Durham University

Durham E-Theses

Geophysical Studies of Oceanic Core Complexes: The Mid-Atlantic Ridge, 13 - 14°N

CHRISTOPHER MALLOWS

How to cite:

MALLOWS, CHRISTOPHER (2011) Geophysical Studies of Oceanic Core Complexes: The Mid-Atlantic Ridge, 13 - 14°N. Doctoral thesis, Durham University.

Use policy

The full-text may be used and/or reproduced, and given to third parties in any format or medium, without prior permission or charge, for personal research or study, educational, or not-for-profit purposes provided that:

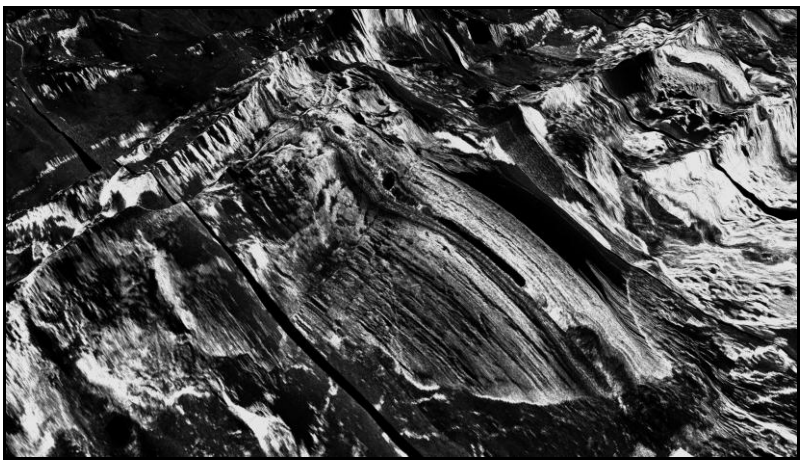
- a full bibliographic reference is made to the original source
- a https://etheses.durham.ac.uk/id/eprint/819/ is made to the metadata record in Durham E-Theses
- the full-text is not changed in any way

The full-text must not be sold in any format or medium without the formal permission of the copyright holders.

Please consult the full Durham E-Theses policy for further details.

Academic Support Office, The Palatine Centre, Durham University, Stockton Road, Durham, DH1 3LE
e-mail: e-theses.admin@durham.ac.uk Tel: +44 0191 334 6107
https://etheses.durham.ac.uk

Geophysical Studies of Oceanic Core Complexes: The Mid-Atlantic Ridge, 13-14°N



Christopher Mallows

A thesis submitted for the degree of Doctor of Philosophy

Durham University, Department of Earth Sciences

October 2010

Geophysical Studies of Oceanic Core Complexes: The Mid-Atlantic Ridge, 13-14°N

Christopher Mallows

Marine geophysical studies have revealed that crustal accretion processes at mid-ocean ridges are largely dependent on the relative contribution of magmatism and tectonism to plate separation. At high levels of magmatic accretion, the ridge is associated with large amounts of surficial volcanism and the formation of closely spaced, continuous abyssal hills that parallel the ridge axis. In contrast, when magmatic accretion is low, tectonic extension prevails and crustal structure is markedly different. In this latter scenario, long-lived detachment faulting forms oceanic core complexes (OCCs) that expose lower crustal rocks and mantle material at the seafloor. Whilst many of the general features of this 'magma-poor' terrain have been identified, there is still widespread debate as to the exact conditions that necessitate and regulate OCC formation.

This study presents the results of a deep-towed and shipboard geophysical survey of the Mid-Atlantic Ridge between 13 – 14°N. This area is an ideal place to test and develop models for OCC structure and formation as the ridge axis exhibits multiple core complexes at various evolutionary stages. The data presented here include: deep-towed TOBI sidescan sonar and tri-axial magnetometer data, shipboard gravity and bathymetric data, and detailed seabed sampling results.

High resolution sidescan sonar data reveal that active core complexes in this region are associated with a neovolcanic hiatus within the axial valley. In contrast, a recently terminated near-axis OCC is associated with widespread neovolcanism, thus confirming that OCC formation is regulated by variations in melt supply to the ridge axis. Forward modelling of gravity data shows that beneath the domal sections of OCC footwalls (from which serpentinised peridotites were ubiquitously sampled), a low density zone (LDZ) exists. This area is interpreted as comprising predominantly gabbroic material that has been captured by each detachment fault at depth beneath the ridge axis (thus explaining the gap in neovolcanism at the surface). Furthermore, magnetic data suggest that OCC footwalls are highly heterogeneous, reflecting significant compositional and thickness variations of the LDZ.

Analyses of sidescan sonar imagery, combined with models of gravity and magnetic anomalies, reveal significant across- and along-axis asymmetry in the region. In general, the quadrants of the survey area within the inside-corners of the non-transform offset at 13°38'N are associated with widespread OCC formation, elevated tectonic strain ($T\varepsilon$ = 25 – 30%), thin crust and faster spreading (20 – 40%) compared with conjugate ridge flanks; these areas are characterised by crust that is typically ~0.5 – 1.0 km thicker than OCC-forming areas, and tectonic strain ($T\varepsilon$ = 10 – 15%) is partitioned across numerous, small faults.

On the basis of these results, a model is presented for the structure of the 13 – 14°N region, and for the life cycle of oceanic core complexes. These models have implications for our current understanding of the magmato-tectonic conditions within which OCCs are expected to operate, and, in a broader sense, for the long wavelength processes that govern crustal accretion at low levels of magmatism.

Declaration

This thesis describes my own original work except where acknowledgment is made in the text. It does not exceed the word limit and is not substantially the same as any work that has been, or is being submitted to any other university for any degree or other qualification.

Christopher Mallows

Durham University
Department of Earth Sciences
October 2010

Copyright © C. Mallows 2010
The copyright of this thesis rests with the author. No quotation from it should be published without the prior written consent of the author and information derived from it should be acknowledged.

Acknowledgements

First and foremost I would like to thank my supervisor, Roger Searle, for his help and encouragement during my time in Durham, and for his prompt and thorough reviews of numerous drafts of this thesis. I extend my gratitude to the following people for contributing to various aspects of this thesis: Tim LeBas provided support with sidescan sonar theory and processing techniques, Bram Murton and Chris MacLeod provided useful discussion regarding all things MOR-related, and Maurice Tivey and Donna Blackman gave useful insights into the magnetic- and gravity-related parts of this thesis, respectively.

This Ph.D. has been funded by the UK's Natural Environment Research Council. Thanks must go to the captain, crew and scientific party of the RRS *James Cook* during research cruise JC07.

I would also like to thank my friends and acknowledge their various contributions to life in Durham: Rich (for keeping the scientific discussion to a minimum whilst at home), Alan, Jude, Jaqs (cake baking and gossip), Izzy and Niamh. I also thank the other members of 'geophysics corner' – Matt, Leanne, Jim, Dean and Sarah – for providing numerous solutions to some of the technical aspects of this thesis.

My family have provided moral (and financial) support and encouragement throughout my time in Durham and I am grateful for this. Finally, I wish to thank Claire for her love and friendship, which has been a continual source of inspiration.

Table of Contents

List of figures xiv
List of tables xix
List of abbreviations and definitions xx

Chapter One: Introduction and geological setting

1.1. Introduction 1
1.2. Mid-ocean ridge structure and morphology 2
1.2.1. Tectonism and the plate boundary zone 2
1.2.2. Volcanism and axial morphology 9
1.2.3. Ridge segmentation and implications for melt supply 12
1.2.4. Composition of oceanic lithosphere 17
1.2.5. The marine magnetic field 19
1.2.6. The marine gravity field 21
1.3. The geological setting of oceanic core complexes 23
1.3.1. Magma-poor regions 25
1.3.2. Surficial morphology of oceanic core complexes 27
1.3.3. Internal structure of oceanic core complexes 29
1.3.4. Melt supply and oceanic core complex formation 31
1.3.5. The Mid-Atlantic Ridge at 13°N 34
1.4. Summary of thesis aims 38
1.5. Thesis outline 39

Chapter Two: Data acquisition and processing

2.1. Introduction 39
2.2. JC07 Survey configuration and instrumentation 39
2.2.1. Deep-towed operations 42
2.2.2. Seabed sampling operations 44
2.3. Bathymetric data acquisition and processing 47
2.4. TOBI sidescan sonar survey configuration 54
2.4.1. The backscatter model 55

2.4.2. Sidescan sonar data acquisition and pre-processing 59
2.4.3. Sidescan sonar imagery processing with PRISM 61
2.4.3.1. Header information 61
2.4.3.2. Sea-surface reflection 63
2.4.3.3. Acoustic drop-out 64
2.4.3.4. Slant-range correction 65
2.4.3.5. Across-track illumination equalisation 66
2.4.3.6. Final PRISM processing configuration 67
2.4.4. Mosaicking of the sidescan sonar imagery 69
2.4.4.1. Re-navigation of sidescan sonar data 70
2.5. Gravity field survey 75
2.5.1. Gravity data acquisition and reduction 75
2.5.1.1. Latitude correction 76
2.5.1.2. Eötvös correction 77
2.5.1.3. Crossover analysis 78
2.5.2. Free-air anomaly 80
2.6. Magnetic field survey 82
2.6.1. Tri-axial magnetometer (TAM) data reduction 83
2.6.1.1. IGRF correction 83
2.6.1.2. Calibration for the effects of vehicle magnetisation 84
2.6.1.3. Assessment of calibration robustness 93
2.6.1.4. Reduction of deep-towed magnetic data to a horizontal plane 97
2.6.2. Magnetic total field anomaly 99
2.7. Summary of data reduction techniques 115

Chapter Three: Seafloor geology from sidescan sonar data

3.1. Introduction 117
3.2. Interpretative methods – seafloor mapping 118
3.2.1. Bathymetry data and seafloor gradient 118
3.2.2. Seafloor sampling results 122
3.2.3. Textural analysis of TOBI sidescan sonar imagery 126
3.2.3.1. Volcanic textures 129
3.2.3.2. Tectonic textures 133

3.2.3.3. Oceanic core complex textures 134
3.2.4. Interpretation of hydrothermal anomalies 136
3.2.5. Map of seafloor geology 138
3.3. Regional morphology & new insights into OCC structure 139
3.3.1. Distribution and morphology of oceanic core complexes 143
3.3.1.1. Newly identified OCCs in the 13°N region 145
3.3.1.2. Newly identified 'Marathon OCC' 147
3.3.1.3. OCC1319: Surficial morphology 150
3.3.1.4. OCC1330: Surficial morphology 155
3.3.1.5. OCC1348: Surficial morphology 159
3.4. Volcanism 163
3.4.1. Short-scale variability in the locus of melt emplacement 163
3.4.2. NVZ width & OCC footwall capture of ascending melt 169
3.5. Tectonism 176
3.5.1. Analysis of fault patterns & morphological asymmetry 176
3.5.2. Tectonic strain (Tε) & inferred component of magmatism (M_{TOTAL}) 180
3.5.3. Role of tectonism and propagating volcanism in OCC termination 182
3.6. Chapter summary 189

Chapter Four: Lithospheric structure from gravity anomalies

4.1. Introduction 191
4.2. Interpretative methods – gravity data 191
4.2.1. Mantle Bouguer anomaly (MBA) 191
4.2.2. MBA method & total crustal attraction 193
4.2.3. MBA results 199
4.2.4. Residual mantle Bouguer anomaly (RMBA) 201
4.2.5. RMBA method 203
4.2.6. RMBA results 206
4.3. Crustal structure & melt supply variability from RMBA 207
4.3.1. Regional structure & asymmetry 207
4.3.2. Crustal thickness 209
4.3.3. Inferred component of magmatic extension (M_{TOTAL}) from RCT 211
4.3.4. Along-axis structure & focused magmatic accretion 214

4.4. Gravity models: Implications for OCC structure 222
4.4.1. RMBA across near-axis OCCs 222
4.4.2. Modelling of gravity anomalies (2.5D) 228
4.4.2.1. OCC1319: Internal density structure (2.5D) 229
4.4.2.2. OCC1330: Internal density structure (2.5D) 232
4.4.2.3. OCC1348: Internal density structure (2.5D) 234
4.4.2.4. Linked detachment surfaces (2.5D) 236
4.4.3. Modelling of gravity anomalies (3D) 239
4.4.3.1. Internal structure of near-axis OCCs (3D) 243
4.4.4. Gravity modelling: Summary 250
4.5. Chapter summary 251

Chapter Five: Spreading history from magnetic anomalies

5.1. Introduction 253
5.2. Interpretative methods – magnetic data 253
5.2.1. Inversion of magnetic anomalies 253
5.2.2. Magnetisation solutions 254
5.3. Anomaly identification & spreading history 265
5.3.1. Spreading rate from anomaly C2n 269
5.3.2. Spreading rate asymmetry & relationship with OCC formation 270
5.3.3. Age of formation of near-axis OCCs 278
5.4. OCC magnetisation & implications for melt emplacement 283
5.4.1. OCC1319: Magnetisation 284
5.4.2. OCC1330: Magnetisation 291
5.4.3. OCC1348: Magnetisation 296
5.5. Chapter summary 298

Chapter Six: Discussion& Conclusions

6.1. Introduction 301
6.2. Crustal accretion in the 13°N region: Regional observations 301
6.2.1. Melt supply 301
6.2.2. OCC distribution & asymmetry 309
6.2.3. Summary & model of regional crustal structure in the 13°N region 313

6.3. The life cycle of oceanic core complexes 316
6.3.1. The role of melt supply in OCC initiation 316
6.3.2. OCC termination 320
6.3.3. Footwall structure 325
6.3.4. Linked detachment surfaces 329
6.3.5. Summary & model for OCC formation 331
6.4. Conclusions 338
6.5. Suggestions for further work 342
6.5.1. Existing data 342
6.5.2. Further data acquisition 343

References 347

Appendix I ..... DVD

Appendix II ..... DVD

List of Figures

Figure 1.2.1: The mid-ocean ridge system 3
Figure 1.2.2a-b: Fault patterns and cross-section of slow-spreading ridges 5
Figure 1.2.3a-d: The life cycle of AVR formation 9
Figure 1.2.4: A hierarchy of segmentation for slow-spreading ridges 13
Figure 1.2.5: A geological model for 'Plum-pudding' crust 17
Figure 1.2.6: The relationship between magnetic susceptibility and serpentinisation 19
Figure 1.3.1: Overview of selected OCC and magma-poor environments 23
Figure 1.3.2: Magma-rich and magma-poor terrain comparison 25
Figure 1.3.3: Morphological and structural characteristics of OCCs 27
Figure 1.3.4: Summary of deep drilling results from OCCs 29
Figure 1.3.5: Seismic structure of TAG 30
Figure 1.3.6: Spectrum of MAR extensional styles as a function of M 31
Figure 1.3.7: Numerical strain modelling of ridge morphology as a function of M 33
Figure 1.3.8: Clay-modelled bathymetry data across the 13°N region 34
Figure 1.3.9: Off-axis seismicity and geochemical enrichment in the 13°N region 36

Figure 2.2.1: Ship's tracks during JC07 40
Figure 2.2.2: Summary of TOBI survey lines and sample locations 41
Figure 2.2.3: TOBI survey configuration 42
Figure 2.3.1a-b: A3 Bathymetry (fold-out map) 49
Figure 2.3.2: A3 Integrated bathymetry (fold-out map) 51
Figure 2.3.3: Comparison of TOBI depth profile with multibeam data 53
Figure 2.4.1: TOBI sidescan sonar beam pattern 55
Figure 2.4.2: Acoustic backscatter patterns from the seabed 57
Figure 2.4.3a-b: Scattering strength as a function of grazing angle and grain size 58
Figure 2.4.4: Sidescan sonar processing flow diagram 60
Figure 2.4.5: Graphical example of TOBI header file information 62
Figure 2.4.6: Sonar processing example – sea-surface reflection 63
Figure 2.4.7: Sonar processing example – acoustic drop-out 64
Figure 2.4.8: Slant-range correction of sonar data 65

Figure 2.4.9: Across-track illumination equalisation coefficients 66
Figure 2.4.10a-b: A3 Sidescan sonar mosaic (fold-out map) 71
Figure 2.4.10c: Sidescan sonar – perspective view of OCC1319 73
Figure 2.4.10d-e: Sidescan sonar – view of OCC1330 and OCC1330 74
Figure 2.5.1: Eötvös correction and associated errors 78
Figure 2.5.2: Crossover analysis in *Fledermaus* 79
Figure 2.5.3a-b: Free-air anomaly (3D) 81
Figure 2.6.1: TOBI tri-axial magnetometer configuration 82
Figure 2.6.2: Disturbance of the magnetic field due to a ship 85
Figure 2.6.3: Average total magnetic field strength for each survey line 87
Figure 2.6.4: Location of magnetometer calibration turn 88
Figure 2.6.5: Observed magnetic field strength during calibration turn 90
Figure 2.6.6: TOBI's induced component of magnetisation as a function of heading .. 91
Figure 2.6.7a-f: Pitch correction for magnetic data 92
Figure 2.6.8a-b: Total field before and after magnetometer calibration in 3D 94
Figure 2.6.9: Example of magnetometer calibration in 2D 95
Figure 2.6.10: Example of magnetometer calibration on each sensor 96
Figure 2.6.11: Fourier transform of TOBI heading data 97
Figure 2.6.12: Comparison of deep-towed and surface-towed magnetic field 99
Figure 2.6.13a-b: Total field anomaly (3D) 100
Figure 2.6.14: Magnetic field in north, east and down directions for each sensor 102

Figure 3.2.1: Slope profiles across each near-axis OCCs 118
Figure 3.2.2: Non-directional seafloor slope (3D) 119
Figure 3.2.3a-b: Seafloor slope in E-W and N-S directions (3D) 120
Figure 3.2.4: Dredging results classified by weight and region 121
Figure 3.2.5: Drill results classified by recovery and region 122
Figure 3.2.6: Location and results of all sampling sites 123
Figure 3.2.7: Across-axis variation in backscatter intensity 126
Figure 3.2.8a-j: Gallery of volcanic sidescan sonar textures and structures 129
Figure 3.2.9: Effect of insonification angle on sidescan sonar texture 130
Figure 3.2.10: Identification of seamounts using slope data 131
Figure 3.2.11a-d: Gallery of tectonic sidescan sonar textures and structures 132
Figure 3.2.12a-f: Gallery of OCC-related sidescan sonar textures and structures 134

Figure 3.2.13: LSS data plotted against vehicle depth 135
Figure 3.2.14: LSS anomaly across OCC1319 136
Figure 3.2.15a-b: A3 Geological interpretation of sidescan sonar (fold-out map) 139
Figure 3.3.1: Interpretation of regional seafloor morphology 141
Figure 3.3.2: Newly identified OCCs in the 13°N region 145
Figure 3.3.3: Relationship between OCCs and ridge-oblique bathymetric lows 146
Figure 3.3.4: Marathon OCC 147
Figure 3.3.5: Model for Marathon OCC formation 148
Figure 3.3.6a-b: OCC1319 – sidescan sonar and bathymetry 150
Figure 3.3.7: Axis-parallel slope profile across dome of OCC1319 151
Figure 3.3.8a-b: Photos of breakaway region and serpentinised peridotite sample 153
Figure 3.3.9: OCC1330 – sidescan sonar and bathymetry 155
Figure 3.3.10: Spreading direction parallel striations bisected by fault on dome 157
Figure 3.3.11: Photo of beehive-shaped mound on dome of OCC1330 158
Figure 3.3.12a-b: OCC1348 – sidescan sonar and bathymetry 159
Figure 3.3.13: NA-SA-AF vector diagram and corrugation azimuths 160
Figure 3.4.1: Volcanic lineaments in southern half of survey area 163
Figure 3.4.2: Sidescan sonar of major and minor volcanic lineaments 164
Figure 3.4.3: Across-axis jump in volcanism adjacent to OCC1319 166
Figure 3.4.4: Volcanic lineaments in northern half of survey area 167
Figure 3.4.5: Variation in width of neovolcanic zone 168
Figure 3.4.6: Calculating seafloor age from backscatter intensity 170
Figure 3.4.7a-d: Model for gaps in volcanism during OCC formation 172
Figure 3.4.8: Sidescan sonar of NVZ adjacent to each near-axis OCC 174
Figure 3.5.1: Equal-age quadrants across the survey area 176
Figure 3.5.2: Frequency of different fault sizes across survey area 178
Figure 3.5.3: Variation in tectonic strain across survey area 180
Figure 3.5.4: Along-axis variation in tectonic strain 181
Figure 3.5.5: Azimuth of volcanic and tectonic lineaments within the axial valley 182
Figure 3.5.6: Model for termination of OCCs 184
Figure 3.5.7: Formation of hooked-ridges 185

Figure 4.2.1: Effect of no. terms in Taylor power series for Bouguer correction 194
Figure 4.2.2a-b: Crustal models for MBA calculation 195

Figure 4.2.3a-d: Predicted and combined attraction of crustal interfaces for MBA.... 197
Figure 4.2.4a-b: Mantle Bouguer anomaly.... 200
Figure 4.2.5: RTR configuration for thermal correction of gravity data.... 202
Figure 4.2.6: Horizontal slices through thermal model.... 204
Figure 4.2.7a-b: Thermo-gravitational model 205
Figure 4.2.8: Residual mantle Bouguer anomaly.... 206
Figure 4.3.1: RMS value for RMBA profiles against latitude 208
Figure 4.3.2: Residual crustal thickness variation 210
Figure 4.3.3: Inferred component of magmatic accretion from crustal thickness.... 213
Figure 4.3.4: Along-axis morphology, RMBA and crustal thickness.... 215
Figure 4.3.5: Along-axis 2.5D gravity model of long wavelength density structure... 216
Figure 4.3.6: Short wavelength RMBA lows and surficial volcanism 217
Figure 4.3.7: Short wavelength component of along-axis RMBA.... 219
Figure 4.3.8a-b: Along-axis model of short wavelength density structure in mantle.. 219
Figure 4.3.9a-b: Along-axis model of short wavelength density structure in crust.... 220
Figure 4.4.1: RMBA profiles across near-axis OCCs.... 223
Figure 4.4.2a-b: RMBA profiles across Kane Massif and FUJI Dome.... 224
Figure 4.4.3a-b: Reduction of gravity data across near-axis OCCs (3D).... 226
Figure 4.4.4a-d: 2.5D gravity modelling of OCC1319.... 230
Figure 4.4.5a-b: Possible models for the low density zone within OCC footwalls.... 232
Figure 4.4.6a-d: 2.5D gravity modelling of OCC1330.... 233
Figure 4.4.7a-d: 2.5D gravity modelling of OCC1348.... 235
Figure 4.4.8a-d: 2.5D gravity modelling of linked detachments.... 238
Figure 4.4.9: Method for 3D modelling of gravity anomalies 239
Figure 4.4.10: Example of basic form of 3D gravity models.... 240
Figure 4.4.11: Observed data used during 3D gravity modelling.... 242
Figure 4.4.12: Predicted and residual anomalies for model G3D_1 244
Figure 4.4.13: Predicted and residual anomalies for model G3D_2 246
Figure 4.4.14: Predicted and residual anomalies for model G3D_3 248
Figure 4.4.15: Predicted and residual anomalies for model G3D_4 249

Figure 5.2.1: 2D magnetisation solution and magnetic annihilator for each profile.... 256
Figure 5.2.2: 3D magnetisation solution with 2D solutions overlain 263
Figure 5.3.1: Magnetisation and anomaly identification after Smith *et al.* (2008)..... 266

Figure 5.3.2: Magnetic anomaly identification in the 13°N region 267
Figure 5.3.3a-d: The MAR axis from sonar, bathymetry, magnetic & gravity data ... 272
Figure 5.3.4: Spreading rate asymmetry plotted against latitude 274
Figure 5.3.5a-b: Model of spreading rate asymmetry across OCC1319 276
Figure 5.3.6: Regional interpretation of spreading rate asymmetry 277
Figure 5.3.7: Duration of near-axis OCCs as function of M_{HW} 279
Figure 5.3.8a-d: Age of formation of OCC1348 280
Figure 5.3.9a-c: History of near-axis OCC formation in 13°N region 281
Figure 5.4.1: Magnetisation pattern across OCC1319 285
Figure 5.4.2: Magnetic model of OCC1319 footwall structure 287
Figure 5.4.3a-c: Model for magnetic evolution of OCC1319 288
Figure 5.4.4: Magnetic model of Brunhes thickness south of OCC1319 290
Figure 5.4.5: Magnetisation pattern across OCC1330 292
Figure 5.4.6: Magnetic model of OCC1330 footwall structure 294
Figure 5.4.7: Magnetisation pattern across OCC1348 296

Figure 6.2.1: Ridge geometry between Fifteen-Twenty and Marathon FZs 303
Figure 6.2.2: Seafloor morphology near the Strakhov FZ 306
Figure 6.2.3: Seafloor morphology south of Kane FZ 311
Figure 6.2.4: Summary of crustal accretion processes along FT-MA segment 315
Figure 6.3.1: History of magmatic accretion during formation of OCC1319 319
Figure 6.3.2: Seafloor morphology near Dante's Domes OCC 330
Figure 6.3.3a: Summary of OCC life cycle (initiation) 332
Figure 6.3.3b: Summary of OCC life cycle (mature – version 1) 334
Figure 6.3.3c: Summary of OCC life cycle (mature – version 2) 336
Figure 6.3.3d: Summary of OCC life cycle (terminated) 337
Figure 6.5.1: Further work – tri-axial magnetometer data 343
Figure 6.5.2: Further work – active OCCs near TAG? 345

List of tables

Table 1.2.1: The hierarchy of ridge discontinuities 12
Table 1.2.2: Magnetisation of crustal lithologies 20
Table 1.2.3: Density of crustal lithologies 21

Table 2.2.1: TOBI survey line start and end points 43
Table 2.2.2: Summary of drill sites with locality description 45
Table 2.2.3: Summary of dredge sites with locality description 46
Table 2.5.1: Published COEs for various cruises 78
Table 2.6.1: Fourier components of heading correction for magnetic data 89
Table 2.6.2: Upward continuation levels for 2D magnetic profiles 98

Table 3.2.1: Sidescan sonar textures and structures 127
Table 3.3.1: OCC distribution in the 13°N region 143
Table 3.5.1: Fault statistics for each quadrant of JC07 survey area 177

Table 4.2.1: Gravity modelling parameters 196
Table 4.4.1: RMBA characteristics across selected OCCs 225
Table 4.4.2: Summary of 3D gravity models 241

Table 5.3.1: Spreading rate calculated from anomaly 2 270
Table 5.3.2: Spreading rate asymmetry 273

Table 6.2.1: Summary of inside-/outside-corner characteristics 312
Table 6.2.2: Summary of magma-rich/magma-poor characteristics 314

List of abbreviations & definitions

AAD ..... Australia-Antarctic Discordance
AF ..... African plate
AFZ..... Active fault zone
AVR..... Axial volcanic ridge
AMAR ..... Alvin Mid-Atlantic Ridge
CAMH..... Central anomaly magnetic high
COE..... Crossover error
D1-D4..... 1st – 4th order ridge discontinuity
FAA ..... Free-air anomaly
FAMOUS ..... French-American Mid-Oceanic Undersea Survey
FFT ..... Fast Fourier Transform
FZ..... Fracture zone
GMT ..... Generic Mapping Tools
IC ..... Inside corner (of ridge-transform intersection)
IGRF..... International Geomagnetic Reference Field
IODP..... Integrated Ocean Drilling Program
JD..... Julian date
LDZ ..... Low density zone
LSS..... Light scattering sensor
M..... Magmatic component of plate separation (0-100%)
Ma..... Millions of years before present (age)
MBA ..... Mantle Bouguer anomaly
MAR..... Mid-Atlantic Ridge
MARK..... Mid-Atlantic Ridge at Kane Fracture Zone
MOR..... Mid-ocean ridge
My..... Millions of years (duration)
NA..... North American plate
NTO..... Non-transform offset
NVZ ..... Neovolcanic zone
OC..... Outside corner (of ridge-transform intersection)
OCC..... Oceanic core complex
ODP ..... Ocean Drilling Program
PBZ..... Plate boundary zone
RCT ..... Residual crustal thickness
RTI..... Ridge-transform intersection
RTR ..... Ridge-transform-ridge
RMBA ..... Residual mantle Bouguer anomaly
RMS..... Root mean square
SA..... South American plate
S1-S4..... 1st – 4th order ridge segment
SWIR..... Southwest Indian Ridge
T..... Tectonic component of plate separation (0-100%)
TAG..... Trans-Atlantic geo-traverse
TAM ..... Tri-axial magnetometer
TOBI..... Towed Ocean Bottom Instrument

Chapter One

Introduction and geological setting

1.1. Introduction

The segment of the slow-spreading Mid-Atlantic Ridge (MAR) located between the Marathon (12°40'N) and Fifteen-Twenty (15°20'N) fracture zones displays two contrasting styles of seafloor morphology. In one instance, the seafloor exhibits an axially symmetric pattern of linear ridges that are continuous along-axis for several tens of kilometres and parallel the axial valley, the formation of which is consistent with a relatively well-understood, magmatically robust mode of plate separation. Adjacent to these 'normal' areas of seafloor are regions that display large expanses of flat terrain, punctuated with isolated, topographically corrugated massifs, intermittent linear ridges and exposures of lower crustal and ultramafic material. This contrast in seafloor morphology is not unique, and is now known to occur over a significant proportion of the slow- and intermediate-spreading rate mid-ocean ridge (MOR) system. Although it is widely accepted that anomalous regions form as a result of increased tectonic strain, prompted by a reduction in melt supply at the ridge axis, the precise mechanisms and magmato-tectonic conditions under which the transition from 'normal' to 'chaotic' seafloor occurs is still largely unknown. Thus it is the purpose of this thesis to further our understanding of the mechanisms that govern crustal accretion along magma-poor sections of the MOR system.

This chapter gives an overview of the background information deemed pertinent to the remainder of this thesis. This information has been divided into two main sections, the first comprising details on the volcanic and tectonic elements commonly associated with slow-spreading sections of the MOR, with the second comprising geological and geophysical information that specifically relates to magma-poor environments and oceanic core complex (OCC) formation. A thesis outline and a summary of the aims of this thesis are given at the end of this chapter.

1.2. Mid-ocean ridge structure and morphology

Volcanic and tectonic processes are the primary mechanisms for shaping the structural and geophysical characteristics of the MOR system (Figure 1.2.1). The style and relative contribution of these processes changes dramatically along the ridge and at a variety of different scales. On a global scale, variations in magma supply divide the ridge such that it can be classified, from increasing to decreasing levels of magmatic robustness, as either: fast-spreading (> 80 km/My full-spreading rate), intermediate-spreading (50 – 80 km/My), slow-spreading (20 – 50 km/My) or ultraslow-spreading (< 20 km/My). Shorter-scale variability in melt supply and tectonism then divide the ridge further, with a morphological expression ranging from fracture zone-bounded spreading segments that are several hundred kilometres long, to single, isolated volcanic peaks no wider than a few tens of metres in diameter. Thickness and composition of newly accreted crustal material are also controlled by the nature of localised volcanic and tectonic processes at the ridge axis (although it should also be noted that locally there can be significant variations that are independent of spreading rate).

1.2.1. Tectonism and the plate boundary zone

At all spreading rates, the MOR is associated with a crest that is 2 – 3 km higher than the surrounding ocean floor (concave upwards) and is paralleled by a plate boundary zone (PBZ) that is defined by the area within which faulting of the lithosphere is seismically and tectonically active (Luyendyk & Macdonald, 1976). The PBZ exists along the entire MOR, although its size and morphology varies greatly with spreading rate. Slow-spreading sections of the MOR system, such as the MAR, have the typical gross morphology of a fault-bounded valley flanking the plate margin (Figure 1.2.2a). This axial valley, which may be several tens of kilometres wide and 1 – 3 km deep, acts as the locus for newly accreted magmatic material and is typically bounded by rugged, lineated abyssal hill terrain (e.g. Needham & Francheteau, 1974; Ballard & Van Andel, 1977; Crane & Ballard, 1981). Mantle temperature variations may further modify slow-spreading ridge morphology such that heating effects produce an axial volcanic crest more typical of a fast-spreading environment (e.g. the Iceland hot-spot on the MAR - Laughton *et al.*, 1979).

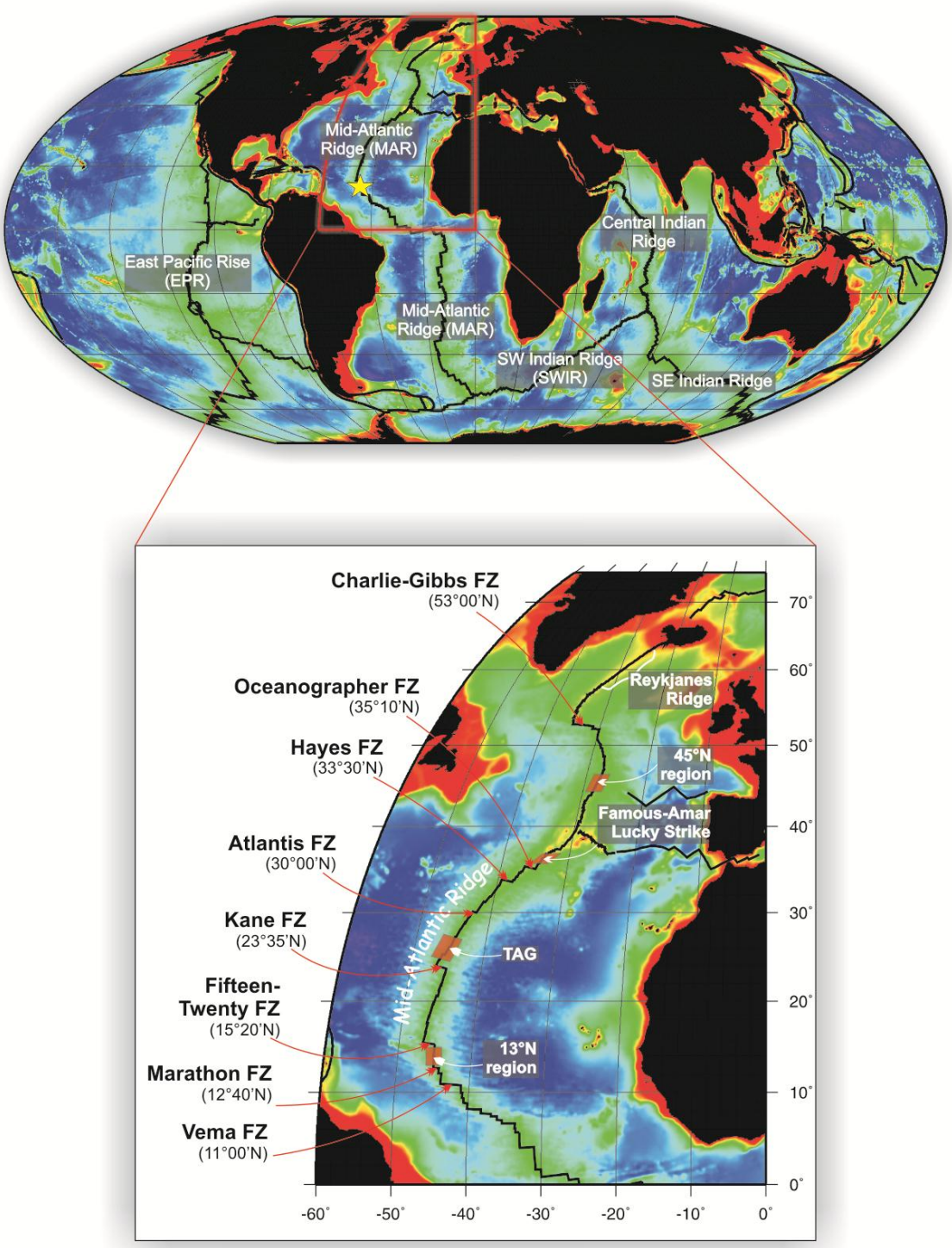


Figure 1.2.1. The mid-ocean ridge system (upper image). Ridge-crest is indicated by solid black line. Bathymetry data (red to green tones) show a decrease in depth of ~2 km towards the ridge from the adjacent oceanic deeps. Location of this study (JC07) is marked by yellow star. The Mid-Atlantic Ridge is the archetypal slow-spreading ridge and runs approximately N-S between 0° and 50°W (MAR detail - lower image, showing positions of major fracture zones and survey areas referred to throughout this study). ETOPO bathymetry data after Amante & Eakins, 2009.

Similarly, cool mantle can produce an axial valley in an otherwise fast-spreading ridge environment.

Width of the PBZ is often difficult to establish as this requires extensive off-axis data collection. Deep-towed imagery of active faulting at the slow-spreading FAMOUS[1] section of the MAR (36°50'N) suggests that the edge of the PBZ lies at a distance of at least 30 km from the centre of the axial valley (e.g. Macdonald *et al.*, 1975; Luyendyk & Macdonald, 1977). Smith *et al.* (2003) resolve a seismically active zone between 15°00'N and 35°00'N that extends for ~±20 km either side of the MAR axis and within which 88% of the total seismicity occurs. Active faulting at intermediate-spreading rates has been observed at distances of up to 12 km from the ridge axis (CYAMEX, 1981). In all instances, the edge of the PBZ is considered to occur at the point where cumulative heave (as a function of across-axis distance) becomes constant (Macdonald & Atwater, 1978).

Close to the ridge axis, a significant amount of tectonism is observed within a narrow zone (the *active fault zone* – AFZ) that begins a few kilometres from the region of zero-age material (or *crustal accretion zone*) and extends away from the axis for several kilometres (Luyendyk & Macdonald, 1976). At slow-spreading ridges, the AFZ takes a form between two end-members; it may display tightly packed faults with vertical offsets of up to a few hundred metres bounding a relatively broad axial valley (e.g. the AMAR[2] segment, 36°25'N MAR), or alternatively, where the axial valley is narrow (e.g. FAMOUS), faults may be spaced by a few kilometres, forming large blocks or terraces (Figure 1.2.2a; Macdonald, 1982). At segment ends, faulting is observed to have larger throws and wider spacing compared with segment centres (Shaw, 1992; Sempere *et al.*, 1993). Thus, each segment may consist of two morphologically distinct yet inter-connected sections (Figure 1.2.2b; Mutter & Karson, 1992).

[1] French-American Mid-Oceanic Undersea Survey
[2] Alvin Mid-Atlantic Ridge
[3] Trans-Atlantic Geo-traverse, in the vicinity of 26°10'N.

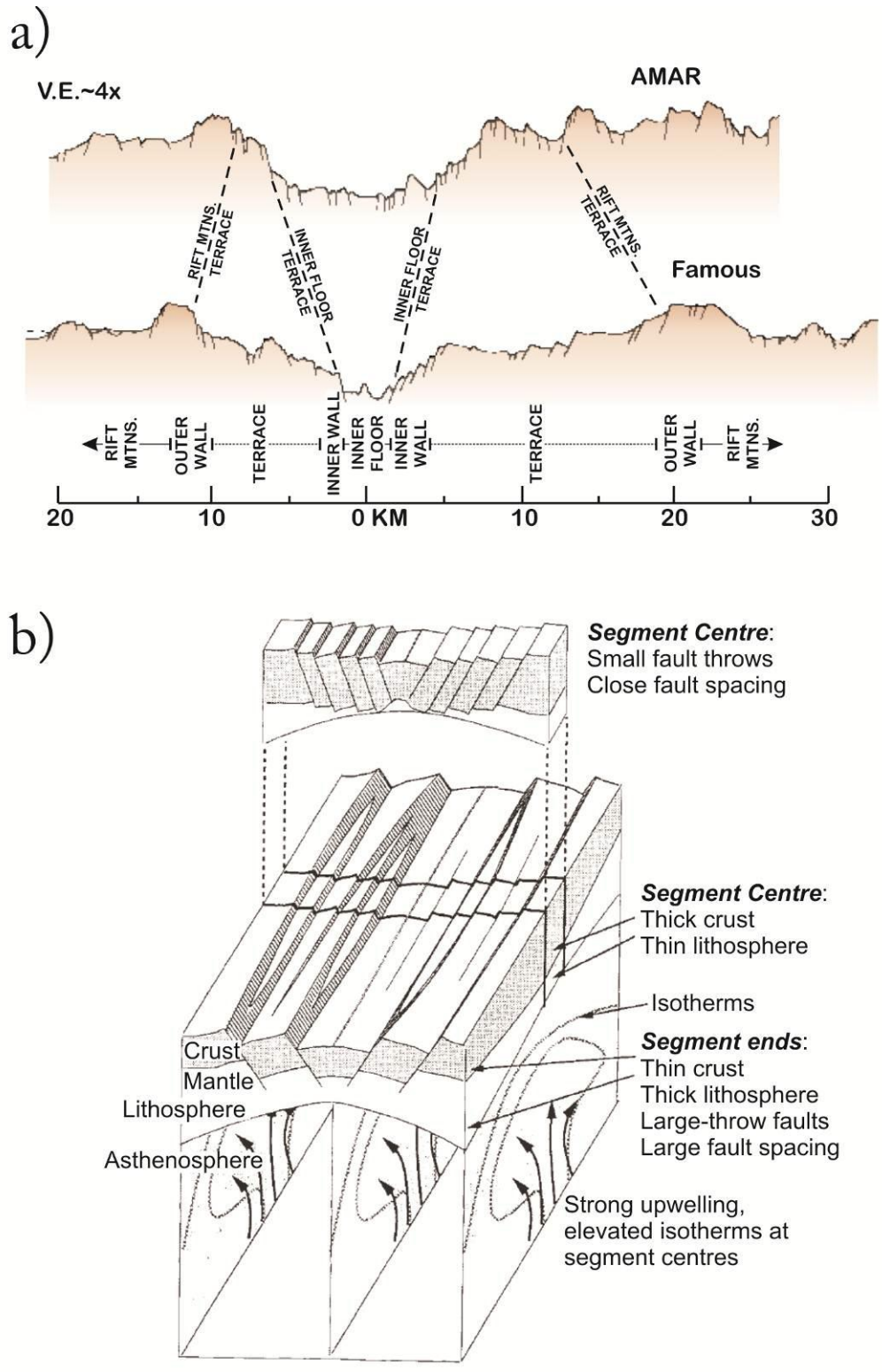


Figure 1.2.2a-b. Segment centres may display contrasting fault styles in a slow-spreading MOR environment. **a)** The AMAR section (upper cross-section) is characterised by tightly packed faults bounding a wide axial valley, whereas the FAMOUS section (lower cross-section) shows more widely-spaced faults on the flanks of a narrow axial valley (from Macdonald, 1982). **b)** There is an overall increase in fault throw and spacing towards segment ends where the lithosphere is expected to be thicker (from Shaw, 1992).

In all cases it is believed that strain initially localises onto a fault close to the ridge axis, which is subsequently rafted away by magmatic accretion and accommodates strain until it becomes mechanically easier to initiate a new fault rather than maintain extension on the original (Behn & Ito, 2008). Along-axis fault growth may occur by propagation of the fault tip and linkage with adjacent features (Cowie, 1998; Searle *et al.*, 1998). Two models can potentially explain the subsequent formation of the axial valley, namely: hydraulic head loss and steady-state necking. The basis for the hydraulic head loss model is that buoyant material supplied to the ridge experiences significant viscous forces around the conduit through which it is being delivered, and hence the axial valley develops a depression (e.g. Sleep, 1969; Sleep & Rosendahl, 1979). Uplift of the bounding fault zone relative to the axial valley floor thus represents a conservation of energy (Macdonald, 1982). Applying this same model to a fast-spreading ridge, where melt delivery conduits are larger and bounded by hotter lithosphere, head loss is much less and subsequently a valley does not develop. Alternatively, steady-state necking may produce an axial valley at slow-spreading rates. In this situation, lithospheric strength is sufficiently high that the ductile layer beneath the ridge can thin ('necking') at a rate determined by the relative levels of tectonic extension and magmatic accretion (e.g. Tapponnier & Francheteau, 1978; Chen & Morgan, 1990; Lin & Parmentier, 1990; Buck *et al.*, 2005). Fast-spreading ridges, characterised by young, hot material, lack the necessary lithospheric strength for necking to be significant.

At slow spreading rates the dominant fault dip direction is towards the ridge axis (Searle & Laughton, 1977; Searle, 1984; Carbotte & Macdonald, 1990; Escartin *et al.*, 1999), with seismic imaging showing that these faults penetrate through the brittle lithosphere and may become less steep with depth (e.g. White *et al.*, 1990; Singh *et al.*, 2006). Faults may be linear for more than 20 km along-axis (e.g. Macdonald *et al.*, 1975), although the measureable length is largely dependent on data resolution (with higher resolution data showing that large faults may only be persistent for up to a few kilometres - Macdonald 1986). Faults dip at approximately 45° – 60° towards the ridge axis and are often back-tilted by 3° – 20° (e.g. Atwater & Mudie, 1973; Macdonald *et al.*, 1975; Kong *et al.*, 1989). Back-tilting is a necessary component of tectonic deformation as it provides a mechanism by which the regional topography can be flattened (essentially, without back-tilting the axial valley would become increasingly deep with successive episodes of normal faulting – Searle, 1992). Where there is little

outward-facing faulting, a block rotation of ~5° would be sufficient to account for the cumulative throw of inward-facing faulting at slow-spreading ridges (Searle, 1992). Minor amounts of antithetic faulting are observed, with their occurrence becoming more predominant beyond the rift outer-wall (Macdonald & Atwater, 1978). As spreading rate increases the percentage of outward facing faults also increases, until at the fastest ridges, the ratio of inward to outward dipping faults within the AFZ is approximately 1:1 (Carbotte & Macdonald, 1994).

Earthquake focal depths of 5 – 10 km are well documented along the MAR (e.g. Toomey *et al.*, 1985; Kong *et al.*, 1992; Wolfe *et al.*, 1995; Tilmann *et al.*, 2004). On the MAR at 22°42'N, Toomey *et al.* (1988) identify normal faulting on planes dipping at an angle of about 45° towards the ridge axis, reaching depths of ~4 – 8 km. Wolfe *et al.* (1995) use microearthquake seismicity to show that tectonism is most extensive in the 29°00'N region in a diffuse, off-axis zone across the inside-corner of a ~15 km ridge offset, which is in agreement with the seismicity pattern recorded at the Lucky Strike segment (37°20'N MAR - Dusunur *et al.*, 2009). Dusunur *et al.* (2009) and Tilmann *et al.* (2004) are able to resolve seismic events beneath the ridge axis at depths of > 10 km and ~8 km, respectively. The presence of faulting at depths well within the upper mantle supports the hypothesis that hydration of mantle material (i.e. serpentinisation) should be prevalent along fault surfaces at slow-spreading rates (e.g. Francis, 1981). This pervasive seawater influx and hydrothermal cooling along fault surfaces may also offer an explanation as to why the depth to the top of the crustal low velocity zone is greater at slow-spreading ridges than at fast-spreading ridges (~4 km relative to ~1 km - Purdy *et al.*, 1992); essentially: deep faults allow seawater to penetrate deep into the crust and upper mantle.

It is now widely accepted that in areas where melt supply to the ridge axis is diminished, tectonic processes accommodate a significant amount of plate separation (e.g. Karson, 1990; Lin *et al.*, 1990; Tucholke *et al.*, 1998; Escartin & Cannat, 1999; Reston *et al.*, 2002; Searle *et al.*, 2003; Okino *et al.*, 2004; Buck *et al.*, 2005; Smith *et al.*, 2006; Tucholke *et al.*, 2008; MacLeod *et al.*, 2009). The subsequent formation of oceanic core complexes and the morphological characteristics of magma-poor ridge environments are discussed in more detail in *Section 1.3*.

1.2.2. Volcanism and axial morphology

Within the plate boundary zone is a narrow area of recent volcanic activity, commonly referred to as the neovolcanic zone (NVZ), which, by definition, for all spreading rates comprises 95% of the surficial component of material erupted within the Holocene epoch (Macdonald, 1982). The NVZ, observed about the ridge axis, is characterised by fresh, untectonised extrusive lava flows and sparse sediment cover. The NVZ differs from the crustal accretion zone in that the latter comprises 95% of the intrusive component which accumulates over the same period (Luyendyk & Macdonald, 1976).

The surficial expression of magmatism at slow-spreading ridges is predominantly volcanoes aligned in *en echelon* elongate ridges (or axial volcanic ridges - AVRs; e.g. Luyendyk & Macdonald, 1977; Shih *et al.*, 1978; Laughton *et al.*, 1979; Crane & Ballard, 1981; Smith & Cann, 1990; Parson *et al.*, 1993; Sempere *et al.*, 1995; Smith *et al.*, 1995; Lawson *et al.*, 1996; Gracia *et al.*, 1999; Briais *et al.*, 2000; Cann & Smith, 2005; Peirce *et al.*, 2005; Searle *et al.*, 2010). AVRs exhibit a diverse morphology that is often variable within an individual ridge segment (Head *et al.*, 1996). Individual ridges may be continuous along-axis for ~30 – 40 km, be 1 – 4 km wide, have reliefs of 100 – 750 metres and exhibit basal width to height ratios of 4:1 (e.g. Karson *et al.*, 1987; Smith & Cann, 1993; Allerton *et al.*, 1995; Lawson *et al.*, 1996; Gracia *et al.*, 1999; Searle *et al.*, 2010). Near the Atlantis Fracture Zone (FZ), Sempere *et al.* (1995) note that major volcanic ridges (18 – 39 km long with heights of 100 – 500 metres) are located at segment centres and are associated with crustal thickening, whereas smaller ridges (9 – 14 km length) are located across minor ridge-discontinuities and correspond to areas of thinner crust.

AVR construction is associated with a combination of dike intrusion and a small degree of faulting (Macdonald *et al.*, 1975), with the primary mechanism for along-axis growth being the coalescence of numerous volcanic cones (Karson *et al.*, 1987; Smith & Cann, 1990; Head *et al.*, 1996). On the basis of sidescan sonar data collected across 42 volcanic lineaments on the Reykjanes Ridge, Parson *et al.* (1993) propose a life cycle in which AVRs grow rapidly during a magmatic phase and then gradually become disseminated during a tectonic phase (Figure 1.2.3a-d). Within this life cycle, 'young' AVRs (Figure 1.2.3a) are thin ridges that display alignments of fissure-type volcanoes; 'adolescent' AVRs (Figure 1.2.3b) comprise broader ridges with conical seamounts; 'mature' AVRs (Figure 1.2.3c) are periclinal in shape and exhibit flat-topped seamounts

and AVR-parallel fracture swarms; and 'old' AVRs (Figure 1.2.3d) are broad ridges that are covered by a thin blanket of sediment and display intense AVR- and axis-parallel faulting (Parson *et al.*, 1993). Gardiner (2003) expands on this by noting that the four stages of the AVR life cycle are merely 'snapshots' of a continuum whereby AVRs may exhibit characteristics typical of more than one stage.

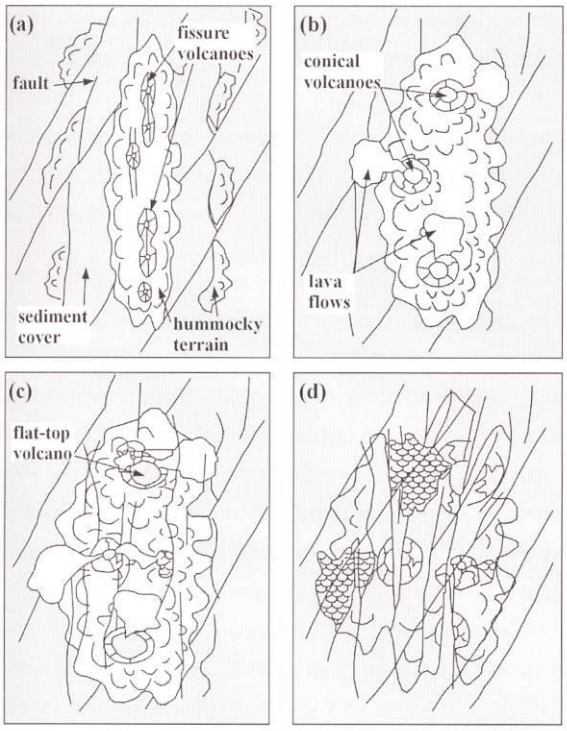


Figure 1.2.3a-d. The life cycle of AVR formation, showing: **a)** 'young', **b)** 'adolescent', **c)** 'mature' and **d)** 'old' stages. See text for discussion. From Gardiner (2003), after Parson *et al.* (1993).

Head *et al.* (1996) deduce from typical MAR spreading rates that slow-spreading axial structures can be accounted for by approximately one vertical dike intrusion every 40 years. In addition to this, Hall (1976) has suggested – based on the occurrence of magnetic reversals within vertical sections through basalt – that growth of neovolcanic structures may occur within short periods (~< 100 years) separated by long intervals (~1000 – 10000 years) of absent or quiescent volcanism. These may effectively be the magmatic and tectonic phases referred to by Parson *et al.* (1993).

Isolated seamounts have been observed with diameters up to a few kilometres (and, although rare, may be elongate along-axis), with most having a diameter in the range of a few hundred metres (e.g. Luyendyk & Macdonald, 1977; Smith & Cann, 1990; Smith *et al.*, 1995; Briais *et al.*, 2000; Rabain *et al.*, 2001). Seamounts with a

relief greater than 50 metres have a density of ~80 per 1000 km^2 of the MAR between 24°00'N and 30°00'N (Smith & Cann, 1990). The formation of larger seamounts on the MAR south of the Oceanographer FZ (35°10'N) has been attributed to higher magma volumes during formation (Rabain *et al.*, 2001).

Briais *et al.* (2000) estimate from TOBI sidescan sonar data collected across the MAR between 27°N and 30°N that the ratio of hummocky to otherwise topographically-smooth terrain (which may be built up from non-hummock-forming pillow and sheet flow basalts) is approximately 9:1. These findings are suggestive of a point-source origin for magmatic accretion at slow-spreading ridge environments, which is in contrast with the continuous, along-axis volcanic morphology of fast-spreading ridges that is suggestive of fissure-fed eruptions (Smith & Cann, 1992). This theory is supported by seismic data collected along the MAR near 35°00'N, which shows no evidence for a continuous, along-axis low velocity zone (which is commonly interpreted as melt accumulation). Instead, a discontinuous low velocity anomaly is identified and interpreted as a discrete partial melt zone feeding a single seamount (Barclay *et al.*, 1998).

For a slow-spreading ridge, the width of the NVZ generally varies between 1 and 10 kilometres, depending on definition and measurement method. From magnetic polarity transition widths, for example, it is estimated that the zone of melt emplacement at the ridge axis may be up to 10 km wide, and hence it may be expected that recent volcanism covers an area this wide (Macdonald *et al.*, 1975; Sempere & Macdonald, 1987). However, submersible and deep-towed camera surveys find that the area of active volcanism characterised by thin sediment cover and fresh, glassy pillow basalt is only a fraction of this, and is rarely wider than 1 – 3 km along the MAR (e.g. Ballard & Van Andel, 1977; Smith *et al.*, 1999). Macdonald (1982) reconciles these differences by suggesting that while the surface expression of neovolcanism may only be 1 – 3 km wide, at slow-spreading rates the crustal accretion zone may periodically widen and wander across-axis. Ancillary evidence for this theory in the form of direct measurement of reversely magnetised crust within the axial valley is further suggestive of temporal 'jumps' in the locus of magmatic accretion (e.g. Ade-Hall *et al.*, 1973). It is therefore likely that in the presence of a narrow axial valley, the NVZ will be similarly constrained and record well-defined magnetic anomalies. This is in contrast with a wide axial valley that allows the NVZ to wander spatially and temporally, smearing-out the magnetic reversal pattern in the process (Macdonald, 1982). Long periods of magmatic

quiescence between eruptions may, due to cooling and subsequent thickening of the brittle lithosphere, provide a means by which the preferential weak zone of melt emplacement is erased and a new zone is initiated.

Axio-centric magmatic activity can account for the majority of neovolcanic structures observed along the MOR. However, off-axis volcanism is not wholly uncommon and is present at all spreading rates. Smith *et al.* (1999) observe that whilst primary neovolcanic activity (i.e. hummocky ridges fed by underlying dikes) is confined to an ≤ 2 km wide zone along the MAR between 29°20'N and 30°00'N, this zone is bounded by a region of secondary volcanism which is interpreted as being fed by lava tubes and channels that siphon lava from the primary accretion zone. This is supported by Lawson *et al.* (1996) and Briais *et al.* (2000) who each suggest that seamount emplacement occurs independently of AVR construction. Furthermore, recent uranium series dating results from the very-slow-spreading (14 – 16 km/My) Southwest Indian Ridge (SWIR) show that neovolcanic activity occurs at distances of up to ~10 km from the ridge axis, and that melt emplacement may be assisted by major axial valley bounding fault scarps (Standish & Sims, 2010). This mode of emplacement is supported by deep-towed sidescan sonar data collected across the Cayman Trough (Mid-Cayman Spreading Centre), where some of the youngest lava flows are observed on the ridge flanks, at the top of prominent axial valley wall faults (R. Searle; cruise JC44, *personal comm.*).

1.2.3. Ridge segmentation and implications for melt supply

The MOR is segmented due to variations in the magmatic and tectonic processes by which it forms. These divisions are commonly referred to as 1st-, 2nd-, 3rd- and 4th-order discontinuities (herein D1 – D4, defining segments S1 – S4), the progression of which is associated with a decreasing magnitude ridge-offset (Table 1.2.1; Macdonald *et al.*, 1988). The relationship between discontinuities forms a continuum whereby lower-order discontinuities may grow to become higher-order discontinuities, and *vice versa*. As such, it should be noted that segmentation characteristics do not always fall within these definitions, and hence it is sometimes more appropriate to use morphologically descriptive terms (Gente *et al.*, 1995).

	Discontinuity (D)			
	1st-order	***2nd-order***	***3rd-order***	***4th-order***
Along-axis separation (S)	400±200 km	50±30 km	15±10 km	7±5 km
Ridge offset – distance	> 30 km	2-30 km	0.5-2 km	< 1 km
- age	> $2x10^6$ yrs	< $2x10^6$ yrs	~0	~0
Typical morphology	Transform fault	Non-transform offset (NTO), oblique shear zone, axial valley jog, overlapping spreading centres	Inter-volcano gaps, AVR discontinuity	Intra-volcano gaps
Depth anomaly	500-2000 m	300-1000 m	50-300 m	<100 m
Off-axis trace	Fracture zone	Bathymetric low	Faint or none	None
High amplitude magnetisation?	Yes	Yes	?	?
Geochemical anomaly?	Yes	Yes	Usually	~50%

Table 1.2.1. The hierarchy of ridge discontinuities after Macdonald (2001). Data are for slow-spreading ridges only. "?" denotes that the nature of high amplitude magnetisation anomalies at D3- and D4-type discontinuities is unknown or ambiguous. Offset age is the age of material juxtaposed against the ridge axis. Off-axis trace of D2 is summarised after Tucholke *et al.* (1997).

The largest offsets (D1) are evident as transform faults that displace the ridge axis at right-angles for distances of > 30 km (Figure 1.2.4). Rigid deformation is recorded in fracture zones that focus horizontal shear strain into narrow zones of strike-slip tectonism (e.g. Macdonald *et al.*, 1988; Grindlay *et al.*, 1991). This type of offset occurs at a frequency of approximately once every 400 km (S1) for the slow-spreading part of the MOR. Segmentation of this magnitude may be controlled by long-lived, long wavelength variations in melt supply to the ridge (the evidence for which is that the ridge axis is generally shallower at segment centres compared with the deeper, transform fault-bounded segment ends), be inherited from continental break-up (e.g. the Vema FZ) or form in response to mantle source compositional variations (Niu *et al.*, 2001). Variation in melt supply may occur as a result of either: 1) less intense mantle upwelling at segment ends, or; 2) melt at segment ends being emplaced predominantly via horizontal transportation from the more magmatically robust segment centre. Conversely, it has been shown that ridge segmentation may itself provide a mechanism for channelling melt to discrete points at the surface (as opposed to the latter controlling the former) so there may be a positive feedback between the two (Magde & Sparks, 1997).

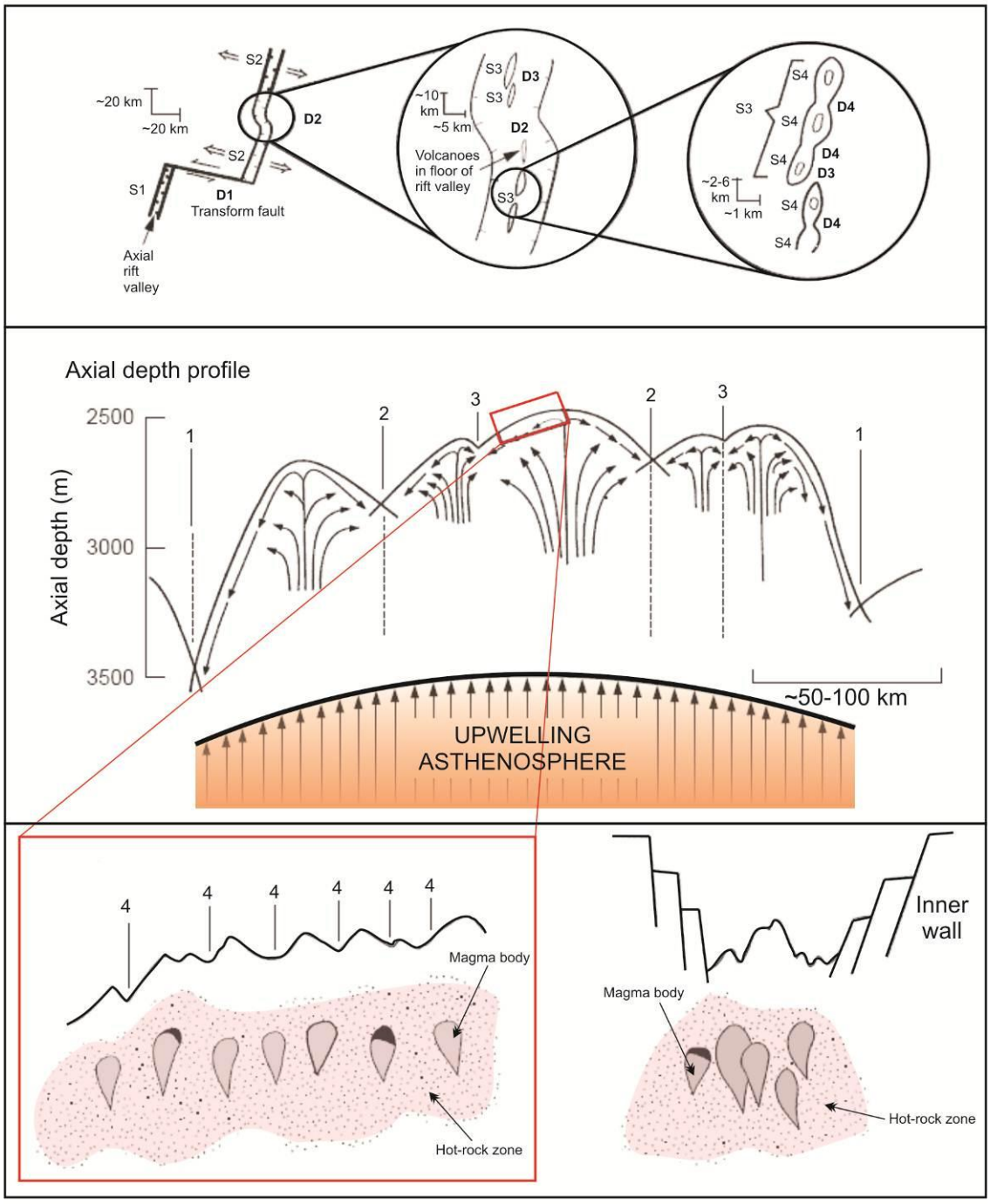


Figure 1.2.4. A possible hierarchy of segmentation for slow-spreading ridges, after Macdonald (2001). In the upper panel, D1-D4 represent 1st-4th order discontinuities defining segments S1-S4, respectively. First-order discontinuities are transform faults, second-order discontinuities are non-transform offsets or oblique shear zones and third- and fourth-order offsets are AVR discontinuities and intra-volcano offsets (middle panel). From 1st-4th the controls on segmentation (e.g. melt supply) become more spatially and temporally unstable. At the lowest order, seamounts and AVRs are fed by discrete magma chambers at shallow depths in the crust (lower panels).

D2 is often referred to as a non-transform offset (NTO), or axial valley 'jog', and may result from short wavelength variability in melt supply or from pre-existing zones of mechanical weakness in the lithosphere (Figure 1.2.4; e.g. Grindlay & Fox, 1993). Segmentation can also occur in response to slight changes in the pole of relative motion of tectonic plates (e.g. Grindlay *et al.*, 1991; Pariso *et al.*, 1995). Second-order discontinuities offset the ridge for distances of 2 – 30 km and occur at along-axis intervals of ~50 km (S2). The off-axis trace of S2 can be differentiated from that of S1 in that it displays non-rigid (i.e. rheologically weak plate boundary conditions in which stresses are distributed across a wide area of oblique, normal and strike-slip faulting), as opposed to rigid (i.e. rheologically strong conditions with stresses focused into a relatively narrow zone), characteristics. Grindlay *et al.* (1991) identify three distinct D2 morphologies, namely: 1) *en echelon* jogs in the plate boundary where adjacent, along-axis AVRs overlap slightly; 2) *en echelon* jogs in the plate boundary where adjacent ridges are separated by an extensional basin that has its long-axis aligned parallel with the strike of adjacent AVRs, and; 3) an oblique offset between AVRs in the form of a basin that is aligned at 45° relative to the strike of the ridge axis.

The off-axis trace associated with S2-type segmentation reveals much about the relatively short wavelength spatial and temporal stability of upwelling asthenosphere. For example, Tucholke *et al.* (1997) have conducted a detailed analysis of the nature and relationship between numerous 2nd-order ridge discontinuities between 25°30'N and 27°00'N on the MAR (TAG[3] area). In this area, each NTO contains an extensional basin within which the adjacent AVR terminates or merges with the old side-margin of the basin. The influence of each NTO can be observed off-axis in crust that is > 20 Ma, forming ridge-perpendicular or sub-perpendicular bathymetric lows that bisect ridge-parallel abyssal hills immediately to the north and south. Individual off-axis traces apparently terminate, initialise and wander (at rates of up to ~2 km/My), suggesting that melt supply from the asthenosphere can migrate along the ridge axis and also wax and wane with a period of ~2 – 3 My. To the south (20°00'N – 24°00'N), a remarkably similar pattern in the off-axis trace of D2-type discontinuities is observed, with individual segments propagating at rates of up to ~25 km/My. The observed variation in segment propagation rate between the two areas is thought to occur due to differences in the ratio of melt flux per unit length (Gente *et al.*, 1995).

[3] Trans-Atlantic Geo-traverse, in the vicinity of 26°10'N.

In addition to tracing the off-axis bathymetric expression associated with type D2 discontinuities, gravity data and residual crustal thickness (RCT) estimates yield similar insights into the nature of regional melt supply variability. Segment centres are typically found to have a lower mantle Bouguer anomaly (and hence thicker crust) when compared with segment ends, forming distinctive 'bull's-eye' anomalies (e.g. Fox & Gallo, 1984; Kuo & Forsyth, 1989; Lin *et al.*, 1990; Tolstoy *et al.*, 1993; Planert *et al.*, 2009). Whitehead *et al.* (1984) suggest that gravitational instabilities within partially molten mantle accumulating at the base of a depleted mantle zone ultimately form undulations, or 'disturbances', in the depleted/non-depleted mantle boundary, which channel melt towards discrete locations via porous flow. Melt then rises diapirically to the surface, where it may form the basis for focused magmatic accretion and generate gravitational bull's-eye anomalies.

Based on gravity data collected about the Atlantis FZ, Pariso *et al.* (1995) use RCT estimates to show that south of the fracture zone segments have undergone focused melt upwelling for periods of up to 10 My (i.e. crust at segment ends is thin compared with that at segment centres for up to 10 My). In contrast, north of the fracture zone this relationship is only maintained within crust that is < 3 Ma, suggesting that focused melting has either recently initiated, or that at ages > 3 Ma focusing occurs over an area of < 25 km^2 (i.e. at a scale less than the data resolution - Pariso *et al.*, 1995). Long wavelength, across-axis variability in RCT was further attributed to using a passive flow model to correct gravity data for lithospheric cooling effects, whereas in the presence of focused melt upwelling it may be expected that significant along-axis changes in mantle density occur. Short wavelength features can be accounted for by magmatic pulses that have a periodicity of ~2 – 3 My (Pariso *et al.*, 1995).

At the short wavelength spectrum of ridge discontinuities, D3 and D4 are typically associated with along-axis variability in neovolcanic zone morphology, and as such are related to short ridge-offsets of 0.5 – 2 km and < 1 km, respectively (Figure 1.2.4). Segment S3 has an average along-axis length of ~15 km, with S4 occurring at intervals of ~7 km. This short wavelength neovolcanic segmentation is most likely the result of shallow heterogeneities in the structure of the upper crust, with Macdonald (2001) surmising that the S3 and S4 end of the segmentation hierarchy represents 'increasingly short-lived, mobile offsets'. Smith & Cann (1993) propose that D3- and D4-type discontinuities are controlled by shallow-scale supply and storage of melt within the crust, and that magma chambers are transient features that rise through the

lithosphere and become trapped by a rheological boundary at a depth of 2 – 5 km. Individual, spheroidal magma chambers (as have been identified using seismics by Barclay *et al.*, 1998) are linked with each other and the seafloor via a series of interconnecting pipes, the surficial expression of which is a single, volcanically constructed cone. In this model, along- and across-axis variations in AVR structure, NVZ morphology and the distribution of isolated seamounts (i.e. D3 – D4) primarily reflects local changes in melt supply and/or the magmatic 'plumbing' system.

1.2.4. Composition of oceanic lithosphere

Seismic refraction surveys have been used to demonstrate that oceanic crust can be subdivided into various lithological units, the boundaries between which may be gradual in nature (e.g. Raitt, 1956; Fowler, 1976, 1978; Kennett & Orcutt, 1976; Kennett, 1977; Spudich & Orcutt, 1980). Of these stratigraphic divisions, the uppermost (Layer 1) is absent at the ridge axis and otherwise consists of sediment that gradually thickens away from the spreading centre (i.e. with increasing age). The topographic boundary between Layer 1 and 2 is highly uneven due to the volcanic processes that construct the latter, which comprises the basaltic section of the oceanic lithosphere. Layer 2 is typically between 1.0 – 2.5 km thick and has a seismic velocity V_p = 5.1±0.63 km/s (Raitt, 1963). This may be subdivided so as to include: Layer 2A, which is ~0.0 – 1.5 km thick and has a seismic velocity of V_p = 3.5 km/s, and Layer 2B, which is ~1.0 – 2.0 km thick and has a seismic velocity of V_p = 5.0 km/s. Layer 2A is made up from basalt that forms lava flows, which interact with seawater at the ridge axis and are hence porous and rubbly in nature. These flows are fed by a sheeted dike complex that forms Layer 2B. The nature of the basalt/dyke (Layer 2A/2B) boundary is uncertain as the seismic reflector commonly interpreted as this transition may instead represent an alteration front within the lava unit (Christeson *et al.*, 2007). Layer 2 grades into Layer 3 which is ~4.0 – 6.0 km thick and has a seismic velocity of V_p = 6.7-7.2 km/s, and is thus interpreted as comprising gabbro that forms upon crystallization of an axial magma chamber. This gabbroic layer may contain significant amounts of serpentinite protrusions from the uppermost, underlying mantle, which comprises partially serpentinised peridotites (Cannat, 1996; Karson, 1998).

At slow-spreading ridges, the total thickness of the oceanic crustal section generally varies between 6 – 8 km (e.g. Purdy & Detrick, 1986; Purdy, 1987; White *et al.*, 1992; Tolstoy *et al.*, 1993; Planert *et al.*, 2009). Changes in thickness may occur as a result of local variations in the tectonic and magmatic conditions by which the crust accretes. For example, increased melting associated with hot-spots may thicken the crustal section to ~10 km (White *et al.*, 1992). Alternatively, cooling effects, such as the juxtaposition of old, cold lithosphere against the ridge axis at fracture zones, may decrease the observed thickness of oceanic crust to as little as 2 km (e.g. Cormier *et al.*, 1984; Purdy & Detrick, 1986; White *et al.*, 1990; Davies *et al.*, 2005). At the 138 – 155 Ma Blake Spur FZ, White *et al.* (1990) show that whilst the original crustal thickness was only ~3 – 4 km, it has since been underlain by ~3 km of relatively low density mantle material that formed during intense circulation of seawater and subsequent serpentinisation.

Cannat *et al.* (1995) and Cannat (1996) propose a model for the composition of oceanic lithosphere at segment ends, where the crustal sequence is thin relative to the total thickness of the lithosphere (Figure 1.2.5). In this model, part of the lower crust contains serpentinised ultramafic material. It is assumed that discrete gabbroic bodies are likely to crystallize within the asthenospheric mantle and that with increasing lithospheric thickness, the amount of melt reaching the surface will decrease (often referred to as the 'plum-pudding' model – Cannat, 1996).

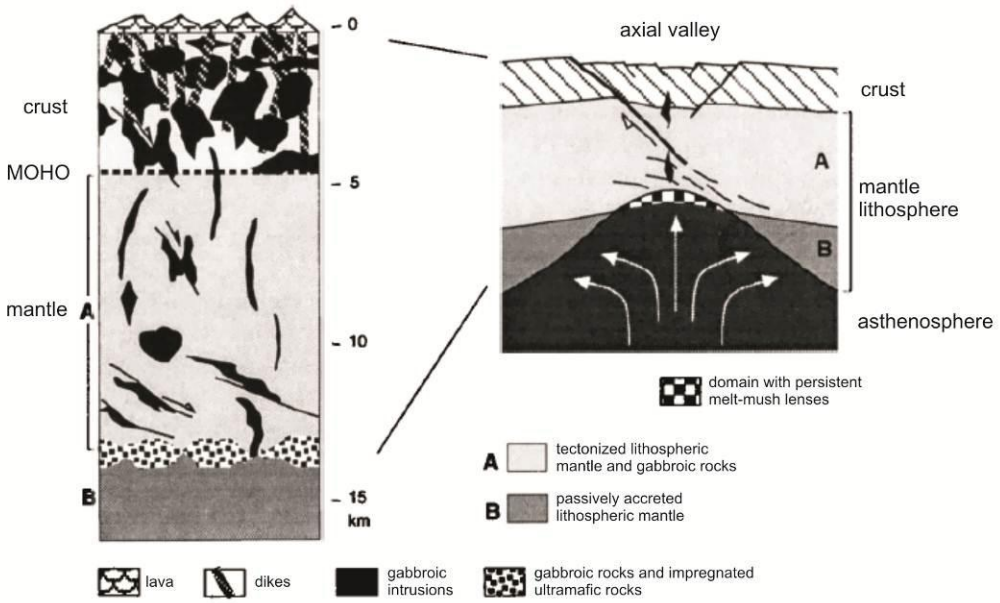


Figure 1.2.5. A geological model for melt circulation and tectonic spreading when the crust is thin relative to the axial lithosphere (right). In this scenario, melt is expected to crystallize within the mantle (left). From Cannat (1996). See text for discussion.

Thus, crustal thicknesses that are determined by seismic and gravity modelling do not directly relate to the amount of melt supplied to the ridge axis, and are instead an underestimate due to some degree of melt becoming trapped in the mantle. Furthermore, crustal thicknesses determined in this way will include some degree of serpentinised ultramafic material. Cannat (1996) further suggests that melt production as determined from major and rare earth element compositions and its apparent relationship with crustal thickness estimates (e.g. White *et al.*, 1992) can be explained if the volume of melt within the asthenosphere is approximately equal to the volume of serpentinised ultramafic material within the lower crust.

1.2.5. The marine magnetic field

The Earth's magnetic field arises due to a dynamo effect caused by circulating electrical current within its molten, metallic core. The field is not fixed, and may reverse in polarity (essentially the magnetic north and south poles switch places). Hot material emplaced at the MOR, upon cooling through its respective Curie temperature, will acquire the same magnetic polarity as that of the ambient geomagnetic field. As tectonic plates separate, newly accreted crust records the temporal variation in the polarity of the ambient field, thus giving rise to a positive- and negatively-striped pattern of magnetic anomalies paralleling the spreading centre (Vine & Matthews, 1963; Morley & Larochelle, 1964). Accurate dating of geomagnetic reversals from terrestrial samples then allows for the spreading rate of the ridge to be calculated (e.g. Cande & Kent, 1992, 1995). In this study, it is the most recent geomagnetic events that are of importance, including the Brunhes (C1n; 0 – 0.78 Ma)[4], Matuyama (C1r; 0.78 – 2.59 Ma) and Gauss (C2An.1-3n; 2.58 – 3.58 Ma) chrons. Within the Matuyama chron, the Jaramillo (C1r.1n; 0.99 – 1.07 Ma) and Olduvai (C2n – 'anomaly 2'; 1.77 – 1.95 Ma) subchrons are also of importance.

By predicting the contribution of the Earth's geomagnetic field (defined by the International Geomagnetic Reference Field – IGRF) to the measured magnetic field, it is possible to isolate the magnetic anomaly pattern associated with local variations in crustal morphology, lithology and magma supply. Further variations in the intensity of the local magnetic anomaly pattern may occur due to temporal fluctuations in the

[4] All geomagnetic polarity reversal ages referred to herein are from Cande & Kent (1995).

strength of the ambient field, with the present day geomagnetic field strength being higher than the longer-term average intensity (Gee *et al.*, 1996; Juarez *et al.*, 1998; Juarez & Tauxe, 2000). This gives rise to a central anomaly magnetic high (CAMH) within the youngest, neovolcanic portion of ridge-centred Brunhes-age material. In addition to this, temporal decay of the magnetisation of rocks formed at the ridge axis occurs due to alteration by seawater. Estimates for the time taken for the magnetisation of basalt to decay to 1/e of its initial 'zero-age' amplitude range from ~0.1 My at the East Pacific Rise (EPR; Johnson & Tivey, 1995) to ~0.6 My at the MAR (Macdonald, 1977).

Magnetic anomaly patterns may be further modified by a variety of localised magmatic and tectonic processes. This may include, for example, degradation of source due to increased tectonism/faulting (e.g. Hussenoeder *et al.*, 1996), wandering of the neovolcanic zone due to weak melt supply (e.g. Macdonald, 1982) and serpentinisation of source material. The latter can greatly influence the magnetic properties of ultramafic material (e.g. Bina & Henry, 1990; Toft *et al.*, 1990; Nazarova, 1994; Oufi *et al.*, 2002; Rao & Krishna, 2002; Beard *et al.*, 2009), and as such its relative extent may have a major affect on the magnetic anomaly patterns associated with magma-poor, oceanic detachment terrains (Figure 1.2.6).

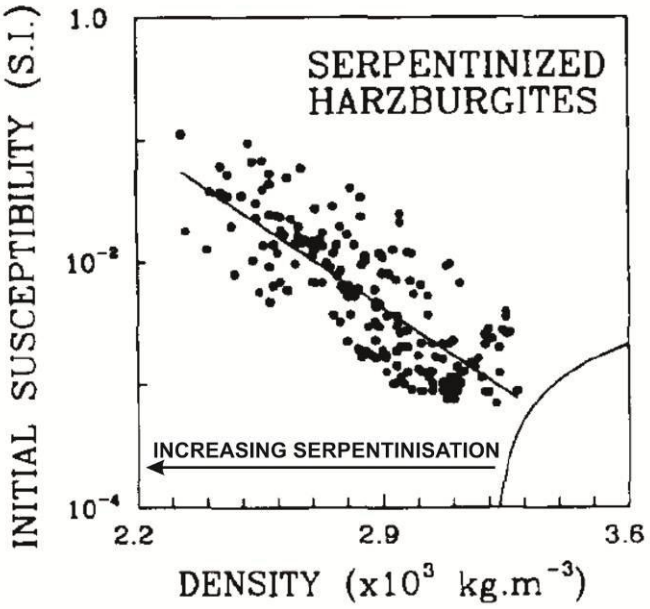


Figure 1.2.6. Magnetic susceptibility is highly dependent on density, which may vary as a function of serpentinisation (discussed in *Section 1.2.6*). Data are from the Josephine Ophiolite, with image from Toft *et al.*, 1990.

Oufi *et al.* (2002) show that the magnetic susceptibility of peridotite increases dramatically at levels of serpentinisation > 75%, concluding that the contribution of serpentinised peridotite to magnetic anomalies may be significant (~4 – 10 A/m) within a depth range of up to 1.5 – 2 km (Table 1.2.2). In contrast to this, Bina & Henry (1990) show that extensively serpentinised samples from MAR at 23°10'N often have magnetisations of between ~1.5 – 5.0 A/m.

Lithology (age)	Magnetisation (A/m)	Magnetisation decay rate to 1/e	Source	Reference	Ridge environment
Basalt (zero-age)	16.6-41.8	0.1 Ma	LAB	(Johnson & Tivey, 1995)	EPR – various
Basalt (central anomaly)	4-30	0.6 Ma	MAG	(Macdonald, 1977)	MAR – FAMOUS area
Basalt (various ages)	1.4-39.5	-	LAB	(Carlut & Kent, 2002)	Juan de Fuca – including 1993 'new flow'
Basalt (various ages)	2-37	No clear axio-centric decay rate	LAB	(Honsho *et al.*, 2009)	MAR – 21°40'N
Basalt (central anomaly)	5-21	No clear axio-centric decay rate	MAG	(Honsho *et al.*, 2009)	MAR – 21°40'N
Gabbro	average of 5.8	-	LAB	(Rao & Krishna, 2002)	SWIR – Atlantis Bank
Olivine gabbro	0.3-1.7	-	"	"	"
Oxide gabbro	0.7-1.3	-	"	"	"
Serp. peridotite	1.5-5 when 'extensively serpentinised'	-	LAB	(Bina & Henry, 1990)	MAR – 23°10'N
Serp. peridotite	4-10 at serp. >75%	-	LAB	(Oufi *et al.*, 2002)	Various

Table 1.2.2. Oceanic crustal lithologies and estimates of magnetisation. Sources include laboratory measurements (LAB; direct) and also those inferred from deep-towed magnetic surveys (MAG; indirect). Surveys across magma-poor areas or from oceanic core complexes are highlighted in green.

1.2.6. The marine gravity field

Gravitational anomalies arise due to subsurface density heterogeneities, and hence gravity data provide a useful means by which to assess the volcanic and tectonic processes at the MOR. It is necessary to predict the regional gravitational field arising from the Earth's shape and spin so that this can be removed from observed data, isolating the anomaly arising from local changes in topography and mass distribution (i.e. the free-air anomaly – FAA). At long wavelengths, the FAA is approximately zero

over the MOR system, indicating that ridges are in a state of isostatic equilibrium. It has been shown that compensation may occur in the uppermost mantle by a Pratt-type mechanism, taking the form of a low-density body (that may be analogous to hotter material) with edges that dip away from the strike of the ridge axis (e.g. Talwani *et al.*, 1965). Short wavelength components of the FAA may then result from localised variations in volcanic and tectonic processes.

Estimating the density of common, oceanic lithosphere-forming subsurface materials (a summary of which is shown in Table 1.2.3) then allows for their relative extent to be calculated by inversion and forward modelling of the observed anomaly. As with magnetic susceptibility the density of ultramafic material – and thus their associated gravity anomalies – is highly influenced by serpentinisation (e.g. Christenson, 1972; Escartin *et al.*, 1997a; 2001).

Lithology	Density (kg/m^3)	Source	Reference
Seawater	~1030	Various	(Telford *et al.*, 1990)
Sediments	~2500	"	"
Basalt	2700-3300	"	"
Gabbro	2700-3500	"	"
Peridotite	2780-3370	"	"
Serpentinite	2400-3100	"	"
Atlantis Massif OCC basaltic hanging-wall	~2600	3D gravity forward modelling	(Blackman *et al.*, 2008)
Atlantis Massif OCC domal section	~2900	"	"
Atlantis Massif OCC domal section (<380 m)	2800-2850	Laboratory – core sample	(Blackman *et al.*, 2006)
	<2800	Borehole logs (lower due to presence of large-scale cracks?)	"
Atlantis Massif OCC domal section (380 m to 1300 m)	~2900 to ~3000	Laboratory – core sample	"
Serp. peridotite (0% altered)	3300	Laboratory – core sample	(Escartin *et al.*, 2001)
Serp. peridotite (75% altered)	~2700-2800	"	"
Serp. peridotite (100% altered)	2500	"	"

Table 1.2.3. Density estimates for common oceanic lithosphere forming rock types. Samples from OCCs are highlighted in green. Note that gabbro and serpentinised peridotite may have very similar density ranges when the latter is serpentinised by 20-75%.

1.3. The geological setting of oceanic core complexes

Plate separation along the MOR is achieved through a combination of magmatic and tectonic processes. In the early 1980s, it was recognised that increased tectonism and the subsequent formation of long-lived (~1 – 2 My) detachment faults plays a major role in the evolution of oceanic lithosphere at slow-spreading ridges (e.g. Dick *et al.*, 1981; Karson & Dick, 1983). Lower crustal and upper mantle lithologies are commonly exposed at the seafloor by detachment faulting within the inside-corner area of first- and second-order ridge discontinuities (e.g. Tucholke & Lin, 1994; Cann *et al.*, 1997). This zone of detachment faulting is often referred to as an oceanic core complex (OCC) due to similarities with terrestrial metamorphic core complexes (Karson, 1998; Tucholke *et al.*, 1998; Karson, 1999; Cheadle & Grimes, 2010). Weak magmatism and the associated lithospheric stretching and thinning has previously been suggested as the primary mechanism for plate separation along detachment faults (Karson, 1990). This magmatic 'starvation' may occur as a result of the juxtaposition of relatively old, cold lithosphere against the spreading axis at a ridge-transform intersection (RTI), which acts as a heat sink that impedes the formation and delivery of melt from within the mantle (Fox & Gallo, 1984). This model explains the apparent prevalence of OCCs towards the magma-poor ends of spreading segments, as opposed to segment centres (Lin *et al.*, 1990; Tucholke *et al.*, 1998). However, OCCs are not necessarily confined to the inside-corner areas of RTIs, and are now known to exist on outside-corners (e.g. Escartin & Cannat, 1999) and also at some distance from the nearest transform offset (e.g. Okino *et al.*, 2004; Smith *et al.*, 2006; Escartin *et al.*, 2008b), suggesting that melt delivery to the ridge may be highly variable at the segment scale.

Geographically, OCCs are most commonly observed along slow-spreading ridges (e.g. Cann *et al.*, 1997; Tucholke *et al.*, 1998; Ranero & Reston, 1999; Tucholke *et al.*, 2001; MacLeod *et al.*, 2002; Reston *et al.*, 2002; Fujiwara *et al.*, 2003; Searle *et al.*, 2003; Smith *et al.*, 2006), with Escartin *et al.* (2008b) estimating that magma-poor processes account for ~50% of the plate separation along the MAR between the Marathon (12°40'N) and Oceanographer (35°10'N) fracture zones (Figure 1.3.1). Similarly, on the SWIR Cannat *et al.* (2009) calculate that ~40% of the seafloor between 61°E and 66°E is built from magma-poor processes, of which ~4% forms major detachment faults.

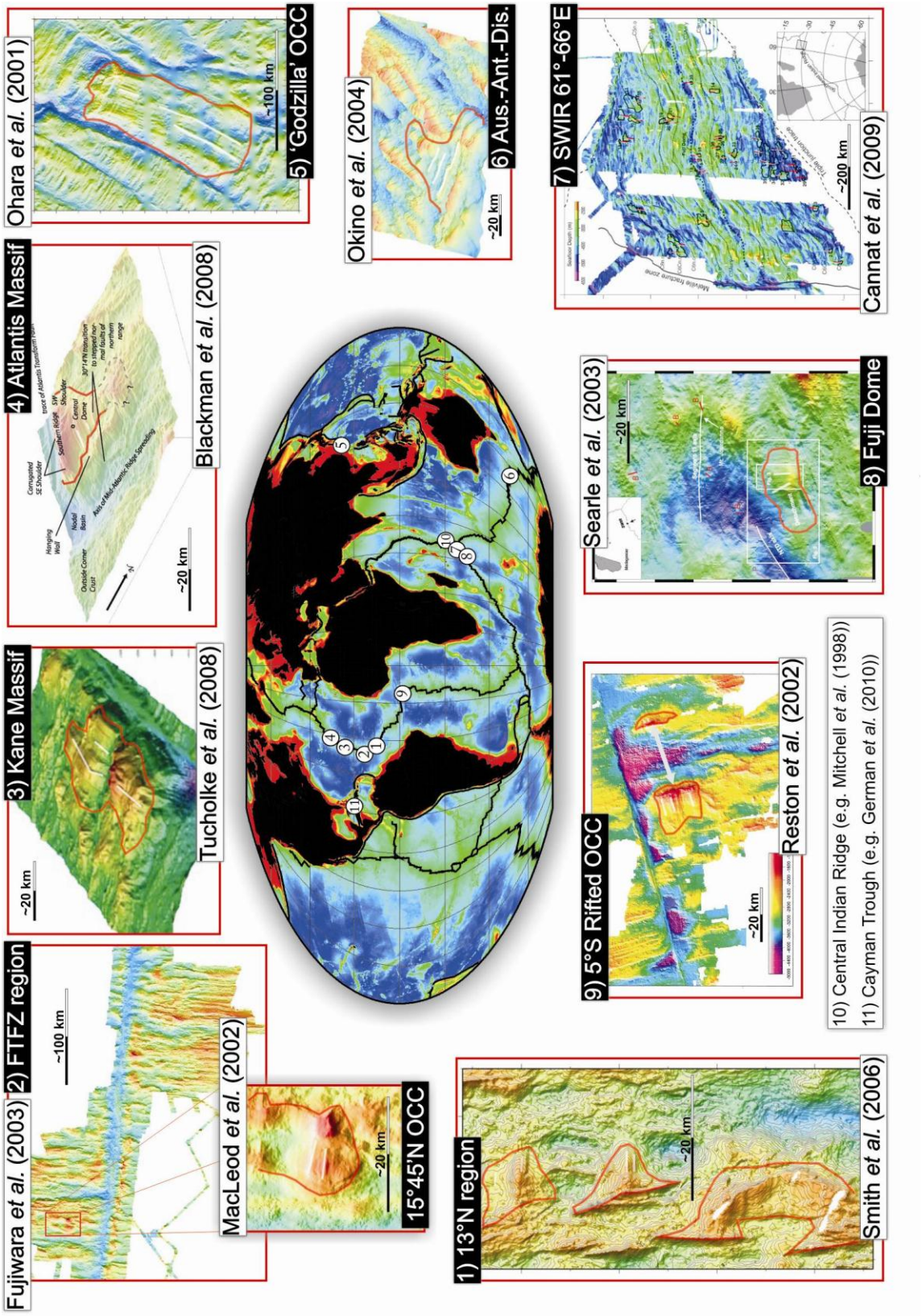


Figure 1.3.1. Selected OCC and magma-poor MOR environments. Diagrams have been annotated to highlight areas of interest: red lines define oceanic core complexes, with white lines showing major topographic corrugations. This is not a comprehensive list but highlights the global distribution of well known OCCs.

OCC formation is not confined to the slow-spreading MAR, with other notable locations including: the Australia-Antarctic Discordance (AAD) between 115°E and 130°E on the Southeast Indian Ridge (Christie *et al.*, 1998; Okino *et al.*, 2004), the slow-spreading Cayman Trough basin (German *et al.*, 2010), the Parece Vela back-arc basin setting (i.e. the Godzilla Megamullion - Ohara *et al.*, 2001), the FUJI Dome on the SWIR (Searle *et al.*, 2003) and the Central Indian Ridge at 25°15'S (Mitchell *et al.*, 1998b) and 3°S – 10°S (Drolia & DeMets, 2005). At present, no OCCs have been identified at the fastest-spreading ridges (although an area of corrugated seafloor has been identified on the intermediate-spreading Chile Ridge - Martinez *et al.*, 1998), which may be explained by the relatively high levels of melt supply at faster spreading rates. It seems unusual, then, that there have also been no core complexes identified on the ultraslow-spreading Gakkel Ridge, where widespread emplacement of the mantle occurs continuously along the ridge axis (Dick *et al.*, 2003). This may be an example of too little magmatism for OCC formation, thus supporting a 'Goldilocks' hypothesis for the magmatic conditions that initiate long-lived detachment faulting (i.e. magmatism can be too weak or too strong for OCC formation; e.g. Tucholke *et al.*, 2008). The relationship between melt supply and OCC formation is discussed in greater detail in *Section 1.3.4*.

1.3.1. Magma-poor regions

The topographic expression of a magma-poor region is generally described as being irregular, blocky and 'chaotic' (e.g. Christie *et al.*, 1998; Fujiwara *et al.*, 2003; Okino *et al.*, 2004; Smith *et al.*, 2006). Cannat *et al.* (2006) refine this description by dividing magma-poor ridge sections into two morphologically distinct regions: corrugated, OCC-forming seafloor (i.e. the blocky component) and 'smooth' seafloor (the combination of which give rise to the irregular and chaotic components). In most cases, the easiest way to identify a magma-poor region is by its pronounced morphological juxtaposition against magma-rich, or 'normal', linear, abyssal hill-type seafloor (Escartin *et al.*, 2008b). This is clearly demonstrated on the MAR at 14°30'N (Figure 1.3.2). Here, Fujiwara *et al.* (2003) note that magma-poor terrain exhibits shorter, more widely spaced fault scarps relative to the magma-rich, segment centre terrains, and that magma-poor regions may display considerable across-axis topographic asymmetry.

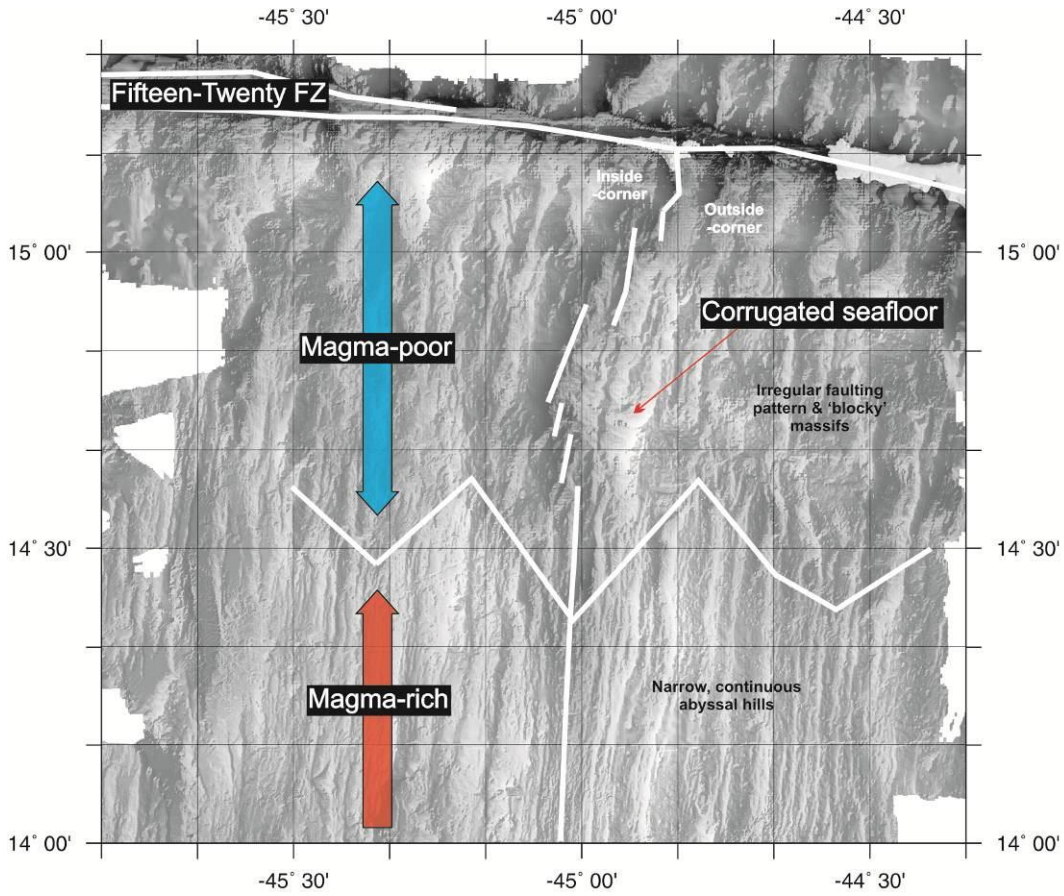


Figure 1.3.2. Contrasting morphological styles of magma-rich (lineated, abyssal hill topography) and magma-poor (irregular and chaotic) environments. Bathymetry data, ridge axis location and morphological boundaries after Fujiwara *et al.*, 2003 and Smith *et al.*, 2008.

Ultramafic exposures, a ubiquitous element of magma-poor environments, are found to outcrop on both sides of the ridge axis (Garces & Gee, 2007), and are not preferentially emplaced on the inside-corner of the RTI, as is predicted by early models for amagmatic plate separation (e.g. Tucholke & Lin, 1994).

In magma-poor regions, magnetic anomalies often have an irregular form like their topographic counterparts. In most cases, magnetic reversal anomalies are asymmetric about the ridge axis, with a tendency to show increased spreading rate over flanks that display OCCs (e.g. Fujiwara *et al.*, 2003; Searle *et al.*, 2003; Tivey *et al.*, 2003; Okino *et al.*, 2004; Smith *et al.*, 2008). Central anomaly magnetic highs are often poorly expressed with, in some instances, apparently zero-age, negative polarity material existing within the axial valley (Fujiwara *et al.*, 2003; Smith *et al.*, 2008). Crustal thinning caused by elevated regional tectonism may degrade the magnetic signal in the presence of long-lived detachment faulting (e.g. Hussenoeder *et al.*, 1996; Tivey *et al.*, 2003), although lower crustal gabbros and mantle peridotites may still acquire a

magnetisation (either thermo-remanant during uplift and cooling or chemical-remanant during serpentinisation of ultramafics) and contribute to the magnetic source layer, producing Vine-Matthews-Morley type lineations as is observed across the FUJI Dome (Searle *et al.*, 2003) and Kane Massif (Williams *et al.*, 2006).

Gravity data may show significant across-axis asymmetries in mass distribution, with inside-corner areas typically exhibiting a mass excess that is indicative of thinned crust (e.g. Tucholke & Lin, 1994; Cannat *et al.*, 1995; Blackman *et al.*, 2008). On a regional scale, crustal thickness can be used as a proxy for melt supply, with thin crust the result of magma-poor accretion. Escartin & Cannat (1999) and Fujiwara *et al.* (2003) estimate that the inside-corners of the Fifteen-Twenty FZ are thinner than the magmatically robust segment centres by ~3 km and ~2.5 km, respectively. OCCs are often associated with a localised, gravity anomaly high that implies the presence of high density material at shallow depth (e.g. Escartin & Cannat, 1999; Fujiwara *et al.*, 2003; Searle *et al.*, 2003; Okino *et al.*, 2004; Blackman *et al.*, 2008; Cannat *et al.*, 2009). This relationship will be discussed in greater detail in S*ection 1.3.3*.

Along the magma-poor region of the SWIR between 61°E and 66°E, the plate conjugate to that which displays OCC formation is primarily of volcanic construction (and has regionally thicker crust/lower gravity), displaying numerous volcanic cones and a combination of tightly packed inward-facing and antithetic faulting that define horst- and graben-type structures (Cannat *et al.*, 2006). This pattern is repeated on the plate opposite Atlantis Massif on the MAR (Canales *et al.*, 2004). There are, however, areas where OCCs may be exposed on both plates (e.g. Fujiwara *et al.*, 2003; Okino *et al.*, 2004; Smith *et al.*, 2006), suggesting that plate separation mechanisms in magma-poor environments may be susceptible to temporal changes in polarity.

1.3.2. Surficial morphology of oceanic core complexes

Oceanic core complexes typically form a topographic high that is abnormally smooth compared to the surrounding seafloor (Cann *et al.*, 1997). They are often bounded on their oldest (axial-distal) side by a linear, outward-tilted volcanic ridge often termed a ‘breakaway’ ridge (e.g. Smith *et al.*, 2006). On their younger (axial-proximal) side they are bounded by the footwall/hanging-wall boundary (or ‘termination’), or a high-angle fault scarp – sometimes termed a ‘termination scarp’ (e.g. Cannat *et al.*, 2009; Figure

1.3.3a-b). The area of seafloor immediately surrounding OCCs sometimes displays a wide range of debris flow morphologies (e.g. Cann *et al.*, 1997; Smith *et al.*, 2006). OCCs may exhibit a convex-upwards or sub-horizontal detachment surface that is corrugated at wavelengths of ~1 km with amplitude of a few tens of metres and further adorned with fine-scale striations that have wavelengths of ~50 – 100 metres (e.g. Cann *et al.*, 1997; Ohara *et al.*, 2001; MacLeod *et al.*, 2002; Reston *et al.*, 2002; Cannat *et al.*, 2003; Searle *et al.*, 2003; Smith *et al.*, 2006; Cannat *et al.*, 2009). Cann *et al.* (1997) suggest that striations observed with sidescan sonar are alternating exposures of bare rock and intervening sediment filled depressions, similar to slickensides on terrestrial fault surfaces. This has subsequently been shown with seafloor video footage across an OCC on the MAR at 15°45'N (MacLeod *et al.*, 2002). It should be noted, however, that the aforementioned 'bare rock' outcrops identified by sidescan sonar may actually lie beneath a thin veneer of sediment.

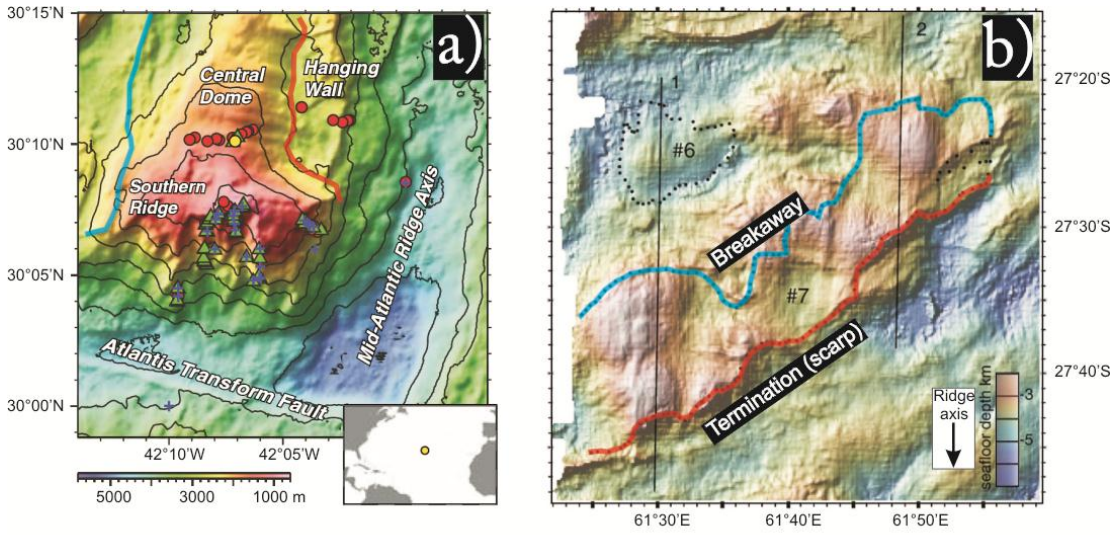


Figure 1.3.3. Morphological and structural elements of OCCs, from **a)** Ildefonse *et al.* (2007) - Atlantis Massif (with breakaway location after Canales *et al.*, 2004) and **b)** Cannat *et al.* (2009) - off-axis OCC#7, SWIR. Red,blue and green dots in **a)** are basalt, grabbro and serpentinised peridotite, respectively, with the single yellow dot marking the location of IODP hole U1309D. Blue and red lines are breakaways and terminations, respectively. Both OCCs display prominent spreading direction parallel corrugations. See text for discussion.

The formation of larger-scale corrugations has previously been attributed to the 'continuous casting' of relatively ductile footwall material against a brittle hanging wall (Spencer, 1999). MacLeod *et al.* (2002), however, find no evidence for ductile deformation of the footwall, and suggest that corrugations form by linkage of precursory structures during extension on the detachment surface. In all cases, efficient

strain localisation along the detachment plane is accompanied by hydrous formation of weak minerals such as serpentine, talc, chlorite and tremolite, as have been sampled from a number of OCCs (e.g. Escartin & Cannat, 1999; MacLeod *et al.*, 2002; Reston *et al.*, 2002). Escartin *et al.* (2001) show that an abrupt transition from strong mantle lithologies to relatively weak mantle-derived serpentinites occurs at low-levels of serpentinisation – perhaps < 15%.

1.3.3. Internal structure of oceanic core complexes

Integrated Ocean Drilling Program (IODP) expeditions 304 and 305 have given an insight into the internal composition of oceanic core complexes. Site U1309D, centred on the corrugated, domal footwall section of Atlantis Massif (yellow dot – Figure 1.3.3a), recovered ~1.4 km of predominantly gabbroic material, with thin, ultramafic layers comprising only a small proportion of all lithologies (Blackman *et al.*, 2006; Ildefonse *et al.*, 2007). These finding are consistent with previous drilling results across OCCs in the Fifteen-Twenty FZ area, which typically comprise up to ~200 metres of serpentinised peridotite overlying deeper successions of gabbro (ODP leg 209 - Kelemen *et al.*, 2004). Deep-drilling results from across Atlantis Bank, at 57°15'E on the SWIR, also predominantly comprise gabbroic rock (Figure 1.3.4; Dick *et al.*, 2000). Based on these observations, Ildefonse *et al.* (2007) suggest that the domal cores of OCCs are composed of gabbroic intrusions enveloped within a peridotite host (i.e. the 'plum-pudding' model of crustal architecture – see *Section 1.2.4*). With increasing tectonic extension and hydrothermal circulation, strain efficiently localises within the rheologically weak serpentinised peridotite as opposed to the strong gabbro intrusion, which may eventually become unroofed by a single, OCC-forming master detachment fault (Ildefonse *et al.*, 2007).

Geophysical investigations of OCCs are inherently ambiguous due to the fact that lower crustal gabbroic rock and upper mantle peridotite, when serpentinised within the range ~20 – 75% (Escartin *et al.*, 2001; Canales *et al.*, 2008), have approximately the same density and seismic velocity. Even so, seismic imaging can still be used to investigate the internal nature of OCCs, which in all cases studied to date reveals a high velocity body beneath the domed, detachment surface (e.g. Canales *et al.*, 2004; Canales *et al.*, 2007; deMartin *et al.*, 2007; Canales *et al.*, 2008; Planert *et al.*, 2009). Canales *et*

al. (2008) are able to distinguish gabbro from serpentinised peridotite on the basis of P-wave velocity variations, seafloor morphology, in-situ sampling and the fact that serpentinised peridotite samples generally show high degrees (> 70%) of serpentinisation. This subsequently confirms drilling results which suggest that OCCs comprise predominantly gabbro beneath their corrugated detachment surfaces which focus significant localisations of serpentinised peridotite. Gravity studies suffer from a similar ambiguity in distinguishing the subsurface lithological composition of core complexes, but are still able to confirm the presence of high density material at shallow depths (e.g. Tucholke *et al.*, 2001; Nooner *et al.*, 2003; Searle *et al.*, 2003; Blackman *et al.*, 2008).

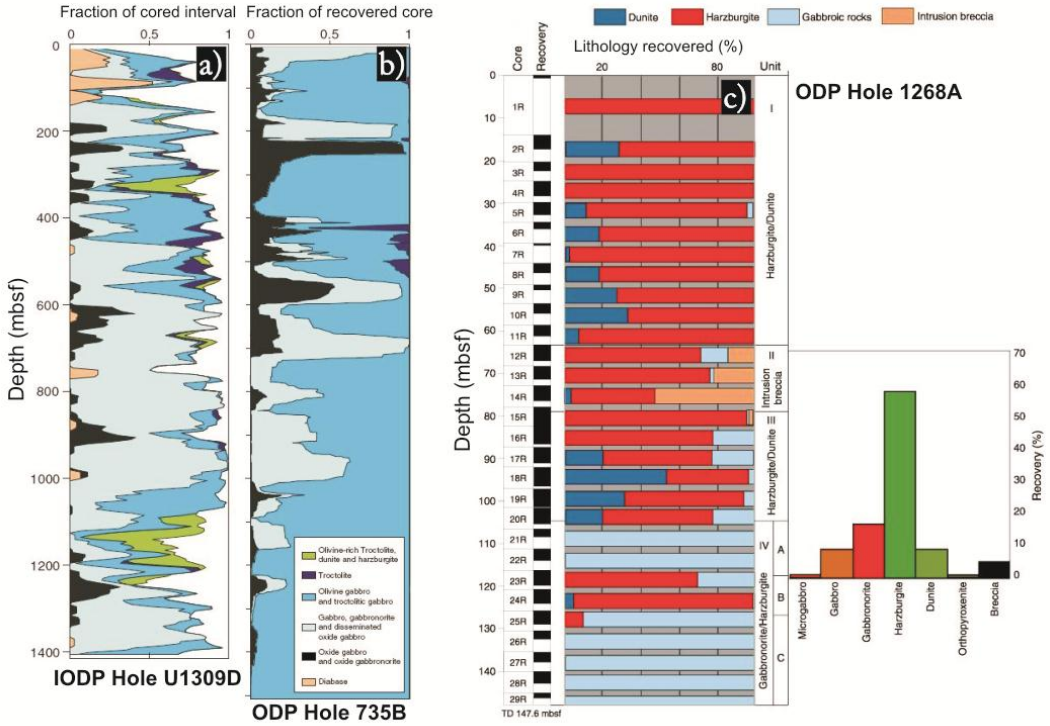


Figure 1.3.4. Summary of deep-drilling results from OCCs. **a)** relates to Atlantis Massif on the MAR (IODP hole U1309D), **b)** shows data from Atlantis Bank on the SWIR, adjacent to the Atlantis II transform (ODP hole 735B) and **c)** an OCC in close proximity to the ridge axis south of the Fifteen-Twenty FZ (ODP hole 1268A). **a)** and **b)** are from Ildefonse *et al.* (2007) and **c)** is from Kelemen *et al.* (2004). Data in **a)** and **b)** have been averaged over 20 metres and hence do not show shallow ultramafic material. See text for discussion.

Combined with microseismicity data, seismic imaging also begins to reveal the subsurface nature of the detachment plane, which, in the TAG area of the MAR, appears to dip at ~20° towards the ridge axis to a depth of ~3 km, below which it steepens rapidly to angle of ~70° to a maximum depth of ~7 km (Figure 1.3.5; deMartin *et al.*,

2007). This detachment geometry is consistent with palaeomagnetic studies which suggest that the footwall of Atlantis Massif has undergone ~46±6° of rotation away from the ridge axis (Morris *et al.*, 2009). Garcés & Gee (2007) also use palaeomagnetism to document footwall rollovers ranging from 50° to 80° for core complexes in the vicinity of the Fifteen-Twenty FZ, suggesting that higher values may be accounted for by isostatic readjustment of the unroofed plate. Furthermore, approximately equal-age samples on opposite sides of the ridge axis exhibit similar degrees of rotation, implying that asymmetric accretion mechanisms may not be necessary to expose lower crustal and upper mantle material during periods of magma-starvation (Garces & Gee, 2007).

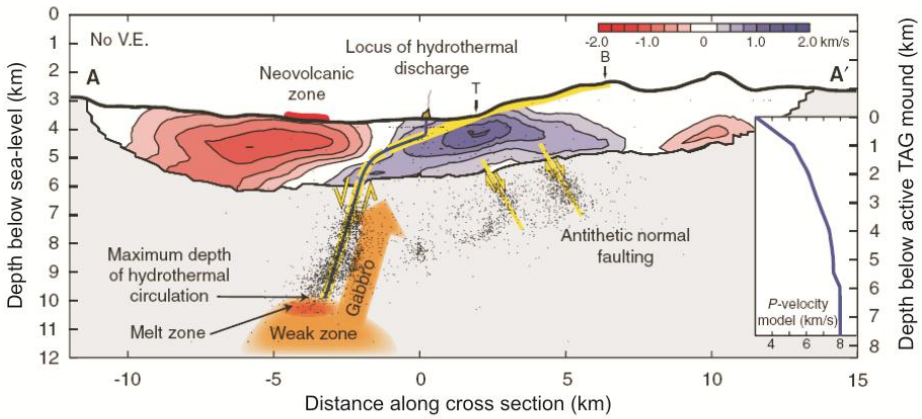


Figure 1.3.5. Seismic imaging has been used to demonstrate the presence of high velocity material at shallow depth beneath OCCs (shown here is the TAG area of the MAR, with contours indicating a deviation from the assumed P-wave velocity model - inset). Microseismicity (black dots) and palaeomagnetic studies (e.g. Garcés & Gee, 2007; Morris *et al.*, 2009) can also be used to constrain the subsurface detachment geometry, which may be steep (~70°) at depths >7 km and rollover by ~50° at a depth of ~3 km. Image from deMartin *et al.* (2007).

1.3.4. Melt supply and oceanic core complex formation

OCCs are assumed to form when melt supply falls below a critical threshold value, necessitating tectonic plate separation at the ridge axis (e.g. Buck *et al.*, 2005; Tucholke *et al.*, 2008). Based on the identification of active fault surfaces in the MARK area (MAR at Kane FZ), Karson & Winters (1992) show that a shallow-dipping detachment fault formed on the inside-corner of the RTI at 23°30'N when the magmatic component of plate separation (herein referred to as M_{TOTAL}) fell to $\leq 20\%$ for a period of about 0.5 My. This detachment fault eventually became terminated by the emplacement of a neovolcanic ridge at the plate margin (MARK (N) – Figure 1.3.6).

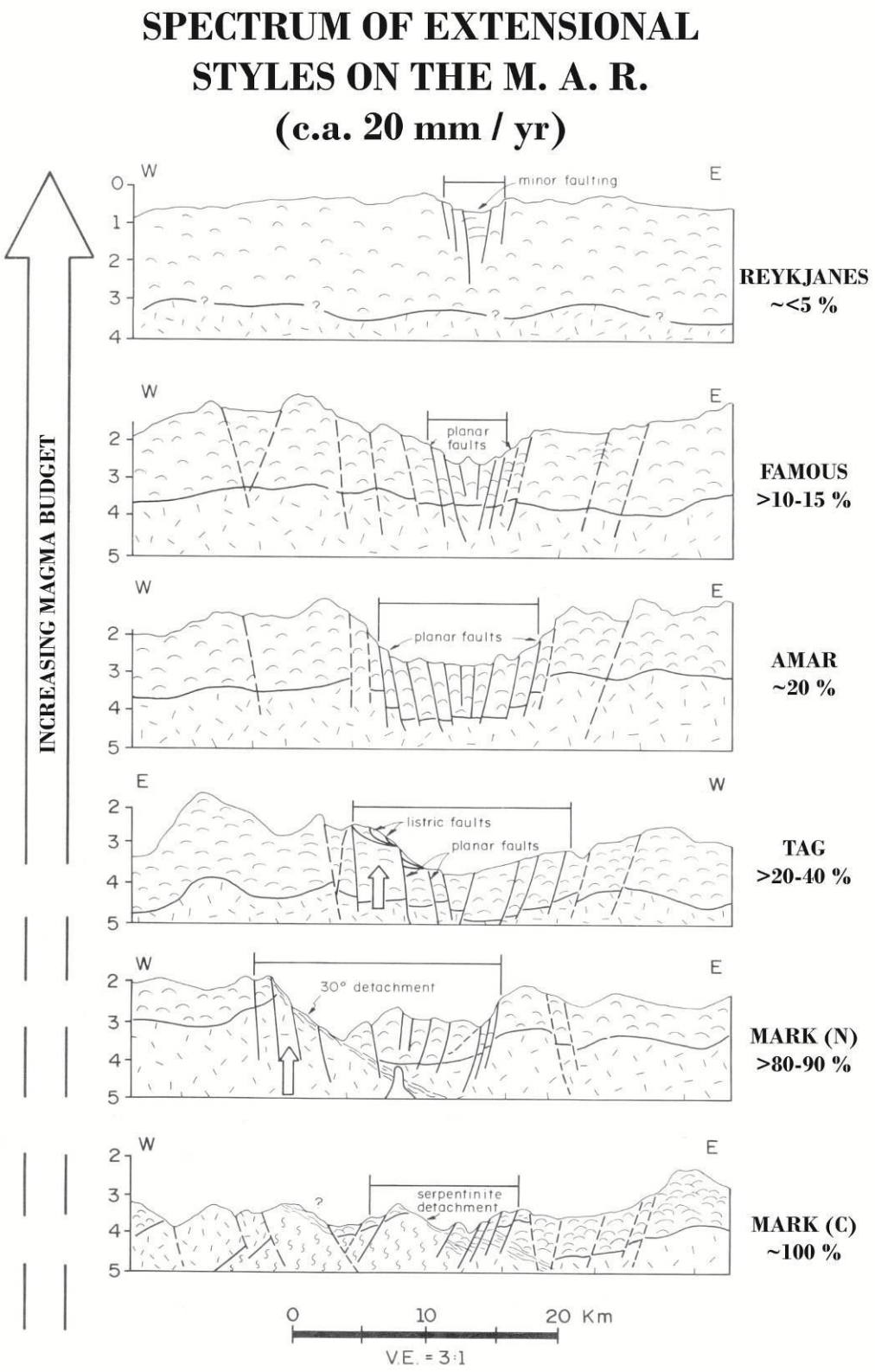


Figure 1.3.6. Spectrum of MAR extensional styles as a function of magmato-tectonic ratio. Percentage to right of section is the component of tectonic extension, the compliment of which is the inferred component of magmatic extension (referred to as M_{TOTAL} in text). From Karson & Winters, 1992.

To the south (MARK (C) – 23°15'N; Figure 1.3.6) lies an accommodation zone with no discernible component of magmatic extension (i.e. $M_{TOTAL} \approx 0\%$). This gives way to seafloor formed about the magmatically robust ($M_{TOTAL} > 88 – 90\%$) segment centre at 23°00'N. This value of M_{TOTAL} for magmatically robust environments is consistent with that which has been calculated at 29°15'N on the MAR (where MTOTAL = 83 – 92%: Escartin *et al.*, 1999).

In addition to seafloor observations of faulted surfaces, numerical algorithms have been used to assess the effect of M_{TOTAL} on seafloor morphology (e.g. Buck *et al.*, 2005; Behn & Ito, 2008; Ito & Behn, 2008; Tucholke *et al.*, 2008; Olive *et al.*, 2010). These models assume that M_{TOTAL} is entirely focused within a narrow, columnar NVZ inside the axial valley. Buck *et al.* (2005) and Tucholke *et al.* (2008) show that for such a model, approximately equal amounts of M_{TOTAL} and T (where T is the tectonic component of plate separation – i.e. the complement of M_{TOTAL}) are required to form OCCs (Figure 1.3.7). In summary, when $M_{TOTAL} > 50\%$, faults are rafted away from the ridge axis by conventional processes, subsequently becoming inactive in the cooler, rheologically strong lithosphere. At $M_{TOTAL} \approx 50\%$, a stable detachment and OCC form. When M_{TOTAL} becomes significantly < 50%, the footwall/proto-OCC migrates towards the hanging-wall to compensate for the magmatic deficiency in the latter, becoming terminated by high-angle antithetic faulting in the process. With no melt supply to the ridge axis ($M_{TOTAL} = 0\%$), advective heating of the footwall prohibits long-lived extension on a single fault and a number of large-offset faults form.

This 'Goldilocks' scenario is supported by gravity profiles which demonstrate that OCCs may be preceded and succeeded by a relative gravity anomaly low, interpreted as indicating magmatic conditions before and after OCC formation (e.g. Kane and Atlantis Massifs), or alternatively a relative gravity anomaly high, indicating particularly magma-poor conditions before and after OCC formation (e.g. the 15°45'N OCC; Tucholke *et al.*, 2008). The prevalence of OCCs in slow- to intermediate-spreading environments and at intermediate axial depths, can also be used to suggest that OCCs form at intermediate melt supplies (Tucholke *et al.*, 2008). In addition to this, Cannat *et al.* (2009) show that OCCs usually form along the transitions between 'normal' (i.e. magmatic) and 'smooth' seafloor, concluding that they are generated at intermediate levels of magmatism (in the context of the low regional melt supply of the SWIR).

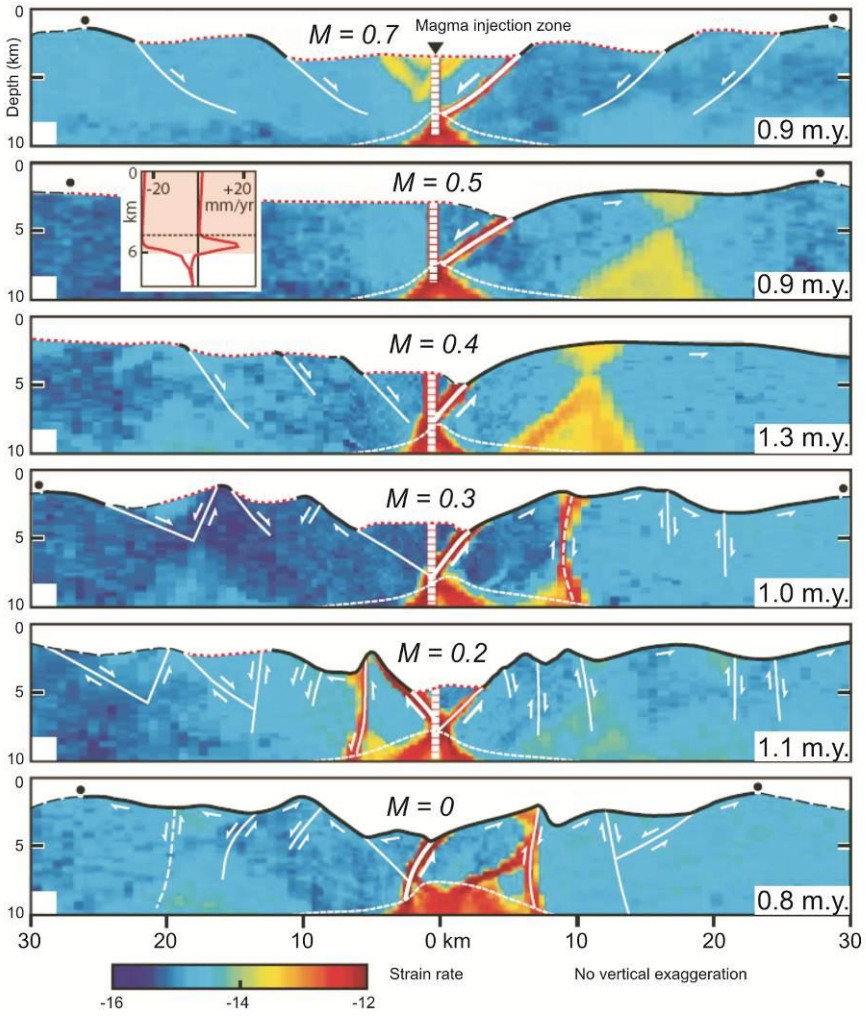


Figure 1.3.7. Numerical strain modelling of ridge morphology as a function of M (M_{TOTAL}), the magmatic component of plate separation. OCC formation is expected to occur when M_{TOTAL} ~= 30-50%. See text for discussion. From Tucholke *et al.* (2008).

1.3.5. The Mid-Atlantic Ridge at 13°N

The '13°N region' is a general term used here to describe the magma-poor terrain that extends for ~120 km along-axis from 12°56'N to 14°00'N on the MAR. The full-spreading rate in the area is believed to be 26 km/My (DeMets *et al.*, 1990, 1994). In addition to research cruise JC07 (RRS *James Cook*, March-April 2007), notable surveys conducted in this region include: M/V *Tyro* (Collette *et al.*, 1979), R/V *Akademik Boris Petrov* (1986) (Bougault *et al.*, 1988), R/V *Knorr* leg 182 (2005) (Smith *et al.*, 2006; Smith *et al.*, 2008), the 30th and 32nd cruises of the R/V *Professor Logatchev* (2007) (Beltenev *et al.*, 2007; Beltenev *et al.*, 2009) and the Serpentine cruise onboard the R/V *Pourquoi Pas?* (2007) (Fouquet *et al.*, 2008) (the latter three of which were primarily concerned with the nature and distribution of hydrothermal vent sites in the area).

The first detailed study of the 13°N region was carried out in 1977 onboard the M/V *Tyro* (Collette *et al.*, 1979). Low resolution, clay-modelled bathymetry data were sufficient to identify the major morphological components of what has since become diagnostic of a magma-poor area, namely: irregular, asymmetric topography that lacks linearity and parallelism (Figure 1.3.8). Collette *et al.* (1979) suggest that temporal (~0.5 My) changes in the locus of accretion over distances of several kilometres may explain the irregular terrain, with a 'twist' (i.e. ridge discontinuity) in the axial valley at 13°45'N being responsible for *en echelon* structures that have a zigzagging fossil expression through 'ragged' seafloor for up to 100 km off-axis.

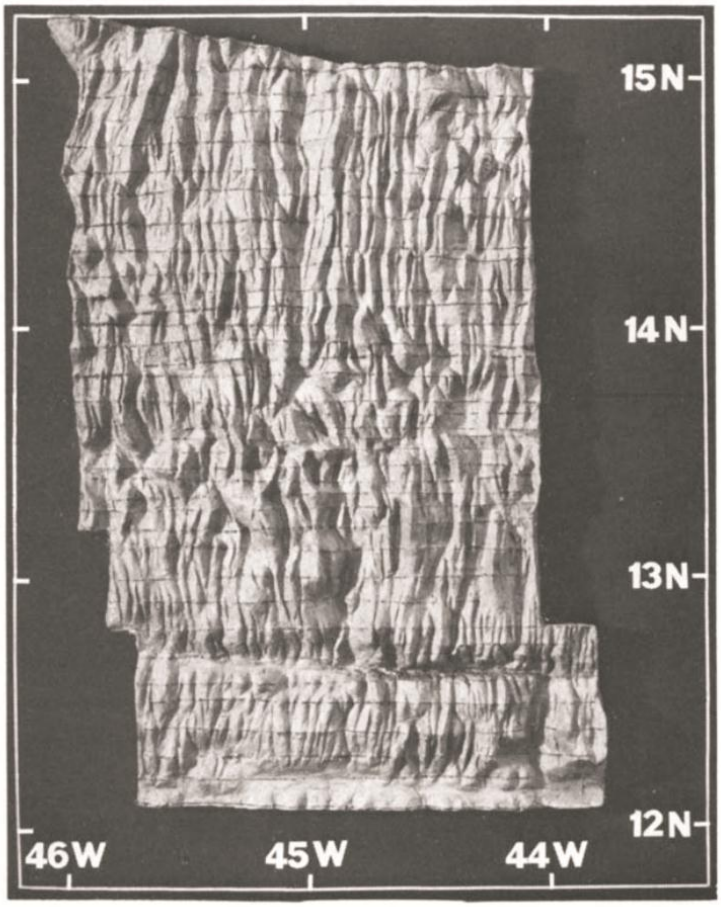


Figure 1.3.8. Clay-modelled bathymetry data across the 13°N region (from Collette *et al.*, 1992). MAR is N-S depression in topography at ~45°W. Note the distinct change in morphology from linear abyssal hills at the segment centre (~14°N) and surrounding the Marathon FZ (E-W depression in topography at 12°40'N) with the intervening areas of irregular seafloor. Illumination is from WNW, with vertical exaggeration of x7.

In a more recent study, Smith *et al.* (2006) have used hydroacoustic energy from small earthquakes (magnitude > 2.5) to define a zone of active OCCs that extend for ~75 km along the ridge axis in the 13°N region, with bathymetry data being used to

recognise an additional field of extinct OCCs extending for at least 100 km off-axis. Furthermore, Escartin *et al.* (2003b) have identified an anomalous zone of seismicity ~70 km west of the ridge axis, with focal mechanisms indicative of spreading between the North American (NA) and South American (SA) plates, concluding that plate separation along the MAR in the 13°N region may be influenced by the NA-SA-AF (African) triple junction. Previous geochemical studies in the area have also detected a geochemical anomaly that suggests the presence of an incipient ridge-centred plume (Figure 1.3.9; Bougault *et al.*, 1988; Dosso *et al.*, 1991).

With regard to regional morphology, Smith *et al.* (2006) expand on the observations of Collette *et al.* (1979) by noting that topography is chaotic, with the west flank displaying widely spaced, narrow faults that are continuous along axis for < 20 km. These faults are separated by areas of smooth seafloor which may be corrugated parallel to the spreading direction. Smith *et al.* (2006) suggest that linear, basin-bounded ridges identified within the axial valley may be the precursors to genesis of OCCs, which form primarily by outward rotation and flattening of the footwall until it becomes truncated by a later, normal fault. On the basis of seafloor morphology, Smith *et al.* (2006) conclude that in the 13°N region, crustal accretion on the SA plate involves regular nucleation and extension on OCC-forming detachment faults.

Smith *et al.* (2008) observe a pronounced degradation in the amplitude and continuity of magnetic anomalies in the 13°N region compared with anomalies measured by Fujiwara *et al.* (2003) over the magmatically robust segment centre at 14°N (Figure 2.6.13b). The Brunhes-age magnetic anomaly in this magma-poor area is particularly disrupted, becoming asymmetric about the topographic ridge axis and, in some places, not being identified at all (Smith *et al.*, 2008).

Gravitational anomalies indicate that the crust in the 13°N region may be at least 1 km thinner than the segment centre (Smith *et al.*, 2008). This is consistent with previous studies of MAR spreading-segments that usually identify a decrease in crustal thickness with distance from the segment centre, forming bull's-eye anomalies (e.g. Kuo & Forsyth, 1989; Lin *et al.*, 1990; Tolstoy *et al.*, 1993; Planert *et al.*, 2009). However, Smith *et al.* (2008) also show that lineated, magmatic terrain bounds the Marathon FZ, implying that magmatism may actually increase towards the segment end in the south. The transitions between magma-rich and magma-poor provinces to the north and south of the segment centre and also the seafloor bounding the Marathon FZ are oblique to the spreading direction, indicating along-axis propagation of magmatic

discontinuities (see, for example, the heavy, dotted black lines in Figure 1.3.9; Fujiwara *et al.*, 2003).

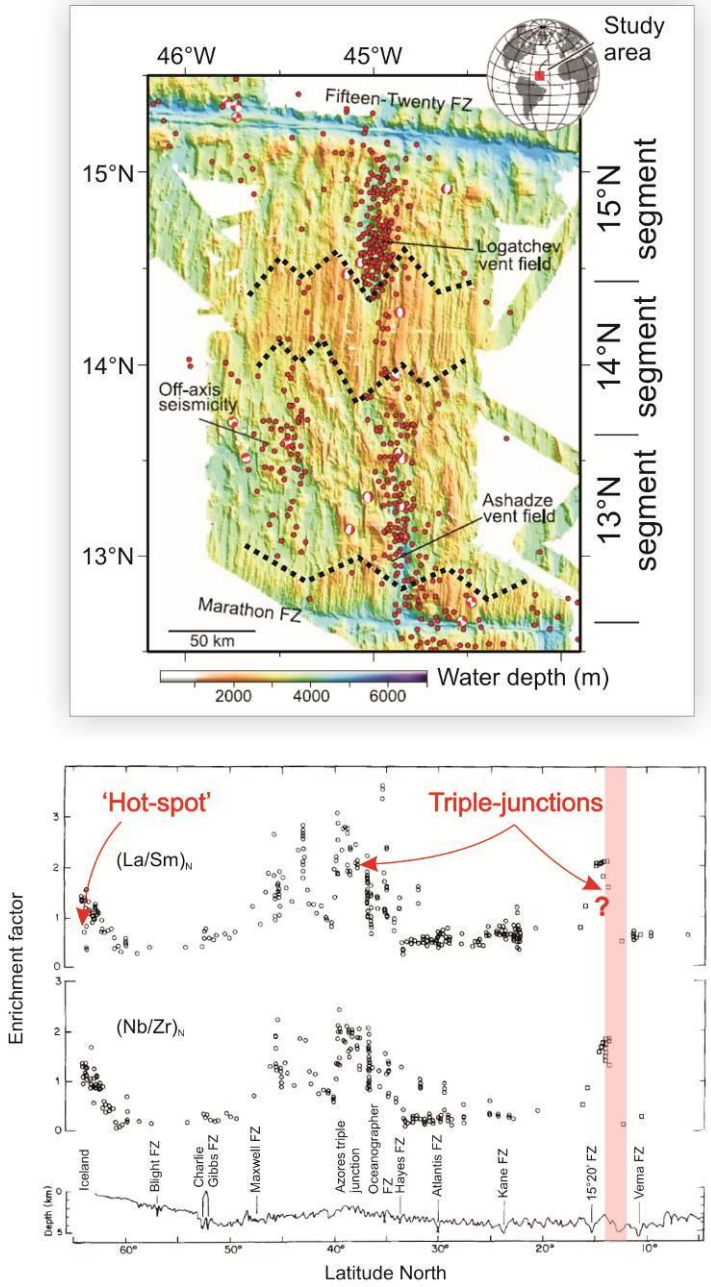


Figure 1.3.9. Off-axis seismicity (upper panel) and geochemical enrichment (lower panel, vertical pink bar highlights 13°N region) suggest that the MAR between 14-15°N is influenced by the presence of the NA-SA-AF triple junction. Heavy, dotted black line in upper panel demarcates magma-rich and magma-poor settings. From Smith *et al.* (2008) and Bougault *et al.* (1988).

1.4. Summary of thesis aims

The MAR at 13°N is an ideal environment in which to examine the fundamental processes that govern plate separation along a magma-poor section of the MAR. Currently important issues regarding magma-poor regions relate to both the internal structure and formation (or 'life cycle') of oceanic core complexes as well as the regional, segment-scale conditions that favour OCC formation. Hence, this thesis uses a variety of interpretive techniques to examine the following topics:

OCC life cycle

- Under what conditions does OCC formation initiate at the ridge axis? There is widespread debate as to whether OCCs are regulated by either local increases or decreases in melt supplied to the ridge axis, and as to the relative contribution of magmatic and tectonic processes to OCC formation.

- How are OCCs terminated? Laterally propagating dikes and faults and renewed magmatism at the ridge axis have previously been suggested as termination mechanisms for slip on detachment surfaces but have not yet been substantiated.

OCC structure

- What is the internal composition of OCCs? Deep-drilling results have recovered predominantly gabbro, yet this is rarely sampled from the surface of core complexes which generally comprise highly-altered peridotite. The internal composition has major implications for magmatic conditions during OCC formation, and might also offer insight into the fundamental structure of oceanic crust along the MAR.

- Are detachment surfaces linked beneath the seafloor, with apparently isolated OCCs actually being the surficial expression of a more extensive corrugated surface? If so, this would mark a paradigm shift in the way in which oceanic crust is believed to form.

Regional morphology

- Beyond the localised variations associated with OCC formation, how does the regional, segment-scale morphology reflect the way in which melt is delivered to the ridge axis, and does this differ greatly from other sections of the MAR? In addition to this, are the regional magmatic conditions the same as those observed locally around OCCs?

- Is the generation of crust along this magma-poor section of the MAR an asymmetric process, and if so, how does this asymmetry manifest itself in the regional morphology? This can be considered in terms of the physical structure of the ridge and also the spreading rate.

1.5. Thesis outline

This chapter has provided background information on the current understanding of how magma-poor regions and OCCs form, which is contrasted to the typical (and relatively well understood) volcanic and tectonic processes that occur on a wider scale along the MOR. In the following chapter I discuss the survey configuration deployed during research cruise JC07 in addition to the data acquisition methods and techniques used to process deep-towed TOBI sidescan sonar data and tri-axial magnetic data, and shipboard gravity data.

The central part of the thesis is split into three chapters, each of which is specific to a particular dataset (i.e. Chapter Three: Sidescan sonar, Chapter Four: Gravity data and Chapter Five: Magnetic data). Each of these chapters has an introductory section documenting the analytical methods used during the latter part of the chapter – which comprises the discussion relating to the dataset in question. The results from Chapters Three, Four and Five are then tied together in Chapter Six, which is subdivided by geological theme and has discussion topics specific to the thesis aims outlined in *Section 1.4*.

Chapter Two

Data acquisition and processing

2.1. Introduction

The purpose of this chapter is to give an overview of the various acquisition and processing techniques applied to each of the geophysical datasets collected during research cruise JC07, namely: sidescan sonar, gravity and magnetics[5]. The methods used to acquire and process bathymetry data are of less importance to this study, but are presented here for completeness. Survey location and configuration is presented at the start of this chapter, followed by a breakdown of the techniques applied to each dataset. In general, these dataset subsections are further subdivided; so as to include, 1) an overview of the theory behind the geophysical instrument being used, 2) a JC07-specific description of how the instrument was deployed and operated, 3) a list and discussion of the various processing stages applied to the dataset in question, and 4) a summary of the processing scheme and its effectiveness.

2.2. JC07 Survey configuration and instrumentation

Research cruise JC07 was carried out aboard the RRS *James Cook* across the 13°N region of the MAR between 5th March and 12th April 2007 (ship's track – Figure 2.2.1). During this period, a deep-towed TOBI (Towed Ocean Bottom Instrument) survey was conducted that lasted for approximately two weeks (TOBI track-lines – Figure 2.2.2), the results of which are discussed in *Section 2.4* and *2.6*.

[5] Gravity and magnetic data processing is considered to be everything up to acquiring the free-air and total field anomalies, respectively. Bouguer corrections and magnetisation solutions are discussed as part of the interpretation in Chapters Four and Five, respectively.

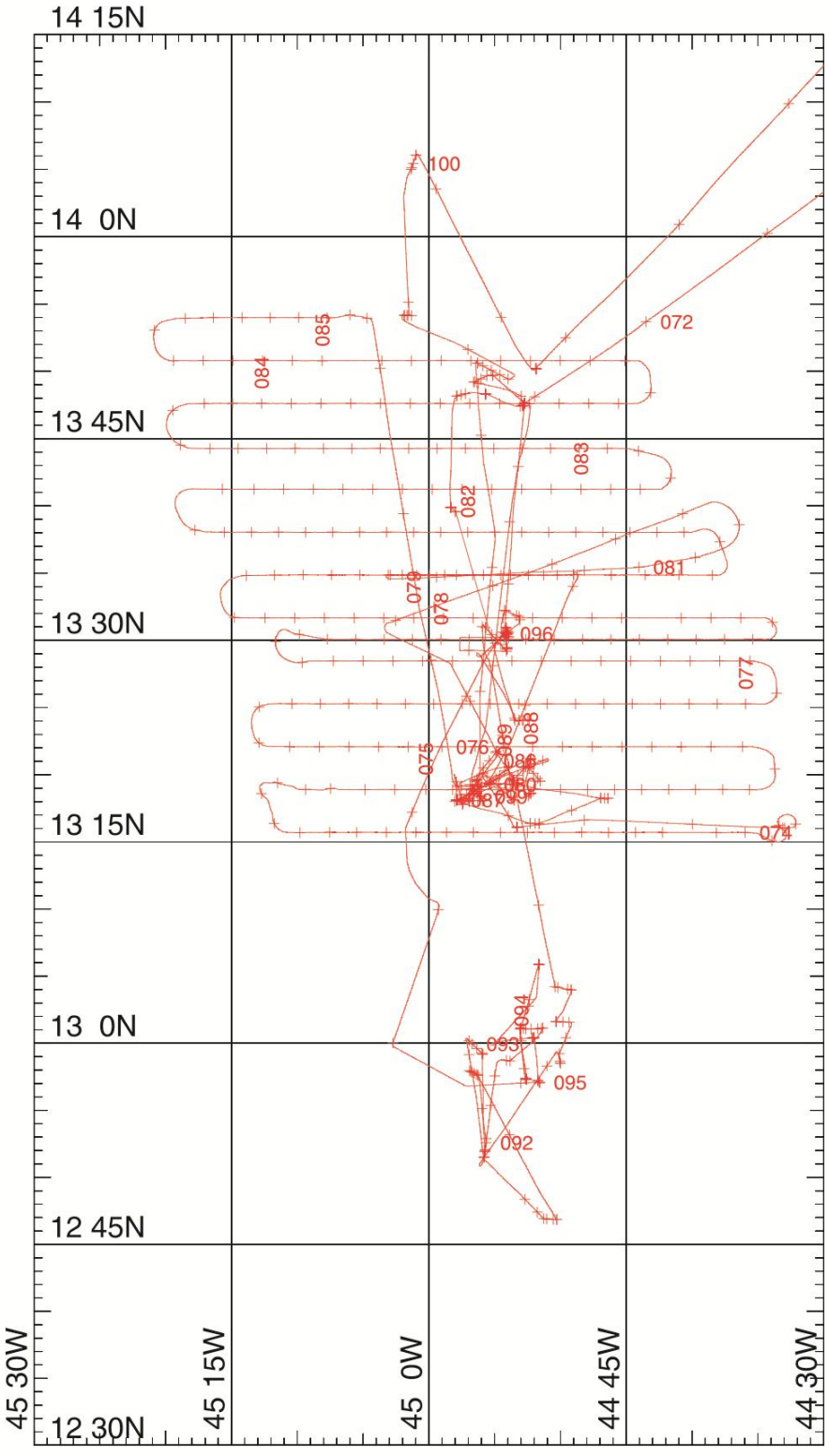


Figure 2.2.1. JC07 survey summary. Red line marks ship's track throughout duration of survey with red crosses at one hour intervals. Annotation of Julian date (e.g. 077) is in red, where JD1 is taken as January 1st 2007.

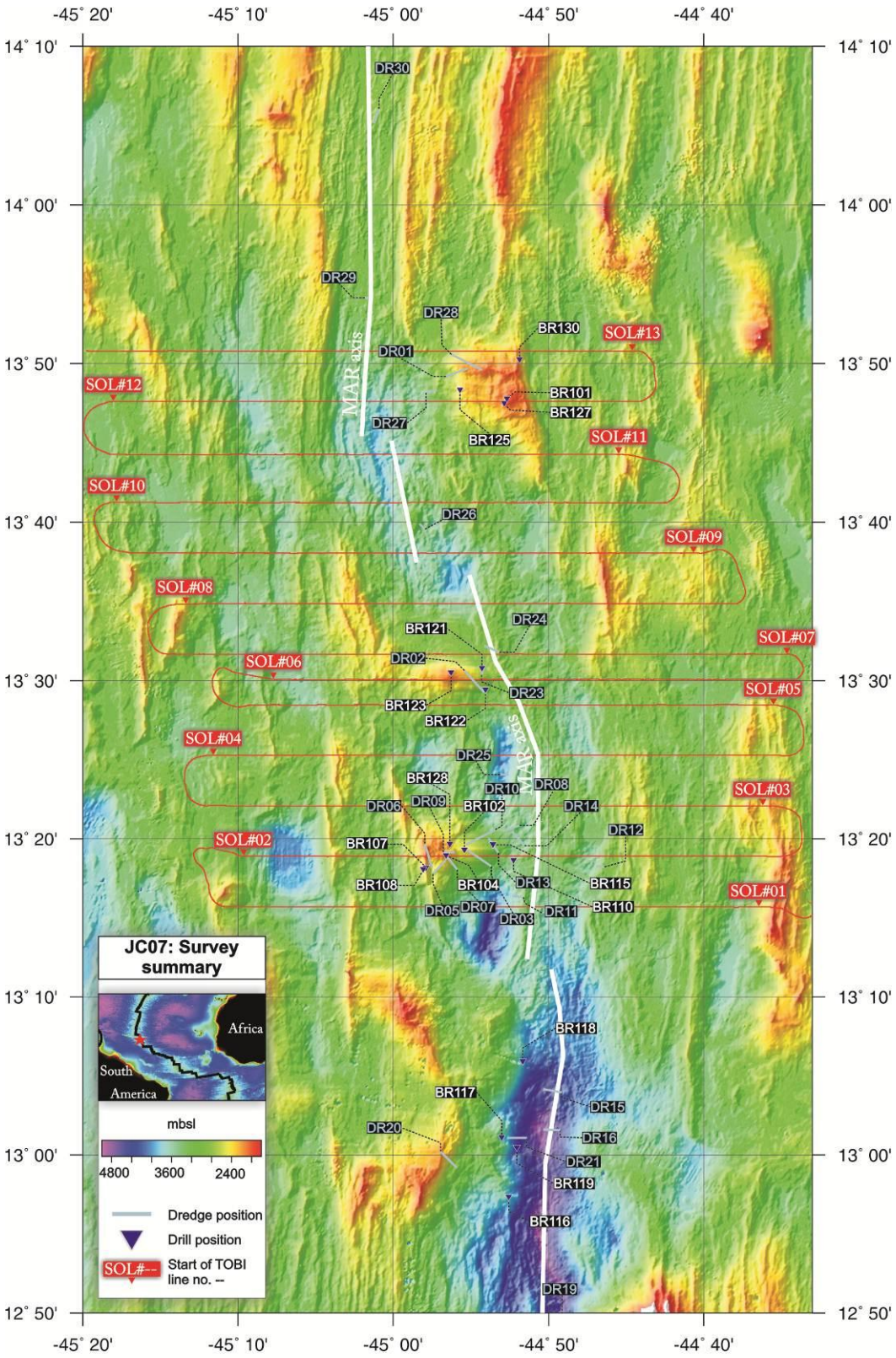


Figure 2.2.2. JC07 survey summary (global position indicated by red star - inset). Thirteen deep-towed survey profiles (TOBI tracks - red lines) were acquired at a line spacing of 6 km, with the exception of lines 5-7 which were 3 km apart. Distribution of dredge (Dxx) and drill (BRxxx) positions are shown. In total, 18 drill cores and 26 dredges were recovered. 100 metre resolution bathymetry (D. Smith, *personal comm.*) is illuminated from NW.

A two-week seabed sampling survey using dredging and the BGS oriented BRIDGE wire-line drill techniques was also conducted, with sample locations shown in Figure 2.2.2. Shipboard bathymetry (*Section 2.3*), gravity (*Section 2.5*) and magnetic data (*Section 2.6*) were collected continuously during the entire survey, with the exception of short periods of instrument downtime. The following subsections give an overview of the configuration of each survey.

2.2.1. Deep-towed operations

TOBI is a stable instrument platform capable of operating in depths of up to 6000 metres (Flewellen *et al.*, 1993). The instrument arrangement used during JC07 contained: 30 kHz sidescan sonar with swath echo-sounder, chirp sub-bottom profiler, tri-axial fluxgate magnetometer, CTD (conductivity/temperature/depth) instruments, light scattering sensor (LSS), gyrocompass and vehicle attitude sensors. Thirteen deep-towed survey profiles were acquired at an average spacing of 6 kilometres between 13°15'N and 13°50'N, the start and end points of which are displayed in Figure 2.2.2 and summarised in Table 2.2.1. Throughout the survey it was necessary that TOBI retained an altitude of approximately 400 metres above the seafloor; this was achieved by maintaining a constant survey speed of roughly 1.7 knots, and by varying the length of the tow cable so that at any given point TOBI was approximately 3 kilometres behind the ship (Figure 2.2.3). A discussion on the transducer configuration and data resolution is presented in *Section 2.4*.

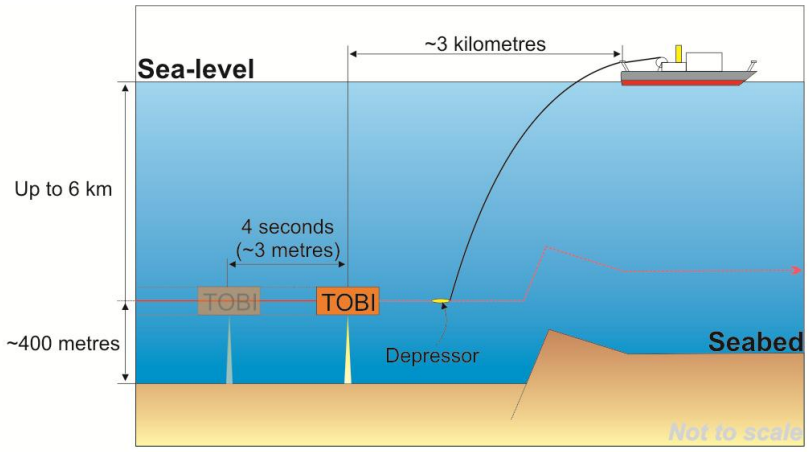


Figure 2.2.3. TOBI (deep-towed) survey configuration. In order to maintain a constant sidescan sonar swath width of approximately 6 km, TOBI 'flew' at an altitude of 400 metres above the seafloor. Measurements were taken at 4-second intervals, equating to roughly 3 metres along track.

In addition to remotely sensed geophysical data, measurement of vehicle attitude and position is essential for geographical referencing of the sidescan sonar information and correction of the tri-axial magnetometer data for the effects of vehicle magnetisation. Vehicle attitude measurement was achieved using a fish-mounted gyrocompass and electrolytic inclinometers. The gyrocompass, which measures vehicle heading (herein called "gyro" for distinction with ship's "heading"), is generally accurate to within ±1° at latitudes less than 70°. Vehicle pitch and roll measurements are assumed to be accurate to within ±0.2° within a range of ±20°, with positive measurements for pitch and roll being vehicle nose-down and vehicle top-to-port, respectively. There is a known misalignment between the recorded TOBI gyro values and the true heading of the vehicle of 10.1°. This was incorrectly added to the gyro values when recording the data during cruise JC07, and hence 20.2° has been removed from the gyro values used throughout the remainder of this study (D. Matthew, *personal comm.*).

Line #	TOBI Start pos.	TOBI End pos.	Start time (Julian date)	End time
1	44°36.7'W, 13°15.9'N	45°07.3'W, 13°15.7'N	74/0115	74/1615
2	45°07.9'W, 13°18.9N	44°37.0'W, 13°18.9'N	74/2150	75/1210
3	44°37.0'W, 13°22.0'N	45°07.6'W, 13°22.1'N	75/1510	76/0440
4	45°07.8'W, 13°25.3'N	44°37.0'W, 13°25.3'N	76/1018	77/0022
5	44°36.8'W, 13°28.4'N	45°07.8'W, 13°28.5'N	77/0325	77/1648
6	45°08.0'W, 13°30.1'N	44°37.0'W, 13°30.1'N	77/2100	78/1106
7	44°36.7'W, 13°31.8'N	45°11.2'W, 13°31.7'N	78/1416	79/0508
8	45°12.3'W, 13°34.8'N	44°40.7'W, 13°34.9'N	79/0930	81/1400
9	44°42.6'W, 13°38.0'N	45°15.2'W, 13°38.0'N	81/1800	82/0930
10	45°14.8'W, 13°41.2'N	44°45.0'W, 13°41.2'N	82/1320	83/0230
11	44°47.5'W, 13°44.2'N	45°16.8'W, 13°44.3'N	83/0630	83/1945
12	45°15.8'W, 13°47.6'N	44°45.1'W, 13°47.6'N	83/2330	84/1245
13	44°47.8'W, 13°50.8'N	45°14.8'W, 13°50.8'N	84/1600	85/0352

Table 2.2.1. Summary of survey line start and end points. A total of thirteen deep-towed profiles were collected at a spacing of ~6 kilometres, with the exception of lines 5, 6 and 7 which were 3 kilometres apart. Date format is JD/hhmm, with all times in GMT.

2.2.2. Seabed sampling operations

The BRIDGE rock drill is designed to take metre-long oriented cores from the seabed in water depths of up to 5500 metres. Knowing the orientation of the core allows for a greater wealth of information to be extracted from the sample (the palaeomagnetic declination, for example), although the results are used here primarily for lithological ground-truthing of sidescan sonar images. The system used a fibre-optic connection which allowed for live video to assist in the selection of a suitable drill location. Throughout JC07, thirty deployments of the drill were made at localities distributed between 12°57'N and 13°50'N, focussing on the OCCs located at 13°19'N, 13°30'N and 13°48'N (Figure 2.2.2). Following the nomenclature introduced during research cruise JR63, drill sites were named BRxxx, with 'xxx' incrementing sequentially between 101 and 130 (MacLeod *et al.*, 2001). From the thirty attempted drill deployments: eighteen cores were recovered, of which only seven were successfully scribed to indicate the orientation of the sample. The average core recovery for the successful deployments was 0.29 metres, much lower than the potential 1 metre penetration of the drill. The lower than normal amount of successful drill deployments and core recovery was primarily attributed to a combination of technical difficulties and a higher than expected degree of sediment cover (Searle *et al.*, 2007). A drill site summary is presented in Table 2.2.2.

Dredging was primarily focused across the detachment surfaces of the three main OCCs and within the neovolcanic zones immediately adjacent to these areas. Additional dredges were deployed towards the segment centre and also the southern segment end in order to fully assess geochemical variation across the entire region (Figure 2.2.2). Dredges were sequentially numbered between 01 and 30 with the prefix DR. Seafloor dredge tracks were typically of the order of a few kilometres in length, and although there is no definitive way of working out the precise location at which samples were collected, the results still provide a useful indication of seabed lithologies. In total: thirty dredges were deployed, two of which were lost at sea (DR18 and DR22) and seven of which did not retrieve any significant volume of material (DR03-04, DR08, DR14, DR17, DR25 and DR27). Dredging positions are summarised in Table 2.2.3, with dredge and drill sample data discussed in *Section 3.2.2*.

Site #	Location description	Drill site JD	lat°	lat'	lon	lon'	dept	Seafloor morphology	Lithology drilled	Recovery (m)
JC07-BR101	OCC1348	072	13	47.64	44	52.71	2005	Talus and pelagic sediment	Peridotite	0.44
JC07-BR102	Corrug. summit OCC1319	080	13	19.24	44	55.41	2486	Talus and pelagic sediment	Basalt	0.13
JC07-BR103	Corrug. toe OCC1319	080	13	19.26	44	53.70	2862	Talus and pelagic sediment	-	0.00
JC07-BR104	Summit plateau OCC1319	086	13	18.92	44	56.62	2249	Angular talus	Basalt	0.11
JC07-BR105	S plateau OCC1319	086	13	18.16	44	56.94	2546	Pelagic sediment	-	0.00
JC07-BR106	Spine W OCC1319	086	13	18.14	44	57.87	2300	Talus and pelagic sediment. Steep slope	-	0.00
JC07-BR107	Spine W OCC1319	086	13	18.12	44	57.90	2329	Pelagic sediment	Sediment	0.45
JC07-BR108	Spine W OCC1319	087	13	18.12	44	57.91	2298	Tilted pillow lavas	Sediment	0.34
JC07-BR109	Tip N AVR	088	13	21.19	44	52.26	3478	Pillow lavas	-	0.00
JC07-BR110	Tip S AVR	088	13	18.61	44	52.27	3421	Pillow lavas	Basalt	0.12
JC07-BR111	Spine W OCC1319	089	13	18.10	44	57.92	-	-	-	0.00
JC07-BR112	Corrug. toe OCC1319	089	13	19.38	44	53.25	-	-	-	0.00
JC07-BR113	Spine W OCC1319	090	13	18.12	44	57.91	2325	Pillow lavas	-	0.00
JC07-BR114	Corrug. toe OCC1319	090	13	19.60	44	53.60	3073	Talus and pelagic sediment	-	0.00
JC07-BR115	Corrug. toe OCC1319	090	13	19.60	44	53.58	3081	Talus and pelagic sediment	Peridotite	0.19
JC07-BR116	Bench near Ashadze	093	12	57.31	44	52.58	3674	Smooth sediment	Sediment	0.16
JC07-BR117	W rift valley wall	094	13	01.08	44	53.01	3621	Talus and pelagic sediment. Rugged outcrop	Gabbro	0.47
JC07-BR118	W rift valley wall	094	13	05.88	44	51.65	3873	Large boulders	Peridotite	0.36
JC07-BR119	W rift valley wall	094	13	00.40	44	52.03	4219	Pelagic sediment	Gabbro	0.17
JC07-BR120	W rift valley wall	095	12	57.07	44	51.57	4337	Pelagic sediment	-	0.00
JC07-BR121	Corrug. toe OCC1330	095	13	30.60	44	54.20	2776	Beehive pinnacle and chimneys	Peridotite	0.20
JC07-BR122	Corrug. toe OCC1330	095	13	29.36	44	54.07	3099	Rubble and rough outcrops	Peridotite	0.29
JC07-BR123	Corrug. toe OCC1330	095	13	30.50	44	54.15	3292	~40 m vertical cliff	Dolerite	0.36
JC07-BR124	Corrug. toe OCC1330	096	13	30.50	44	54.13	2774	Talus and pelagic sediment	-	0.00
JC07-BR125	OCC1348	098	13	48.32	44	55.68	2419	Talus and pelagic sediment	Peridotite	0.66
JC07-BR126	OCC1348	098	13	47.45	44	55.86	2087	Talus and pelagic sediment	-	0.00
JC07-BR127	OCC1348	098	13	47.45	44	52.84	2094	Talus and pelagic sediment	Peridotite	0.40
JC07-BR128	OCC1319 W of corrug. surf.	098	13	19.62	44	56.35	2336	Gravel/rubble	Basalt	0.12
JC07-BR129	OCC1319 W of corrug. surf.	099	13	18.37	44	56.07	2839	Isolated outcrop in pelagic sediment	-	0.00
JC07-BR130	OCC1348 breakaway ridge	100	13	50.20	44	51.86	2257	Steep, rubbly slopes	Basalt	0.26

Table 2.2.2. Summary of drill sites and locality description. JD (Julian day), lat° (latitude degrees), lat' (latitude decimal minutes), lon° (longitude degrees), lon' (longitude decimal minutes) and depth (metres) for each drill position. Seabed morphology is from BRIDGE drill video (Searle *et al.*, 2007). Core recovery (metres) is colour coded such that: green (successful and scribed), orange (successful and not scribed) and red (no recovery/aborted/drill failure).

Site #	Location description	Dredge on bottom						Dredge off bottom						Primary lithology
		JD	lat	lat'	lon	lon'	dept	JD	lat°	lat'	lon	lon'	dept	
JC07-D01	OCC1348 corrug. toe	072	13	49.49	44	56.59	2932	072	13	49.70	44	55.22	2190	Peridotite
JC07-D02	OCC1330 corrug.	073	13	29.23	44	54.14	3172	073	13	30.64	44	55.41	2381	Peridotite
JC07-D03	OCC1319 corrug. S	073	13	18.25	44	53.69	3324	073	13	19.64	44	55.32	2568	Sediment
JC07-D04	OCC1319 block to NE	085	13	21.40	44	55.11	2975	086	13	20.68	44	55.73	2534	Peridotite/sediment
JC07-D05	OCC1319 S flank	087	13	17.77	44	57.45	2612	087	13	18.63	44	56.64	2238	Basalt
JC07-D06	OCC1319 lava spine to W	087	13	18.20	44	57.50	2526	087	13	19.70	44	57.97	1988	Basalt
JC07-D07	OCC1319 SE flank	087	13	18.04	44	55.87	2962	087	13	19.12	44	56.73	2164	Basalt
JC07-D08	by AVR N OCC1319	087	13	20.56	44	52.74	3450	087	13	20.86	44	51.88	3340	Sediment
JC07-D09	OCC1319 E above corrug.	088	13	19.15	44	56.06	2354	088	13	19.15	44	56.79	2173	Dolerite
JC07-D10	OCC1319 corrug. N	088	13	20.57	44	53.42	3187	089	13	19.36	44	55.30	2531	Basalt
JC07-D11	AVR S of OCC1319	088	13	16.39	44	52.31	3740	089	13	16.33	44	51.61	3202	Basalt
JC07-D12	Valley wall F opp. OCC1319	089	13	18.27	44	46.93	3457	089	13	18.24	44	46.40	3049	Basalt
JC07-D13	Toe OCC1319 corrug. surface	089	13	19.13	44	53.23	3196	090	13	20.02	44	53.84	3153	Peridotite
JC07-D14	Inter-AVR terrain E OCC1319	090	13	19.54	44	51.55	3500	090	13	20.49	44	52.36	3414	Basalt
JC07-D15	AVR far south	091	13	04.18	44	05.33	4496	091	13	03.98	44	49.17	4270	Basalt
JC07-D16	Valley floor/wall E	091	13	01.62	44	50.33	4820	091	13	01.57	44	49.27	4498	Basalt
JC07-D17	Valley floor	091	12	58.52	44	50.01	4610	091	12	59.37	44	50.22	4581	Basalt
JC07-D18	W wall above Ashadze	092	12	57.61	44	56.27	3343	092	12	57.83	44	56.69	3060	(Lost)
JC07-D19	AVR centre N of Marathon FZ	092	12	46.85	44	50.31	4094	092	12	46.89	44	51.10	4081	Basalt
JC07-D20	W wall above Ashadze	092	12	59.18	44	55.91	2866	093	13	00.20	44	56.95	2158	Basalt/dolerite/gabbro
JC07-D21	Lower slope W valley wall	093	13	01.11	44	51.43	4357	093	13	01.05	44	52.75	3821	Peridotite
JC07-D22	Toe OCC13130 corrug.	096	13	30.94	44	54.13	2949	096	13	30.35	44	54.29	2641	(Lost)
JC07-D23	Toe OCC13130 corrug.	096	13	30.58	44	53.93	2854	096	13	30.60	44	54.36	2659	Basalt
JC07-D24	AVR N OCC1330	096	13	21.19	44	54.14	3011	097	13	31.78	44	53.16	2882	Basalt
JC07-D25	AVR between OCC1319/30	097	13	24.06	44	53.13	3857	097	13	24.05	44	52.56	3790	Basalt
JC07-D26	AVR between OCC1330/48	097	13	39.57	44	57.96	3496	097	13	39.88	44	58.32	3240	Basalt
JC07-D27	Terrace below OCC1348	097	13	48.18	44	57.88	3164	097	13	48.34	44	57.17	2942	Basalt
JC07-D28	Flank of OCC1348	099	13	50.58	44	56.27	2768	099	13	49.59	44	54.27	2044	Peridotite
JC07-D29	AVR N of OCC1348	099	13	54.15	45	01.83	3181	099	13	54.15	45	01.58	3135	Basalt
JC07-D30	AVR centre 14N segment	099	14	05.12	45	01.24	2970	100	14	06.05	45	00.91	2876	Basalt

Table 2.2.3. Summary of dredging sites with locality descriptions. JD (Julian day), lat° (latitude degrees), lat' (latitude decimal minutes), lon° (longitude degrees), lon' (longitude decimal minutes) and depth in metres are for ship position at start and end dredge points. Primary lithology summary is from Searle *et al.* (2007). A detailed lithology summary is given in *Section 3.2.2*.

2.3. Bathymetric data acquisition and processing

High-resolution mapping of seafloor topography forms an integral part of marine geophysical research. Throughout JC07, a hull-mounted Simrad EM120 multibeam echo-sounder collected swath-bathymetry data. The system operated at a frequency of 12 kHz, with 191 individual beams calculating a depth to the seafloor. At an average water depth of 4000 metres, this equates to a single beam footprint of approximately 70 x 70 metres and maximum swath width of roughly 16 kilometres. Vertical resolution is typically 0.2% of the water depth (Mienert & Weaver, 2002). Data were processed onboard the ship using Simrad's Neptune software package, which primarily involved spike removal and navigational smoothing. Geo-referenced data were then supplied in ASCII-xyz format (Searle *et al.*, 2007).

Using the Generic Mapping Tools (GMT – Wessel & Smith, 1998), data were gridded at a resolution of 50 metres (Figure 2.3.1a-b). This has in some instances been sub-sampled to allow integration with the 100-metre resolution data collected during R/V *Knorr* leg 182 (D. Smith, *personal comm.*), which is itself an amalgamation of data collected during the *Faranaut* research cruise (Escartin & Cannat, 1999), YK98-05 (Fujiwara *et al.*, 2003) and JR63 (MacLeod *et al.*, 2001). All GMT grid files were converted into digital elevation models so that they could be analysed using *Fledermaus* 3D visualisation software (these data, including sidescan sonar mosaics and geological maps of the 13°N region are included on DVD in Appendix II). Viewing the data in 3D proved beneficial as it allowed for the subtle details of the seafloor topography to be detected more readily compared with a contoured, two-dimensional grid image. Final areal coverage of the bathymetry data collected throughout JC07 is approximately 6500 km^2 between geographic limits of 12°50'N to 14°10'N and 45°20'W to 44°35'W. The integrated bathymetry data set covers the entire MAR segment between the Fifteen-Twenty and Marathon Fracture Zones (Figure 2.3.2). Across axis, the data extend up to a distance of ~50-80 kilometres from the ridge axis.

In addition to the ship-mounted echo-sounder, it was also possible to obtain a depth estimate from the TOBI sidescan sonar. Pressure readings were converted into vehicle depth (depth (m) = pressure (Pa) / 1.028) and added to altitude values (determined by the first return of the sidescan sonar data). Close to the vehicle path, the sidescan samples an area of approximately 4 x 9 metres (along-track x across-track)

at a sampling frequency (0.25 Hz) that equates to an along-track resolution of ~3 metres and a sample footprint less than 1% of the multibeam data. The high-resolution TOBI profiles match closely with the data collected with the ship's echosounder, although it should be noted that differences may occur because TOBI doesn't follow the ship's path perfectly (Figure 2.3.3). When the data are considered over a broader scale (e.g. along the entire length of a survey line), these differences are insignificant. However, when it is desirable to obtain accurate information, for example regarding the gradient and number of faults about the ridge axis, the TOBI depth profiles are advantageous, as they resolve fault scarps into a number of higher angle, short slopes, rather than a single, less steep scarp as imaged with the Simrad EM120 (Figure 2.3.3). It should also be noted that seafloor video reconnaissance (using the rock drill) demonstrated that vertical cliffs several tens of metres high occurred yet were not resolved in either bathymetry dataset (Searle *et al.*, 2007).

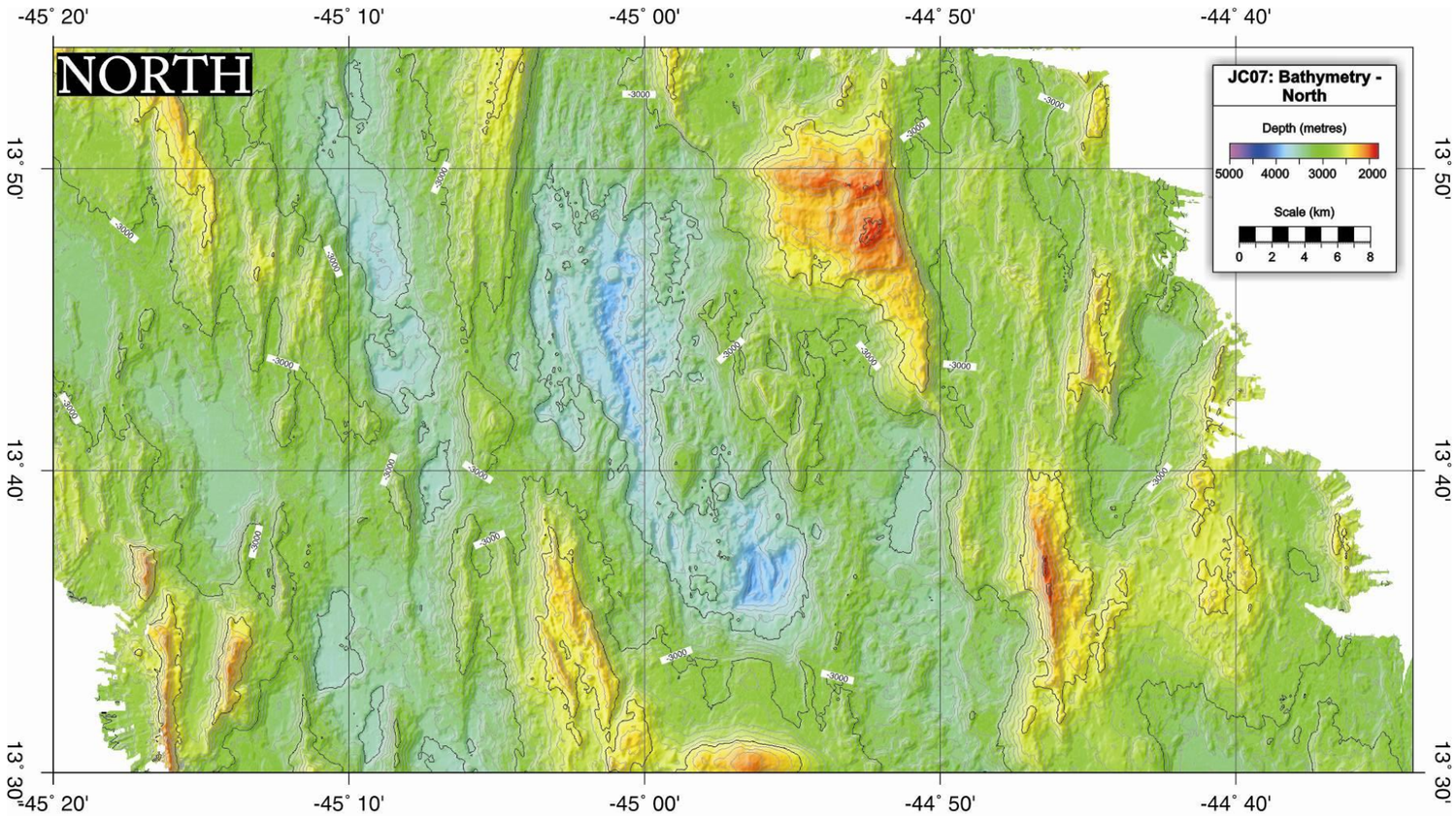


Figure 2.3.1a. Bathymetric map of northern half of JC07 survey area. Raw data were processed using Neptune to remove acquisition artefacts. Data were then gridded using a surface-fitting algorithm with a tension parameter of 0.2 in GMT. Blue-tones are bathymetric deeps, red tones are bathymetric peaks. MAR axial valley is bathymetric deep running North to South between 45°05'W and 44°50'W longitude. Scale is 1:360000. Contouring at 100 metre intervals, illumination from NW.

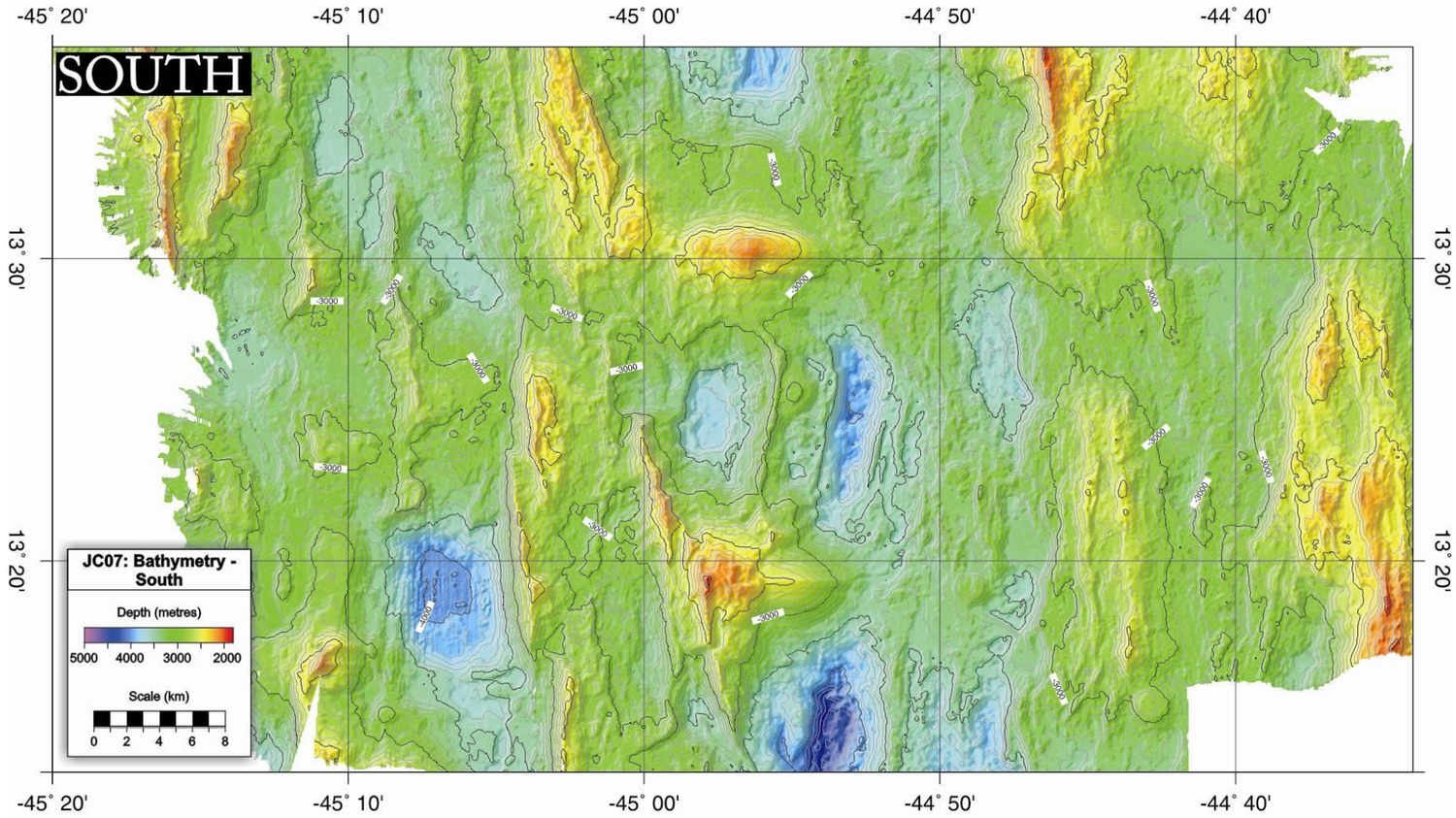


Figure 2.3.1b. Bathymetric map of southern half of JC07 survey area. Raw data were processed using Neptune to remove acquisition artefacts. Data were then gridded using a surface-fitting algorithm with a tension parameter of 0.2 in GMT. Blue-tones are bathymetric deeps, red tones are bathymetric peaks. MAR axial valley is bathymetric deep running North to South between 45°00'W and 44°45'W longitude. Scale is 1:360000. Contouring and illumination are the same as **Figure 2.3.1a**.

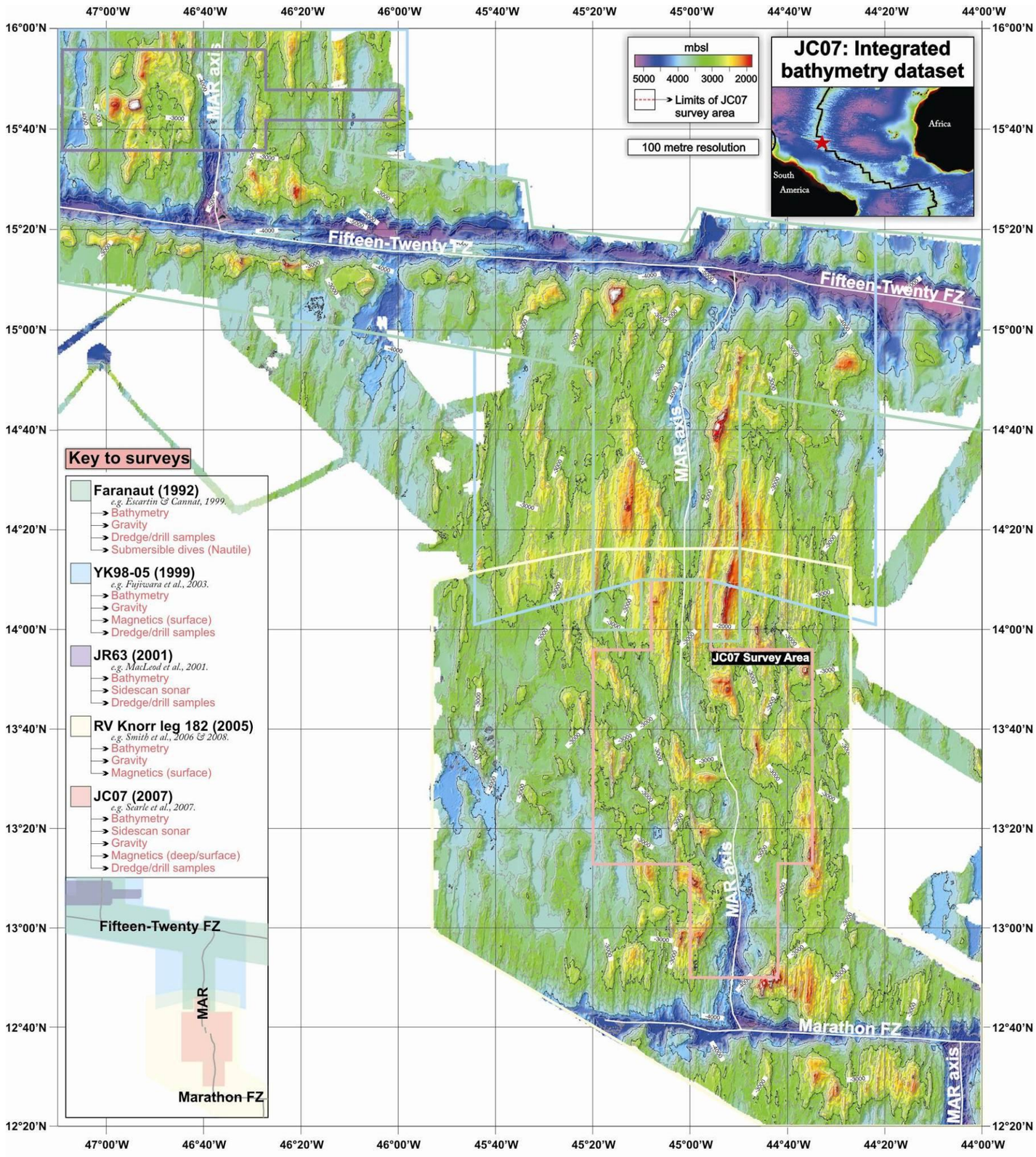


Figure 2.3.2 Integrated bathymetry dataset gridded at 100 metre resolution. The limits of noteworthy previous studies are shown and have been annotated to highlight published datasets from the Fifteen Twenty FZ region (key - lower left). All bathymetry data prior to JC07 were compiled by D. Smith (*personal comms.*). Contours are at 250 metre intervals, with illumination from NW.

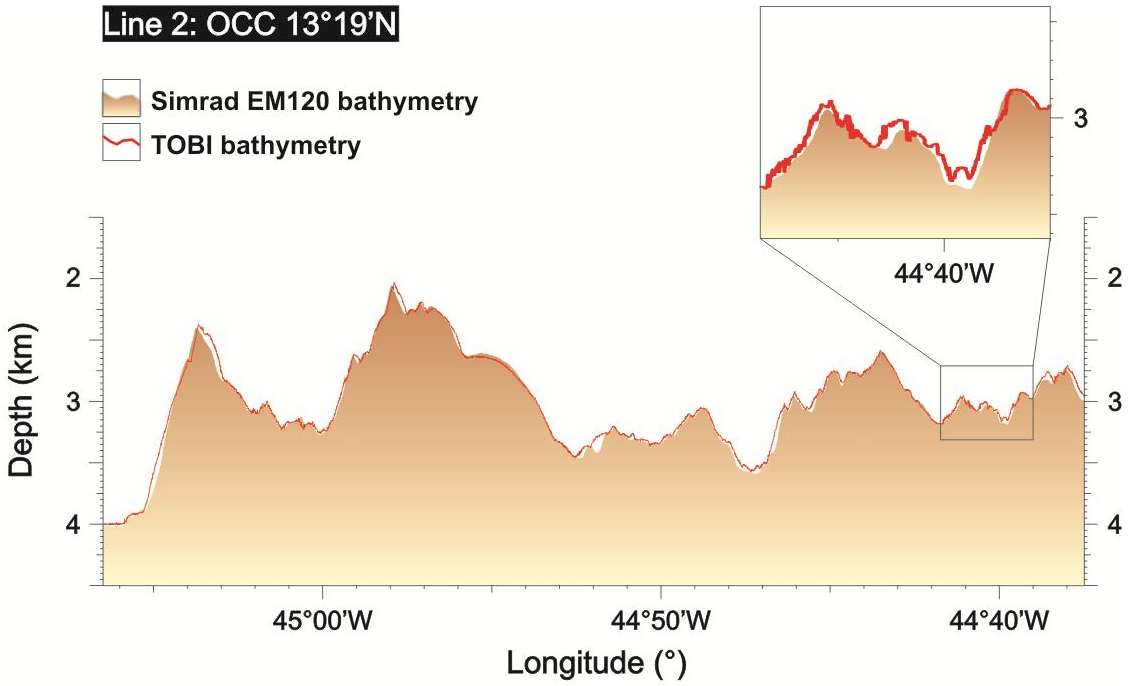


Figure 2.3.3. Comparison of hull-mounted Simrad EM120 multibeam echo-sounder profile (shaded section) and bathymetry profile calculated from TOBI depth and altitude estimates (red line). The TOBI depth profiles contain a greater amount of detail (inset). Larger-offsets are likely to be caused by miscalculations in TOBI position. See text for discussion.

2.4. TOBI sidescan sonar survey configuration

TOBI contains a 30 – 32 kHz sidescan sonar system that transmits two fan-shaped pulses of high-frequency acoustic waves towards the seafloor. Upon incidence with the seafloor, the waves are scattered back towards the vehicle where they are collected by the acoustic receivers. Acoustic energy is advantageous compared with other energy sources as its relatively low attenuation in seawater allows for surveying to be conducted at a higher altitude, imaging larger swathes of the seabed in the process (e.g. Urick, 1983; Tolstoy, 1987). As with most geophysical techniques, a trade-off exists between resolution and penetration (as in this case range – i.e. penetration through seawater). Higher frequency systems resolve smaller seafloor features but have a reduced swath width relative to their lower frequency counterparts.

TOBI's sidescan sonar is able to insonify a strip of seafloor 6 km wide (3 km each to port and starboard) whilst maintaining a reasonable signal-to-noise ratio (Flewellen *et al.*, 1993). A time-dependent gain function is applied to the backscattered signal to account for transmission loss due to geometrical spreading and attenuation in seawater. Data coverage is achieved by 'flying' the vehicle at an approximately constant altitude of 400 metres above the seafloor (Figure 2.2.3). The area of the insonified strip is governed by the beam and grazing angles (that is, the angle in which the beam spreads in a horizontal plane and the angle between seafloor and incident wave, respectively), the acoustic pulse transmission length (2.8 ms) and also the sampling window and survey speed (Figure 2.4.1). Hence, near- and far-range pixels differ in size such that close to the vehicle path they are elongate in the across-track direction and short in the along-track direction, and at the distal ends of the swath they have a short across-track dimension and are elongate along-track. The backscattered signal is digitally sampled by the port and starboard receivers at a frequency of 1 kHz, which, combined with an acoustic transmission cycle, or 'ping' repetition rate of 4 seconds provides 8000 samples per 6 km swath. Having the port and starboard transducer arrays operate at different frequencies minimises the possibility of interference between the two halves of the swath. Considering that the pulse transmission length is 2.8 ms and that the nominal sampling resolution is 0.75 metres, TOBI data are slightly oversampled (Le Bas, 2005).

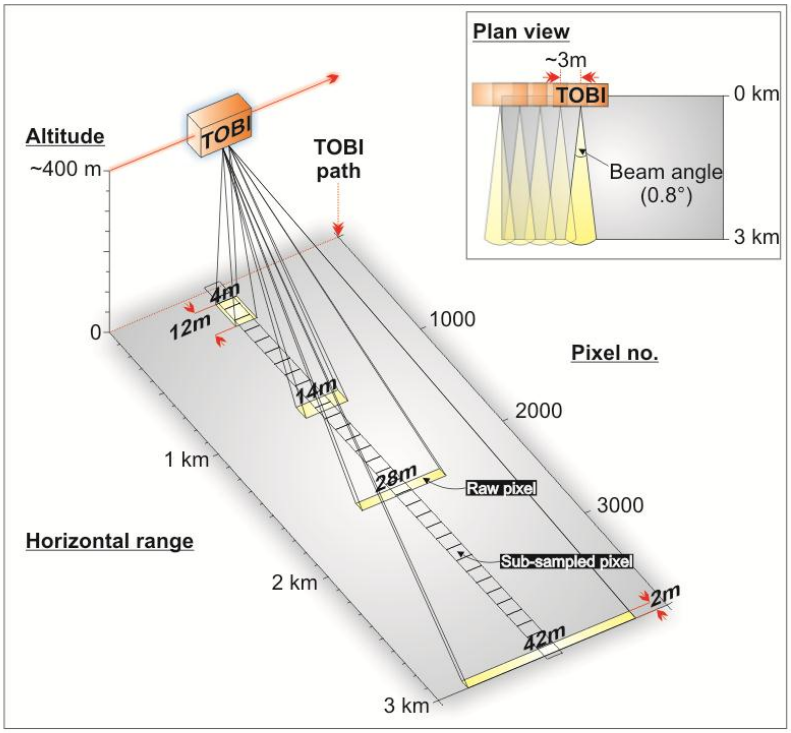


Figure 2.4.1 TOBI sidescan sonar beam pattern. Near- and far-range pixels differ in across- by along-track ratio due to variation in beam and grazing angles. Data are recorded at a frequency of 1 kHz and are hence over-sampled. Sub-sampling by a factor of 4 down-range (i.e. averaging 4 successive pixels) is done to match the approximate along track sampling interval, giving a final pixel resolution of 3-by-3 metres.

It is common practice to sub-sample sidescan sonar data (i.e. to average successive pixels) in the across-track direction so that it matches the along-track sampling resolution (which is a function of survey speed) as this increases the signal-to-noise ratio and eliminates redundant data. For example, at an average along-track sampling interval of 3 metres, the across-track data (at 0.75 metre resolution) must be averaged over 4 pixels to give an equal along- by across-track resolution. The practical application of this process is discussed in *Section 2.4.2*.

2.4.1. The backscatter model

Depth of acoustic penetration into the immediate subsurface has a large affect on the final sidescan sonar imagery. Essentially, imagery represents the average acoustic scattering strength of the upper portion of the seabed, rather than the exact nature of the surficial seawater/seafloor boundary. Direct evidence of this effect was obtained during cruise 6/90 of the MV *Farnella*, where it was observed that TOBI's relatively high frequency sidescan sonar did not image 'seafloor' features which had previously

been mapped using the lower frequency GLORIA sidescan sonar array, confirming that the features in question must lie at different depths beneath the surface (Masson & Gardner, 1991). The extent of acoustic infiltration into the seafloor is largely unknown, the precise value being a function of the frequency of the incident sound waves and the composition of the seabed and immediate subsurface. It is widely believed that "significant" sediment penetration occurs when the incident waves have a frequency of less than 12 kHz (Johnson & Helferty, 1990; Blondel & Murton, 1997). Furthermore, Mitchell (1993) shows that for a grazing angle of 30° the expected depth of penetration for a 6.5 – 12 kHz acoustic wave would be 5 – 30 metres, decreasing to ~0.5 – 0.8 metres at frequencies of 100 kHz. Penetration with TOBI's 30 – 32 kHz sidescan sonar should in theory reach no further than 1 metre (Urick, 1983), although in some instances it has been estimated to penetrate 2 – 5 metres (Lawson, 1996). At a sedimentation rate of 5 – 10 m/Ma (Mitchell *et al.*, 1998a), this implies that TOBI can effectively identify volcanic features at ages of < 1 Ma. The causes of acoustic attenuation are discussed more fully below.

The intensity of the recovered signal, or backscatter, is dependent on a combination of factors, such as the grazing angle between acoustic wave and seafloor and the physical composition of the seafloor (with the ratio of backscattered to incident energy being the "backscatter coefficient"). The majority of acoustic energy is reflected in the across-track direction, away from the receivers, and it is only a relatively small proportion that is backscattered. Figure 2.4.2 demonstrates the three primary mechanisms by which sound is directed back towards the vehicle, namely: volume reverberation in sediments, diffraction of sound when the seafloor exhibits a high acoustic impedance contrast and roughness, and specular reflection as from a mirror or plane faceted surface (Johnson & Helferty, 1990). Acoustic shadowing occurs when the beam emitted from the vehicle's transducers does not have the necessary line of sight to image the seafloor. This is most commonly observed across terrains that exhibit significant variations in topographic relief. It is sometimes necessary to conduct a number of passes over the same area of seafloor, so that key features can be insonified from various directions, minimising the amount of shadowing within the data. However, over small areas, this shadowing effect may enhance the textural content of the data, aiding interpretation (e.g. surveys over hummocky neovolcanic terrain).

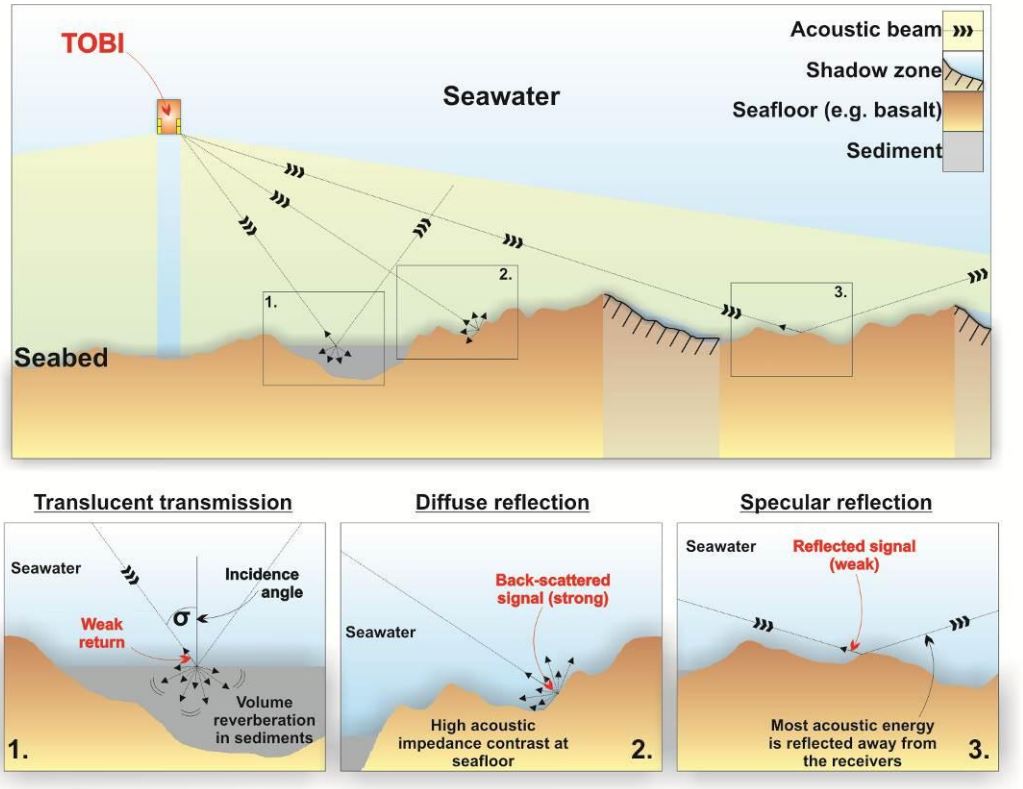


Figure 2.4.2. Acoustic backscatter patterns at the seabed. There are a number of factors which affect the degree of backscatter. Compositionally 'soft' features, such as sediment, absorb acoustic energy and begin to reverberate, returning only a small amount of energy to the vehicle in the process (**1**). Alternatively, high acoustic impedence contrasts at a rough seabed (e.g. if basalt is exposed at the surface) generate a large back-scattered signal through diffuse reflection (i.e. diffraction), which is increased further if the grazing angle is near normal to the seafloor and/or the wavelength of the incident signal matches closely that of the microscale roughness of the seafloor (**2**). The majority of the acoustic energy is reflected in the across-track direction away from the vehicle, with a small amount returning from specular reflection (this situation may also occur in older, compacted sediment) (**3**). Micro-scale roughness and sediment grain size also affect the degree of backscatter. See text for discussion. (Adapted from; Johnson & Helferty, 1990 and Lawson, 1996.)

Jackson *et al*. (1986) show that the backscattering potential of the seafloor is highly dependent on the grazing angle of the incident waves (Figure 2.4.3a). Based on shallow water observations at high frequencies: scattering strength is seen to decrease with decreasing grazing angle, and subsequently increase as grazing angle becomes near normal to the seafloor. These conclusions may be expanded to explain some of the observed seafloor backscatter properties in a geological sense. For example, flat surfaces inclined towards the vehicle such that the grazing angle of the sonar energy is near normal to the seafloor, which may be analogous to scarps or fault surfaces, generate a high acoustic backscatter pattern.

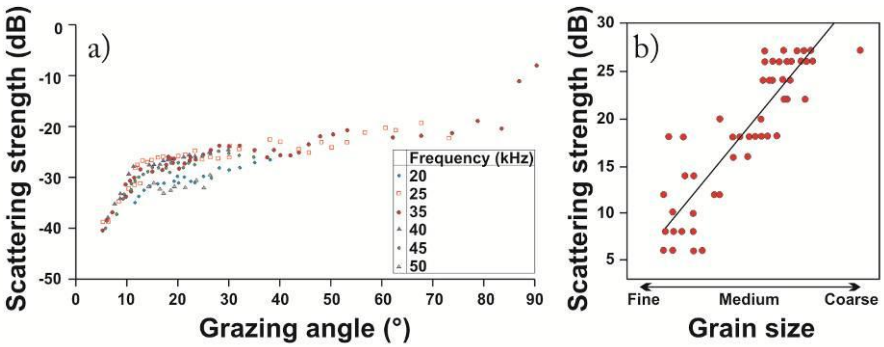


Figure 2.4.3a-b. There are a number of factors which affect backscatter strength, such as: **a)** the local geometry of the incident wave (i.e. grazing angle) and **b)** the composition of the seafloor (e.g. grain size). See text for disucssion. **a)** and **b)** are re-drawn from Jackson *et al*. (1986) and Davis *et al*. (1996), respectively.

Depending on across-track location, the effect of a sub-horizontal sediment pond may be to reduce the grazing angle and therefore the backscattering potential, with Lambert's Law stating that backscatter strength 'varies as the square of the sine of the grazing angle'. This relationship, however, is only applicable to very simple situations such as smooth seafloors and large-scale undulations (Blondel & Murton, 1997).

In the same study, Jackson *et al*. (1986) observe little spatial variability in backscattering strength along a survey profile that crosses coarse- and fine-grained sand, concluding that grain size is not a major factor in the backscattering potential of the seafloor. Contrary to this, Davis *et al*. (1996) have demonstrated that variations in backscatter strength may be directly related to grain size and surficial composition, with coarse-grained sediments reflecting more acoustic energy than fine-grained sediments (Figure 2.4.3b). Thus it seems likely that the exact contribution of grain size is largely dependent on the sonar wavelength. Composition and micro-scale roughness also greatly affect the seafloor backscatter coefficient, where compositionally 'soft' features like sediment absorb more energy (and hence re-radiate less acoustic energy) relative to 'hard' features such as bare rock outcrops. At MORs, persistent sedimentation blankets the seafloor, and hence it is generally only recent, un-sedimented neovolcanic material that is associated with a significant high backscatter. Older off-axis material has undergone millions of years of sedimentation, and it is this sediment cover which absorbs much of the acoustic signal, resulting in a low-backscatter environment. Micro-scale roughness of the seabed may increase the backscatter coefficient if the micro-topographic wavelength is greater than that of the incident waves (which is in TOBI's case ~ 4cm; Blondel & Murton, 1997).

2.4.2. Sidescan sonar data acquisition and pre-processing

Sidescan sonar data were collected by TOBI with a four-second ping rate, at an altitude of approximately 400 metres above the seafloor. The total swath width of the sonar footprint at this altitude is roughly 6 km (i.e. 3 km in both the port and starboard directions). Survey lines were conducted at a spacing of 6 km in order that the greatest area of seafloor could be surveyed in the time available, minimising the overlap of adjacent sonar profiles and hence meaning that the seafloor was in most cases only insonified in one direction (Figure 2.2.2). The TOBI system performed flawlessly throughout the first week of the two week deep-towed survey, but after this point numerous failures of the system (attributed to seawater influx into the tow cable) meant that the survey eventually had to be cancelled two days before the scheduled completion date.

A flowchart summarising the sidescan sonar data processing methods is shown in Figure 2.4.4. Data were supplied by the TOBI team in netCDF format, which is an I/O library accessible via FORTRAN. This is beneficial as it allows for the header part of the TOBI data file (containing information on, for example, vehicle attitude at the time of each ping – *Section 2.4.3.1*) to be processed independently of the imagery part, which is stored in flat-file form (e.g. a table format, with a backscatter value for each pixel). Each TOBI data file related to approximately 16 hours of surveying, with a line of header information for each of the ~14000 pings per file. Sub-sampling of TOBI data is usually done by a factor of 8 to give an image-resolution of 6 metres (based on a nominal across-track resolution of 0.75 metres – *Section 2.4*). However, during research cruise JC07 the survey speed was slow enough that sidescan sonar data were effectively collected at 3 metre increments along-track, and hence upon import to the PRISM (Processing of Remotely-sensed Imagery for Seafloor Mapping - Le Bas, 2005) processing suite, the data were sub-sampled by a factor of 4 to give an image-resolution of 3 metres. Furthermore, it was found that sub-sampling by a factor of 8 greatly reduced the dynamic range of the data, with imagery seemingly taking on either a black or white appearance. Full resolution data (i.e. no sub-sampling) required too much disk space to be practicable.

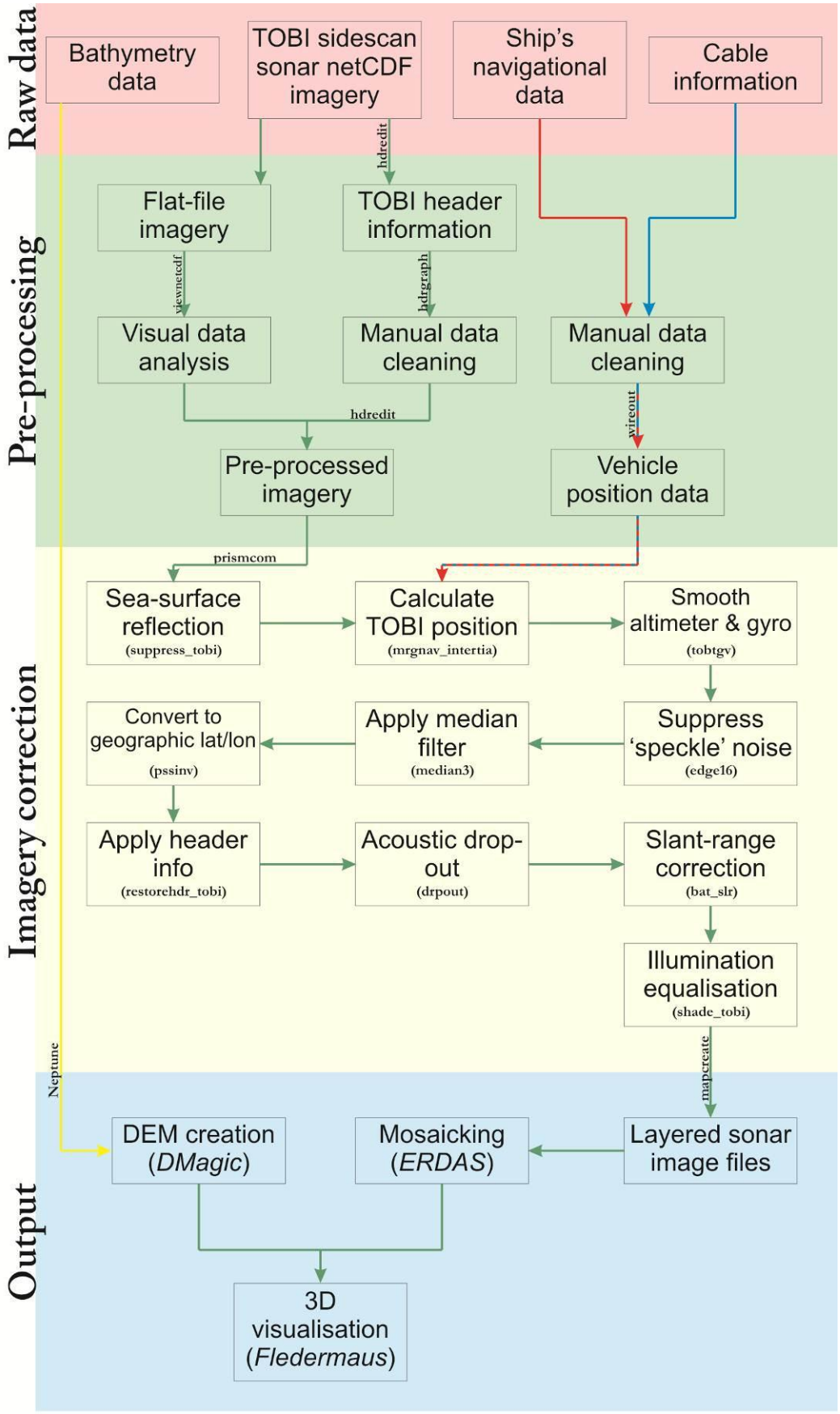


Figure 2.4.4. Flow-chart for processing of TOBI sidescan sonar imagery from raw data format to visualisation with *Fledermaus*. Imagery correction is performed with PRISM. The names of processing commands are given in small font. See text for discussion.

Prior to processing the imagery data, it was necessary to merge the TOBI data files with the ship's navigation file (pink and green sections – Figure 2.4.4). PRISM contains a program that, when provided with cable information in an additional file, predicts the position of TOBI based on dynamic modelling of cable length. This essentially geo-references the sidescan sonar pings, and is therefore an important step in making a precise picture of the seabed. Ship's navigation and cable information occasionally contained erroneous values that were accounted for by either removing them manually or by using one of PRISM's many automated routines, the use of which are discussed in the following section.

2.4.3. Sidescan sonar imagery processing with PRISM

PRISM contains a collection of customisable subroutines that are designed to minimise acquisition artefacts and increase signal-to-noise ratio. Trial and error was generally found to be the most successful method by which to assess the suppression of various artefacts, with the processing parameters varied at each stage to assess their effect on data quality. The next few sections give an overview of the main causes of noise inherent within the sidescan sonar imagery and the measures taken to suppress them, before the final processing configuration is outlined. Header information is part of the pre-processing (green) section of the flowchart in Figure 2.4.4, with all other PRISM commands falling under the imagery processing (yellow) section.

2.4.3.1. Header information

The `headergraph` subroutine in PRISM allows for rapid assessment of the quality of all the data contained within the header part of each TOBI data file. It was found that header information usually contained 10-15 data spikes per file (Figure 2.4.5). These spikes are seemingly innocuous given the shear volume of data that was collected, but failure to remove them was discovered to result in miscalculations of TOBI's depth and position. In one instance it was found that a spike in all the header information at the start of a file caused a small section (~100 metres) of the final mosaic to be repeated twice. Likewise, an uncorrected spike in pressure information means that there will subsequently be a spike in predicted TOBI depth and hence seafloor depth, and related imagery pixels will be misplaced.

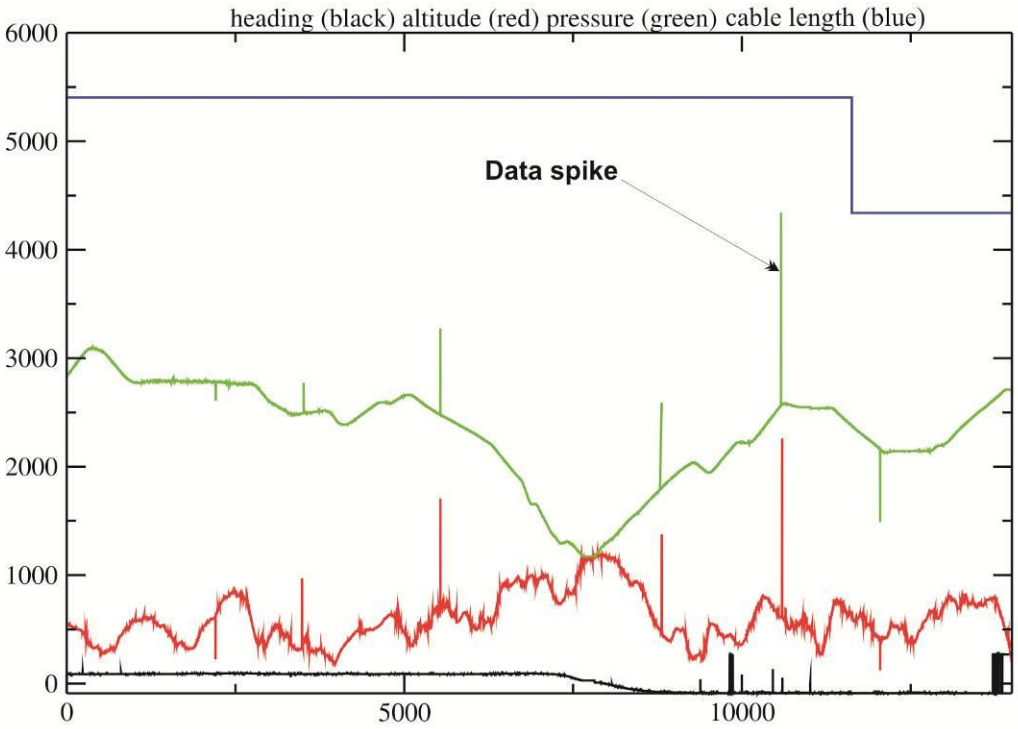


Figure 2.4.5 Example of TOBI data file header information, displayed using PRISM's *headergraph* subroutine (x-axis is along-track ping number). There are clearly a number of spikes in the pressure and altitude data. This type of erroneous measurement was corrected manually in a text editor. The header file was then re-applied to the sonar imagery (netCDF) file. All TOBI header data were cleaned using this method.

Single erroneous values were generally easiest to correct manually in a text editor. The corrected header data could then be re-applied to the netCDF file using PRISM's `hdredit` command. However, in addition to single spikes of anomalous values, it was found that there were also large sections of data that showed no variation, where the TOBI sensors had apparently 'locked-up'. In these instances, the data were linearly interpolated between the first and last 'good' values either side of the erroneous values. In a few extreme cases, where the data gaps related to distances greater than, for example, 100 metres along profile, it was necessary to fill in the gaps in calculated water depth using information from the ship's bathymetry file/echosounder data.

In addition to cleaning the TOBI data file header information of erroneous values, the ship's navigation and cable length information (co-registered with time) were processed to remove data spikes and anomalous values. Latitude and longitude values were smoothed over 20 readings to suppress jitter between successive sonar pings and improve the clarity of the final mosaic. Cable information also contained data gaps for periods of the order of several minutes that had to be corrected manually in a text editor.

2.4.3.2. Sea-surface reflection

Sea-surface reflections are generated by a small proportion of acoustic energy that, rather than travelling towards the seafloor, travel upwards to the sea-surface and then back down towards TOBI. The high acoustic impedance contrast between seawater and air means that this artefact is usually visible as a high backscatter line running along the edges of the sidescan sonar profiles. Detection of this artefact is achieved by analysing the backscatter intensity along the extent of each sonar ping, and if the variation within a given spatial window exceeds a threshold value before returning to background levels then this area is flagged as being a sea-surface reflection. Removal is achieved by interpolation of values either side of the reflection using the `suppress_tobi` command. PRISM is generally quite efficient at removing most sea-surface reflections, with the final image containing only faint dark lines along the edges of profiles (Figure 2.4.6). There are some instances where PRISM struggles to suppress sea-surface reflections, usually when the background backscatter level is quite high (e.g. over the neovolcanic zone).

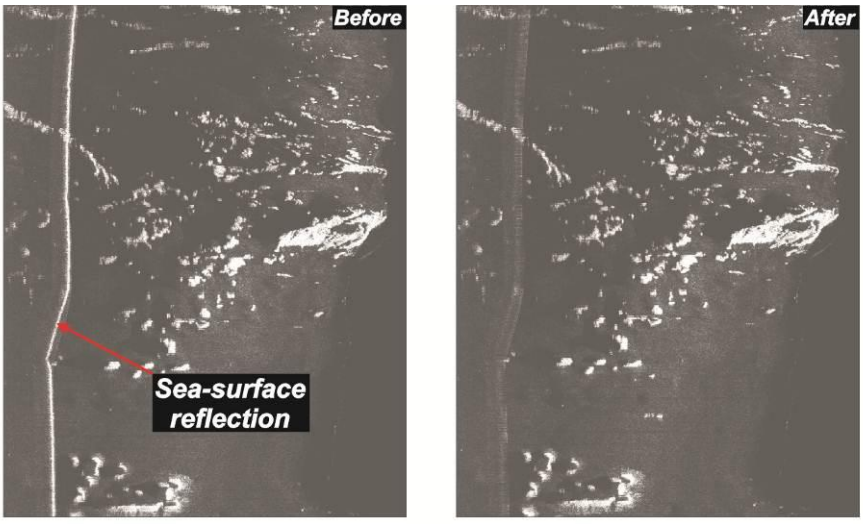


Figure 2.4.6 Sea-surface reflection suppression using PRISM. The reflection is apparent as a high-backscatter white stripe along the edges of sidescan sonar profiles (left image). In most cases the artefact is adequately suppressed, leaving only a faint blur in the final mosaic (right image).

2.4.3.3. Acoustic drop-out

Excessive vehicle motion can have an adverse effect on the amount of signal collected by TOBI's receivers. For example: if vehicle yaw exceeds the fore-aft beam width during a single acoustic transmission cycle, then the vehicle will be so physically misaligned that it cannot receive any of the backscattered signal. This effect is most prevalent when veering cable to go down steep slopes, resulting in the data containing stripes of zero amplitude. These stripes may occur across the entire across-track duration of an acoustic transmission cycle or only partially – depending on the point at which vehicle yaw exceeded beam width. Similar to the removal of sea-surface reflections, drop-out removal is first achieved by searching along-track for an area of anomalously low backscatter (defined by a threshold value) and then by averaging across successive pings (using the `drpout` command). Acoustic dropouts were in most cases corrected to within acceptable limits (Figure 2.4.7).

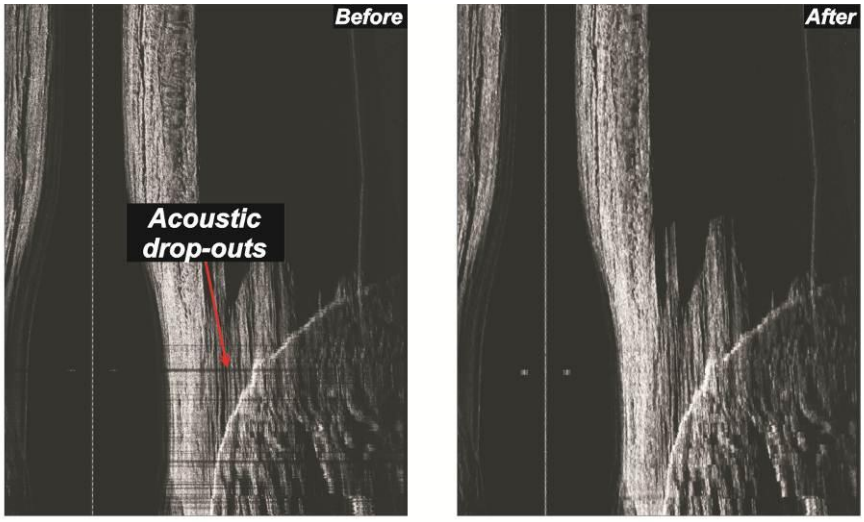


Figure 2.4.7 Acoustic drop-out suppression using PRISM. Drop-outs occur when vehicle yaw exceeds beam sensitivity (left image). Correction is mainly for aesthetic purposes. The final mosaic (right image) displays only very faint blurring where drop-outs have been removed by interpolation of adjacent sonar pings.

2.4.3.4. Slant-range correction

Backscattered acoustic energy arrives at the vehicle having travelled in a direct line between transducer and seafloor target. This slant-range distance is not a true measure of the across-track position of the target and hence it must be converted into horizontal distance. Traditionally, a conversion is applied using the vehicle's altitude and by assuming that the seafloor acts as a flat horizontal plane. In areas of large-scale topographic relief, the assumption of a planar horizontal seafloor is clearly inadequate, as demonstrated by Figure 2.4.8 (Johnson & Helferty, 1990). Targets which are upslope of the vehicle are displaced closer to the vehicle track, where as downslope targets are displaced further outward than their true across-track position. The overall effect of this is to cause imagery distortion, whereby the summits of seamounts may be positioned outside their flanks, for example (Blondel & Murton, 1997); this effect is known as layover.

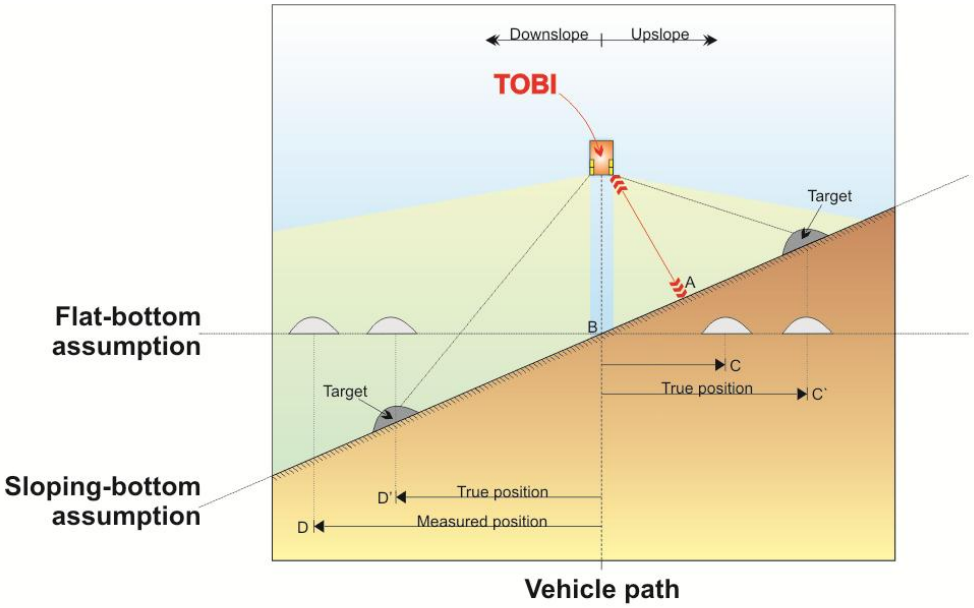


Figure 2.4.8 Regional slope causes objects to appear closer to or further from the track within the sidescan imagery than they actually are on the seafloor. In the above scenario, the first acoustic return is from point A. This point is assumed to be directly beneath the vehicle, however, it is clear that point B (which is further from the vehicle than point A) is actually beneath the vehicle. This starts the sidescan 'clock' too early, and hence the target (in this case the two dark grey seamounts) positions will be relative to point A rather than point B. Upslope targets will appear closer to the vehicle path (C) compared with their true position (C`). Conversely, downslope features will appear further away (D) than their true position (D`). Modified from Johnson & Helferty, 1990.

A correction applied assuming a horizontal seafloor is generally acceptable if the strikes of prominent topographic features are perpendicular to the vehicle path (that is to say there is little across-track topographic variation). This situation may be analogous to E-W survey lines across an N-S spreading ridge flanked by N-S trending abyssal hills. However, in the 13°N region, one of the distinguishing features is that topography is largely chaotic and that linear ridges are shorter, meaning that there is more across-track topographic variation. Thus a slant-range correction was applied based on the bathymetry data rather than assuming a flat, horizontal seafloor; application of this method was achieved by using PRISM's `batslr` subroutine.

2.4.3.5. Across-track illumination equalisation

The sensitivity of TOBI's sidescan sonar transducer array varies as a function of angle of incidence, such that pixels close to the vehicle (near-range) and at the edge of the swath (far-range) are weaker than those which scatter from the centre of the swath (mid-range). This is corrected for by applying the shading coefficient shown in Figure 2.4.9, which equates to factors of 1.2-1.4 for both near- and far-range pixels and 0.8 for mid-range pixels (Le Bas, 2005).

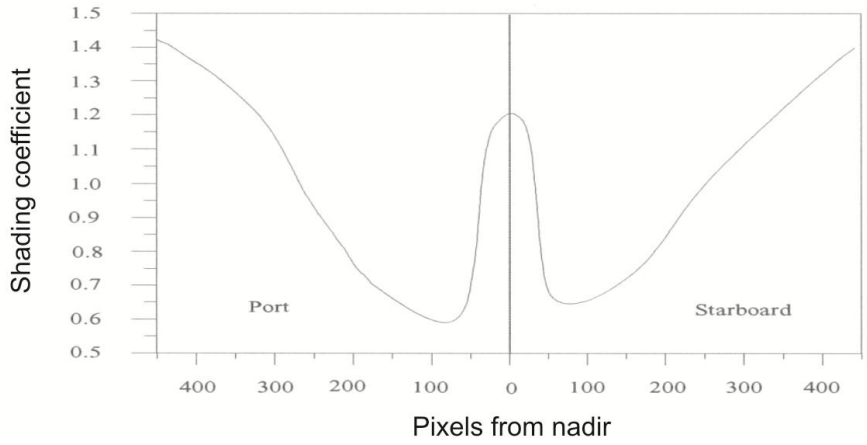


Figure 2.4.9. Shading coefficient applied to each sidescan sonar ping to compensate for varying beam sensitivity at different angles of incidence. From Le Bas, 2005.

2.4.3.6. Final PRISM processing configuration

The final processing scheme applied to the raw sidescan sonar imagery is given below (in the order in which it was applied), so that it may be used in future studies if necessary. Annotation has been added (%) to outline the purpose of each line of code. The sequence is applied using the `prismcom` command which locates the TOBI netCDF files and assigns them to the parameter `-i %1` (`-o %0` relates to the output file after each stage). All header information must be cleaned prior to applying the processing scheme.

% **Sea-surface reflection suppression**. See *Section 2.4.3.2* for a discussion on this acquisition artefact:

```
suppress_tobi -i %1 -o %0
```

% **Calculate TOBI position**. This was computed by dynamic modelling of cable data and ship's navigation information (contained within the file specified by -n), assuming an umbilical length (-u) of 202 metres:

```
mrgnav_inertia -i %1 -o %0 -u 202 -n navfile.veh_nav
```

% **Smooth altimeter and heading data**. This stage is essential as there is a certain amount of 'jitter' contained within the altimeter and heading information (which occurs due to minor deviations in course). Without smoothing, the sonar pings collected during these course deviations overlap the data collected immediately before and after (forming what are known as 'bow-ties'). Data were averaged over 10 pings (-l) in order to minimise this effect:

```
tobtvg -i %1 -o %0 -l 10
```

% **Suppress 'speckle' noise**. Acoustic signals returning from the seafloor are not in phase and thus constructive and destructive interference occurs (Blondel & Murton, 1997). Speckle noise is the name given to these anomalously high- and low-backscatter returns that are not representative of seafloor morphology. A 3-by-3 cross-pattern median filter (-m) was used to assess if the central pixel along swath edges exceeded the median value by a certain amount, in which case the pixels were averaged (Le Bas *et al.*, 1995):

```
edge16 -i %1 -o %0 -m
```

% **Apply a 3-by-3 median filter**. A median filter is applied to the entire sidescan sonar dataset to suppress anomalous backscatter values:

```
median3 -i %1 -o %0
```

% **Conversion to geographical coordinate system**. In order to apply a slant-range correction based on the bathymetry data (as opposed to assuming a flat seafloor – *Section 2.4.3.4*), it is first necessary to determine the geographical coordinate of each sidescan sonar pixel. Map limits (-m) are specified, as is the type of projection, which is in this case Mercator WGS84. The relatively low resolution bathymetry data are re-gridded at the same resolution as the sonar data using a triangulation method (-t):

```
pssinv -i %1 -t -r res -o %0 -m ../cdf/map.dat -proj=merc -
ellps=WGS84 -lat_ts=0.0
```

% **Apply sidescan sonar header information**. This restores the header information to the imagery after it has been stripped during the geographical pixel registration:

```
restorehdr_tobi -i %1 -h %3
```

% **Acoustic drop-out suppression**. Refer to *Section 2.4.3.3* for a discussion on this acquisition artefact. This routine is applied twice with different sampling windows (-k) in order to account for partial and complete acoustic drop-outs. In each case, the threshold ratio value (-t) remains fixed, and the adjacent pings are interpolated (-f). A parallel processing technique (-p) is used to reduce computation time:

```
drpout -i %1 -o %0 -t 100 -f -p -k 201
drpout -i %1 -o %0 -t 100 -f -p -k 51
```

% **Slant-range correction**. Refer to *Section 2.4.3.4* for a discussion on this acquisition artefact. Bathymetry data file is represented by '%4' and the pixel resolution of the sidescan sonar imagery (-r) is specified as 3 metres:

```
batslr -i %4 , %2 -o %0 -r 3 –p
```

% **Across-track illumination equalisation**. This compensates for the effect of near- and far-range pixels appearing darker than mid-range pixels (which is caused by the varying sensitivity of the receiver at different angles of incidence) as discussed in *Section 2.4.3.5*. Near-, far- and mid-range pixel amplitudes were scaled using the coefficients shown in Figure 2.4.9:

```
shade_tobi -i %1 -o %0
```

2.4.4. Mosaicking of the sidescan sonar imagery

Using the `mapcreate` command, PRISM is able to subset the sidescan information into a series of maps which fill the survey area (the blue 'output' section of Figure 2.4.4). Sidescan sonar data were split and placed on separate 'layers' of each map when course deviation exceeded 20° over 20 successive pings. This frequency was chosen as it segmented the data around the turns at the end of survey lines (allowing for the best imagery to be kept), but did not unnecessarily segment the data when TOBI deviated slightly midway along profiles. Adjacent, overlapping layers of the processed image were viewed using *ERDAS Imagine*, which allowed for the layers that contained the most useful sidescan sonar imagery to be accepted, and the layers containing the least useful imagery to be rejected (the alternative is that the overlapping pixel information is averaged). As TOBI tracks were in most cases 6 km apart there was little overlapping imagery, and so most of the sidescan data were only split at the ends of survey profiles. At this stage, images were manually trimmed to remove any spurious segments of data that would otherwise have confused the final geological interpretation of the mosaic. These spurious segments were most commonly located around the turns at the end of survey profiles, due to rapid changes in vehicle altitude and the 'splaying' of pings (whereby data density is decreased around the far edges of the swath and increased in the centre of the turn).

Image files (which typically contained 2 – 4 layers of overlapping data) had to be reduced to one layer before the final mosaicking process could take place. Given the relatively little amount of overlap, this usually involved arbitrarily separating layers that overlapped by only a few tens of metres, little more than the resolution of the data. Survey lines 4, 5 and 6 were, however, only 3 km apart, and so the layers overlapped by the same margin. This required that the layers of the sonar mosaic around the OCC at 13°30'N had to be carefully selected, choosing only the segments of data which accentuated the OCC sidescan texture, particularly the footwall/hanging-wall contrast. After each map had been reduced to a single layer, mosaicking was performed using *ERDAS Imagine* to form a single sidescan sonar image of the region (Figure 2.4.10a-b). A gamma correction of the form: corrected image = Constant (1.2) x uncorrected image$^{\gamma}$ (where $\gamma = 0.9$) was applied to the imagery in order to improve the backscatter contrast, allowing more subtle textures to be identified. Bathymetry data were then overlain with the final sonar mosaic using the 'create textured SD file' command in

DMagic, allowing three-dimensional analysis with *Fledermaus* (Figures 2.4.10c-e). Detailed analysis of these images is given in the following chapter.

2.4.4.1. Re-navigation of sidescan sonar data

After mosaicking the sidescan sonar imagery it became apparent that some features within the imagery did not match the position of their topographic counterparts, perhaps highlighting a limitation of the slant-range correction in the presence of complex topography (despite the correction being applied based on bathymetry data). Miscalculations in TOBI's physical position had a similar effect on the imagery. This was corrected manually by identifying areas of mismatched data and measuring the offset and azimuth between sidescan sonar imagery and bathymetry. The points immediately before and after the mismatch where the sonar and bathymetry data were in agreement were also noted, so that the relevant segment of navigation data could be fit with a spline, removing the mismatch in the process. Corrections were usually of the order of 80 – 400 metres, although in a few extreme cases offsets between the sidescan sonar feature and bathymetric counterpart were ~700 metres. Approximately 4 or 5 offsets per survey profile had to be corrected in this way, and while the correction procedure was adequate to relocate most of the easily identifiable areas of mismatched data, its necessity serves to highlight a limitation of the acquisition and processing techniques, which may otherwise have led to large sources of error in the interpretation of the sidescan sonar imagery.



Figure 2.4.10a. Final TOBI sidescan sonar mosaic of northern half of JC07 survey area. Low-backscatter areas (dark shades) represent 'soft' features such as sediment or flat topography. Bright, high-backscatter areas are indicative of 'hard' features or surfaces inclined towards the sonar array, typically lava flows (i.e.young rock that has not yet been covered in sediment) and fault scarps. Raw data were processed using the PRISM processing suite. Rectangular black areas are zones of no data. Scale is 1:360000.

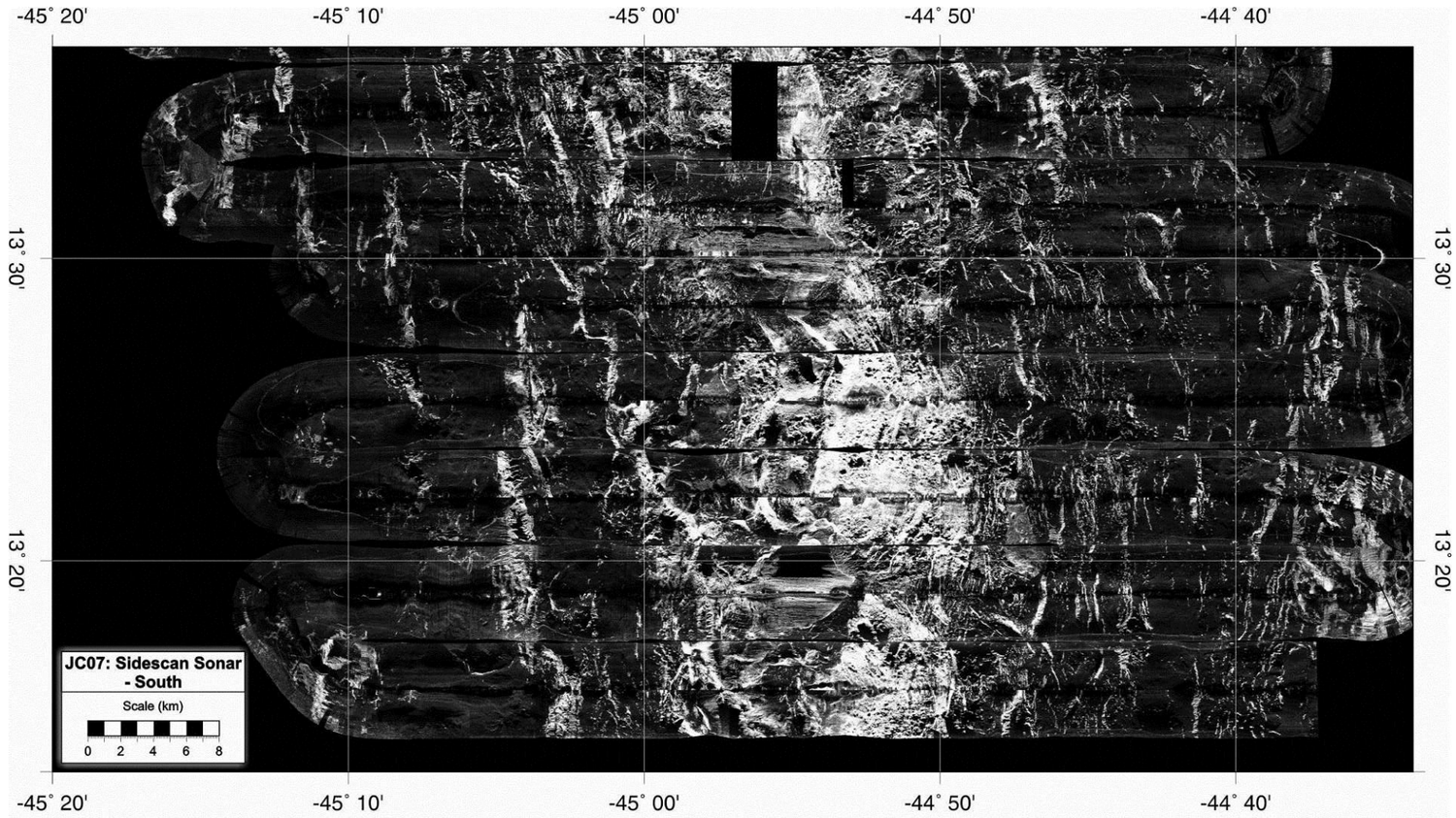


Figure 2.4.10b. Final TOBI sidescan sonar mosaic of southern half of JC07 survey area. Low-backscatter areas (dark shades) represent 'soft' features such as sediment or flat topography. Bright, high-backscatter areas are indicative of 'hard' features or surfaces inclined towards the sonar array, typically lava flows (i.e.young rock that has not yet been covered in sediment) and fault scarps. Raw data were processed using the PRISM processing suite. Rectangular black areas are zones of no data. Scale is 1:360000.

Figure 2.4.10c. Sidescan sonar imagery draped over bathymetry: view of an OCC at 44°55'W, 13°19'N; looking NW. Axial neovolcanic zone is just off lower-right of image; older sedimented seafloor is visible in upper-left. The core complex comprises two distinct sections: a smooth, domed section that is both corrugated and striated parallel with the direction of spreading and a section of generally more 'rugged' terrain and incoherent backscatter intensity. Vertical exaggeration is x2. Approximate width of field of view along lower edge of image is 8 km.

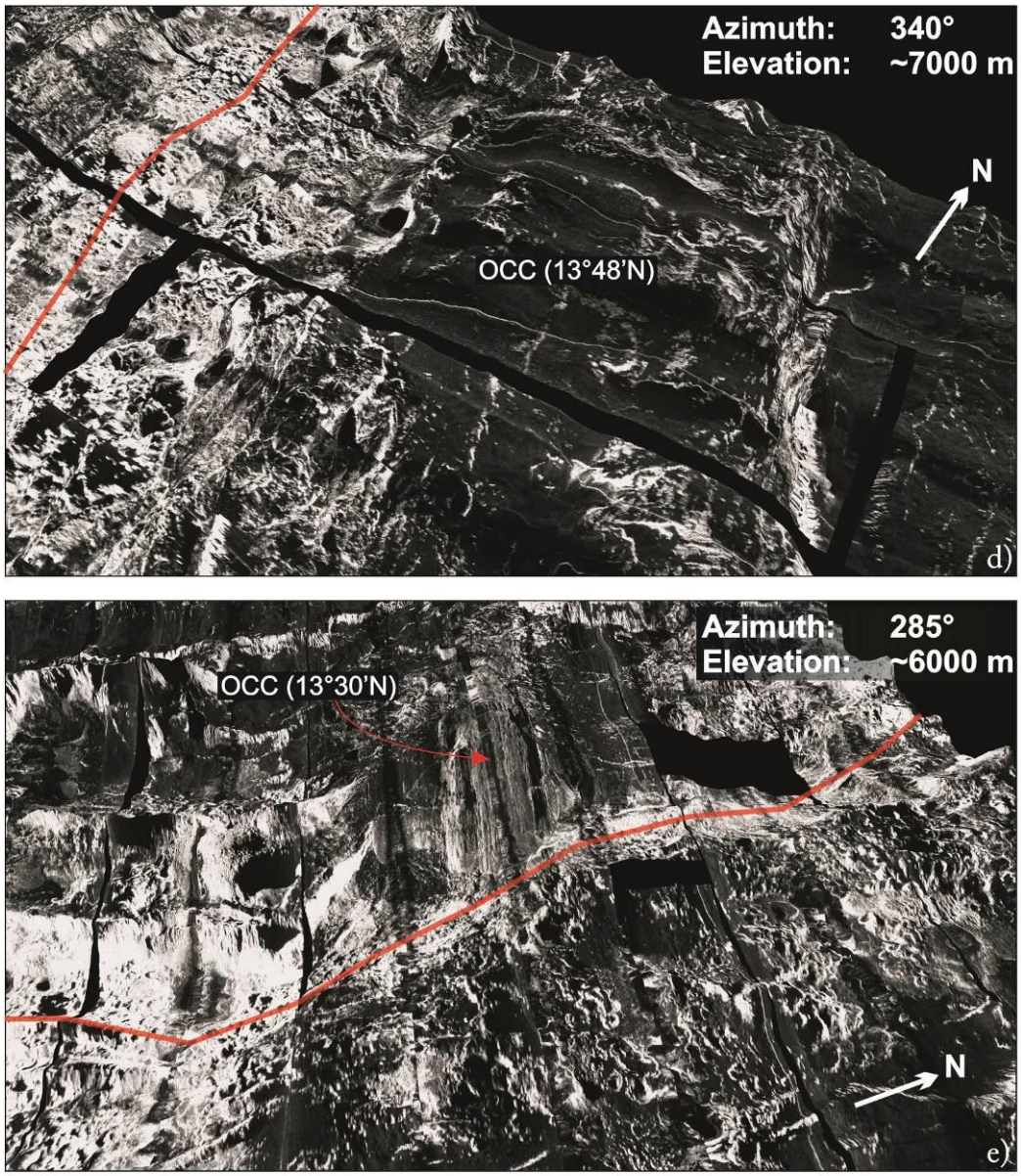


Figure 2.4.10d-e. Sidescan sonar imagery draped over bathymetry: **d)** view of OCC at 13°48'N and **e)** OCC at 13°30'N. Red line indicates position of ridge axis. Variable backscatter intensity between OCCs most likely represents difference in sediment cover (which is in turn a proxy for OCC age). Vertical exaggeration is x2.

2.5. Gravity field survey

Gravity data reflect the distribution of subsurface density heterogeneities that on a MOR-scale may be present due to lateral changes in lithology or significant crustal thickness variations. The standard procedure for processing marine gravity data is designed to isolate the sources of intra-crustal anomalies from anomalies of known origin (such as seafloor topography). In addition to geological sources of gravitational anomaly, gravity data contain a degree of noise generated by acceleration of the gravimeter, which may be due to ship motion, latitude variation and instrument drift. The processes by which these artefacts are removed forms the basis of this section.

2.5.1. Gravity data acquisition and reduction

Gravity measurements were carried out during research cruise JC07 using a shipboard gyroscopically stabilised Lacoste-Romberg gravimeter (S75). The gravimeter functioned continuously throughout the cruise and without any major problems. In transit to the survey area, it was observed that exporting data to two serial ports caused excessive noise in the gravity readings, which was subsequently mitigated by exporting to only one port throughout the duration of the survey (Dave Wallis, *personal comm.*). Following the standard convention for acquisition of marine gravity data, a 5-minute convolution filter was automatically applied to the raw gravity readings in order to increase the signal to noise ratio and suppress sinusoidal acceleration created by wave motion. Data were recorded every ten seconds in netCDF format and subsequently converted to ASCII format using the multi-dimension toolbox in *ArcMap*. It was necessary to delay the data (i.e. subtract five minutes from the posted time) to compensate for the effects of the convolution filter. Missing data of the order of a few seconds to several minutes were commonly observed between successive files. In this instance, the digital data were interpolated between the two readings either side of the data gap, using the hardcopy gravimeter print-out as a reference for the missing values. Attitude data downloaded daily from the ship's computer (which included ship's speed and heading) were found to be unreliable, often including time-gaps embedded within files. Processing the gravity data using this unreliable attitude information resulted in large crossover errors, which occurred due to sections of gravity data being reduced with incorrect values for the Eötvös

correction – essentially the gravity data and ship's attitude data were out of sync. For example: gravity data collected on station may be processed with an Eötvös correction that relates to a time two hours later, when the ship may have been steaming and the associated Eötvös correction may be up to ~10 mGal greater. To mitigate this effect, speed and heading were calculated at ten second intervals using successive longitude and latitude values for the ship's position. Gravity data were checked against the hardcopy gravimeter print-out at approximately 2 hour intervals to ensure that data had been correctly reduced. Gravimeter readings were converted from counter units ($g_{c.u.}$) to milligals – mGals (g_{mGal}) – based on harbour ties conducted at Santa Cruz de Tenerife on JD63 and JD107 (the start and end of the cruise, where the absolute value of gravity was determined to be 979399.25 mGal and 979399.16 mGal, respectively). The conversion was as follows (2.1):

$$g_{mGal} = ((g_{c.u.} - 10093.4) \cdot 0.9911) + 979399.21 \quad (\mathbf{2.1})$$

Gravimeter drift rate was assessed by linear interpolation between the harbour ties. The total variation observed for the six week duration of the cruise was < 1 mGal, and hence no correction was applied to the data to account for instrument drift.

2.5.1.1. Latitude correction

The Earth's theoretical gravitational potential can be determined by approximation to a rotating ellipsoid of uniform density layers. Removal of this value from survey data allows for the gravitational anomaly arising from local geological structure and topography to be assessed. Assuming an ellipticity of 1/298.247, the 1967 Geodetic Reference System Formula defines the variation in gravity with latitude as (2.2):

$$g_{\Phi} = 978031.846 \cdot (1 + 0.005278895 \cdot \sin 2\Phi + 0.000023462 \cdot \sin 4\Phi) \quad (\mathbf{2.2})$$

Where g_{Φ} is the correction in mGal at latitude Φ (Woollard, 1979). Gravitational variation caused by changes in ship's latitude is responsible for ±20 mGal about a mean value of ~978310 mGal for cruise JC07 data.

2.5.1.2. Eötvös correction

The ship's gravimeter is influenced by the Coriolis force generated by the Earth, the magnitude and polarity of which is dependent on the latitude, heading and speed of the ship, such that (2.3):

$$E_c = 7.503 \cdot S \cdot \sin H \cdot \cos \Phi + 0.004154 \cdot S^2 \quad \textbf{(2.3)}$$

Where E_c is the Eötvös correction in mGal, H is the ship's heading, S is the ship's speed in knots and Φ is latitude (Dehlinger, 1978). The Eötvös correction is greatest when the ship is moving in an E-W direction (i.e. when the ship is moving parallel with the direction of the Earth's rotation) at relatively high speeds and at low latitudes. Conversely, the Eötvös correction is at a minimum when the ship is moving N-S at relatively slow speeds and at high latitudes (Figure 2.5.1). In addition to applying (2.3) to each gravity datum, accelerometers built into the gravimeter were used to minimise the short wavelength cross-correlation between ship motion and gravity data (e.g. the method of Lacoste, 1973).

Gravity readings taken during research cruise JC07 can be loosely divided into two groups: the first group comprises readings taken within the two week period of the deep-towed survey and the second group comprises those taken during the two week seafloor-sampling survey. Throughout the deep-towed survey, the ship's speed was consistently 1.7±0.3 knots along a series of E-W trending lines. The result of surveying at such a slow speed is relatively 'clean' gravity data that do not display noise associated with sudden changes in ship's speed or heading, except at the ends of lines. The Eötvös correction associated with this slower part of the survey was thus ~±15 mGal in amplitude (Figure 2.5.1). In contrast, throughout the sampling survey sudden increases in speed of up to ~10 knots (as the ship steamed to a new sampling location) followed by long periods of near-zero speed across a 360° range of headings were encountered. The use of bow-thrusters to remain on-station during sampling operations also created sudden changes in velocity. The result of this type of surveying is that the associated Eötvös correction for the data is often as great as ~±50 mGal (Figure 2.5.1).

Having applied the Eötvös correction the corrected gravity data still displayed spikes and erroneous values. This was possibly caused by errors associated with measurement of the ship's position (and subsequently the speed and heading, as

discussed in *Section 2.5.1*). To correct for this, the Eötvös correction was passed through a temporal five minute filter (so as to imitate the filter already applied to the raw gravity data), and the corrected gravity data were edited manually if necessary.

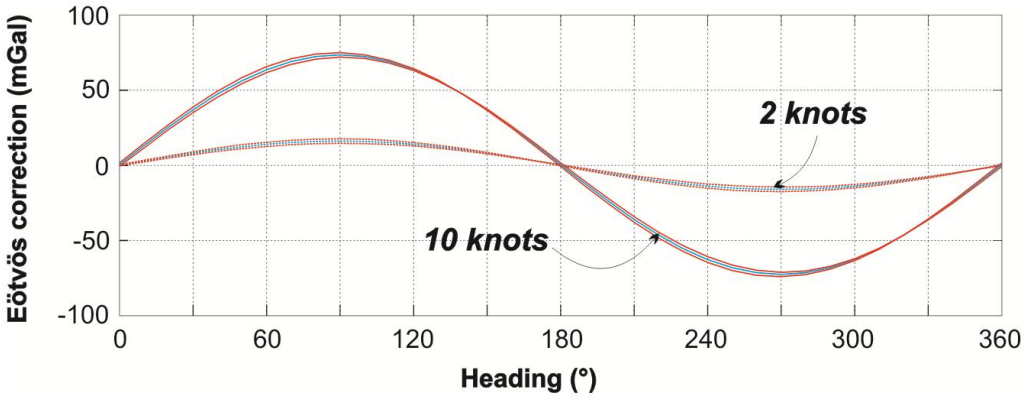


Figure 2.5.1. Eötvös correction for gravity measurements. During the deep-towed survey, where the ship-speed was a steady ~1.7 knots, correction was typically ±15 mGal for East and West survey lines (dashed lines). Ship speed and heading data were sufficient to perform the Eötvös correction during the slower TOBI survey. However, during the seabed sampling survey, speeds often reached in excess of 10 knots (between localities) meaning that data often contained large spikes (>50 mGal - solid lines). Correction for these larger errors was generally most successful when performed manually. Red lines indicate errors associated with a 1° uncertainty in heading and 0.2 knot uncertainty in speed.

2.5.1.3. Crossover analysis

The nature of the survey configuration allowed for a high number of crossover points to be analysed (Figure 2.2.1.). Assuming instrument drift to be negligible, crossover errors (COEs) therefore primarily represent the accuracy of the Eötvös correction and ship navigation (i.e. position; assuming Earth tides to be negligible). In general, a COE within the range of ±2 mGal between readings from crossing tracks is considered to be acceptable (Table 2.5.1.).

Study	Survey area	Crossovers	SD Crossover error (mGal)
(Fujiwara *et al.*, 2003)	MAR (15°20'N)	203	3.4-3.5
(Blackman *et al.*, 1998)	MAR (30°00'N)	650	1.82 (with 3.2% > 4 mGal)
(Searle *et al.*, 1998)	MAR (60°00'N)	Not listed	0.8
(Kuo & Forsyth, 1989)	MAR (32°00'S)	360	5.7
(Prince & Forsyth, 1988)	MAR (11°00'N)	Not listed	3.8

Table 2.5.1. Published values for standard deviation of COEs for various cruises. It is desirable to minimise COEs between datasets collected during separate cruises and also intra-survey crossovers.

Figure 2.5.2 displays a new method for rapid crossover analysis whereby the gravimetry data file is visualised using *Fledermaus*. The diameter of every sphere (each of which represents a gravity measurement) is scaled to represent ±1 mGal, making crossover points easily identifiable and analysed to see if they are within a ±2 mGal limit. Whilst this method does not provide a direct means by which to correct COEs, the ease at which identification of potential errors and a qualitative assessment of the data is made should not be underestimated, especially given that most alternative methods require at least some degree of pre-formatting of the survey data (the X-over package in GMT, for example – Wessel, 1989).

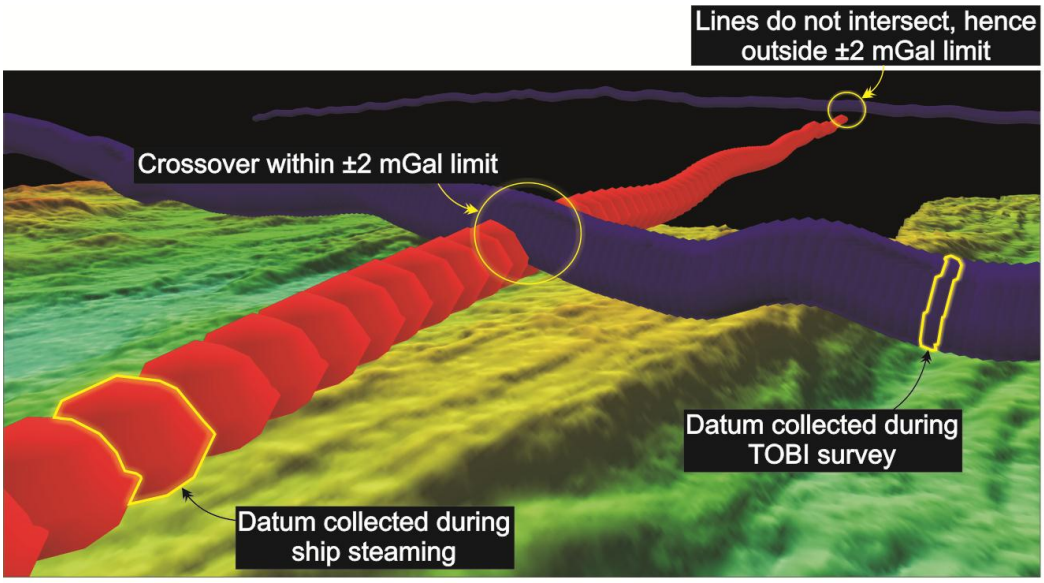


Figure 2.5.2. An alternative method for crossover analysis of gravity measurements. Gravity data (red and blue spheres) were plotted in Fledermaus above bathymetry data. Data points were scaled so that the diameter of each sphere equated to a ±1 mGal error. Gravity measurements could then be explored in 3D, providing a rapid method by which to assess the quality of the data with regard to crossover errors. Notice how the crossover in the foreground is 'touching', and hence the crossover must be within an acceptable ±2 mGal range. The crossover in the background does not intersect, and so must be investigated further. Each sphere represents one gravity datum. Blue spheres are closer together because they were collected during the slower, deep-towed survey.

Throughout JC07, 217 crossovers were encountered with a standard deviation of 1.3 mGal. Of these 217: a total of thirty crossover points distributed across the survey area which fell outside the ±2 mGal band were identified using *Fledermaus*, the COE standard deviation of which was 3.2 mGal. In order to reduce this value, COEs were correlated with time, heading and speed. There was very little correlation between COE and time, which is understandable given the negligible levels of instrument drift. Instead, it was discovered that quite a large correlation (correlation

coefficient of 0.63) existed between the difference in ship's heading for the two gravity observations in question and COE. Furthermore, this error was evident in the gridded data, which displayed linear E-W 'striping' (magnitude ~±0.5 mGal) that correlated exactly with the positions of E-W survey lines (indicating that the calculated Eötvös correction did not match exactly the gravitational acceleration experienced by the gravimeter, which may have occurred due to small errors in the calculated speed and heading of the ship). In order to correct the data it was necessary to increase the east-going Eötvös corrections and decrease the west-going Eötvös corrections by ±0.25 mGal, respectively. After applying this correction, the standard deviation of all COEs was reduced to 1.1 mGals. Large individual COEs (of the order of 4 – 6 mGal) were eliminated by removing the section of data between the nearest two crossover points that were within a ±2 mGal limit (this did not significantly effect data density as the few large COEs were generally in areas of high data coverage comprising multiple crossovers, usually during sampling operations). The final standard deviation of COEs, having removed spurious sections of data, was 1.0 mGal.

2.5.2. Free-air anomaly

The free-air anomaly (FAA), at sea-surface, is the observed gravity field adjusted for the effects of survey latitude and the Eötvös correction. It comprises all gravitational contributions from structural and lithological elements of the survey area.

To summarise the reduction of the gravity data: data were initially converted from counter units to milligals and corrected for variation in survey latitude, ship speed and heading and crossover errors. A certain amount of manual editing was required to remove spurious readings. Data were then blockmean filtered across an area of one arc-minute using GMT (Wessel & Smith, 1998) and gridded using a minimum curvature surface algorithm with a tension parameter of 0.2 (Figure 2.5.3a). Unfortunately, existing gravity data from within the 13°N region (i.e. Smith *et al.*, 2008) were not available. Figure 2.5.3b shows, however, that there is an excellent visual match between the gravity data collected during leg 182 of the R/V *Knorr* (Smith *et al.*, 2006; Smith *et al.*, 2008) and the JC07 data. It is difficult to quantify this exactly without a digital copy of Smith *et al.* (2008)'s data.

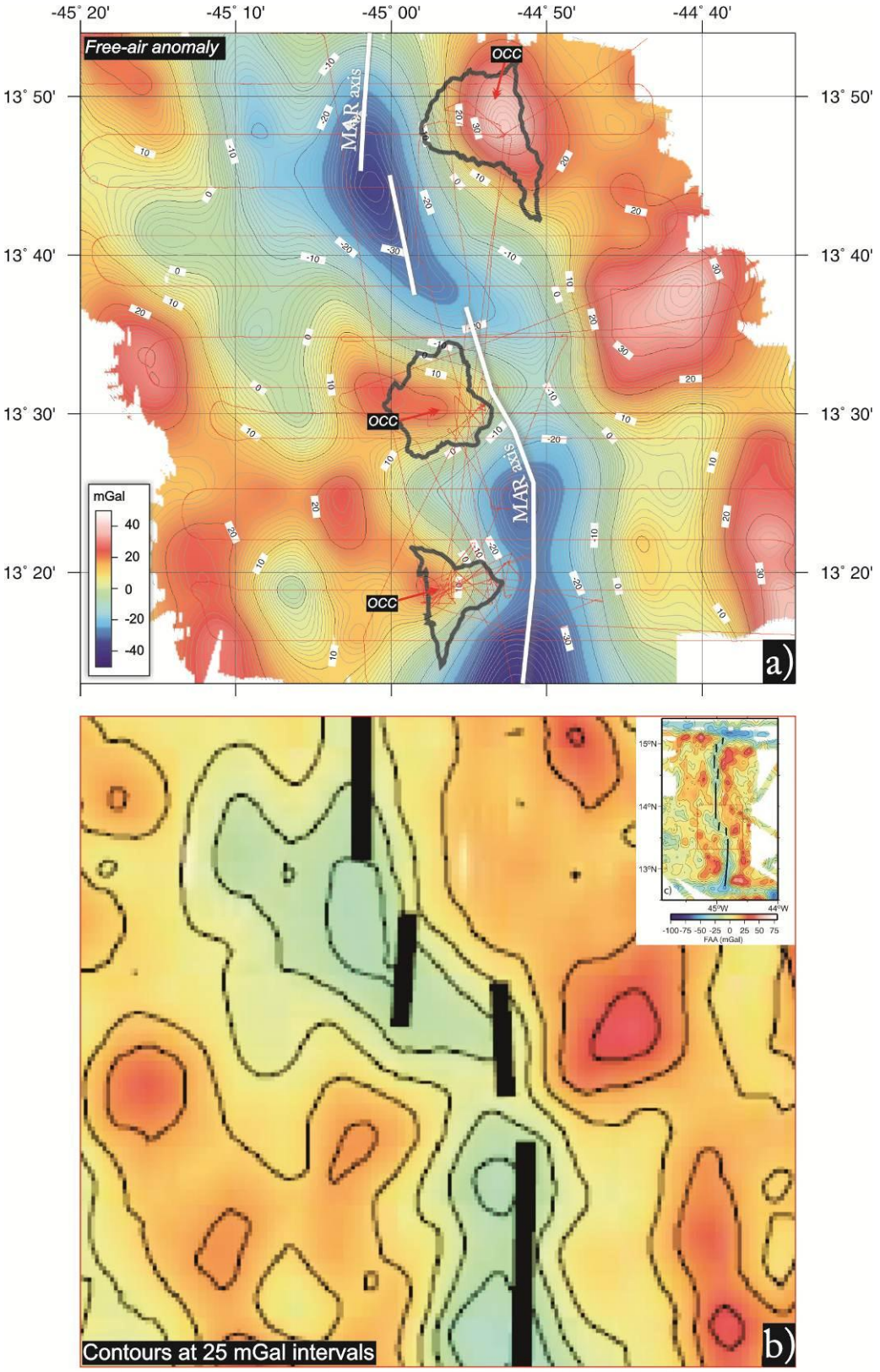


Figure 2.5.3a-b. a) Gravitational FAA from JC07 data. OCCs (outlined in black) and MAR axis (white) are identified in Chapter Three. Red line is survey track. **b)** FAA of Smith *et al.* (2008) (with regional position inset). Scale is only approximately the same as the lower image is a screen-grab from published results. There is a good match between the two datasets. Note that the closer track-line spacing during JC07 (red lines) means the upper image contains more information (see, for example, the FAA over the OCC at 13°48'N). See text for discussion

2.6. Magnetic field survey

TOBI contains a tri-axial fluxgate magnetometer (TAM) that is capable of simultaneously measuring the magnetic vector field strength in three orthogonal directions (and hence total field strength as the square root of the sum of the squares of each vector). The three sensors are oriented such that $TOBI_x$ is aligned with the vehicle's port-starboard axis (positive to port), $TOBI_y$ is aligned fore-aft (positive to fore) and $TOBI_z$ is aligned vertically (positive down – as summarised in Figure 2.6.1). Magnetic field measurement using TOBI's TAM has an accuracy of ±0.5 nT within a range of ±100000 nT on each axis. TAM data are advantageous compared with total magnetic field data as they allow for a greater wealth of information to be extracted from sub-surface sources of magnetic anomaly; rather than averaging a potentially complex signal into a single direction (much like a proton-precession magnetometer), TAM data can be used to more accurately analyse multifaceted three-dimensional bodies. However, this requires that deep-towed TAM data must be carefully reduced to remove sources of unwanted magnetic interference, including that produced by the deep-towed vehicle itself. The processes by which raw magnetic field measurements are reduced to obtain the magnetic field anomaly form the basis of this section.

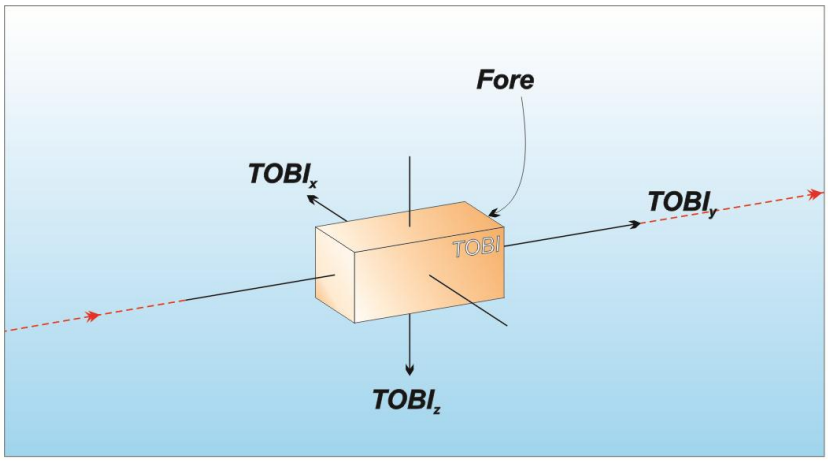


Figure 2.6.1. TOBI tri-axial magnetometer configuration. The axes are aligned such that: **$TOBI_x$** is parallel with the vehicle's port-starboard axis (positive to port), **$TOBI_y$** is parallel with the vehicle's fore-aft axis (positive fore) and **$TOBI_z$** is aligned vertically (positive measurement when magnetic field direction is downwards).

2.6.1. Tri-axial magnetometer (TAM) data reduction

Raw data were decimated to 10 metre resolution and then converted into magnetic field strength in nanotesla (nT). Firstly, readings were transformed to voltages for each of the three sensors using the following linear conversion given by the manufacturer (2.4):

$$V_{xyz} = Measured_{xyz} \frac{2.5}{524288} \tag{2.4}$$

Where V_{xyz} is the voltage equivalent of the raw measurement made by the sensor - $Measured_{xyz}$ (the conversion being the same for each of the three magnetic sensors). Recorded voltages were then converted into magnetic field strength based on the matrix conversion (2.5):

$$\overline{B} = 40000 \cdot \overline{A} \cdot \overline{V} \tag{2.5}$$

Where $\overline{B}$ is a 3-by-1 matrix of corrected magnetic values in nanotesla, $\overline{A}$ is a 3-by-3 matrix of manufacturer's calibrations and $\overline{V}$ is a 3-by-1 matrix of manufacturer's offsets, such that (2.5) can be expressed as (2.6):

$$\begin{pmatrix} B_x \\ B_y \\ B_z \end{pmatrix} = 40000 \cdot \begin{pmatrix} 0.9996297 & -0.0057871 & -0.0745943 \\ 0.0037991 & 1.0322001 & 0.0465985 \\ 0.0070859 & 0.0068992 & 1.0296533 \end{pmatrix} \cdot \begin{pmatrix} V_x - 0.0001508 \\ V_y + 0.0002495 \\ V_z - 0.0000618 \end{pmatrix} \tag{2.6}$$

2.6.1.1. IGRF correction

In order to assess only the magnetic field arising from local geological sources, it is necessary to remove from the observed TAM data the contribution of the Earth's ambient geomagnetic field. The IGRF (International Geomagnetic Reference Field) is an internationally agreed set of global spherical harmonic models which describe both

the spatial and secular variation of the Earth's geomagnetic field (Macmillan & Maus, 2005).

The total field across the survey area was of the order of ~32250±150 nT. This can be broken down into vector components in the north, east and downward direction, which are ~27950±50 nT, ~-8975±25 nT and ~13500±500 nT, respectively. Secular variation for a period of two-weeks during March 2007 was ~1.3 nT, and hence considered to be negligible for the duration of the survey. The IGRF correction was calculated for the median date of the deep-towed survey (JD81.5). In addition to this, it was assumed that the declination (17.4°W) and inclination (21.6° down) of the magnetic field remained constant throughout the survey.

2.6.1.2. Calibration for the effects of vehicle magnetisation

Bullard and Mason (1961) show that the magnetic field produced by a ship at a given distance astern is proportional to the length of the ship and the position of the magnetic poles within the hull, as expressed by (2.7):

$$\Phi(x) = \frac{(2x/l + 1)}{(x/l + \alpha)^2 \cdot (x/l + 1 - \alpha)^2} \tag{2.7}$$

Where the magnetic potential of the ship is Φ, the length of the ship is l, the distance astern of the magnetometer is x and the position of the ship's magnetic poles is given by α (so that the product of α and l is the distance to the pole from the bow or stern - Figure 2.6.2). During calibration of TOBI's TAM, the vehicle was towed in a loop at a mean distance of 400 metres from the ship. Given the length of the RRS *James Cook* (89.5 metres), the horizontal field produced by the ship would be negligible (~< 1 nT) throughout the calibration (regardless of the position of the magnetic poles), and subsequently for the rest of the cruise, where TOBI's distance astern was significantly greater (several km). TOBI itself, however, contains magnetic materials and as such has a permanent and induced magnetic moment that is a function of TOBI's orientation within the geomagnetic field.

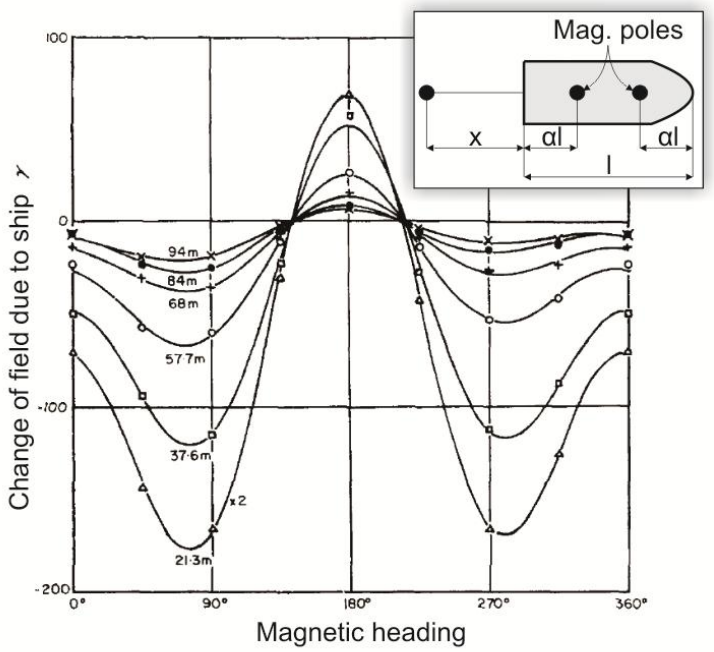


Figure 2.6.2. Disturbance of the magnetic field as a function of distance astern of ship and ship's heading. Calculations are for the *Discovery II*, which, at 67.4 metres, is shorter than the RRS *James Cook* (89.5 metres) and therefore the field shown here should be less than that encountered throughout JC07. From Bullard & Mason, 1961.

Essentially, the magnetic vector being measured by each of the three magnetometers at any given time can be expressed in the TOBI coordinate frame of reference as (2.8):

$$H_{ob} = F + H_i + H_p \tag{2.8}$$

Where H_{ob} is the observed magnetic vector, F is the local geomagnetic field, H_i is the induced magnetic moment created by placing TOBI within the geomagnetic field and H_p is the permanent magnetic moment of TOBI. The Earth's magnetic field, F, is a weak field, and as such the induced magnetic component of TOBI, H_i, is proportional to F. Isezaki (1986) states that (2.9):

$$H_i = \overline{A} \cdot F \tag{2.9}$$

Where $\overline{A}$ is a 3-by-3 matrix specific to the vehicle and is dependent upon: (1) the distribution of magnetisation about the vehicle, (2) the location of the magnetic sensors within the vehicle and (3) the shape of the vehicle. Clearly, as the attitude of TOBI

varies throughout the course of the survey, the measured value of H_i will also vary. If the geomagnetic field in (2.8) is projected onto the geometric orientation of TOBI (as expressed by the measured values of roll, pitch and yaw of the vehicle) then combining with (2.9) gives (2.10):

$$H_{ob} = \left(\overline{R} \cdot \overline{P} \cdot \overline{Y}\right) \cdot F + \overline{A} \cdot \left(\overline{R} \cdot \overline{P} \cdot \overline{Y}\right) \cdot F + H_p \qquad (\mathbf{2.10})$$

Where $\overline{R}$, $\overline{P}$ and $\overline{Y}$ are the matrices of rotation for the roll, pitch and yaw of the vehicle, respectively.

In practice, determination of $\overline{A}$ and H_p is achieved by turning and pitching the vehicle in a magnetically quiet region where F is known so that (2.10) may be solved by the method of least squares. A defect of (2.10) occurs due to the fact that in one 360° turn the measured value of yaw will vary greatly relative to pitch and roll, and hence it is necessary to carry out a number of calibration turns so that the solution to (2.10) may be optimised for more accurate determination of $\overline{A}$ and H_p (Isezaki, 1986). Furthermore, the determination of $\overline{A}$ and H_p does not take into account local magnetic anomalies and the fact that the viscous remnant magnetisation (VRM) of the vehicle may change gradually over the course of the survey. Korenaga (1995) presents a solution whereby the vehicle carries out a series of figure-eight turns and the resultant H_{ob} is analysed with respect to its noise power spectra and filtered to minimise errors associated with vehicle roll bias in one particular direction.

Unlike a ship-mounted magnetometer a deep-towed magnetometer takes significant time to carry out a calibration turn. Therefore, throughout research cruise JC07 only one calibration loop was conducted and the TAM data cannot be accurately calibrated to remove the effects of vehicle magnetisation using the method of Isezaki (1986) or Korenaga (1995). It was also found that the magnetic data were not compatible with existing MATLAB routines designed to automatically remove the effects of vehicle magnetisation, which may have occurred due to a localised anomaly in the vicinity of the calibration turn (M. Tivey, *personal comm.*). Instead, an empirical approach is adopted to remove the effects of vehicle magnetisation, H_i, similar to that which was used during research cruise CD99 (Searle *et al.*, 1996). With this method it is assumed that although H_p should vary temporally with the effects of VRM, the relatively short period of the survey means it can be treated as a constant.

Plotting the average total magnetic field for each survey line allows for an estimate of the heading correction to be made (Figure 2.6.3). West-going lines measure consistently higher values for magnetic field strength than east-going lines by ~1750 nT. This value is an estimate of the vehicle's contribution to the magnetic field over a range of 180° in heading. Given that the IGRF for the survey area ranges from ~32150 nT in the south to ~32450 nT in the north, based on Figure 2.6.3 it would be expected that the calibration of the total field data should be roughly +300 nT for east-going lines (i.e. the measured value of 31971 nT for east-going lines in Figure 2.6.3 has to be increased by ~300 nT to match the IGRF) and -1450 nT for west-going lines. The relationship between heading and vehicle-induced magnetic field strength is non-linear (and the average field strengths in Figure 2.6.3 also include local, geologically-induced anomalies as well as the effect of the vehicle), hence a calibration turn is conducted to assess the vehicle's magnetic moment over a 360° range of headings.

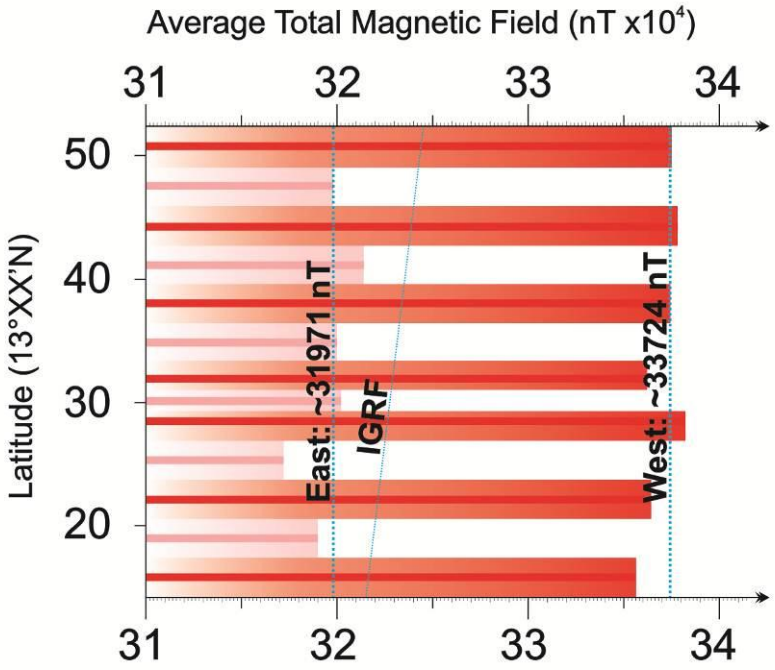


Figure 2.6.3. Average total magnetic field strength for each survey line. West-going lines (red bars) measure consistently higher values for magnetic field strength than east-going lines (pink bars) by ~1750 nT. This value is essentially a rough measure of the vehicle's contribution to the magnetic field over a range of 180° in heading. See text for discussion.

In order to derive a more robust estimate of the vehicle's contribution to the magnetic field, the magnetometer was towed in a loop at the beginning of the deployment in an area that was assumed to be magnetically 'quiet' (Figure 2.6.4).

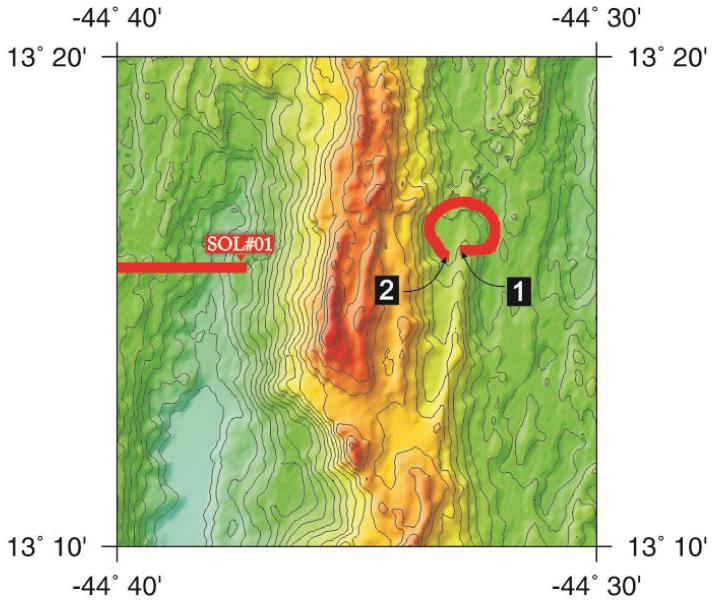


Figure 2.6.4. Location of vehicle magnetometer calibration turn. Start (1) and end (2) position of anti-clockwise turn are indicated (bold red line is vehicle path). Note that no TOBI data (or surface magnetometer data) were collected between (2) and start of survey line #1. Bathymetry data is illuminated from NW, vertical scale as **Figure 2.2.2**.

Un-calibrated total field strength (herein referred to as H_{ob_tf}) and observed magnetic vector on each of the three magnetometers in the $TOBI_x$, $TOBI_y$ and $TOBI_z$ directions (H_{ob_x}, H_{ob_y} and H_{ob_z}, respectively) for the period of the calibration turn are shown in Figure 2.6.5. Pitch data were used to perform a geometrical vector rotation on the $TOBI_y$ and $TOBI_z$ sensors (i.e. H_{ob_y} was made horizontal and H_{ob_z} was made vertical). The predicted field, F, was determined by sampling the north, east and downward component of the IGRF and rotating this onto the same track heading as TOBI during the calibration loop (the predicted field in the $TOBI_z$ direction is assumed constant and the effects of vehicle pitch and roll are ignored at this stage). As implied by (2.8), the residual between observed magnetic field, H_{ob}, and predicted magnetic field, F, thus represents the magnetic moment generated by TOBI, H_i (as H_p is assumed constant throughout the calibration turn). Figure 2.6.6 shows the residual between H_{ob} and F for the total field and each of the three magnetic components (e.g. $H_{i_xyz} = H_{ob_xyz} - F$), and therefore shows the induced magnetic component of TOBI in each direction as a function of vehicle heading. In order to physically remove the contribution of vehicle magnetisation from the observed magnetic field, a truncated Fourier series was fitted to all the magnetic components shown in Figure 2.6.6, ($Calibration_{tf}$, $Calibration_x$,

Calibration$_y$ and *Calibration*$_z$) following the method used during research cruise CD99 (Searle *et al.*, 1996). Each Fourier series had the general form (2.11):

$$Cal. = a0 + a1 \cdot \cos\left(gyro/c1\right) + b1 \cdot \sin\left(gyro/c1\right) + a2 \cdot \cos\left(gyro/c2\right) + b2 \cdot \sin\left(gyro/c2\right) \quad (\mathbf{2.11})$$

It was found that for the sensors in the $TOBI_x$ and $TOBI_y$ directions, it was necessary to have five components in the Fourier series to accurately fit H_{i_x} and H_{i_y}, respectively (red line - Figure 2.6.6). H_{i_z} was accurately fitted with a three-term series. It is not clear why an additional expansion of (2.11) should be required to remove the effects of vehicle magnetisation from the data in the $TOBI_x$ and $TOBI_y$ directions, although this may be caused by a strong horizontal magnetic gradient (the effect of which on H_{i_z} would negligible), or due to poorly constrained data between gyro values of 80° – 140° (M. Tivey, *personal comm.*). The ship may be one possible source of such an external magnetic field, but the contradiction with (2.7) makes this unlikely. The Fourier components used to correct each component of the magnetic field are shown in Table 2.6.1.

	Magnetic sensor		
Fourier component	**$TOBI_X$**	**$TOBI_Y$**	**$TOBI_Z$**
a0	3226	980	-873
a1	5777	86920	30
b1	782	-86300	1383
c1	-4304	-76150	360
a2	-121	83780	-
b2	416	284	-
c2	217	287	-

Table 2.6.1. Components of the Fourier series used to remove the effects of vehicle magnetisation from the magnetic dataset. H_{i_x} and H_{i_y} were each fitted with a five-term series, whereas H_{i_z} was fitted with a three-term series. See text for discussion.

Using this method, the contribution of TOBI to the total magnetic field was calculated as ~-450 nT for east-going lines and ~1360 nT for west-going lines, which is in agreement with the estimate made by averaging the total field strength for each line (e.g. Figure 2.6.3).

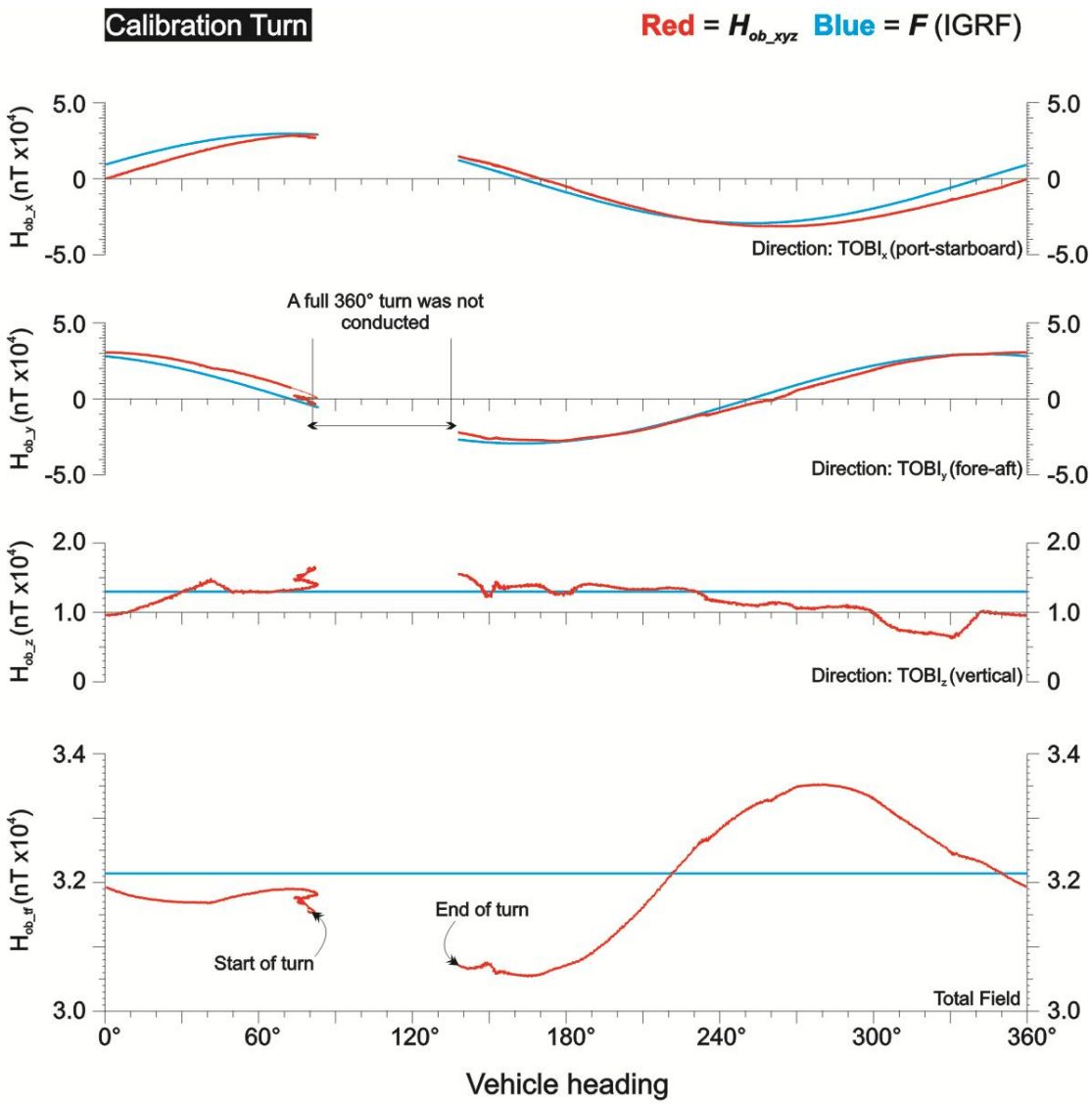


Figure 2.6.5. Observed magnetic field strength (nT) during the calibration turn for each of the magnetic components (H_{ob_xyz}) in the TOBI reference frame and the total field (H_{ob_tf}) (red lines). Predicted magnetic field strengths, F (blue lines), were calculated by sampling the north, east and downward components of the IGRF and performing a vector rotation based on the TOBI heading data (x-axis). An entire 360° turn was not conducted, hence the gap in data coverage between 80° and 130°. This reduces the accuracy of the calibration for magnetic data collected along east-going survey lines. Note that the range on the y-axis varies between plots. See text for discussion.

The relative contribution of TOBI to the individual magnetic sensors in the $TOBI_x$, $TOBI_y$ and $TOBI_z$ directions between east- and west-going lines was ~4000 nT, ~10750 nT and ~2750 nT, respectively. The Fourier series' in Figure 2.6.6 form the basis of the heading correction, and were applied to the TOBI magnetic data collected along each of the thirteen survey profiles in order to eliminate the magnetic contribution of the vehicle (i.e. in the geographical reference frame: $Calibrated_{xyz} = H_{obs_xyz} - Calibration_{xyz}$).

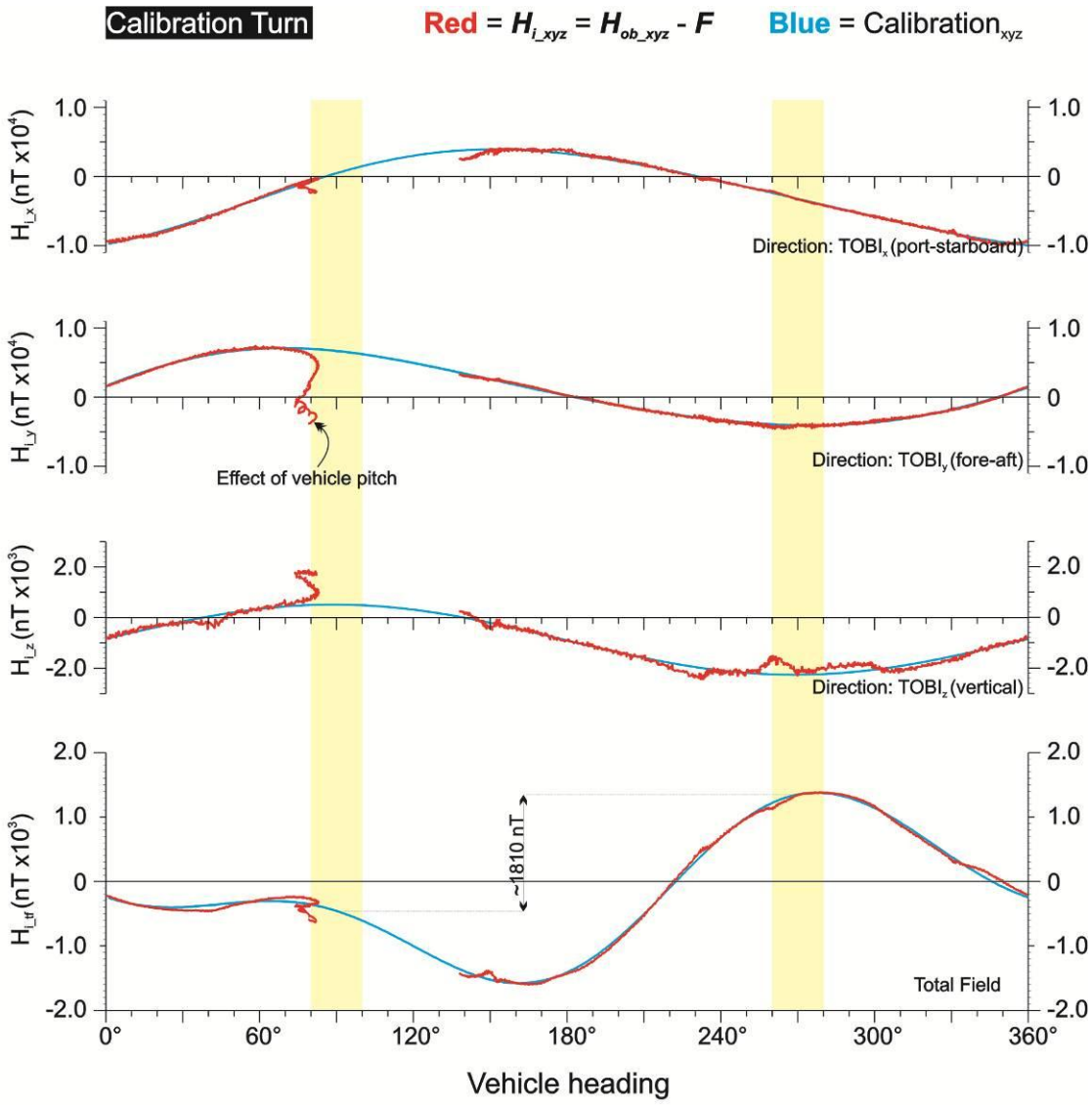


Figure 2.6.6. Plot of TOBI's induced component of magnetisation as a function of heading - H_{i_xyz} and H_{i_tf} (red line) - calculated by subtracting from H_{ob_xyz} the predicted field, F. Blue line is a Fourier best-fit model for each component (Calibration$_{xyz}$) and the total field (Calibration$_{tf}$). For each deep-towed magnetic survey profile, the relevant Fourier model is subtracted from the corresponding component of the magnetic field, removing the effects of vehicle magnetisation. Vertical highlighted areas show the approximate correction for east- and west-going survey lines. Note that the influence of TOBI on the total field between east- and west-going lines is ~1810 nT, which is similar to the 1750 nT calculated by seperately averaging the east- and west-going survey lines (**Figure 2.6.3.**). Note that the scale on the y-axis varies between plots. See text for discussion.

Removal of each Fourier series from H_i measured during the calibration turn then allowed for the relationship between pitching of the vehicle and magnetisation to be assessed (e.g. $Pitch_anom_{xyz} = H_{i_xyz} - Calibration_{xyz}$). Roll values (Figure 2.6.7a) appeared to be cross-coupled with pitch values (Figure 2.6.7b), presumably due to a misalignment between the two sensors. However, for most of the survey roll was < 2°, and so its affect on magnetisation was considered to be negligible and ignored.

Anomalies generated by pitching of the vehicle, *Pitch_anom*$_{tf}$ and *Pitch_anom*$_{xyz}$, are shown in Figure 2.6.7c-f and are plotted against pitch. There is a weak correlation between pitch and *Pitch_anom*$_x$, which would be expected due to pitch primarily affecting the vehicle along the fore-aft axis and the TOBI$_x$-magnetometer being aligned with the port-starboard axis (Figure 2.6.7c). The low-degree of correlation may be attributable to vehicle roll but it is difficult to accurately quantify this relationship. In the TOBI$_y$ direction, *Pitch_anom*$_y$ is also very weakly correlated with pitch, although the high amount of data scattered around zero nanotesla across the ~20° range of pitch values again makes it hard to quantify the precise nature of the relationship (Figure 2.6.7d).

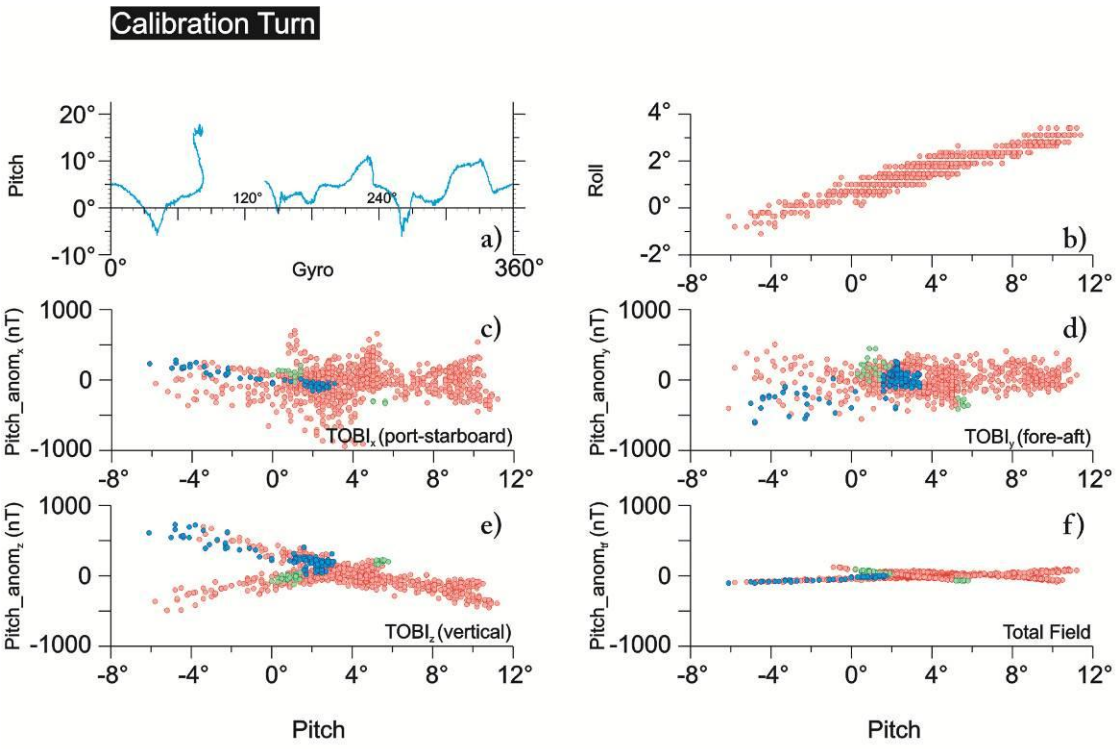


Figure 2.6.7a-f. Magnetic data correction for the effects of vehicle pitch. Blue-dots in **c-f)** represent west-going data (260-280°), green-dots represent east-going data (50-60° and 130-140°) and red-dots represent all data (0-360°). Pitch anomalies (Pitch_anom$_{xyz}$ and Pitch_anom$_{tf}$) were calculated by subtracting the heading calibration (Calibration$_{xyz}$ and Calibration$_{tf}$) from the vehicles induced component of magnetisation (H_{i_xyz} and H_{i_tf}). **a)** Pitch variation throughout the calibration turn was -5 to +10° (positive measurements are 'nose-down' - which usually occurs when cable is being payed-out and the vehicle is descending). **b)** Cross-coupling of pitch and roll measurements occurs due to a misalignment between the two sensors. **c)** Pitch_anom$_x$ and pitch are weakly correlated, as are **d)**, Pitch_anom$_y$ and pitch. **e)** Pitch_anom$_z$ is strongly related to pitch, having a positive correlation for west-going data and a negative correlation for east-going data. The opposite sense is true for **f)**, the relationship between Pitch_anom$_{tf}$ and pitch. Note that all x-axes are pitch (except in **a**). See text for discussion.

Pitching angle is strongly correlated with $Pitch_anom_z$, the relationship between which appears to be positive when the vehicle is heading between 0 – 180° (green dots, Figure 2.6.7e) and negative for heading values of 180-360° (blue dots). (Note that as a complete turn was not conducted, the pitching anomaly when the vehicle was travelling east is less well constrained than for when it was travelling west.) A similar relationship is observed, albeit with the opposite sense, between $Pitch_anom_{tf}$ and pitch (Figure 2.6.7f). The degree and polarity with which pitching anomalies and pitch are related is identical to that observed during CD99 (Searle *et al.*, 1996).

Linear regression fits of $Pitch_anom_z$ and $Pitch_anom_{tf}$ for both the east- and west-going observations were used as the basis of the pitch correction. These were removed from the raw magnetic data collected along each of the thirteen deep-towed survey profiles (e.g. $Mag_{xyz} = Calibrated_{xyz}$ – Pitch correction).

2.6.1.3. Assessment of calibration robustness

The vehicle heading and pitch calibrations were applied to the magnetic data and the results carefully analysed so as to assess the validity of the method derived in the previous section. Figure 2.6.8a-b shows the total field anomaly before and after (Mag_{tf}) the calibration process. Prior to calibration (Figure 2.6.8a), the data are striped in an E-W direction, corresponding with the fluctuating nature of TOBI's induced component of magnetisation that was generated by the back-and-forth nature of the survey. Applying the heading and pitch calibrations successfully removes this feature (Figure 2.6.8b), so that the true nature of the magnetic anomaly pattern can be observed.

In order to quantitatively gauge the robustness of the calibration, a two-dimensional section of the total field data for survey line 6 is considered (the location of which is marked in Figure 2.6.8a-b) and shown in Figure 2.6.9. In theory, before the calibration the data should be moderately correlated with the vehicle's heading, whereas after the calibration there should be no correlation (i.e. H_i – which is a function of heading and, to a lesser extent, pitch – is removed from the data). A correlation coefficient between the un-calibrated total field and heading was calculated as -0.66 for the full length of survey line 6 and -0.21 after the calibration, indicating that H_i had been considerably suppressed by the calibration process yet not removed entirely.

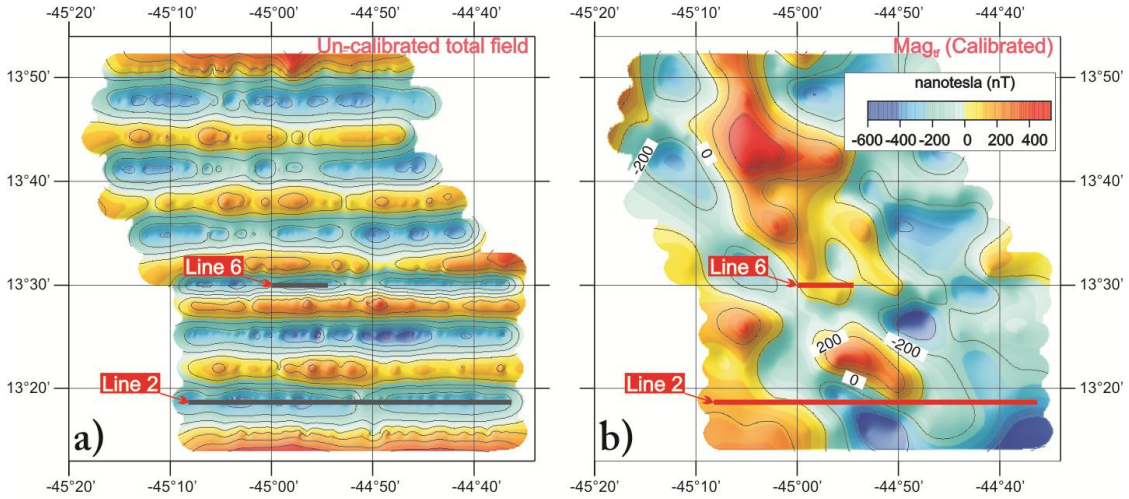


Figure 2.6.8a-b. Example of calibration of magnetic total field data for the effects of vehicle magnetisation. **a)** The un-calibrated data are striped due to variation in TOBI's induced component of magnetisation between east and west-going lines. **b)** Calibration successfully removes the effect of TOBI's magnetisation. Contours are at 200 nT intervals.

Furthermore, the close-up of the survey profile in Figure 2.6.9 shows that a number of peaks in the un-calibrated field (e.g. at 44°55.9'W and 44°53.7'W) are caused by slight variations in vehicle heading, as they are no longer evident in Mag_{tf}, the calibrated field. Considering that this distinct 'visual' correlation between raw magnetic data and heading had been removed, this level of correlation was considered acceptable for the purposes of interpretation of the total field magnetic data.

To assess the robustness of the calibration applied to each component of the magnetic field, un-calibrated and calibrated field strength for survey line 2 is shown in Figure 2.6.10. For each component: applying the calibration for the effect of vehicle attitude causes the residual to fluctuate about the predicted field (i.e. the IGRF). This is expected as it means that removal of the IGRF then causes the magnetic anomaly to oscillate about zero. However, upon closer inspection of the heading values for survey line 2, it becomes apparent that the vehicle proceeds along an unusual zigzag path through the water column during the survey (upper panel, Figure 2.6.10 – dashed black hyperbolae and yellow highlighted areas). This same anomaly pattern is seen intermittently within the magnetic data, both before and after calibration (the 'ringing' effect in Mag_{tf} at 44°44'W, for example), indicating that there may still be some vehicle-induced magnetic effects embedded within the calibrated data.

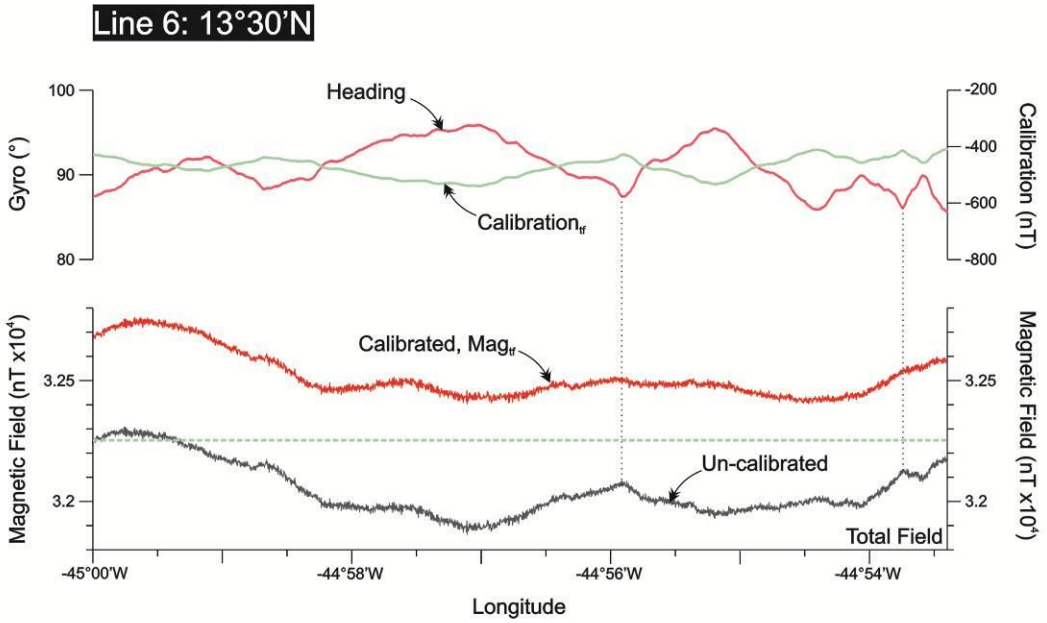


Figure 2.6.9. Example of calibration of magnetic total field data for the effects of vehicle magnetisation for a small section of survey line 6 (the position of which is marked in **Figure 2.6.8a-b**). Upper panel shows the vehicle heading (pink line) and the subsequent calibration that is applied to the total field data (Calibration$_{tf}$ - green line). Lower panel shows the un-calibrated magnetic field (grey line) and calibrated total field, Mag$_{tf}$ (red line, with IGRF/predicted field indicated by dashed green line). Note that some of the fluctuation in heading manifests itself in the un-calibrated field (vertical dotted lines) and is removed by the calibration process

It is possible that the physical nature of the towing configuration creates vortex-shedding along the length of the tow-cable. Essentially, as deep-water currents rush past the cable, they create an area of low-pressure on one side of the cable – similar to the way in which an aeroplane wing creates uplift. The cable swings towards the area of low pressure, and by doing so creates a conjugate area of low pressure that it subsequently swings back towards. If the frequency of this vortex-shedding matches the natural frequency of the towing configuration, then it is plausible that high amplitude oscillations in the cable may cause TOBI to fish-tail along-track, creating the type of anomalies observed in the gyro and magnetic datasets. The fact that this type of gyro-related anomaly is present within the data after application of the calibration highlights a limitation of the calibration process. However, given that the wavelength of the sinusoidal 'fish-tailing' of TOBI remains approximately constant (the precise value of which is presumably a function of the layback of the vehicle), the data can be filtered to remove this artefact. A Fourier transform of the gyro values reveals a spike in amplitude at 0.48 mHz that is responsible for the noise within the data (Figure 2.6.11).

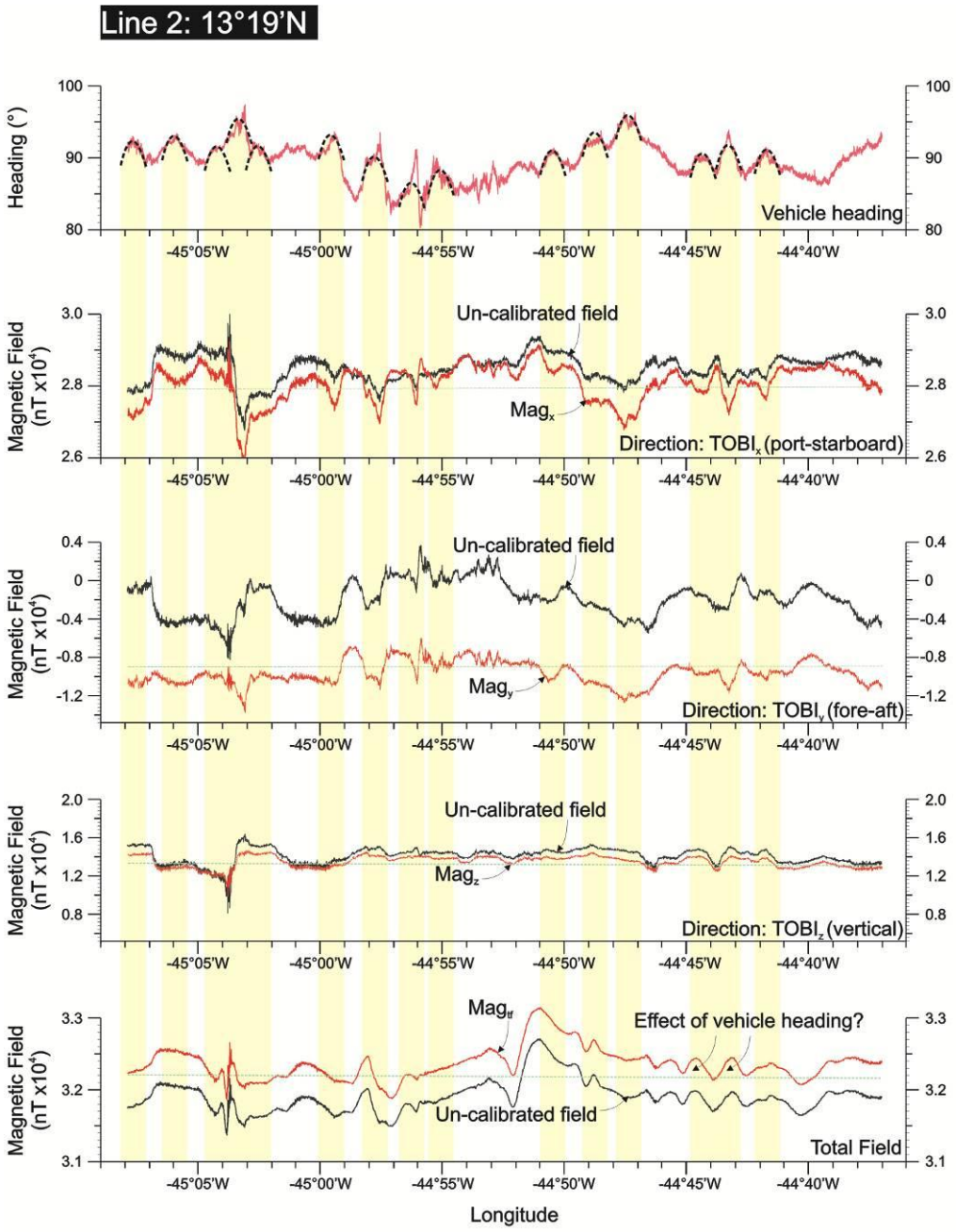


Figure 2.6.10. Assessment of heading and pitch calibration on each component of the magnetic field and the total field: survey line 2 (position marked in **Figure 2.6.8.**). Upper panel shows the vehicle heading throughout the line (pitch is excluded from the plot as its amplitude is only a few degrees). Note that the vehicle seems to zigzag along-track (dashed black hyperbolae and yellow highlighting). As would be expected, the calibration process shifts the un-calibrated magnetic field (grey lines - lower four panels) so that the calibrated field (red lines) oscillate about the IGRF. However, some of the short-wavelength features of the calibrated field may arise from the zigzagging nature of the vehicle (Mag_{tf} at 44°44'W, for example). The calibration process is not robust enough to remove this effect. However, if the motion happens over a consistent along-track distance, data can be filtered to remove its effect.

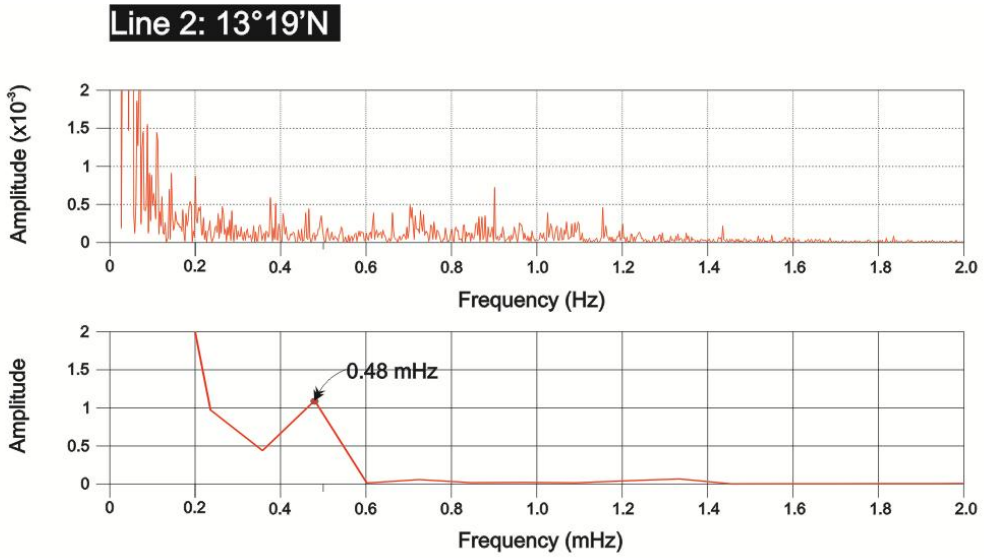


Figure 2.6.11. Fourier transform of survey line 2 vehicle heading data. Lower panel is a magnified view of the low-frequency end of the upper panel (note different x and y scales between the two plots). There is a distinct peak in amplitude that correlates to a frequency of 0.48 mHz. This low-frequency signal, possibly caused by zigzagging of the vehicle, may be responsible for the sinusoidal signal identified within the deep-towed magnetic data.

Assuming a relatively constant survey-speed of 1.7 knots (or 0.9 $m.s^{-1}$), this equates to an along-track distance of roughly 1.8 kilometres, and hence during the upward continuation process the data were bandpass filtered with a short-wavelength filter of 2 kilometres.

A final, comprehensive assessment of the validity of the deep-towed data reduction process is given in the next section, where deep-towed magnetic anomaly is compared with the ship's surface-towed magnetic anomaly data.

2.6.1.4. Reduction of deep-towed magnetic data to a horizontal plane

TOBI magnetic data were acquired along an uneven vertical path, and as such vary in intensity with varying altitude above the seafloor. Essentially, as the vehicle descends towards the seabed, the measured magnetic field strength increases with TOBI's increasingly close proximity to the magnetic source. It is necessary to remove this effect so that adjacent data can be compared to each other as if they existed on the same horizontal plane. Guspi (1987) provides a frequency-domain method for reduction of potential field data to a horizontal plane above irregular topography.

Each of the thirteen two-dimensional survey profiles were separately upward continued to: (1) the minimum along-track depth of TOBI for that particular line (levels are shown in Table 2.6.2), and (2) the minimum depth encountered during the entire survey (survey line 12 – 1.32 km). The first method allowed for each line to be analysed individually (e.g. without unnecessary loss in resolution associated with upward continuation to a level shallower than that encountered along the specific profile), whereas the second method allowed for gridding of all the magnetic data (i.e. three-dimensional interpretation). In each case the data were mirrored to reduce edge-effects and bandpass filtered between 55 and 2 kilometres for stability (and to remove the cable oscillation effect).

Survey line #	Up-con level (below sea-surface)	Max. vehicle depth	Max. water depth	Min. water depth
1	2.14 km	3.36 km	4.13 km	2.41 km
2	1.81 km	3.21 km	4.13 km	2.01 km
3	1.89 km	2.86 km	3.64 km	2.08 km
4	1.83 km	3.09 km	3.94 km	2.24 km
5	1.40 km	3.03 km	3.58 km	2.41 km
6	1.58 km	2.70 km	3.54 km	2.10 km
7	1.66 km	2.83 km	3.59 km	2.47 km
8	1.74 km	2.96 km	3.72 km	2.06 km
9	1.56 km	3.03 km	3.70 km	2.09 km
10	2.12 km	2.98 km	3.79 km	2.65 km
11	1.57 km	3.14 km	3.85 km	2.33 km
12	1.32 km	2.98 km	3.69 km	1.97 km
13	1.80 km	2.87 km	3.49 km	2.21 km

Table 2.6.2. Upward continuation levels taken as the minimum vehicle depth for each of the thirteen survey profiles (with absolute minimum depth marked in red). Maximum vehicle depth and maximum and minimum water depth are also shown for comparison. All values are kilometres below sea-surface.

Having reduced the deep-towed data to a horizontal plane, it was possible to compare this with the magnetic total field data collected by the ship's surface-towed proton-precession magnetometer. In general, the longer-wavelength features are closely matched between the two datasets (such as the CAMH; Figure 2.6.12). Short wavelength features, which may be attributable to, for example, magnetic degradation due to faulting or short-period geomagnetic reversals, are as expected more clearly resolved within the deep-towed data rather than the surface data. Features common to both datasets have higher amplitudes in the deep-towed data, due to TOBI's closer

proximity to the magnetic source. Bandpass filtering has also suppressed the anomalous sinusoidal variation in magnetic anomaly detected at 44°44'W, but without eliminating short wavelength features.

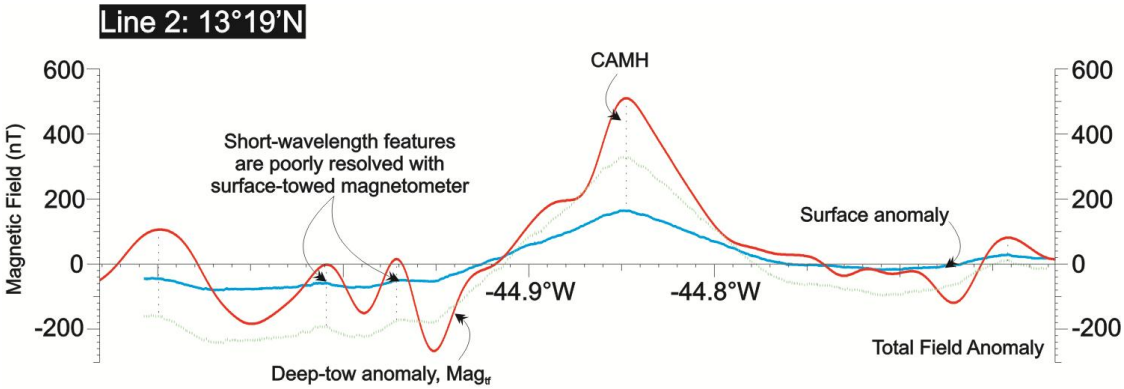


Figure 2.6.12. Comparison of deep-towed magnetic total field anomaly (upward continued to minimum survey depth and bandpass filtered - red line) with ship's surface-towed magnetometer data (blue line). The data match very closely in terms of their overall shape, but as expected, the deep-towed data contain a greater amount of information due to their relatively close proximity to the magnetic source. Dashed green line is 2x exaggerated surface anomaly, highlighting the close relationship between the two datasets. Vertical black dots connect common features.

2.6.2. Magnetic total field anomaly

To summarise the data reduction process: three orthogonal components of the regional magnetic field were measured in orientations parallel with TOBI's port-starboard ($TOBI_x$), fore-aft ($TOBI_y$) and vertical ($TOBI_z$) axes at a mean altitude of 400 metres above the seabed ($Measured_{xyz}$, respectively). Total field intensity ($Measured_{tf}$) was obtained by taking the square-root of the sum of the squares of the individual magnetic vectors. Data were converted to nanotesla, decimated to an along-track resolution of 10 metres, corrected for variation in the IGRF, and calibrated for the magnetic moment of the vehicle as a function of heading and pitch so that (2.12):

$$Mag_{xyz} = (Measured_{xyz} \text{ . nT conversion}) - \text{IGRF} - Calibration_{xyz} - \text{Pitch correction} \quad \textbf{(2.12)}$$

Where Mag_{xyz} is the final, calibrated field. Two-dimensional survey profiles were then upward continued to a level plane 1.32 kilometres below sea-level (upon which they were bandpass filtered between long and short wavelengths of 55 and 2 kilometres, respectively), and gridded using a surface-fitting algorithm (with tension parameter of 0.2) in GMT (Figure 2.6.13a).

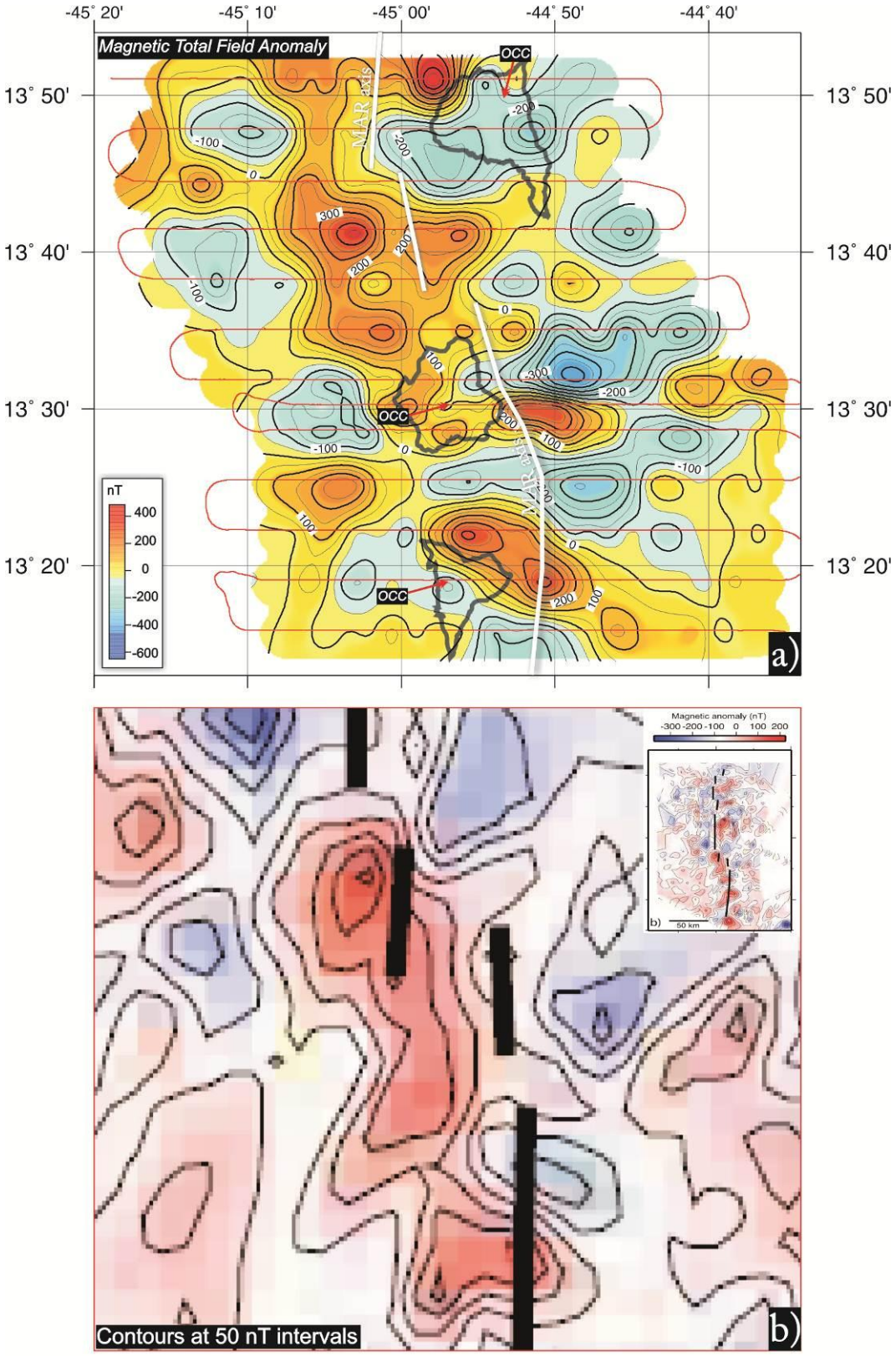


Figure 2.6.13a-b. a) Deep-towed magnetic total field anomaly from JC07 data. OCCs (outlined in black) and MAR axis (white) are identified in Chapter Three. Red line is survey track. **b)** Sea-surface total field anomaly of Smith *et al.* (2008) (with regional position inset). Scale is only approximately the same as the lower image is a screen-grab from published results. There is a good match between the two datasets, particularly the negative polarity material close to the ridge axis and the discontinuous nature of the CAMH. See text for discussion.

Figure 2.6.13a shows the three-dimensional deep-towed magnetic total field anomaly collected throughout cruise JC07. Individual two-dimensional magnetic survey profiles and their surface measured counterparts are shown in Figure 2.6.14[1-13]. As with the gravity data, existing magnetic anomaly data from R/V *Knorr* leg 182 were not available and hence a direct, quantitative comparison for the two surveys cannot be estimated. There is, however, an excellent visual match between the total field anomaly published in Smith *et al.* (2008) and that which has been measured during JC07 (Figure 2.6.13b).

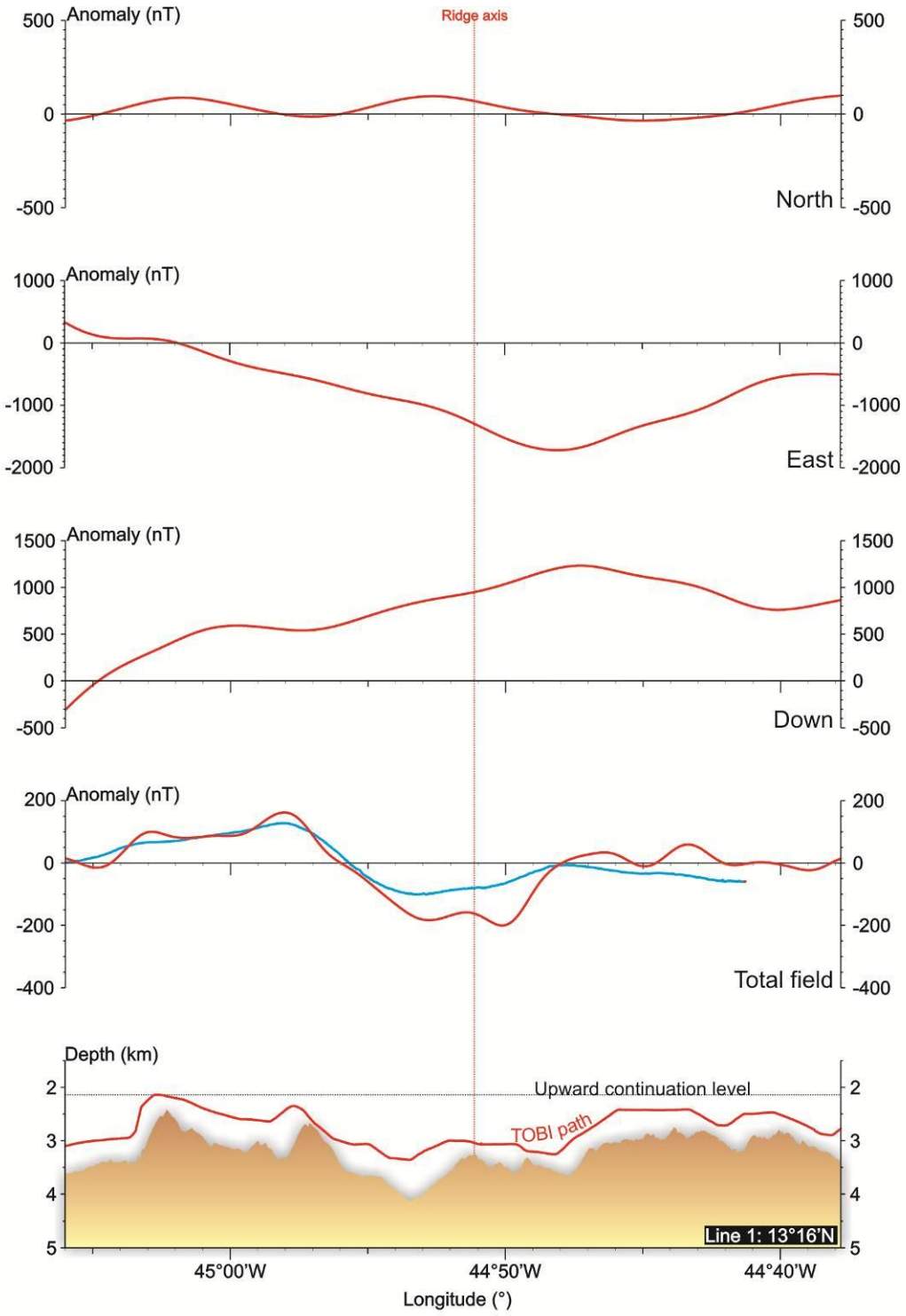


Figure 2.6.14[1]. Two-dimensional magnetic total field anomaly and components in north, east and downward direction for survey line 1. In each case red line is deep-towed anomaly (upward continued to the minimum depth encountered along the profile and bandpass filtered between 55 and 2 kilometres) and blue is the surface-towed anomaly. Note that the vertical scale is different between plots.

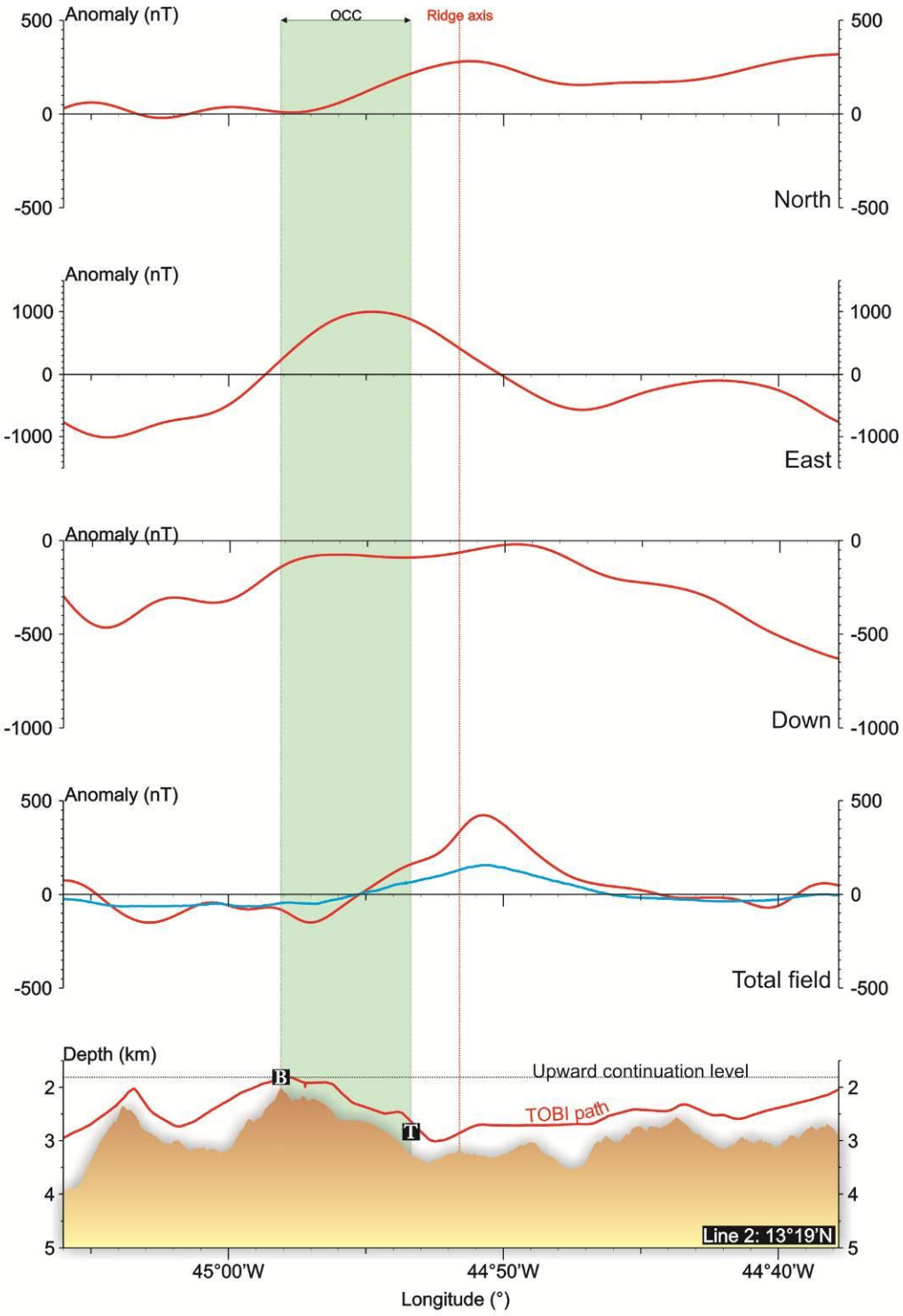


Figure 2.6.14[2]. Two-dimensional magnetic total field anomaly and components in north, east and downward direction for survey line 2. In each case red line is deep-towed anomaly (upward continued to the minimum depth encountered along the profile and bandpass filtered between 55 and 2 kilometres) and blue is the surface-towed anomaly. Note that the vertical scale is different between plots. Vertical green bar marks near-axis OCC location.

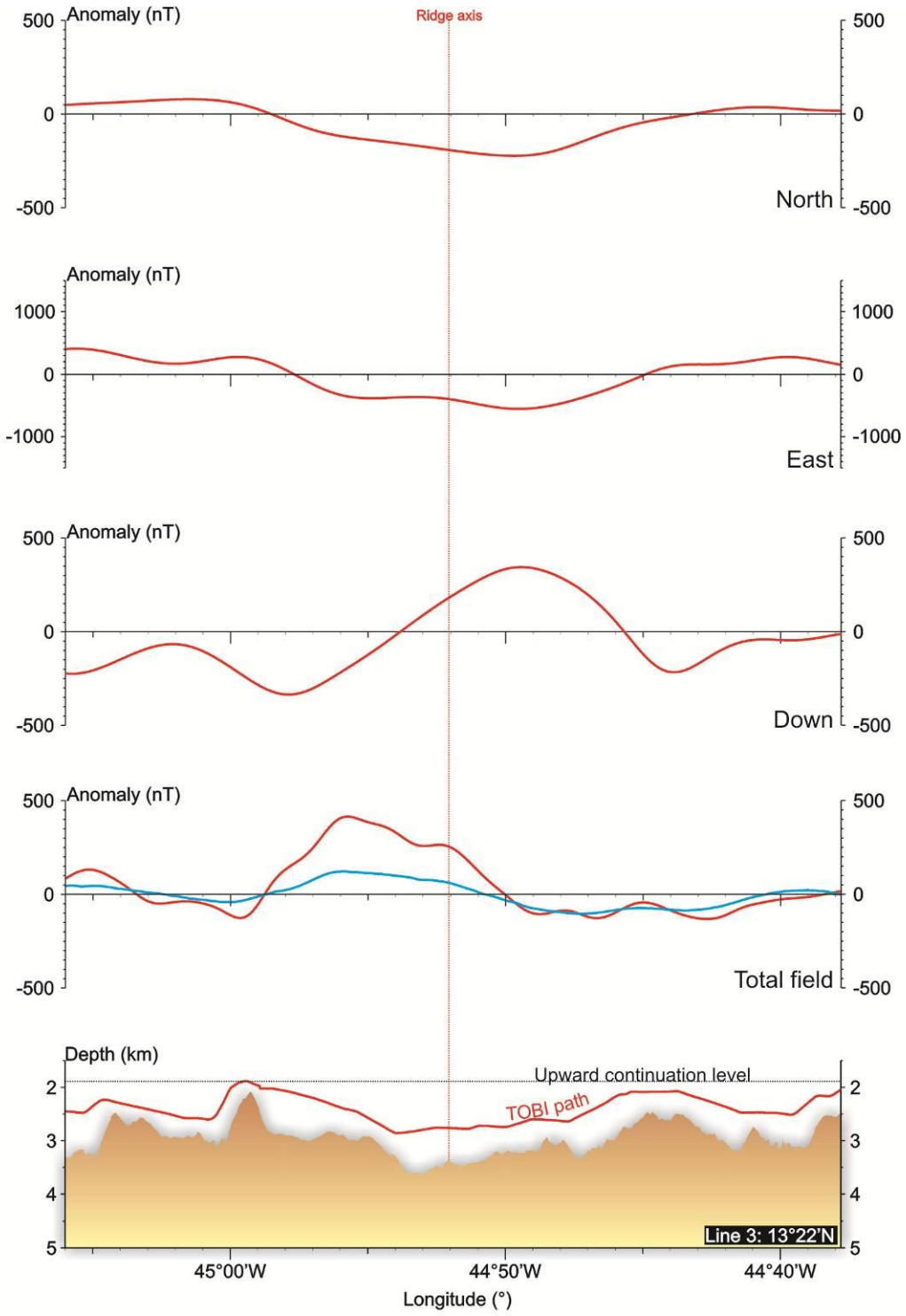


Figure 2.6.14[3]. Two-dimensional magnetic total field anomaly and components in north, east and downward direction for survey line 3. In each case red line is deep-towed anomaly (upward continued to the minimum depth encountered along the profile and bandpass filtered between 55 and 2 kilometres) and blue is the surface-towed anomaly. Note that the vertical scale is different between plots.

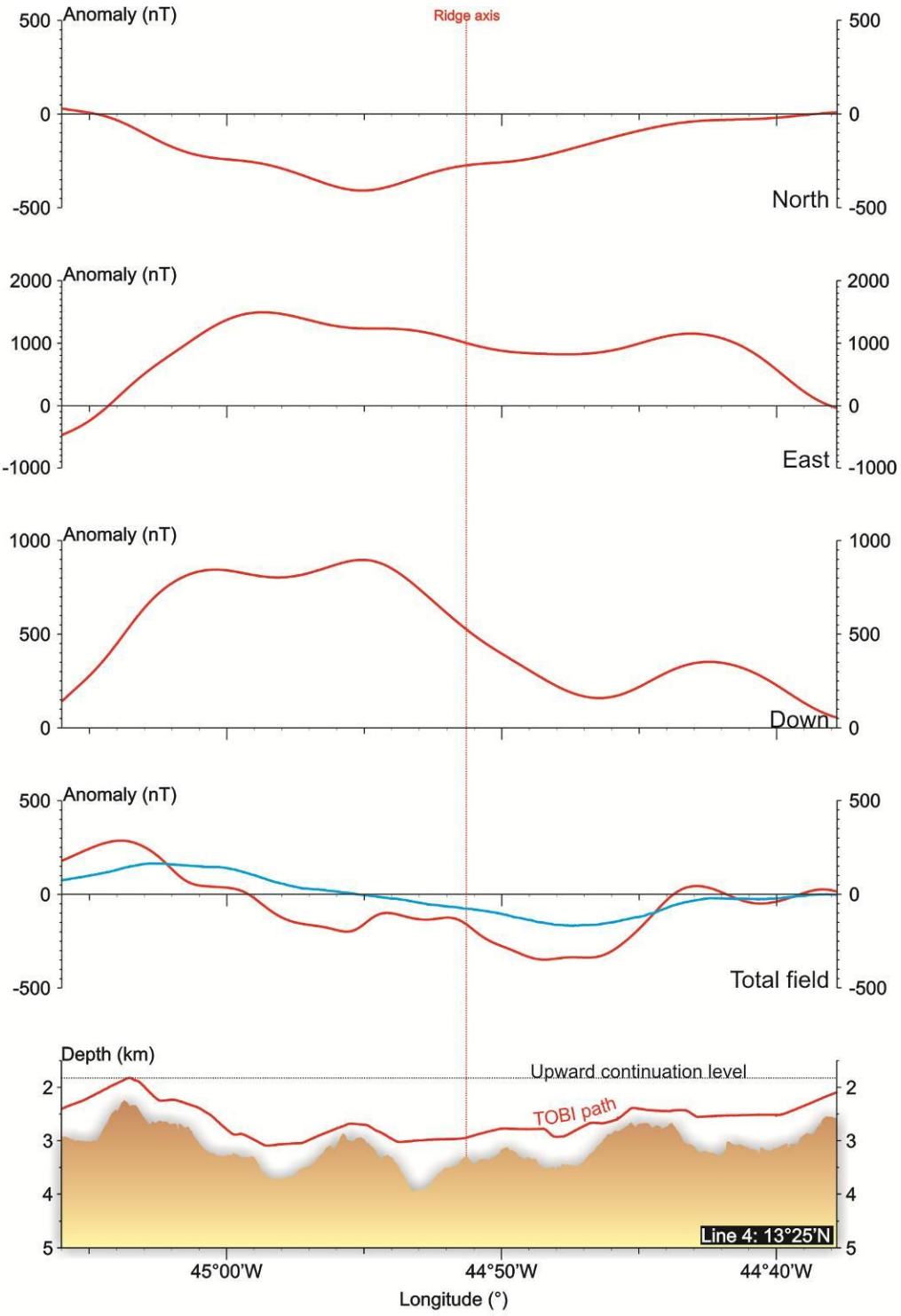


Figure 2.6.14[4]. Two-dimensional magnetic total field anomaly and components in north, east and downward direction for survey line 4. In each case red line is deep-towed anomaly (upward continued to the minimum depth encountered along the profile and bandpass filtered between 55 and 2 kilometres) and blue is the surface-towed anomaly. Note that the vertical scale is different between plots.

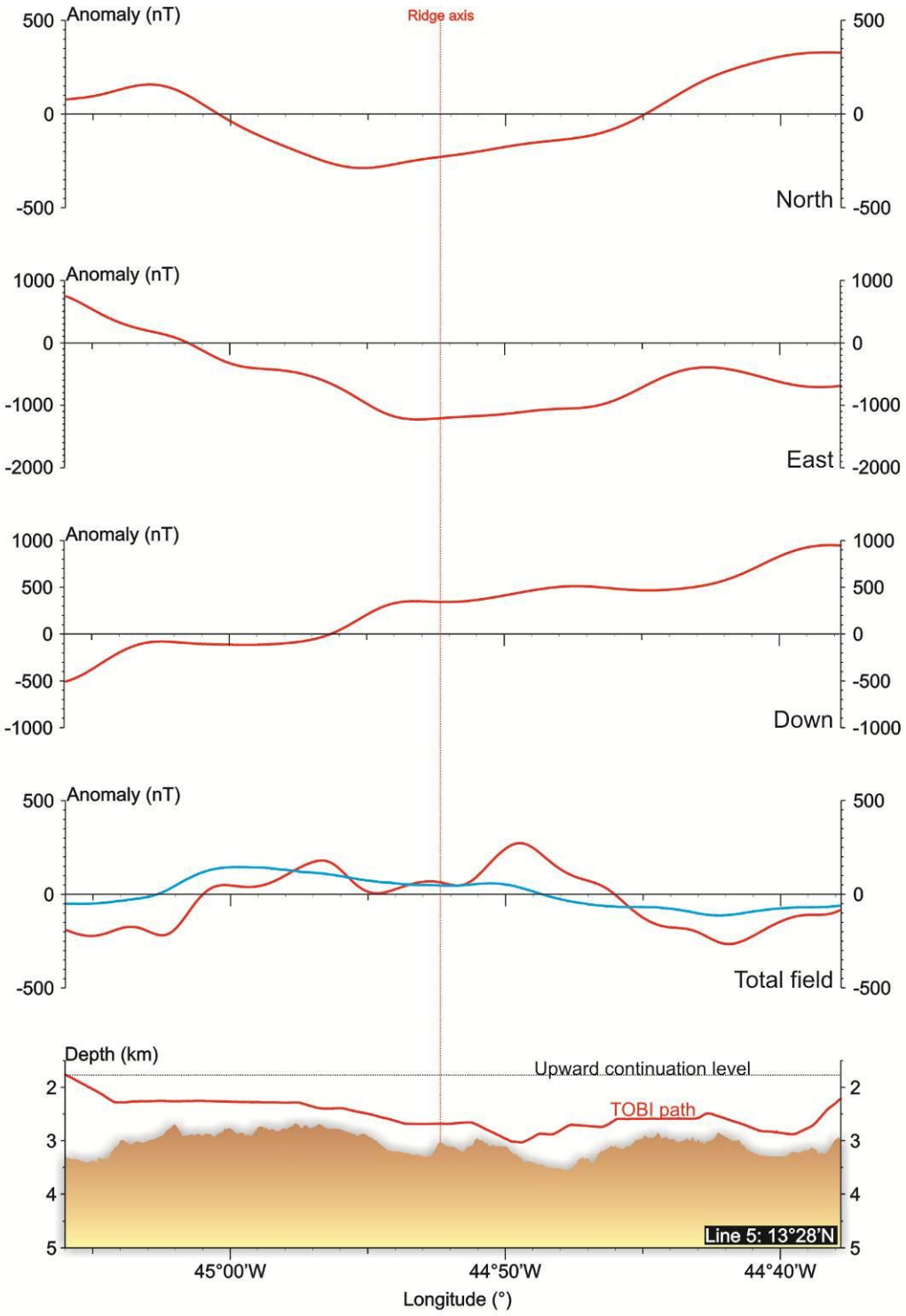


Figure 2.6.14[5]. Two-dimensional magnetic total field anomaly and components in north, east and downward direction for survey line 5. In each case red line is deep-towed anomaly (upward continued to the minimum depth encountered along the profile and bandpass filtered between 55 and 2 kilometres) and blue is the surface-towed anomaly. Note that the vertical scale is different between plots.

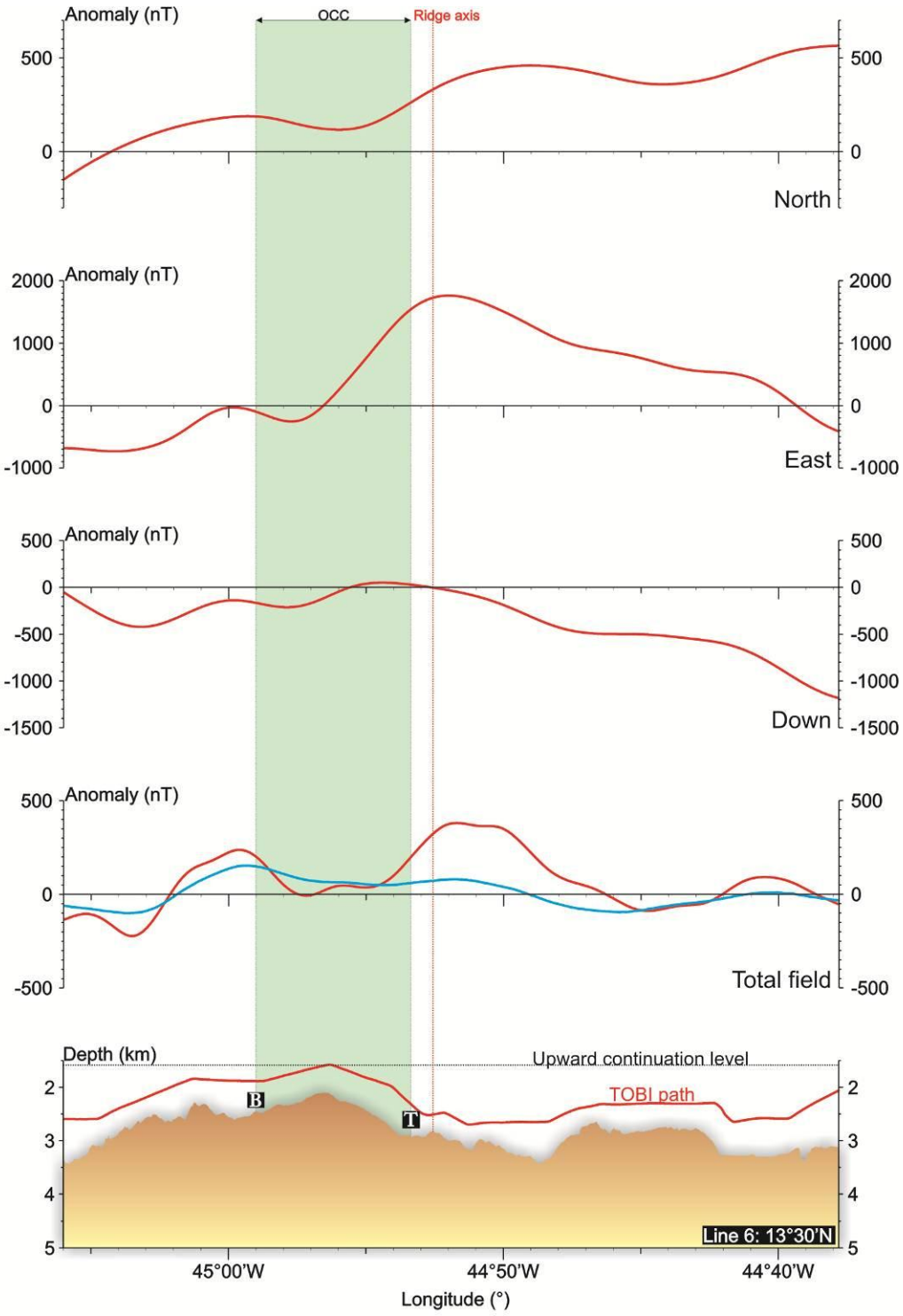


Figure 2.6.14[6]. Two-dimensional magnetic total field anomaly and components in north, east and downward direction for survey line 6. In each case red line is deep-towed anomaly (upward continued to the minimum depth encountered along the profile and bandpass filtered between 55 and 2 kilometres) and blue is the surface-towed anomaly. Note that the vertical scale is different between plots. Vertical green bar marks near-axis OCC location.

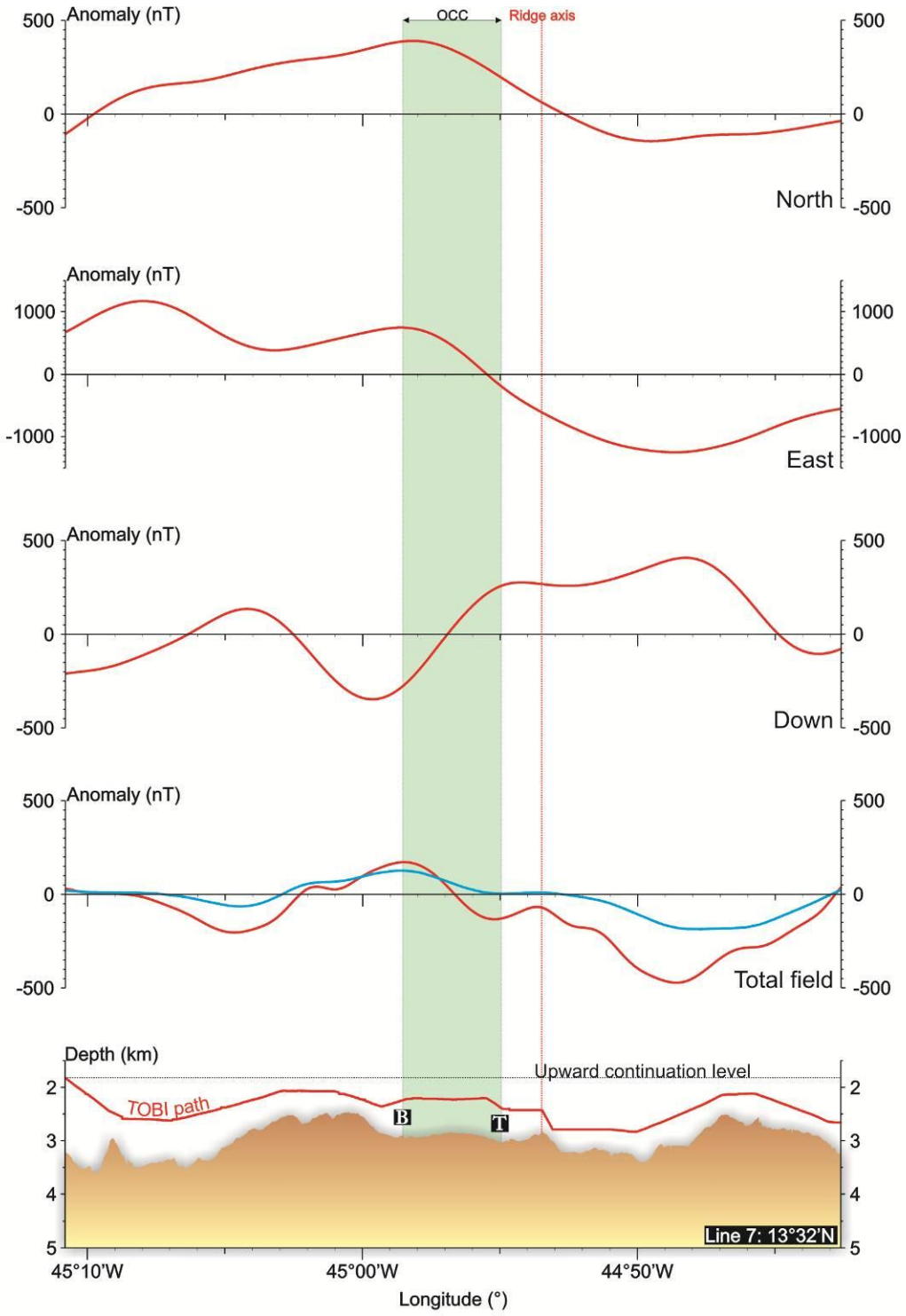


Figure 2.6.14[7]. Two-dimensional magnetic total field anomaly and components in north, east and downward direction for survey line 7. In each case red line is deep-towed anomaly (upward continued to the minimum depth encountered along the profile and bandpass filtered between 55 and 2 kilometres) and blue is the surface-towed anomaly. Note that the vertical scale is different between plots. Vertical green bar marks near-axis OCC location.

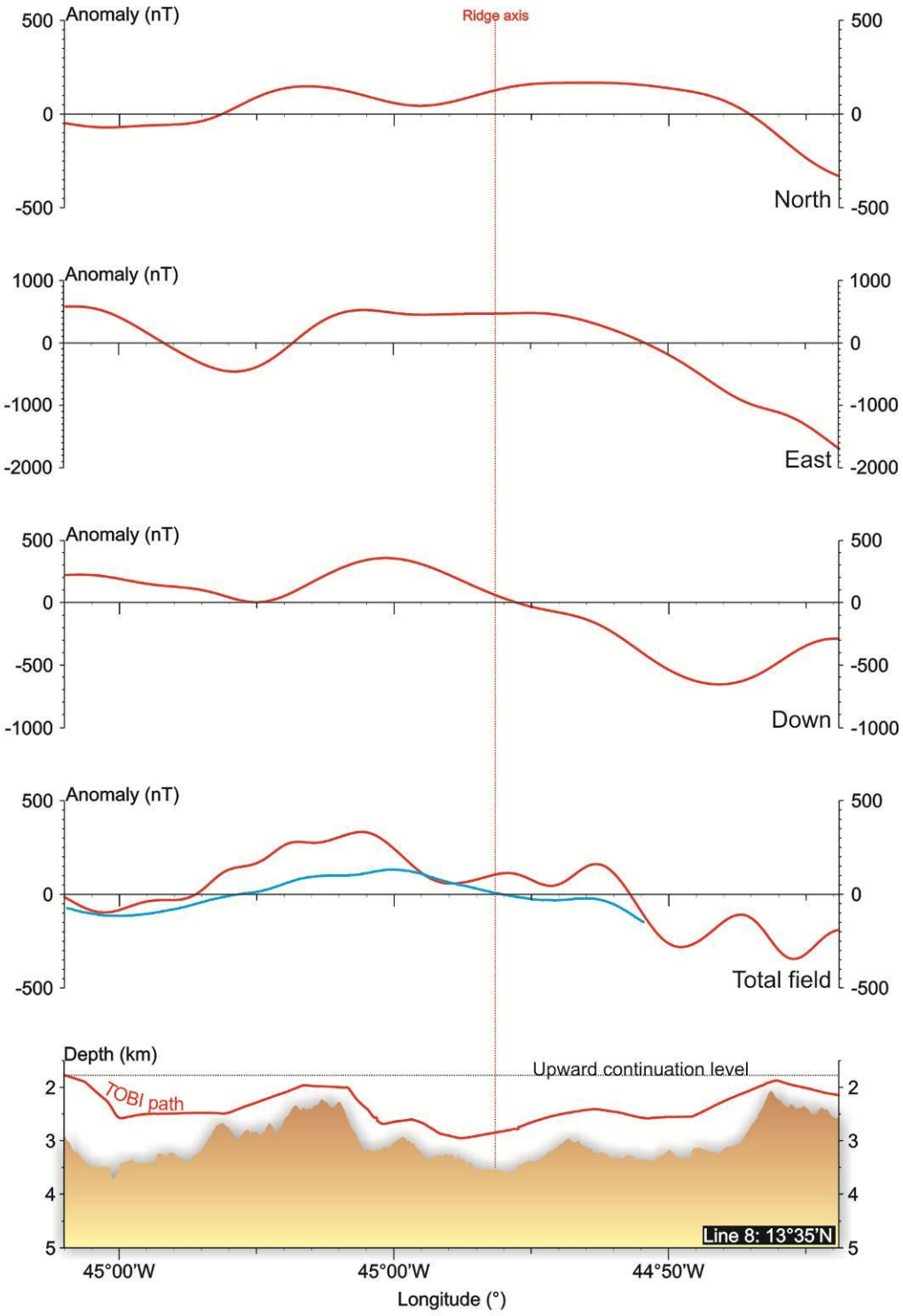


Figure 2.6.14[8]. Two-dimensional magnetic total field anomaly and components in north, east and downward direction for survey line 8. In each case red line is deep-towed anomaly (upward continued to the minimum depth encountered along the profile and bandpass filtered between 55 and 2 kilometres) and blue is the surface-towed anomaly. Note that the vertical scale is different between plots.

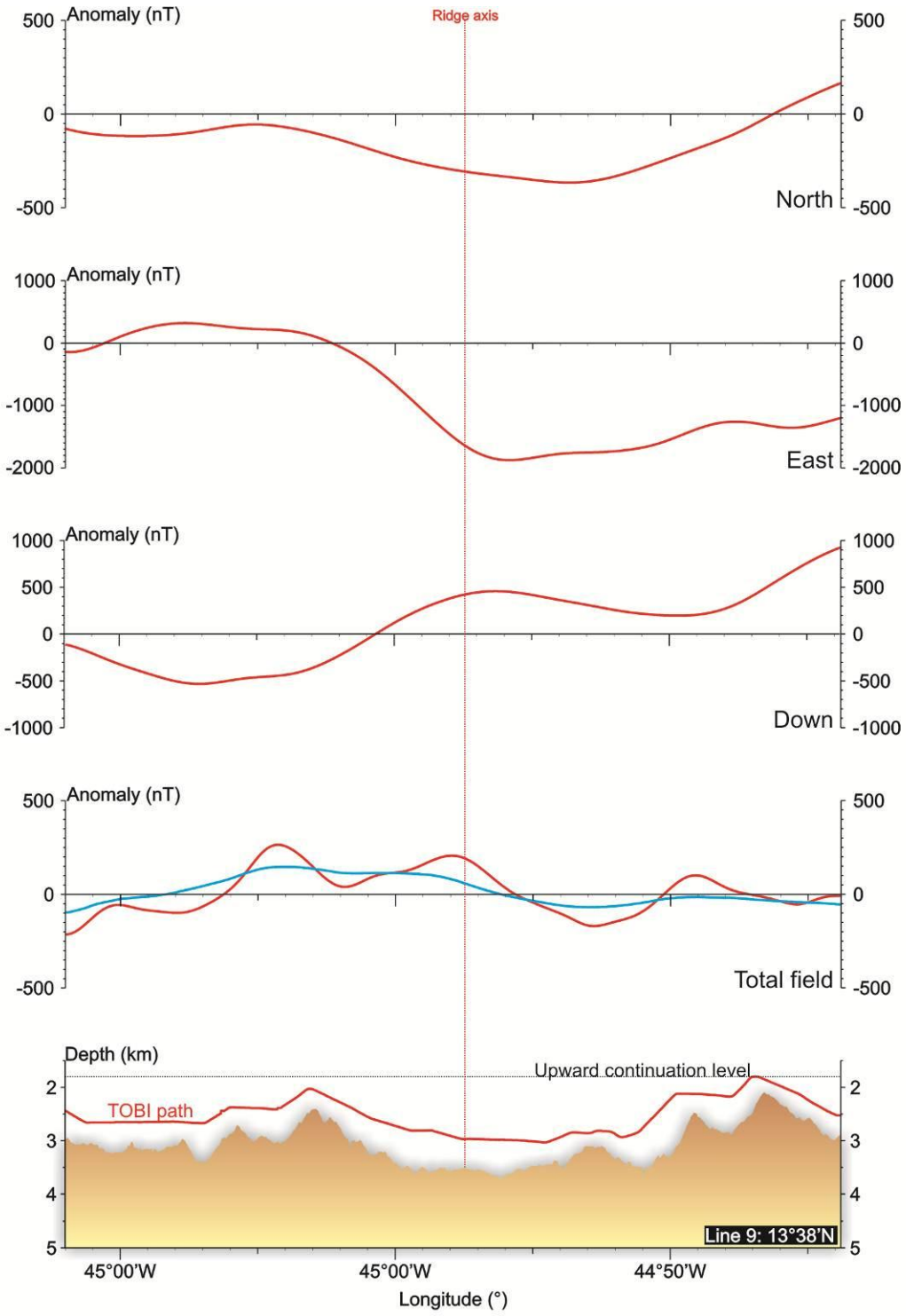


Figure 2.6.14[9]. Two-dimensional magnetic total field anomaly and components in north, east and downward direction for survey line 9. In each case red line is deep-towed anomaly (upward continued to the minimum depth encountered along the profile and bandpass filtered between 55 and 2 kilometres) and blue is the surface-towed anomaly. Note that the vertical scale is different between plots.

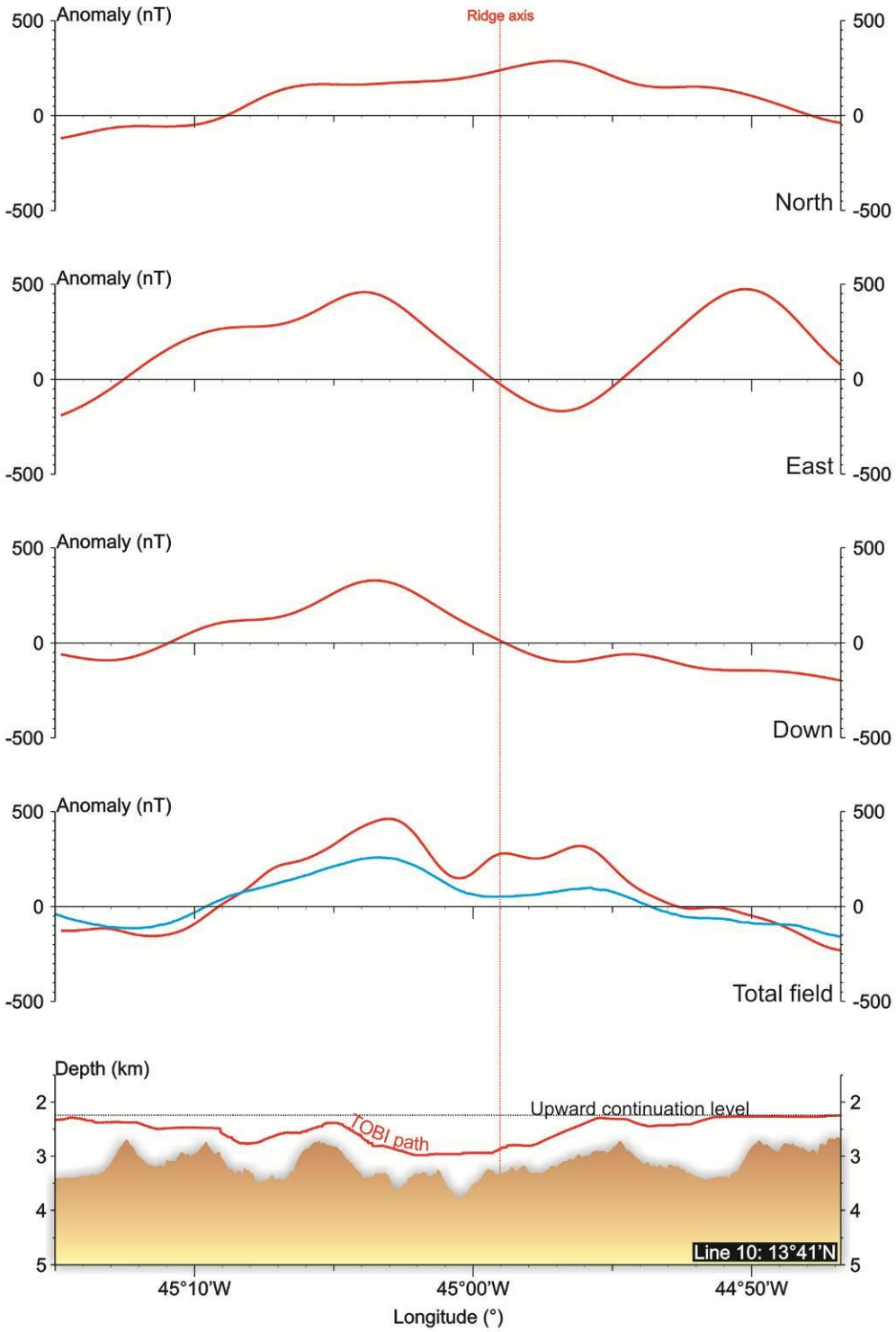


Figure 2.6.14[10]. Two-dimensional magnetic total field anomaly and components in north, east and downward direction for survey line 10. In each case red line is deep-towed anomaly (upward continued to the minimum depth encountered along the profile and bandpass filtered between 55 and 2 kilometres) and blue is the surface-towed anomaly. Note that the vertical scale is different between plots.

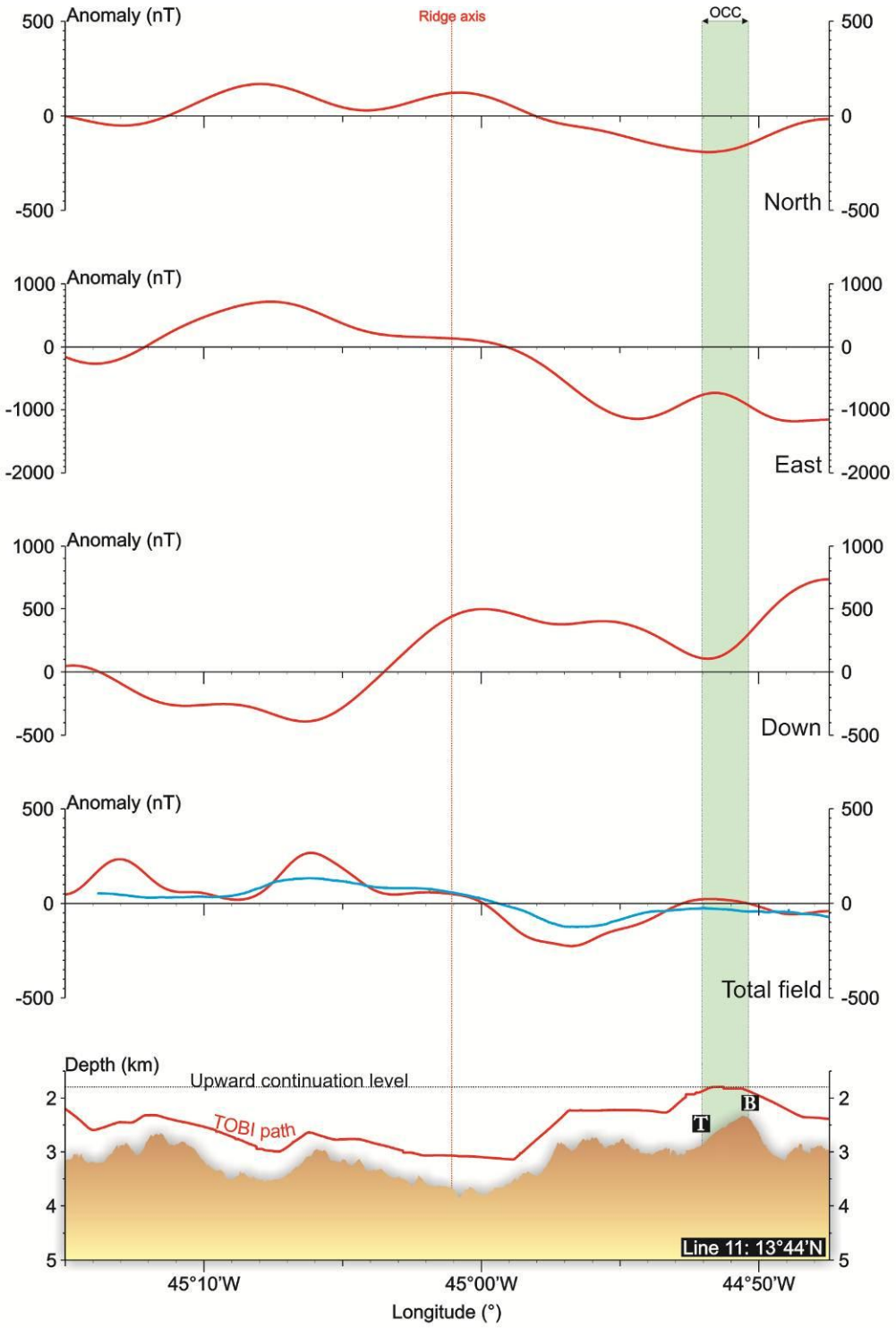


Figure 2.6.14[11]. Two-dimensional magnetic total field anomaly and components in north, east and downward direction for survey line 11. In each case red line is deep-towed anomaly (upward continued to the minimum depth encountered along the profile and bandpass filtered between 55 and 2 kilometres) and blue is the surface-towed anomaly. Note that the vertical scale is different between plots. Vertical green bar marks near-axis OCC location.

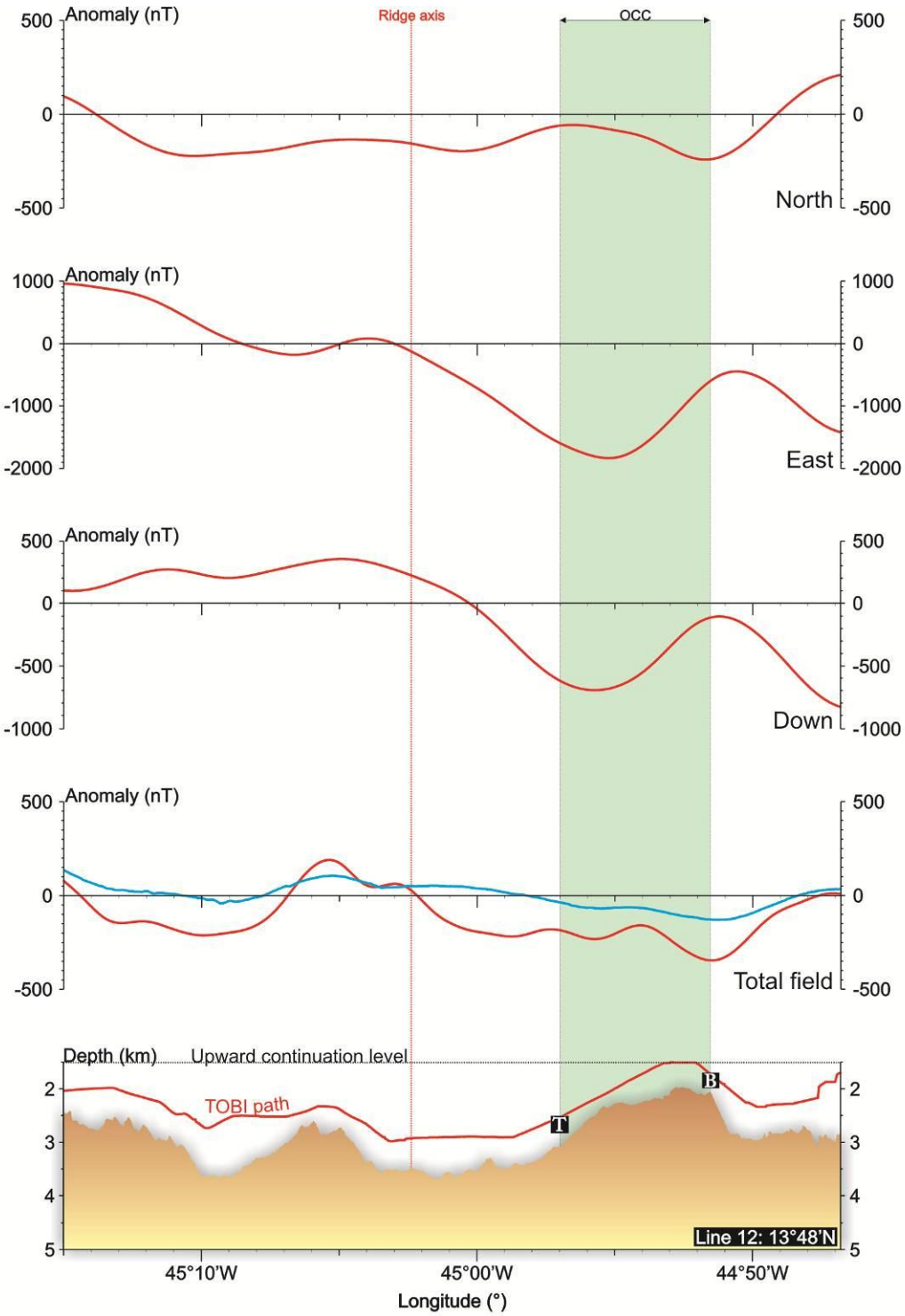


Figure 2.6.14[12]. Two-dimensional magnetic total field anomaly and components in north, east and downward direction for survey line 12. In each case red line is deep-towed anomaly (upward continued to the minimum depth encountered along the profile and bandpass filtered between 55 and 2 kilometres) and blue is the surface-towed anomaly. Note that the vertical scale is different between plots. Vertical green bar marks near-axis OCC location.

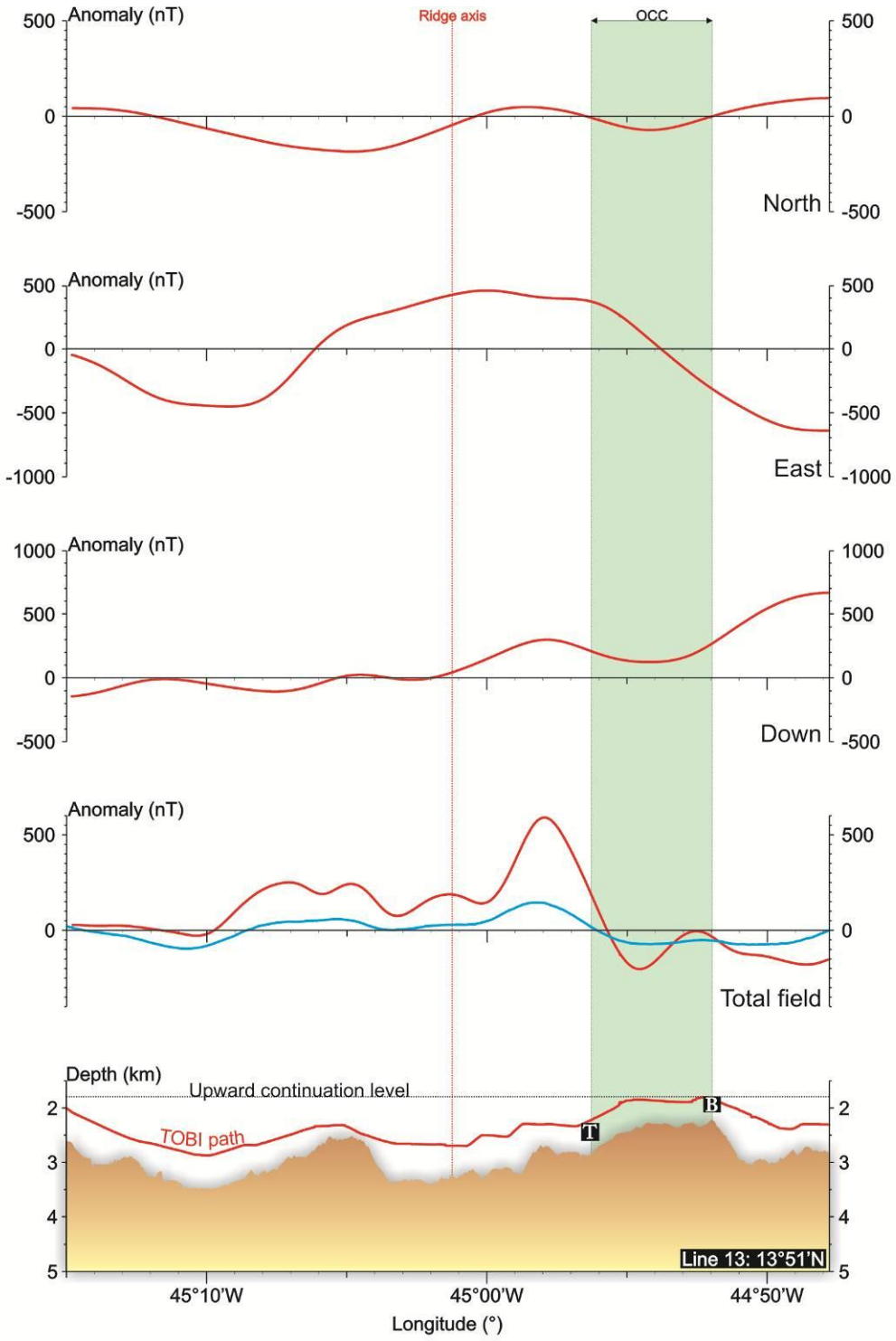


Figure 2.6.14[13]. Two-dimensional magnetic total field anomaly and components in north, east and downward direction for survey line 13. In each case red line is deep-towed anomaly (upward continued to the minimum depth encountered along the profile and bandpass filtered between 55 and 2 kilometres) and blue is the surface-towed anomaly. Note that the vertical scale is different between plots. Vertical green bar marks near-axis OCC location.

2.7. Summary of data reduction techniques

This chapter has provided an overview of the data reduction stages I have performed for JC07 gravity, deep-towed sidescan sonar and tri-axial magnetometer data.

The sidescan sonar imagery is some of the most spectacular ever recorded by a deep-towed vehicle (e.g. Figure 2.4.10c). Within the images, minor acquisition artefacts still exist which have not entirely been removed during the processing stage (attributable to either acoustic noise or inaccuracies with estimating the vehicle position). This is most commonly evident as sea-surface reflections or minor mismatches between sidescan imagery and bathymetry. Acoustic noise and artefacts within the final mosaic can generally be regarded as an aesthetic feature, and given that the interpretation of the imagery is entirely manual these artefacts should not affect the final interpretation of seafloor geology.

Gravity readings have been reduced to the free-air anomaly using the standard method for marine gravimetry data. This has involved removing the predictable effects of variation of gravitational potential due to survey latitude and the Eötvös effect. Internal crossover errors were reduced from 1.3 to 1.0 mGal.

Deep-towed tri-axial magnetic data have been reduced to total field anomaly after removal of the theoretical IGRF and derivation of vehicle-related heading and pitch anomalies.

Chapter Three

Seafloor geology from sidescan sonar data

3.1. Introduction

In combination with bathymetry data and seafloor sampling information, TOBI sidescan sonar imagery reveals a profusion of information regarding the surficial structure and composition of seafloor geology. The analytical techniques used to extract useful information from sidescan sonar imagery can be quite subjective, however, and so it is necessary to document the criteria that have been used to delineate various volcanic and tectonic features of the seafloor. The first part of this chapter is thus concerned with the interpretative methods associated with mapping seafloor geology, and is subdivided into sections on: seafloor gradient, seafloor sampling, hydrothermal data and – primarily – sidescan sonar. Useful information derived from the seafloor map then forms the latter part of this chapter, which is divided into sections on: regional seafloor morphology and newly identified OCCs in the 13°N region, volcanic processes and tectonic processes – the latter two of which reveal insights into OCC initiation conditions and termination mechanisms. A condensed version of some of these results is included in the paper published by MacLeod *et al.* (2009) to which I contributed and is included here as Appendix I.

3.2. Interpretative methods – seafloor mapping

3.2.1. Bathymetry data and seafloor gradient

Seafloor gradient and slope information were independently derived from both the ship's bathymetry data and TOBI digital data (*Section 2.3*). For each of the thirteen TOBI survey profiles, seafloor gradient was calculated by adding the vehicle depth (determined from the pressure sensor) and vehicle altitude (first acoustic return of sidescan sonar data) – and by dividing the change in depth by the change in longitude for successive sidescan sonar pings. It was necessary to average the data over 9-points

in order to remove some of the 'jitter' inherent within the original pressure readings, giving a final along-track resolution of ~30 metres (Figure 3.2.1). The resultant signal fluctuates rapidly over distances of ~<100 metres between ±50° (positive slope to west). Given that this value diminishes over OCC surfaces (max. amplitude ~8°) that are predicted to be relatively smooth, it is therefore likely that some of this 'jitter' is real (e.g. arising from volcanic topography). If OCCs have smooth surfaces this indicates a resolution of ±4°. Mismatches between the deep-towed and ship's profiles may occur if the vehicle deviates from the track-line, possibly due to deep-water currents (upper panel, Figure 3.2.1).

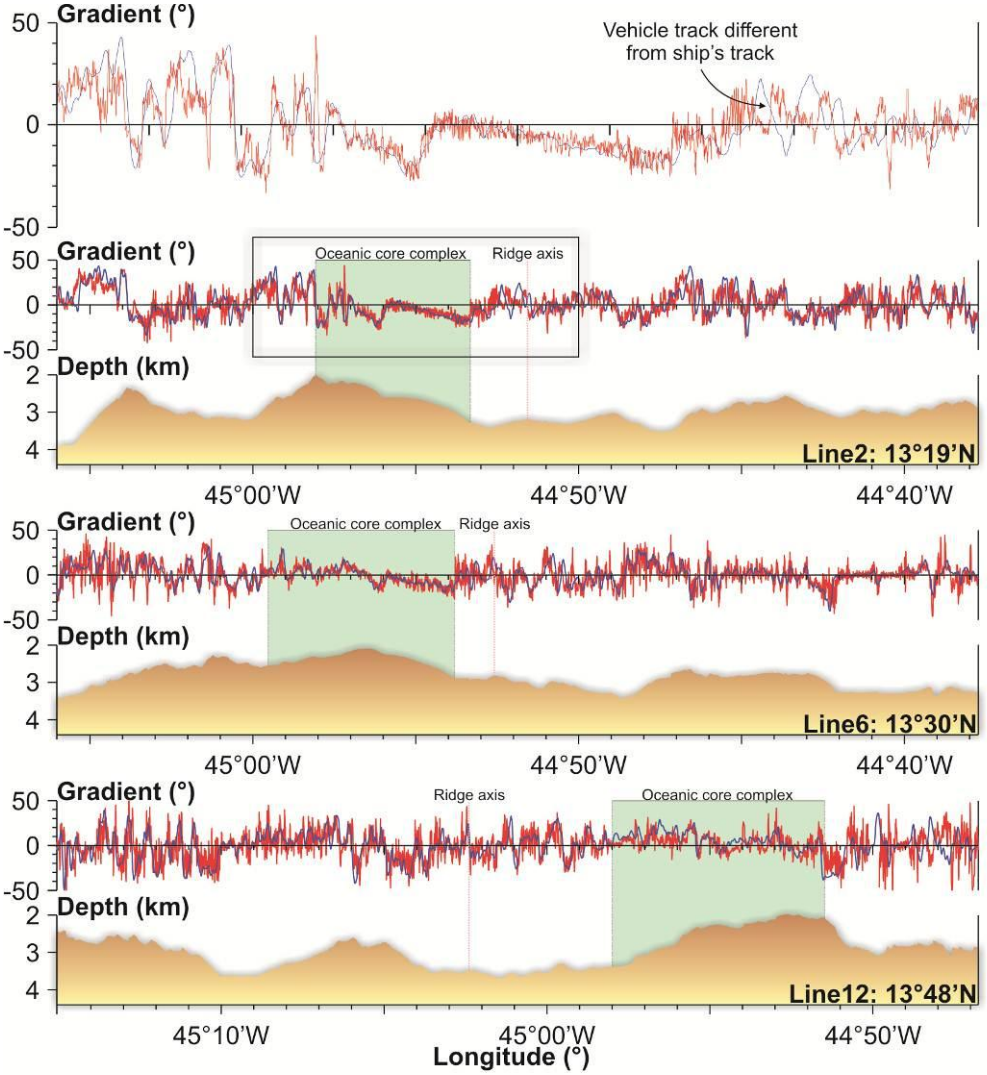


Figure 3.2.1. Seafloor gradient profiles across OCCs derived from ship's bathymetry data (blue lines) and high resolution TOBI depth profiles (red lines and corresponding cross-section). Upper panel shows an enlargement of survey line 2 across OCC at 13°19'N, with the position marked by the rectangle. See text for discussion.

In addition to slope profiles, the modulus (i.e. non-directional component) of the seafloor slope was determined using the 'surface slope calculator' function in *DMagic* (Figure 3.2.2). This information allowed for qualitative estimations of seafloor roughness to be made, which was particularly useful when distinguishing between hummocky and smooth seafloor terrains (see *Section 3.2.3*). Azimuthal derivatives of seafloor gradient in the E-W and N-S directions were also obtained from the bathymetry grid file using the `grdgradient` command in GMT (Wessel & Smith, 1998) and by varying the –A operator from 90 to 0, respectively (Figure 3.2.3a-b). As a general rule, the E-W derivative is useful for identifying features that are aligned parallel to the ridge axis, such as major fault scarps, and the N-S derivative highlights spreading direction-parallel features, such as prominent OCC corrugations.

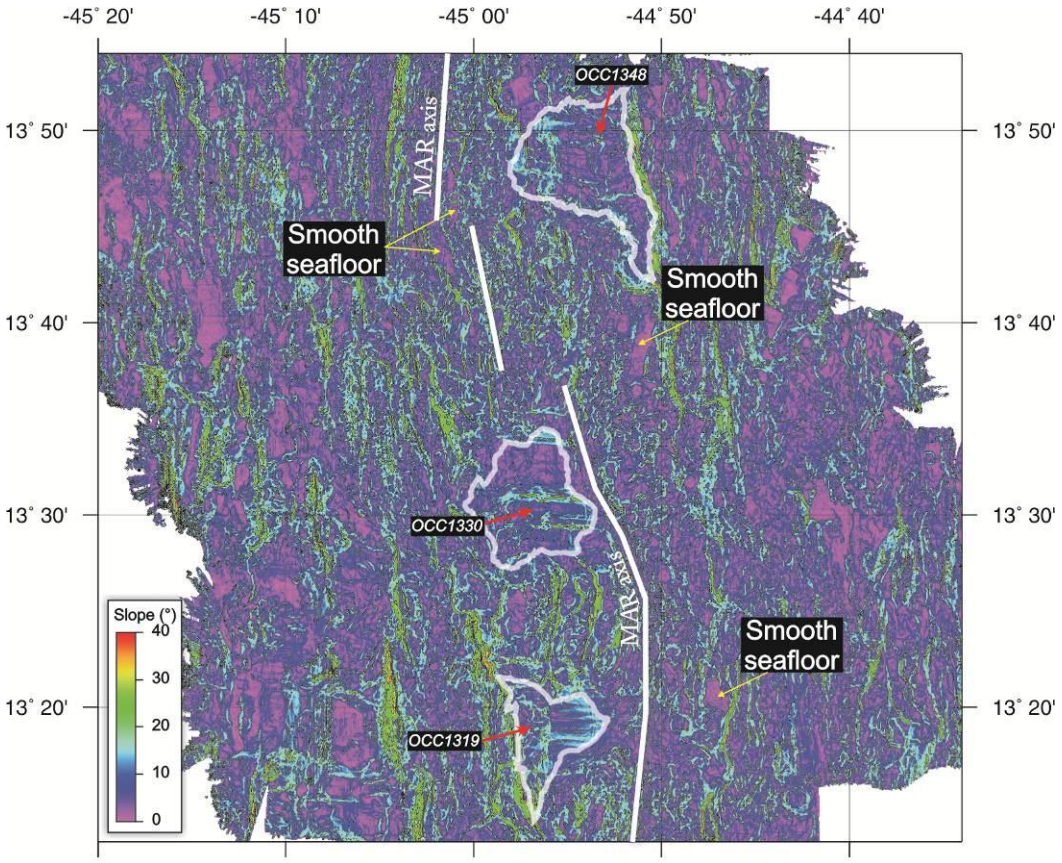


Figure 3.2.2. Seafloor slope derived from bathymetry data. The non-directional slope is useful for assessing seafloor 'roughness', making it easier to dinstinguish areas of hummocky seafloor from smooth seafloor.

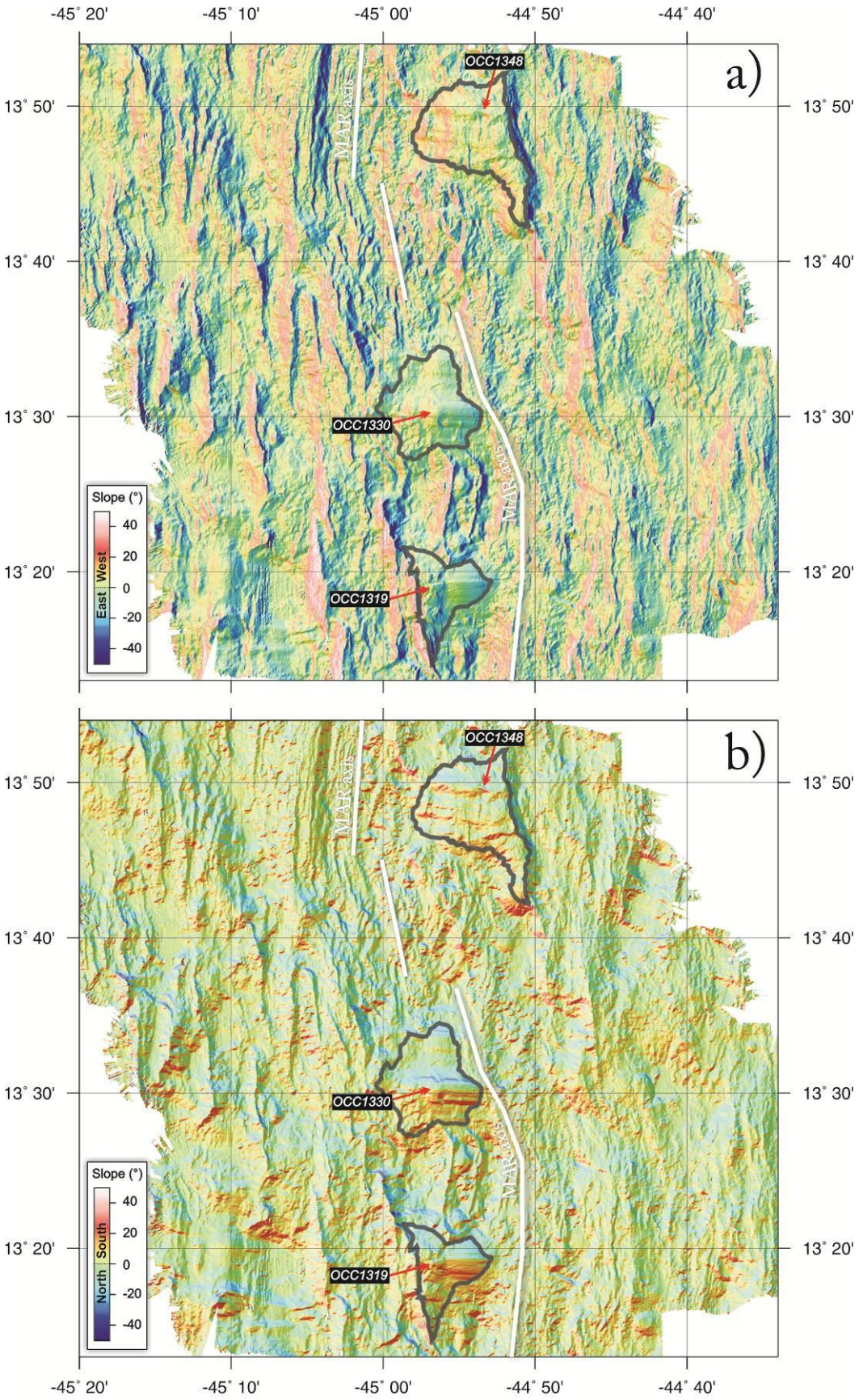


Figure 3.2.3a-b. Seafloor slope derived from bathymetry data. **a)** East/west azimuthal derivative is useful for looking at ridge parallel features (e.g. faults), where as **b)** north/south derivative helps to identify features that are perpendicular to the ridge (e.g. OCC corrugations). Slope is in colour, shading is bathymetric illumination from NW.

3.2.2. Seafloor sampling results

This section provides an overview of the lithologies collected throughout the sampling survey, the results of which provide a useful means by which to ground-truth not only the sidescan sonar textures, but also the various lithologies implied by forward and inverse modelling of the gravitational and magnetic field (survey configuration and relevant location information for drill and dredging sites can be found in Tables 2.2.2 and 2.2.3, respectively). Figure 3.2.4 shows the distribution of lithologies collected throughout the dredging survey, classified by weight and grouped into the morphological areas: OCC domal (the domed, corrugated section of the OCC's detachment surface), OCC upper massif (the area between the breakaway ridge and domal section) and axial valley (see also Figure 3.2.6 for geographical distribution). The terms 'OCC domal' and 'OCC upper massif' are defined more fully in *Section 3.2.3*.

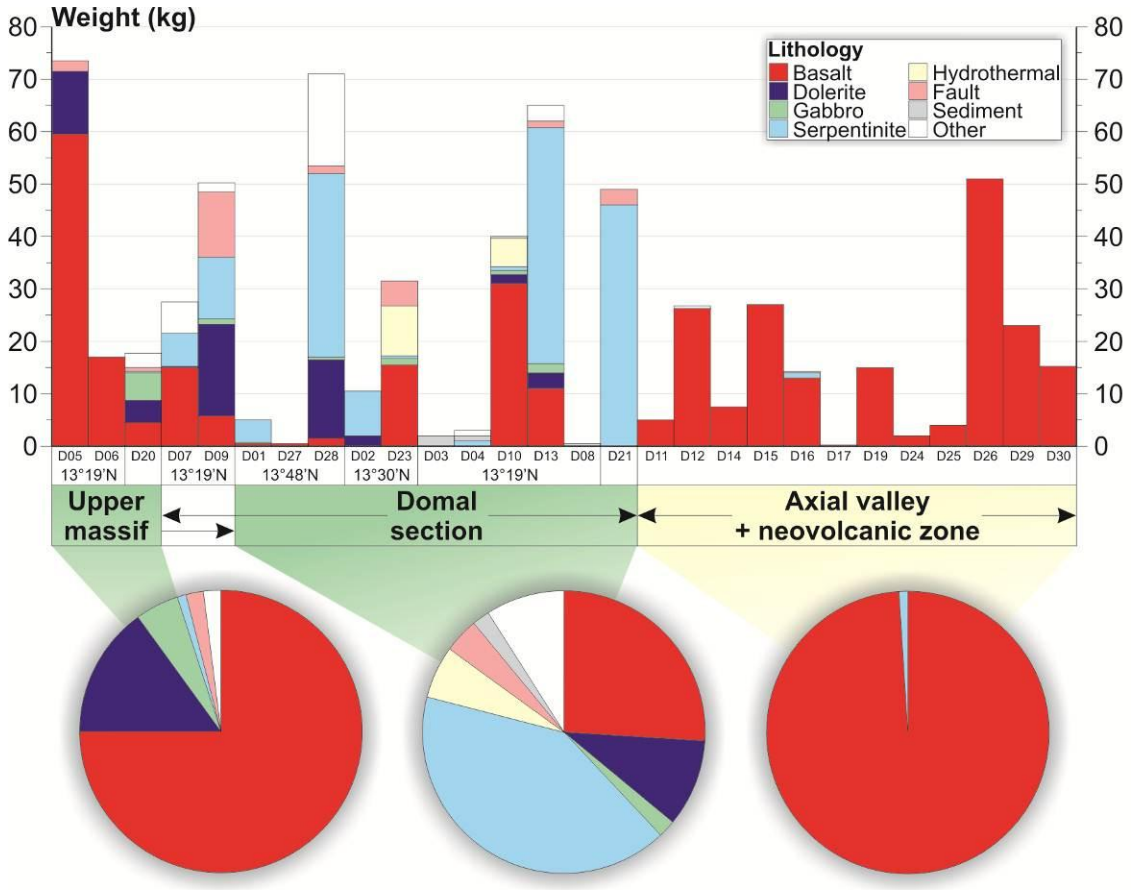


Figure 3.2.4. JC07 dredging results classified by weight and grouped into the morphological regions: OCC upper massif, OCC domal section and axial valley. Note that D07 and D09 cross the boundary between upper massif and domal section (and may therefore comprise lithologies common to both regions) and so are ommitted from the summary pie charts. Data are from Searle *et al.* (2007). See text for discussion.

Lithologies have been generalised into the following groups: basalt, dolerite, gabbro, peridotite, fault rock, hydrothermal, sediment and other. A drill survey summary is presented in Figure 3.2.5, with a map of combined dredge and drill results in Figure 3.2.6.

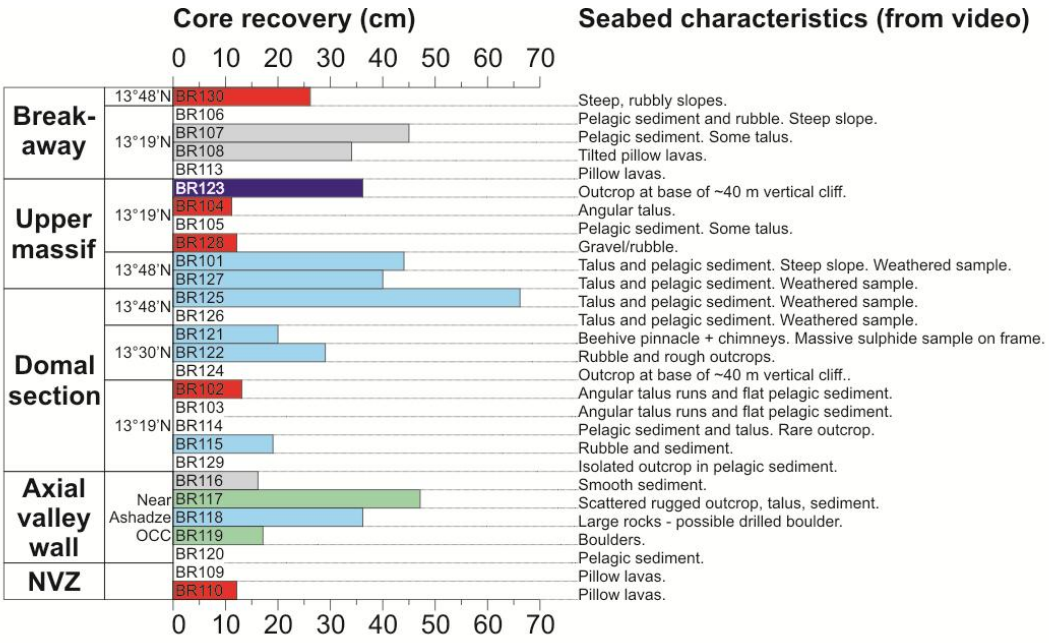


Figure 3.2.5. JC07 drill results classified by core length and grouped into the morphological regions: breakaway, OCC upper massif, OCC domal section, axial valley and NVZ. Seabed classification from drill video footage is from Searle *et al.* (2007), with colour code as for **Figure 3.2.4**.

It should be noted that dredge-tracks were typically a few kilometres long and hence the precise location of dredged samples is ambiguous. Most dredges were confined to a single morphological province (e.g. the NVZ or the domal section of an OCC) to help mitigate this problem. Dredges D07 and D09, however, crossed the boundary between the upper massif and domal section of the OCC at 13°19'N, and may therefore contain lithologies common to both regions. A similar problem applies to the drilled samples, with the possibility of some rocks sampled (especially on the smooth domes) not being in-situ. Seabed characterisation from the drill video partially mitigates this problem (Figure 3.2.5).

In general, basalt is predominantly exposed (75% by weight of all samples) across the upper massif area of OCCs, with small amounts of dolerite (15%) and gabbro (5%) also being recovered. Domal sections comprise the most diverse array of lithologies, exposing significant volumes of serpentinite (41%), basalt (26%), dolerite

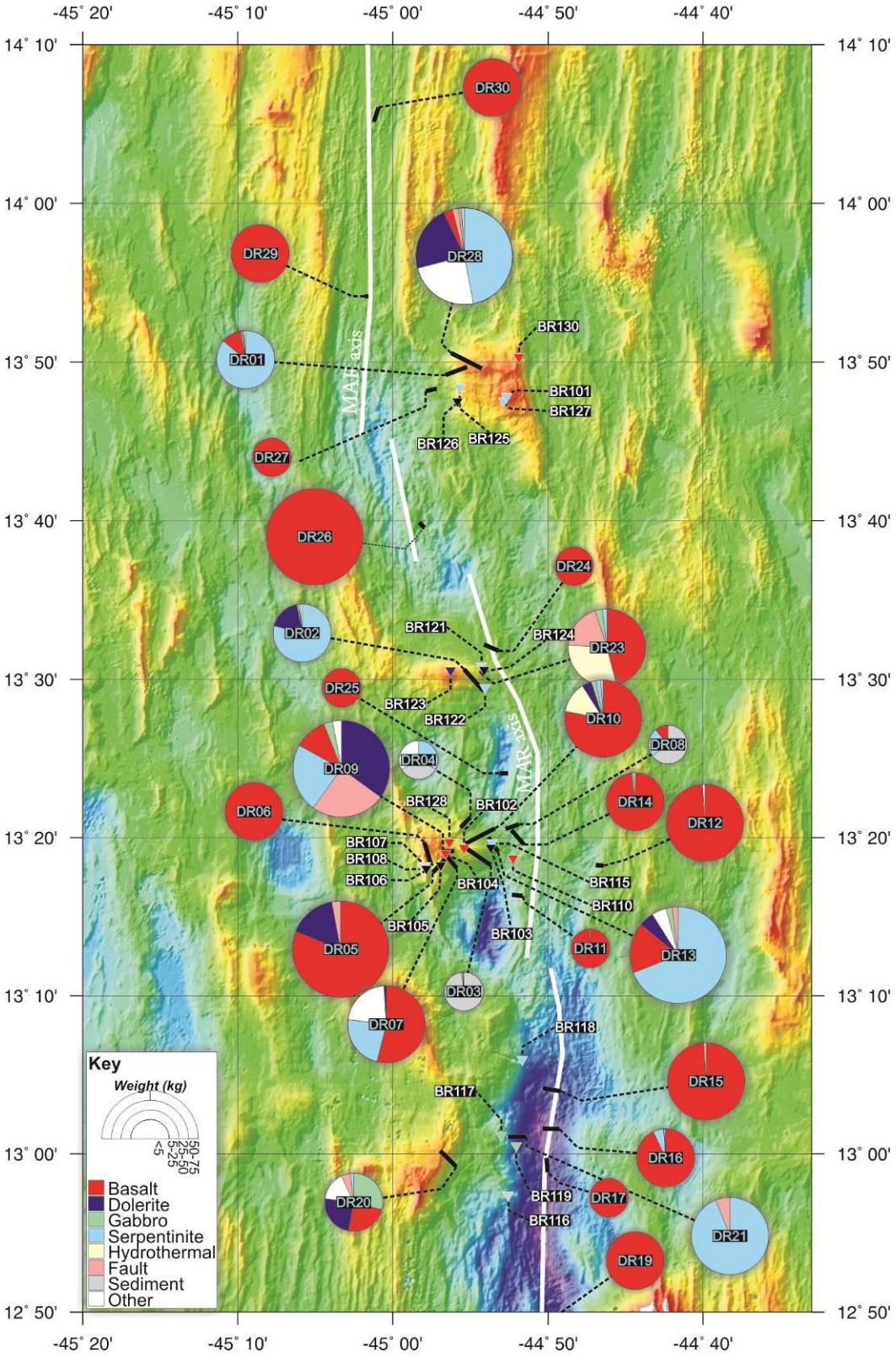


Figure 3.2.6. JC07 sampling survey results. Pie charts represent the relative weights of the various lithologies recovered during dredging. BRIDGE drill sampling results are marked by triangles (black triangles show sites where no samples were recovered, but the seabed video has been referred to in this study). 100 metre resolution bathymetry is illuminated from NW. See text for discussion.

(10%) and hydrothermal deposits (6%). As would be expected, dredges from within the axial valley recovered almost entirely basaltic material (> 99%). The drill results show a similar pattern to the dredging survey, with the upper massif and breakaway regions being dominated by upper crustal lithologies, and with ultramafic exposures becoming prevalent across the domes of OCCs. Video footage showed the breakaway ridge to consist of spheroidal pillow lavas – the lack of elongation indicating that basaltic material had been erupted horizontally and subsequently tilted during OCC formation (Searle *et al.*, 2007). Angular talus accumulations were identified across the domal sections of all OCCs.

In terms of lithology and geographical distribution, the samples collected and seabed characteristics (from the drill video) encountered throughout JC07 are similar to those which have been observed during other sampling and submersible studies across OCCs and magma-poor environments (e.g. Bougault *et al.*, 1993; Cann *et al.*, 1997; Cannat *et al.*, 1997; Escartin & Cannat, 1999; Ohara *et al.*, 2001; Tucholke *et al.*, 2001; MacLeod *et al.*, 2002; Reston *et al.*, 2002; Searle *et al.*, 2003; Dick *et al.*, 2008). The results are consistent with an OCC model in which a detachment fault cuts through the crust and displaces and rotates upper crustal, basaltic material towards the oldest (axial-distal) part of the OCC. From the oldest (i.e. the breakaway) to the youngest (i.e. the termination or footwall/hanging-wall boundary) part of the OCC, the lithologies encountered originate from progressively deeper parts of the crustal and upper mantle sequence. Domal sections often comprise talc, serpentine and other weak minerals which most likely promote strain localisation onto detachment surfaces (e.g. Escartin *et al.*, 2001; Escartin *et al.*, 2008a). The relative lack of gabbroic material recovered during JC07 implies that either the gabbroic layer within the crust must be thin or that gabbroic material is predominantly encountered at depths greater than those sampled by the BRIDGE drill, or that gabbro is systematically under sampled by dredging. This may be further evidence for a 'plum-pudding' (*Section 1.2.4*) style crust beneath magma-poor environments in which gabbro crystallizes in a peridotite host (e.g. Cannat *et al.*, 1995; Ildefonse *et al.*, 2007). Alternatively, if the series of ridges at 44°58.5'W are the crests of basaltic rider-blocks, as has been suggested by Smith *et al.* (2008), the gabbroic sequence may be largely obscured. Spalling of material from the brittle hanging wall onto the footwall may also account for the basaltic samples collected across the domal section of OCCs.

3.2.3. Textural analysis of TOBI sidescan sonar imagery

TOBI sidescan sonar data sample the uppermost few metres of the seabed, and hence they can be used to identify major tectonic and recent volcanic events. As the seafloor becomes older, it accumulates more sediment and subsequently absorbs greater amounts of sonar energy (*Section 2.4.1*). For this reason, the axial valley is generally characterised by high intensity backscatter that steadily decreases in amplitude away from the ridge axis. This is readily demonstrated by considering the backscatter amplitude for a swath of data that crosses the axial valley (Figure 3.2.7). The neovolcanic zone has a maximum backscatter intensity of ~4600 units (from a maximum of 5000) that, when averaged over the full-width of the sonar swath, typically becomes ~1000 – 2000 (the effects of beam-sensitivity at different across-track ranges – discussed in *Section 2.4.3*.5 – is ignored at this stage as it is assumed that it affects each successive ping equally). This value decreases away from the ridge axis so that at an along-track distance of ~6 km (2000 pings) the average backscatter intensity is ~< 200. Beyond this point the gradient of the backscatter-distance relationship remains constant, implying that sediment thicknesses are greater than the effective depth of penetration of the incident acoustic energy. Assuming a sedimentation rate of 5 – 10 m/Ma (Mitchell *et al.*, 1998a), then for a half-spreading rate of 13 km/My this would indicate that TOBI's sidescan sonar samples the uppermost 2.3 – 4.6 metres of the seabed. This value is greater than the 1 metre estimate that is made based on work by Urick (1983) (*Section 2.4*), but is comparable with the 2 – 5 metre estimate made by Lawson (1996).

In reality, sediment does not accumulate evenly across the ridge axis, instead preferring to build up in topographic depressions and form isolated sediment ponds. This adds a degree of complexity to the sidescan sonar imagery that must be taken into account when geologically interpreting the data. Furthermore, topographic variations, such as those created by fault scarps and volcanic cones, affect the angle of incidence of acoustic energy and can greatly change the backscattering potential of the seafloor. This can be observed in Figure 3.2.7, where major faults, such as that located on survey line 12 at ping number 10500, may locally increase the backscatter intensity to the point where it has an amplitude similar to zero-age, un-sedimented seafloor. This topographic effect may increase or decrease the backscatter intensity depending on the alignment of the feature in question and the incident acoustic energy.

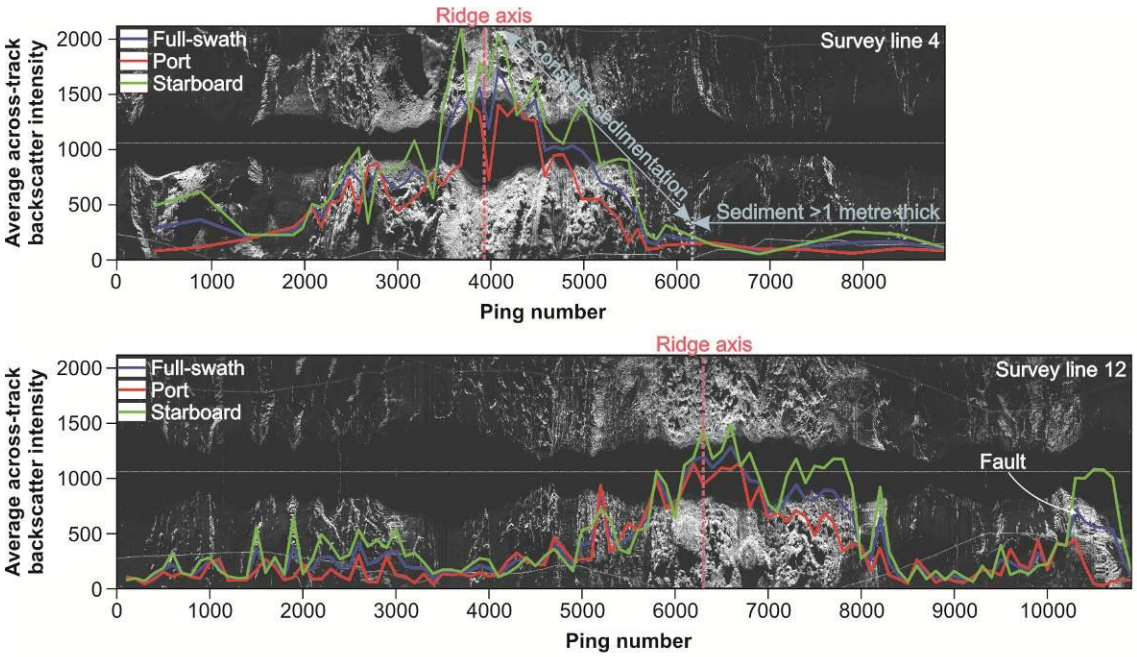


Figure 3.2.7. Across-axis variation in backscatter intensity. The intensity is calculated over an interval of 100 pings (~300 metres) by extracting a profile from the raw sidescan sonar data (background image) and taking the average for the full-swath (blue line) and the separate port (red) and starboard (green) swaths. The black area running along the centre of the imagery corresponds to the period when the acoustic energy is travelling through the water column, and is hence excluded from the calculation. See text for discusssion.

For example, the fault on survey line 12 trends NNW-SSE causing the backscatter intensity on the starboard side (green line – Figure 3.2.7) to increase dramatically compared with the shadow zone on the port side (red line).

In order to map seafloor lithology, I have classified various seabed types into volcanic features (V1 – V7), tectonic features (T1 – T3) and features related to OCCs (O1 – O3). These are listed with their characteristics in Table 3.2.1 and illustrated in Figures 3.2.8, 11 and 12; they are described in detail in the next section. Seafloor topography and gradient information have been used to help ground-truth the sidescan sonar data, as have sampling results and seafloor video reconnaissance where available. In addition to this, mean intensities have been determined for a 1 km^2 sample of each texture.

	Texture identifier	Texture/feature description	Geological interpretation	Mean intensity	Intensity relative to V1	General location (Figure number)
Volcanic textures & structures	V1	Very bright, hummocky	NVZ, volcanic cone seafloor	1270	100 %	Axial valley (3.2.8a)
	V1a	Bright, hummocky	Young, volcanic cone seafloor	1000	79%	Axial valley (3.2.8b)
	V2	Moderate intensity, hummocky	Intermediate age, volcanic cone seafloor	570	45 %	Axial valley & flanks (3.2.8c)
	V2a	Moderate-low intensity, intermittent hummocks	Old, volcanic cone seafloor	370	30 %	Edges/outside axial valley (3.2.8d
	V3	Moderate-high intensity hackly texture with bright bands	NVZ, smooth seafloor displaying faults and possible flow-fronts	820	65 %	Axial valley (3.2.8g)
	V3a	Moderate intensity hackly texture	Young, smooth seafloor	590	46%	Axial valley (3.2.8h)
	V4	Low intensity, dullish-grey hackly texture	Old, smooth seafloor	470	37 %	Mainly axial valley, some on flanks (3.2.8i)
	V5	Variable intensity alignments of hummocks	Minor volcanic cone lineament	-	-	Axial valley (3.2.8e)
	V6	Variable intensity alignments and large build-ups of hummocks	Major volcanic cone lineament	-	-	Axial valley (3.2.8f)
	V7	Bright, semi-circular arc and conjugate shadow zone. May have flat summit.	Seamounts	-	-	Axial valley and some off-axis (3.2.8j)
Tectonic textures & structures	T1/T2	High backscatter intensity with narrow, vertical shadow bands	Fault (inward/outward facing), displaying gulleys	940	74%	Widespread, mainly off-axis (3.2.11a-b)
	T3	Moderate intensity channels cutting through seafloor at base of T1 and T2	Sediment chutes and erosional features	-	-	Off-axis faults, thick sediment regions (3.2.11d)
Oceanic core complex textures and structures	O1	Variable, from banded high/low intensity striations to solid, low intensity	OCC – domal section at various ages	Variable: 100-480	Variable: 8-38%	Obscured >~10km from ridge axis (3.2.12a-b)
	O2	Variable and incoherent	OCC – upper massif	Variable: 100-520	Variable: 8-40%	Obscured >~10km from ridge axis (3.2.12c-e)
	O3	Moderate intensity, hackly texture with bright, cross-cutting bands.	OCC–related hanging-wall degradation with cross-cutting faults	~390	~30%	Axial valley (3.2.12f)
Sed.	Sed.	Very low intensity, 'fuzzy' texture	Thick (~>4 m), off-axis sediment	100	8 %	Outside axial valley

Table 3.2.1. Summary of sidescan sonar textures and features. The backscatter intensity range for the entire survey was 0 – 5000. Average backscatter intensity for a section (~1 km^2) typical of each texture is shown, with the percentage relative to V1 calculated for each. See text for discussion.

3.2.3.1. Volcanic textures

- **Hummocky seafloor** (V1/V1a/V2/V2a) is the most common feature of the volcanic terrain observed within the axial valley, most likely due to the point-source nature of volcanic events at slow-spreading ridges (*Section 1.2.2*). The backscatter intensity of hummocky seafloor is the highest of any texture observed within the survey area, with an average backscatter value for neovolcanic, zero-age material of ~1270 (Figure 3.2.8a). Where possible, a slightly older section of the NVZ has been identified based on its lower backscatter intensity (V1a – with an intensity relative to V1 of ~79%; Figure 3.2.8b). The high intensity of V1 occurs as a result of minimal sediment cover and the alignment of multiple surfaces towards the incident sonar pulse, as each individual hummock represents a topographically distinctive, individual volcanic cone with a typical diameter of a few hundred metres and a height of several tens of metres. Seafloor sampling and video footage confirm that this terrain is built from basaltic extrusives in the form of pillow basalts, with a single 'haystack' usually forming at the summit of cones and marking the locus of eruptive events (Searle *et al.*, 2010 – included in Appendix I). Pillow-basalts acting as corner-cube reflectors over wavelengths similar to the incident sonar energy (≈ 5 cm) may also locally increase the backscatter intensity. The 'hummocky' nature of this texture arises from the variation in the shape of the seafloor and the shadowing pattern that this creates with the sidescan sonar. This leads to an interesting effect whereby volcanic cones beneath the path of the vehicle (i.e. within the nadir) lose their hummocky texture due to insonification from a high angle, and instead take on the appearance of 'smooth' seafloor (which is discussed in the next section). Ideally, multiple passes over the seafloor at various insonification angles would mitigate this effect. In the absence of this, seafloor topography and gradient (*Section 3.2.1*) can be used to show that despite the apparently different sidescan sonar texture beneath the vehicle, the surface morphology is usually no different from the areas at the port and starboard edges of the swath (Figure 3.2.9). V2 (Figure 3.2.8c) and V2a (Figure 3.2.8d) are hummocky textures that have intensities of ~45% and ~30% relative to V1, and represent older, more sedimented volcanic cone seafloor.

Hummocky lineaments (V5 – V6) are common, with alignments of volcanic cones occurring for distances of up to 8 km in the neovolcanic area situated at 13°24'N (sonar mosaic – Figure 2.4.10b). These lineaments are the result of melt preferentially being supplied along weak zones that run parallel to the ridge axis (Head *et al.*, 1996).

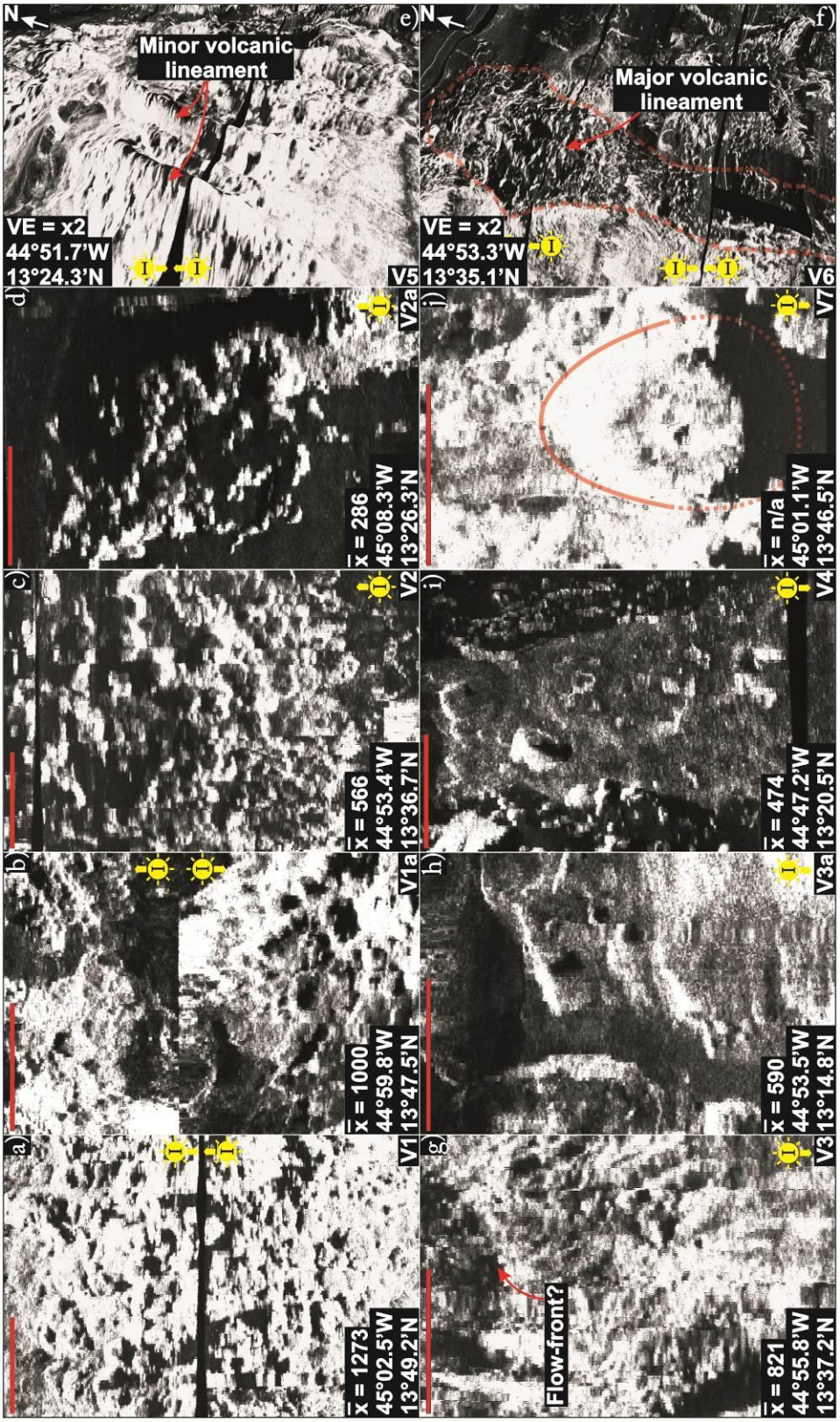


Figure 3.2.8a-j. (Landscape except for e) and f)). Gallery of volcanic sidescan sonar textures and structures: **a)** V1 - neovolcanic, hummocky seafloor; **b)** V1a - young, hummocky seafloor; **c)** V2 - intermediate age, hummocky seafloor; **d)** V2a - oldest resolvable hummocky textures; **e)** V5 - hummocky lineament (minor); **f)** V6 - major hummocky lineament; **g)** V3 - neovolcanic, smooth seafloor; **h)** V3a - young, smooth seafloor; **i)** V4 - old, smooth seafloor; **j)** V7 - major seamount (outlined). $\bar{x}$ is the average backscatter intensity for each texture and sun icon indicates the insonification direction. Red bar in upper-left represents ~1 km. Plan view with north to top of page except where VE= x2. Further texture examples can be obtained by comparing the geological map (Figure 3.2.15a-b) with the TOBI sidescan sonar mosaic (Figure 2.4.10a-b) - a digital copy of each is contained in Appendix II.

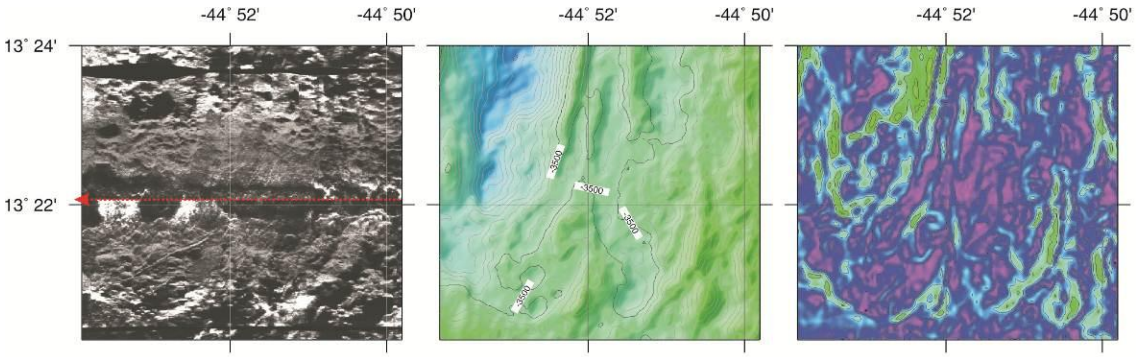


Figure 3.2.9. Effect of insonification angle on sidescan sonar texture. Hummocky seafloor (sidescan sonar data, left image) loses its shadow when insonified from high angles (i.e. close to the vehicle path - red line), even after across-track beam sensitivity has been taken into account, and begins to look like smooth seafloor. Bathymetry data (centre) and seafloor slope (right, with colour scale the same as **Figure 3.2.2.**) can be used to show that there is no morphological difference between the hummocky and apparently smooth areas.

These volcanic lineaments may be only a single volcanic cone wide (minor – V5, Figure 3.2.8e), or, in some places (e.g. 44°53'W, 13°34'N – Figure 2.4.10b), may have been built up by successive magmatic eruptions to the point where they form a topographically distinctive, major volcanic lineament that is a few kilometres wide (major – V6, Figure 3.2.8f).

- **Smooth seafloor** (V3/V3a/V4) comprises a mixture of pillow- and sheet-flow forming lavas. It is much less extensive than hummocky seafloor, which may be due to the fact that it is potentially created by highly effusive, fissure-fed magmatic eruptions that are more typical of a fast-spreading environment. Alternatively, I propose that smooth seafloor may be formed by precisely the same mechanism in which hummocky seafloor forms, with smooth seafloor representing the initial evolutionary phase of, say, a hummocky lineament (growth of volcanic structures is discussed in *Section 3.4.1*). Within the sidescan sonar imagery, neovolcanic smooth seafloor (V3) has a mottled backscatter texture (Figure 3.2.8g). It is sometimes possible to detect narrow, high intensity lineaments, which may represent the flow-fronts of major magmatic events, but their character often makes them difficult to distinguish from minor faults (Figure 3.2.8g).

V3 typically has a backscatter intensity of around 65% of that associated with hummocky seafloor. This lower intensity is probably due to a greater amount of energy being reflected away from the vehicle in the across-track direction when the seafloor is 'smooth' (*Section 2.4.1*). In addition to this, lava flows that do not form mounds are

likely to be more readily concealed by sediment, and thus if the rate of sedimentation remains constant across the ridge, it may be expected that smooth seafloor has a lower backscatter intensity than equal-age hummocky seafloor. V3a (Figure 3.2.8h) and V4 (Figure 3.2.8i) are older areas of seafloor that have relative intensities of ~46% and ~37%, respectively.

- **Seamounts** (V7) are isolated features that have a distinctive sidescan sonar and topographic morphology. An individual seamount usually has a bright, semi-circular arc of high intensity backscatter that corresponds to the flank that is facing the sidescan sonar, with a conjugate, low intensity arc that relates to the shadow zone on the opposite flank (Figure 3.2.8j). Seamounts are usually flat-topped or have a summit plateau that domes upwards slightly. Backscatter intensity across the summit varies depending on the age of the seamount, but it is usually possible to identify a summit crater that is evident as a shadow within the sidescan sonar imagery. Generally, only the youngest seamounts can be detected with the sidescan sonar and so it is necessary to use seafloor gradient data to extend seamount observations off-axis. This also applies to seamounts that are 'lost' within the nadir of the vehicle (Figure 3.2.10).

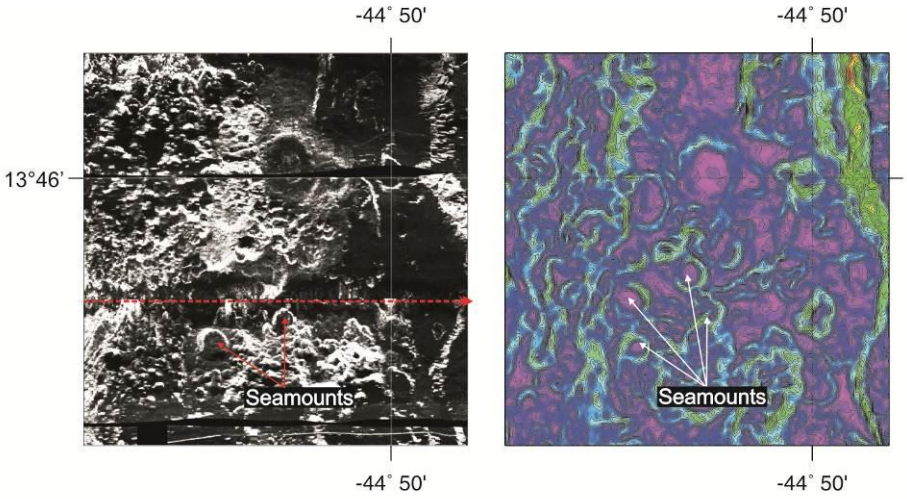


Figure 3.2.10. In areas of old seafloor, or within the vehicle nadir (TOBI track - red line), it becomes difficult to identify seamounts using the sidescan sonar data alone (left image). Seafloor slope derived from ship's bathymetry data can usually resolve seamounts in these areas (right image). Seafloor slope has the same colour-scale as **Figure 3.2.2**.

3.2.3.2. Tectonic textures

- **Faults** (inward/outward facing – T1/T2) are associated with a high intensity backscatter texture that arises due to lack of sediment cover and, in some instances, the fault surface being favourably aligned to reflect the incident acoustic energy back towards the sidescan sonar receivers (Figure 3.2.11a-b). Fault surfaces typically display high and low backscatter bands that relate to numerous large gullies, which, from seafloor video reconnaissance, may be several tens of metres wide (Allerton *et al.*, 1995; Searle *et al.*, 2008). Due to these shadowing effects, the backscatter intensity of a fault surface over 1 km^2 is around 75% of that associated with un-sedimented, hummocky seafloor (V1). Around the bases of fault scarps it is sometimes possible to detect an area of moderate intensity backscatter: sparse seafloor video reconnaissance makes it difficult to ground-truth this terrain, but Lawson *et al.* (1996) and Searle *et al.* (1998) have shown that this texture most likely represents an accumulation of talus (Figure 3.2.11c). Due to the relatively low abundance of this feature, it is not assigned a texture number. The base of fault scarps may also exhibit sediment chutes (T3 – Figure 3.2.11d) that form wavy, high intensity backscatter bands, which may be visible within low backscatter, sedimented areas for distances of up to ~1 km from the fault.

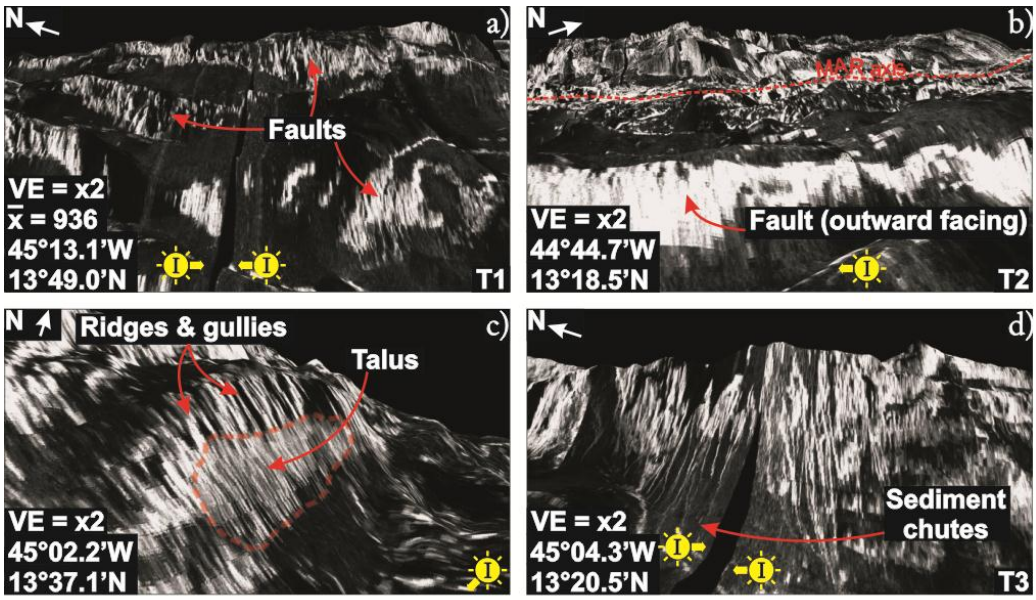


Figure 3.2.11a-d. Perspective views of tectonic sidescan sonar textures and structures. **a)** T1 - normal, inward facing faulting, **b)** T2 - outward facing fault, **c)** talus acummulation at base of fault scarp and **d)** T4 - sediment chutes and erosional features. $\bar{x}$ is the average backscatter intensity for faulted surfaces and sun icon indicates the insonification direction.

3.2.3.3. Oceanic core complex textures

- **Domal sections** (O1) are defined as the domed or sub-horizontal areas that form on the youngest, ridge-proximal side of OCCs. They may be topographically corrugated at wavelengths of a few hundred metres and adorned with fine-scale striations, evident in the sidescan sonar, at wavelengths of a few tens of metres (*Section 1.3.2*). They vary widely in texture as a function of the age of the OCC and the related degree of sedimentation across the detachment fault. The youngest OCC in the region, at 13°19'N, displays distinctive, well-defined, spreading direction parallel striations that have wavelengths of a few tens of metres (Figure 3.2.12a). Over a 1 km^2 area this texture has an intensity of approximately 38% relative to V1. In comparison, the domal section of the OCC at 13°30'N has a similar intensity of 36% (Figure 3.2.12b); but the striations are less well-defined and the sidescan sonar imagery displays a greater proportion of mid-tones rather than black-and-white striations that are observed across the OCC at 13°19'N. The domal section of the OCC at 13°48'N is almost entirely sediment covered, and, with an intensity of 8% relative to V1, from the sidescan sonar data alone is almost indistinguishable in texture from that of highly sedimented, off-axis seafloor.

- **Upper massifs** (O2) are defined as the rugged, blocky areas of topography that form between the breakaway and domal sections, on the oldest, axial-distal side of OCCs (*Section 1.3.2*). As with domal sections, upper massifs display a highly variable sidescan sonar texture at different stages of OCC formation (Figure 3.2.12c-e). Unlike domal sections, however, this change in texture is not simply a function of sediment cover, but may also reflect physical degradation of the upper massif with time (which is discussed in *Section 3.3*). Each upper massif displays a combination of textures that are typical of faults, talus accumulations, thick sediment and in some places the striated nature of domal sections. The relative contribution of these individual components combine to give a backscatter intensity of 41% relative to V1 across the upper massif of the OCC at 13°19'N (Figure 3.2.12c). This is similar to that which is observed across the OCC at 13°30'N (Figure 3.2.12d-e), even though here the upper massif appears to be heavily degraded and the texture comprises fewer solid blocks of equal-intensity backscatter, but rather a mottled pattern of backscatter intensity highs within a low-intensity background.

- **OCC-related hanging-wall degradation** (O3) may form a fringe around the OCC (Figure 3.2.12f). This texture has a moderate intensity and may display striations similar to those observed on the domal section of the OCC, presumably due to the thin hanging-wall becoming intensely faulted and degraded by the relative motion of the underlying footwall. The footwall/hanging-wall boundary may be marked by a high-intensity band of backscatter that represents talus accumulation from the hanging-wall (Figure 3.2.12f).

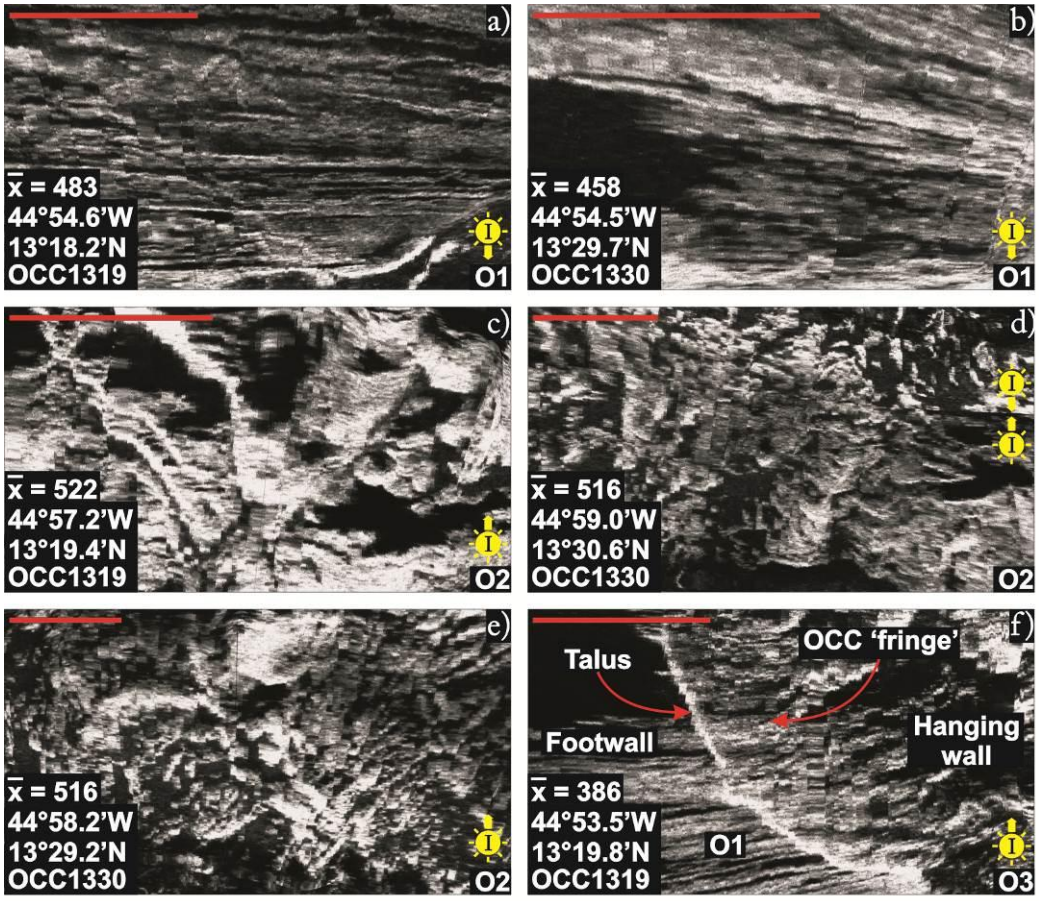


Figure 3.2.12a-f. Gallery of OCC-related sidescan sonar textures and structures. **a)** O1 - domal section of OCC at 13°19'N displaying striations, **b)** O1 - domal section of OCC at 13°30'N displaying striations, **c)** O2 - upper massif of OCC at 13°19'N, **d-e)** O2 - upper massif of OCC at 13°30'N and **f)** the footwall/hanging wall boundary at OCC at 13°19'N (high backscatter band), showing moderate intensity OCC-related structural degradation of hanging wall (O3). $\bar{x}$ is the average backscatter intensity for each texture and sun icon indicates the insonification direction. Red bar in upper-left represents ~1 km. All panels are in plan view with north to top of page.

3.2.4. Interpretation of hydrothermal anomalies

Light scattering sensor (LSS) data are sensitive to particulate matter in the water column and can thus be used to detect sources of hydrothermal activity. Data were collected during the TOBI survey at four second intervals, but due to the inherently noisy nature of the signal it was necessary to average the data over a distance of ~300 metres (i.e. 100 readings). There is a distinct first-order relationship between TOBI depth and LSS value (Figure 3.2.13 – correlation coefficient: -0.68), which may be caused by variability in turbidity distribution within the water column (B. Murton, *personal comm.*). By removing this linear LSS-depth relationship from the data, it is possible to detect a clear plume-like anomaly in the water column centred on 44°54.5'W, 13°18.9'N. This area is located over the domal section of the OCC situated at 13°19'N, approximately 3.3 km west of the footwall/hanging-wall boundary, and is therefore similar in geological setting to a peridotite-hosted, Rainbow-type hydrothermal vent (German *et al.*, 1996). This type of vent is expected to form on a mature detachment fault where gabbroic intrusion into the footwall helps drive fluid convection from a recharge zone within the hanging-wall, with deformation of the footwall then focusing hydrothermal discharge to discrete locations along the detachment surface (Figure 3.2.14; McCaig *et al.*, 2007).

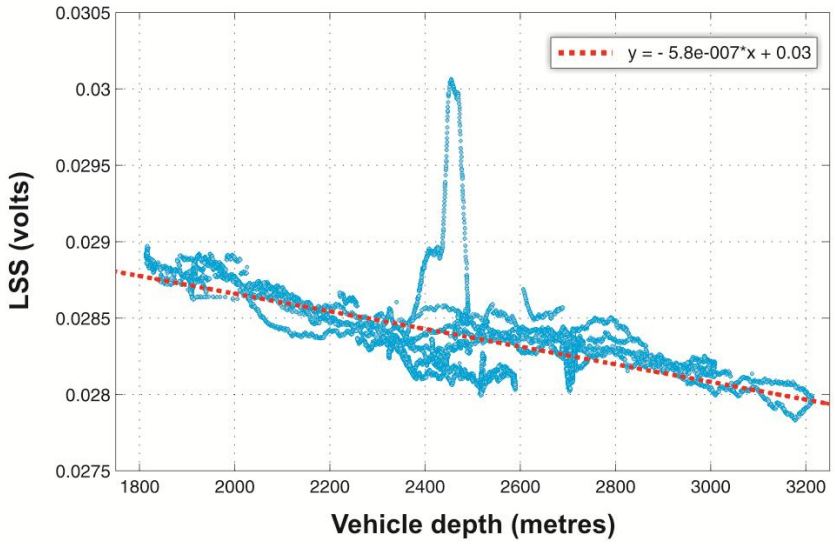


Figure 3.2.13. LSS value plotted against depth of TOBI (blue dots). There is a clear linear relationship between the two (red dashed line, with equation in upper right) that is most likely caused by absorption of light energy with increasing depth. This can be removed to leave the anomaly associated with hydrothermal activity.

Ancillary evidence for hydrothermal activity in this area comes from manganese staining on many of the dredge samples and recoveries of jasper, epidosite and sulphide chimneys during DR10 (which crossed the zone of intensely faulted hanging wall approximately 2.5 km to the north). This hydrothermal plume has been marked on the final geological map with an orange triangle (geological map – Figure 3.2.15a-b).

LSS profiles across the OCCs at 13°30'N and 13°48'N do not show similar plume-like anomalies to that which is observed across the OCC at 13°19'N. This seems unusual given that direct evidence for hydrothermal activity was observed during BR121 in the form of beehive-shaped mounds across the domal section of the OCC at 13°30'N (*Section 3.3.1.2*). These mounds were in close proximity to a narrow fault that most likely acts as a hydrothermal pathway from the core of the OCC to the seafloor. Furthermore, Beltenev *et al.* (2009) use electric potential anomalies to confirm the existence of at least five individual hydrothermal sites (i.e. the 'Semyenov sulphide district') situated along the central axis of the OCC at 13°30'N, with Semyenov-3 appearing to be in the equivalent place to the aforementioned BR121. The lack of a distinct LSS anomaly may indicate that the plume associated with this type of system is either more diffuse and thus less intense compared with that which is observed within the footwall of the OCC at 13°19'N, or that vents near 13°30'N are not currently active. It should also be noted that the plume across the OCC at 13°19'N is < 2 km wide, and thus similar plumes may have been missed elsewhere.

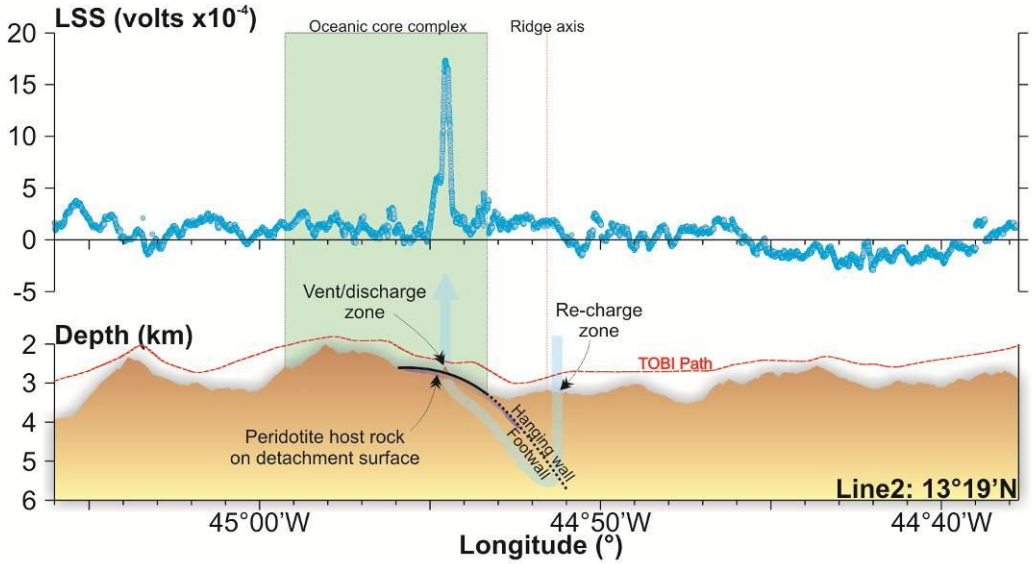


Figure 3.2.14. LSS anomaly along TOBI profile 2. There is a spike centred across the footwall of the OCC at 13°19'N that may be associated with peridotite-hosted hydrothermal venting, similar to that which is observed at the Rainbow vent on the MAR at 36°15'N. Possible fluid pathway (blue shading) for mature detachment fault after McCaig *et al.* (2007).

3.2.5. Map of seafloor geology

Figure 3.2.15a-b shows the final interpretation of the TOBI sidescan sonar mosaic (see also Appendix II for high resolution digital version). In areas of thick sediment cover, the map has been supplemented with information from bathymetry and seafloor gradient data. This allows for off-axis OCCs to be included in the final map, with the caveat that their extent is less well defined compared with relatively un-sedimented, near-axis OCCs. The nomenclature used herein to refer to a specific OCC is of the form OCCYYXX, where YY and XX are the degrees and minutes of latitude at which the OCC is situated, respectively. In the event that numerous OCCs occur at the same latitude, the names of progressively older OCCs are appended with 'a', 'b', etc.

Many OCC locations were originally identified by Smith et al. (2006) and Smith et al. (2008). Their extents have been mapped more accurately in this study due to higher resolution bathymetry data (and the inclusion of sidescan sonar data). In addition to this, I identify four new OCCs in the 13°N region (marked with orange shading in Figures 3.2.15a-b – with the criteria used to define them discussed in *Section 3.3*). Bathymetric contours and annotation have been added to provide extra detail and relevant information. In the few areas where a mismatch between the sidescan sonar mosaic and bathymetry data were identified (i.e. layover effects, *Section 2.4.3.4*) the feature in question has been mapped from the bathymetry data – assuming this to be more accurately geo-referenced than the corresponding sidescan sonar imagery.

For the purpose of Figure 3.2.15a-b and the remainder of this thesis, I have defined the ridge axis as occurring within the neovolcanic zone. Where there is clearly a bathymetric ridge within the NVZ this has been selected as the ridge axis. However, I note that spatial and temporal variations in the locus of melt emplacement are integrated across the whole width of the axial valley (and, perhaps, outside of the axial valley; *Section 3.4.1*). Thus, the neovolcanic ridge axis may not be a good estimate of the time-averaged/stable ridge axis (i.e. for the purpose of calculating the gravitational thermal correction or spreading rate asymmetries from magnetic data), particularly in a magma-poor environment where the surficial expression of melt emplacement and the position of the ridge axis may be controlled by regular formation and extension on detachment faults. Because of this, I have averaged (i.e. smoothed) the position slightly so that it can be used mainly as a tool for cross-referencing various plots to each other. Use of any variation of this ridge axis location is clearly stated in the text.

3.3. Regional morphology & new insights into OCC structure

The Fifteen-Twenty and Marathon FZs are first-order ridge discontinuities (D1) that define a ~300 km first-order segment (S1) of the MAR (Figure 3.3.1). Within this segment there are a number of second-order discontinuities (D2), including a ~20 km NTO at 13°38'N (i.e. within the 13°N magma-poor region). The 13°N region is bounded along-axis by magmatic, linear abyssal hill terrain that has formed around the first-order segment centre (14°10'N) and the Marathon FZ. These boundaries form V-shapes that are oblique to the spreading direction and thus indicate that the magmatic source is not fixed in space, but is able to wander along the ridge axis (Fujiwara *et al.*, 2003; Smith *et al.*, 2008; white lines in Figure 3.3.1 and see also Video 1 - Appendix II). Expanding on these observations, and by assuming a half-spreading rate of 13 km/My, I calculate that the magmatic segment centre at 14°10'N has propagated southwards at a rate of ~15 km/My for the last 1.8 My, prior to which it propagated northwards at ~19 km/My for 0.9 My. Similarly, the magmatic terrain bounding the Marathon FZ shows evidence for a magmatic source that has either gradually waned or propagated southward over the last 1.8 Ma. The similar timescale over which these surficially isolated magma-rich provinces have varied suggests that they may be controlled by the same processes at depth within the mantle.

Previously undocumented, isolated exposures of linear abyssal hill terrain are also detected within the 13°N region, located at 45°15'W, 13°50'N and 44°35'W, 13°19'N (red dashed lines – Figure 3.3.1), suggesting that short periods of enhanced magmatism within magma-poor regions are not wholly uncommon. These areas are associated with numerous, closely spaced small faults (locations annotated on Figure 3.2.15a-b). The isolated area of magmatic terrain at 45°15'W, 13°50'N appears to trend southwards with decreasing age, mimicking the southern boundary of abyssal hills which make up the first-order segment centre. To the north and south of this isolated, magmatic province are bathymetric lows that trend NW-SE across the seafloor, bearing a striking resemblance to off-axis valleys observed along the MAR between 25°25'N – 27°10'N (interpreted as the off-axis trace of second-order ridge discontinuitues – Gente *et al.*, 1995; Tucholke *et al.*, 1997) (blue lines – Figure 3.3.1).

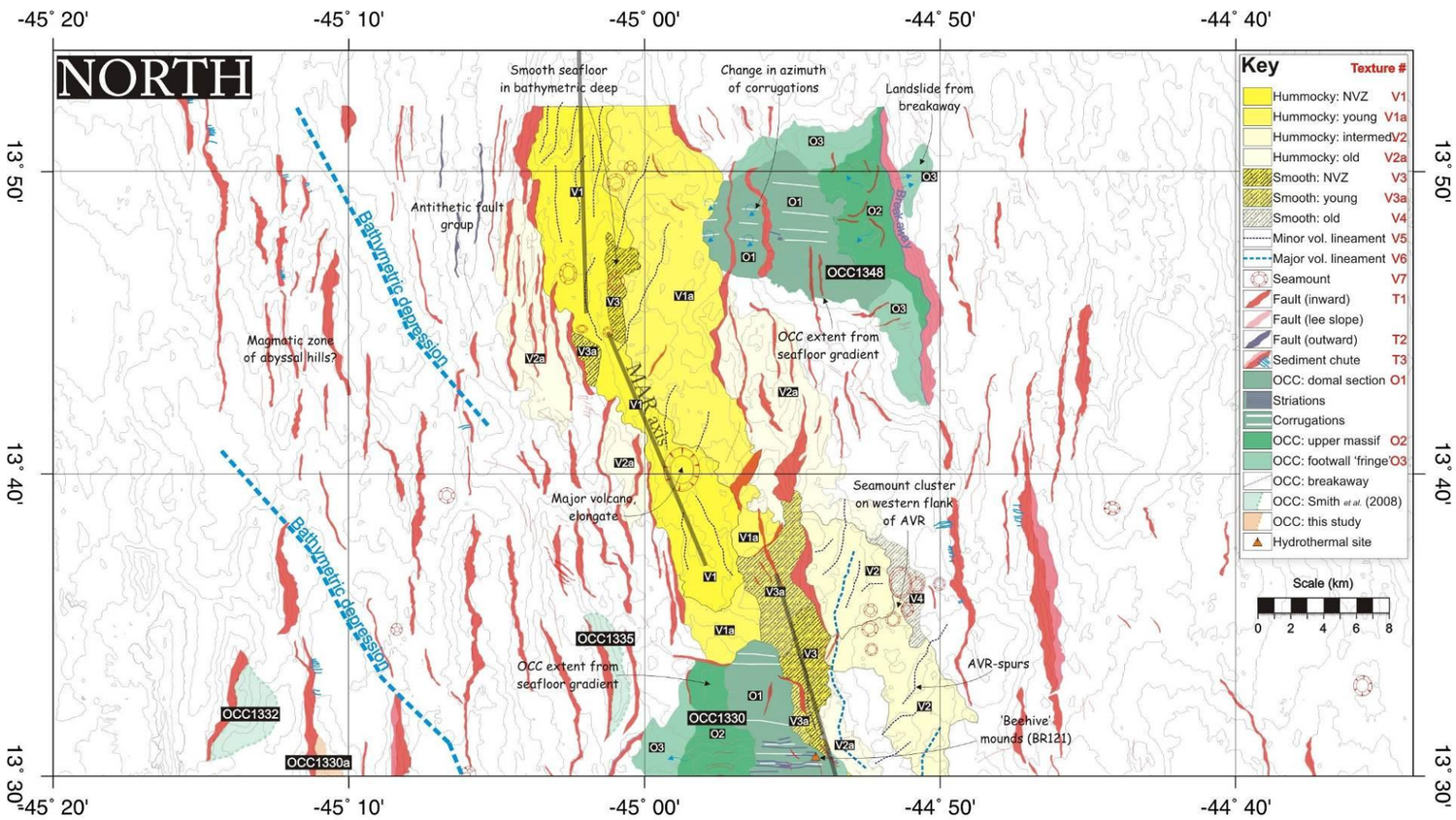


Figure 3.2.15a. Geological interpretation of sidescan sonar textures, including observations from: topography, seafloor gradient, sampling results and seabed video reconnaisance, for northern half of survey area. For the older core complexes (i.e. OCC1330, OCC1348 and off-axis OCCs), sidescan sonar data alone cannot determine the limits of the detachment surface, and so this is estimated from the seafloor gradient map (**Figure 3.2.3**). Bathymetric contours are at 200 metre intervals. MAR axis is dark line within NVZ. See text for discussion.

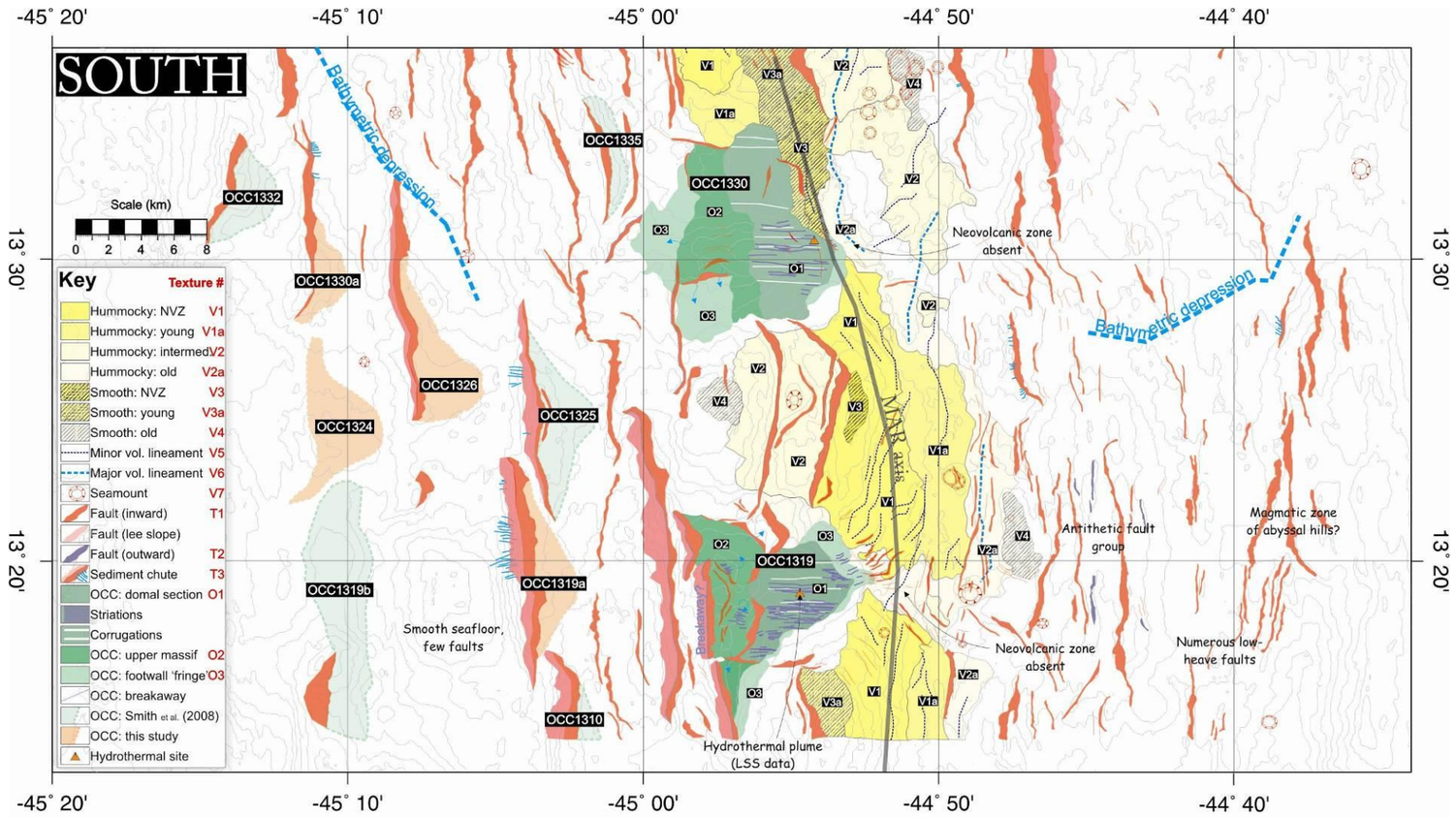


Figure 3.2.15b. Geological interpretation of sidescan sonar textures, including observations from: topography, seafloor gradient, sampling results and seabed video reconnaisance, for southern half of survey area. For the older core complexes (i.e. OCC1330, OCC1348 and off-axis OCCs), sidescan sonar data alone cannot determine the limits of the detachment surface, and so this is estimated from the seafloor gradient map (**Figure 3.2.3**). Bathymetric contours are at 200 metre intervals. MAR axis is continuous dark line within NVZ. See text for discussion.

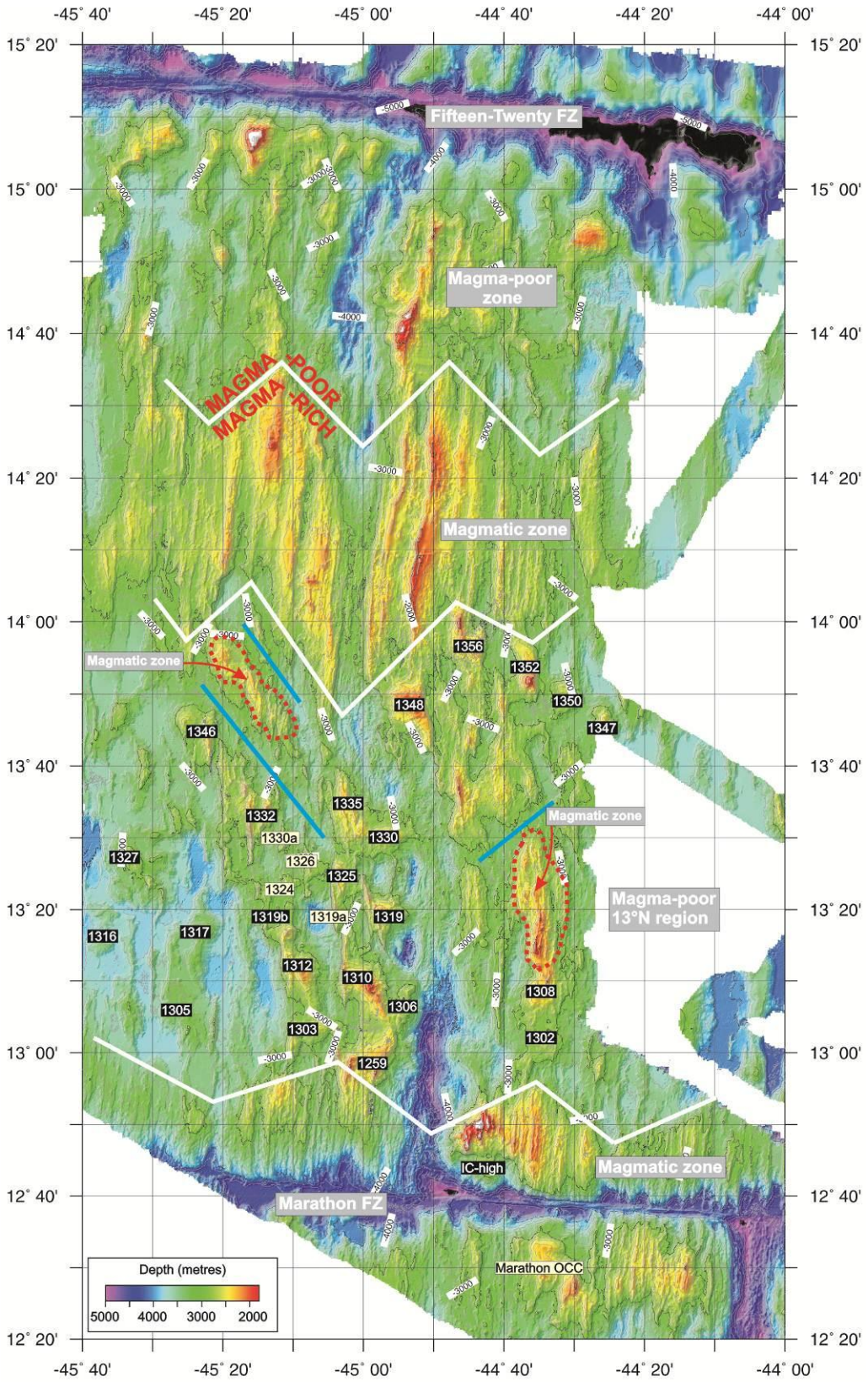


Figure 3.3.1. Regional seafloor morphology, showing boundaries between magmatic (abyssal hill) terrain and magma-poor (OCC-forming) terrain (heavy white lines). Localised magmatic zones may also exist within magma-poor environments (red, dashed lines). OCCs with black labels were identified by Smith *et al.* (2006) and Smith *et al.* (2008), those with pale yellow labels have been identified in this study. Heavy blue lines are bathymetric depressions referred to in text. MAR axis is axial-depression running N-S between 44°50'W-45°02'W.

Maintaining the assumption that abyssal hill terrain is a proxy for relatively robust magmatism, the oblique nature of this localised zone of abyssal hills suggests it was created by a discrete zone of magmatism that moved southwards along the ridge axis. The along-axis extent of this set of abyssal hills is ~10 – 15 km, which may indicate the diameter of the localised zone of melting. The conjugate plate to each of these isolated magmatic regions displays typically magma-poor topographic characteristics (*Section 1.3.1*). The magmatic zone at 44°35'W, 13°19'N on the AF plate, for example, is between 22.2 – 32.0 km from the ridge axis and corresponds with a zone of OCCs on the SA plate centred at 45°13'W, 13°23'N; this suggests some degree of asymmetric crustal accretion at the ridge axis (which is discussed further in *Section 3.5.1*).

3.3.1. Distribution and morphology of oceanic core complexes

Smith *et al.* (2008) identify a total of 24 core complexes between the Marathon FZ and the magmatic segment centre (annotated with black rectangles – Figure 3.3.1) by using the criteria that OCCs are associated with a topographically uplifted, domed area of smooth or corrugated seafloor that extends towards the ridge axis from a linear or hooked, breakaway ridge (Table 3.3.1). Of these 24 OCCs, 23 are located within the magma-poor 13°N region and one is located on the inside-corner of the RTI between the MAR and Marathon FZ (in predominantly abyssal hill terrain). On the basis of sidescan sonar imagery and higher resolution bathymetry data collected during JC07, it is possible to identify four additional core complexes in the area around 45°08'W, 13°25'N (annotated with pale yellow rectangles – Figure 3.3.1). These OCCs are drawn in orange on the accompanying geological map (Figure 3.2.15b). An additional fifth, previously undocumented OCC is identified immediately south of the Marathon FZ at 44°33.4'W, 12°32.5'N, approximately 50 km from the ridge axis (Figure 3.3.1).

The average duration of all OCCs, calculated from their across-axis extents and assuming they form at a half-spreading rate of 13 km/My (this assumption is discussed in *Section 5.3.3*) is 0.44 My (Table 3.3.1). This is less than the ~1.0 – 2.6 My durations of OCCs on the MAR between 20° – 30°N (Tucholke *et al.*, 1998). Tucholke *et al.* (1998) suggest that the durations of OCCs are related to the duration of a magmatic/amagmatic cycle of the order of 2 – 3 My, with OCC formation becoming terminated by renewed magmatism. Thus the greater number of OCCs within the smaller JC07 survey area may be the result of shorter-wavelength, higher-frequency

variations in predominantly magmatic and predominantly tectonic crustal accretion. This relationship between OCC formation and melt supply is discussed in more detail in *Section 3.4*, and the ages and durations of OCCs are discussed in terms of the magnetic data in *Section 5.3.3*.

	Identifier	Longitude	Latitude	Plate	Distance from ridge (km)	Approximate surface area (km^2)	Age of formation (Ma)		Duration (My)
							Breakaway	Termination	
Near-axis	OCC1306	44°53'W	13°06'N	SA	6.0	55.5	0.46	~0.00	0.46
	OCC1319	44°56'W	13°19'N	SA	10.0	79.9	0.77	~0.00	0.77
	OCC1330	44°56'W	13°30'N	SA	10.6	100.0	0.82	~0.00	0.82
	OCC1348	44°54'W	13°48'N	AF	19.0	147.3	1.46	0.54	0.90
	OCC1259	45°02'W	12°59'N	SA	20.3	53.2	1.56	1.37	0.19
	OCC1303	45°07'W	13°03'N	SA	31.2	79.3	2.45	1.87	0.58
	OCC1305	45°28'W	13°05'N	SA	69.6	94.6	5.35	4.64	0.71
	OCC1310	45°02'W	13°10'N	SA	21.3	116.7	1.64	1.01	0.63
	OCC1312	45°07'W	13°12'N	SA	32.4	134.5	2.49	1.87	0.62
	OCC1316	45°37'W	13°16'N	SA	85.9	39.8	6.61	6.18	0.43
	OCC1317	45°22'W	13°17'N	SA	57.3	100.4	4.41	3.99	0.42
Off-axis	OCC1319a*	45°04'W	13°19'N	SA	23.7	22.5	1.82	1.60	0.22
	OCC1319b	45°11'W	13°19'N	SA	36.7	54.4	2.82	2.48	0.34
	OCC1324*	45°10'W	13°24'N	SA	37.2	19.6	2.86	2.56	0.30
	OCC1325	45°03'W	13°25'N	SA	22.4	31.0	1.72	1.44	0.28
	OCC1326*	45°07'W	13°26'N	SA	30.3	31.3	2.33	1.91	0.42
	OCC1327	45°33'W	13°27'N	SA	77.3	73.2	5.95	5.66	0.29
	OCC1330a*	45°11'W	13°30'N	SA	34.1	24.7	2.62	2.47	0.15
	OCC1332	45°14'W	13°32'N	SA	14.7	15.3	1.13	1.02	0.11
	OCC1335	45°01'W	13°35'N	SA	37.6	25.6	2.89	2.64	0.25
	OCC1346	45°25'W	13°46'N	SA	42.3	36.4	3.25	2.92	0.33
	OCC1302	44°35'W	13°02'N	AF	32.0	76.5	2.46	1.93	0.53
	OCC1308	44°36'W	13°08'N	AF	30.0	117	2.30	1.67	0.63
	OCC1347	44°27'W	13°47'N	AF	65.4	37.5	5.03	4.70	0.33
	OCC1350	44°31'W	13°50'N	AF	57.5	36.4	4.42	4.03	0.39
	OCC1352	44°37'W	13°52'N	AF	46.8	67.2	3.60	3.22	0.38
	OCC1356	44°45'W	13°56'N	AF	33.9	37.4	2.60	2.23	0.37
				Average =	36.5	63.2	2.81	2.66	0.44

Table 3.3.1. Summary of OCCs in the 13°N region. Ages are calculated from the distance to the bathymetric ridge axis and assuming a half-spreading rate of 13 km/My. Surface areas are calculated using *ArcMap*. * denotes OCC identified in this study, all other OCCs were identified by Smith *et al.* (2006) and Smith *et al.* (2008).

In order to assess their regional and morphological relationships, core complexes can be divided into two groups: near- and off-axis. The near-axis group comprises three OCCs that are interpreted as being within the active, or very recently active, evolutionary phase of OCC formation (an additional fourth near-axis OCC is identified by Smith *et al.* (2008) – OCC1306 – but this was not surveyed during JC07). Near-axis OCCs are characterised by relatively low amounts of sediment cover, allowing for a wealth of information about their surface morphology to be extracted from the sidescan sonar data (*Sections 3.3.1.3-5*). Off-axis OCCs are considerably older than near-axis OCCs, existing in the mature, terminated phase of the OCC life cycle. They are subsequently associated with a high degree of sediment cover and higher tectonic/erosional degradation, and can therefore only be analysed in relation to their extent and distribution (*Sections 3.3.1.1-2*). The following sections discuss the morphology of newly identified OCCs and new insights into the morphology of near-axis OCCs using high resolution bathymetry and sidescan sonar data.

3.3.1.1. Newly identified OCCs in the 13°N region

Four newly identified OCCs (OCC1319a, OCC1324, OCC1326 and OCC1330a) occur in close proximity to each other on the SA plate (Figure 3.3.1, with detailed view in Figure 3.3.2). This group is centred within an intense zone of detachment faulting and OCC formation previously identified by Smith *et al.* (2008). Morphologically, with the exception of OCC1326, these OCCs are generally smaller than those previously documented (having surface areas < 30 km^2, compared with the regional average of ~65 km^2). OCC1326 and OCC1330a exhibit distinct, hooked breakaway ridges (Points 1 – Figure 3.3.2). Bathymetry data resolve faint corrugations on this newly identified set of OCCs (inset – Figure 3.3.2), and OCC1324 might itself be the expression of a larger corrugation on the surface of OCC1319b.

This set of newly-identified OCCs helps define a zone of OCC formation that runs oblique to the spreading direction (perspective view – Figure 3.3.3). This is similar to the alignment of OCCs immediately south of the magma-rich/magma-poor transition on the AF plate near 44°35'W, 13°50'N (Figure 3.3.1). As with the V-shaped magma-rich/magma-poor boundary near the first-order segment centre, this implies a certain degree of along-axis melt migration. OCCs, which are predicted to form during periods of reduced magmatic activity (Karson & Winters, 1992; Buck *et al.*, 2005; Tucholke *et*

al., 2008), may therefore develop around the edges of migrating zones of focused, upwelling melt. As the zone of melting migrates along the ridge axis, renewed volcanism within the axial valley may terminate slip on adjacent OCC-forming detachment surfaces. A new OCC may then initiate further along-axis, towards the edge of the zone of focused melting.

A seamount (~650 metres in diameter, ~80 metres in height) is identified beyond the outward-facing breakaway of OCC1326 (Point 2 – Figure 3.3.2 and Figure 3.2.15b). This suggests that there is still some degree of melt reaching the surface within this magma-poor region and during periods of intense OCC formation (at least prior to the formation of OCC1326), which is also supported by the exposure of hummocky terrain on the back-tilted breakaway ridges of most OCCs in the 13°N region.

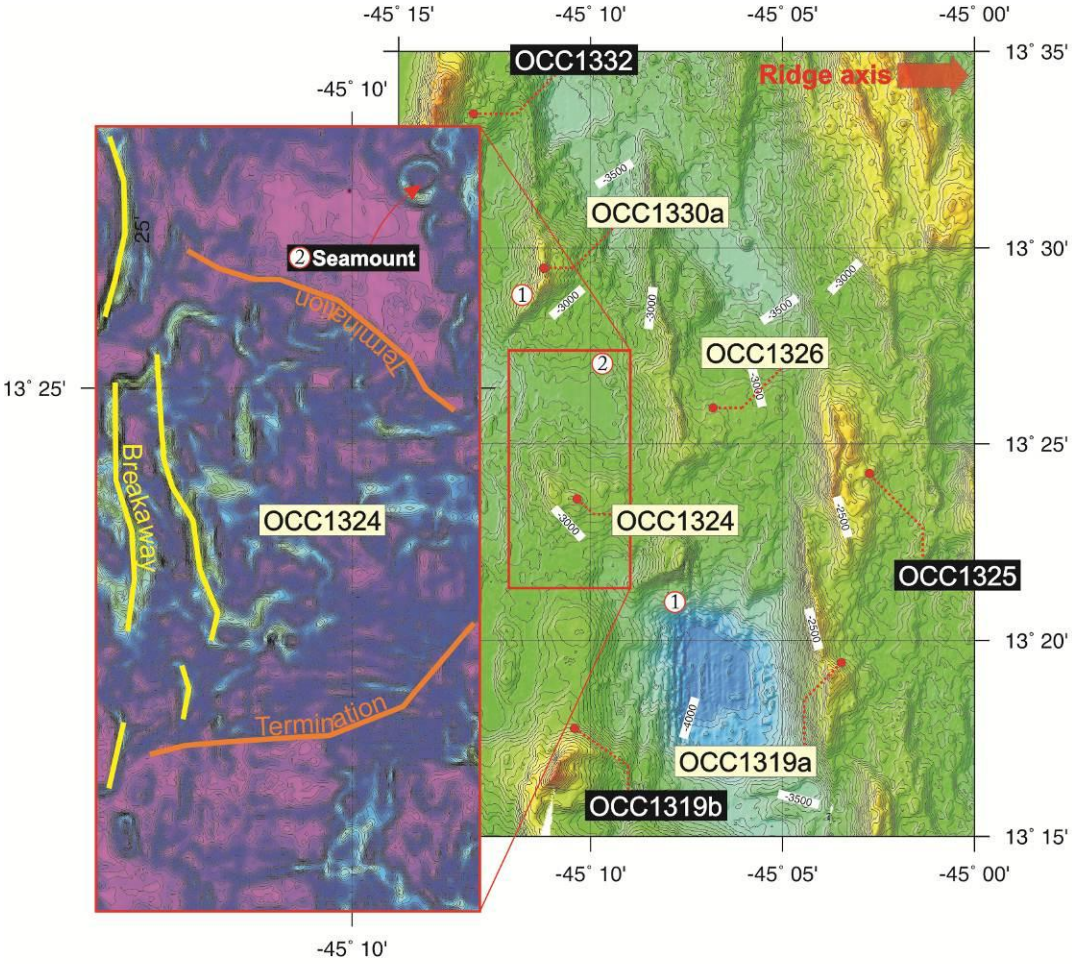


Figure 3.3.2. Newly identified OCCs in the 13°N region (annotated with pale yellow rectangles, black rectangles are OCCs identified by Smith *et al.* (2006) and Smith *et al.* (2008)). Numbered points are referred to in the text. Inset (seafloor slope with contours at 1° intervals and colour scale the same as **Figure 3.2.2.**) highlights a seamount within the zone of newly identified OCCs and extent of OCC1324. Contours are at 50 metre intervals with colour scale the same as **Figure 2.2.2**. See text for discussion.

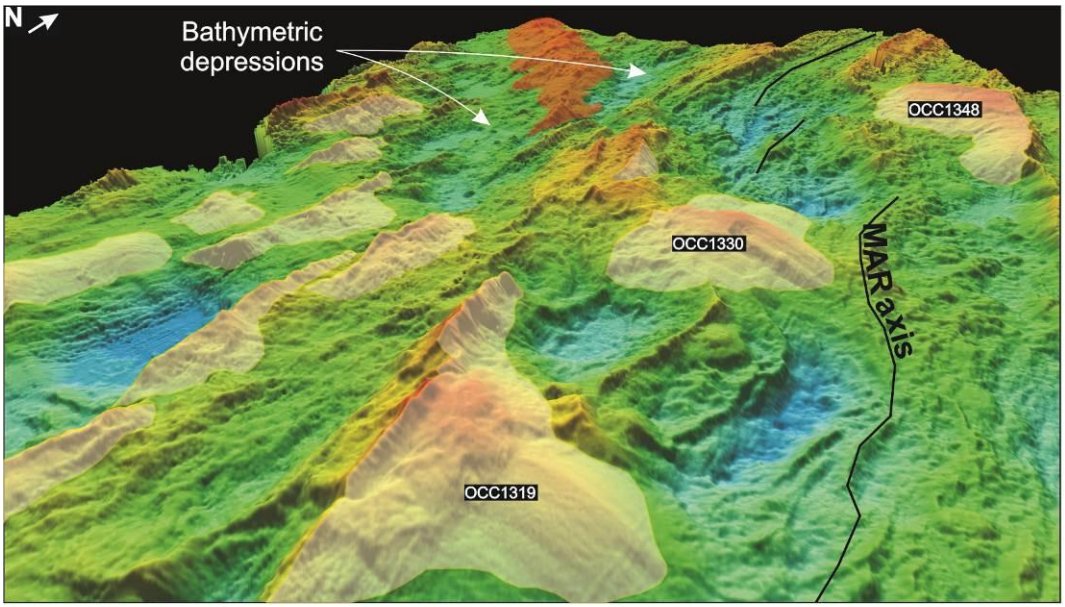


Figure 3.3.3. Perspective view of OCC (yellow shading) and off-axis magmatic zone (red shading) alignments which are oblique to the spreading direction (ridge axis marked by black line). Note the bathymetric depression that runs parallel with the magmatic zone. See text for discussion.

3.3.1.2. Newly identified 'Marathon OCC'

The Marathon OCC (44°33'W, 12°33'N) differs from OCCs situated within the 13°N region as it is located in an inside-corner RTI setting similar to other notable OCCs on the MAR, such as Kane Massif (23°30'N) and Atlantis Massif (30°00'N) (Point 1 – Figure 3.3.4). Morphologically, the Marathon OCC comprises a corrugated 'double-dome' (similar to Kane Massif) that extends across-axis for ~8.4 km and along-axis for ~14.8 km. The Marathon OCC is bounded to its east (younger) and west (older) by magmatic, abyssal hill seafloor. All other OCCs in the 13°N region (i.e. those which are annotated on Figure 3.3.1), with the exception of the inside-corner high at the western end of the Marathon FZ, are located within typical, magma-poor terrain. OCC1356 is the only other OCC in the region that is bounded on its younger side by magmatic terrain (Figure 3.3.1).

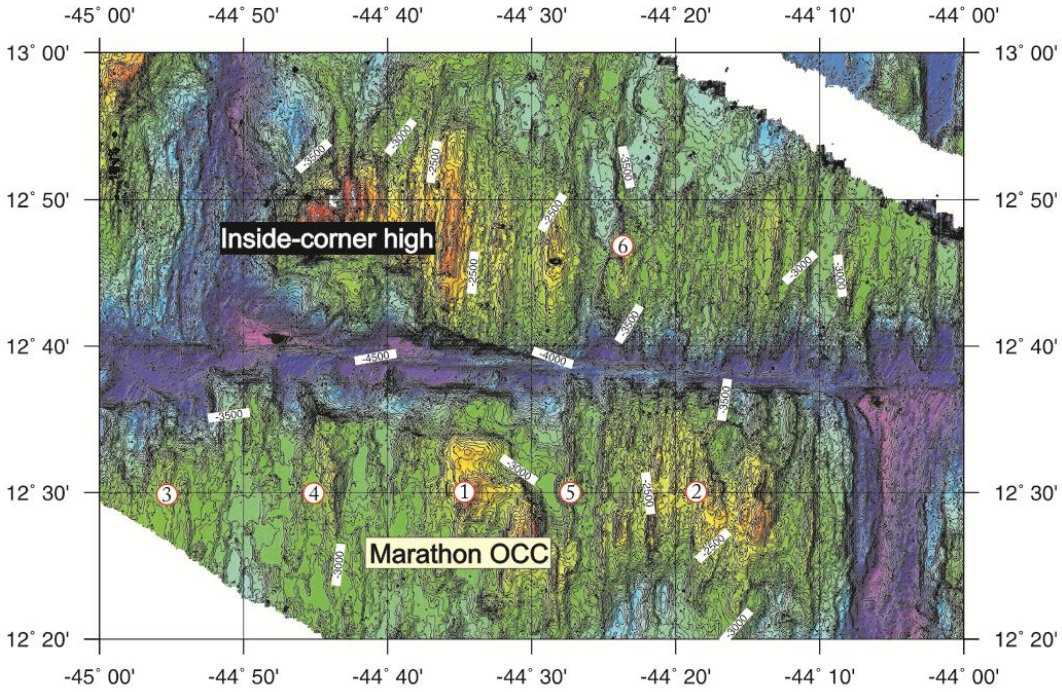


Figure 3.3.4. Marathon OCC and surrounding seafloor morphology. E-W bathmetric low is Marathon FZ, N-S bathymetric low is MAR axis (with colour scale the same as **Figure 2.2.2**). Numbered circles are referred to in text. Contours are at 50 metre intervals.

The breakaway and termination of Marathon OCC lie at distances of 57 km and 49 km from the ridge axis, respectively, suggesting that the OCC was active between 3.7 – 4.4 Ma (assuming a half-spreading rate of 13 km/My). On the younger, axial-proximal side of the OCC (Point 2 – Figure 3.3.4), magmatic terrain extends from the ridge axis westwards to a distance of 41.3 km. In this area abyssal hills are continuous along-axis for distances of up to ~30 km (they appear to be truncated southwards by a 35 km offset in the ridge axis at 12°09'N – not shown in Figure 3.3.4) with crests that are ~1 – 2 km apart. The existence of magmatic terrain on the younger side of the OCC supports observations which show that OCCs are terminated by renewed magmatism at the ridge axis (e.g. Karson & Winters, 1992; Tucholke *et al.*, 2001; MacLeod *et al.*, 2009). On the older side of the OCC, linear ridges are topographically less well-defined but are apparent at a distance of ~84 km from the ridge axis (Point 3 – Figure 3.3.4). The area of seafloor between the apparently magmatic zone and the breakaway ridge features large expanses of smooth seafloor and intermittent ridges (Point 4 – Figure 3.3.4). It is possible that if abyssal hill terrain forms when the amount of plate separation accommodated by magmatic accretion (M_{TOTAL}) is ~95%, and OCC formation is prevalent when $M_{TOTAL} \approx 50\%$ (Buck *et al.*, 2005; Tucholke *et al.*, 2008), then this area of smooth seafloor and intermittent ridges may represent a gradual

transition between the two – i.e. 95% > M_{TOTAL} > 50%. There does not appear to be a similar gradual transition from the termination to abyssal hills on the younger side of the OCC, suggesting that melting may have resumed relatively quickly after OCC formation (Point 5 – Figure 3.3.4; schematic model of formation shown in Figure 3.3.5).

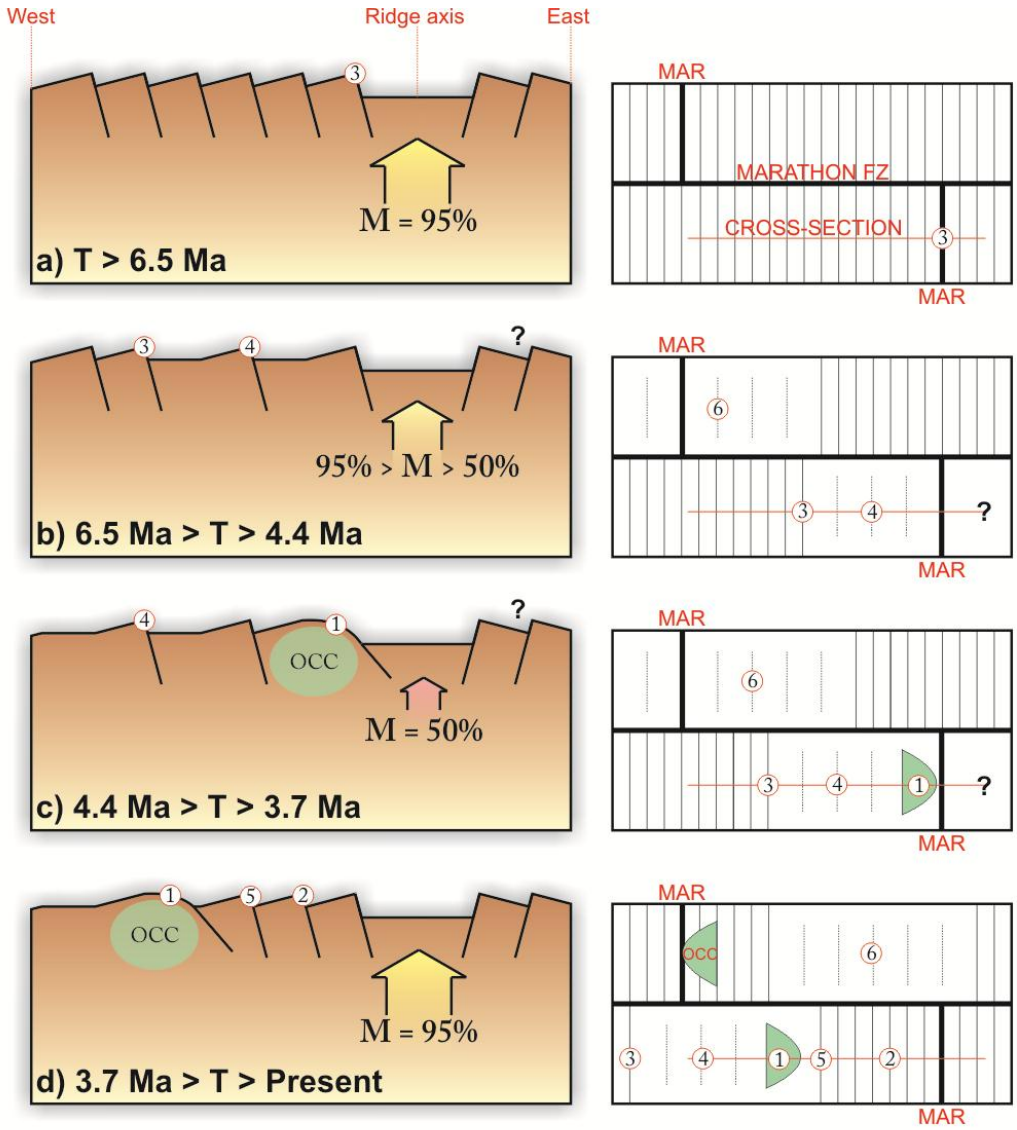


Figure 3.3.5. Schematic interpretation of Marathon OCC formation from 6.5 Ma to present. **a)** Before 6.5 Ma: terrain north and south of the FZ displays abyssal hills indicative of magmatic conditions at the ridge axis. **b)** 6.5 Ma to 4.4 Ma: magmatic supply begins to wane, creating a 'V'-shape in abyssal hills to the north of the FZ. Abyssal hills to the south become more widely spaced. **c)** 4.4 Ma to 3.7 Ma: magmatic supply south of the FZ reaches threshold for OCC formation. **d)** 3.7 Ma to present: melt supply at ridge axis is enhanced and abyssal hills form. Inside-corner high formation at western end of FZ may indicate localised or very recent reduction in melt supply (as evidenced by the decreasing length of abyssal hills in this area over the last 1.8 Ma - **Figure 3.3.1.**). All components of magmatic accretion (M), are from Buck *et al.* (2005) and Tucholke *et al.* (2008). Numbered circles relate to positions in **Figure 3.3.4.** (note that these are not sequential, but relate to the order in which these points are referred to in *Section 3.3.1.2*).

Waning of the melt supply from 6.5 Ma (i.e. the age of the innermost abyssal hill on the older side of the OCC – Point 3 – Figure 3.3.4) to 3.2 Ma (i.e. the age of the nearest abyssal hill on the younger side of the termination – Point 5 – Figure 3.3.4) is also recorded north of the Marathon FZ by the gradual decrease in along-axis extent of abyssal hills (Point 6 – Figure 3.3.4 and also white lines in Figure 3.3.1). Gente *et al.* (1995) suggest that waxing magmatism leads to growth of magmatic terrain, and thus the gradual shortening and lengthening of abyssal hills surrounding the Marathon FZ gives the impression of a magma supply that has remained fixed in space (in contrast to the apparent along-axis migration of magmatic zones to the north – *Section 3.3*) but has increased and decreased in strength over a period of ~3 My (Figure 3.3.5). This value is comparable to the ~2 – 3 My amagmatic/magmatic cycle predicted for some 17 OCCs identified on the MAR between 21°18'N and 31°17'N (Tucholke *et al.*, 1998).

3.3.1.3. OCC1319: Surficial morphology

OCC1319 can be divided into three morphological regions: a corrugated, domal section to the east of 44°55.9'W (Point 1 – Figure 3.3.6a), a blocky, irregular upper massif between 44°57.9'W and 44°55.9'W (Point 2 – Figure 3.3.6a) and a breakaway zone west of 44°57.9'W (Point 3 – Figure 3.3.6a). The terms 'domal section' and 'upper massif' are defined in *Section 3.2.3.3*, see also Figure 3.2.15b for geological interpretation, Figure 2.4.10c for oblique view and MacLeod *et al.* (2009), Appendix I, for published account. The domal section has a maximum across- by along-axis distance of 5.3 km by 5.8 km, and increases in depth from 2.47 km at the summit to 3.27 km at the footwall/hanging-wall boundary. The change in slope has a near constant gradient of 4.4°.km^{-1}, with the summit being sub-horizontal and the footwall dipping at ~18° towards the ridge axis (Figure 3.2.1). Corrugations, which act as kinematic indicators recording the relative plate motions during unroofing of the footwall, have a mean wavelength of 470 metres and amplitude of 25 metres (Video 2 – Appendix II). Corrugations and striations on the domal section trend at 270.6±0.8° and 270.4±4.9°, respectively, which is within the 273.4±1.7° range of values for spreading direction predicted from the NUVEL-1a model for SA-AF at 13°19'N (DeMets *et al.*, 1990, 1994). Slope data show that shorter-wavelength corrugations appear to be impressed on top of longer-wavelength features (Figure 3.3.7).

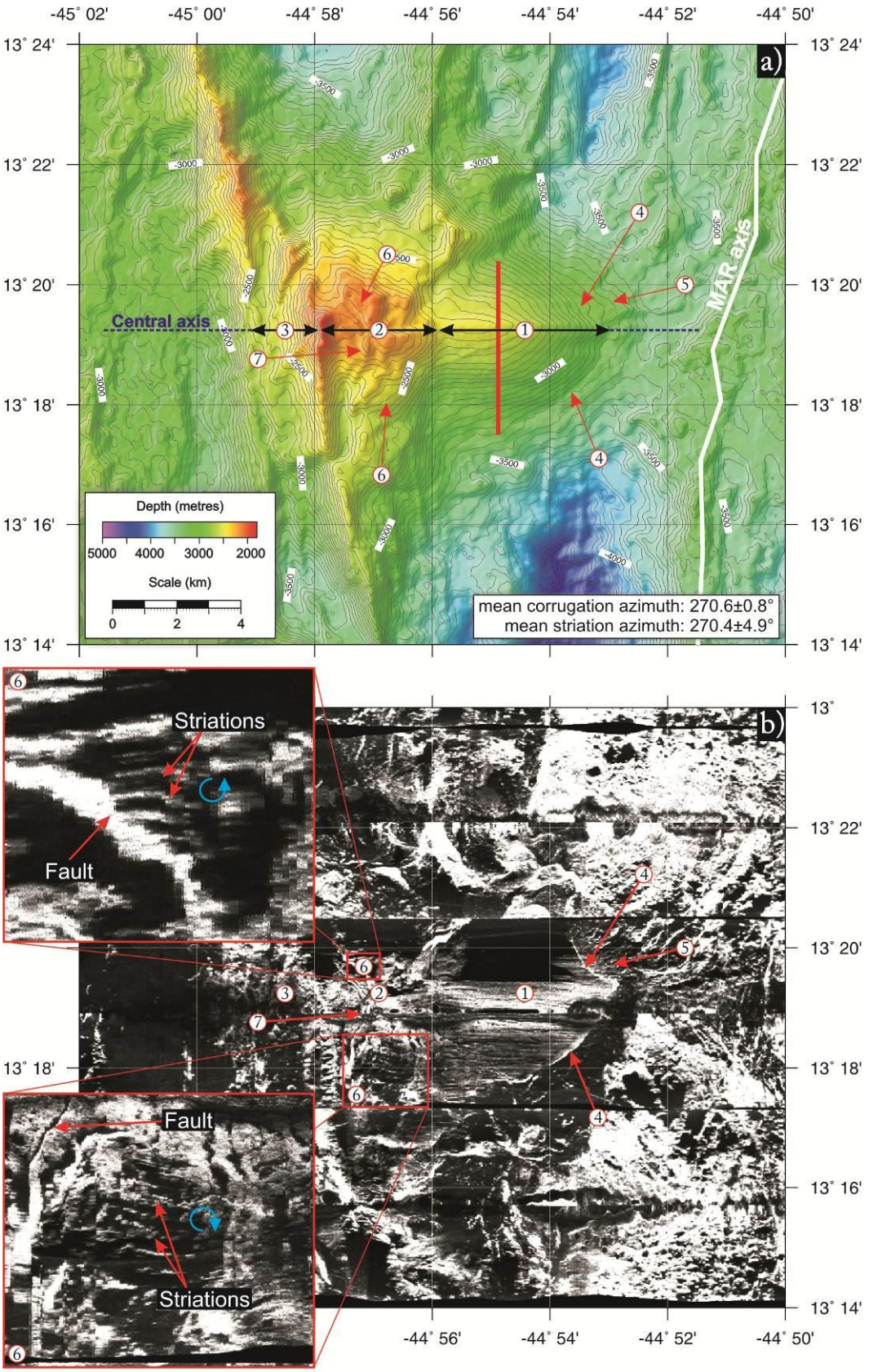


Figure 3.3.6a-b. Morphology of OCC1319: **a)** bathymetry data with contours at 50 m intervals, illumination from NW; **b)** sidescan sonar data, with inset showing detailed view of rotated striations on upper massif (blue arrow indicates sense of rotation). Numbered points are referred to in the text. Vertical red line in **a)** marks position of profile in **Figure 3.3.7.**

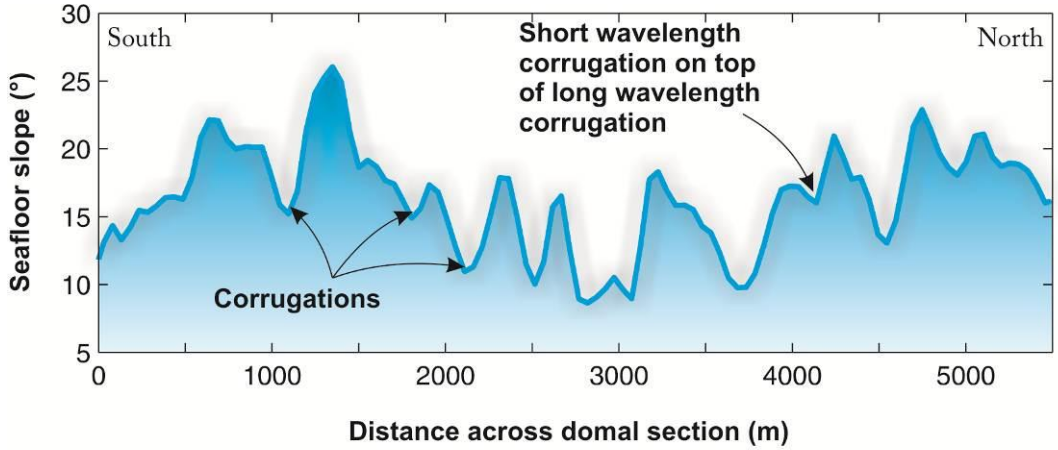


Figure 3.3.7. Axis-parallel profile of seafloor slope across domal section of OCC1319 (position indicated by red line in **Figure 3.3.6.**). Summit and troughs of corrugations appear as troughs/minima in the slope data. Corrugations appear to have a wavelength of ~100-700 metres, although shorter wavelengths (<100 m) may not be resolved with the bathymetry data. See text for discussion.

Prominent spreading-parallel striations revealed by the sidescan sonar, which have wavelengths of ≤ 50 metres, may be topographic corrugations that cannot be resolved with the ship's echo-sounder (e.g. Cann *et al.*, 1997; see Video 3 – Appendix II). The footwall/hanging-wall boundary is clearly defined with the sidescan sonar data around the eastern part of the dome, forming a narrow, high intensity band of backscatter (Point 4 – Figure 3.3.6b). The influence of the footwall can be observed within the hanging-wall at distances of up to ~2 km from this "zone of emergence", forming a fan of moderate intensity backscatter that most likely represents widespread talus accumulation and tectonic degradation of the thin, uplifted hanging-wall (texture O3; Point 5 – Figure 3.3.6b).

To the west of 44°55.9'W, the upper massif displays a blocky topography that is ~3.5 km across-axis by ~13.7 km along-axis, reaching a minimum depth of 1.92 km (Point 2 – Figure 3.3.6a). Backscatter across this region is highly variable, with the shallower areas generally being brighter than the deeper areas towards the north and south, which are interpreted to have undergone large amounts of wasting and deformation. Striations similar to those observed on the dome to the east are intermittently detected on the upper massif at 44°56.7'W, 13°18.2'N and 44°57.2'W, 13°19.7'N (Points 6 and inset – Figure 3.3.6b). The southern group of striations have seemingly been rotated clockwise by ~11° to trend at 281.6±5.4°, whereas the northern half have been rotated anticlockwise by ~8° so that they trend at 262.4±5.1°. This rotation may have occurred due to block faulting and degradation of the upper massif

during uplift of the footwall (i.e. gravitationally driven; MacLeod *et al.*, 2009), which is further evidenced by a series of curvilinear faults that are centred along the central axis of the OCC (Point 7 – Figure 3.3.6b). These rotations are evidence of significant brittle deformation occurring in the upper footwall of the OCC.

The presence of striations on the upper massif of OCC1319 has interesting implications for the mechanisms by which they must form. For example, if it is assumed that striations develop in the same way as corrugations – i.e. by casting of relatively ductile footwall material (e.g. serpentinised peridotite) against the impression of the underside of the brittle (e.g. basaltic) hanging-wall (e.g. Spencer, 1999; Tucholke *et al.*, 2008) – then striations on the upper massif indicate a transition into relatively ductile crust at depths of ~1.5 – 3.5 km (i.e. the distance from the breakaway to the oldest, most-westerly striations). This supports a lithospheric model in which the lower crust has a plum-pudding composition, comprising a mixture of gabbro and peridotite (Section 1.2.4 – Cannat *et al.*, 1995). However, the lack of sampled ultramafic material on the upper massif (Figure 3.2.6) suggests that these striations exist in basaltic (i.e. brittle) material. Thus it seems plausible that corrugation and striation formation is a two level process, with corrugations forming by casting at depth and striations forming by scratching against shallow brittle crust as the footwall becomes unroofed.

The breakaway zone comprises two major, steeply back-tilted fault blocks that define an area which is 2.3 km wide (E-W) at the central axis (Point 3 – Figure 3.3.6a). Seabed video showed that the outer slopes of these faults blocks comprise back-tilted pillow lavas (Figure 3.3.8a), with sidescan sonar data also showing that they have a hummocky texture suggestive of volcanic composition. The eastern ridge is bisected by two E-W trending offsets that occur at the same latitude as the northern (13°20.2'N) and southern (13°17.1'N) edges of the dome, forming three segments that have a cumulative length of 15.9 km, with an average trend of 342° and dip of 35 – 42°W. This ridge is joined at 44°59.2'W, 13°21.4'N by the western ridge, which is continuous along axis for 20.4 km with a trend of 356° and dip of 35 – 40°W. The eastern breakaway ridge is convex towards the ridge axis at 13°19.4'N, which may have occurred in response to uplift and flattening of the footwall being more pronounced along the central axis of the OCC (this effect is also seen along the breakaway of OCC1325 – Figure 3.2.15b).

Two possible models for the nature of the breakaway zone make it difficult to determine the exact position of a single ridge that defines the point at which extension began on the detachment fault. For example, if the western ridge marks this point, then

the eastern ridge may represent the crest of a 'rider-block' that was at one point attached to the hanging-wall. Alternatively, the eastern ridge may mark the point of OCC inception, and then the western ridge would simply be a normal fault dipping towards the ridge axis that existed prior to strain localising onto a single, OCC-forming detachment fault.

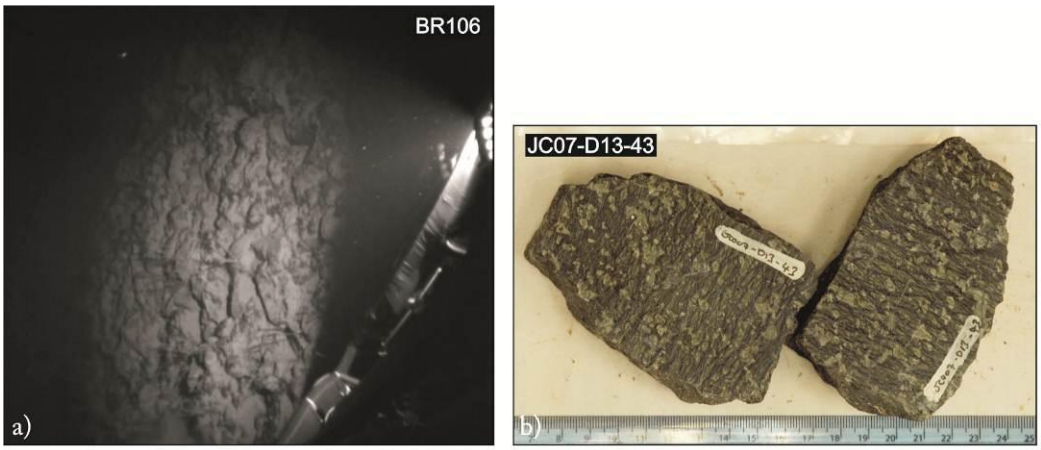


Figure 3.3.8a-b. a) Seabed video footage taken during BRIDGE drill deployment showing westward tilted pillow-lava outcrops across the breakaway zone of OCC1319 and **b)** a sample of harzburite dredged from the domal section of OCC1319. Ultramafic samples were in most cases highly (~<75%) serpentinised (Searle *et al.* 2007).

Sampling results show that OCC1319 comprises a diverse spectrum of lithologies (Figure 3.2.4; Searle *et al.*, 2007). Across the upper massif and breakaway zone, dredging and drilling recovered almost entirely basalt and diabase. Sampling across the younger domal massif to the east recovered a greater abundance of mid- to lower-crustal rocks and mantle lithologies. It therefore seems feasible that the morphological change at 44°55.9'W represents a rheological boundary between predominantly brittle crustal lithologies that form the upper massif and ductile serpentinised mantle material that form the surface of the domal section. This would suggest a crustal thickness prior to OCC formation of ~3 – 6 km (the exact value will depend on the precise location of the breakaway ridge and the dip of the detachment fault through the crust during the early evolution of the OCC), which seems a reasonable estimate for a slow-spreading, magma-poor environment (*Section 1.2.4*). It is important to note, however, that sampling during JC07 does not preclude the possibility of lower-crustal rocks at depth beneath the domal section.

Peridotite samples from the OCC dome were in most cases highly serpentinised (Figure 3.3.8b), with some specimens being 100% amorphous serpentine (Searle *et al.*, 2007). In addition, red-staining was observed on many of the samples, indicating that hydrothermal mineralisation occurred at some point after deposition of the rocks.

3.3.1.4. OCC1330: Surficial morphology

From its across-axis extent, OCC1330 is interpreted as being slightly older than OCC1319, and hence in a different evolutionary phase of the OCC life cycle (Figure 3.3.9a-b and also Figure 3.2.15a-b). This difference in age manifests itself in the morphological differences between the two core complexes, namely: the upper massif and breakaway region of OCC1330 is not topographically distinct (Point 1 – Figure 3.3.9a-b) and OCC1330 also exhibits less well-defined striations on the domal section (Point 2 – Figure 3.3.9a-b). The area of seafloor corresponding to the upper massif has a pronounced, highly irregular, mottled backscatter pattern, seemingly indicative of prolonged tectonic deformation (Point 3 – Figure 3.3.9a), forming a topographic depression that is on average several hundred metres shallower than the 2.11 km deep summit of the domal section.

The overall plan-shape of the OCC is also very different from that observed at OCC1319 – where the northern and southern limits of the breakaway ridge and the eastern limit of the footwall/hanging-wall boundary forms an eastward pointing equilateral triangle. Instead, OCC1330 is much more oval in shape, with the domal section possibly continuing along-axis for up to ~11.56 km (Point 2a – Figure 3.3.9a-b; see also Figure 3.2.15b), although it is unclear if this area of low backscatter intensity and thus thick sediment cover to the north forms part of the OCCs footwall or not. Along its central axis, the dome of OCC1330 displays a change in gradient of 4.7°.km^{-1}, dipping at ~2°E at the summit to ~14°E at the footwall/hanging wall boundary (similar to OCC1319; Figure 3.2.1).

The mean azimuth of corrugations and striations across OCC1330 is 272.3±1.5 and 271.2±6.0°, respectively, and is thus within the range of values determined for OCC1319 and for the regional spreading direction between SA-AF. Corrugations on the domal part of OCC1330 have mean wavelengths and amplitude of 615 metres and 32 metres, respectively, and are thus slightly larger than those observed at OCC1319.

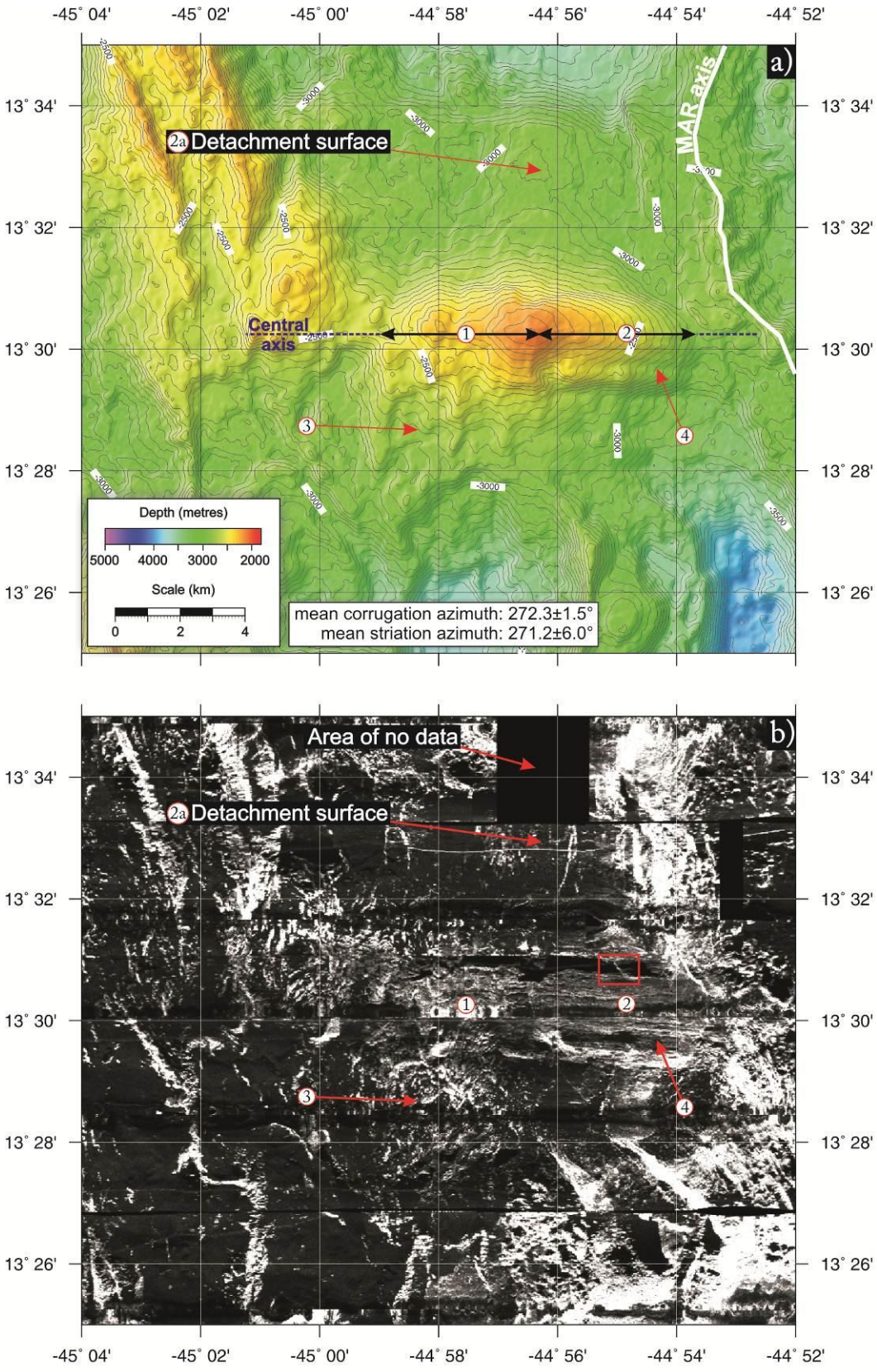


Figure 3.3.9a-b. Morphology of OCC1330: **a)** bathymetry data with contours at 50 m intervals, illumination from NW; **b)** sidescan sonar data. Numbered points are referred to in the text. Red box marks position of **Figure 3.3.10.**

Assuming that corrugations form by continuous casting of ductile footwall material against brittle hanging-wall material (Spencer, 1999), this variation in mean corrugation dimension may represent subtle changes in the topography of the brittle-ductile transition, which may be related to an irregular pattern of magma intrusion in magma-poor environments (Tucholke *et al.*, 2008). Furthermore, corrugation amplitude may indicate that the ubiquitous ultramafic layer across the domal sections of near-axis OCCs (identified during the sampling survey – *Section 3.2.2*) is ~> 30 metres thick. For example, if rheologically strong gabbroic material was encountered within the upper few metres, it may be expected that distinct topographic corrugations of the order of several tens of metres in amplitude would not form.

The striated nature of the dome is less well resolved with the sidescan sonar compared with OCC1319 (Point 4 – Figure 3.3.9b). Although the backscatter intensity of the striated surface is approximately equal between OCC1319 and OCC1330 (38% compared with 36% – *Section 3.2.3*), the latter exhibits more grey tones rather than sharply defined white and black striations, indicative of a greater amount of sediment accumulation (as would be expected across the older OCC). The dome is also cut by a number of N-S trending, minor faults that post-date the formation of the striated structures (Figure 3.3.10 and also Figure 3.2.15b). It is possible that these cross-cutting faults may grow to the point where they potentially terminate extension on the OCC's detachment surface (*Section 3.5.3*). Thus, they may be the precursors to 'termination faults' documented on the SWIR, which are believed to form due to mass wasting of the footwall as it becomes rheologically stronger and uplift becomes greater towards the end of the OCC life cycle (Cannat *et al.*, 2009). Termination mechanisms are discussed in more detail in *Section 3.5.3* and *Section 6.3.2*.

There are a number of ridges that could potentially mark the breakaway of OCC1330 (i.e. 45°02.2'W, 45°01.3'W and 45°00.5'W; Figure 3.3.9a). Neither ridge, however, is as distinctive as the breakaways to OCC1319 and OCC1348. The true breakaway ridge may therefore have become degraded to the point where it is no longer clearly apparent within the bathymetry and sidescan sonar data. This could be a temporal effect – with OCC1330 being at a more mature stage of the OCC life cycle compared with OCC1319 and thus assumed to have undergone a greater degree of denudation – yet this is not a completely satisfactory explanation as it would predict that the breakaway ridge of the oldest near-axis OCC (13°48'N) should be similarly morphologically degraded (which is not the case, as noted in the following section). As

an alternative explanation, the prominent breakaway ridges of OCC1319 and OCC1348 may in fact be the crests of rider-blocks discussed by Smith *et al.* (2008), with the absence of such a ridge at OCC1330 therefore implying that no such rider-block formed on this OCC.

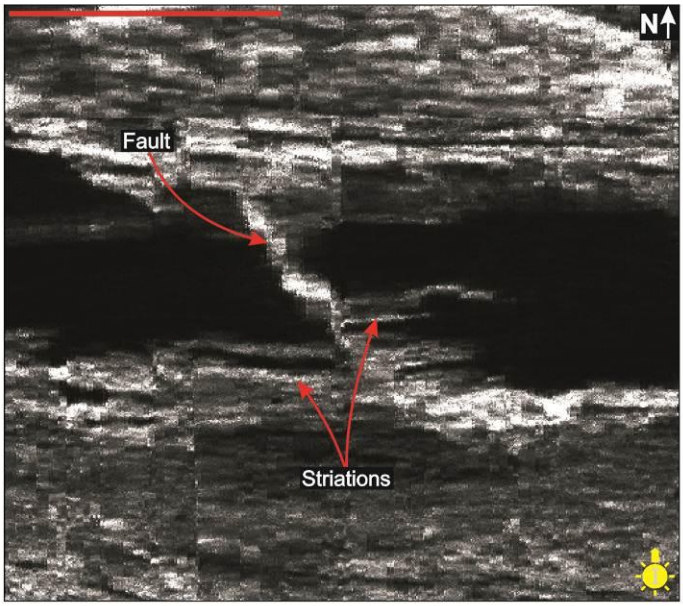


Figure 3.3.10. Spreading direction-parallel footwall striations are bisected (and hence post-dated) by cross-cutting faulting across the domal section of OCC1330. These features are too small to be resolved by the ship's echo-sounder, but can be detected with the 3 metre resolution sidescan sonar data. Red bar in upper left represents 0.5 km. Geographical location of image marked by red box in **Figure 3.3.9b**.

Seabed sampling and video reconnaissance were less extensive over OCC1330 compared with OCC1319. A single dredge (DR02) along the domal section recovered a large volume of serpentinised peridotite and small fragments of dolerite, similar to the pattern observed across OCC1319 (Figure 3.2.6). Significant volumes of hydrothermally altered samples were collected during dredge DR23, including specimens of sulphides, native copper, mineralised basalt and jasper. In addition to this, seabed video recorded during BR121 identified a number of beehive-shaped mounds that were believed to be black smoker-like vent chimneys (Figure 3.3.11; Searle *et al.*, 2007). The large amounts of basalt dredged from the surface of the domal section (DR23; which from seabed video were seen to occur as boulders and rubble, rather than in-situ outcrops) may represent talus that has broken-off the hanging-wall near the footwall/hanging-wall boundary.



Figure 3.3.11. Frame from seabed video footage taken during BRIDGE drill deployment BR121 showing beehive-shaped mounds across domal section of OCC1330.

3.3.1.5. OCC1348: Surficial morphology

OCC1348 is the oldest of the near-axis core complexes, and as such its primary difference from OCC1319 and OCC1330 is that it is almost entirely obscured on the sidescan sonar imagery by sediment cover and it exhibits various topographic differences (Figure 3.3.12a-b). For example, the domal section (Point 1 – Figure 3.3.12a) has a less regular slope (Figure 3.2.1) and is bisected in several places by ridge-parallel faults (Point 2 – Figure 3.3.12b; also Figure 3.2.15a). At 44°56.1'W, an N-S trending fault cuts the detachment surface with a vertical offset of ~300 metres (Point 3 – Figure 3.3.12a-b). In terms of its offset and position on the western, younger side of the OCC, this fault is also similar to the termination faults discussed by Cannat *et al.* (2009; range of termination fault heaves: 100 – 1600 metres) and in the previous section. However, to the west of this apparent termination, corrugated (Point 4 – Figure 3.3.13a) and striated (Point 5 and inset – Figure 3.3.13b) seafloor is again observed, which might imply that the OCC detachment is present on both sides of the fault. This is supported by DR01 and BR125 which recovered serpentinite from this fault scarp (Figure 3.2.6).

Corrugations trend at 280.7±1.1° across the domal surface of OCC1348, which is several degrees greater than that which is observed across the younger OCCs to the south (mean azimuth for corrugations and striations across both younger OCCs: 271.1°) and the spreading direction calculated from the NUVEL-1a plate model for SA-AF (273.4±1.7° – DeMets *et al.*, 1990, 1994).

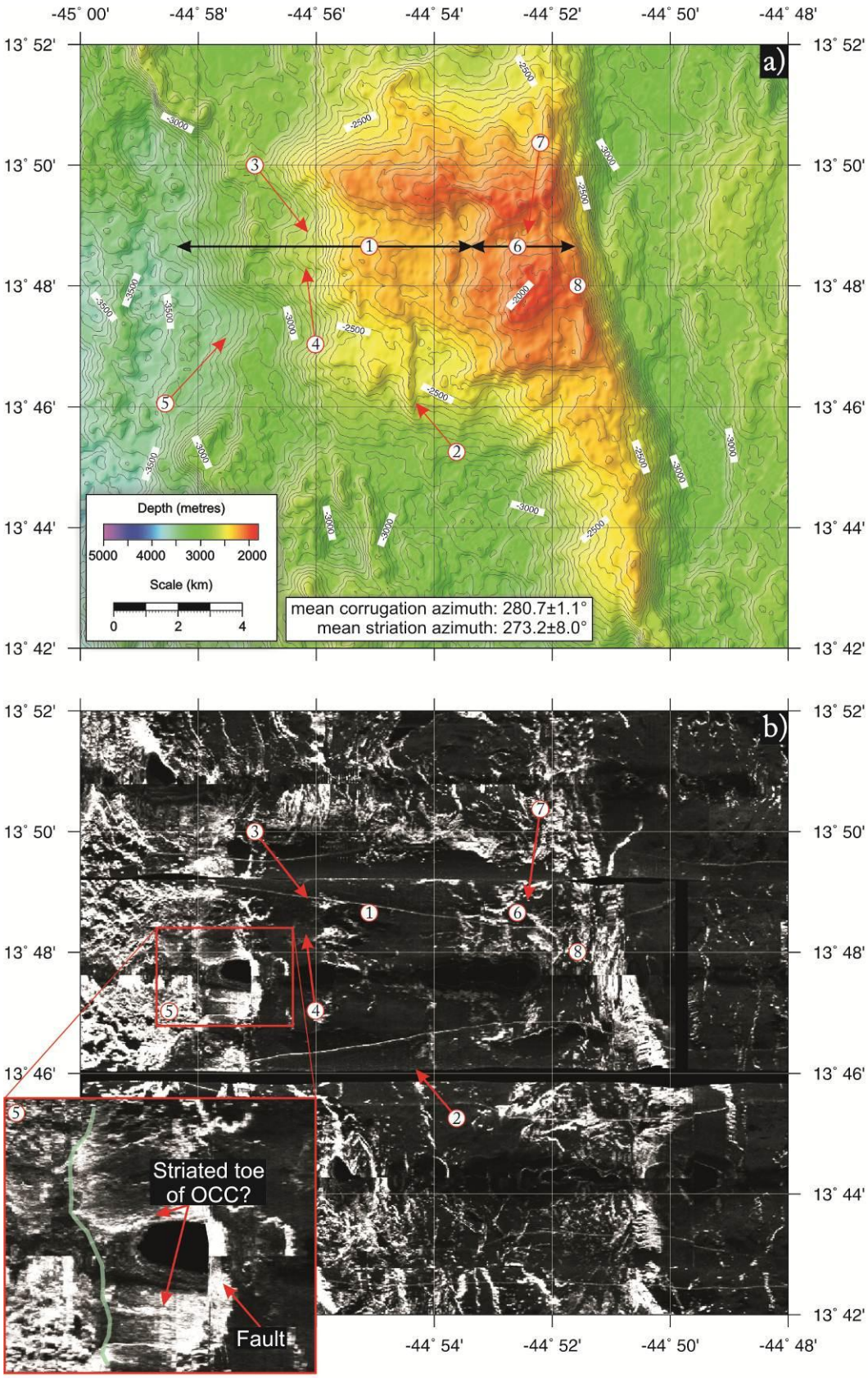


Figure 3.3.12a-b. Morphology of OCC1348: **a)** bathymetry data with contours at 50 m intervals, illumination from NW; **b)** sidescan sonar data with inset showing possible striations on toe of OCC (green line represents footwall/hanging-wall boundary). Numbered points are referred to in the text. Note that residual sea-surface reflections are seen in the centre of **b)**.

This implies either a spatial and/or temporal variation in along-axis spreading direction (with OCC1348 being both older and on the conjugate plate to OCC1319 and OCC1330) or a significant amount of post-extensional intra-plate deformation localised within or around OCC1348 (which may have been accommodated by the aforementioned ridge-parallel faulting: Point 2 – Figure 3.3.13b; also Figure 3.2.15a). Alternatively, the proximity of the NA-SA-AF triple junction to the 13°N region may explain this discrepancy, with the azimuth of corrugations and striations across OCC1348 being more closely aligned with the spreading direction for NA-AF (281.5±1.1° - DeMets *et al.*, 1990; 1994; Figure 3.3.13). In addition to this, low-magnitude seismic events show that focal mechanisms are highly oblique to the spreading axis at 14°N (i.e. in close proximity to OCC1348; Figure 1.3.9) and are sub-parallel to the spreading direction further south, which is consistent with the azimuth of corrugations and striations across OCC1319 and OCC1330 (Escartin *et al.*, 2003b). Lineament azimuths on the detachment surfaces of near-axis OCCs therefore suggest that the 13°N region is strongly influenced by the presence of the NA-SA-AF triple junction and thus highlights the complex regional stress and tectonic regime under which the area has evolved.

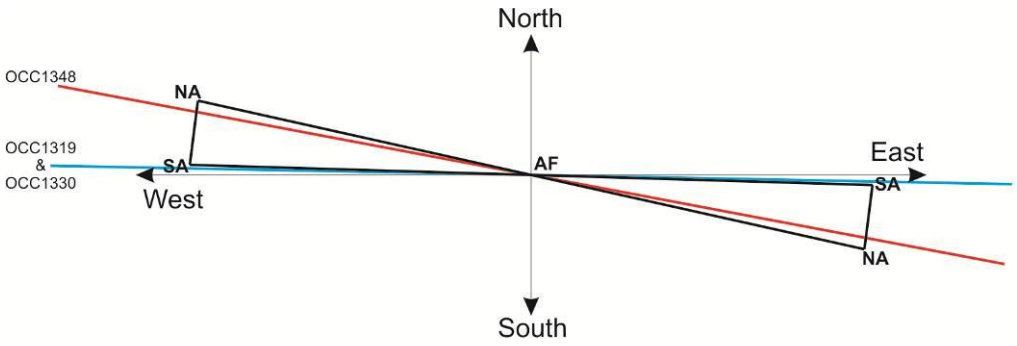


Figure 3.3.13. NA-SA-AF relative plate motions. Blue line is the average corrugation and striation azimuth for OCC1319 and OCC1330 (271.1°), red line is the average corrugation azimuth for OCC1348 (280.7°). Note that the lineaments across OCC1348 are more closely aligned with NA-AF, whereas lineaments on the detachment surfaces of OCC1319 and OCC1330 are aligned with SA-AF. See text for discussion.

The upper massif of the OCC (Point 6 – Figure 3.3.12a) has an irregular, elevated topography that is morphologically similar to that which is observed at OCC1319, rather than at OCC1330. As discussed in the previous section, this might

suggest that the breakaway ridge is actually part of a rider-block. Sidescan sonar imagery shows this area to be associated with moderate backscatter intensity that is indicative of variable rock exposures and areas of thick sedimentary cover (Point 6 – Figure 3.3.12b). A depression running E-W through the centre of the upper massif at 13°48.8'N may possibly indicate displacement of the rider-block towards the north and south about the central axis of the OCC (Point 7 – Figure 3.3.12a).

The breakaway is clearly defined by a single ridge at 44°51.8'W that is continuous for ~20.3 km along-axis and whose eastern side has a dip of ~38°E (Point 8 – Figure 3.3.13a-b). The ridge has an N-S trend (001°) to the south of 13°46.0'N and becomes convex towards the ridge axis north of this point. Seabed video footage shows the outward-facing part of this ridge to be built up of pillow lavas, and as with the breakaway zone at OCC1319, it is possible to identify hummocky features within the sidescan sonar on this outer slope.

3.4. Volcanism

In the previous section I discussed the seafloor morphology of oceanic core complexes on the basis of sidescan sonar, bathymetry data and sampling results. Using the same datasets, in this section I give an overview of the morphology and extent of the surficial component of volcanism across the 13°N region. To a certain extent, the expression of volcanic processes observed in the 13°N magma-poor region are typical of slow-spreading ridge environments, namely: there is a predominance of hummocky terrain, a relative lack of smooth seafloor and numerous volcanic ridge-forming lineaments (*Section 1.2.2*). There are, however, a number of volcanic features that are atypical for a slow-spreading MOR environment and are indicative of spatial and temporal instabilities in melt supply to the ridge axis in the presence of active, or very recently active, oceanic core complexes.

3.4.1. Short-scale variability in the locus of melt emplacement

The morphology, distribution and relative ages of volcanic terrains record the recent history of spatial and temporal variations in the locus of melt emplacement at the ridge axis. As with most sections of the slow-spreading MAR, in the 13°N region volcanic terrain is expressed primarily as hummocky seafloor, which constitutes approximately 90% of the volcanic seabed that is visible to TOBI's sidescan sonar (similar to ~90% on the MAR between 27°N – 30°N – Briais *et al.*, 2000). The surface expression of this hummocky seafloor typically comprises a number of distinct, topographic lineaments that range dramatically in scale, as has been observed on other parts of the MAR (e.g. Luyendyk & Macdonald, 1977; Shih *et al.*, 1978; Crane & Ballard, 1981; Karson *et al.*, 1987; Parson *et al.*, 1993; Head *et al.*, 1996)[6]. For example, there is a large volcanically constructed ridge within the axial valley that extends for ~22 km between the eastern part of the NTO in the ridge axis (44°53'W, 13°39'N) to an area of seafloor south of OCC1330 (44°51'W, 13°27'N), forming a crescent shape that has a width of ~4 km and height of up to ~450 metres (Point 1 – Figure 3.4.1).

[6] Volcanic ridges are marked with blue, dashed lines on the geological map – Figure 3.2.15a-b.

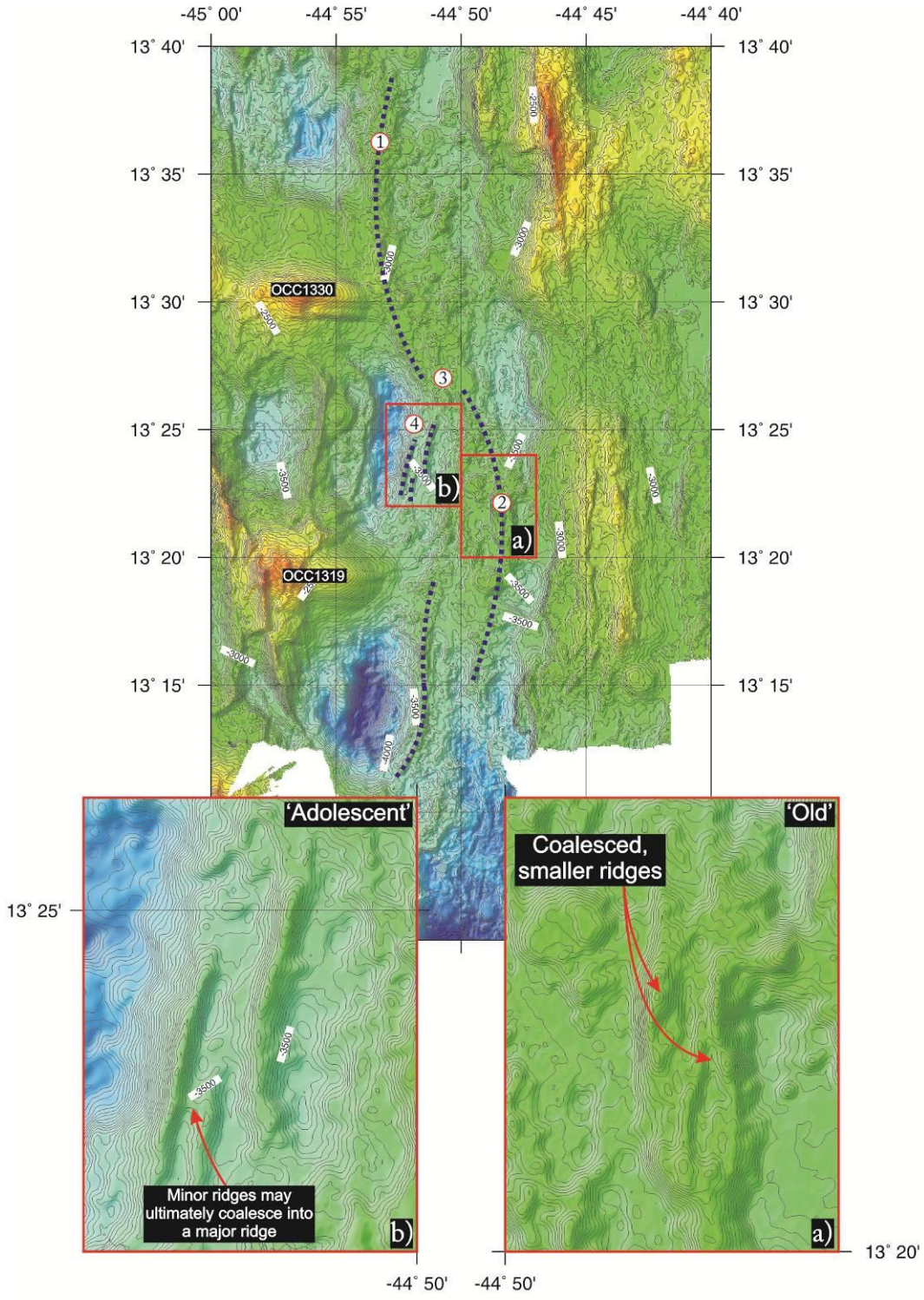


Figure 3.4.1. Volcanic lineaments in the southern part of the survey area. There is an array of major and minor ridges (annotated in main plot with purple, dashed lines), which most likely reflects volcanic material of different ages. Numbered points are referred to in the text. Red boxes show locations of insets. Contours are at 50 metre intervals (20 metres for inset) with colour scale and illumination (from NW) the same as **Figure 2.2.2**. Sidescan sonar of the insets is shown in **Figure 3.4.2**. See text for discussion.

Further south, another major, volcanically-constructed ridge is observed at 44°48'W, 13°22'N that is ~18 km long and forms a crescent shape with the opposite sense compared with the ridge to the north (Point 2 – Figure 3.4.1). It is possible that these two ridges are actually the northern and southern halves of one single ridge, in which case the area of low-lying topography in the centre may indicate along-axis variability in the strength of magmatism (Point 3 – Figure 3.4.1). Alternatively, they may have originally been discrete features that have propagated along-axis and rotated towards each other (explaining the double-crescent shape) similar to overlapping-spreading centres (Macdonald *et al.*, 1988).

On the basis of backscatter texture, it is apparent that these major volcanic ridges are composed of numerous volcanic cones that have coalesced together – as has been suggested for other parts of the MAR (e.g. Karson *et al.*, 1987; Smith & Cann, 1990; and many others) – and are generally sediment covered and thus relatively old compared with the brighter NVZ (Figure 3.4.2a). Sidescan sonar data also show that as well as being sediment covered the volcanic ridge opposite OCC1319 is highly tectonised. These major volcanic ridges are thus comparable in morphology and age to the 'old' classification of AVRs on the Reykjanes Ridge (Figure 1.2.3d – Parson *et al.*, 1993).

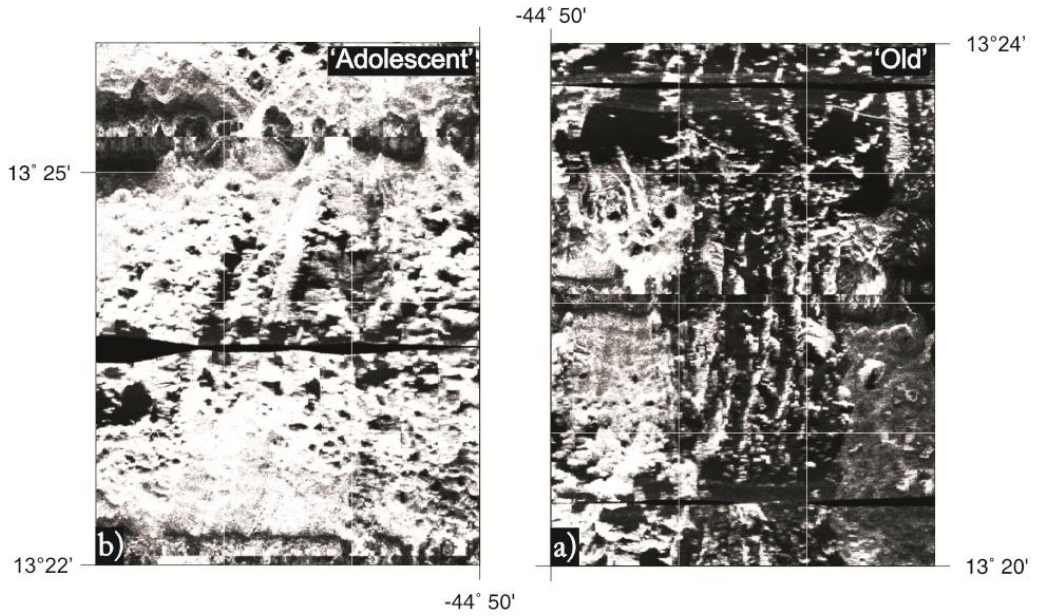


Figure 3.4.2. Sidescan sonar imagery for the two insets to **Figure 3.4.1**, showing 'old' **(a)** and 'adolescent' **(b)** volcanic lineaments (relative ages based on the classification by Parson *et al.* (1993)). Older lineaments comprise large mounds of hummocks that are sedimented and are highly tectonised in places. Younger lineaments are less sedimented and are usually only a single volcanic cone wide. Gridlines are at 1' increments. See text for discussion.

Immediately to the west of the major volcanic ridge between OCC1319 and OCC1330 (Point 2 – Figure 3.4.1) is a series of relatively minor volcanic lineaments that are continuous along-axis for distances of ~5 – 15 km with widths of ~400 – 1000 metres and well-defined summit crests that are typically 50 – 200 metres above the surrounding seafloor (Point 4 – Figure 3.4.1). This group comprises 4 ridges that co-exist at the same latitude and are spaced across-axis by ~1 – 2 km. Minor volcanic ridges are in most cases only a single volcanic cone wide and generally occur within the brightest, neovolcanic parts of the axial valley (Figure 3.4.2b), suggesting that they are much younger than the major ridges observed in the region. Backscatter data are of insufficient resolution to determine if only one or many of these volcanic ridges are active at the same time (i.e. the intensity is approximately equal across all ridges). These lineaments are similar to 'young' or 'adolescent' AVRs on the Reykjanes Ridge (Figure 1.2.3a-b - Parson *et al.*, 1993) and have previously been classified as 'hummocky ridges' by Head *et al.* (1996). Thus they might eventually coalesce by prolonged melt emplacement to become a single, major volcanic ridge.

In order to create the pattern and relative ages of volcanic lineaments discussed above, melt emplacement at the ridge axis must have recently shifted by ~6 km to the west within the axial valley immediately north of OCC1319, moving from the older, larger volcanic ridge to the younger, smaller volcanic lineaments. This value is a maximum as melt emplacement and growth of the minor volcanic ridges will have shifted the major ridge eastwards as a natural consequence of seafloor spreading. Previous studies have shown that significant backscatter attenuation occurs due to sedimentation within ~0.5 My (e.g. Smith *et al.*, 1995; Lawson *et al.*, 1996; Escartin *et al.*, 1999), and thus is might be expected that the major volcanic ridge between the two southernmost, near-axis OCCs has been inactive for a similar period. Furthermore, Collette *et al.* (1979) suggest that crustal accretion in the 13°N region involves regular switching to a new spreading centre several kilometres from the existing one over a period of ~0.5 My. These timescales are similar to the duration of near-axis core complexes (Table 3.3.1), and it may therefore be possible that OCC formation and the locus of melt emplacement are closely related. For example, an OCC, the formation of which may occur during periods of weak magmatism (e.g. Karson & Winters, 1992; Buck *et al.*, 2005; Behn & Ito, 2008; Tucholke *et al.*, 2008), may form during a volcanic hiatus as the melt supply episodically switches to a new location within the axial valley (Figure 3.4.3).

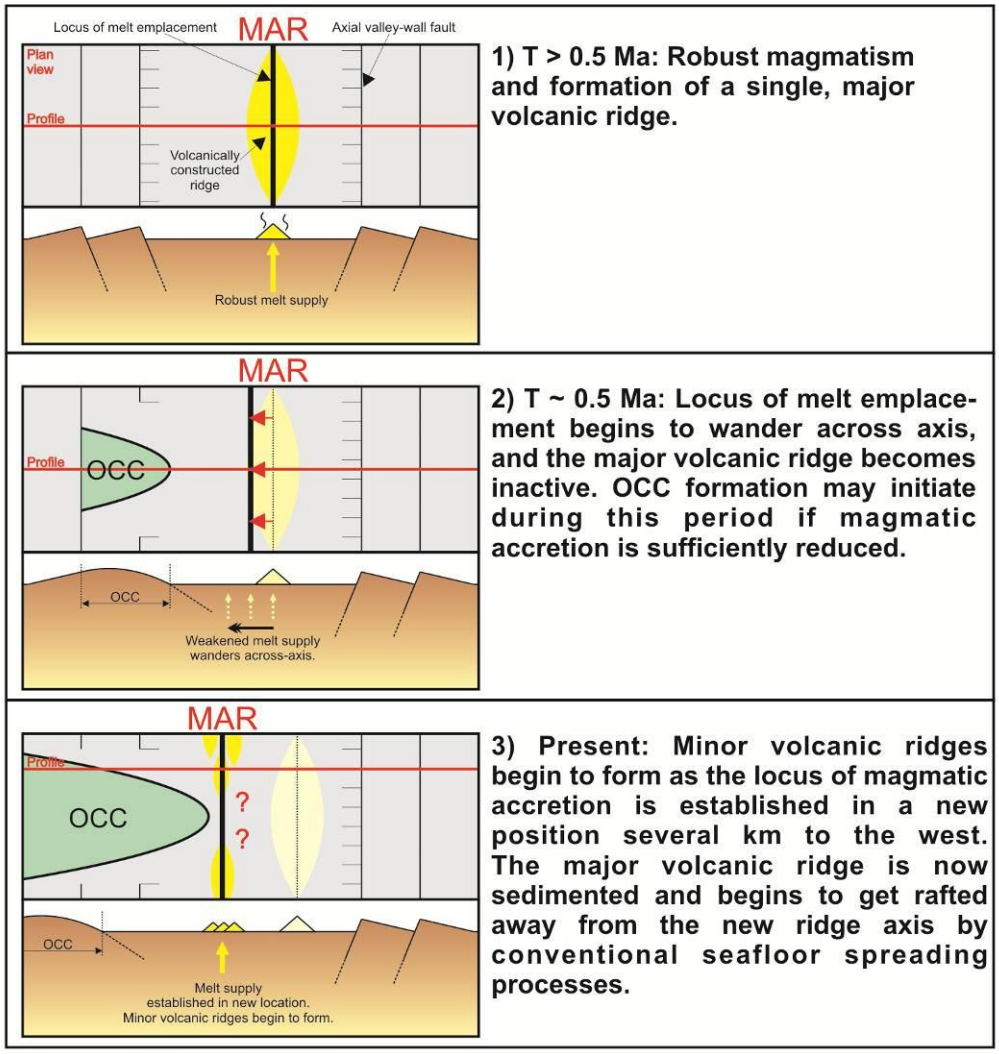


Figure 3.4.3. OCC formation may occur during periods in which the locus of melt emplacement switches to a new location. Note that the present day seafloor has a break in neovolcanism adjacent to the active OCC at 13°19'N, which is indicated by the red question marks in the diagram above. Formation of this gap in neovolcanism is discussed in the following section.

In the northern part of the survey area, numerous minor hummocky lineaments span the axial valley (e.g. Point 1 – Figure 3.4.4). There do not, however, appear to be any major volcanic ridges. Assuming the pattern of volcanic ridge growth discussed above (i.e. young, minor ridges eventually coalesce into older, major ridges) applies in this part of the axial valley, this suggests that either: 1) melt emplacement has rapidly switched back and forth across the entire width of the axial valley, so that there is no preferential zone of volcanic construction and subsequently only minor ridges ever form, or; 2) melt emplacement at the ridge axis has only recently initiated after a prolonged hiatus – which may be related to the formation of OCC1348 (which is discussed more fully in the following section).

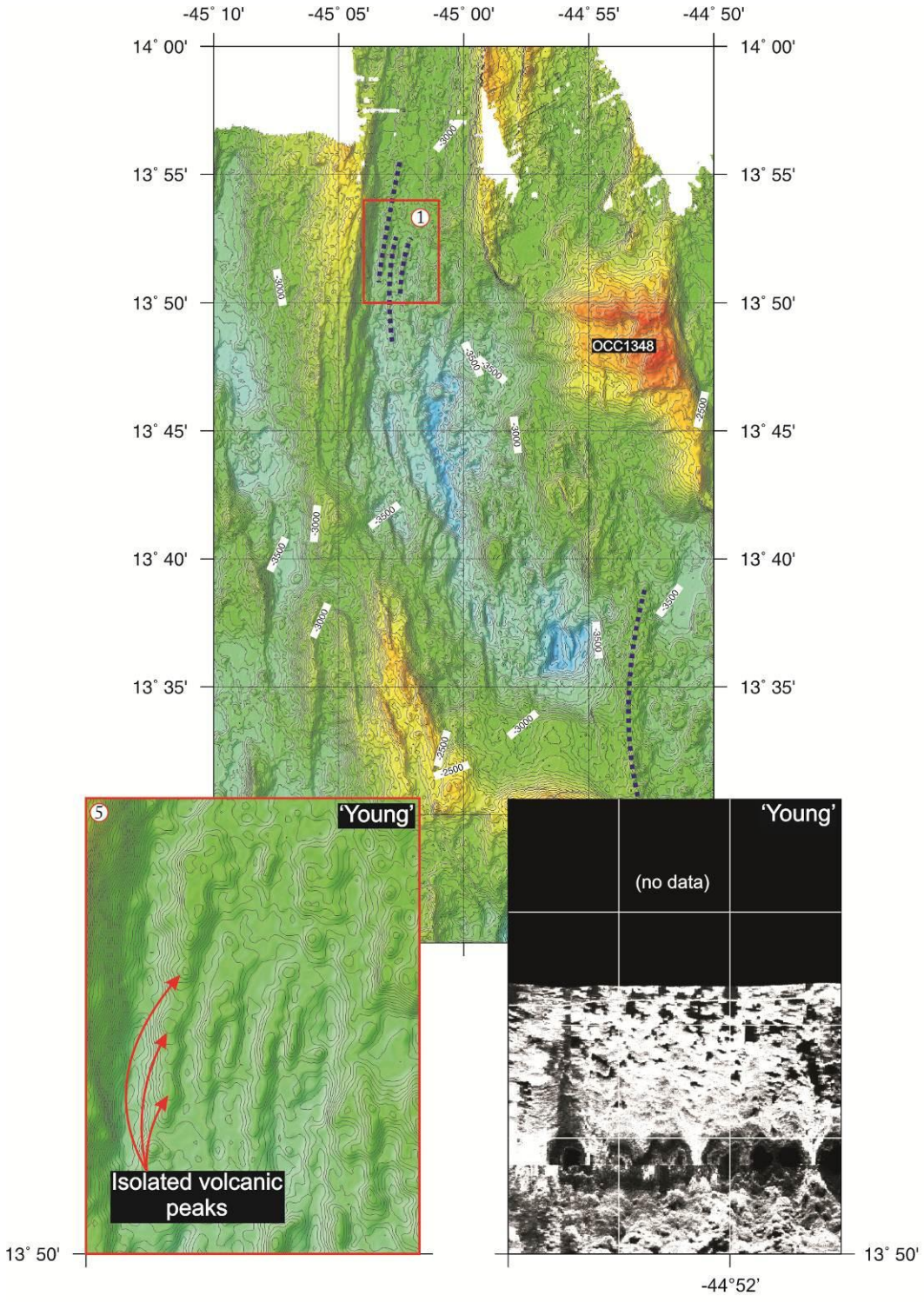


Figure 3.4.4. Volcanic lineaments in the northern part of the survey area. There are a number of minor ridges (annotated in main plot with purple, dashed lines) but no major volcanic ridges similar to those observed south of the NTO at 13°38'N. Numbered points are referred to in the text. Contours are at 50 metre intervals (20 metres for inset) with colour scale and illumination (from NW) the same as **Figure 2.2.2**. See text for discussion.

3.4.2. NVZ width & OCC footwall capture of ascending melt

In the previous section I used the morphology of volcanic lineaments to suggest that the locus of melt emplacement has shifted several kilometres to the west between OCC1319 and OCC1330 over a period of ~0.5 My. I also noted that whilst young, hummocky volcanic ridges span the axial valley in close proximity to OCC1348, neovolcanism appears to be absent opposite OCC1319. In this section I will discuss the implications of this observation, which is also documented by MacLeod *et al.* (2009; Appendix I for published account).

The NVZ marks the locus of the most recent magmatic accretion within the axial valley and is evident as a bright, hummocky (and to a lesser extent smooth) texture within the sidescan sonar imagery (*Section 3.2.3.1*). This area is bounded across-axis by a series of progressively less bright regions, interpreted as being older, sedimented lava flows (Figure 3.2.15a-b). Figure 3.4.5 shows the along-axis variability in the width of volcanic textures identified from the sidescan sonar (with the NVZ being classified as the brightest hummocky (V1) and smooth (V3) backscatter textures – defined in *Section 3.2.3.1*). Note that Figure 3.4.5 shows the combined widths of each individual texture for that latitude, so that, for example, at 13°48'N the combined width is 12 km, which is partitioned between the NVZ (V1) that is 5 km wide, slightly older (V1a) material that is 5 km wide and highly sedimented (V2a) material that is 2 km wide.

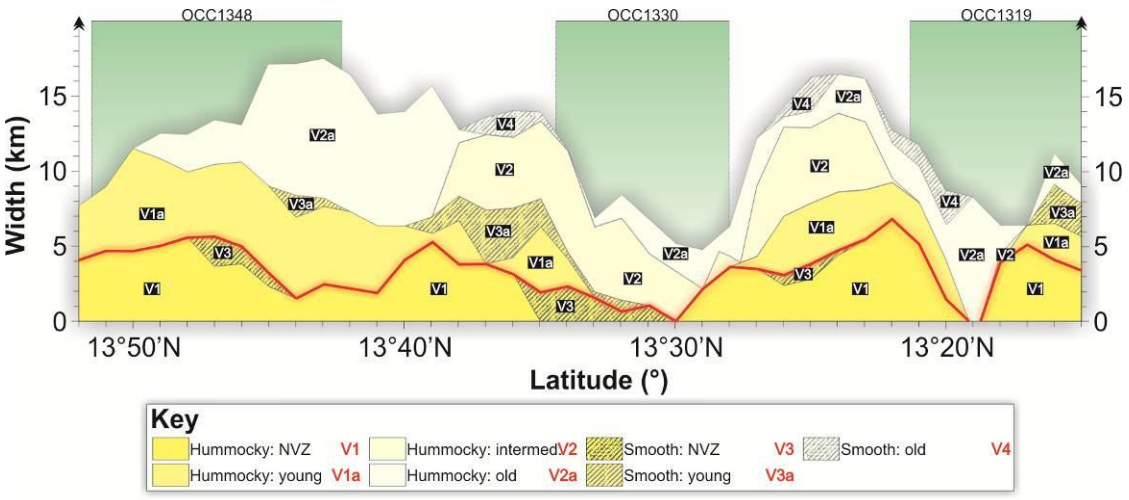


Figure 3.4.5. Along-axis profile showing variation in the width of volcanic textures identified with TOBI's sidescan sonar (texture definitions are given in *Section 3.2.3*). Note that widths of various textures are stacked. Width of NVZ is marked by red line and includes textures V1 and V3. Latitudinal extent of near-axis core complexes are highlighted with vertical green bars. See text for discussion.

Estimates of the width of volcanic textures in Figure 3.4.5 differs slightly from that which is presented by MacLeod *et al.* (2009), as the identification here is based on backscatter intensity profiles rather than a purely qualitative estimation (and is hence more precise). For example, at 13°25'N MacLeod *et al.* (2009) report that the NVZ is ~8 km wide, yet from the backscatter intensity profile along survey line 4 (Figure 3.2.7) it is clear that the intensity decays quite rapidly about a zone that is only ~5 km wide. It should be noted, however, that the relative along-axis change in the width of the NVZ is more-or-less the same.

The NVZ is on average 2.5 km wide, expanding to a maximum width of ~6 km across the axial valley immediately north of OCC1319 (at 13°22'N), and is hence similar to estimates for the width of the NVZ in various other slow-spreading environments (e.g. Ballard & Van Andel, 1977; Macdonald *et al.*, 1991; Smith *et al.*, 1999). However, opposite the OCCs forming at 13°19'N and 13°30'N, the neovolcanic zone is entirely absent along-axis for ~2.5 km and ~1.5 km, respectively (see Video 4 – Appendix II). Adjacent to both OCC1319 and OCC1330, the seafloor has a backscatter intensity and texture similar to that which forms the inactive major volcanic lineament in the eastern part of the axial valley (e.g. Point 2 – Figure 3.4.1), implying that these areas of seafloor were volcanically active at approximately the same time. As I have discussed in the previous section, studies have suggested that significant backscatter attenuation may occur within ~0.5 My (e.g. Smith *et al.*, 1995; Lawson *et al.*, 1996; Escartin *et al.*, 1999), and thus volcanism may have been absent over a similar period.

It is also possible to estimate the duration of this volcanic hiatus from the sidescan sonar data by assuming a constant sedimentation rate and depth of penetration of the sonar into the seabed (Figure 3.4.6). If the backscatter intensity linearly decreases from a maximum of 1270 (V1) to a background level of 100 (sediment intensity – see Table 3.2.1), then the sediment thickness for a particular texture/intensity can be determined by plotting it on the red line in Figure 3.4.6. The age of the seafloor is thus given by (3.1):

$$Age(Ma) = Max_{pen} \cdot \left(\frac{V1_{\text{int}} - V_{\text{int}}}{V1_{\text{int}} - Sed_{\text{int}}} \right) / S \qquad \textbf{(3.1)}$$

Where Max_{pen} is the depth of penetration of the acoustic signal, $V1_{int}$ is the backscatter intensity of zero-age/neovolcanic material, V_{int} is the intensity of the texture which is to

be dated (in this case V2a), Sed_{int} is the backscatter intensity of background/sedimented seafloor and *S* is the sedimentation rate in m/My. For V2a (with a backscatter intensity of 370), and assuming a depth of penetration of TOBI's sidescan sonar of 5 metres (Lawson, 1996) and sedimentation rate of 5 m/My (Mitchell *et al.*, 1998a), this gives an age of the seafloor opposite OCC1319 and OCC1330 of 0.77 Ma. This value decreases by half to 0.38 Ma for a maximum assumed sedimentation rate of 10 m/My. If the depth of penetration of TOBI's sidescan sonar is assumed to be only 2.5 metres, then for sedimentation rates of 5 m/My and 10 m/My the age of V2a becomes 0.38 Ma and 0.19 Ma, respectively. Furthermore, the across-axis distance of V2a material from the youngest, V1 (neovolcanic) material is 6 km at 13°25'N. If V2a material was erupted in the present day location of the neovolcanic zone and rafted across the axial valley-floor by normal seafloor spreading mechanisms at a half-spreading rate of 13 km/My, this would also imply that the seafloor opposite the southernmost near-axis OCCs is several hundred thousand years old (0.46 Ma).

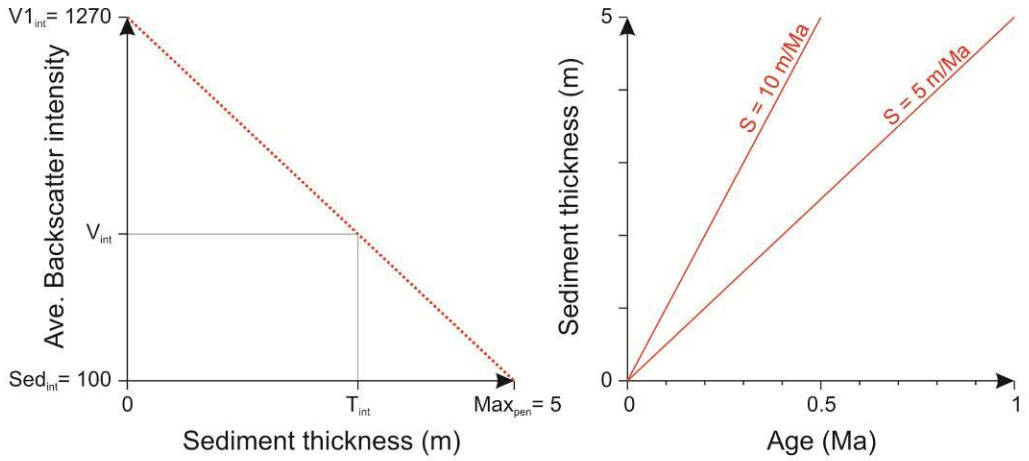


Figure 3.4.6. Calculating the age of the seafloor from backscatter intensity. Y-axis (left-hand graph) is backscatter intensity with minimum and maximum set as background/sediment intensity (Sed_{int}) and neovolcanic intensity ($V1_{int}$). Intensity is assumed to decrease linearly (red line) with increasing sediment thickness to the maximum penetration depth of the sidescan sonar (Max_{pen} - x-axis). Calculating the thickness of sediment (T_{int}) for a given intensity (V_{int}) then allows the age to be estimated if the sedimentation rate (S) is assumed (Equation 3.1 and right-hand graph). See text for discussion.

Assuming that the time taken to form OCC1319 and OCC1330 is between 0.38 – 0.77 Ma and 0.41 – 0.82 Ma (the maximum age is calculated from the across-axis distance of the OCC and the half-spreading rate, whereas the minimum age is calculated from the full-spreading rate – i.e. the OCC takes up 100% of the plate separation),

respectively, this suggests that surficial volcanism may have been absent prior to OCC formation. For example, it is possible that volcanism has been absent since ~0.80 Ma and that OCC1319 and OCC1330 began forming at ~0.40 Ma. Alternatively, volcanism may have ceased shortly after OCC initiation. In this latter scenario, OCC1319 and OCC1330 may have been forming since ~0.80 Ma and volcanism may have persisted throughout the initial stages of OCC formation and ceased at ~0.20 Ma.

In contrast to OCC1319 and OCC1330, the seafloor opposite the oldest of the three near-axis core complexes, OCC1348, displays higher backscatter intensities and thus seemingly robust neovolcanism that extends across- and along-axis for ~5 km and > 15 km, respectively (Figure 3.4.5, see also Figure 3.2.15a-b for geological interpretation and Figure 2.4.10a-b for sidescan sonar mosaic).

The absence of recent volcanism within the hanging-wall adjacent to OCC1319 and OCC1330 is unusual as previous studies have suggested that magmatic accretion should persist, albeit at a reduced strength, during OCC formation (Buck *et al.*, 2005; Behn & Ito, 2008; Tucholke *et al.*, 2008; Olive *et al.*, 2010; see also *Section 1.3.4*). Reduced backscatter intensity has also been detected within the axial valley further south at ~13°00'N, in close proximity to the OCC actively forming at 13°06'N (Smith *et al.*, 2008). This suggests that OCC formation may at some point during its life cycle form entirely amagmatically, although, as we have discussed in MacLeod *et al.* (2009) it is important to note that 'footwall capture' of ascending melt (i.e. fault-assisted melt emplacement) may play a critical role in OCC formation (i.e. OCC formation is not amagmatic but 'avolcanic').

Fault-assisted melt emplacement has been proposed to explain off-axis volcanism on a magma-poor section of the SWIR (Standish & Sims, 2010), the effect of which may also explain the prevalence of gabbroic plutons within the footwall of OCCs (e.g. Dick *et al.*, 2000; MacLeod *et al.*, 2002; Reston *et al.*, 2002; Ildefonse *et al.*, 2007). At Atlantis Massif, Grimes *et al.* (2008) use U-Pb zircon ages from IODP hole U1309D to show that magmatic accretion within the footwall was in the form of sills that formed during episodic periods of magmatism and at variable depths beneath the ridge axis.

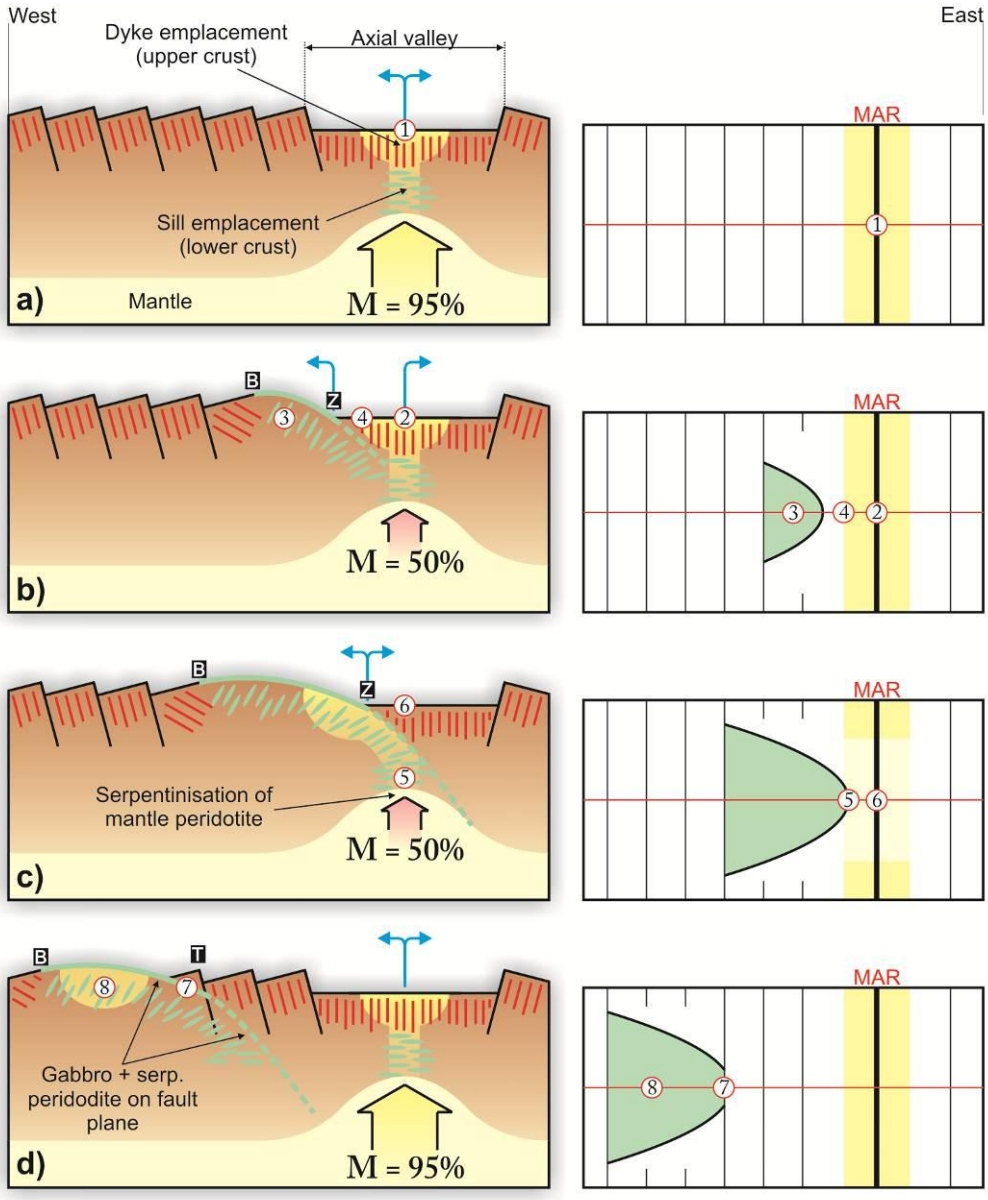


Figure 3.4.7a-d. Melt emplacement during the formation of oceanic core complexes. **a)** 'Normal' magmatic plate separation with high melt supply (Point 1), where blue arrows show plate motion. **b)** Melt supply wanes (Point 2) and regional plate separation is accommodated tectonically on the axial wall fault forming an OCC (Point 3, with 'B' and 'Z' marking the breakaway and zone of emergence, respectively). Note that at this point there is a fixed micro-plate (Point 4). **c)** As the OCC continues to grow, it eventually crosses the vertical projection of the ridge axis at depth (Point 5; see also MacLeod *et al.*, 2009), and the footwall captures ascending melt (possibly by sill emplacement, e.g. Grimes *et al.*, 2008). Volcanism ceases at the surface which becomes sedimented (Point 6). This stage is analagous to present day OCC1319 and OCC1330. **d)** Renewed melt emplacement may eventually overwhelm the OCC, initiating a new fault close to the ridge axis in the process that terminates extension on the detachment fault (termination (T) - Point 7), leaving an inactive, gabbro-cored OCC off-axis (Point 8). Widespread volcanism covers the axial valley floor. This stage is analagous to present day OCC1348. All values for magmatic accretion (M) are from Buck *et al.* (2005).

Footwall capture can also potentially explain the gaps in neovolcanism evident within the sidescan sonar data (Figure 3.4.7a-d; MacLeod *et al.*, 2009). Essentially, an OCC becomes initiated during magma-poor conditions (Figure 3.4.7a-b). In the early stages of OCC formation, there are then two possible explanations for melt becoming captured by the footwall, namely: 1) magmatism is entirely absent for a significant period of time and the OCC's footwall/hanging-wall boundary acts as the ridge axis and migrates towards the opposite side of the axial valley (i.e. to the east in Figure 3.4.7a-d). If the detachment crosses the along-axis projection of the ridge axis, any renewed magmatism will then be preferentially accreted within the footwall of the OCC, rather than the hanging-wall. Alternatively, 2) if magmatism persists throughout OCC formation, a fixed micro-plate will form between the volcanic ridge axis and the OCC's footwall/hanging-wall boundary (Figure 3.4.7b). Continued subsurface growth of the detachment surface, possibly combined with an across-axis jump to the west in the locus of melt emplacement (as has been demonstrated in *Section 3.4.1*) could then lead to melt being preferentially injected into the footwall of the OCC (Figure 3.4.7c). 'Jumping' of the spreading centre would remove the need for the detachment surface to cross through the zone of melt emplacement at depth.

The boundaries of the neovolcanic zones immediately to the north and south of OCC1319 and OCC1330 have V-shapes directed towards the footwall/hanging-wall boundaries of the OCCs (Figure 3.4.8). This suggests that the neovolcanic melt supply is currently propagating from more magmatically robust regions towards the zone of emergence. The angle subtended by the tip of the southernmost NVZ (i.e. immediately south of OCC1319) shows that the melt supply is propagating northwards at a rate of 15 km/My (MacLeod *et al.*, 2009). The southern tip of a moderately-sized volcanic lineament within the axial-valley south of OCC1319 is also curved towards the young (and presumably active) OCC1306 (44°52'W, 13°12'N; Figure 3.4.1 with OCC location in Figure 3.3.1). Each of these NVZs may ultimately cut through the 'toe' of their respective OCCs and thus terminate slip on the detachment surface (Figure 3.4.7d). The mechanisms by which this may occur and the faulting patterns within the axial valley adjacent to actively forming OCCs are discussed in the following section.

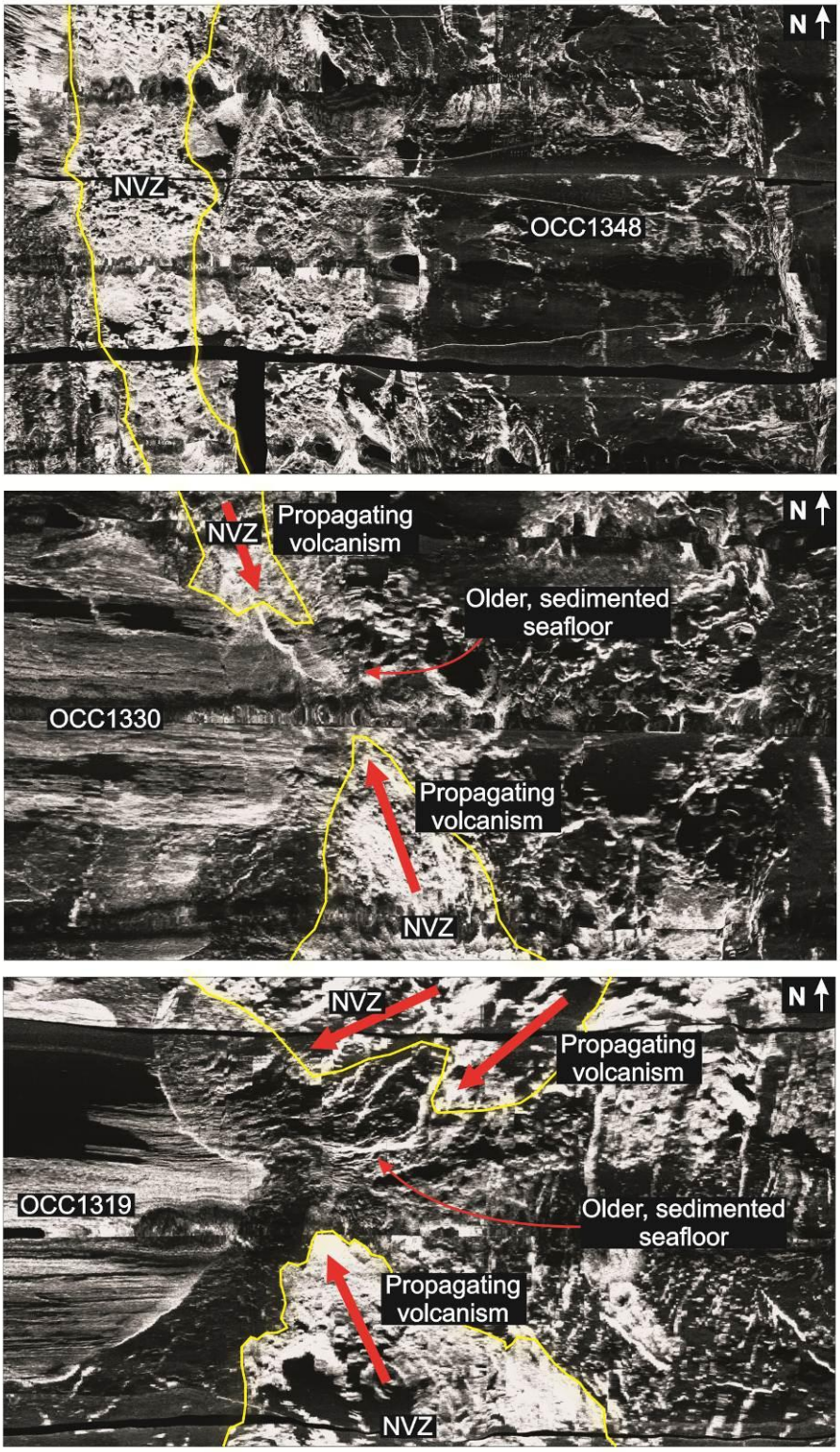


Figure 3.4.8. Variation in the style of the NVZ opposite near-axis OCCs. Opposite OCC1348 widespread neovolcanism covers the axial valley floor (upper image). Adjacent to OCC1330 (central image) and OCC1319 (lower image) however, the NVZ zone is absent. NVZs to the north and south have V-shaped tips suggesting they are propagating towards the active OCCs. NVZ outlined in yellow for clarity (see also geological map - **Figure 3.2.15a-b**). See text for discussion.

3.5. Tectonism

OCC formation is expected to be prevalent when magmatic accretion accommodates ~30 – 50% of the total plate separation (Buck *et al.*, 2005; Behn & Ito, 2008; Tucholke *et al.*, 2008; see also *Section 1.3.4*). More specifically, Olive *et al.* (2010) show that this melt must be accreted within the hanging-wall, rather than the footwall, to promote long-lived extension on a single fault (i.e. $M_{TOTAL} \approx M_{HW}$). Contrary to this, in the previous section it was shown that there is no apparent surficial component of magmatism during at least some, or perhaps all, of the OCC life cycle. By using sidescan sonar data to identify fault exposures, it is possible to measure tectonic strain ($T\varepsilon$) and therefore infer the relative strength of magmatism in the 13°N region (since tectonic strain is the complement of M_{TOTAL}, i.e. $M_{TOTAL} + T\varepsilon = 1$). Fault exposures and $T\varepsilon$ can then also be used to determine if there is any regional morphological asymmetry, as has been observed in other magma-poor environments (e.g. Fujiwara *et al.*, 2003; Okino *et al.*, 2004; Cannat *et al.*, 2006; Garces & Gee, 2007).

In addition to analysing seafloor fabrics outside of the axial valley, in *Section 3.4* many volcanic lineaments were identified in close proximity to the NVZ. These volcanic lineations are controlled by faults (or fissures) that form parallel with the direction of least compressive stress, and hence their orientation can be used to infer stress directions that may affect the OCC life cycle. The purpose of the following sections is thus: to examine regional asymmetries in crustal accretion based on the exposure of faulted surfaces, to quantify M_{TOTAL} – the relative contribution of magmatism to crustal accretion, and to assess potential termination mechanisms for extension on OCC-forming detachment faults. The following section also gives a brief overview of the techniques used to extract fault data from the sidescan sonar mosaic.

3.5.1. Analysis of fault patterns & morphological asymmetry

In *Section 3.3* five new oceanic core complexes were identified, giving a total of 27 OCCs in the magma-poor 13°N region. These OCCs are asymmetrically distributed both along- and across-axis, with most (20 out of 27 – 75%) seeming to cluster near the ridge axis on the SA plate and becoming relatively sparse (7 out of 27 – 25%) on the AF plate (Figure 3.3.1). Sedimentation and structural degradation of inactive OCCs as they become rafted off-axis by seafloor spreading processes most likely explains the

apparent prevalence towards younger parts of the seafloor. The across-axis asymmetry of 3:1 is reduced to approximately 2:1 if the sum of the surface areas of OCCs on each plate is calculated from Table 3.3.1, with numerous small OCCs on the SA plate being partially 'balanced out' by fewer, larger OCCs on the AF plate. Even so, these values suggest significant asymmetrical crustal accretion processes in the 13°N region, as has been suggested for other magma-poor environments (e.g. Fujiwara *et al.*, 2003; Searle *et al.*, 2003; Okino *et al.*, 2004; Cannat *et al.*, 2006).

To quantify asymmetry in fault exposures and tectonic strain each plate was divided into equal-age areas by inferring the location of anomaly 2 (1.77 – 1.95 Ma) from the magnetic data (*Section 5.3*). The survey area was further subdivided at 13°34'N (i.e. within the NTO) to give four quadrants that each extended for ~40 km along-axis (Figure 3.5.1). OCCs in the 13°N region have a wide range of shapes and sizes (surface area: $\mu = 65$ km^2, $\sigma = 38$ km^2) and so to accurately quantify asymmetry in tectonic strain it is necessary to consider all fault exposures (essentially removing the need to distinguish between large normal faults and OCC-forming detachment faults).

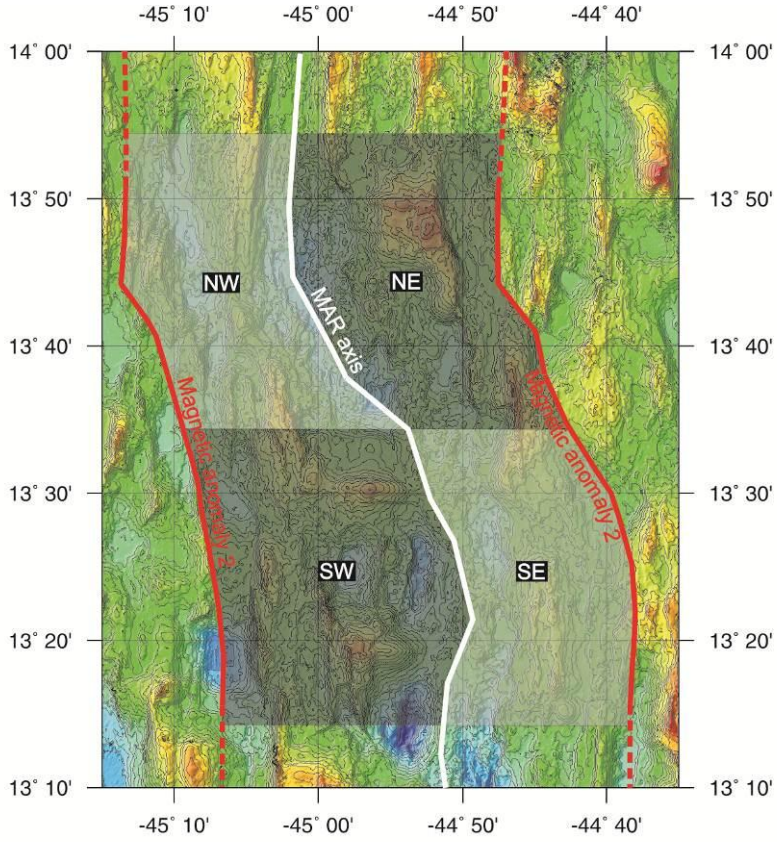


Figure 3.5.1. Division of the survey area into equal-age quadrants for analysis of tectonic patterns. Areas are based on the position of magnetic anomaly 2 (1.77 – 1.95 Ma - see *Section 5.3* for identification of this anomaly).

Faults were identified using the criteria defined in *Section 3.2.3.2* and then mapped as polygons in *ArcMap*. By specifying a projected (or 'planimetric') coordinate system for the shapefile containing the polygons, it was subsequently possible to estimate the surface area of each fault in km^2. This method differs from that which has been used in MacLeod *et al.* (2009), where fault heaves were measured directly from E-W multibeam bathymetry profiles co-registered with sidescan sonar data. The method used here is more efficient as after the geological map has been derived from the data (Figure 3.2.15a-b) the area calculation for each fault surface can be done automatically in *ArcMap*. Splitting the survey area into quadrants, rather than basing the analysis solely on faults that cross survey profiles, is also more robust than the method in MacLeod *et al.* (2009). For example, 24 E-W profiles that are spaced at ~3 km intervals will not include ridge-parallel faults smaller than this, or larger faults that are not aligned N-S (e.g. some of the faults within the axial valley opposite OCC1319 or those which flank the NTO).

Table 3.5.1 shows the summary statistics for faults within the SW-, SE-, NW- and NE-quadrants of the survey area (for the purpose of Table 3.5.1, OCCs are arbitrarily defined as faults that have a surface area of > 15 km^2).

	Symbol	Quadrant of TOBI survey area			
		Southwest	Southeast	Northwest	Northeast
Area of quadrant (km^2)	Q_a	1081.8	760.7	989.2	874.5
Faulted surface area (km^2)	F_a	337.5	79.3	143.6	205.5
E-W tectonic strain	$T\varepsilon$	31.2%	10.4%	14.5%	23.5%
Fault density (1 fault per XX km^2)	μ_d	49.2	13.3	18.3	23.0
Along-axis length of quadrant (km)	-	36.3	36.3	36.4	36.4
No. OCC (> 15 km^2)	n_{OCC}	6	0	0	1
No. inward-facing faults (< 15 km^2)	n_{in}	16	51	48	35
No. outward-facing faults	n_{out}	0	6	5	2
Average OCC area (km^2)	μ_{OCC}	48.2	N/A	N/A	147.3
St. deviation OCC area (km^2)	σ_{OCC}	33.1	N/A	N/A	N/A
Average inward fault area (km^2)	μ_{in}	2.7	1.4	2.2	1.6
St. deviation inward fault area (km^2)	σ_{in}	3.2	2.2	2.9	2.2
Average all fault areas (inc. OCC; km^2)	μ_{all}	14.7	1.4	2.7	5.4
St. deviation all fault areas (km^2)	σ_{all}	25.9	2.2	4.3	23.7

Table 3.5.1. Summary of fault statistics for each of the four, equal-age quadrants of the survey area. OCCs are defined as having surface areas that are > 15 km^2. Values are minima as they are limited by the resolution of the data and do not take into account intra-crustal deformation. All area calculations were performed with the coordinate geometry function in *ArcMap*.

The percentage of faults that are outward-facing is ~8%, which is statistically similar to that which has been measured across other slow-spreading ridge environments (e.g. < 10% on the MAR at 29°N – Escartin *et al.*, 1999). It should be noted, however, that identification of outward-facing faults was often difficult as in most cases these faults have throws similar to the resolution of the bathymetry data, causing them to have zero-relief on the final (3D) sonar mosaic. Ambiguous faults were arbitrarily classified as inward-facing, normal faults. Of the very few outward-facing faults that were identified, most group together on the outer slopes of large normal faults, forming horst-like structures (e.g. 44°44'W, 13°23'N and 45°06'W, 13°47'N – Figure 3.2.15a-b). These faults seem to predominantly lie on plates adjacent to those which exhibit OCCs, suggesting that OCC formation occurs with little-to-no extension accommodated on outward-facing faulting.

There is a distinct asymmetry in the style of faulting observed across the survey area. In the SE-quadrant, for example, tectonic strain is partitioned entirely onto numerous small faults (n_{in} = 51, μ_{in} = 1.4 km^2), where as in the SW-quadrant there are relatively few small faults (n_{in} = 16, μ_{in} = 2.7 km^2), with tectonic extension being taken up primarily on detachment surfaces (n_{occ} = 6; see Figure 3.5.2). Average fault density (μ_d – calculated as the total surface area for each quadrant divided by the number of faults in that quadrant), shows a similar asymmetric pattern, with approximately one fault occurring for every 50 km^2 of seafloor in the SW, compared with 13 km^2 in the SE.

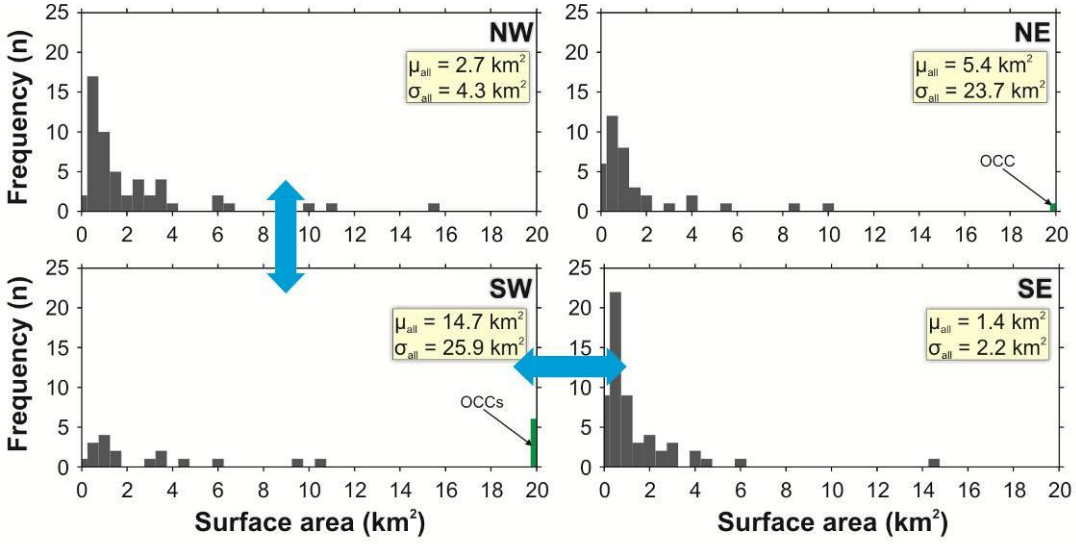


Figure 3.5.2. Frequency of fault sizes identified with the sidescan sonar for the four quadrants of the 13°N survey area (**Figure 3.5.1**). There is a distinct N-S and E-W asymmetry between the SW-NW and SW-SE pairs of quadrants, respectively (blue arrows). See text for discussion.

In terms of surface area and distribution of faulting, the NW-quadrant is statistically similar to the SE-quadrant (n_{in} = 48, μ_{in} = 2.2 km^2). Neither area displays evidence of active or inactive OCC formation and hence tectonism is partitioned entirely onto numerous inward- and few outward-facing small (~1.8 km^2) faults spaced at approximately 13-18 km^2. The NE-quadrant contains one OCC and thus exhibits a moderate number of inward-facing faults (n_{in} = 35) that have an average area of 2.2 km^2 (Figure 3.5.2).

3.5.2. Tectonic strain (Tε) & inferred component of magmatism (M_{TOTAL})

Tectonic strain (Tε) measured across the survey area is shown in Table 3.5.1 and was calculated as the ratio of the tectonically-stretched area to its original value (3.2):

$$\varepsilon = \sum (F_a + Q_a) \Big/ Q_a \qquad (\mathbf{3.2})$$

Assuming that the contribution of faults too small to be resolved with TOBI's sidescan sonar is negligible, Tε is a lower bound, as diffuse intra-crustal deformation (which does not have a quantifiable surface expression) is not taken into account. With this in mind, tectonic strain for the SW-, SE-, NW- and NE-quadrants is 31%, 10%, 15% and 24%, respectively, and hence there is a gross across-axis asymmetry of 3:1 between the SW- and SE-quadrants and 1.6:1 between the NE- and NW-quadrants. Furthermore, there is an along-axis asymmetry of 2:1 and 1.6:1 for the SW-NW and NE-SE quadrant pairs, respectively. This across-axis degree of asymmetry is similar to that which has been observed at 29°N on the MAR by Escartin *et al.* (1999), where Tε ≈ 15% for an inside-corner environment and ≈ 7% for an outside-corner environment. Note, however, that the total tectonic strain in the 13°N region (i.e. the combined strain for the SW- and SE-quadrants: ~40%) is approximately double the total strain in the 29°N region (where total Tε ≈ 20%). Escartin *et al.* (1999) suggest that increasing fault size and spacing are primarily controlled by rheological changes and secondarily by lithospheric thickness variations. Further, Behn & Ito (2008) show that fault heave and spacing increase when lithospheric thicknesses decrease. Fault patterns and asymmetry in the 13°N region may therefore be explained by the lithosphere being relatively thin beneath the SW- and NE-

quadrants compared with their conjugate quadrants, and may thus be closely related to gravity anomalies which reflect density variations in the upper lithosphere (discussed in *Section 4.3*).

As plate separation is accommodated by tectonic and magmatic processes, the complement of tectonic strain thus gives an estimate of the relative contribution of magmatic accretion at the ridge axis (Escartin *et al.*, 1999; MacLeod *et al.*, 2009). The magmatic component of crustal accretion (M_{TOTAL}), based on the identification of faulted surfaces, is therefore ~80% for the southern half of the survey area (this value is averaged across-axis; Figure 3.5.3). This value is a maximum (given that the precise contribution of diffuse tectonism is unknown) and represents a robust area of magma-starvation along ~40 km of the MAR for the last ~2 Ma (assuming that a value for M_{TOTAL} of 95% represents a 'normal' level of magmatic accretion, e.g. Buck *et al.*, 2005; Tucholke *et al.*, 2008).

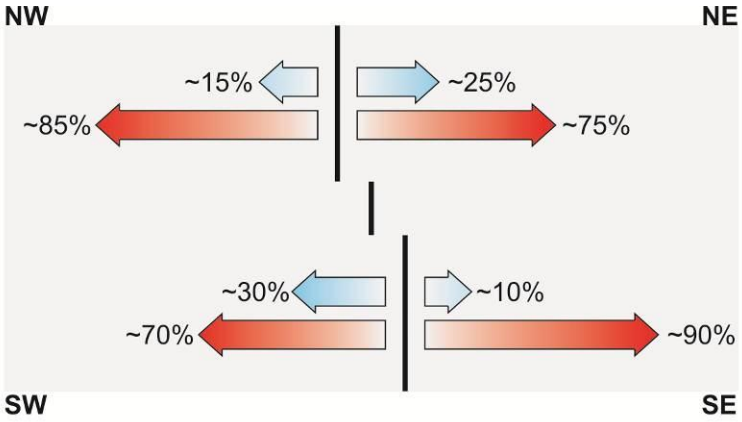


Figure 3.5.3. Tectonic strain (blue arrows) calculated from faults exposed on the TOBI sidescan sonar imagery and inferred component of magmatic extension (red arrows) for the four quadrants of the survey area. See text for discusssion.

If the area of analysis (i.e. the 'quadrant' size used in this study) was reduced, then the same analytical technique would yield greater spatial and temporal variations in M_{TOTAL}. The value of M_{TOTAL} calculated by only considering fault exposures that cross survey line 2 (13°19'N), for example, is 60% (as shown by MacLeod *et al.*, 2009 – Figure 3.5.4). It would be expected that if the length of this profile was reduced yet further that Tε would increase and the inferred value of M_{TOTAL} would become very small. However, younger tie-points from the magnetic data are difficult to resolve (*Section 5.3*), and thus it becomes increasingly difficult to estimate the location and extent of the area of

seafloor that forms conjugate to a single OCC. When coupled with the fact that the precise quantity of magmatic accretion within the footwall of each OCC is unknown, it becomes clear that it is not possible to quantify from fault patterns alone the precise magmatic conditions under which OCC formation should initiate. It is possible, however, to demonstrate that OCC formation occurs during prolonged periods of volcanic starvation and is primarily an asymmetric process.

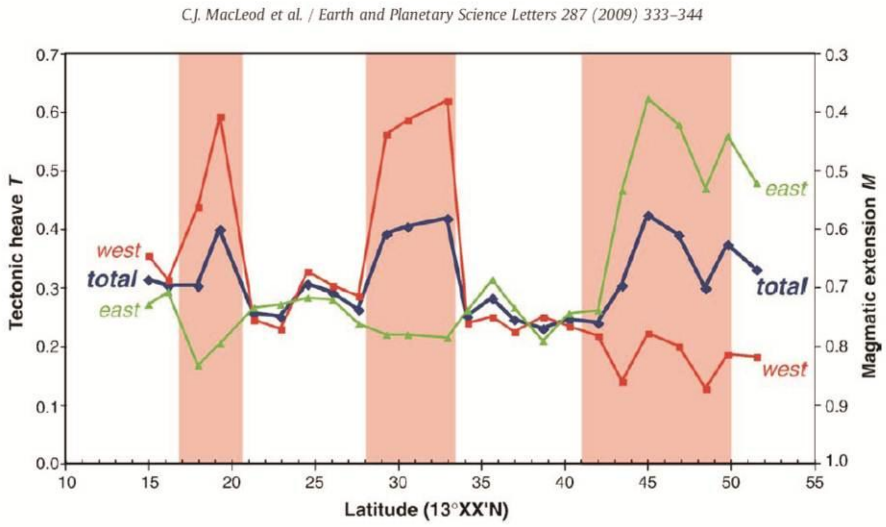


Figure 3.5.4. Components of tectonic and magmatic (inferred) extension based on single profiles of TOBI sidescan sonar imagery. The inferred components of tectonic and magmatic extension over OCCs, averaged across-axis (i.e. 'total' in diagram), are 40/60%, respectively. From MacLeod *et al.*, 2009.

3.5.3. Role of tectonism and propagating volcanism in OCC termination

In *Section 3.4.1* it was shown that numerous volcanic ridges exist within the axial valley, and that the strike of these lineaments often deviates from being aligned perpendicular to the spreading direction. Opposite near-axis OCCs, faults within the axial valley show a similar deviation from being aligned ridge-parallel (Figure 3.5.5; and also geological map – Figure 3.2.15a-b). Within the NVZs to the north (Point 1 – Figure 3.5.5) and south (Point 2 – Figure 3.5.5) of 13°19'N, lineaments identified from the sidescan sonar and bathymetry datasets gradually rotate from a spreading-direction-perpendicular N-S trend to a NE-SW and NW-SE trend, respectively, with increasing proximity to the actively forming OCC. There are still a substantial number of N-S trending

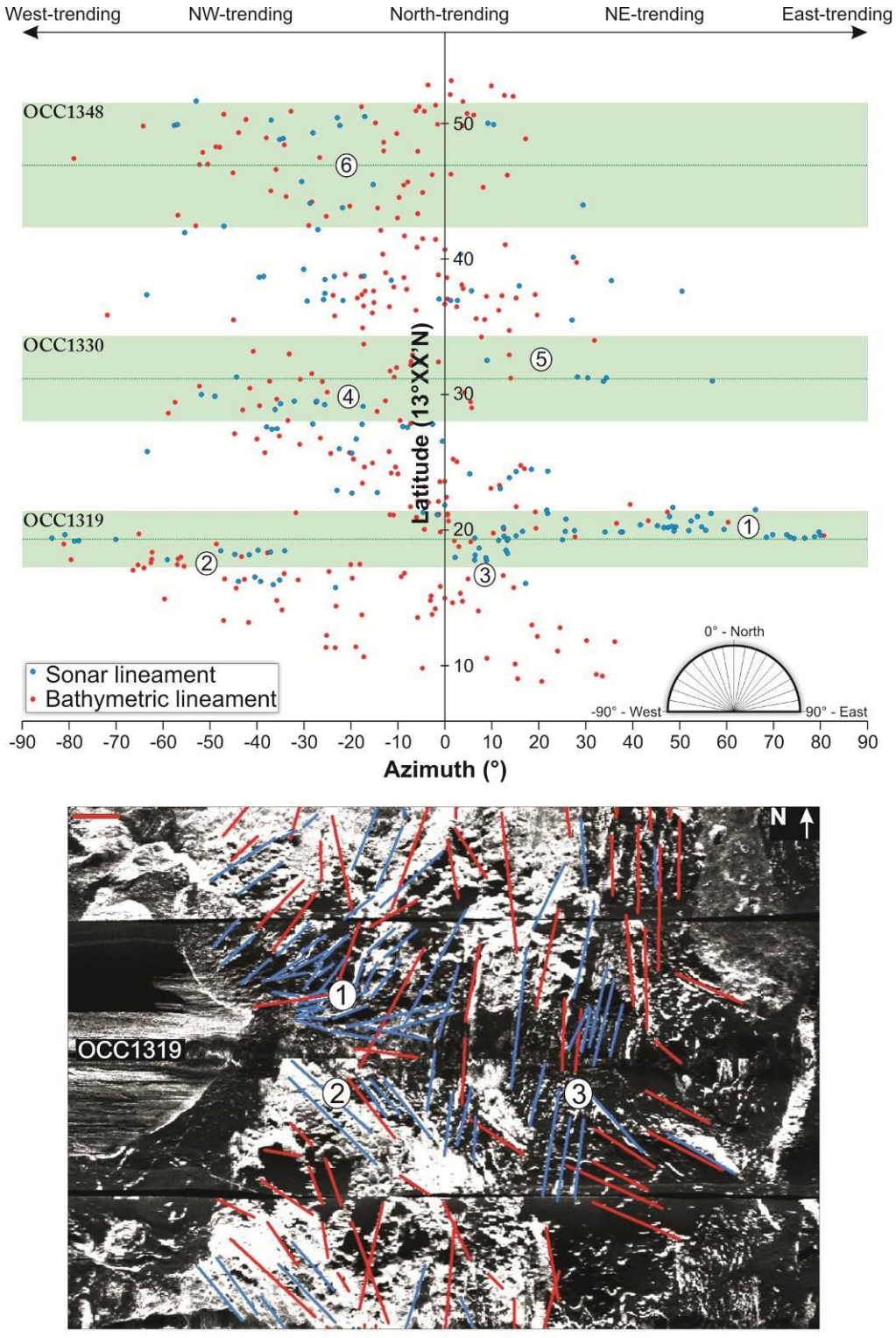


Figure 3.5.5. Azimuth of volcanic and tectonic lineaments within the axial valley plotted against latitude (upper image). Azimuths of 0° – 90° trend from NE-SW (e.g. Point 1), -90° – 0° from NW-SE (Point 2) and -10° – 10° are approximately N-S (e.g. Point 3). Green bars represent approximate latitudes of near-axis OCCs. Note the change in azimuth of lineaments between the northern and southern halves of OCC1319. Lower image shows example of lineaments in the axial valley adjacent to OCC1319, with blue lines corresponding to picks from the sidescan sonar imagery and red lines picks from the bathymetry data (red bar in upper left indicates ~1 km). Numbered points are referred to in the text.

lineaments within the axial valley opposite OCC1319, but, based on their position within low-intensity backscatter, these appear to be localised within older seafloor forming the relict major volcanic ridge on the eastern side of the axial valley, suggesting that they might pre-date the rotated lineaments (Point 3 – Figure 3.5.5).

A similar pattern of gradually rotated lineaments is observed with increasing proximity to the footwall/hanging-wall boundary of OCC1330. NW-SE trending lineaments that form to the south of the OCC are numerous and well resolved (Point 4 – Figure 3.5.5), but there are fewer NE-SW trending lineaments to the north (Point 5 – Figure 3.5.5). It would be expected that the left-stepping NTO in close proximity to OCC1330 creates NW-SE trends in fault patterns (which can be seen on the geological map – Figure 3.2.15a-b – in the area around 44°40'W, 13°32'N) and so it is possible that this partially masks any 'azimuthal anomaly' created by the nearby OCC. Note, however, that the NVZ to the north has a V-shaped tip that is directed southwards. As with OCC1319, there are numerous N-S trending faults that are situated within the older, sedimented AVR to the east of the OCC.

Adjacent to OCC1348, there is a similar asymmetry in the ratio of NW-SE to NE-SW trending lineaments within the axial valley, with rotated lineaments generally being aligned NW-SE (Point 6 – Figure 3.5.5).

MacLeod *et al.* (2009) attribute these anomalous faults and lineaments to a re-organisation of the plate boundary at the initial stage of OCC formation. In this model, a significant reduction in magmatic accretion causes an OCC to initiate on a major axial valley-wall fault (Point 1 – Figure 3.5.6), effectively transferring a 'sliver' of the SA plate to the AF plate and creating accommodation zones across the axial valley (similar to an NTO) between magmatically-robust regions to the north and south of the proto-OCC (Point 2 – Figure 3.5.6). Oblique faulting (tensional gashes) may form along the new plate boundary (Point 3 – Figure 3.5.6). The stress-free footwall/hanging-wall boundary may also initiate fault growth towards the OCC, potentially explaining faults that are nearly parallel with the spreading direction and presumably well within the AF plate (i.e. not directly on the new plate boundary, e.g. 44°47.7'W, 13°17.8'N; Figure 3.2.15b). In addition to this, if the hanging-wall becomes uplifted by the footwall (as has been documented near OCC1319: Point 5 – Figure 3.3.6b), local reorientations in the stress field may further refract faulting within the axial valley – similar to radial dikes around major terrestrial volcanoes. The volume increase associated with serpentinisation of peridotite along the detachment front and bending moments

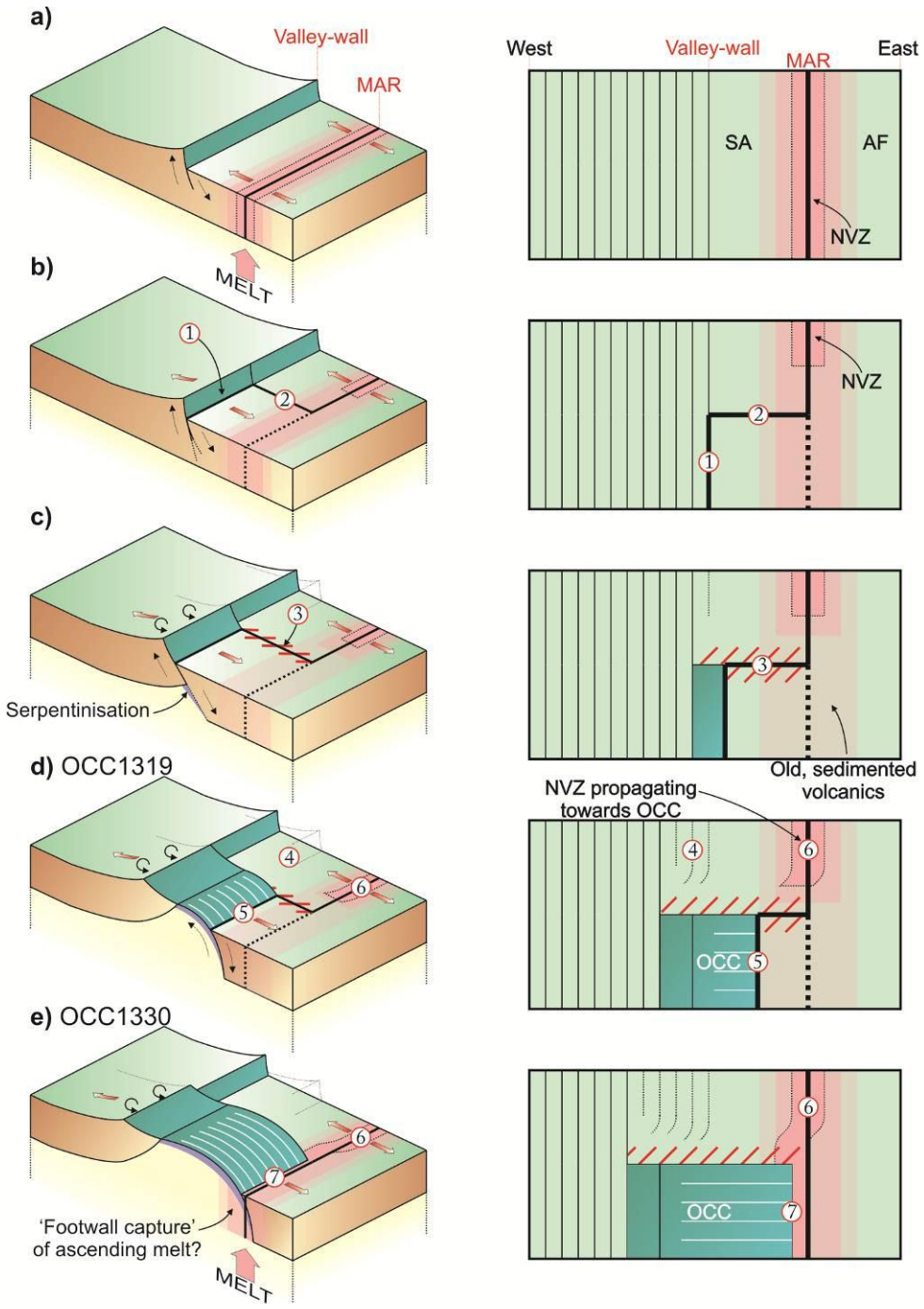


Figure 3.5.6. Seafloor lineament patterns and termination of oceanic core complexes (modified from MacLeod *et al.*, 2009): perspective view (left) and corresponding plan view (right). **a)** 'Normal' magmatic ridge environment with continuous NVZ (pink shades). **b)** Conditions for OCC formation (possibly reduced/zero melt supply at ridge axis). Plate boundary jumps to axial valley-wall fault (Point 1) creating a shear zone across the axial valley-floor (Point 2). **c)** Tensional gashes and hooked ridges that are oblique to the spreading direction form along the shear zone (Points 3 and 4, pattern is assumed to be the same south of the OCC - not shown). **d)** Assuming the OCC accommodates all of the plate separation, the footwall/hanging-wall boundary migrates eastwards with the African plate (Point 5). This is similar to the present-day plate configuration near OCC1319. **e)** The OCC is eventually terminated by NVZs that propagate laterally along-axis (Point 6), possibly due to renewed magmatism in the vicinity of the OCC, and cut through the detachment surface (Point 7). Ascending melt may be captured by the footwall at any point through **a-e)**, although it would be expected to be more likely when the OCC is mature - e.g. stages **d-e)**. See text for discussion.

associated with plate flexure may provide the required vertical force to 'warp' the hanging-wall upwards in this way.

Hooked ridges, which often form the breakaways of OCCs (e.g. Smith *et al.*, 2008), may form in a similar fashion to rotated lineaments within the axial valley. For example, at 44°55'W, 13°27'N two major faults (the innermost of which constitutes the axial valley-wall fault, which has been proposed as a site for future OCC formation by Smith *et al.*, 2006) have been rotated counter-clockwise by ~48° from trending at 011° (clockwise from north) to 323° within a few kilometres of OCC1330 (e.g. Point 4 – Figure 3.5.6 with example shown in Figure 3.5.7); this most likely occurs in response to the stress-free footwall/hanging-wall boundary associated with OCC1330.

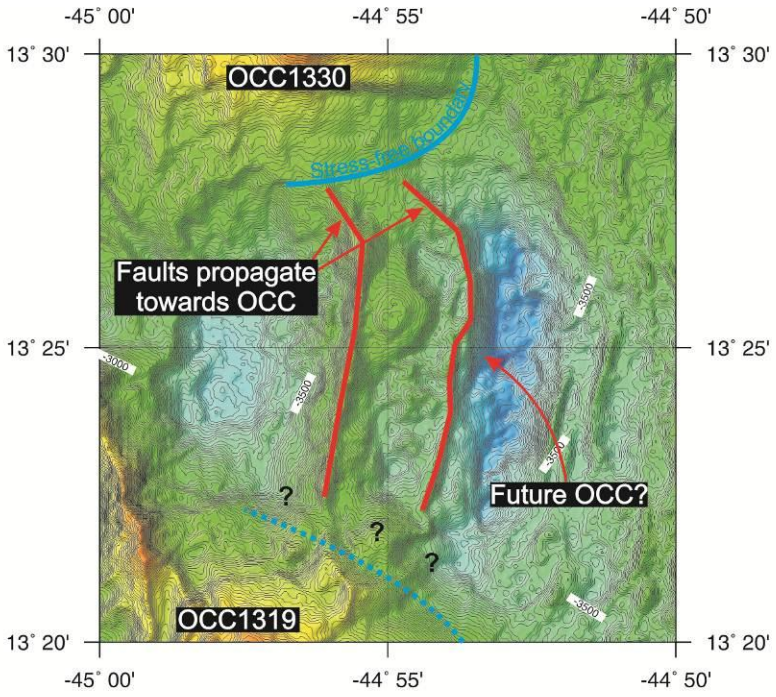


Figure 3.5.7. The axial valley wall-fault (easternmost red line) between OCC13°19'N and OCC1330 has previously been recognised as a future site for OCC formation (Smith *et al.*, 2006). This ridge, and the normal fault to the west, is hooked towards OCC1330, most likely due to the stress-free footwall/hanging-wall boundary around the OCC (blue line). A similar pattern is recorded by volcanic lineaments within the axial valley (not shown). Hooked faults may be obscured in the south by mass wasting associated with the upper massif of OCC1319. Colour scale the same as **Figure 2.2.2**. Contours are at 20 m intervals.

The subsequent termination of extension on an OCC's detachment surface is expected to be attributed to either locally waxing or waning magmatic conditions at the ridge axis. In the event of waning magmatism, it is likely that extension along a single fault cannot be maintained and the detachment is cut by a new master fault (Tucholke *et*

al., 2008). On the basis of an increase in residual mantle Bouguer anomaly across its footwall/hanging-wall, Tucholke *et al.* (2008) consider that amagmatism was responsible for terminating an OCC on the MAR at 15°45'N. This also appears to be the case on the MAR at 05°00'S, where a 'split' OCC has been rifted primarily by tectonic, rather than magmatic, processes (Reston *et al.*, 2002).

A combination of propagating volcanism and renewed melt emplacement at the ridge axis (e.g. Karson & Winters, 1992; Tucholke *et al.*, 1998; Tucholke *et al.*, 2001; MacLeod *et al.*, 2009) and/or rheological changes associated with the cooling of melt accreted within the footwall (e.g. Cannat *et al.*, 2009), are also expected to promote termination of OCCs. In the 13°N region, it appears that the recurrence of magmatic conditions at the ridge axis regulate OCC formation. For example, NVZs are currently propagating from melt-rich areas towards the zones of emergence of active OCCs, and may thus eventually form a continuous zone of volcanic activity (as is observed adjacent to OCC1348). If along-axis propagation of volcanism is the primary mode of OCC termination, then on the basis of V-shaped NVZs and rotated seafloor lineaments, this suggests that OCC1319 is currently being terminated by lateral propagation of melt from both the north and south. Asymmetry in the ratio of NW-SE and NE-SW trending lineaments may therefore indicate that OCC1330 is presently being terminated primarily by propagating melt from the south (although proximity to the NTO may obscure the true nature of melt propagation from the north). Similarly, the abundance of NW-SE trending lineaments and the scarcity of NE-SW trending lineaments within the axial valley adjacent to OCC1348 may suggest that this OCC was overwhelmed entirely by melt which propagated southward from the magmatically robust segment centre (as evidenced by the southward progression of abyssal hills near the segment centre – *Section 3.3*), with little-to-no melt coming from the south.

In addition to propagating volcanism, surficial volcanism is absent within the axial valley adjacent to active OCCs, suggesting that ascending melt may be preferentially accreting within the footwall's of active OCCs. As with the model shown in Figure 3.5.6, if the position of the footwall/hanging-wall boundary migrates eastwards with the AF plate (at a rate determined by the ratio of extension on the SA and AF plates), it may thus eventually cross the along-axis projection of the ridge axis, further increasing the likelihood that it will capture melt. Captured melt may periodically break through to the seafloor, weakening the detachment surface (MacLeod *et al.*, 2009). Any combination of renewed magmatism at the ridge axis (which may

occur due to a natural magmatic/amagmatic cycle), along-axis propagation of volcanism or a significant volume of melt becoming captured by the OCC footwall, is expected to thermally alter and weaken the lithosphere near the ridge axis and 'toe' of the OCC. Thus it becomes mechanically easier to accommodate plate separation by forming a new fault rather than by maintaining extension on the OCC's detachment fault, which subsequently becomes disseminated by faults and rafted off-axis by conventional seafloor-spreading processes (Points 6 and 7 – Figure 3.5.6). These factors are discussed in more detail in *Section 6.3.2*, where they are combined with observations that relate to OCC termination from gravity and magnetic data.

3.6. Chapter summary

TOBI sidescan sonar data have been fully integrated with bathymetric data and seafloor sampling results. This information has been used to map the major structural and lithological features exposed on the seafloor (Figure 3.2.15a-b). This map has been used to show that:

Regional melt supply & morphological asymmetry

- Magmatism is variable at the segment-scale. Magmatic abyssal hill terrain appears to wander along-axis at rates of ~15 – 20 km/My, and may occur in isolated exposures that are asymmetric across-axis (*Section 3.3*).

- Based on fault exposures, the average inferred component of magmatic accretion (M_{TOTAL}) has been ~80% for a 40 km section of the ridge axis along which 6 major OCCs have formed over the last ~2 My (*Section 3.5.2*). Shorter-scale, higher amplitude variations in M_{TOTAL} are expected to occur. Estimates of M_{TOTAL} vary across the survey area and thus indicate that crustal accretion is an asymmetric process in the 13°N region.

Local melt supply & OCC formation

- About the Marathon FZ, decreasing magmatism, as evidenced by the shortening of abyssal hills between 3.2 – 6.5 Ma, appears to have resulted in the formation of a large OCC (‘Marathon OCC’; *Section 3.3.1.2*). This may suggest a magmatic/amagmatic cycle with a period of ~3 My.

- On the basis of the distribution of OCCs in the 13°N region and their proximity to a zone of abyssal hills which is oblique to the spreading direction, it is plausible that OCC formation occurs around the edges of migrating zones of localised melt emplacement (*Section 3.3.1.1*). Waxing and waning of magmatism at the ridge axis due to the along-axis migration of melt may thus regulate OCC formation (which is discussed in more detail in the following chapters).

- Hummocky volcanic ridges and lineaments have a wide range of sizes and backscatter intensities. This suggests that local melt emplacement may wander across-axis for distances of up to ~6 km over time-scales of ~0.50 My (*Section 3.4.1*). The average duration of OCCs in the 13°N region is 0.44 My, and thus local wandering of melt emplacement and OCC formation may be closely linked.

Renewed melt emplacement & OCC termination

- Volcanism is absent adjacent to active OCCs, suggesting that either local magmatic supply is approximately zero or that magmatic accretion occurs mainly in the footwall of OCCs. The age of the volcanic 'hiatus' suggests that volcanism and magmatic accretion may have been synchronous with the early stages of OCC formation in this region, and 'switched-off' later in the OCC life cycle. Older OCCs, which are associated with progressively more cross-cutting, ridge-parallel faulting, are adjacent to widespread, robust neovolcanism within the axial valley (*Section 3.4.2*). Thus, it appears that OCCs are terminated by renewed melt emplacement and magmatic accretion at the ridge axis. This causes new faults to form within thermally-weakened lithosphere that bisect the main detachment surface. Renewed magmatism as a mechanism for OCC termination is also evident in the bathymetry data, with the Marathon OCC and OCC1356 being bounded on their younger sides by abyssal hill terrain. It should be noted, however, that numerous inactive OCCs occur without abyssal hill terrain coinciding with their terminations.

- Avolcanism, expressed as gaps in the NVZ opposite active OCC formation, does not necessitate amagmatism, as subsurface detachment faults may control melt emplacement pathways at depth and hence the surficial expression of volcanism (*Section 3.4.2*).

Sidescan sonar and bathymetry data give a surficial representation of OCC structure and magmatic conditions in the 13°N region. In the following chapter I use gravity data to assess the internal structure of OCCs and infer the deep structure of the lithosphere.

Chapter Four

Lithospheric structure from gravity anomalies

4.1. Introduction

In the previous chapter, I have used sidescan sonar data to assess the regional seafloor morphology and examine the close relationship between OCC formation and neovolcanism. The data revealed significant regional-scale, morphological asymmetry and evidence for highly variable melt supply to the ridge axis in the presence of OCCs. Following on from these findings, in this chapter I use gravity data to assess subsurface mass distribution in the 13°N region, providing: regional crustal thickness and composition estimates, further insights into the nature and variability of melt supplied to the ridge axis, and constraints on the composition and structure of oceanic core complexes.

Prior to modelling of the gravity data, the Bouguer correction must be applied to the free-air anomaly in order to remove the predictable effects of the seafloor and Moho interfaces, obtaining the mantle Bouguer anomaly (MBA). Predicting the gravitational response due to cooling of the lithosphere then allows for the residual mantle Bouguer anomaly (RMBA) to be derived and modelled. The theory and application of these methods form the basis of the first part of this chapter.

4.2. Interpretative methods – gravity data

4.2.1. Mantle Bouguer anomaly (MBA)

To isolate the MBA, the crust can be modelled as a series of interfaces that partition major lithological changes, the individual, gravitational attraction of which may be added together to give the Bouguer correction (or total crustal attraction). The residual between observed anomaly (i.e. the FAA) and predicted total crustal attraction can

therefore be interpreted as the deviation between the actual sub-surface mass distribution and that which has been assumed in the starting model.

To calculate the gravitational attraction of an uneven crustal layer, Parker (1972) uses a Fourier transform-based method; decomposition of the source into its constituent wavenumber components allows for rapid computation of anomalies generated by complex source bodies (compared with other, more cumbersome methods, e.g. Talwani & Ewing, 1960). The method assumes that the point of field observation is made on a level plane which lies everywhere above a slab of material that is bounded by an irregular upper interface and horizontal lower interface. The plane of observation is defined as $z = z_0$, relative to the upper and lower interfaces of the layer in question, which are defined as $z = h(\vec{r})$ and $z = 0$, respectively (where $\vec{r}$ represents the projection of a Cartesian [x, y, z] vector onto the x-y plane and z is positive upwards). In this scenario, the gravitational potential, U, at position r_o can be defined in a simplified form over the whole x-y domain (indicated by dS) as (4.1):

$$U(r_0) = G\rho \int_D dS \int_0^{h(r)} \frac{dz}{|r_0 - r|} \qquad (\mathbf{4.1})$$

Where G is the gravitational constant and ρ is density. Taking the Fourier transform of (4.1) and expressing one of the resultant exponential terms as a Taylor series, then yields (4.2):

$$f[U] = 2\pi G\rho \exp\left(-|\vec{k}|z_0\right) \sum_{n=1}^{\infty} \frac{|\vec{k}|^{n-2}}{n!} f\left[h^n(\vec{r})\right] \qquad (\mathbf{4.2})$$

Where $\vec{k}$ is the wavenumber and f [] is the Fourier transform (Parker, 1972). The practical application of (4.2) to gravity studies (e.g. for the purpose of applying the Bouguer correction) requires that the vertical gravitational attraction is known, not the potential. Given that above the topography the rate of change of the gradient of potential is zero (that is, $\nabla^2 U = 0$), and by defining vertical gravitational attraction as the partial differential of potential with depth ($\Delta g = +\partial U/\partial z$), (4.2) can be expressed as (4.3):

$$f[\Delta g] = -2\pi G \exp\left(-|\vec{k}|z_0\right)\sum_{n=1}^{\infty}\frac{|\vec{k}|^{n-1}}{n!} f\left[\rho(\vec{r})\{h^n(\vec{r}) - g^n(\vec{r})\}\right]$$

(**4.3**)

In its generalised form, (4.3) has been expanded to include the attraction of an uneven lower interface ($z = g(\vec{r})$), and may be expanded further in the same fashion so as to include the attraction of multiple layers (Parker, 1972). In the following section I will discuss the practical implementation of (4.3).

4.2.2. MBA method & total crustal attraction

The Bouguer correction was obtained by calculating the inverse transform of (4.3) using '`grav2`' (Kuo & Forsyth, 1989). This method relies on a Fast Fourier Transform (FFT) and hence the input model/interface must be specified as an array of equally spaced points where *nx* and *ny* are each a power of 2 (e.g. 512, 1024). A suitable input file was obtained by sub-sampling the integrated bathymetry dataset using GMT's `grdsample` command; the region argument (-R) was carefully modified to sample a grid that was centred over the survey area and had exactly 1024 points in both the x and y directions (so as to extend well beyond the limits of gravity data acquisition). This .grd file was converted into ASCII format using `grd2xyz`, before having the z-values isolated and inverted (as `grav2` requires that depths are positive). The x and y coordinates of the grid were saved in a separate file so that they could eventually be pasted back together with the output from `grav2`, allowing for geographic re-gridding of the predicted anomaly. As an option, during the FFT `grav2` allows for the input array to be mirrored about the x and y planes, essentially quadrupling the amount of data. This minimises the artificial edge effect which arises due to the assumption of periodicity in the FFT process, which, combined with sampling the bathymetry over an area much larger than the limits of gravity data acquisition, vastly reduces the possibility of misinterpretation of edge effects.

The number of terms used for the Taylor series expansion in (4.3) must also be taken into consideration. It is recommended that four to five terms should be absolutely sufficient for convergence of the FFT (Parker, 1972; Kuo & Forsyth, 1989). To test this, a trial was conducted using an arbitrary 1024 by 1024 depth interface. The predicted anomaly was calculated using 1 to 7 terms in the Taylor series expansion, with the

density contrast remaining constant during each run. For each term in the Taylor power series, the root mean square (RMS) value of the output (in mGal) was calculated (Figure 4.2.1). It was found that between 3 and 6 terms, the RMS variation for each additional term was < 0.1 mGal. RMS variation was greatest between 1 and 2 terms, indicating that the series of Fourier transforms does not reach convergence with < 3 terms in the Taylor series. Including 7 terms repeatedly caused the output to contain non-amplitude nodes (NaNs), which may occur due to a conflict between the specified precision of the output and division by very small numbers (D. Blackman, *personal comm.*). Thus, five terms have been used for robustness in the Taylor power series expansion throughout the remainder of this study.

The `grav2` method allows for a complete crustal model of multiple interfaces to be calculated. This model is defined by simply applying a constant offset to the seafloor/bathymetry data, meaning that sub-seafloor interfaces are assumed to be parallel and layers have a constant thickness.

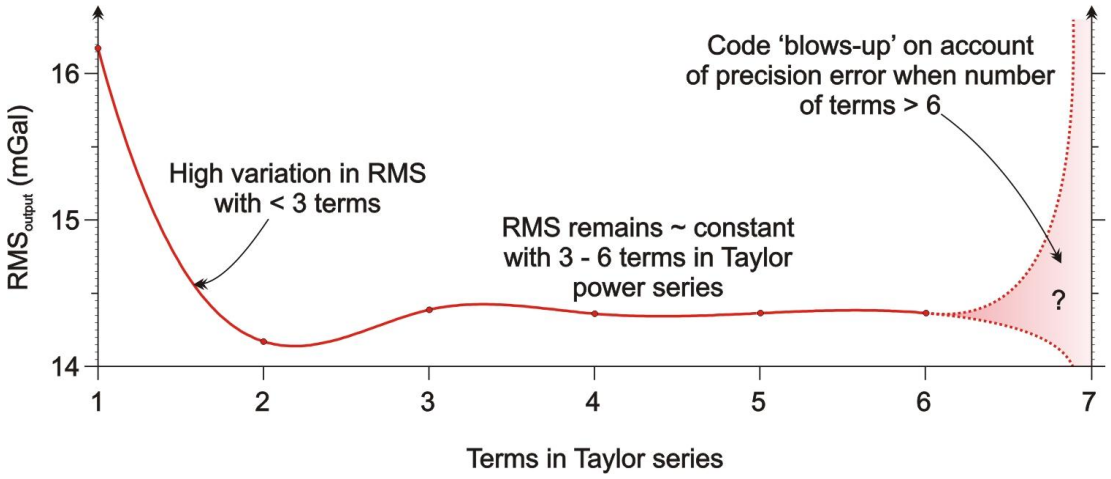


Figure 4.2.1. Variation in output RMS (mGal) with increasing terms in the Taylor power series expansion of equation (**4.3**). Five terms were used throughout this study, as the code appears to be relatively robust over the range of terms 3-6.

For the purpose of this study, two starting models are assumed. MBA1 has a constant 6 km thick crust with a density of 2700 kg/m^3 – this represents a standard model that has been used in numerous marine gravity studies (Figure 4.2.2a, with modelling parameters in Table 4.2.1) (e.g. Lin *et al.*, 1990; Tolstoy *et al.*, 1993; Detrick

et al., 1995; Tucholke *et al.*, 1997; Searle *et al.*, 2003). MBA2 has an additional intra-crustal density interface at a depth of 1.5 km that partitions lower density, upper crust (analogous to fractured, basaltic material: $\rho_{uppercrust}$ = 2700 kg/m^3) and higher density, lower crust (analogous to gabbro: $\rho_{lowercrust}$ = 2900 kg/m^3; Figure 4.2.2b). In both cases, the density of seawater and the mantle are assumed to be 1030 kg/m^3 and 3300 kg/m^3, respectively. In previous studies, the effect of an intra-crustal interface has been shown to be negligible (e.g. Blackman & Forsyth, 1991), with its minor contribution being balanced out by having a slightly lower density contrast at the Moho in a stratified model (e.g. MBA1 $\Delta\rho_{moho}$ = 600 kg/m^3, MBA2 $\Delta\rho_{moho}$ = 400 kg/m^3). This intra-crustal interface forms the basis of the forward modelling of the gravity data (*Section 4.4*) and hence it is used here during formulation of the MBA.

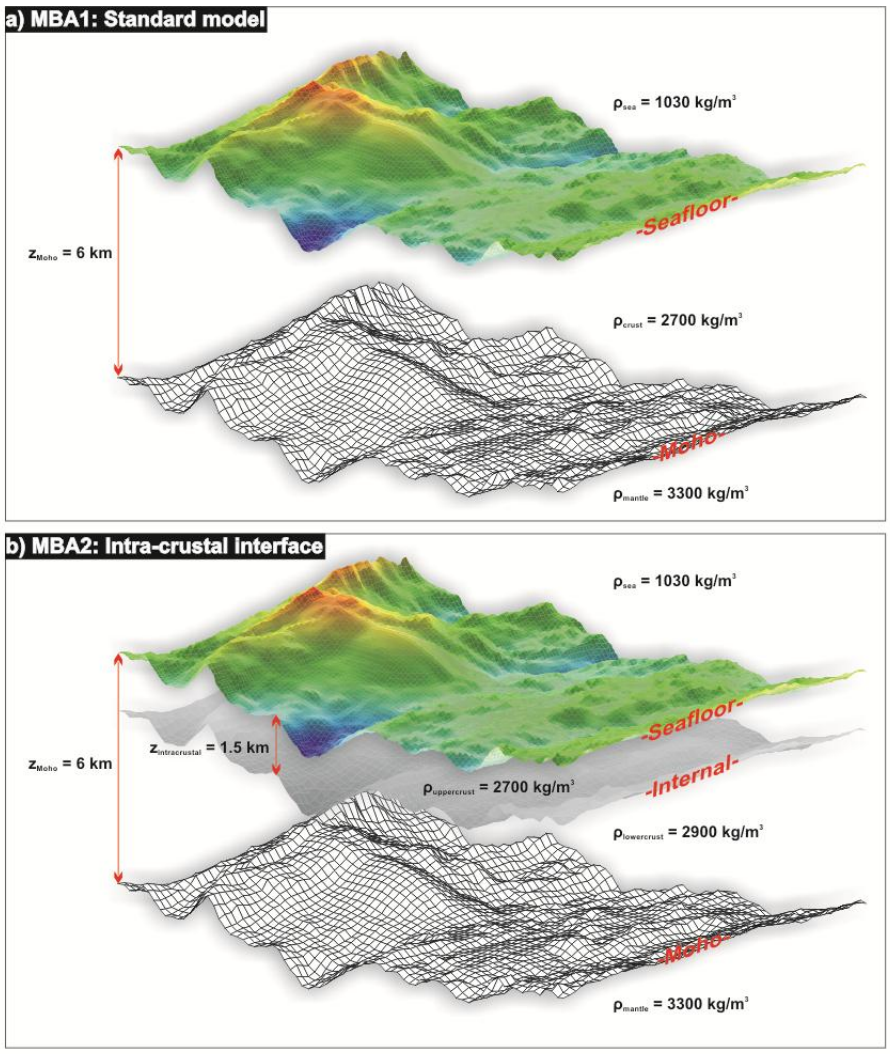


Figure 4.2.2a-b. Mantle Bouguer anomaly crustal models. **a) MBA1** has a constant thickness (6 km), constant density (2700 kg/m^3) crust. **b) MBA2** assumes the crust is stratified at a depth of 1.5 km between upper crustal material (2700 kg/m^3) and lower crustal material (2900 kg/m^3).

		Parameter	Value
General	Model resolution for predicted anomalies	-	90 x 90 m
	Interface grid size for predicted anomalies	-	1024 x 1024
	Half-spreading rate	-	13 km/my[1]
	Gravitational constant	-	6.67×10^{-11} $N.m^2.kg^{-2}$
	Gravitational acceleration	-	9.80 m^2/s
Thermal	Thermal model grid size	-	256 x 256 nodes
	Coefficient of thermal expansion	-	3.4×10^{-5}/°C
	Thermal boundary layer thickness	-	100 km
	Asthenospheric temperature	-	1350°C
Model layer densities (ρ)	Seawater	ρ_{sea}	1030 kg/m^3
	Average crust	ρ_{crust}	2700 kg/m^3
	Mantle	ρ_{mantle}	3300 kg/m^3
	Upper crust	$\rho_{uppercrust}$	2700 kg/m^3
	Lower crust	$\rho_{lowercrust}$	2900 kg/m^3
Model interface depths (z)	Upper/lower crust	$z_{intracrustal}$	1.5 km
	Lower crust/mantle	z_{moho}	6.0 km

Table 4.2.1. Summary of gravity modelling parameters (including layer densities and thicknesses) used for formulation of the MBA and RMBA. Density and thickness values may be varied during the modelling phase.

Figure 4.2.3a-c shows the predicted gravitational response for each of the interfaces shown in Figure 4.2.2b and the total crustal attraction for MBA model 2 (Figure 4.2.3d; see also FAA – Figure 2.5.3a). The predicted anomaly for each interface is based on a 1024 by 1024 (90 by 90 metre) bathymetry grid.

The seafloor interface is calculated for a seawater/seafloor density contrast of 1670 kg/m^3; this is equivalent to a seawater density of 1030 kg/m^3 and average upper crustal density of 2700 kg/m^3 (which represents basaltic material; Figure 4.2.3a). The seafloor anomaly contains a large amount of relatively short wavelength information and has a peak-to-peak amplitude range of ~70 mGal; it is therefore comparable to the FAA which has a range of ~80 mGal. In contrast, the predicted anomaly for an intra-crustal interface at a depth of 1.5 km with a density contrast of 200 kg/m^3 (equivalent to an upper crust of density 2700 kg/m^3 overlying lower crust that has a density of 2900 kg/m^3 – i.e. gabbroic material) contains much less detail (Figure 4.2.3b). Only long wavelength anomalies are resolved at this depth, i.e. the axial valley and off-axis topographic highs such as OCCs. The peak-to-peak amplitude range of the intra-crustal anomaly is ~6 mGal. In comparison, due to its depth of 6 km, the Moho anomaly (Figure 4.2.3c) contains the least short wavelength information (compare, for example, the predicted intra-crustal and Moho anomalies across OCC1330 – Figure 4.2.3b-c).

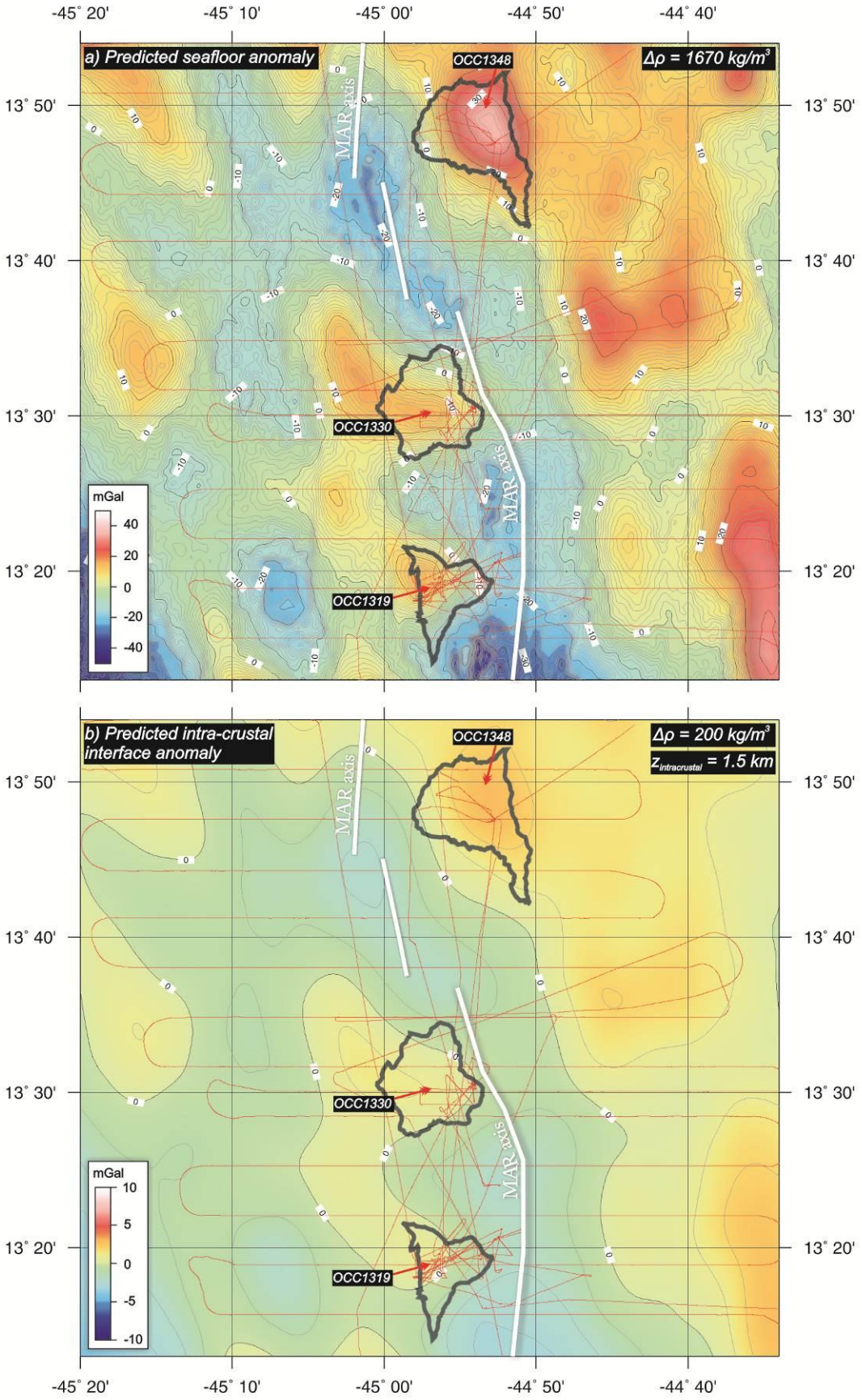


Figure 4.2.3a-b. Predicted gravitational attraction of **a)** seafloor and **b)** intra-crustal interface. Red line is the ship's track, black outlines show near-axis OCC locations. Contours are at 1 mGal intervals. See text for discussion.

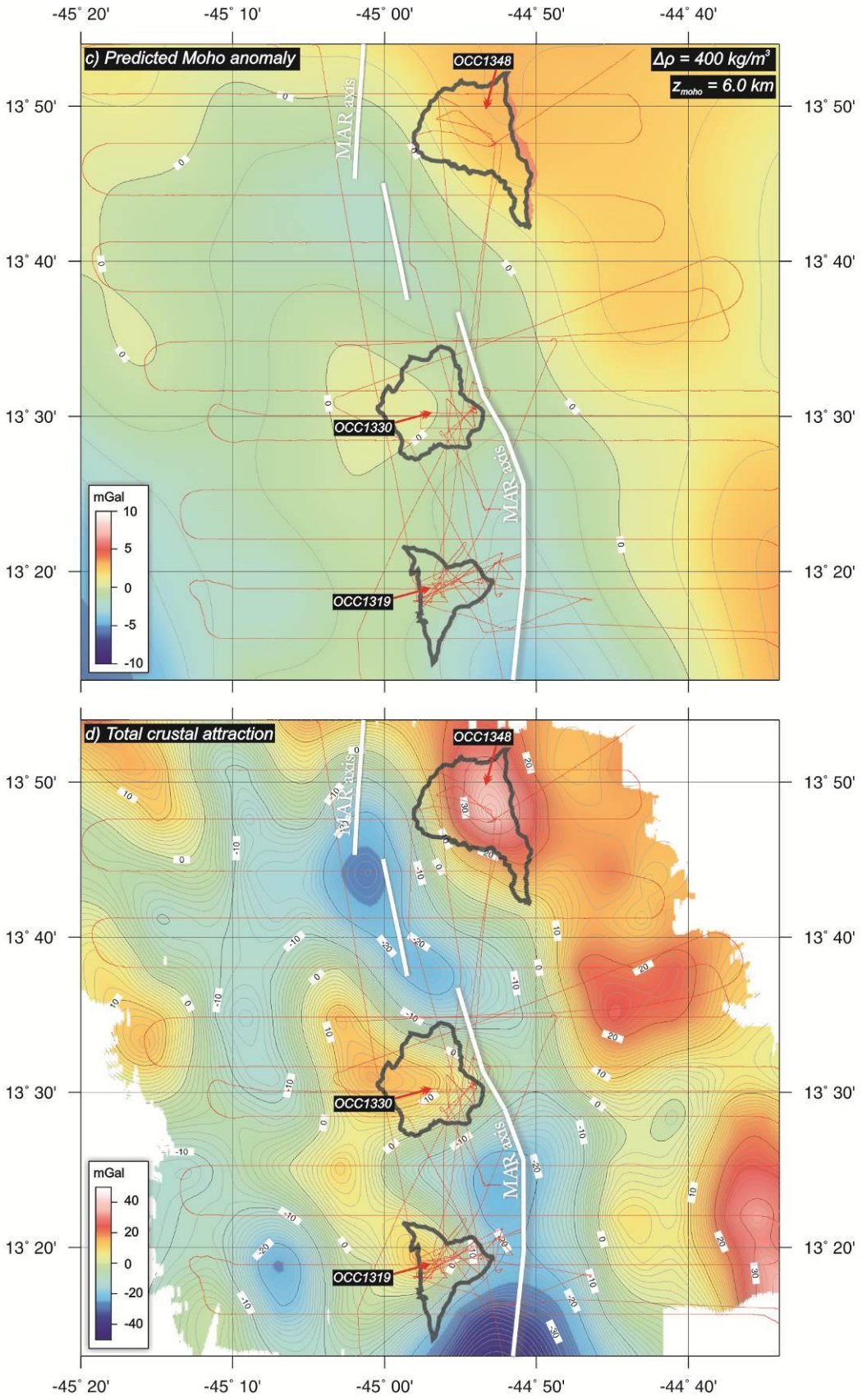


Figure 4.2.3c-d. Predicted gravitational attraction of **c)** Moho interface and **d)** total crustal attraction. Model interface anomalies (**a-c**) are sampled along-track and added together to give the total crustal attraction, which has been masked where there are no gravity data points. Red line is the ship's track, black outlines show near-axis OCC locations. Contours are at 1 mGal intervals. See text for discussion.

The Moho anomaly is calculated for a density contrast of 400 kg/m^3 (lower crust overlying mantle peridotite with a density of 3300 kg/m^3), however, and thus has an amplitude range slightly larger than the intra-crustal interface (peak-to-peak: ~7 mGal). In summary: Within the range of depths and densities examined, interface depth controls the frequency content, and density contrast across the interface controls the amplitude of the anomaly.

It was found that varying the density contrast across the seafloor interface from 1470 – 1870 kg/m^3 (i.e. an upper crustal density range of 2500 – 2900 kg/m^3) could account for an additional ~5 mGal in the predicted anomaly. For example, when the assumed density of the upper crust is reduced by 200 kg/m^3 to 2500 kg/m^3, the predicted anomaly has a peak-to-peak range of ~65 mGal (i.e. the peaks and troughs are reduced in magnitude by ~2.5 mGal). Similarly, varying the depth to the Moho interface (i.e. the assumed crustal thickness) from 4 – 7 km alters the predicted anomaly by ~1.5 mGal. Thus it may be expected that realistic modification of the starting crustal model can account for approximately several mGal of the residual MBA (discussed in *Section 4.2.3*). Note, however, that gravity anomalies are interpreted relative to the assumed starting crustal model, and therefore the selection of density contrasts and depths at this stage is arbitrary.

4.2.3. MBA results

The mantle Bouguer anomaly (Figure 4.2.4a-b) is calculated by subtracting the predicted anomaly of each interface for models MBA1 and MBA2 from the FAA (Figure 2.5.3a). Predicted anomalies were subtracted along-track using GMT's `grdtrack` command (Wessel & Smith, 1998); this mitigates the possibility of accumulating errors introduced by gridding the data (i.e. in areas of low data coverage away from the ship's track; Kuo & Forsyth, 1989). There is very little difference between the two sets of results; MBA1 has an RMS value of 10.3 mGal and MBA2 has an RMS value of 10.2 mGal. This is consistent with previous studies with, for example, Prince & Forsyth (1988) and Blackman & Forsyth (1991) finding the difference between a constant density and layered density crustal model to be < 1 mGal.

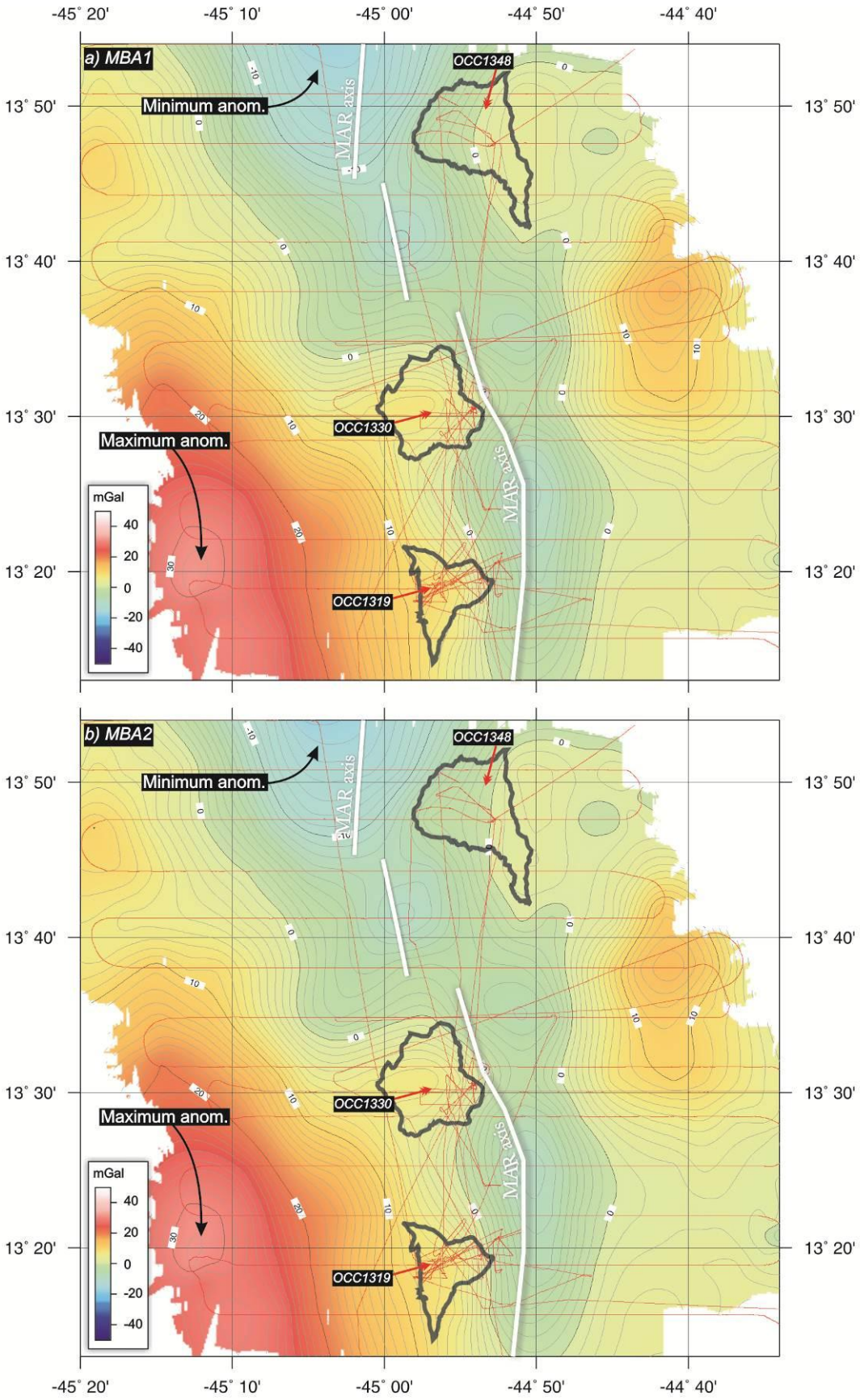


Figure 4.2.4a-b. Mantle Bouguer anomalies: **a) MBA1** and **b) MBA2** (see **Figure 4.2.2.** for crustal model). Red line is the ship's track, black outlines show near-axis OCC locations. Contours are at 1 mGal intervals. See text for discussion.

For both MBA1 and MBA2, the maximum positive anomaly is 31 mGal and is located near the beginning of survey line 2 at 45°12'W, 13°19'N. This point is situated within seafloor that displays multiple, off-axis OCCs (*Section 3.3.1*). The most negative anomaly is -16 mGal, centred slightly to the west of the ridge axis in the most northerly part of the survey area at 45°03'W, 13°52'N, in close proximity to the magmatically robust segment centre. The main long wavelength component of the MBA is a ridge-centred low that grades into higher values off-axis. This is a ubiquitous feature of the MBA along slow-spreading ridge segments and primarily shows that as the crust gets older it cools, contracts, and becomes denser. A monotonic decreasing temperature with increasing age relationship cannot, however, account for all the features that are present within the MBA. For example, there is a high degree of asymmetry about the ridge axis south of the NTO at 13°38'N, with anomalies on the SA plate consistently higher than anomalies on the conjugate AF plate. In addition to this, each of the three main near-axis core complexes appears to be associated with a slight increase in MBA of a few mGal in relation to the local background anomaly. There is also an isolated positive anomaly that has amplitude of several mGal located at 44°42'W, 13°38'N (Figure 4.2.4a-b). These observations are discussed in a wider context later in this chapter.

4.2.4. Residual mantle Bouguer anomaly (RMBA)

A thermal anomaly arises due to dissipation of heat energy from upwelling asthenospheric material, which, in the previous section, was shown to manifest itself as a long wavelength, temporal anomaly that dominates the MBA. In order to isolate the residual mantle Bouguer anomaly (RMBA), which contains short wavelength density anomalies that relate to lithological and structural variations, it is first necessary to predict the thermal structure of the ridge.

Forsyth & Wilson (1984) predict the gravitational response of conductively driven temperature variations at a ridge-transform-ridge (RTR) environment. This model is based on passive upwelling driven solely by plate separation; it does not, for example, consider buoyancy-driven upwelling. The method assumes boundary conditions for a finite plate whose upper (z = 0 km) and lower (z = 100 km) conditions are 0°C and 1350°C, respectively (Figure 4.2.5).

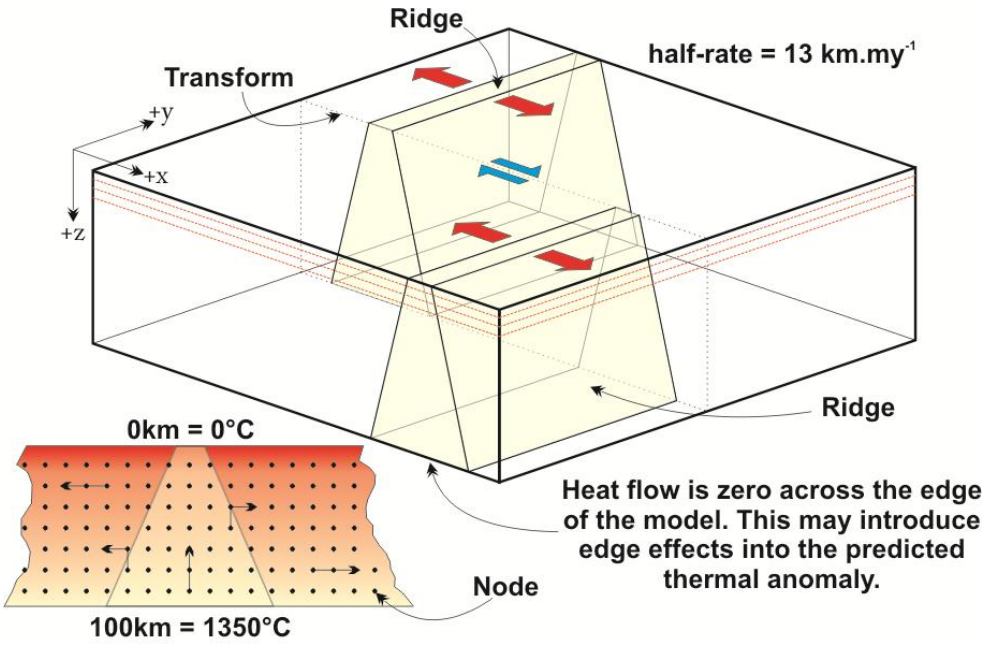


Figure 4.2.5. Three dimensional temperature structure of a ridge-transform-ridge system, with boundary conditions of T=0°C at z=0 km and T=1350°C at z=100 km. Advection of heat is assumed to be vertical within the triangular region and horizontally away from the ridge everywhere else (modified from Forsyth & Wilson 1984).

Vertically upwelling material is confined to a triangular region beneath the ridge, with its volume matching that of the material transported horizontally beneath the plates and away from the axis (thus the width of the triangle is determined by the spreading rate). At the RTR intersection, material is cooled by the juxtaposition of old, cold lithosphere with young, warm, upwelling material. The precise rate by which this material is cooled is governed by the length of time in which the two mediums are in contact (i.e. the ascent rate of the warmer material). A thermal model is derived numerically by first representing the RTR model as a grid of nodes and calculating the heat transfer by advection. Advection is assumed to be along prescribed flow-lines and is a function of spreading rate and the length of the time step represented (Forsyth & Wilson, 1984). Following the advective transfer of heat, conductively driven cooling of material is then calculated using an FFT algorithm over the same time period. During the conductive stage it is necessary to satisfy the transient heat flow equation (4.4):

$$\nabla^2 T = \frac{1}{k} \cdot \frac{\partial T}{\partial t} \qquad \textbf{(4.4)}$$

Where k is the thermal diffusivity constant and T is the temperature at a given node in Figure 4.2.5, which is a function of time, t, and the spatial coordinates x, y and z.

4.2.5. RMBA method

A thermal model that satisfies (4.4) was calculated using '`rtrflow`' and '`upwsor`', and its gravitational effect calculated using '`pratt`' (Forsyth & Wilson, 1984). Material flow in the asthenosphere, induced by the motion of the overlying lithospheric plates, is calculated by defining the ridge position by a series of orthogonal offsets, requiring that the true ridge position is simplified by approximation of curvilinear features to a series of stepped, parallel segments. This input model is used as the basis for `rtrflow`. The dimensions of the model must be a power of 2 in the x and y directions in order to satisfy the FFT algorithm. The extent of gravity data collected throughout JC07 was approximately 70 km by 72 km, and hence a model was created centred about the survey area that was 256 km in both the x and y directions. Extending the model by this amount, in addition to folding the data in the x and y direction, vastly minimises artificial edge effects that may be introduced as `rtrflow` assigns zero heat flow boundary conditions along model edges parallel with the transform (Forsyth & Wilson, 1984). Flow rates are normalised about their mean value so as to represent deviations from an 'infinite ridge model'.

The output from `rtrflow` (flow velocity in the asthenosphere) is then converted into advective and conductive steady-state temperature variations using `upwsor`. Output from `upwsor` was combined with the lat/lon pairs of a bathymetry grid over the same area to allow gridding of the temperature variation induced by the ridge. (Note that GMT lists grid points from NW to SE, where as the ridge model must be defined relative to an origin that is at the SW corner of the model. Therefore it was necessary to sort the latitude and longitude pairs so that they were arranged from SW to NE in order to prevent the gridded anomalies from being a mirror image of the ridge model.) Figure 4.2.6 shows three horizontal slices through the calculated thermal model at depths of: 6 km, 12.5 km and 20 km. The average temperature at a depth of 6 km is approximately 600 – 700°C at the ridge axis. This decreases with increasing age, and increases with depth towards the 1350°C boundary condition at the base of the model (100 km).

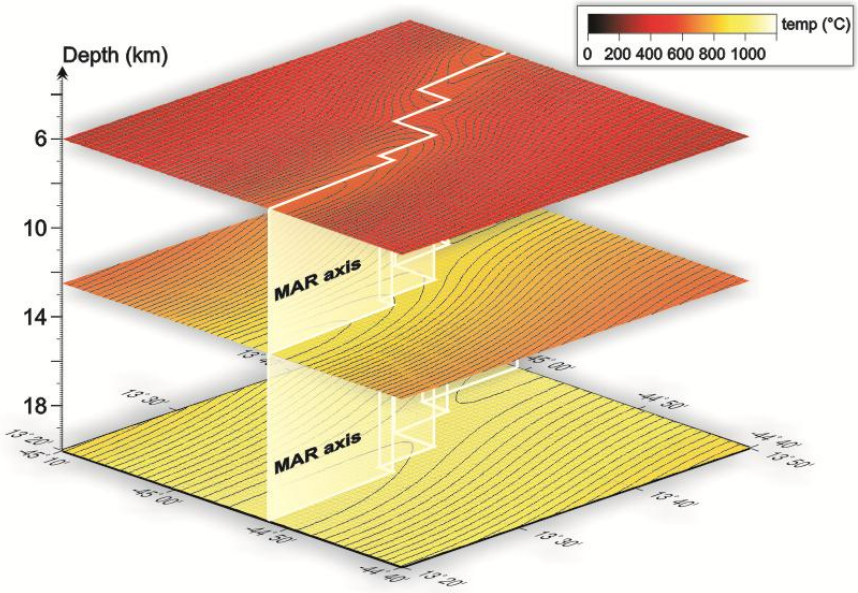


Figure 4.2.6. Horizontal slices through the output of `upwsor` at depths of 6 km, 12.5 km and 20 km. Colour scale is same the same for each plot, with contours at 10°C intervals. Heavy white line denotes model ridge position used in the thermal calculations.

The `pratt` program is then used to transform temperature into density variation by multiplication with the thermal expansion coefficient of 3.4 $x10^{-5}$ $°C^{-1}$ and finally calculates the resultant gravity. Figure 4.2.7a-b shows two thermo-gravitational anomalies: Thermal model 1, which is a coarse model with the NTO at 13°38'N approximated by one offset (Figure 4.2.7a), and thermal model 2, which is a detailed model of the ridge position with the NTO modelled with three offsets (Figure 4.2.7b). Each model has an amplitude range of ~20 mGal, from -14 mGal at the ridge axis to 6 mGal at the edge of the model. The main difference is the increased cooling effect when the NTO is approximated with a single 20 km offset, causing the area about 44°57'W, 13°38'N to have an amplitude of -6 mGal, as opposed to three gradual steps of 4 km, 10 km and 6 km which cause the same area to have a thermal anomaly of -8 mGal. Changing the spreading rate made little difference to the thermal anomaly. For the purpose of calculating the RMBA, the thermal model with one ridge-offset (Figure 4.2.7a) has been used as this matches the position of the along-axis low in the MBA (Figure 4.2.4a-b) more precisely than if three offsets are modelled.

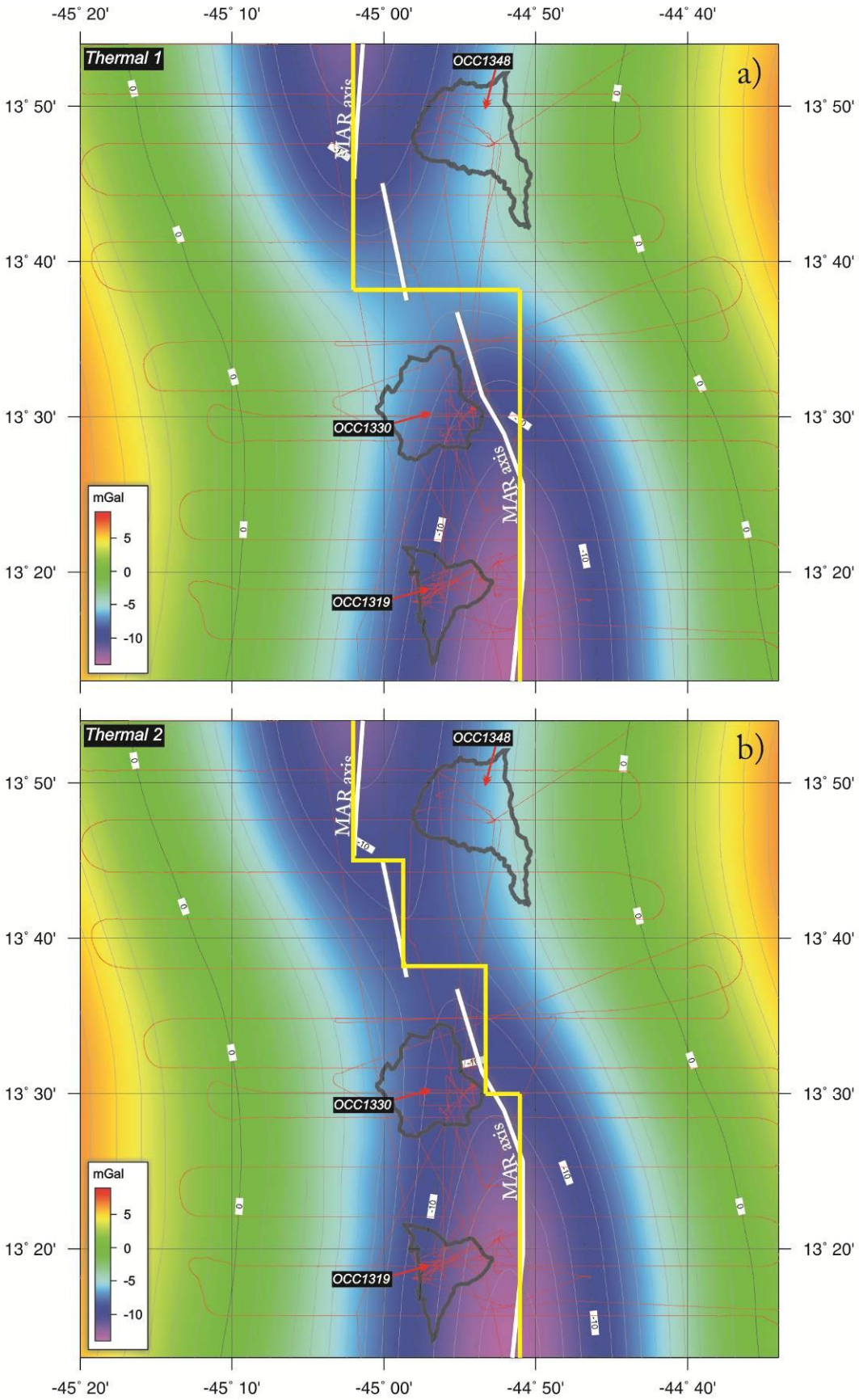


Figure 4.2.7a-b. Predicted thermal anomalies: **a)** Thermal 1 and **b)** Thermal 2. White line is ridge axis picked from bathymetry and sidescan sonar data, yellow line is that which is used to make the model. Red line is the ship's track, black outlines show near-axis OCC locations. Contours are at 1 mGal intervals. See text for discussion.

4.2.6. RMBA results

The thermal model shown in Figure 4.2.7a was sampled along-track and subtracted from MBA2 (Figure 4.2.4b), giving the residual mantle Bouguer anomaly (Figure 4.2.8). Theoretically, the RMBA reflects deviation of the actual subsurface mass distribution from that which is assumed in the starting crustal model (Figure 4.2.2b). Positive anomalies indicate a mass excess that may occur due to thinned crust and/or higher density material near the surface, and negative anomalies indicate a mass deficit that may occur in the presence of thick crust and/or lower density material. In the 13°N region where melt supply is expected to be weak and intermittent, strong, lateral temperature gradients may exist that are not taken into account in the thermal model. This caveat should be kept in mind when attributing the RMBA entirely to changes in layer thickness and lithology (as discussed in the following section).

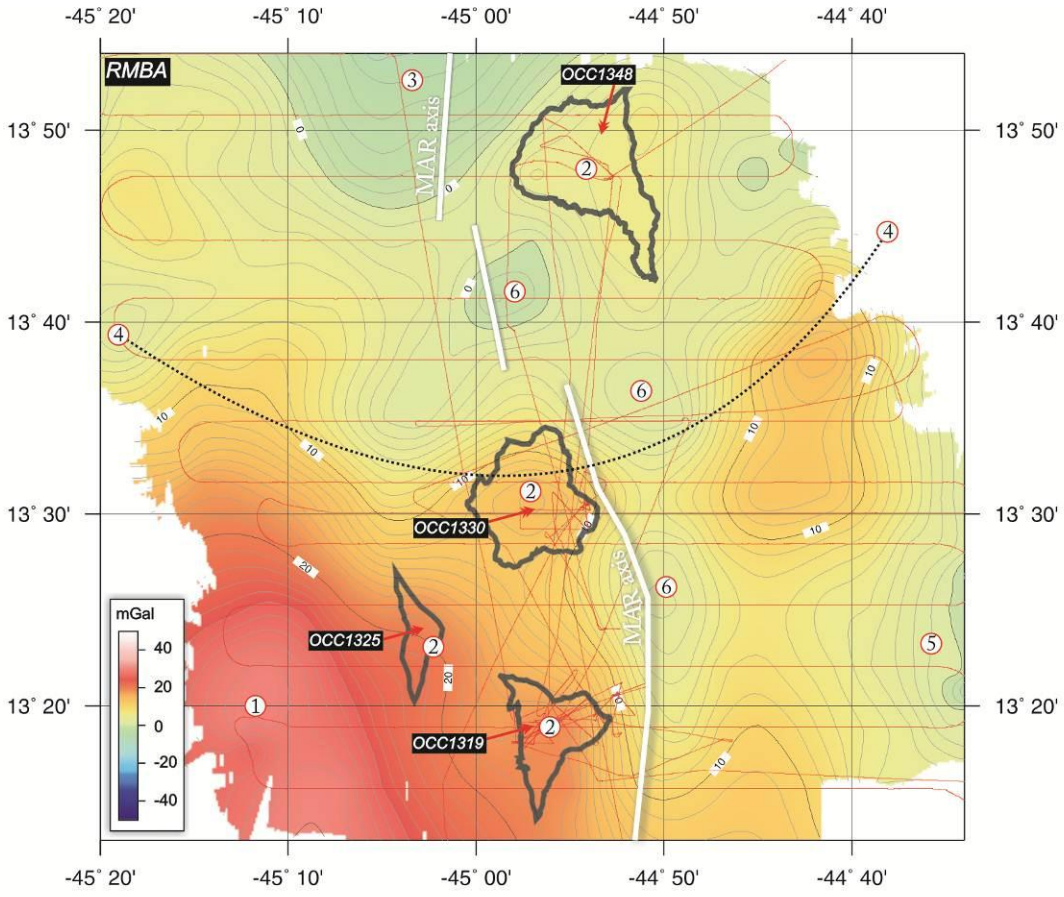


Figure 4.2.8. Residual mantle Bouguer anomaly calculated from MBA2 (**Figure 4.2.4b**, which is calculated for a stratified crustal model - **Figure 4.2.2b**) and thermal model 1 (**Figure 4.2.7a**). Red line is the ship's track, black outlines show near-axis OCC locations. Contours are at 1 mGal intervals. Numbered points are referred to in the text. Dotted line denotes possible influence of focused magmatism beneath segment centre to the north. See text for discussion.

4.3. Crustal structure & melt supply variability from RMBA

In this section, the RMBA is used to assess crustal structure (including thickness variations and regional asymmetry) and the implications this has for melt supply in the 13°N region. Compared with the information derived from sidescan sonar imagery (*Section 3.3-5*), gravity data represent a more robust estimate of the mode of magmatic accretion as they respond to a larger volume of material (whereas sidescan sonar data sample only the uppermost few metres of the seabed) and are thus averaged over a longer period. There are still, however, a number of similarities between the two datasets, namely: evidence for localised zones of magmatic accretion and regional, across-axis asymmetry in crustal accretion processes.

4.3.1. Regional structure & asymmetry

The most striking feature of the RMBA is the positive anomaly across the SW part of the survey area (Point 1 – Figure 4.2.8; maximum of 29 mGal at 45°12'W, 13°20'N, compared with < 10 mGal at its conjugate). This mass excess indicates the presence of high density material close to the surface, which may arise due to the crust being thinned in this area of intense OCC formation. Given that individual OCCs, such as OCC1330 and OCC1348, have a clear, isolated RMBA high (as do OCC1319 and OCC1325, albeit to a lesser extent; Point 2 – Figure 4.2.8), it seems possible that the gravity signature associated with multiple off-axis OCCs coalesces into a single, broad RMBA high in the SW (the form of the RMBA across near-axis OCCs is discussed in *Section 4.4.1*). This RMBA high is oblique to the ridge axis (for example, follow the trace of the 20 mGal contour) which appears to match the oblique trend of OCCs and bathymetric depressions discussed in *Section 3.3*.

Towards the north of the survey area the RMBA is associated with a broad low (Point 3 – Figure 4.2.8; minimum of -6 mGal at 45°05'W, 13°52'N) that becomes increasingly negative towards the segment centre at ~14°N (as shown by Smith *et al.*, 2008). This is consistent with numerous marine gravity surveys which show that segment centres are often associated with a ridge-centred RMBA low that is indicative of thicker crust and focused magmatic accretion (e.g. Fox & Gallo, 1984; Kuo & Forsyth, 1989; Lin *et al.*, 1990; Tolstoy *et al.*, 1993; Planert *et al.*, 2009). On a wider scale, the influence of the magmatically-robust segment centre may be evident as the

broad, circular RMBA low that extends south to 13°32'N at the ridge axis (Point 4 – dashed black line – Figure 4.2.8). It is probable that this circular anomaly not only represents crustal thickness variations induced by waxing and waning of the segment centre (*Section 3.3*), but also the 3D nature of temperature anomalies that are not taken into account with the passive-thermal model used to calculate the RMBA (3D variations in mantle temperature and upwelling velocity are potentially the largest source of density variation beneath spreading centres: Sparks *et al.*, 1993). For example, calculating an RMS value for the RMBA along each of the 13 survey profiles reveals a distinct regional trend where the RMS increases away from the segment centre (Figure 4.3.1). To a certain degree this relationship reflects a greater abundance of OCCs in the southern part of the survey area (and the associated increase in RMBA), but it may also suggest that asthenospheric temperatures decrease away from the segment centre in the north (which is discussed in more detail in *Section 4.3.4*).

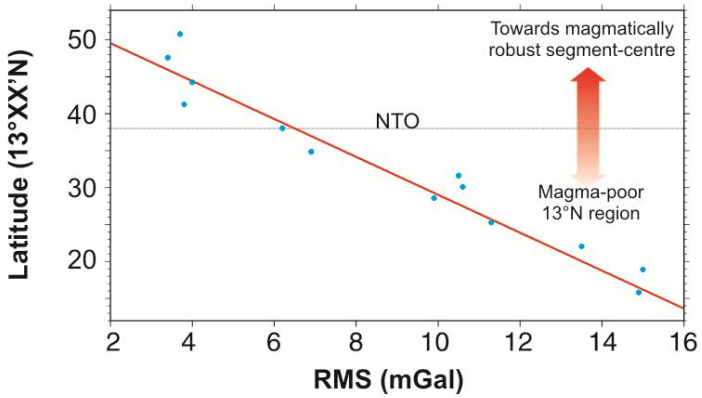


Figure 4.3.1. RMS value for RMBA profiles plotted against latitude (blue dots with linear best fit shown by red line). Close to the segment-centre, RMS is low compared with values towards the southern end of the 13°N region. This may be due to a greater number of OCCs south of the NTO, or a strong thermal gradient originating from the segment centre.

The broad regional asymmetry in the RMBA between the SW- and SE-quadrants matches the asymmetric pattern of faulting and tectonic strain identified in *Section 3.5*. The minimum RMBA in the SE-quadrant (Point 5 – Figure 4.2.8; ~0-2 mGal at 44°36'W, 13°25'N) coincides with the localised zone of abyssal hills identified in *Section 3.3*, thus giving further evidence for a spatially and temporally localised period of asymmetric magmatic-robustness (a similar gravity anomaly has been detected on the SWIR by Cannat *et al.*, 2009). To the north of the NTO in the ridge axis, across-axis asymmetry in the RMBA is less well pronounced, which also matches the lower degree of asymmetry in tectonic strain between the NW-NE pair of quadrants.

The increase in RMBA in the SW is associated with increasing fault heave and spacing (*Section 3.5*). This is similar to the pattern observed on the MAR between the Kane and Atlantis FZs, where, at the ends of segments, large throw faults show a positive correlation with RMBA (Shaw, 1992). As a possible explanation, Shaw (1992) suggests that in areas where melt supply is low, isotherms are deeper and hence faults can penetrate deeper and grow larger. Furthermore, numerical modelling results suggest that morphological asymmetry develops when magmatic and tectonic accretion is approximately equal and OCC formation is prevalent (Buck *et al.*, 2005; Behn & Ito, 2008; Tucholke *et al.*, 2008). Behn & Ito (2008) show that during OCC formation, an area of high temperature forms within the underlying lithosphere (beneath the footwall) that is not present on the conjugate plate – i.e. the ridge becomes thermally asymmetric. It may be expected that this contributes to the asymmetry in the RMBA observed in the 13°N region. However, increasing the temperature of the thermal model (Figure 4.2.7a) across the area of OCCs in the SW would further increase the magnitude of the RMBA high. This suggests that the across-axis asymmetry in the RMBA is primarily created by crustal thinning and the emplacement of high density material close to the surface, and that the 'heating effect' created by OCC formation is negligible in terms of gravity. Cooling effects, such as those caused by seawater percolation along detachment surfaces, may however contribute to the regional asymmetry in RMBA.

4.3.2. Crustal thickness

Assuming that the RMBA arises entirely from variations in depth to the Moho interface, it is possible to use the infinite slab formula (4.5) to calculate regional variations in crustal thickness (Figure 4.3.2):

$$\Delta g \cdot 10^{-5} = 2\pi G \rho t \qquad \textbf{(4.5)}$$

Where Δg is the observed anomaly in mGal, G is the gravitational constant, ρ is the assumed density variation across the Moho in kg/m^3 and t is the thickness perturbation in metres. Prior to this, the observed RMBA must be downward continued to a level 9 km beneath the sea-surface observation level – i.e. the assumed base of the crust (3 km average water depth plus 6 km crustal thickness). Downward continuation is inherently unstable as it amplifies noise within the observed signal, hence it is necessary to make a

filtered approximation of the form of the RMBA at the base of the crust (Smith & Sandwell, 1994). Thus, data were low-pass filtered, passing wavelengths > 30 km and rejecting wavelengths < 15 km, before translating them to residual crustal thickness (RCT) using (4.5).

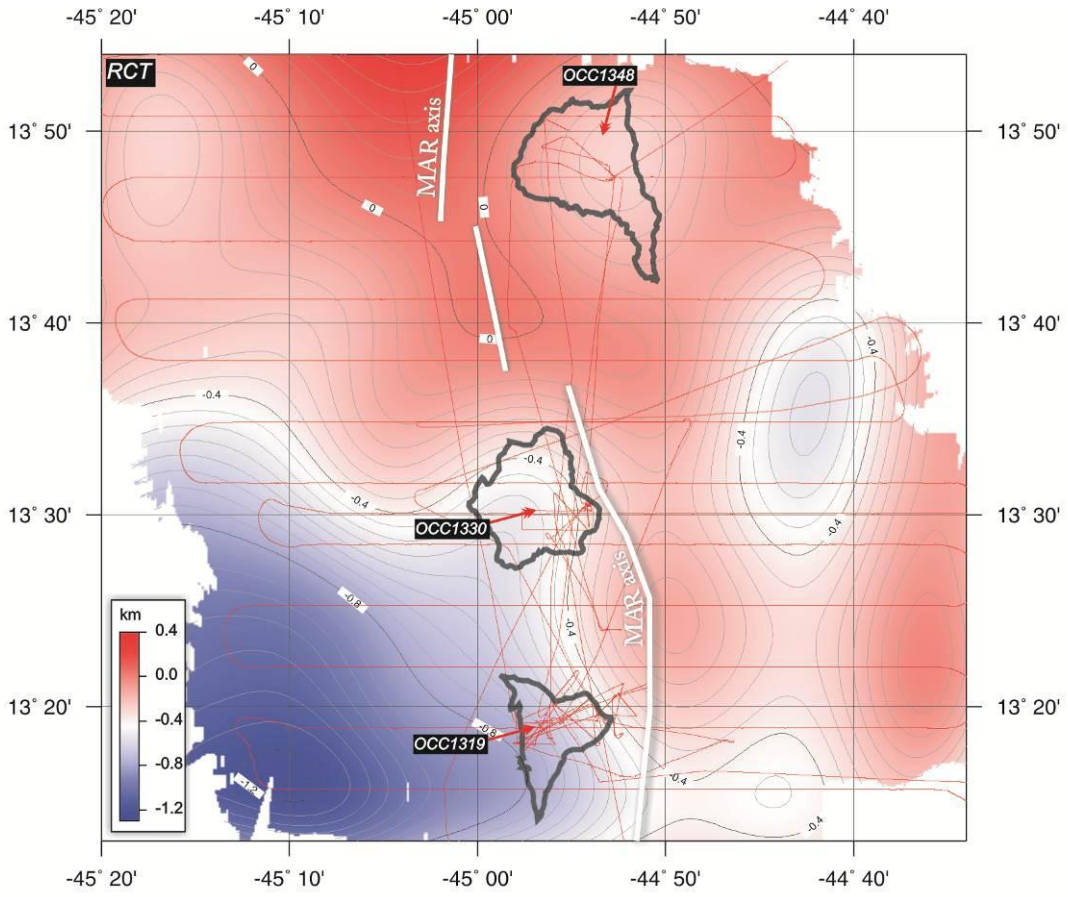


Figure 4.3.2. Residual crustal thickness variation assuming Moho depth of 6 km and density contrast of 600 kg/m^3. Red line is the ship's track, black outlines show near-axis OCC locations. Contours are at 50 metre intervals. See text for discussion.

The filtering process smoothes many of the short wavelength features present within the RMBA, but significant large-scale variations are still resolved by the RCT estimate (Figure 4.3.2). The SW-quadrant of the survey area, which displays the highest RMBA, can be attributed to crustal thinning of ~1.2 km from the ridge axis at 44°50'W, 13°25'N to the zone of intense detachment faulting at 45°10'W, 13°15'N. This is consistent with an estimate of 'at least 1 km' of crustal thinning for the same area made by Smith *et al.* (2008), and is also comparable to Fujiwara *et al.* (2003)'s estimate for the amount in which the segment ends surrounding the Fifteen-Twenty FZ are thinner than the corresponding segment centres (~1.0 – 2.5 km). At this stage it is important to

note that when referring to 'crustal' thickness, Figure 4.3.2 (and also the work of Fujiwara *et al.* (2003) and Smith *et al.* (2008)) *actually* refers to the thickness of material that has a density of 2700 kg/m^3 (which in an otherwise 'normal'/magmatic environment would constitute the crust) and may hence include serpentinised peridotite (i.e. non-crustal material; Table 1.2.3). Thus, the magnitude of crustal thinning is underestimated (it might be expected, for example, that if OCCs exhume mantle the actual crustal thickness across the domal section of an OCC is zero). This is aptly demonstrated across OCC1348, where the RCT suggests that the crust is only thinned by 0.4 km (i.e. the crust is 5.6 km thick). In this area serpentinised peridotite was extensively sampled from the seafloor (*Section 3.2.2*) and thus it seems likely that this 'crustal' thickness must comprise a significant proportion of mantle material. Furthermore, if the gravity signatures of numerous OCCs in the SW of the survey area are spatially aliased into one single anomaly, this might also mask shorter-wavelength, higher amplitude variations in RCT.

With this ambiguity in mind, it is difficult to quantify exactly the across-axis asymmetry in the RMBA if it is attributed entirely to crustal thickness variations. The thickness of the crust in the SE-quadrant of the survey area is, however, approximately 0 – 0.5 km thinner than the 6 km assumed in the starting calculation. Thus, the apparent asymmetry between the SW- and SE-quadrant of several hundred metres is comparable to an across-axis asymmetry of ~0.5 – 1.0 km measured near the Fifteen-Twenty FZ (Fujiwara *et al.*, 2003). Along the ridge axis, where it might be expected that RCT estimates more accurately reflect 'crustal' thicknesses in the traditional sense, the RCT shows a thickening towards the magmatically-robust segment centre of ~0.3 km relative to the starting crustal model.

4.3.3. Inferred component of magmatic extension (M_{TOTAL}) from RCT

Crustal thickness variations have previously been used to infer the relative variation in melt supply to the MOR, with thicker crust usually occurring at magmatically robust segment centres and thinner crust in magma-poor regions (e.g. Lin *et al.*, 1990; Tucholke *et al.*, 1997). Thus, the gradual decrease in crustal thickness from north to south over the 13°N region can be interpreted as a decrease in melt supply to the ridge axis. Fujiwara *et al.* (2003) and Smith *et al.* (2008) estimate that at the segment centre (14°N) the thickness of the crust is ~7 km and ~8.5 km, respectively. Assuming that this

thickness of crust is built up at a 'normal' ratio of magmatic to tectonic extension for a magmatically-robust environment, such as M_{TOTAL} = 95% (Buck *et al.*, 2005) or M_{TOTAL} = 90% (Escartin *et al.*, 1999), it is possible to scale the RCT estimates made in the previous section to give their corresponding inferred component of magmatic extension (Figure 4.3.3). This transformation is summarised in (4.6):

$$M_{TOTAL} = \left(\frac{RCT + ACT_{RMBA}}{ACT_{S.C}} \right) \cdot M_{S.C} \qquad (\mathbf{4.6})$$

Where M_{TOTAL} is the inferred component of magmatic accretion across the survey area, *RCT* is the residual crustal thickness variation (e.g. Figure 4.3.2), ACT_{RMBA} is the thickness of crust assumed for the RMBA calculation (e.g. 6 km), $ACT_{S.C}$ is the assumed thickness of crust at the segment centre and $M_{S.C}$ is the assumed melt supply at the magma-rich segment centre.

Figure 4.3.3 shows the minimum inferred component of M_{TOTAL} for the 13°N region, which is estimated by assuming that at the segment centre a component of M_{TOTAL} = 90% forms magmatic crust that is 8.5 km thick. In this scenario, M_{TOTAL} ranges from ~60 – 65% along the ridge axis to ~50% across the area of minimum crustal thickness – the SW-quadrant. If a value for M_{TOTAL} of 95% and crustal thickness of 7 km is assumed for the segment centre, then the maximum estimate of M_{TOTAL} in the 13°N region becomes ~73 – 78% along the ridge axis and ~65% in the SW-quadrant. The average inferred value for M_{TOTAL} is also shown in Figure 4.3.3, calculated assuming M_{TOTAL} = 92.5% and crustal thickness is 7.75 km at the segment centre.

As the RCT may be an underestimate (*Section 4.3.2*) of the true crustal thickness, the inferred component of M_{TOTAL} is consequently an overestimate. As stated in the previous section, however: along the ridge axis the crustal thickness estimates are unlikely to comprise a high amount of relatively low density, serpentinised mantle material, and thus the inferred component of magmatic extension may be more realistic in these areas. This value is ~75% in the northern part of the survey area and ~70% at the ridge axis between 13°19'N and 13°30'N (i.e. within the localised, magmatically-robust zone detected by the sidescan sonar – Figure 3.2.15b) and is hence comparable to the estimate of the relative contribution of magmatism to plate separation made from fault exposures detected by sidescan sonar (~80% averaged across the entire survey area

– *Section 3.5.2*, or ~60% for single profiles through the more magmatically-robust parts of the survey area – MacLeod *et al.* (2009)).

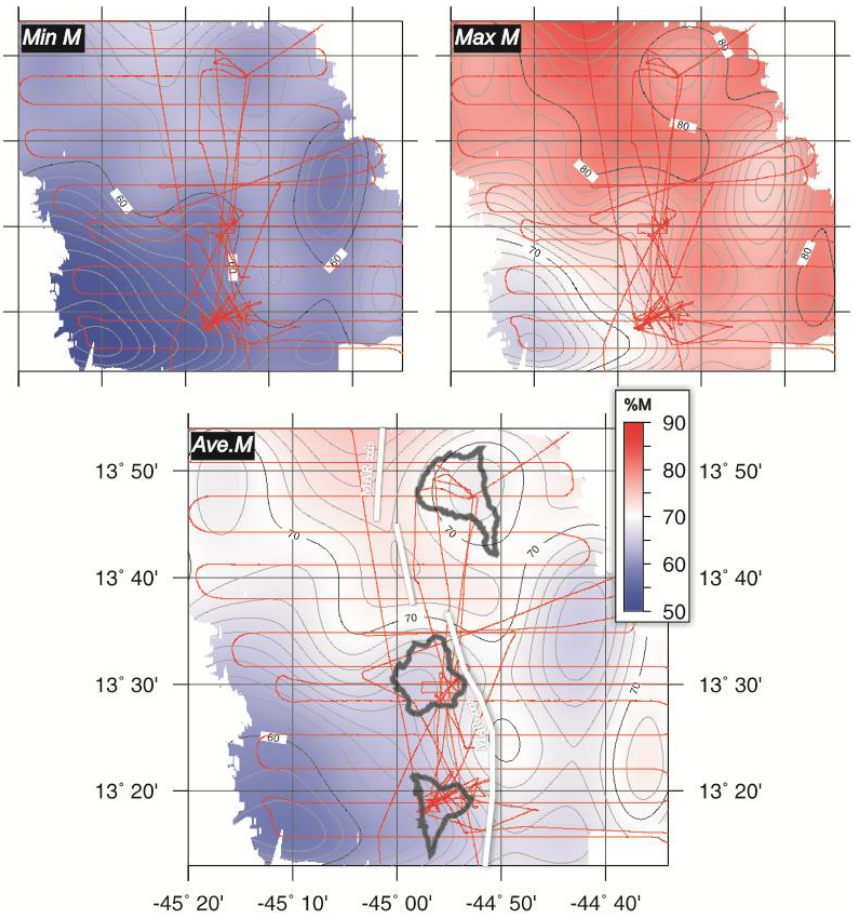


Figure 4.3.3. Inferred component of magmatic accretion (M) from residual crustal thickness estimates. 'Min', 'Max' and 'Ave.' values are given depending on the assumptions about the thickness and melt supply of crust at 14°N. Red line is the ship's track, black outlines show near-axis OCC locations. Contours are at 1% M intervals. See text for discussion.

In the SW part of the survey area M_{TOTAL} is calculated as 60%. This value is a maximum (given that the RCT is an underestimate) and is hence similar to the proposed value of M_{TOTAL} = 50% for OCC initiation and formation from numerical modelling (Buck *et al.*, 2005; Behn & Ito, 2008; Tucholke *et al.*, 2008). As previously stated: spatial aliasing of gravitational anomalies most likely masks shorter-wavelength, higher-amplitude variations in M_{TOTAL}, and to this extent the true value of M_{TOTAL} is uncertain. However, the high RMBA and low inferred component of magmatic accretion can still be used to confirm that magma-poor accretion has dominated in the

SW part of the survey area for at least the last 2 My (which has also been concluded by measuring tectonic strain across the region – *Section 3.5.2*). In addition to this, it is possible to use the RMBA to give a qualitative estimate of the magmatic conditions that preceded, occurred during and then followed OCC formation (i.e. by using the method of Tucholke *et al.*, 2008). Using the principle that higher RMBA represents lower melt supply (i.e. the same principle used to derive Figure 4.3.3): the local increase in RMBA across each of the near-axis OCCs (Point 2 – Figure 4.2.8) suggests that they formed in response to a period of low magmatism relative to slightly enhanced magmatic conditions before and after OCC formation.

4.3.4. Along-axis structure & focused magmatic accretion

Along-axis, the RMBA increases in amplitude from north to south by ~20 mGal at a steady rate of ~0.25 mGal/km (Figure 4.3.4). This strong, regional gradient represents a transition from magmatically robust accretion at the segment centre to magmatically-poor accretion in the 13°N region, and may thus reflect progressive thinning of the crust and/or thermally induced density variations in the upper mantle. Although the magnitude of this anomaly may at first seem insignificant, this is in fact more than twice the gradient that is observed on the Reykjanes Ridge south of the Iceland hotspot (where the RMBA increases away from the hotspot at a rate of ~0.1 mGal/km; Gardiner, 2003; Peirce *et al.*, 2005).

Without additional constraints on the regional crustal structure (i.e. seismic data), it is impossible to isolate the relative contribution of thermal effects and crustal thickness variations to the along-axis RMBA. However, if the thermal effect is considered negligible, the along-axis profile through the RCT shows that the regional gradient can be attributed to the crust thinning by ~0.75 km form north to south across the survey area – equivalent to a decrease in Moho depth of ~10 metres per km of latitude (lower panel – Figure 4.3.4). This is clearly a maximum that will decrease if a horizontal density gradient is introduced into the upper mantle. For example, using *Gravmag* (Pedley, 1991; described in *Section 4.4.2*) it is possible to model the long wavelength component of the RMBA exclusively by density variations in the mantle (Figure 4.3.5). In the model shown in Figure 4.3.5, sub-crustal polygons are 10 km wide and extend to 25 km deep.

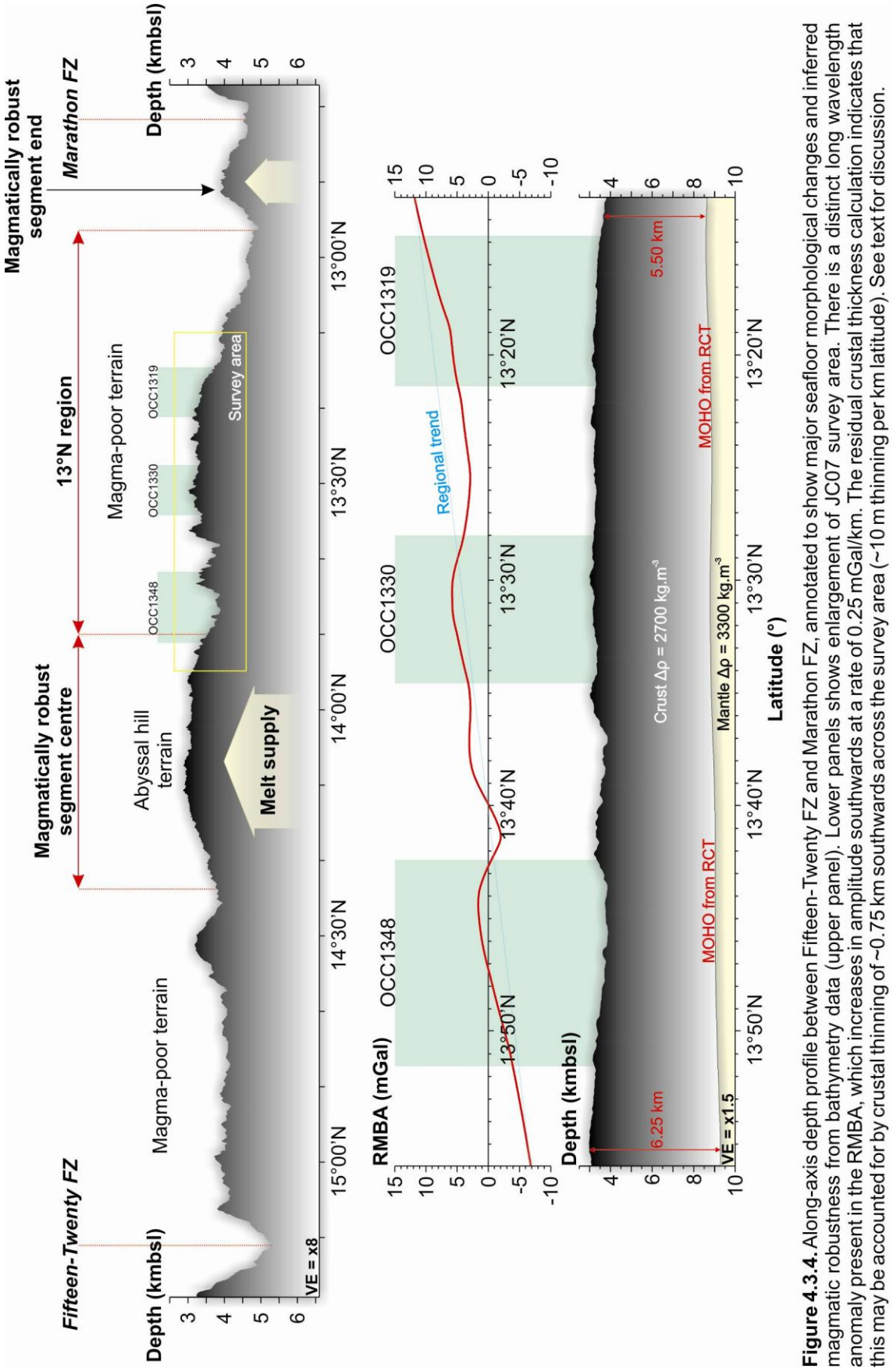


Figure 4.3.4. Along-axis depth profile between Fifteen-Twenty FZ and Marathon FZ, annotated to show major seafloor morphological changes and inferred magmatic robustness from bathymetry data (upper panel). Lower panels shows enlargement of JC07 survey area. There is a distinct long wavelength anomaly present in the RMBA, which increases in amplitude southwards at a rate of 0.25 mGal/km. The residual crustal thickness calculation indicates that this may be accounted for by crustal thinning of ~0.75 km southwards across the survey area (~10 m thinning per km latitude). See text for discussion.

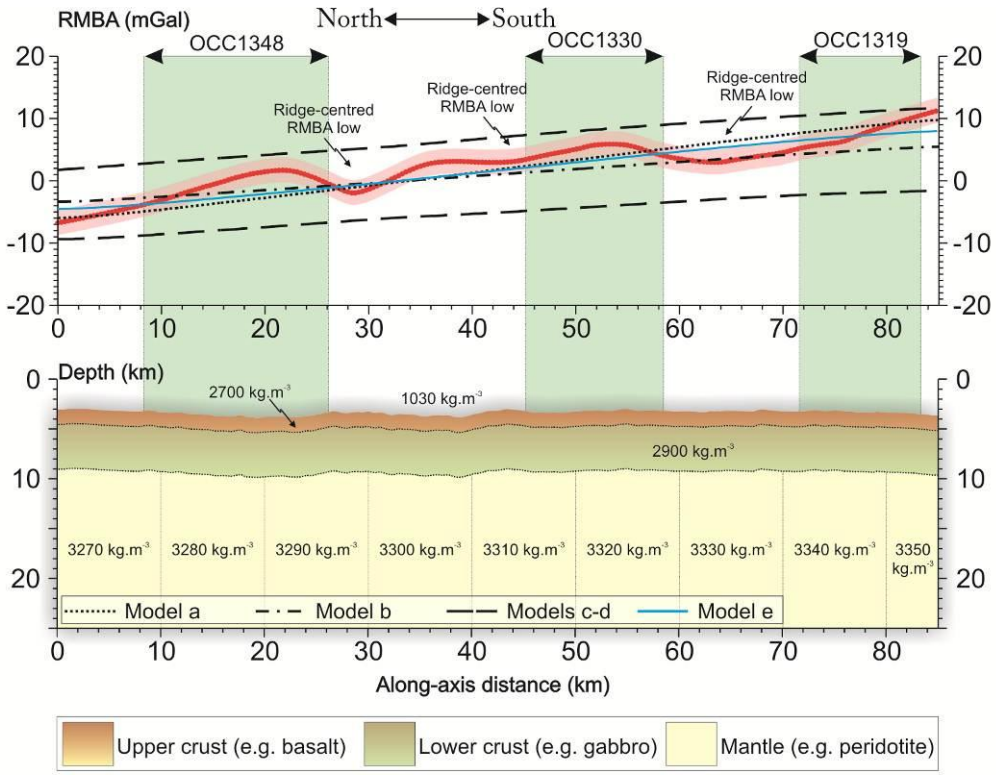


Figure 4.3.5. Along-axis 2.5D gravity model of subsurface mass distribution. The regional, long wavelength component can be accounted for by a gradual increase in density from north to south of 80 kg/m^3, representing a thermal gradient from the magmatically robust (i.e. hotter) segment centre to the north. Models a-b show the effect of varying the half-width of polygons between 10.0 km and 5.0 km, respectively. Models c-d show the effect of increasing and decreasing the density by ±50 kg/m^3 for the 5 km half-width model. Model e shows the effect of increasing the depth to the base of mantle polygons to 50 km. Observed anomaly data (red dots - upper panel) are at 350 m intervals with ±2 mGal confidence limits indicated by pink shading. The use of *Gravmag* software is discussed in *Section 4.4.2*.

For along-axis/zero-age modelling of gravity profiles along the MAR, Mello *et al.* (1999) and Peirce *et al.* (2005) place the base of anomalous mantle material at depths of 60 – 100 km and 50 km, respectively. I note, however, that increasing the depth to the base of the model from 25 km to 50 km has a negligible affect on the predicted anomaly (Figure 4.3.5). In this model, no regional variation in Moho depth is required if upper mantle densities increase from north to south by 80 kg/m^3 (thus representing an area of focused magmatism beneath the segment centre at 14°10'N). A corresponding temperature change can be calculated from:

$$\Delta T = \Delta\rho / (\alpha\rho_0) \qquad \textbf{(4.7)}$$

Where $\Delta\rho$ is the change in density, α is the coefficient of thermal expansion and ρ_0 is a reference density. Thus assuming a coefficient of thermal expansion of 3.4 x 10^{-5}/°C and a reference density for the upper mantle of 3300 kg/m^3, this gives a temperature change of ~700°C. The magnitude of this anomaly is clearly too great to be geologically realistic, which implies that significant along-axis crustal thinning from north to south in the 13°N region must also contribute to the long wavelength RMBA gradient.

In addition to long wavelength signals, superimposed on the regional gradient are three circular lows in the RMBA centred near the ridge axis, each of which has amplitude of only a few mGal (Point 6 – Figure 4.2.8, also annotated as 'ridge-centred RMBA low' in Figure 4.3.5). RMBA lows remain even if the detailed thermal model is applied to the gravity data (i.e. their wavelength and magnitude do not appear to be associated with cooling effects along offsets of the ridge model; Figure 4.2.7b). These types of anomaly have previously been identified in MBA data and used to pinpoint focused zones of magmatic accretion (e.g. Kuo & Forsyth, 1989; Lin *et al.*, 1990; Tolstoy *et al.*, 1993; Planert *et al.*, 2009; *Section 1.2.3*). In the 13°N region, RMBA lows generally show a good correlation with the surficial expression of volcanism in between near-axis OCCs (Figure 4.3.6).

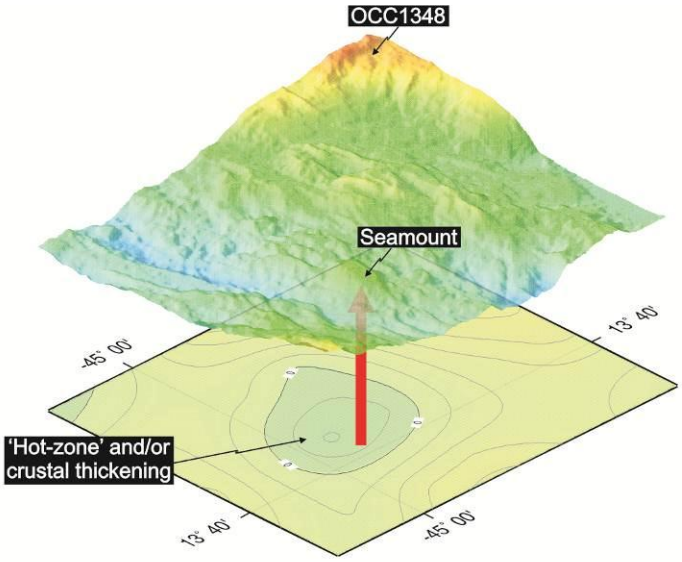


Figure 4.3.6. Short wavelength, along-axis RMBA lows show a good correlation with robust volcanism on the seafloor. For example: bathymetry data (upper surface) show a prominent seamount on the ridge axis at 13°40'N that extends for ~3 km along-axis and ~2 km across-axis and corresponds with a distinct, circular low in the RMBA data (lower surface). This indicates a mass deficit in the RMBA, and hence the crust must be thicker and/or hotter - both of which imply localised/focused magmatic accretion. This anomaly may thus be of similar origin to the localised, seismic low velocity zone observed beneath a prominent seamount on the MAR at 34°50'N (Barclay *et al.*, 1998).

Ridge-centred RMBA lows in the 13°N region are not 'smeared' across the ridge axis like traditional Bull's-eye anomalies, suggesting that they may be temporally unstable magmatic features that can switch on and off (and may thus explain the apparently localised zone of abyssal hills formed on the AF plate and the increasing and decreasing strength of magmatism about the Marathon FZ – *Section 3.3*). It is possible that the ridge-centred RMBA low at 44°51'W, 13°36'N has an off-axis trace that is oblique to the spreading direction and coincides with the off-axis bathymetric depressions identified in *Section 3.3*, but, as stated in *Section 4.3.1*, this off-axis trace may also be created by a longer-wavelength anomaly generated by focused accretion at the segment centre (Point 4 – Figure 4.2.8). The RMBA low centred on the ridge axis at 13°25'N may be asymmetrically smeared across-axis, accounting for the slight decrease in the RMBA around 44°45'W, 13°25'N.

The RMBA lows are generally slightly to the east of the neovolcanic ridge axis (white line, Figure 4.2.8) south of 13°45'N, with the opposite sense to the north of this point. This effect may be produced if the locus of melt emplacement is temporally and spatially variable, with the gravity dataset responding to a thicker accumulation of, albeit older, magmatic material. If this is true, it implies that at some point in the recent history of the 13°N region, melt emplacement has shifted by ~1 – 7 km westwards to the south of 13°45'N (as has been suggested based on the age of volcanic lineaments in *Section 3.4.1*) and ~1 – 2 km eastwards to the north of 13°45'N. This shift is towards near-axis OCCs, and may therefore result from OCCs capturing melt at depth and channelling it preferentially towards one side of the axial valley (e.g. MacLeod *et al.*, 2009).

Removing the regional field from the RMBA allows for the source of ridge-centred-lows to be modelled more accurately (Figure 4.3.7). The residual, short wavelength RMBA lows at 13°42'N, 13°36'N and 13°25'N have wavelengths of 16 km, 15 km and > 25 km and amplitudes of 5 mGal, 2 mGal and 4 mGal, respectively. The relatively short wavelength of these features means it is unlikely that they are caused by a low density zone in the upper mantle (which is a possible source for the regional anomaly). For example, modelling a narrow zone within the mantle centred beneath the RMBA low at 13°42'N (29 km in Figure 4.3.7) that extends for 5 km along- and 5 km across-axis (i.e. 2.5 km half-width) to a depth of 25 km creates an anomaly that has a wavelength much greater than the wavelength of the observed anomaly (Figure 4.3.8a).

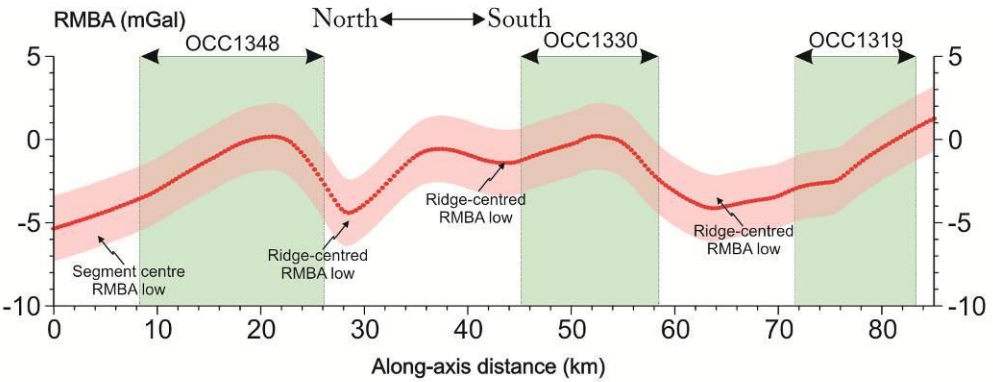


Figure 4.3.7. Short wavelength component of along-axis RMBA having removed the regional trend of 0.25 mGal/km. Observed anomaly data (red dots - upper panel) are at 350 m intervals with ±2 mGal confidence limits indicated by pink shading. Vertical green bars are along-axis positions of near-axis OCCs. Depth profile is shown in **Figure 4.3.5**. See text for discussion.

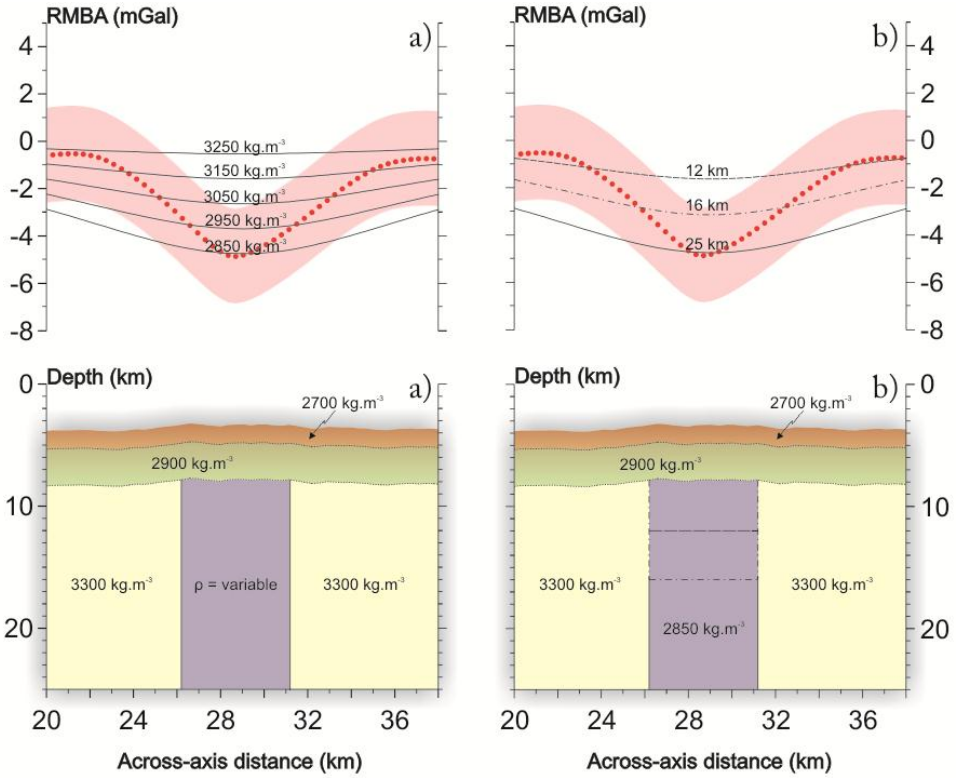


Figure 4.3.8a-b. Short wavelength 2.5D gravity models of along-axis subsurface mass distribution within the mantle. The regional, long wavelength component has been removed from the observed data. **a)** A low density column in the mantle (purple) creates a predicted anomaly much wider than the observed anomaly. **b)** Reducing the depth to the base of the anomalous mantle zone does not significantly alter the predicted anomaly. Observed anomaly data (red dots - upper panel) are at 350 m intervals with ±2 mGal confidence limits indicated by pink shading. Cross-sectional colour code is the same as **Figure 4.3.5**. See text for discussion.

Varying the density contrast between the anomalous column of material and surrounding mantle alters the amplitude of the predicted anomaly, but not the wavelength. Narrowing the anomalous zone was found to decrease the amplitude but make little difference to the wavelength of the predicted anomaly, as did altering the depth to the base of the column (Figure 4.3.8b).

Applying the same method to an anomalous column of material within the upper and lower crust, rather than the mantle, achieves a much better fit between predicted and observed anomalies. Figure 4.3.9a shows a low density zone in the crust that is 5 km along- by 5 km across-axis.

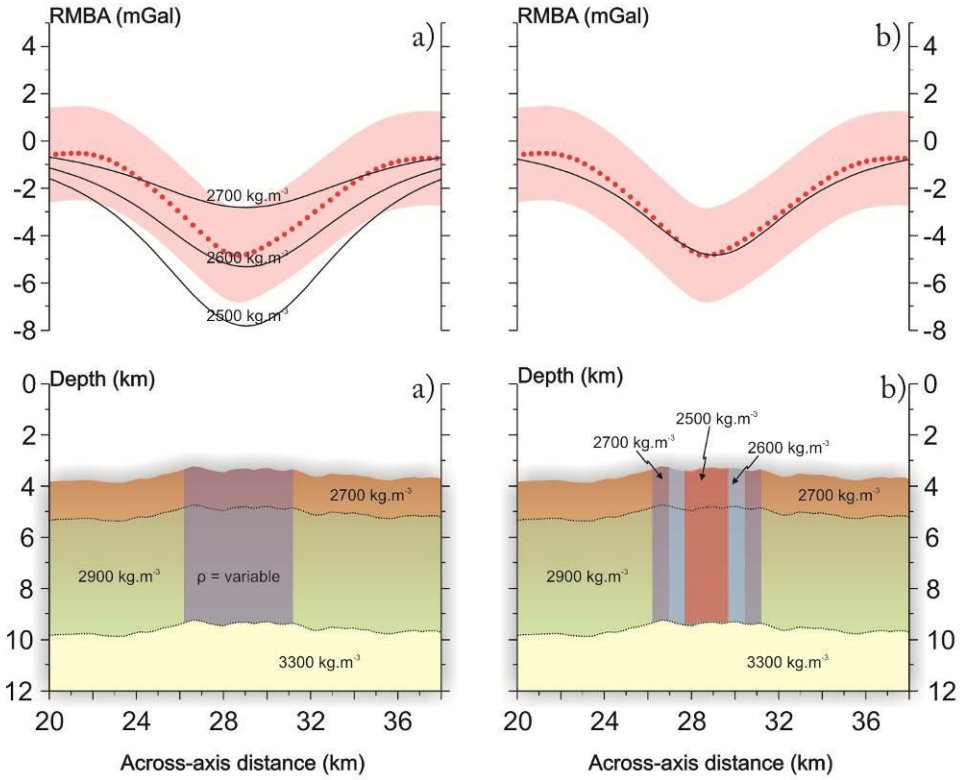


Figure 4.3.9a-b. Short wavelength 2.5D gravity models of along-axis subsurface mass distribution within crustal layer. **a)** A shallower column of anomalous material (purple) more accurately matches the observed wavelength compared with mantle compensation. **b)** This can be optimised by having a gradual density decrease across the melt conduit. Observed anomaly data (red dots - upper panel) are at 350 m intervals with ±2 mGal confidence limits indicated by pink shading. Colour code is the same as **Figure 4.3.5**, purple/blue/red is anomalous crustal mass. See text for discussion.

In this case the shallow source generates a predicted anomaly that has a wavelength of ~20 km (compared with 16 km for the observed width of the RMBA low at 13°42'N). For a density of 2700 kg/m^3, however, the amplitude of the predicted anomaly is ~2 mGal (Figure 4.3.9a). Decreasing the density of the anomalous material to 2600 kg/m^3 and 2500 kg/m^3 causes an increase in the amplitude of the predicted anomaly to ~4 mGal and ~6 mGal, respectively. The best-fit between the wavelength and amplitude of the observed and predicted anomalies is obtained by dividing the single 5 km wide zone of anomalous crustal material into three vertical columns that decrease in density towards the centre (Figure 4.3.9b).

Without independent measurements of layer thicknesses it is difficult to determine the true intra-crustal density variation as at least some portion of the RMBA may be created by localised changes in the Moho and basalt/gabbro interface topography. Regardless of the source, however, short wavelength RMBA perturbations suggest localised, robust melt emplacement at a crustal level in areas between near-axis OCCs. These findings are discussed in more detail in *Section 6.2.1* and *Section 6.3.1*.

4.4. Gravity models: Implications for OCC structure

The RMBA arises due to density variations in the subsurface that are not present in the assumed crustal model. By predicting the gravitational response of causative bodies and matching this with the observed anomaly, it is possible to estimate the magnitude and extent of anomalous mass beneath the surface. In the absence of additional constraints on subsurface geology, however, modelling results are inherently ambiguous. Information from drill cores and seismic surveys across other OCCs and magma-poor environments can be, however, used to guide the modelling process in the 13°N region (*Section 1.3.3*). Thus modelling results are useful for assessing the range of densities and shapes of crustal and mantle material that could explain the observed anomaly, but are not a unique solution.

In this section I give a quantitative description of the RMBA across OCCs in the 13°N region and contrast this with observations and models across OCCs on other parts of the MOR. I then use a combination of 2.5D and 3D forward modelling techniques to assess possible models for the subsurface structure and formation of near-axis OCCs, and address the possibility of linked detachment surfaces (Smith *et al.*, 2008).

4.4.1. RMBA across near-axis OCCs

Figure 4.4.1 shows RMBA profiles across the three near-axis OCCs in the 13°N region. Each OCC is associated with a positive RMBA, confirming that they are underlain with material of higher density than that which is assumed in the starting crustal model, as has also been shown in previous gravity studies across OCCs (e.g. Blackman *et al.*, 1998; Tucholke *et al.*, 1998; Tucholke *et al.*, 2001; Baines *et al.*, 2003; Fujiwara *et al.*, 2003; Searle *et al.*, 2003; Cannat *et al.*, 2006). The anomalies across OCC1319 and OCC1330 are a few kilometres wider than the surficial width of each OCC (vertical green bars in Figure 4.4.1). The anomaly across OCC1348 is, however, considerably broader than the surficial limits of the OCC – extending for up to ~8 km either side of the OCC. The maximum "absolute" RMBA observed across each OCC is: OCC1319, 18 mGal; OCC1330, 14 mGal; and OCC1348, 6 mGal.

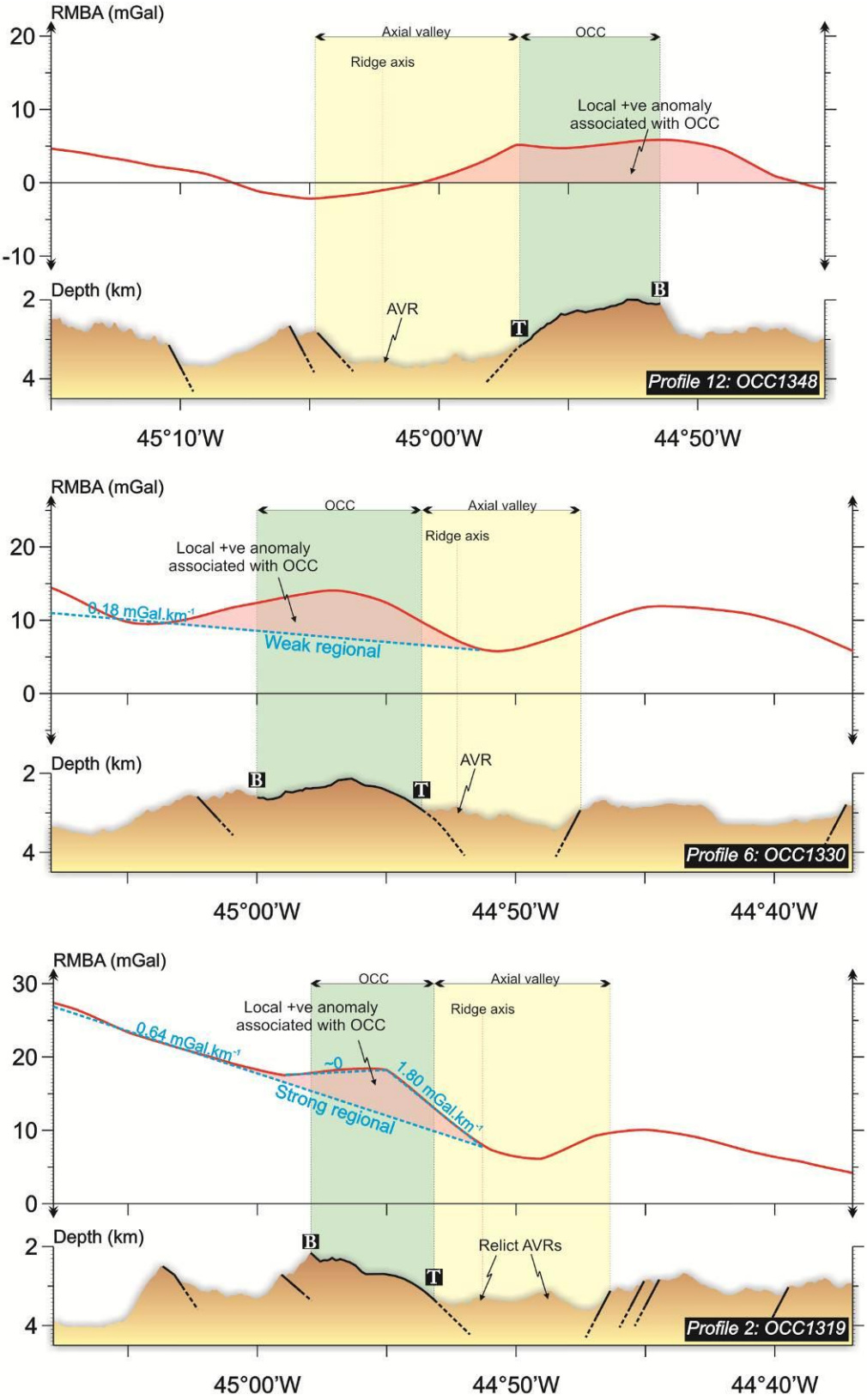


Figure 4.4.1. 2D RMBA profiles across near-axis core complexes. Each OCC exhibits a local anomaly increase of several mGal (pink shading), and also a conjugate RMBA-high on the opposing ridge flank. OCC1319 and OCC1330 have a long wavelength component on the SA plate, similar to Kane Massif (Tucholke *et al.*, 1998) and FUJI Dome (Searle *et al.*, 2003). See text for discussion.

RMBA highs observed across OCC1319 and OCC1330 are superimposed on longer-wavelength anomalies that increase away from the ridge axis on the SA plate at rates of 0.6 mGal/km and 0.2 mGal/km, respectively, and are thus markedly different from the nature of the observed anomaly across OCC1348 where there is no long wavelength component of the RMBA. This long wavelength component gives the SW part of the survey area its distinctive, regional RMBA high that was noted in *Section 4.3* as possibly arising from the coalescing signatures of multiple OCCs, or, later, possibly attributed to an overall crustal thinning of ~1.2 km (*Section 4.3.2*). Previous studies have also detected long wavelength components of the RMBA across OCCs and attributed this to thinner crust on the older side of the OCC (Tucholke *et al.*, 1998, 0.5 mGal/km; Tucholke *et al.*, 2001, 0.2 mGal/km; Searle *et al.*, 2003, 1.5 mGal/km). Assuming the anomaly on the older side of an OCC hints at conditions that instigated OCC formation, and given the striking similarity between the shape of the RMBA profile across OCC1319, Kane Massif (Figure 4.4.2a) and FUJI Dome, this would appear to suggest a common life cycle for these OCCs. However, OCC1348 does not have a long wavelength component and may have thus undergone a different mode of formation (the RMBA profile over OCC1348 is similar to that which has been observed across Atlantis Massif by Blackman *et al.* (1998); Figure 4.4.2b). Blackman *et al.* (1998) note that the RMBA across Atlantis Massif is centred over the termination of the OCC, and thus conclude that this area is underlain by high density serpentinised peridotite and gabbroic material. Based on a purely qualitative comparison with Figure 4.4.1, this does not appear to be the case for near-axis OCCs in the 13°N region, with the RMBA generally being centred over the summit of each OCC.

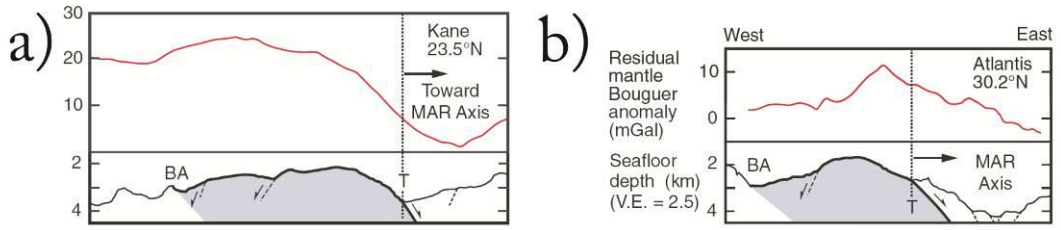


Figure 4.4.2a-b. RMBA profiles across other notable OCCs: **a)** Kane Massif (x-axis ~45 km) and **b)** Atlantis Massif (x-axis ~35 km); which have similarities to OCC1319 and OCC1348, respectively. Image is from Tucholke *et al.* (2008), with data from a) Tucholke *et al.* (1998) and b) Blackman *et al.* (1998).

Measuring relative to the regional, long wavelength average, the RMBA associated with OCC1319 and OCC1330 becomes ~6 mGal and ~7 mGal, respectively

(thus, the RMBA across all three near-axis OCCs becomes approximately equal). In comparison, the RMBA amplitude (measured from the OCC peak-anomaly to a best estimate of the regional average) across other notable OCCs are generally higher than those observed in the 13°N region (Table 4.4.1). It is difficult to directly compare RMBA values from other studies as in each case the assumed crustal and thermal models might be different; the crustal model used at Dante's Domes OCC (Tucholke *et al.*, 2001), however, is the same as that which has been used in this study, thus suggesting that the different RMBA values may be due to a different internal structure between the OCCs. Conversely, Cannat *et al.* (2009) show that the RMBA associated with some 39 corrugated surfaces on the SWIR (spanning an age range of 5 – 30 Ma) is on average ~4 – 5 mGal above the regional level, which is thus similar to that observed in the 13°N region and suggestive of a common structure and composition.

OCC	Source	RMBA (mGal)	Termination-centred anomaly?	Long wavelength component (mGal/km)	Breakaway (Ma)	Termination (Ma)
OCC1319	*This study*	6±2	No	0.6	0.77	~0.00
OCC1330	*This study*	7±2	No	0.2	0.82	~0.00
OCC1348	*This study*	6±2	Slightly?	None	1.46	0.54
Atlantis Massif	(Blackman *et al.*, 1998)	10 – 15±2	Yes	Very weak?	1.75 – 2.08	0.92
Kane Massif (south)	(Tucholke *et al.*, 1998)	8-12	No	0.5	2.92	2.31
Dante's Domes	(Tucholke *et al.*, 2001)	15 – 20±1	No	0.2	2.0 – 2.2	0.7 – 1.3
FUJI Dome	(Searle *et al.*, 2003)	30-35	Slightly	1.5	2.58	1.95
SWIR (39 OCCs)	(Cannat *et al.*, 2009)	4 – 5	N/a	N/a	> 5	< 30

Table 4.4.1. Summary of RMBA characteristics across selected OCCs, measured between the peak anomaly and an estimate of the regional average/long wavelength component. 'Termination-centred anomaly' column refers to if the OCC-related anomaly appears to be centred over the footwall/hanging-wall boundary as opposed to the entire OCC.

As stated previously: in 2D all OCCs are associated with a slight local increase to the RMBA. When the RMBA is considered in 3D, however, there does not appear to be a unique shape that can define the anomaly across all three near-axis OCCs (Figure 4.2.8, see also the detailed plot of FAA to RMBA in Figure 4.4.3a-b). Across OCC1348 for example, the RMBA forms a T-shape that points towards the ridge axis. The eastern-part of this T-shape comprises an oval that has maximum amplitude centred over the breakaway ridge, with its long-axis (~18 – 23 km) aligned parallel with the ridge axis and short-axis (~7 – 10 km) aligned parallel with the spreading direction.

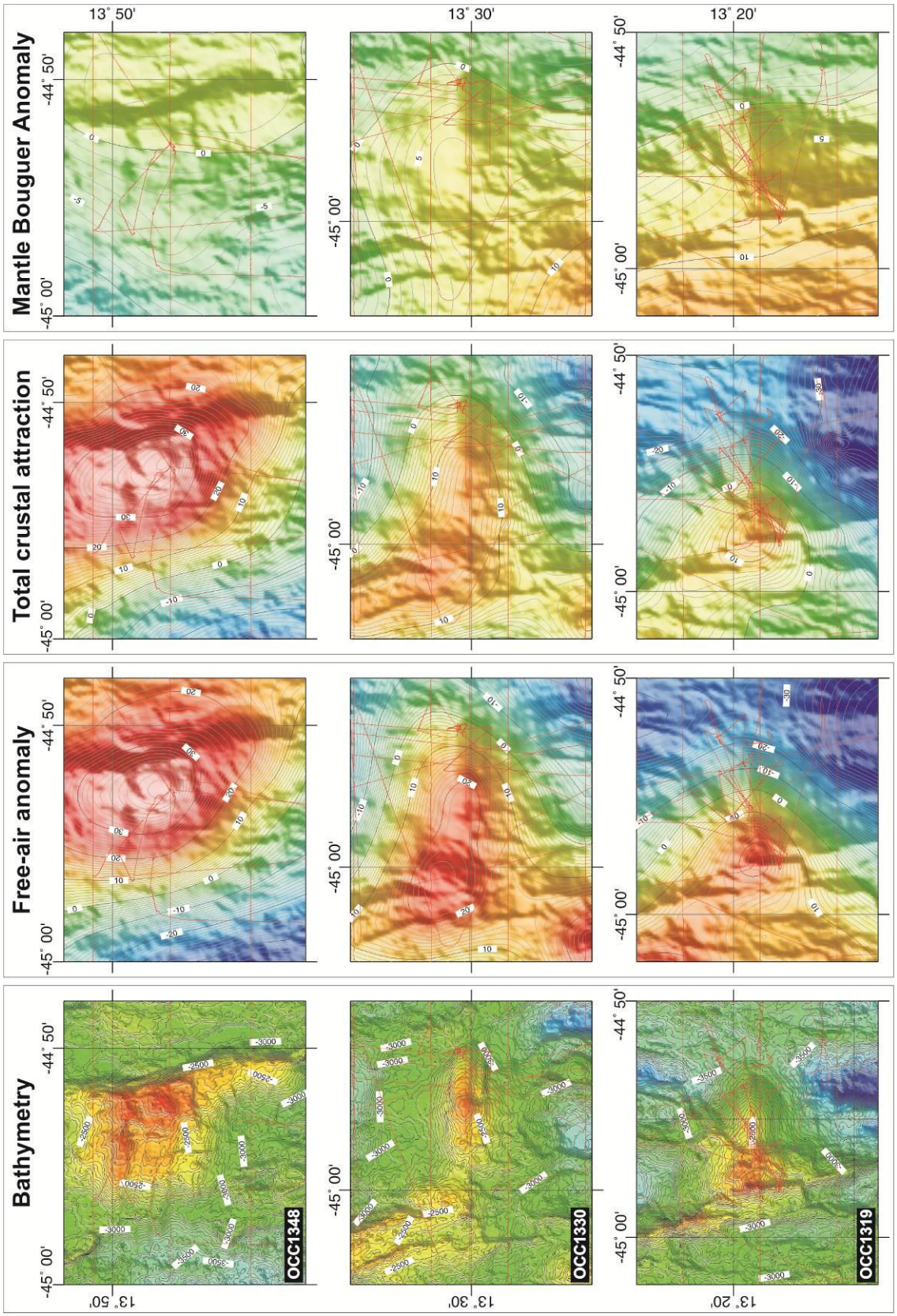


Figure 4.4.3a. Gravity data reduction from FAA to MBA: detailed plot across each of the three near-axis OCCs. In each case, bathymetry is shown with colour scale the same as **Figure 2.2.2.** and with contours at 50 m intervals. FAA, total crustal attraction (for model MBA2) and MBA2 are also shown, with 1 mGal contours and colour scale the same as **Figure 4.2.8**. See text for discusssion.

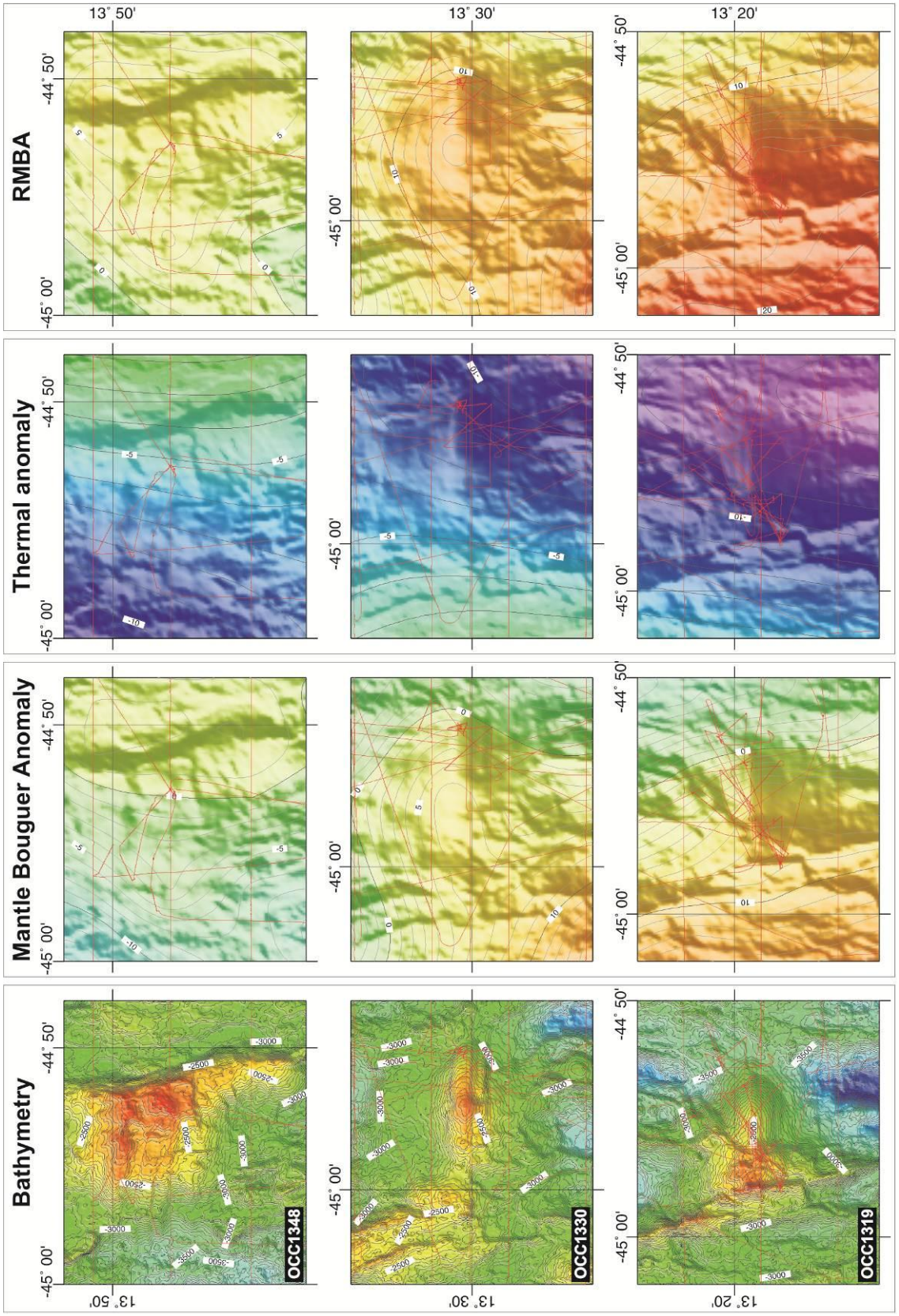


Figure 4.4.3b. Gravity data reduction from MBA to RMBA: detailed plot across each of the three near-axis OCCs. In each case, bathymetry is shown with the same colour scale as **Figure 2.2.2.** and with contours at 50 m intervals. **MBA2** (colour scale: **Figure 4.2.8.**), thermal anomaly (colour scale: **Figure 4.2.7a.**) and **RMBA** (colour scale: **Figure 4.2.8.**) are also shown, with 1 mGal contours. See text for discusssion.

There is a slight depression in the RMBA across the domal section of the OCC that gives way to a small, circular peak located across the footwall/hanging-wall boundary (~2.5 km in diameter), giving the OCC-related anomaly an across-axis width of ~18 – 22 km. In contrast, OCC1330 is associated with an oval-shaped RMBA that extends for ~18 – 23 km along-axis by ~14 – 20 across-axis. OCC1319, which is situated within the long wavelength RMBA in the SW of the survey area, appears to have an RMBA similar in shape to that which is observed across OCC1348 – a T-shape pointing towards the ridge axis. The OCC influences the RMBA for ~12 – 14 km along-axis by ~11 – 13 km across-axis (although it is difficult to measure this accurately given the long wavelength component of the RMBA). In *Section 4.4.3* I use a 3D modelling technique to assess suitable models for the intra-crustal interface that give rise to these various shapes, and assess the implications this has for subsurface detachment structure.

4.4.2. Modelling of gravity anomalies (2.5D)

2.5D modelling has been performed using *Gravmag* software, which allows for the crust beneath the RMBA profile to be modelled as a series of polygons (Pedley, 1991). Each polygon is assigned a density contrast and a half-width perpendicular to the plane of the profile (giving a '2.5D' element). Observed data are constrained by *Gravmag* to 500 data points per model, and hence the RMBA has been sub-sampled to 250 metre intervals for the following across-axis models. Polygons have been extended to ±1000 km where necessary to minimise artificial edge effects, and have a default half-width of ±10 km unless otherwise stated. Using the RMBA, as opposed to the FAA, as the observed anomaly is advantageous as the ridge-thermal effect has already been taken into consideration (continuously varying densities are difficult to accurately model with *Gravmag*). Hence density contrasts are relative to densities in the starting crustal model used for calculation of the RMBA (Figure 4.2.2b – interfaces used for calculation of the RMBA are also shown as dotted black lines in the following 2.5D modelling diagrams). An error of ±2 mGal is assigned to the observed data, which I estimate from the standard deviation of 217 crossover errors in the gravity survey (which was reduced from 1.3 mGal to 1.0 mGal, with 30 of these crossover points having a COE of 3.2 mGal - *Section 2.5.1.3*).

4.4.2.1. OCC1319: Internal density structure (2.5D)

Figure 4.4.4a-d shows three *Gravmag* models of the expected mass distribution beneath OCC1319 for a 3-layered crust, with layer-densities and thicknesses the same as those assumed in Figure 4.2.2b and with the subsurface detachment geometry assumed to be the same as that which has been seismically imaged at TAG (deMartin *et al.*, 2007; *Section 1.3.3*). In Figure 4.4.4b the half-width of anomalous polygons are varied to assess their contribution to the predicted anomaly. By changing the half-width from 5.0 km to 3.5 km for the anomalous material between the vertical projection of the breakaway ridge and the detachment surface, the predicted anomaly varies greatly in amplitude (peak amplitude: 38 mGal and 32 mGal, respectively). This highlights a major limitation of the 2.5D modelling process as no single half-width can accurately define the axis-parallel shape of the OCC. Thus, the half-width of OCC1319 is approximated to 3.5 km (roughly half the axis-parallel extent of the OCC) for the models discussed below. The long wavelength component of the RMBA is accounted for by thinning the crust by ~1.5 – 2.5 km on the SA plate. The fact that this is greater than that which is predicted by the RCT calculation (maximum: ~1.2 km) may be due to the misassumption that the area of thinned crust only extends by ±10 km along-axis (i.e. the half-width of the polygon). A crustal thickness of 6 km implies that the Moho should be exposed on the seafloor midway across the dome of the OCC (i.e. ~6 – 7 km from the breakaway ridge in the model set-up – dependent on the angle in which the detachment surface cuts through the crustal sequence). As discussed in *Section 3.3.1.3*, it seems more likely that the boundary between upper massif and domal section marks the position of the Moho, and hence this is set accordingly in the model.

The most striking feature of the model set-up in Figure 4.4.4b is that the predicted anomaly greatly mismatches the observed data (by roughly 13 mGal). This is somewhat unsurprising given that the model invokes the exposure of high density (3300 kg/m^3), unaltered mantle material at the seafloor, which conflicts with the sampling results in *Section 3.2.2*. Note, however, that such a model is plausible for explaining the high RMBA values observed across FUJI Dome (Searle *et al.*, 2003). The peak of the predicted anomaly also lies ~1.5 km to the east of the peak of the OCC-related observed anomaly. In order to reduce the amplitude and shift the peak of the predicted anomaly, thus improving the match with the observed data, it is necessary to introduce an area of low density (~2900 kg/m^3) that is ~3 km thick within the footwall (Figure 4.4.4c).

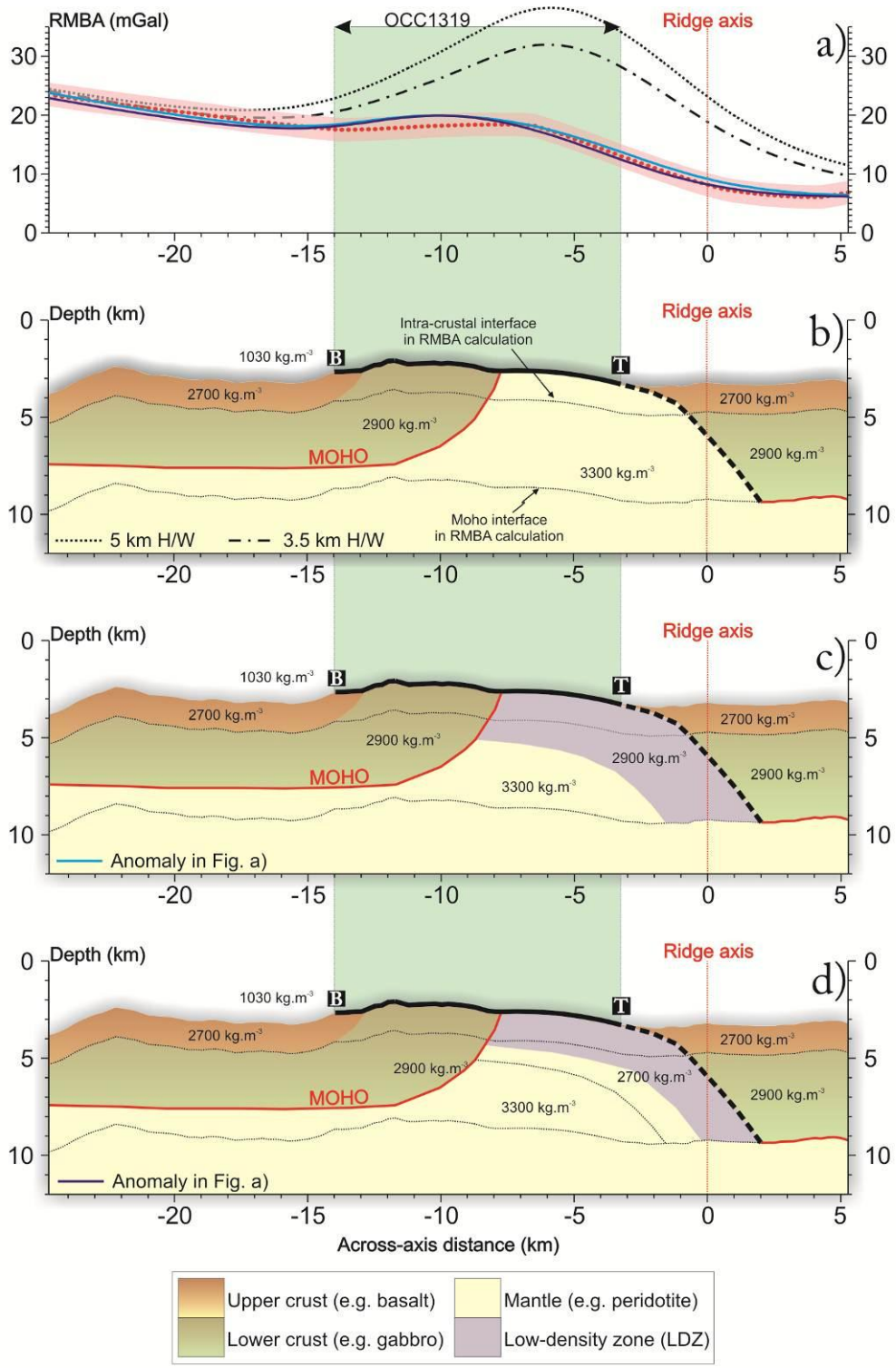


Figure 4.4.4a-d. Gravity models (2.5D) of OCC1319 internal mass distribution: **a)** observed anomaly data (red dots) are at 250 m intervals with ±2 mGal confidence limits indicated by pink shading, **b)** [dashed black lines in a)] starting model for a 3-layered crust, H/W is half-width of anomalous material between breakaway and detachment surface, **c)** [blue line in a)] effect of introducing a low density zone into the footwall and **d)** [purple line in a)] the relationship between thickness of the LDZ and density. Heavy, solid black line is detachment surface exposed at surface, dashed black line is inferred location of detachment surface after deMartin *et al.* (2007). See text for discussion.

This low density zone (LDZ) effectively removes the density contrast between the footwall and hanging-wall at depths > 1.5 km, with the predicted anomaly now arising from the area of uplifted mantle and lower crustal rocks within the upper 1.5 km to the west. By manually altering the model, I estimate that the density and thickness of the LDZ can be changed by ±100 kg/m^3 and ±1 km without exceeding the ±2 mGal error assigned to the observed data. There is a trade-off whereby if the LDZ is made thinner it must also have a lower density to match the observed data. For example, if the LDZ has a density of 2700 kg/m^3, it must be made ~1 – 2 km thinner (Figure 4.4.4d). Given that the LDZ can be modelled with a density that is the same as that of the lower crustal layer (2900 kg/m^3), this essentially makes the surficial position of the Moho moot (i.e. the Moho may exhibit no density contrast near the surface in Figure 4.4.4c-d).

The LDZ within the upper part of the footwall may potentially occur due to: 1) serpentinisation of peridotite, 2) footwall capture of ascending melt and/or plutonic gabbro, or; 3) a combination of these two processes. At Atlantis Massif, gravity modelling has revealed a similar low density zone in the footwall that has been attributed to a serpentinisation front running sub-parallel to the detachment surface (Nooner *et al.*, 2003). If the LDZ was built-up entirely from serpentinised peridotite (i.e. scenario 1) this would imply that OCC formation occurred entirely amagmatically (assuming that no melt is accreted to the hanging-wall during at least some part of the OCC life cycle, as shown by sidescan sonar data in *Section 3.4.2*; Figure 4.4.5a). Scenario 2, however, where the LDZ comprises melt intrusion into the footwall, suggests that magmatism persisted throughout OCC formation (Figure 4.4.5b). Given that peridotite, when serpentinised by ~50%, has a density of ~2900 kg/m^3 and is thus, in terms of gravity data, indistinguishable from gabbro (Escartin *et al.*, 2001), it is not possible to choose from these two scenarios from gravity modelling alone (note that '50%' serpentinisation is an average over the ~3 km thickness of the LDZ, and that in reality it probably grades from 75 – 100% at the surface – as shown by dredge results – to 0% at the base). However, based on deep-drilling results (Dick *et al.*, 2000; Kelemen *et al.*, 2004; Blackman *et al.*, 2006; Ildefonse *et al.*, 2007) and sampling of faults that cut deep into footwalls (MacLeod *et al.*, 2002; Reston *et al.*, 2002; Escartin *et al.*, 2003a) that recover predominantly gabbro beneath a thin veneer of serpentinised peridotite, it seems more likely that this LDZ comprises mainly gabbroic material with a small degree of serpentinised peridotite. As shown by Figure 4.4.4c-d, gabbroic material would have to extend for ~2 – 4 km beneath the dome of OCC1319 if it had a density of

2900±100 kg/m^3. This estimate seems reasonable given that ~1.4 km of predominantly gabbroic material was drilled beneath the dome of Atlantis Massif (the true thickness of the gabbroic sequence must thus be > 1.4 km).

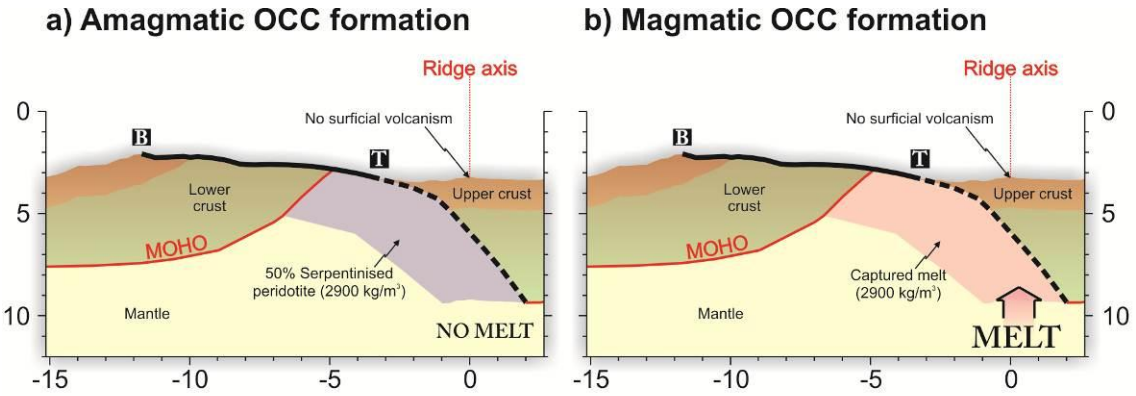


Figure 4.4.5a-b. Two possible models for OCC formation that give rise to the same gravitational anomaly. **a)** OCC formation is amagmatic and the LDZ in the footwall is formed by serpentinisation of mantle peridotite (purple) as seawater infiltrates along the detachment surface (solid black line and dashed black line at depth). **b)** melt persists throughout OCC formation and is captured and stored as gabbro in the footwall, forming the LDZ. Note that in both cases it is assumed there is no surficial volcanism. 'B' and 'T' mark breakaway and termination. Depth profile is across OCC1319.

4.4.2.2. OCC1330: Internal density structure (2.5D)

In Figure 4.4.6a-d a density model is set-up for OCC1330 using the same criteria as previously assumed for OCC1319. The main ambiguity with OCC1330 is that the breakaway ridge is poorly defined; hence I assume that the distinct topographic change at 44°56.1'W is the Moho (-6.5 km in Figure 4.4.6a-d). The long wavelength component of the RMBA is much weaker across OCC1330, and so it is only necessary to thin the crust by ~0.5 – 2 km to get a good match between observed and predicted anomaly on the older side of the OCC (Figure 4.4.6b). Changing the half-width of the anomalous material beneath the OCC greatly affects the predicted anomaly. For example, with a half-width of 2.5 km the mismatch in magnitude between observed and predicted anomaly is 10 mGal. This value becomes 20 mGal for a half-width of 4.25 km (which is the best approximation for the overall along-axis extent of OCC1330).

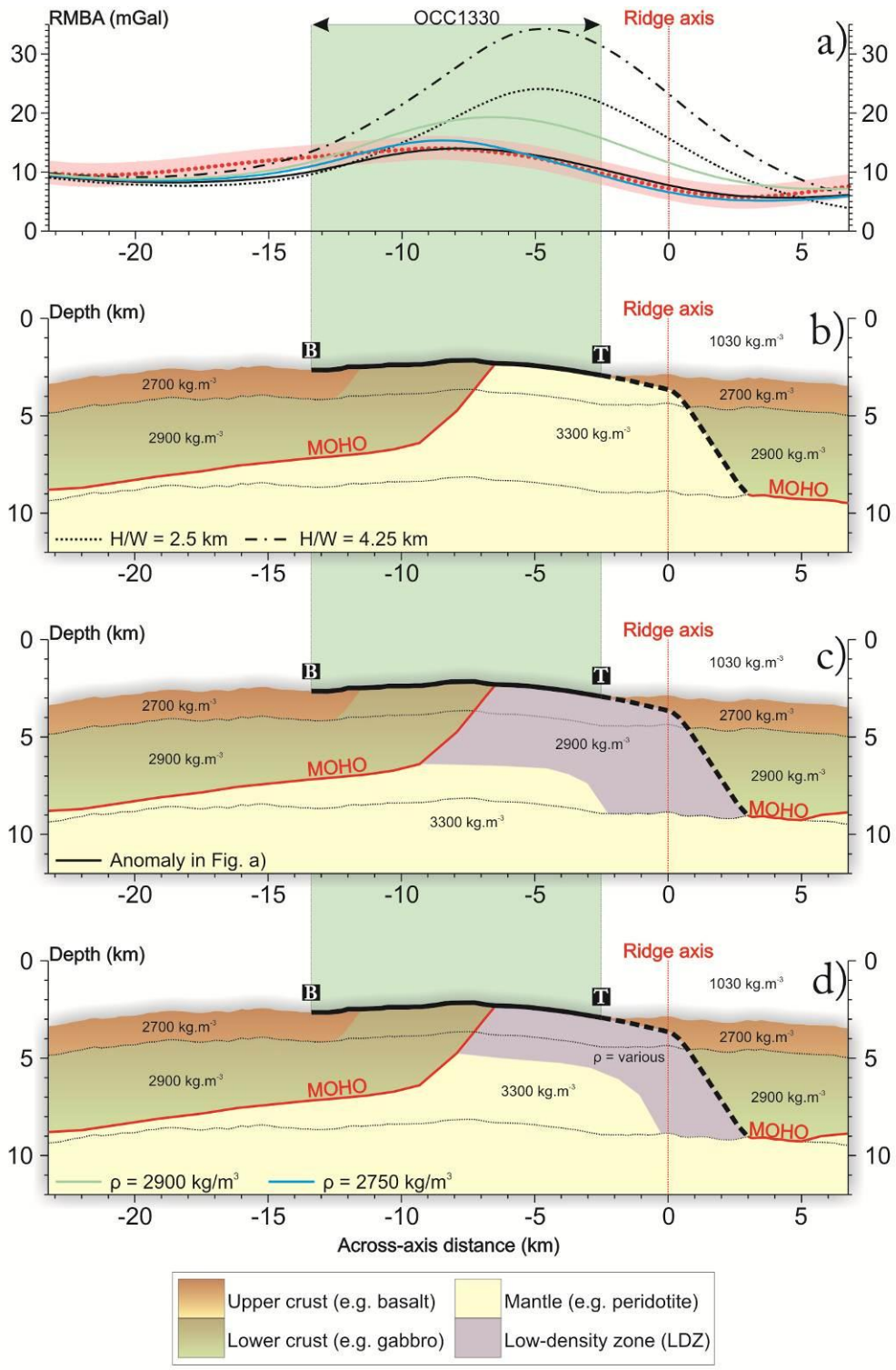


Figure 4.4.6a-d. Gravity models (2.5D) of OCC1330 internal mass distribution: **a)** observed anomaly data (red dots) are at 250 m intervals with ±2 mGal confidence limits indicated by pink shading, **b)** [dashed black lines in a)] starting model for a 3-layered crust, H/W is half-width of anomalous material between breakaway and detachment surface, **c)** [solid black line in a)] effect of introducing a low density zone into the footwall and **d)** [green and blue lines in a) - as shown in lower left of panel d)] the relationship between thickness of the LDZ and density. Heavy, solid black line is detachment surface exposed at surface, dashed black line is inferred location of detachment surface after deMartin *et al.* (2007). See text for discussion.

As with the 2.5D gravity model across OCC1319, the peak in the predicted anomaly is centred over the uplifted mantle material within the footwall (-5 km) and thus lies ~4 km to the east of the peak in the observed data. It is again possible to introduce a LDZ into the footwall to obtain a better match between the observed and predicted fields (Figure 4.4.6c). Note that as the original mismatch between observed and predicted anomaly in Figure 4.4.6a is ~7 mGal greater than the corresponding model for OCC1319 (8 mGal – Figure 4.4.4b), then the LDZ must be thicker (~4 – 5 km) if it is assumed to have the same density of 2900 kg/m^3 beneath OCC1330. If the LDZ comprises predominantly melt captured by the footwall, this increase in thickness may imply a local increase in melt supplied to the ridge axis during formation of OCC1330 compared with OCC1319. Alternatively, the LDZ may be thicker due to more extensive alteration of peridotite beneath the slightly older OCC at 13°30'N. If the thickness of the LDZ is decreased to ~3 km (i.e. the same as in Figure 4.4.4b), the density must be reduced to 2750 kg/m^3 to maintain a reasonable fit to the data (Figure 4.4.6d). The upward-inflection of the RMBA at the eastern-end of the profile (7 km) may be accounted for by having the Moho shoaling by ~300 – 400 metres towards the African plate, possibly due to tectonic thinning beneath the horst-like feature running N-S at 44°46'W, 13°31'N (bathymetry data: Figure 2.3.1a-b).

4.4.2.3. OCC1348: Internal density structure (2.5D)

The breakaway ridge of OCC1348 is well defined and hence it may be expected that it should be easy to predict the subsurface structure of the OCC. The model, however, is complicated by the OCC-related RMBA that extends well beyond the limits of the core complex in both the older and younger directions (*Section 4.4.1*). The termination location is also ambiguous due to the increased blanket of sediment cover, but this is tentatively identified from the sidescan sonar and bathymetry as being at ~10 km east of the ridge axis.

Figure 4.4.7a-d shows the expected mass distribution beneath OCC1348 with half-widths of 4.0 km and 2.5 km for anomalous material within the footwall. Assuming a crustal thickness of 6 km, the Moho lies ~7 km to the west of the breakaway. With a half-width of 4.0 km for the OCC, the predicted anomaly is ~23 mGal greater than the observed data (Figure 4.4.7b).

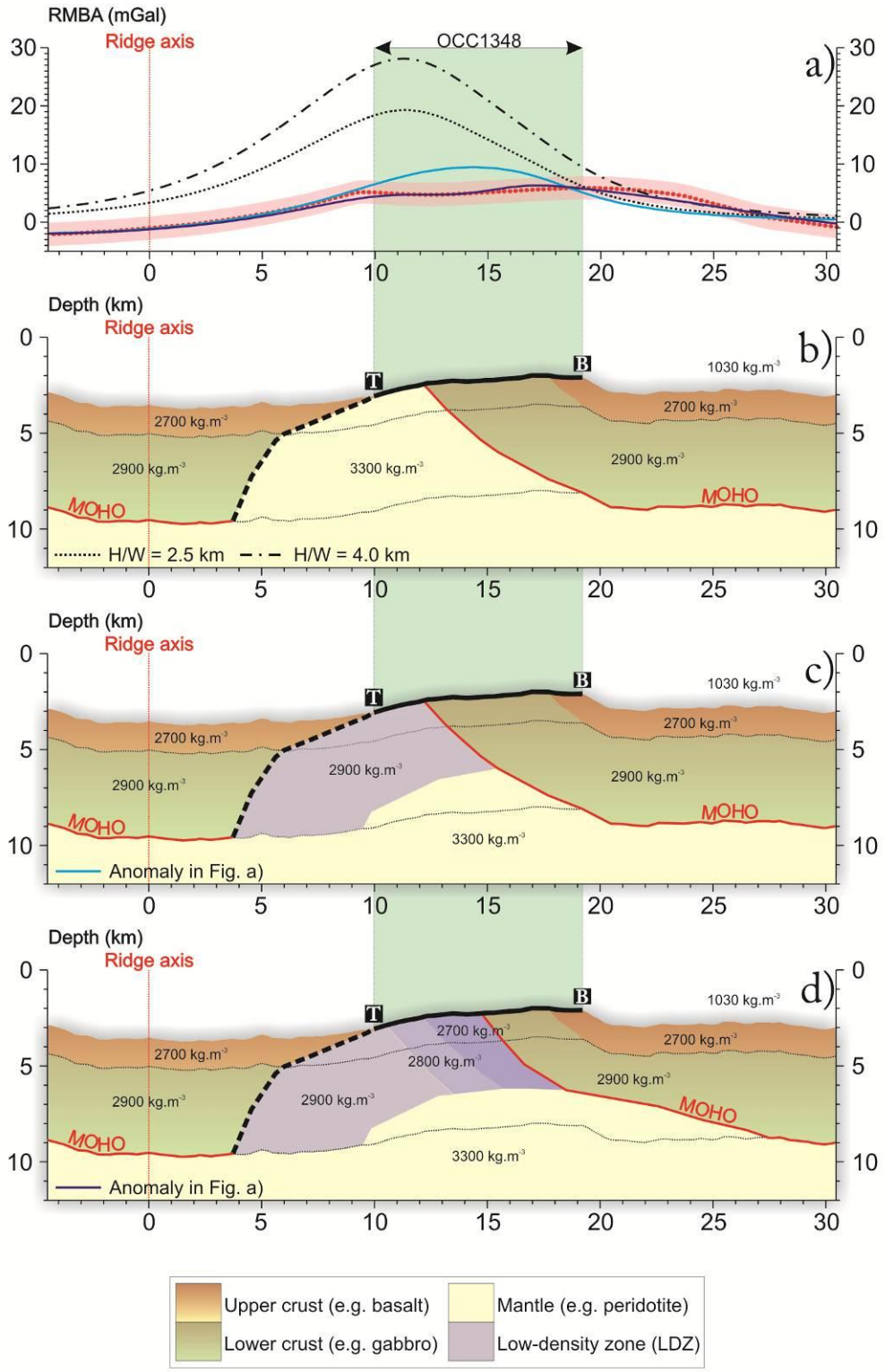


Figure 4.4.7a-d. Gravity models (2.5D) of OCC1348 internal mass distribution: **a)** observed anomaly data (red dots) are at 250 m intervals with ±2 mGal confidence limits indicated by pink shading, **b)** [dashed black lines in a)] starting model for a 3-layered crust, H/W is half-width of anomalous material between breakaway and detachment surface, **c)** [blue line in a)] effect of introducing a low density zone into the footwall and **d)** [purple line in a)] the mass deficit at 20 km can be accounted for by thinning the crust beneath the breakaway by ~2 km. The mass excess across the domal section can be attributed to a lateral density contrast in the footwall. Heavy, solid black line is detachment surface exposed at surface, dashed black line is inferred location of detachment surface after deMartin *et al.* (2007). See text for discussion.

As with the models across OCC1319 and OCC1330, this mismatch can be greatly reduced if a LDZ is introduced into the footwall (Figure 4.4.7c). However, the resultant model has a mass excess equating to ~5 mGal in the footwall at 14 km along the model profile, and a mass deficit of ~3 mGal at 20 – 23 km. The mass deficit can be accounted for by making the crust ~2 km thinner beneath the breakaway ridge and subsequently shifting the Moho by ~2 km to the east so that it is located at the boundary between upper massif and domal section – as determined in *Section 3.3.1.5*. Thinning the crust here is effectively the same process by which the long wavelength component of the RMBA is accounted for across OCC1319 and OCC1330 (Figure 4.4.4b and Figure 4.4.6b, respectively), with the exception that the across-axis extent of thinning is less beneath OCC1348 – extending for only 8 km beyond the breakaway region (Figure 4.4.7d). Progressive crustal thinning of this nature prior to OCC formation may reflect increasingly magma-poor conditions.

The mass excess across the dome of OCC1348 can be corrected for by reducing the density of the LDZ immediately beneath the Moho to 2700 – 2800 kg/m^3 (Figure 4.4.7d). A reduction in density in this area may result from the oldest part of the exhumed mantle having undergone the most pervasive serpentinisation (assuming density decreases at increasing levels of serpentinisation – Escartin *et al.*, 2001). By introducing this lateral density contrast in the footwall, the apparent double-peak in the RMBA can be accounted for, with very low density material creating a saddle-point in the predicted anomaly between higher-density material located beneath the breakaway and termination of the OCC. The increase in density towards the termination of the OCC may occur due to lower levels of serpentinisation on the younger part of the OCC, or an overall increase in gabbroic content compared with the older part of the dome to the east. This latter model is consistent with OCC termination by renewed magmatism at the ridge axis, as has been inferred from increased volcanic activity within the axial valley adjacent to OCC1348 (*Section 3.4.2*).

4.4.2.4. Linked detachment surfaces (2.5D)

Smith *et al.* (2008) and Schouten *et al.* (2010) propose a model for the 13°N region in which multiple OCCs may be linked along- and across-axis. This type of continuous fault model may account for up to 50% of oceanic lithosphere generation for a swathe

of seafloor south of the Kane FZ (Cann *et al.*, 2008), and may thus, if verified, mark a paradigm shift in the way in which it is believed oceanic crust is formed.

The basic model, applied to the 13°N region, implies that the group of ridges between 44°57.9'W and 44°59.1'W – previously interpreted as the breakaway to OCC1319 (e.g. -9 km to -15 km in Figure 4.4.4b-d) – are rider-blocks that have formed due to high-angle faults cutting through the hanging-wall and rooting into the OCC-forming detachment fault (Smith *et al.*, 2008). Hanging-wall-derived rider-blocks on OCC footwalls have also been proposed to explain the topographic and gravity signatures of Atlantis Massif (Blackman *et al.*, 1998). Figure 4.4.8a-d shows the expected subsurface density structure for such a model, with the ridge at 45°04.1'W (-22 km) forming the breakaway to OCC1319 (on the geological map this ridge has been interpreted as the breakaway location of OCC1319a – Figure 3.2.15a-b). As would be expected from the gravity modelling results presented in the previous sections: exposure of high-density mantle material at the seafloor causes the predicted anomaly to be > 10 mGals more than the observed data (red dashed line in Figure 4.4.8a, model is not shown). Introducing a 3 – 4 km thick LDZ (density: 2900 kg/m^3) into the footwall, analogous to a mixture of gabbro and/or serpentinised peridotite, removes this large density contrast at shallow depths and reduces the overall mismatch between the two anomalies (Figure 4.4.8b). The residual between the predicted and observed anomalies can be reduced even further if the LDZ within the older part of the footwall (i.e. -11 km to -22 km) increases in thickness by ~1 km relative to the LDZ immediately beneath the domal section (-3 km to -8 km; Figure 4.4.8c). Introducing a horizontal density gradient in which the older part of the footwall is less dense than the younger domal part would produce a similar effect without necessitating a thickness variation (as shown for OCC1348 in Figure 4.4.7d). As has been stated for OCC1348 (*Section 4.4.2.3*), a horizontal density contrast in which the older part of the footwall is less dense and/or thicker could be explained by increased weathering, more pervasive serpentinisation and/or temporal variations in magmatic accretion/footwall capture of melt.

Without independent estimates of crustal thickness or additional sampling sites to the west of the group of ridges between 44°57.9'W and 44°59.1'W, the ambiguous nature of gravity anomalies does not allow for preferential selection of an isolated- or linked-OCC model. This is readily demonstrated by Figure 4.4.8d, in which the long and short wavelength components of the RMBA are adequately modelled by two OCCs, rather than one continuous OCC at 13°19'N.

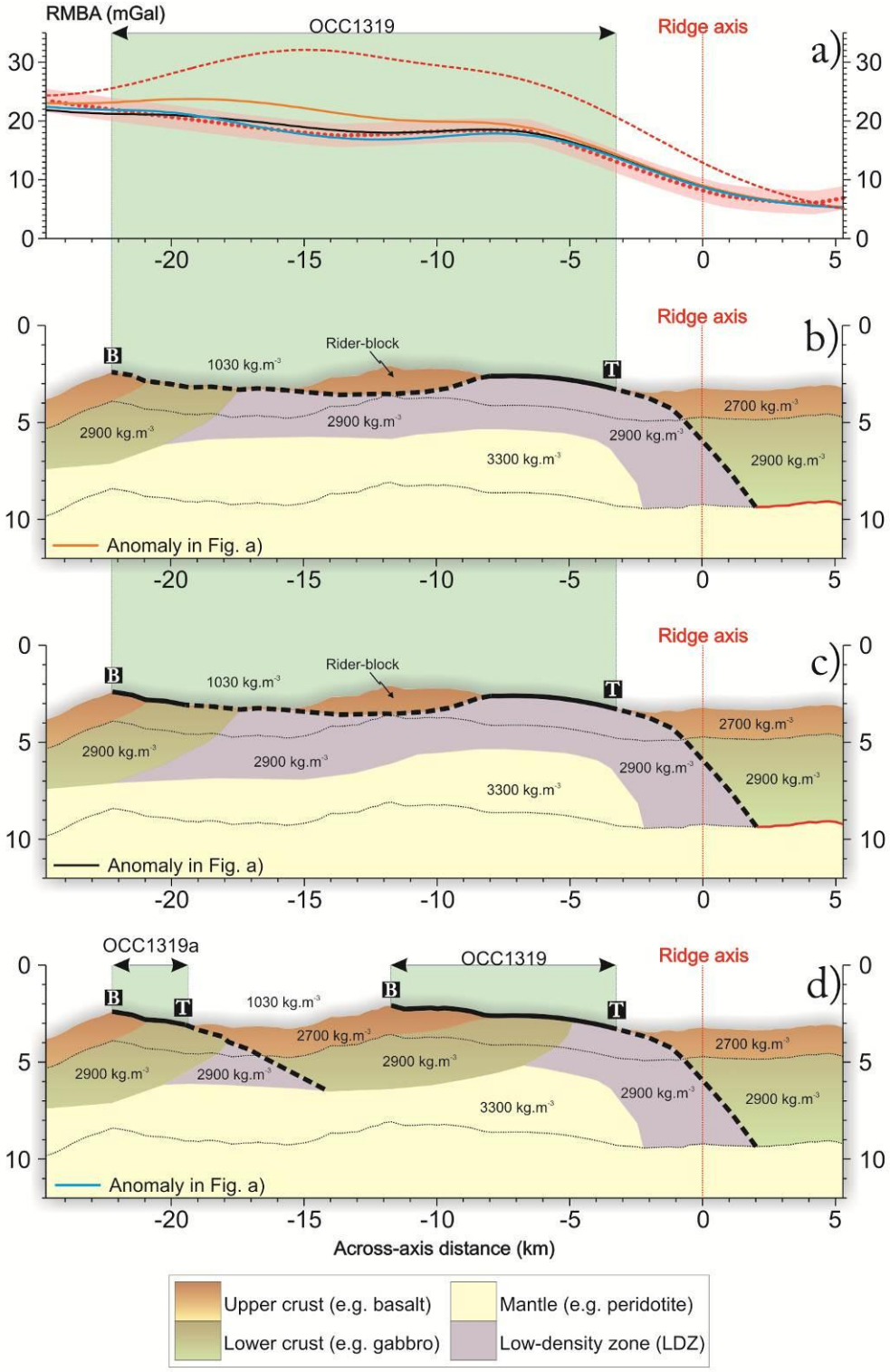


Figure 4.4.8a-d. Gravity models (2.5D) of linked detachment surfaces: **a)** observed anomaly data (red dots) are at 250 m intervals with ±2 mGal confidence limits indicated by pink shading, **b)** [orange line in a)] model assuming OCC1319 and OCC1319a are linked, with the ridge at -12 km forming part of a rider-block, **c)** [black line in a)] mass excess at -15 km to -20 km can be accounted for by thickening the LDZ by ~1 km beneath this area and **d)** [blue line in a)] the subsurface can also be interpreted as two isolated OCCs because there may not be sufficient density contrast between gabbro and serpentinised peridotite to distinguish between c) and d). Heavy, solid black line is detachment surface exposed at surface, dashed black line is inferred location of detachment surface at depth. See text for discussion.

4.4.3. Modelling of gravity anomalies (3D)

Modelling with *Gravmag*, whilst able to place some constraints on the mass distribution beneath OCCs, essentially involves trying to fit a 2D solution to a 3D problem. Hence, in this section I describe a method for accurately representing the expected mass distribution beneath OCCs in 3D. This method is then used to place further constraints on the density of the footwall, and also to examine effects of the subsurface shape of the footwall/hanging-wall boundary on predicted gravity anomalies.

At present, Blackman *et al.* (2008) have carried out the only fully-3D analysis of the gravity signature associated with an OCC (Atlantis Massif). In this study, 3D modelling has been conducted using a slight variation of the method of Blackman *et al.* (2008), which involved manipulation of bathymetry data using the `grdcontour` command in GMT (D. Blackman, *personal comm.*). The method used here relies on manually selecting areas of bathymetry data using the *Mirone* suite of programs in MATLAB (Luis, 2007). For example: using the 'extract profile' command in *Mirone* allows for a list of latitude/longitude pairs to be extracted for a particular area of interest (such as the expected basalt/gabbro transition beneath the domal section of an OCC). These pairs of coordinates can then be used to define a 'mask' which is applied to the bathymetry data (Point 1 – Figure 4.4.9).

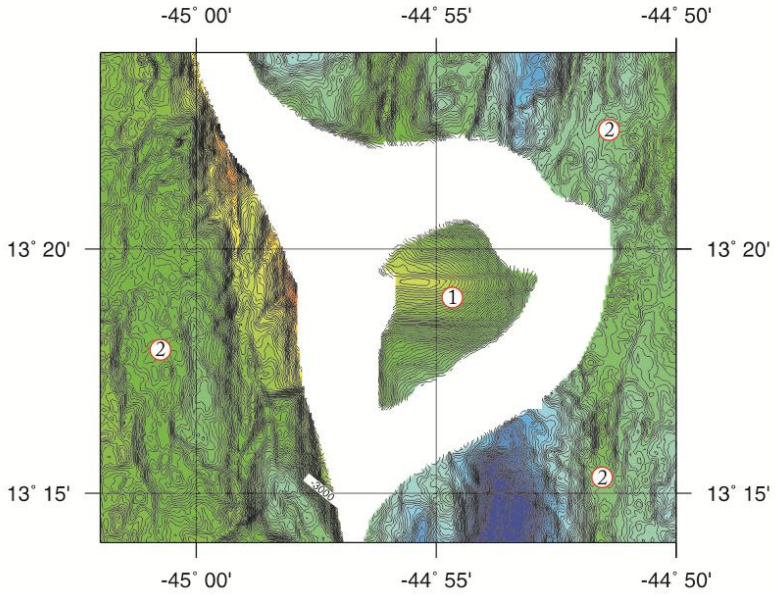


Figure 4.4.9. Manipulating bathymetry data to form an uneven, intra-crustal interface. The two GMT .grd files (numbered 1 and 2) are shifted vertically relative to each other. A surface-fitting algorithm then combines the grids to form the detachment surface (the angle of which can be varied by changing the gap (i.e. the white space) between the grids. Colour scale is the same as **Figure 2.2.2**.

By drawing a second mask that defines an area outside of which the intra-crustal interface is assumed to be at a 'normal' depth (Point 2 – Figure 4.4.9), the two individual grids can be shifted vertically relative to each other and then re-gridded to form an intra-crustal interface that represents the gabbro-cored nature of each OCC (Figure 4.4.10; see also Video 5 – Appendix II). The gap between the two grids and the tension parameter used for the surface-fitting algorithm in GMT can also be modified to alter the subsurface detachment geometry. The predicted anomaly for this new interface is then calculated using the method outlined in *Section 4.2.2*.

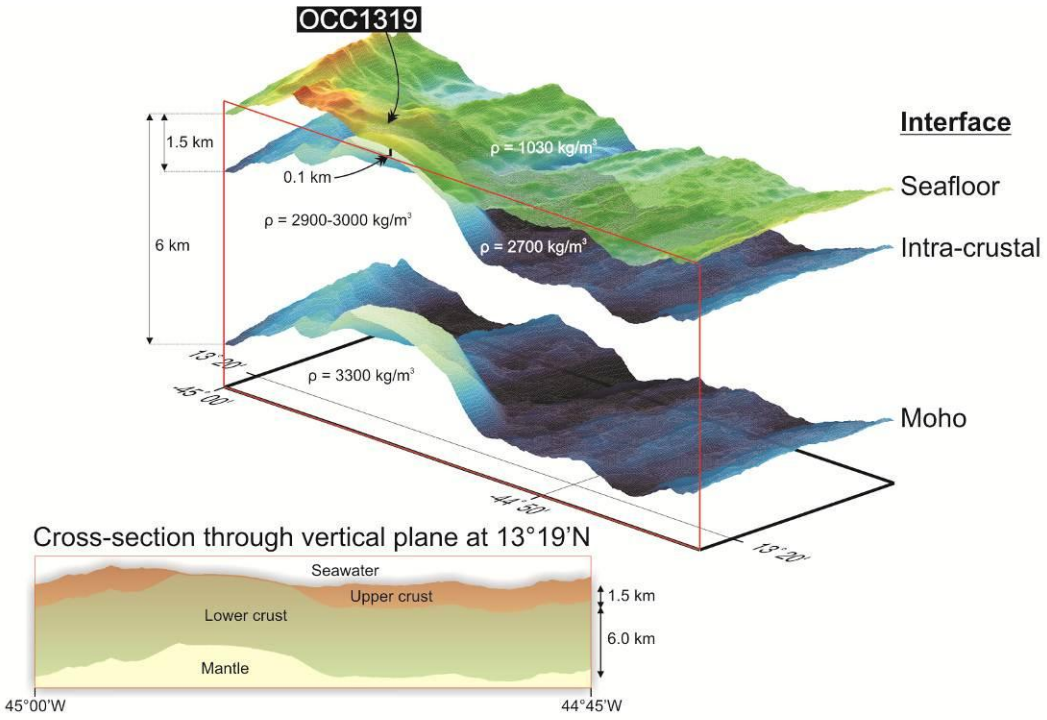


Figure 4.4.10. Crustal model used for forward modelling of gravity anomalies in 3D. The intra-crustal and Moho interfaces are parallel with each other (but not to the seafloor) and have a combined density contrast of 600 kg/m^3. In the model shown here: the intra-crustal interface shoals to a depth of 100 metres beneath the seafloor under the dome of the OCC and is at a depth of 1.5 km everywhere else. The Moho has a mean far-field depth of 6 km beneath the seafloor.

Blackman *et al.* (2008) state that when calculating the RMBA in the presence of OCCs, positioning the Moho interface at a depth of 6 km is entirely arbitrary (as detachment tectonics are expected to dramatically thin the crust). Hence, rather than using the RMBA as the observed anomaly, it is advisable to use the FAA minus the seafloor attraction and thermal anomaly (Figure 4.4.11). Adopting this method, I

calculate the combined attraction of two interfaces – one each for the intra-crustal (upper/lower crust) and Moho (lower crust/mantle) interfaces and compare this with the observed anomaly. Each 3D model has the overall design shown in Figure 4.4.10, with Table 4.4.2 providing a summary of relevant parameters. The intra-crustal and Moho interfaces are parallel with each other, but are uneven with respect to the seafloor; the Moho is assumed to have the same topography as the intra-crustal interface, but lie at a far-field depth of 6 km beneath the seafloor. In all models, the sum of the density contrasts at the intra-crustal and Moho interfaces is 600 kg/m^3. In addition to this, simultaneously modelling the long and short wavelength components of the RMBA (*Section 4.4.1*) is too complex to be conducted in 3D, hence GMT's `grdtrend` command has been used to remove a planar trend from the data and thus isolate the short wavelength component of the observed anomaly (specified by –N3 in `grdtrend`; Figure 4.4.11). The long wavelength component is assumed to form by thinning of the crust by up to ~2 km on the older side of each OCC (*Section 4.4.2.1-3*).

Model/OCC	$\Delta\rho$ intra-crustal	$\Delta\rho$ Moho	Depth to intra-crustal interface beneath dome of OCC	Far-field depth to intra-crustal interface	High density OCC 'core' extent	Range of residual (mGal)		RMS misfit (mGal)
						Min	Max	
G3D_1_1319	200 kg/m^3	400 kg/m^3	0.1 km	1.5 km	From sonar	1.5	3.9	0.39
G3D_1_1330	200 kg/m^3	400 kg/m^3	0.1 km	1.5 km	From sonar	-1.8	3.1	0.18
G3D_1_1348	200 kg/m^3	400 kg/m^3	0.1 km	1.5 km	From sonar	-4.7	3.8	0.46
G3D_2_1319	300 kg/m^3	300 kg/m^3	0.1 km	1.5 km	From sonar	0.9	3.9	0.28
G3D_2_1330	300 kg/m^3	300 kg/m^3	0.1 km	1.5 km	From sonar	-2.8	3.0	0.24
G3D_2_1348	300 kg/m^3	300 kg/m^3	0.1 km	1.5 km	From sonar	-6.4	3.8	0.61
G3D_3a_1348	200 kg/m^3	400 kg/m^3	0.2 km	1.5 km	From sonar	-4.2	3.8	0.40
G3D_3b_1348	200 kg/m^3	400 kg/m^3	0.3 km	1.5 km	From sonar	-3.9	3.8	0.36
G3D_4a_1319	200 kg/m^3	400 kg/m^3	0.1 km	1.5 km	Variable	0.5	3.4	0.21
G3D_4b_1319	200 kg/m^3	400 kg/m^3	0.1 km	1.5 km	Variable	-0.5	3.2	0.16

Table 4.4.2. Summary of 3D gravity models. In each case, the density of seawater and the upper crust are assumed to be 1030 kg/m^3 and 2700 kg/m^3, respectively, and the Moho is assumed to be parallel to the intra-crustal interface and lie at a far-field depth of 6 km beneath the seafloor. Range of residual and RMS misfit are calculated for the geographic extent of the OCC detachment surface in the model (grey shaded areas in Figures 4.4.12-15) and are used to assess degree of fit.

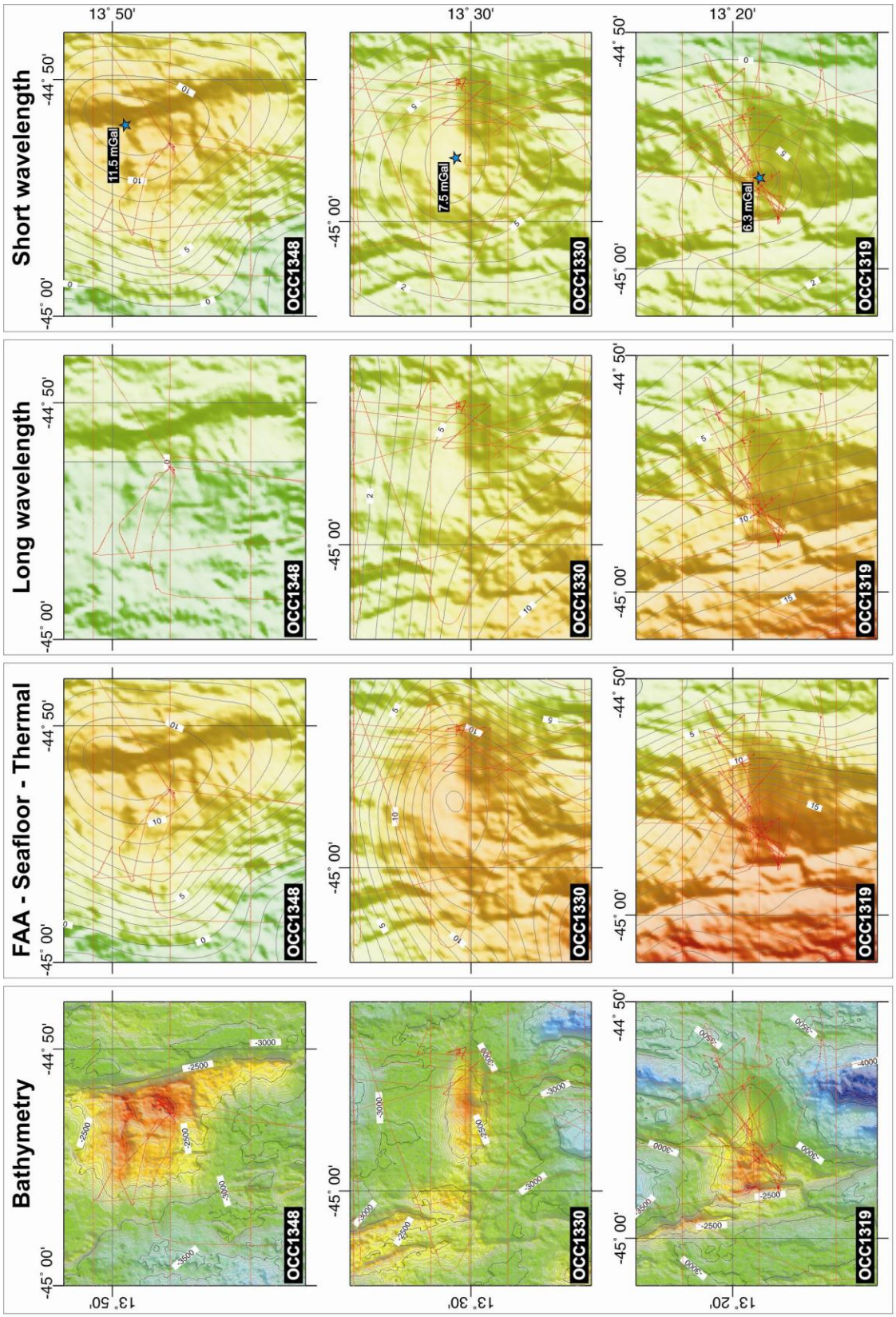


Figure 4.4.11. Observed FAA minus seafloor and thermal anomalies across the three near-axis OCCs. Data are separated into long and short wavelength components using GMT's `grdtrend` command as it is difficult to simultaneously model both fields using the 3D forward modelling method. Colour scale and contours are the same as **Figure 4.4.3a-b**. Blue stars mark peaks in short-wavelength anomalies.

4.4.3.1. Internal structure of near-axis OCCs (3D)

Figure 4.4.12 shows the predicted anomalies for a 3D model (G3D_1) of the subsurface beneath each near-axis OCC. The model has been designed so that the shallow, 100 metre deep section of the intra-crustal interface coincides exactly with the footwall/hanging-wall boundary (as identified with the sidescan sonar and indicated by the red, dashed line over the bathymetry data in Figure 4.4.12). The point at which the intra-crustal interface is at a depth of 1.5 km is chosen so that detachment surface (grey shading within blue, dashed line) on the younger, axial-proximal side of the OCC has a dip similar to that which is observed at TAG (i.e. it dips at ~20° towards the ridge axis; deMartin *et al.*, 2007). In this model, the density contrasts across the intra-crustal and Moho interfaces are 200 kg/m^3 and 400 kg/m^3, respectively, with the anomaly for each interface added together to give the total predicted anomaly (which is subsequently subtracted from the observed data to give the residual shown in Figure 4.4.12).

The peak anomaly in the observed data (which is the FAA with the attraction of the water column, upper crust, thermal model and long wavelength component removed) is 6.3 mGal, 7.5 mGal and 11.5 mGal across OCC1319, OCC1330 and OCC1348, respectively (blue stars in Figure 4.4.12). For all near-axis OCCs, this peak is located towards the older part of the OCC: across the domal section/upper massif boundary for OCC1319 and OCC1330 and over the breakaway ridge for OCC1348. In comparison, the predicted anomaly for the 3D model set-up has a maximum of 3.8 mGal, 8.5 mGal and 13.5 mGal for the near-axis OCCs (yellow stars in Figure 4.4.13). The peaks in observed and predicted anomalies across OCC1319 coincide almost exactly, suggesting that the centre of mass for the high density core in the 3D model is accurately positioned. This is not the case for the two OCCs to the north, with the peak in the predicted anomalies occurring ~2.9 km east and ~3.5 km west of the peak in the observed anomaly for OCC1330 and OCC1348, respectively.

In general, there is a good fit between the observed and predicted anomalies for each OCC. For example, across OCC1319 the residual over the extent of the OCC's detachment surface varies between ~1.5 – 3.9 mGal and has an RMS misfit of 0.39 mGal; the maximum mismatch (~4.5 mGal) occurs in the SE part of the plot in Figure 4.4.12, which is probably due to slight crustal thickness variations beneath the ridge axis that are not accounted for in the 3D model.

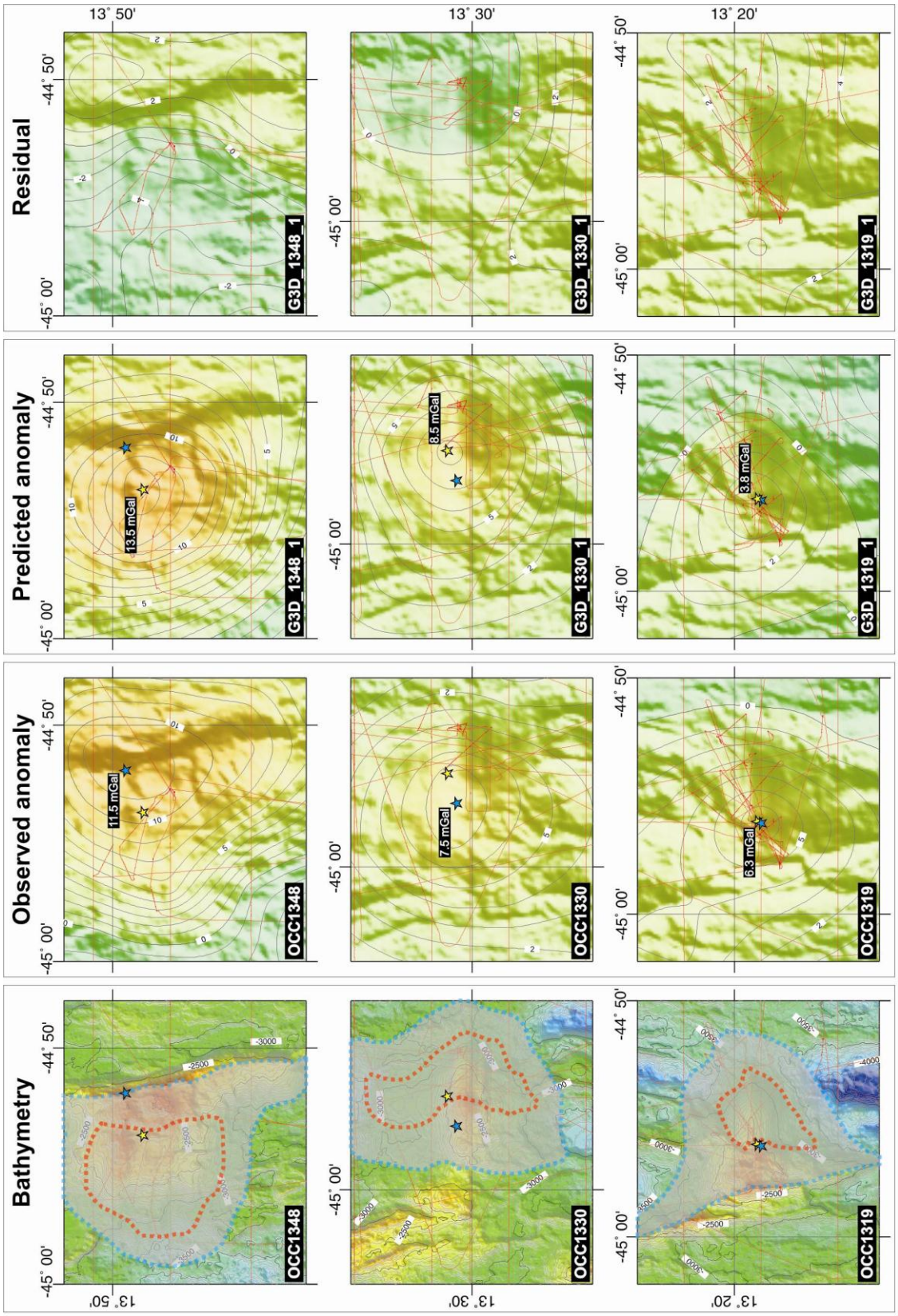


Figure 4.4.12. Observed, predicted and residual 3D gravitational anomaly for model G3D_1. Density contrast at intra-crustal and Moho interface is 200 kg/m^3 and 400 kg/m^3, respectively. Blue stars mark peaks in observed anomaly, yellow stars mark peak in predicted anomaly. Colour scales and contours are the same as **Figure 4.4.10**. Observed anomaly is short wavelength anomaly from **Figure 4.4.11**. See text for discussion.

The residual across OCC1330 is slightly greater than that which is observed across OCC1319 and varies between ~-1.8 – 3.1 mGal with an RMS misfit 0.18. This increased residual range most likely occurs due to the predicted centre of mass of the footwall beneath OCC1330 being slightly misplaced, with the shallow portion of the intra-crustal interface actually extending further west than has been assumed in Figure 4.4.12. OCC1348 displays the greatest variation in residual, which is ~-4.7 – 3.8 mGal (RMS misfit: 0.46) across the dome and upper massif of the OCC. This high mismatch may occur by assuming that the shallow portion of the intra-crustal interface (red dashed line in Figure 4.4.12) extends to 44°58'W.

Changing the density contrast across the intra-crustal and Moho interfaces to 300 kg/m^3 (with the overall density contrast from upper crust to mantle remaining the same) can account for an increase of up to ~1.3 mGal in the predicted anomaly across OCC1319 (model G3D_2 – Figure 4.4.13). This slightly improves the fit between observed and predicted anomalies over the OCC (RMS misfit: 0.28 mGal), although the overall residual range for the model is approximately the same (residual range: 0.9 – 3.9 mGal). For the same partitioning of density contrasts in the subsurface: OCC1330 and OCC1348 are less well-modelled (the RMS misfit has increased from 0.18 to 0.24 mGal for OCC1330 and from 0.46 to 0.61 mGal for OCC1348). This is because the peaks in their respective predicted anomalies have increased further (they were already greater than the peak in observed data when the intra-crustal and Moho interfaces had density contrasts of 200 kg/m^3 and 400 kg/m^3, respectively). Hence, it would be expected that to decrease the residual across OCC1330 and OCC1348 it would be necessary to decrease the density contrast of the intra-crustal interface (for example from 200 kg/m^3 to 100 kg/m^3) and subsequently increase the density contrast at the Moho (from 400 kg/m^3 to 500 kg/m^3). This is consistent with the 2.5D modelling, which showed that the LDZ within the footwalls of OCC1330 and OCC1348 had to be thicker (or of lower density) relative to OCC1319 to match the observed data. As stated in *Section 4.4.2.2*: this apparent decrease in density may reflect prolonged serpentinisation of peridotite beneath the older OCCs (which may increase temporally and also be enhanced by the increase in faulting and degradation of the footwall observed on older OCCs – *Section 3.3.1.4-5*). Mechanical weathering has also been proposed for progressively lowering the density of older OCCs that flank the Atlantis FZ (Blackman *et al.*, 2008).

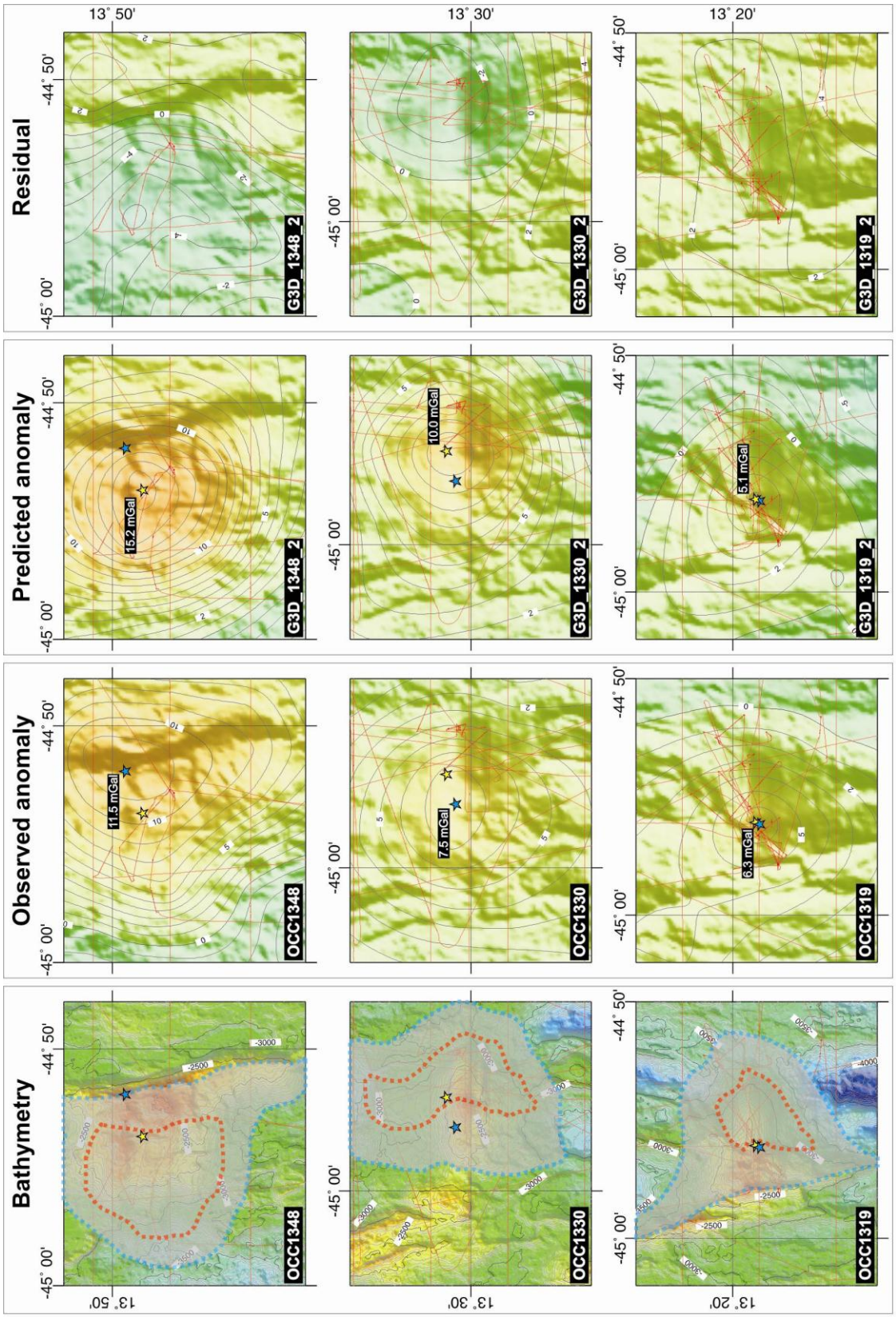


Figure 4.4.13. Observed, predicted and residual 3D gravitational anomaly for model G3D_2. Density contrast at both intra-crustal and Moho interfaces is 300 kg/m^3. Blue stars mark peaks in observed anomaly, yellow stars mark peak in predicted anomaly. Colour scales and contours are the same as **Figure 4.4.10**. See text for discussion.

Cannat *et al.* (2009) suggest that as an OCC becomes older, gabbro intrusions into the footwall become stronger and cause the OCC to become more rigid and subsequently cease extension. It may therefore be expected that cooling of melt within the footwall and the associated rheological changes cause the overall density of older OCCs to increase, but based on modelling results in the 13°N region it appears that increased faulting and/or serpentinisation of the footwall counteract this and reduce the overall density. Note, however, that without additional constraints on the thickness of materials in the footwall, inferring the absolute density is inherently ambiguous.

The variation in subsurface density distribution between near-axis OCCs in the 13°N region can be further demonstrated by increasing the depth to the intra-crustal interface beneath the dome of each OCC. In previous models this value has been 100 metres (as shown in Figure 4.4.10). Figure 4.4.14 shows the effect of increasing this value to 200 and 300 metres beneath OCC1348 – effectively simulating a greater thickness of low density, highly fractured and serpentinised material on the upper part of the domal section (model G3D_3). Increasing the thickness by 100 and 200 metres progressively reduces the peak of the predicted anomaly by up to ~1.4 mGal so that it more accurately matches the observed data. For example, the RMS misfit decreases from 0.46 mGal when the low density zone is 100 metres thick to 0.40 mGal and 0.36 mGal when the thickness of the LDZ is increased to 200 metres and 300 metres, respectively.

In addition to vertical density changes within the footwall, it is possible that uncertainties in the along- and across-axis shape of the core of each OCC may account for some of the residual anomaly (thus eliminating the need for older OCCs to apparently be less dense at shallow depths). For example, increasing the overall volume of the core beneath OCC1319 increases the predicted anomaly in a similar fashion to varying the half-width of polygons in the 2.5D modelling stage (model G3D_4 – Figure 4.4.15). By altering the across-axis extent of the shallow, high density zone by a few kilometres so that it extends beneath the upper massif, the predicted anomaly increases from ~3.8 mGal to ~6.5 mGal, thus reducing the residual anomaly. It may therefore be expected that decreasing the volume of the high density core beneath OCC1330 and OCC1348 should improve the match between predicted and observed anomalies in those regions without having to reduce the density of the core (as has been shown in Figure 4.4.14).

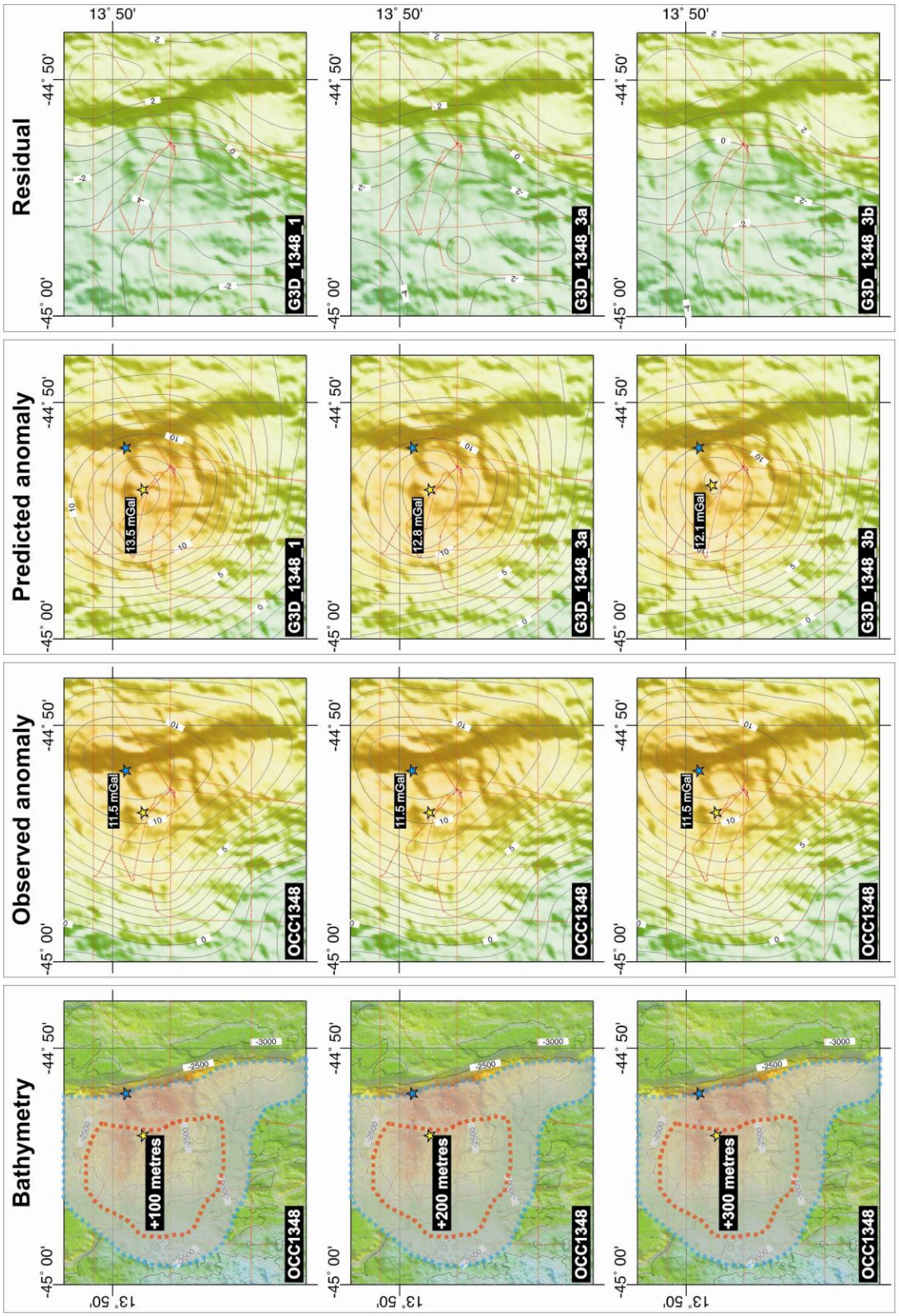


Figure 4.4.14. Observed, predicted and residual 3D gravitational anomaly for model G3D_3 beneath OCC1348. Density contrasts at intra-crustal and Moho interfaces are 200 kg/m^3 and 400 kg/m^3, respectively. The depth to the intra-crustal interface beneath the domal section is indicated in the bathmetry panel. Blue stars mark peaks in observed anomaly, yellow stars mark peak in predicted anomaly. Colour scales and contours are the same as **Figure 4.4.10**. See text for discussion.

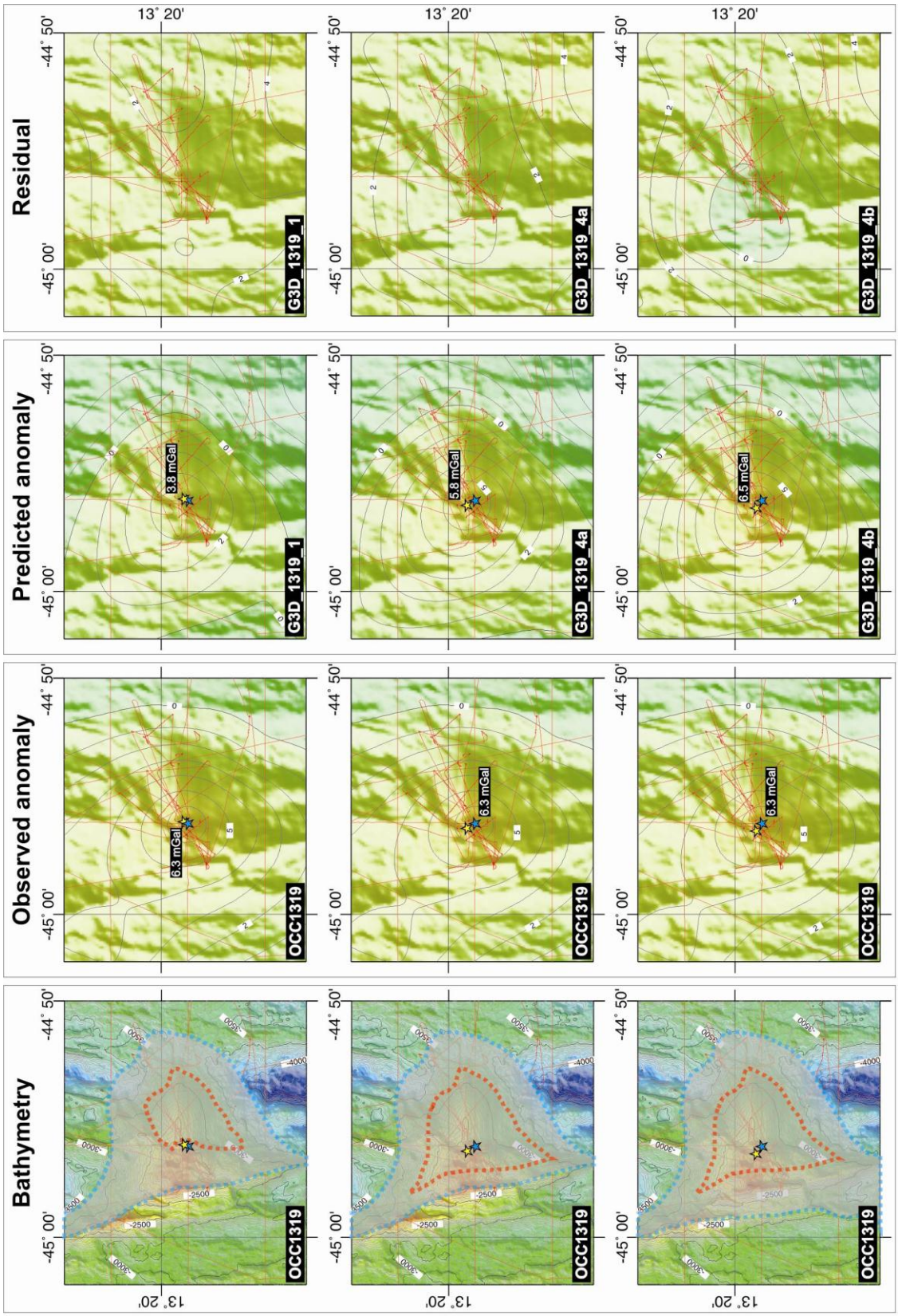


Figure 4.4.15. Observed, predicted and residual 3D gravitational anomaly for model G3D_4 beneath OCC1319. Density contrasts at intra-crustal and Moho interfaces are 200 kg/m^3 and 400 kg/m^3, respectively. The extent of the intra-crustal interface beneath the domal section is indicated in the bathmetry panel. Blue stars mark peaks in observed anomaly, yellow stars mark peak in predicted anomaly. Colour scales and contours are the same as **Figure 4.4.10**. See text for discussion.

However, reducing the along- and across-axis extent of the high density core of these OCCs so that they no longer coincide with the footwall boundaries detected with the sidescan sonar is essentially the same process as making the LDZ more extensive, and thus the overall relationship between LDZ extent and OCC age remains the same.

4.4.4. Gravity modelling: Summary

2.5D and 3D modelling of gravity data show that the footwalls of OCCs in the 13°N region contain a zone of low density material immediately beneath the surface of their domal sections (low density relative to where it might be expected that high density mantle material outcrops on the seafloor). For a density of 2900 kg/m^3, the LDZ must be ~3 – 4±1 km thick beneath OCC1319 and ~4 – 5±1 km thick beneath OCC1330 and OCC1348. Without additional data constraints, it is possible that the density of the LDZ may be decreased if it is assumed to be thinner, and *vice versa*.

A LDZ may form in the footwall by either: 1) serpentinisation of unroofed mantle material, 2) melt accumulation in the footwall, or 3) a combination of these processes. I favour the latter as this is the only model that can potentially explain the observed gravity anomalies and also the sampling results, which show that serpentinised peridotite is exposed at the seafloor (*Section 3.2.2*) and gabbro is abundant within the core of OCCs (e.g. Dick *et al.*, 2000; MacLeod *et al.*, 2002; Reston *et al.*, 2002; Escartin *et al.*, 2003a; Kelemen *et al.*, 2004; Blackman *et al.*, 2006; Ildefonse *et al.*, 2007). This model implies that OCCs form magmatically (as has been suggested by, e.g. Buck *et al.*, 2005; Behn & Ito, 2008; Tucholke *et al.*, 2008; MacLeod *et al.*, 2009), rather than amagmatically.

2.5D and 3D data modelling suggest that the LDZ may be more extensive beneath older OCCs. It is possible that this reflects a greater depth and/or degree of serpentinisation, or a greater accumulation of melt within the footwalls of older OCCs. Regarding the latter, for example, Grimes *et al.* (2008) calculate that the footwall of Atlantis Massif may accrete an ~10 metre thick layer of magma every ~1000 years. Applying this rate of accretion to the near-axis OCCs in the 13°N region (OCC durations: Table 3.3.1) would suggest that the LDZ may be ~1.5 km thicker beneath OCC1348 than it is beneath OCC1319, which is of similar magnitude to the thickness estimates made from gravity modelling in this chapter.

4.5. Chapter summary

In this chapter, FAA gravity data have been reduced to the RMBA. In addition to the findings based on sidescan sonar data in the previous chapter, the gravity data reveal a number of insights into the spatial and temporal variability of melt supply in a magma-poor environment, and can be used to assess the internal structure of OCCs. In summary:

Regional crustal structure, inferred melt supply & asymmetry

- The zones of abyssal hills identified in the previous chapter show a good correlation with areas of thicker crust. Similarly, the areas in which multiple OCCs have been identified show an RMBA high, consistent with thin crust (~1.2 km thinner than at the ridge axis) and the presence of high density material near the surface (*Sections 4.3.1-2*).

- Thin crust suggests that magmatic accretion has been relatively low across the SW-quadrant of the survey area compared with conjugate areas. As each OCC exhibits an RMBA high, this further suggests that individual OCCs are associated with a local, temporal decrease in magmatism below the regional average (*Section 4.3.3*).

- There are a number of circular lows in the RMBA centred on the ridge axis. These types of anomaly may be created by localised, temporally unstable/mobile zones of melt emplacement. They are generally between the locations of near-axis OCCs and do not match the location of the neovolcanic ridge axis, suggesting a recent shift in the locus of melt emplacement (*Section 4.3.4*).

- Strong, across-axis asymmetry in the RMBA matches the pattern of tectonic strain discussed in the previous chapter, with larger, more widely spaced faults rooting in thinner crust (*Section 4.3.1*).

Internal structure of OCCs

- RMBA profiles across near-axis OCCs are remarkably similar to those which have been observed across Kane Massif (Tucholke *et al.*, 1998) and FUJI Dome (Searle *et al.*, 2003). OCCs on the SA plate are associated with a local increase in RMBA

superimposed on a longer-wavelength regional trend that may result from thinner crust on the older side of the breakaway (*Section 4.4.1*).

- For a simple, three-layered crustal model in which the subsurface detachment geometry is assumed to be the same as that which has been seismically imaged at TAG (deMartin *et al.*, 2007), the mantle should be exposed at the surface for each near-axis OCC in the 13°N region. If the exposed mantle has a density of 3300 kg/m^3, the predicted gravity anomaly greatly mismatches the observed anomaly by several tens of mGal (*Sections 4.4.2.1-3*).

- It is possible to fit observed gravity anomalies with models in which a low density zone (LDZ) in the footwall counteracts the effect of high density mantle material. The extent and magnitude of the LDZ may be controlled by a combination of mantle serpentinisation, melt emplacement and mechanical weathering of material within the footwalls of OCCs (*Sections 4.4.2-3*).

- Lack of additional constraints on crustal structure and the inherently ambiguous nature of gravity anomalies does not allow discrimination between an isolated- or linked-OCC model (*Section 4.4.2.4*).

In the following chapter, I use deep-towed magnetic data to further assess regional variability in melt emplacement. Identification of geomagnetic polarity reversals also allows for the regional spreading rate and asymmetry to be calculated, and for the spreading history of OCCs in the 13°N region to be reconstructed.

Chapter Five

Spreading history from magnetic anomalies

5.1. Introduction

In the previous chapters, I have used sidescan sonar and gravity data to constrain magmatic accretion processes and oceanic core complex structure on the MAR at 13°N. Magnetic data can also be used to provide a record of the history of magmatism along the ridge axis, with the identification of magnetic reversal anomalies allowing for the rate of plate separation and sense of asymmetry to be quantified (the principle of which was discussed in *Section 1.2.5*). The internal structure of OCCs and history of melt emplacement at the ridge axis can also be inferred from magnetic anomalies. These topics, including an overview of the 2D and 3D inversion procedures applied to the magnetic total field data, form the basis of this chapter.

5.2. Interpretative methods – magnetic data

5.2.1. Inversion of magnetic anomalies

The irregular shape of the seafloor causes marine magnetic data to contain large topographic anomalies that mask more important signals (Parker & Huestis, 1974). Hence, it is desirable to remove this topographic effect so that rock magnetisation intensities can be calculated. Parker & Huestis (1974) expand upon the method of Parker (1972) (which is described in *Section 4.2.1*) to formulate a Fourier technique for calculating a magnetisation solution in the presence of complex topography. The method assumes that the magnetic source (the basaltic layer of oceanic crust, for example) is confined to an irregular layer of constant thickness h_o with an upper interface defined by $z = h(x)$. The source magnetisation of amplitude $M(x)$ is assumed to have constant direction $\hat{M}_0$. The observed magnetic anomaly, A, measured on a level

line at z_0 above the topography is thus related to the magnetisation (whose intensity is allowed to vary horizontally) as follows (5.1):

$$f[A] = \frac{1}{2}\mu_0 \exp(-|k|z_0)\left[1 - \exp(-|k|h_0)\right]V(k)\sum_{n=0}^{\infty}\frac{|k|^n}{n!} f\left[M(x)h(x)^n\right]$$

$$\text{Where: } f[A] = \int_{-\infty}^{\infty} dx \exp(ikx)A(x),$$

$$\text{And: } V(k) = \hat{B}_0(\hat{z} + i\hat{x}k/|k|)\hat{M}_0(\hat{z} + i\hat{x}k/|k|),$$

(**5.1**)

Where k is the wavenumber, f [] is the Fourier transform and $\hat{B}_0$ is a unit vector in the direction of the ambient geomagnetic field. For practical application to marine magnetic surveys, (5.1) may be rearranged to form an inversion procedure by moving the $n = 0$ component to the left side, giving (5.2):

$$f[M] = \frac{f[A]\exp(|k|z_0)}{(\mu_0/2)\left[1 - \exp(-|k|h_0)V(k)\right]} - \sum_{n=1}^{\infty}\frac{|k|^n}{n!} f\left[Mh^n\right]$$

(**5.2**)

A magnetisation solution is then attained by making an initial estimate of M (usually $M \equiv 0$) for the summation of (5.2) and calculating $f[M]$, which is then substituted back into the right side of (5.2) until the solution converges (Parker & Huestis, 1974). As with the upward continuation process discussed in *Section 2.6.1.4*, the robustness of the method is improved by filtering the solution after each iteration so as to reduce the amplification of high wavenumber components by the summation (which subsequently smoothes the data and eliminates relatively short wavelength signals). In the following section I will discuss the implementation of (5.2) and consider the non-unique nature of the solution.

5.2.2. Magnetisation solutions

Magnetisation solutions have been calculated in 2D and 3D using the MATLAB programs *inv2d* and *inv3d*, which were kindly provided by M. Tivey (*personal comm.*). 2D solutions (Figure 5.2.1) were computed using the magnetic total field profiles shown

in Figure 2.6.14 (at 10 metre resolution, with each profile having been upward continued to the minimum depth of TOBI during the profile) and by assuming a magnetic source layer thickness of 0.5 km whose upper surface was bounded by the seafloor (i.e. sediment cover was assumed to be negligible across the entire survey area). Data were bandpass filtered between wavelengths of 55 km and 2 km to ensure convergence of equation (5.2); the upper filter cut-off was chosen to avoid spatial aliasing of long wavelength components of the magnetic field which may arise due to the assumed periodicity of the FFT (the average length of deep-towed profiles was ~55 km), and the short wavelength filter was chosen as it was found that at wavelengths < 2 km the signal became overly noisy. Magnetic skewness (i.e. spatial asymmetry) arises when the ambient field is at an angle to magnetisation boundaries. This causes anomalies to become transposed from their source (which is heightened in the 13°N region by the low latitude of the survey), and is thus corrected for by the *V(k)* term in equation (5.1) and (5.2), where it is assumed that the geomagnetic field inclination and declination across the survey area are 21.6° down and 17.4°W, respectively.

Magnetisation solutions are inherently non-unique and are largely dependent on the starting choice of h_0. For example, if the assumed thickness of the layer is decreased, the calculated magnetisation must increase so that the layer generates the same magnetic anomaly, and *vice versa*. Another measure of this non-uniqueness is that of the magnetic annihilator. The magnetic annihilator is the magnetisation distribution that, when convolved with the topography, produces no external field (Parker & Huestis, 1974). Subsequently, any amount of magnetic annihilator can be added or subtracted from the magnetisation solution without invalidating the inversion procedure. In general, sufficient annihilator is applied to balance the positive and negative magnetisation amplitudes of the Brunhes and Matuyama reversals, respectively. However, this method can be ambiguous due to the Brunhes anomaly being constructed by younger, and hence more highly magnetised material, than the surrounding seafloor (*Section 1.2.5*). Thus it is more appropriate to balance the amplitude of magnetic anomaly C2n with that of the Matuyama reversal (Tivey *et al.*, 2003). Using this criterion, it was found that no magnetic annihilator had to be added to the magnetisation solution (Figure 5.2.1).

Figure 5.2.2 shows the magnetisation calculated across the entire survey area using *inv3d* for a 0.5 km thick magnetic source layer. The corresponding total field anomaly is shown in Figure 2.6.13a.

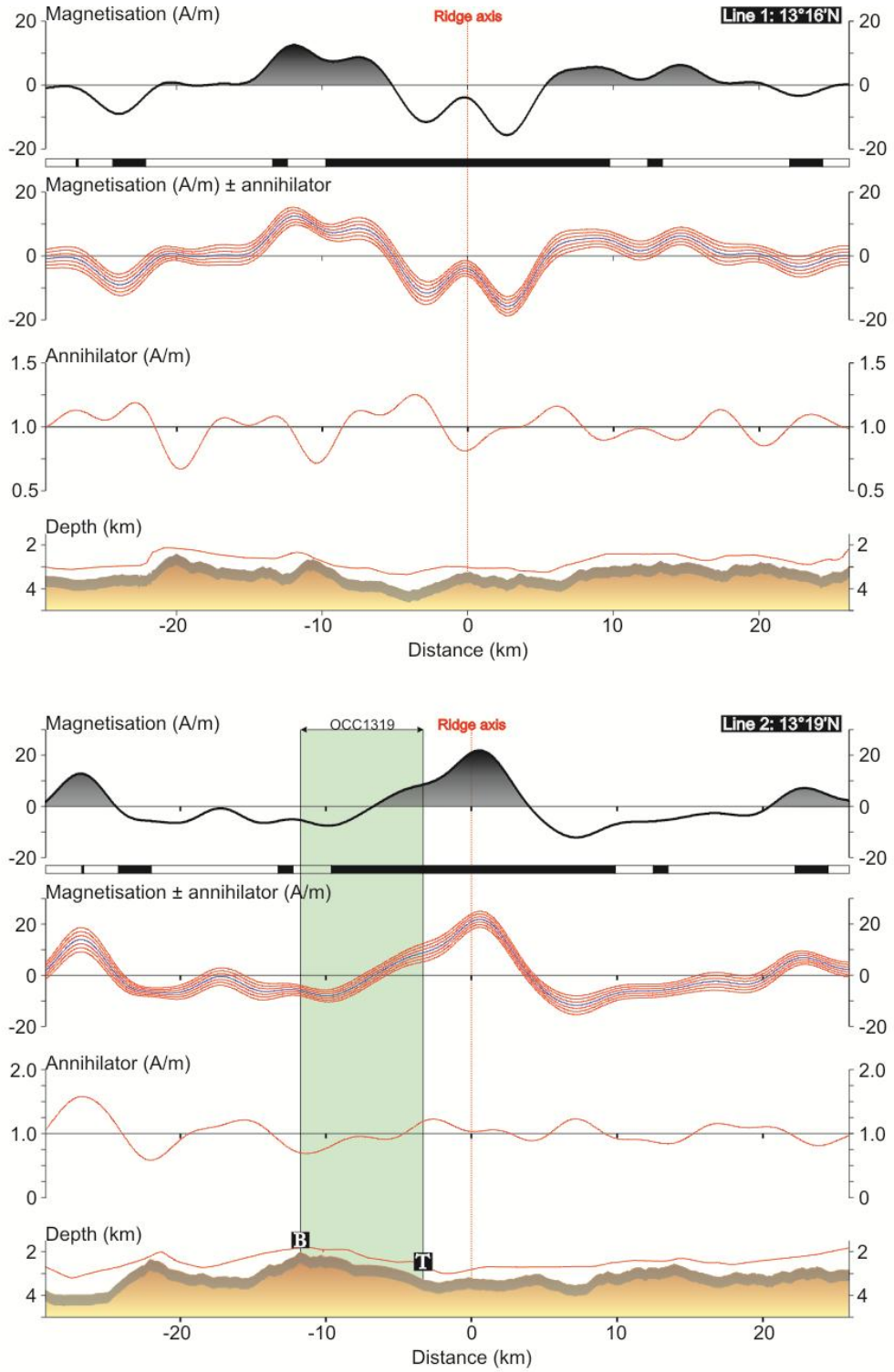


Figure 5.2.1[1]. Crustal magnetisation solution (2D) for survey lines 1 and 2 assuming 0.5 km thick magnetic source layer (grey shading in cross-section). A bandpass filter with wavelength cut-offs of 55 km and 2 km has been used to ensure convergence of the solution. Magnetic annihilator is shown, as is the magnetisation ±3 annihilators. Red line over cross-section is TOBI path above seafloor. Expected magnetic reversal polarity (black +ve, white -ve) is shown for a spreading rate of 26 km/My. Vertical green bars are near-axis OCCs.

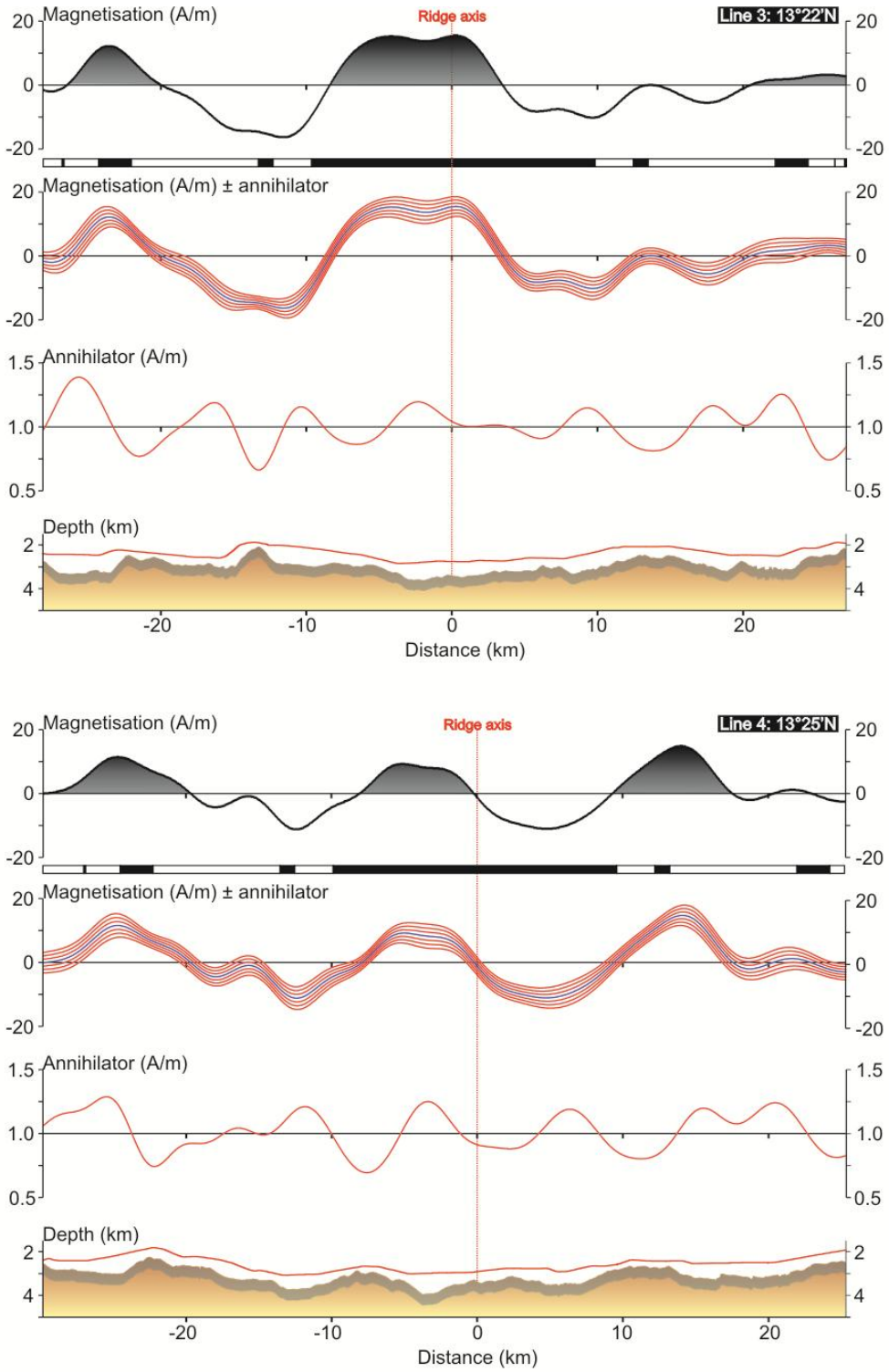


Figure 5.2.1[2]. Crustal magnetisation solution (2D) for survey lines 3 and 4 assuming 0.5 km thick magnetic source layer (grey shading in cross-section). A bandpass filter with wavelength cut-offs of 55 km and 2 km has been used to ensure convergence of the solution. Magnetic annihilator is shown, as is the magnetisation ±3 annihilators. Red line over cross-section is TOBI path above seafloor. Expected magnetic reversal polarity (black +ve, white -ve) is shown for a spreading rate of 26 km/My.

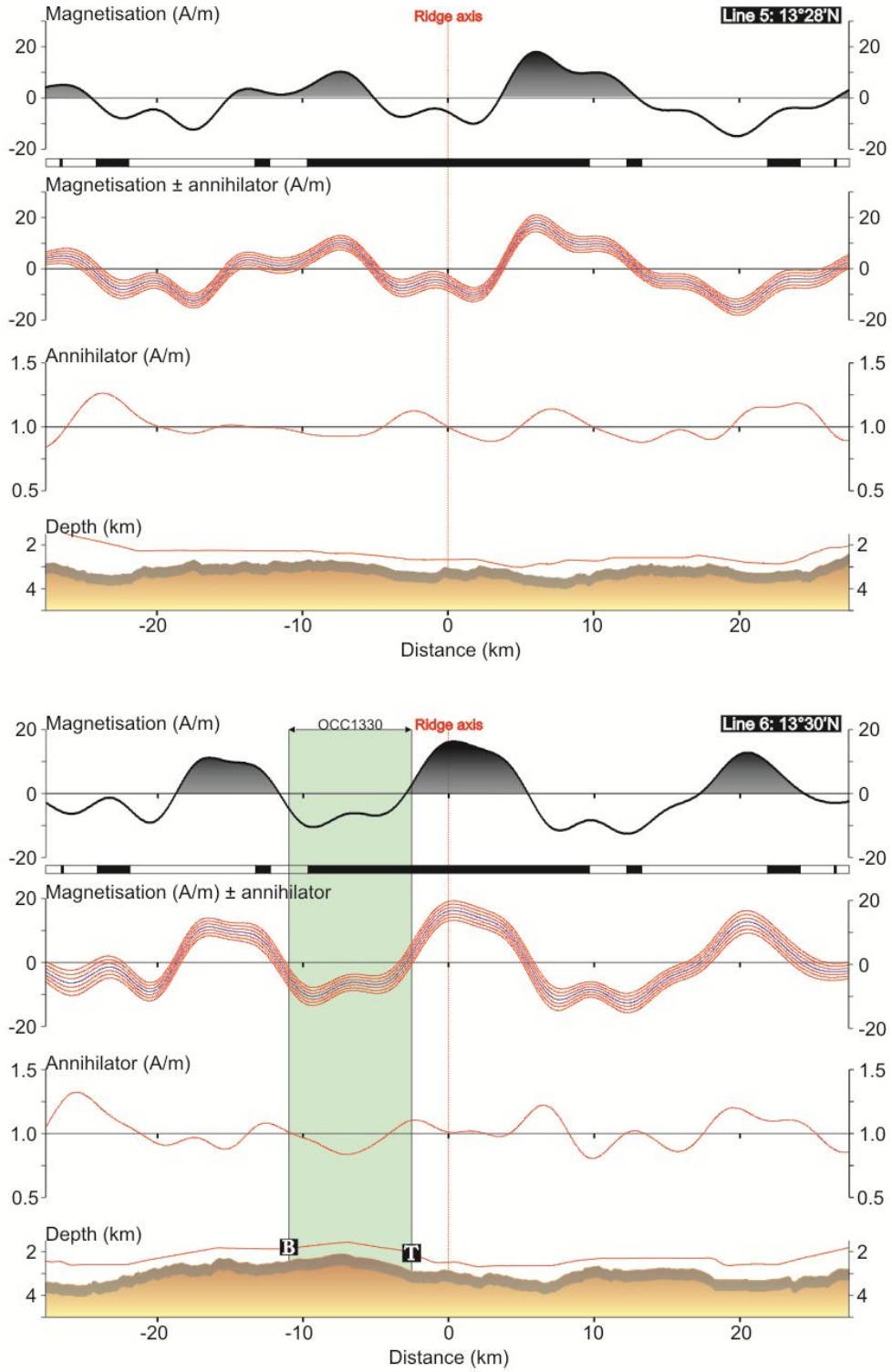


Figure 5.2.1[3]. Crustal magnetisation solution (2D) for survey lines 5 and 6 assuming 0.5 km thick magnetic source layer (grey shading in cross-section). A bandpass filter with wavelength cut-offs of 55 km and 2 km has been used to ensure convergence of the solution. Magnetic annihilator is shown, as is the magnetisation ±3 annihilators. Red line over cross-section is TOBI path above seafloor. Expected magnetic reversal polarity (black +ve, white -ve) is shown for a spreading rate of 26 km/My. Vertical green bars are near-axis OCCs.

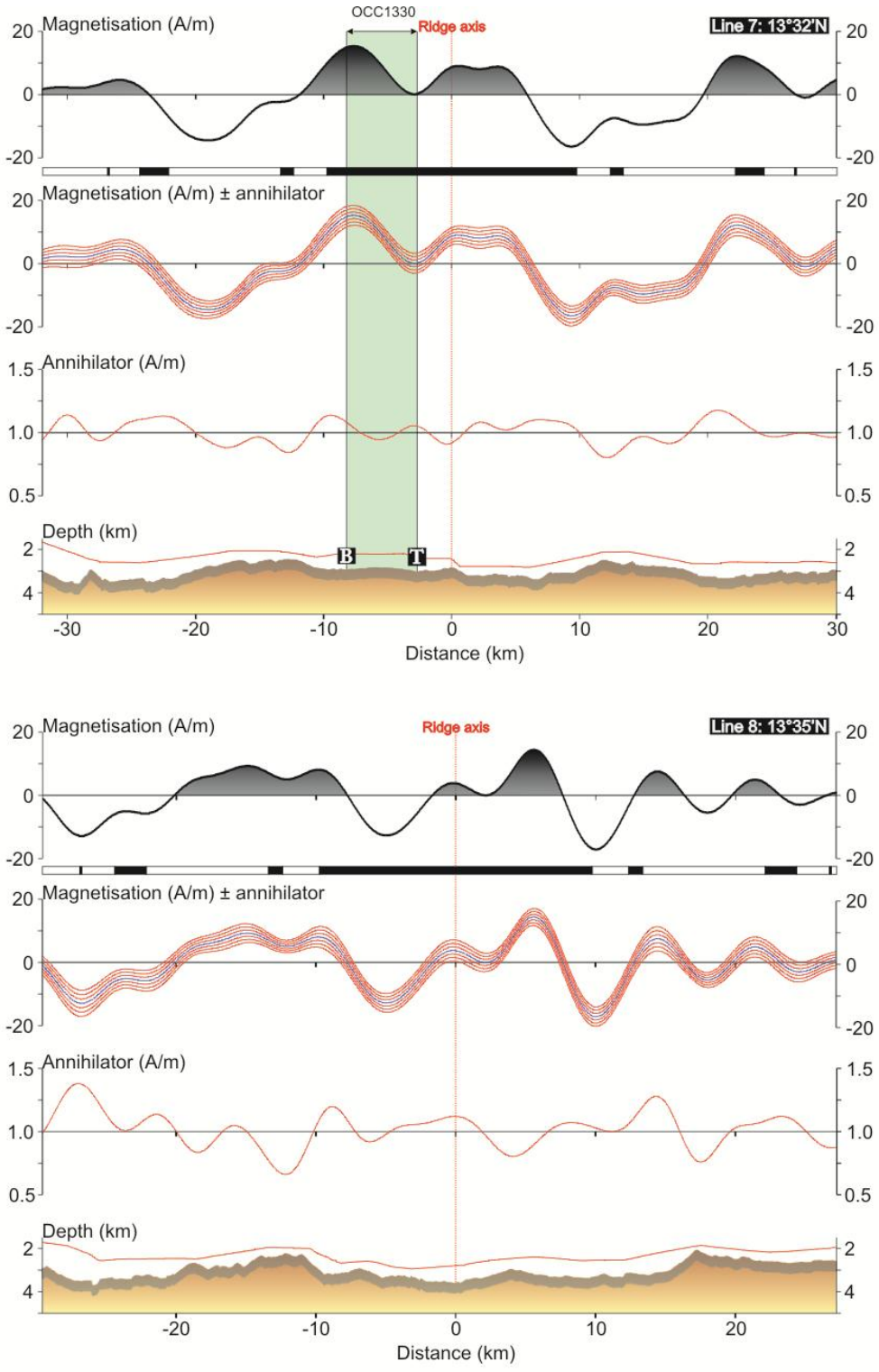


Figure 5.2.1[4]. Crustal magnetisation solution (2D) for survey lines 7 and 8 assuming 0.5 km thick magnetic source layer (grey shading in cross-section). A bandpass filter with wavelength cut-offs of 55 km and 2 km has been used to ensure convergence of the solution. Magnetic annihilator is shown, as is the magnetisation ±3 annihilators. Red line over cross-section is TOBI path above seafloor. Expected magnetic reversal polarity (black +ve, white -ve) is shown for a spreading rate of 26 km/My. Vertical green bars are near-axis OCCs.

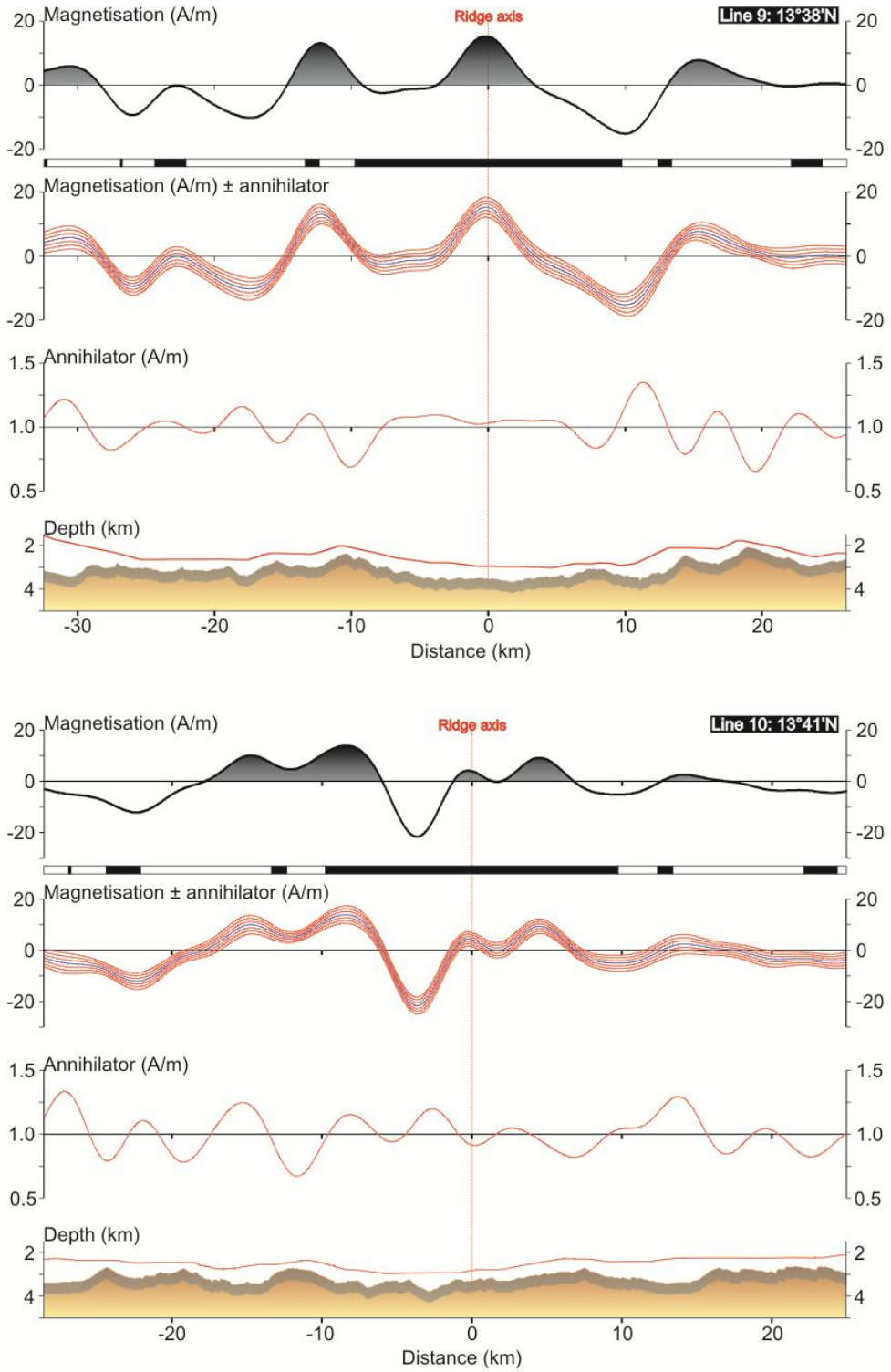


Figure 5.2.1[5]. Crustal magnetisation solution (2D) for survey lines 9 and 10 assuming 0.5 km thick magnetic source layer (grey shading in cross-section). A bandpass filter with wavelength cut-offs of 55 km and 2 km has been used to ensure convergence of the solution. Magnetic annihilator is shown, as is the magnetisation ±3 annihilators. Red line over cross-section is TOBI path above seafloor. Expected magnetic reversal polarity (black +ve, white -ve) is shown for a spreading rate of 26 km/My.

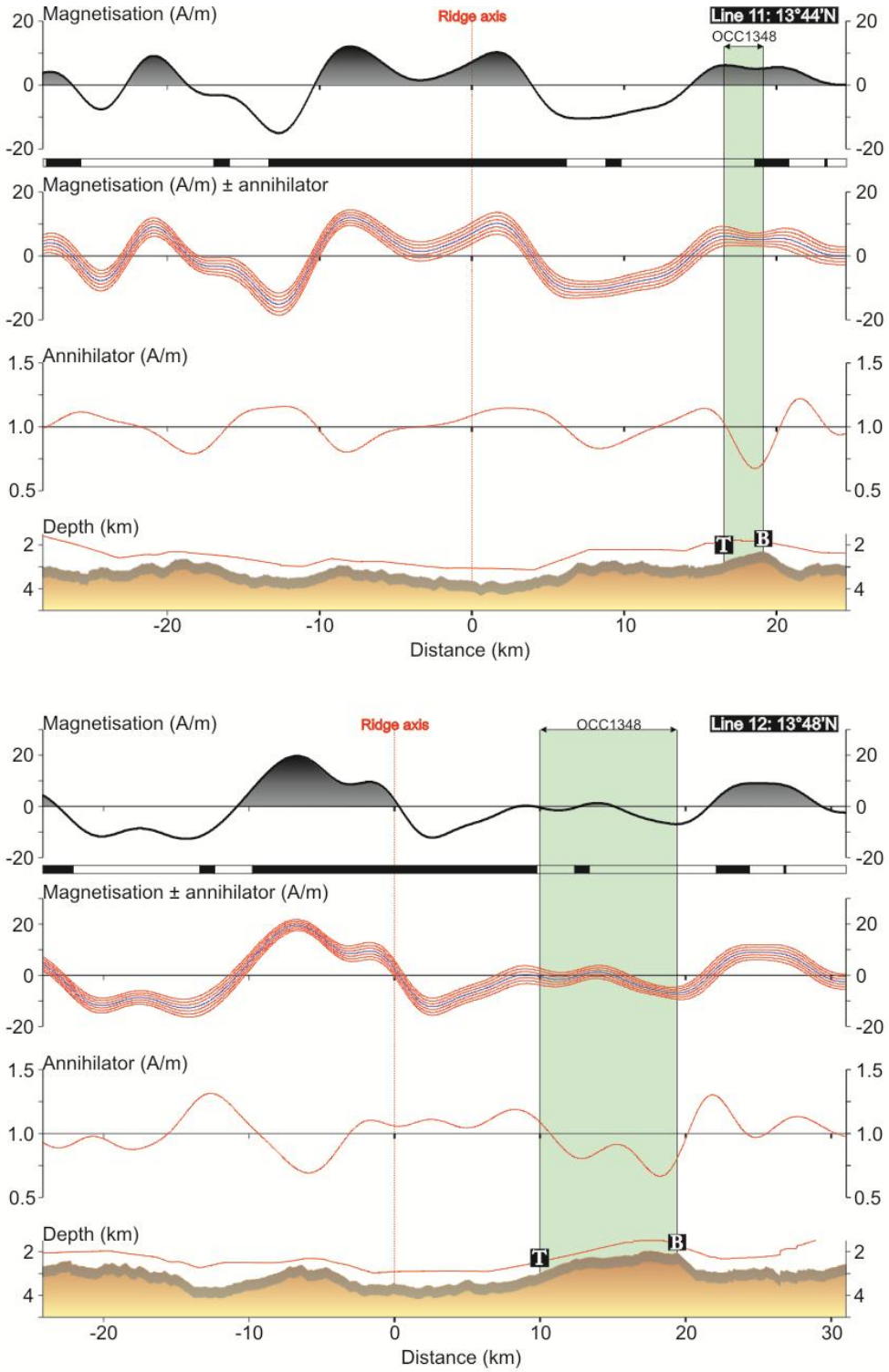


Figure 5.2.1[6]. Crustal magnetisation solution (2D) for survey lines 11 and 12 assuming 0.5 km thick magnetic source layer (grey shading in cross-section). A bandpass filter with wavelength cut-offs of 55 km and 2 km has been used to ensure convergence of the solution. Magnetic annihilator is shown, as is the magnetisation ±3 annihilators. Red line over cross-section is TOBI path above seafloor. Expected magnetic reversal polarity (black +ve, white -ve) is shown for a spreading rate of 26 km/My. Vertical green bars are near-axis OCCs.

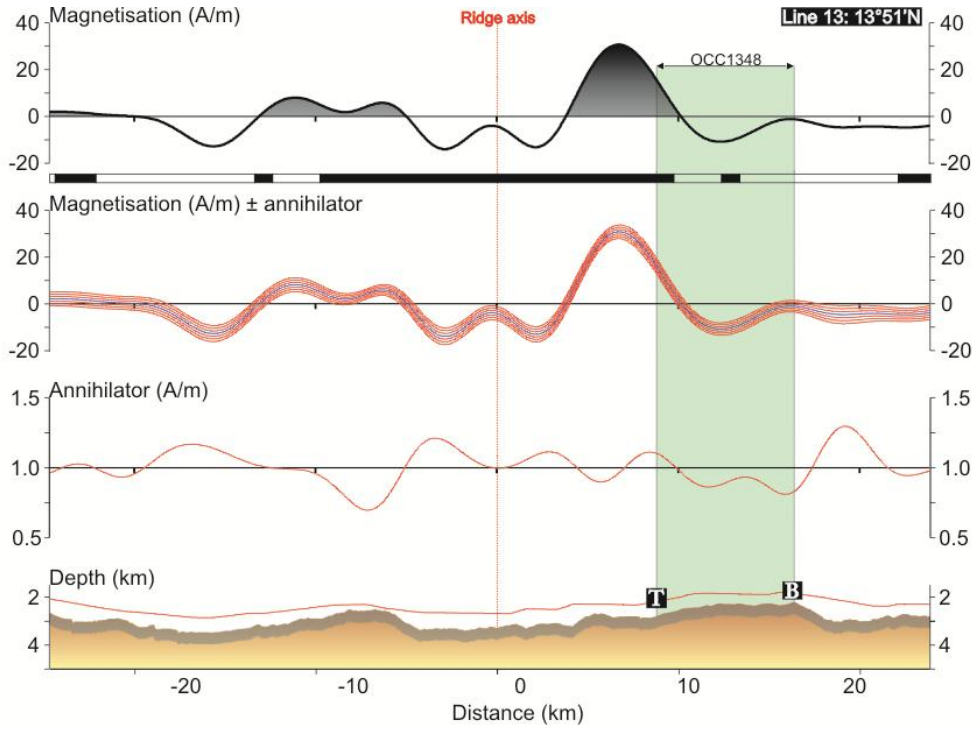


Figure 5.2.1[7]. Crustal magnetisation solution (2D) for survey line 13 assuming 0.5 km thick magnetic source layer (grey shading in cross-section). A bandpass filter with wavelength cut-offs of 55 km and 2 km has been used to ensure convergence of the solution. Magnetic annihilator is shown, as is the magnetisation ±3 annihilators. Red line over cross-section is TOBI path above seafloor. Expected magnetic reversal polarity (black +ve, white -ve) is shown for a spreading rate of 26 km/My. Vertical green bar marks location of near-axis OCC.

3D data were corrected for magnetic skewness due to the latitude of the survey and bandpass filtered between 55 km and 2 km to ensure convergence of the solution. As with the 2D solution, the positive and negative amplitudes of anomaly C2n and the Matuyama reversal are in most cases approximately equal, and so it was decided that no magnetic annihilator should be added to the magnetisation.

The main difference between the 2D and 3D solutions is the amplitude of magnetisation. For example, within the axial valley adjacent to OCC1319, the 2D magnetisation solution shows a well-developed, ridge-centred Brunhes anomaly that has a peak magnetisation of 20 A/m (survey line 2 – Figure 5.2.1). In contrast, the same area within the 3D solution displays a peak that has a magnitude of 10 A/m. In general, however, the shape of the 2D and 3D solutions match well. Slight differences between the 2D and 3D solutions may be caused by a number of factors, such as: 1) 3D data are upward continued to the minimum depth of the entire deep-towed survey, whereas individual profiles have been upward continued to the minimum depth of TOBI for the

survey line in question (so as to contain more high frequency detail); 2) the 2D solutions assume that magnetic and bathymetric features are infinitely continuous along-axis, which may breakdown in the presence of complex, discontinuous topography, and; 3) in the presence of magnetic anomalies that are discontinuous along-axis, the resolution of 3D magnetic data are limited by the profile spacing, which, in most places, is 6 km.

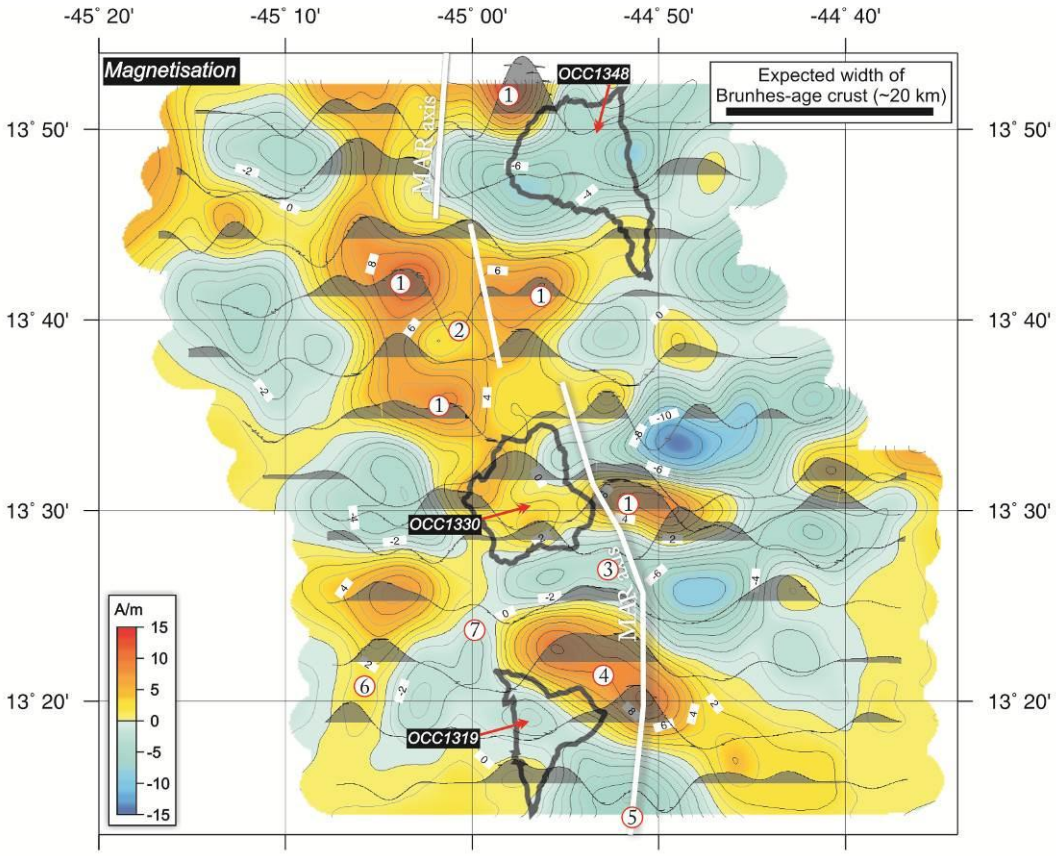


Figure 5.2.2. Contours of the crustal magnetisation solution (3D) assuming 0.5 km thick magnetic source layer. A bandpass filter with wavelength cut-offs of 55 km and 2 km has been used to ensure convergence of the solution. Profiles are 2D solutions shown in **Figure 5.2.1**. Black outlines show near-axis OCC locations. Contours are at 1 A/m intervals. Numbered points are referred to in *Section 5.3*.

For example, the negative/low magnetisation across the axial-valley detected during survey profile 1 (44°52'W, 13°15'N) clearly gives way to material of positive/relatively high magnetisation towards the north. Gridding of the 3D data assumes that the location of this transition is roughly midway between survey profiles 1 and 2, and hence its precise location is uncertain.

The 3D magnetisation solution shown in Figure 5.2.2 is comparable in shape and amplitude (±15 A/m) to that which has been reported using sea-surface data by Fujiwara *et al.* (2003) (±20 A/m) for the area surrounding the Fifteen-Twenty FZ and by

Smith *et al.* (2008) (±10 A/m) for the 13°N region (discussed in *Section 1.3.5*; note that Fujiwara *et al.* (2003)'s solution is for a 0.5 km thick source layer, whereas Smith *et al.* (2008)'s solution is for a 1 km layer). Anomalous magnetic patterns have previously been attributed to spatial and temporal variations in magmatism over periods of several million years and the associated thickness variations within the upper crustal layer (Fujiwara *et al.*, 2003). Building on these observations, it is the purpose of the following section to use the magnetisation solutions to examine the implications for magmatism in the 13°N region.

5.3. Anomaly identification & spreading history

Crustal magnetisation across the 13°N region (Figure 5.2.2) is highly disorganised (thus being typical for a magma-poor environment – *Section 1.3.1*) and therefore magnetic anomaly identification based solely on JC07 survey data is ambiguous. The difficulty with which anomalies are identified is increased by the lack of data coverage across the magma-rich segment centre (where it would be expected that magnetic anomalies are well-developed) and off-axis regions (which would allow for asymmetry patterns to be averaged over a longer period). Thus, in order to assist in anomaly identification within the JC07 survey area, I first consider the anomaly picks of Fujiwara *et al.* (2003) and Smith *et al.* (2008) (as I have noted previously, digital data were unavailable and so my analysis/comparison is based purely on published images).

Figure 5.3.1 shows crustal magnetisation between the Marathon and Fifteen-Twenty FZs compiled by Smith *et al.* (2008), with the following anomalies annotated: 'CA' (Brunhes: 0 – 0.78 Ma), '2' (1.77 – 1.95 Ma), '2a' (2.58 – 3.58 Ma) and '3' (4.18 – 4.29 Ma; 10' gridlines have been added to assist in cross-referencing anomalies between the two datasets; Cande & Kent, 1995). From this plot I deduce that: 1) Anomaly 3 should not be resolved at all within the JC07 survey area, 2) the onset of anomaly 2a may be intermittently resolved at the edges of profiles north of 13°35'N, 3) anomaly 2 should be apparent within profiles south of ~13°30'N, but may be poorly resolved north of this point, and 4) the Brunhes anomaly may be split into numerous discrete anomalies and contain negatively magnetised (presumably Matuyama-age) material.

It would also be expected, based on a full-spreading rate of 26 km/My, that the Brunhes anomaly should be ~20 km wide; even if the locus of magmatic accretion jumps during the Brunhes chron – the combined width of discrete 'packets' of Brunhes-age crust should be ~20 km. However, it is important to note that in areas where long-lived detachment faults form, a significant portion of the Brunhes may accrete within the footwalls of OCCs, and may thus not necessarily have a distinct, positive magnetisation at the surface similar to that which would be expected to form by 'normal' magmatic processes. Therefore the ridge-centred, positive peak in magnetisation does not necessarily have to be ~20 km wide if the deficit can be accounted for by crustal accretion during tectonic events. For this reason, in the following discussion I refer to the positive peaks in magnetisation formed near the ridge

axis collectively as the 'central positive anomaly', or *CPA*. This can be differentiated from the central anomaly magnetic high (CAMH – the formation of which is discussed in *Section 1.2.5*) as the latter may be expected to only include the most recently formed magmatic crust – i.e. the CAMH is a component of the CPA, which is in turn a component of the crust formed during the Brunhes chron.

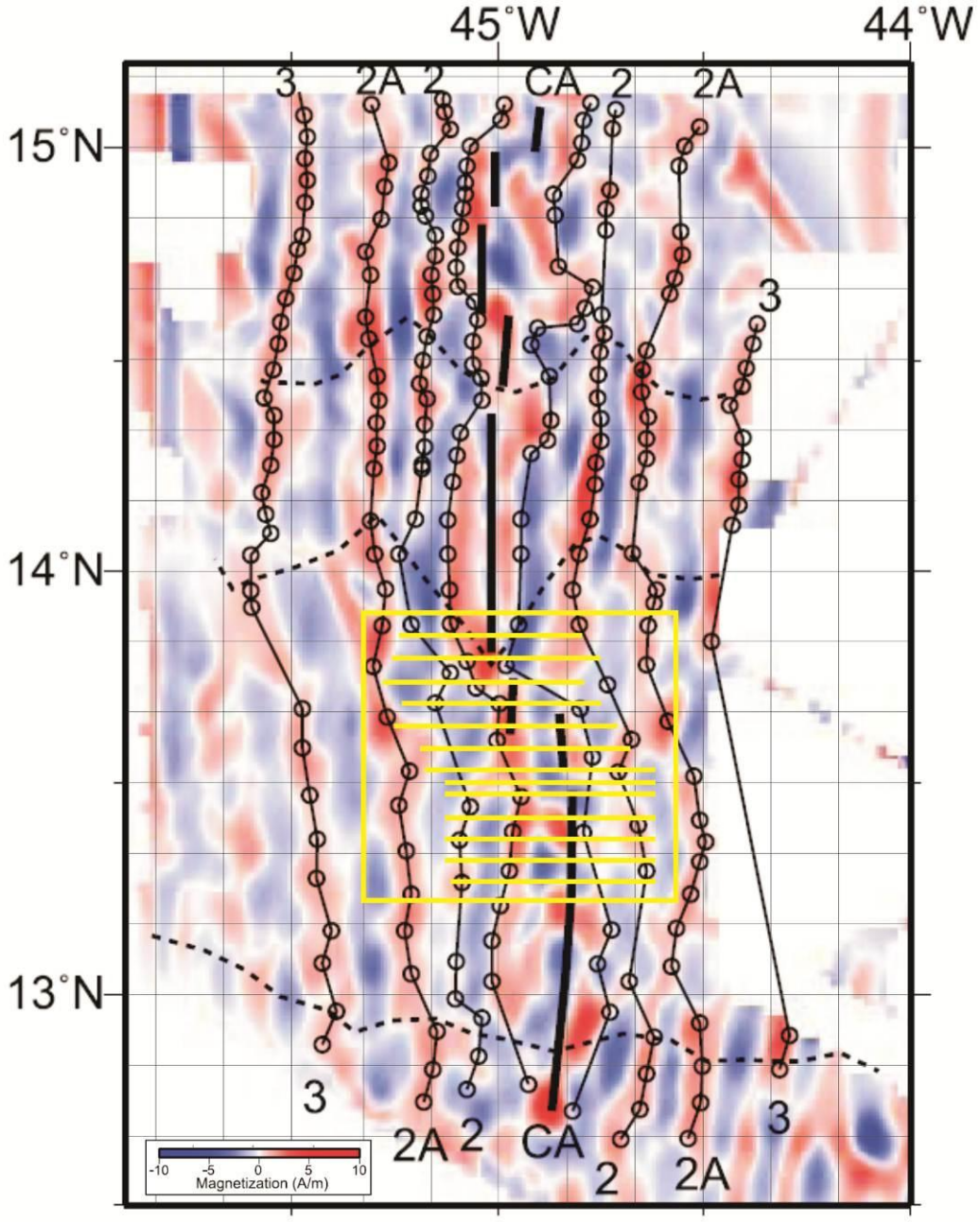


Figure 5.3.1. Magnetic anomaly identification after Smith *et al.*, 2008. Yellow box marks location of **Figure 5.2.2** and horizontal lines show locations of TOBI survey profiles (e.g. **Figure 5.2.1**). The data show that within the JC07 survey area, the central anomaly ('CA') may be highly discontinuous and contain negatively magnetised crust. Anomalies 2 and 2a may be intermittently resolved at the ends of profiles. Diagram modified from Smith *et al.*, 2008.

Using these criteria as a starting point, Figure 5.3.2 shows my anomaly picks for the 13°N region. The ridge-centred CPA (red shading – Figure 5.3.2) is characterised by a number of isolated peaks in magnetisation that are typically 8 – 14 A/m in magnitude (Points 1 – Figure 5.3.2; see also Figure 5.2.2). The maximum magnetisation is located immediately north of OCC1348 at 44°57'W, 13°52'N, having a magnitude of 14 A/m in the 3D solution and 30 A/m in the 2D solution (which may be overestimated in this region due to the discontinuous nature of the axial valley wall-fault over which the anomaly is centred). The irregular pattern of magnetisation causes the CPA to widen to a maximum width of 26 – 30 km about the ridge axis between 13°35'N and 13°44'N. When the 2D solutions are considered it is clear that the CPA is in fact partitioned between 2 – 3 regions of positive magnetisation that are each ~8 – 14 km wide and are separated by areas of negatively magnetised crust (e.g. Point 2 – Figure 5.3.2).

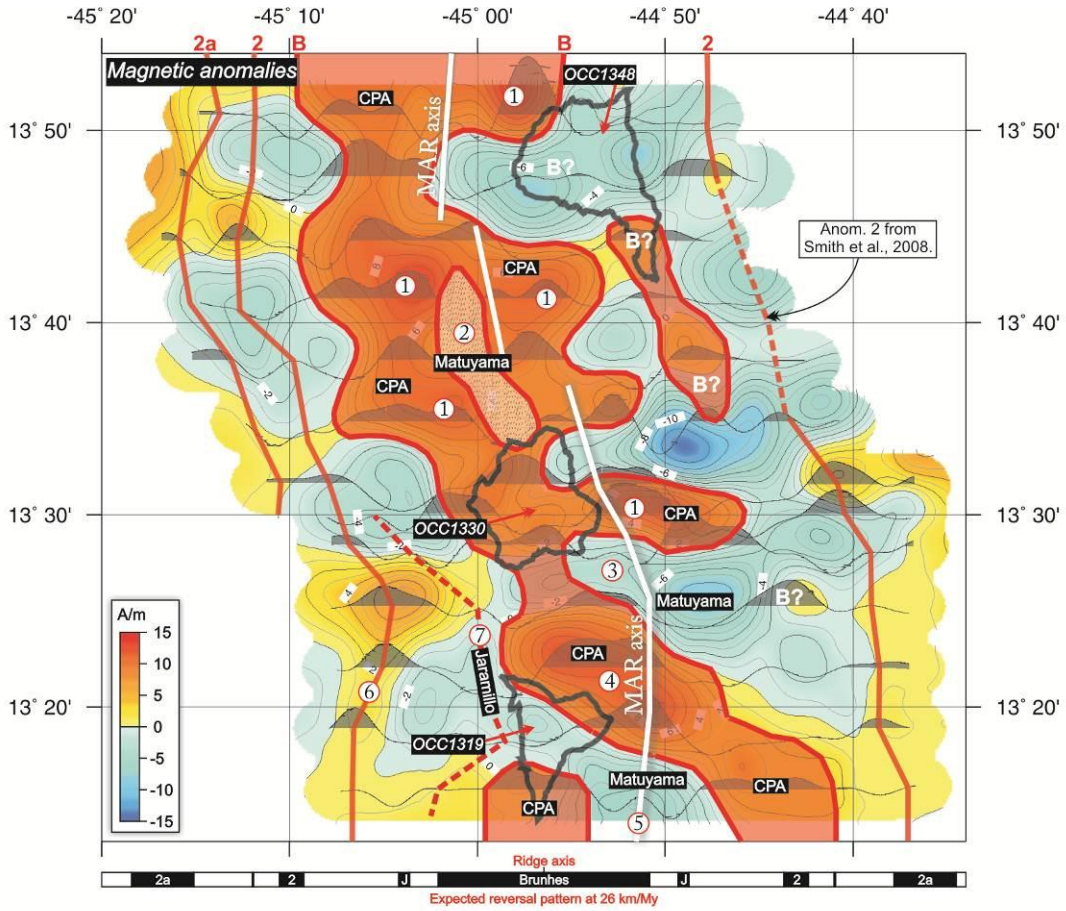


Figure 5.3.2. Magnetic anomaly identification in the 13°N region. The CPA is a component of crust formed during the Brunhes chron and is the shaded red area about the MAR axis. There are distinct areas of negatively magnetised crust where it may be expected that positively magnetised crust (i.e. that which is formed during the Brunhes chron) would exist. Anomaly 2 is well resolved in the SW and intermittently resolved elsewhere. The younger edge/onset of anomaly 2a is resolved in the NW. Numbered points are referred to in the text.

Multiple peaks in magmatic, Brunhes-age crust formed at the same latitude suggest that the locus of melt emplacement jumps across-axis at a frequency of ~0.25 – 0.40 My (i.e. 2 – 3 individual events within 0.78 My) by perhaps as much as ~12 km (the distance between two peaks in Brunhes-age magnetisation observed along survey line 8). These values are comparable to estimates made by Collette *et al.* (1979) who, on the basis of bathymetric data, suggest that crustal accretion in this region is associated with ridge jumps over several kilometres every ~0.5 My (*Section 1.3.5*). This is also supported by sidescan sonar data collected during JC07, which show a range of inactive and active volcanic lineaments across the axial valley-floor, which are assumed to have formed as the melt supply wandered across-axis over periods of ~0.5 My (*Section 3.4*). The 3D inversion solution seemingly does not have the necessary resolution to create a full 'swing' of magnetisation from positive to negative to create these discrete peaks and troughs within the CPA.

To the north and south of 13°35'N – 13°44'N, the CPA gradually narrows, reaching a width of only ~5 km between 13°25'N and 13°27'N (Point 3 – Figure 5.3.2) and becoming ~8 km wide at 13°48'N. I note, however, that there is an area of low magnetisation crust across the dome of OCC1348, and thus part of the Brunhes 'deficit' at 13°48'N may be accounted for by OCC formation (the mechanisms by which this may occur are discussed later in this chapter). Furthermore, adding a small amount of annihilator makes this low magnetisation zone become positively magnetised (although, as I have discussed in Section 5.2.2, using the traditional criteria for determining if annihilator should be added I find that it is not necessary to add any annihilator across this region; survey line 12 – Figure 5.2.1).

A magnetisation high of ~10 A/m exists within the axial valley between OCC1319 and OCC1330 (Point 4 – Figure 5.3.2). A negatively-magnetised area of crust with a magnitude of -7 A/m is observed to the south of OCC1319 (Point 5 – Figure 5.3.2). Within this latter area, the ridge axis (white line in Figure 5.3.2), however, is still associated with a small peak in magnetisation. The existence of this relatively weak area of the CPA and its implications for crustal accretion during OCC formation are discussed in *Section 5.4*.

Anomaly 2 is well-resolved across the SW part of the survey area (e.g. Point 6 – Figure 5.3.2). North of this point, anomaly 2 becomes intermittently resolved on the SA plate, although it is possible to detect the eastern/youngest edge of anomaly 2a. Presumably, the longer (~1.0 My) duration of anomaly 2a relative to anomaly 2 (~0.18

My) makes the magnetic signature of the former more robust, i.e. its formation is less susceptible to short-term fluctuations of the melt supply that creates the magnetic source layer (such as those observed within the CPA). At 13°30'N on the SA plate, anomaly 2 is so poorly expressed that it cannot be resolved with the JC07 magnetic data. The small peak in magnetisation at this latitude is aligned with a short normal chron between the Brunhes and anomaly 2 on survey lines 1 – 5, which may be the Jaramillo event (0.99-1.07 Ma; Point 7 – Figure 5.3.2). However, due to the short period of this chron and the 2 km low pass filter applied to the magnetic dataset, it is unlikely that this event should be recorded across the region. On the AF plate, anomaly 2 is again resolved in the south, although its exact location is slightly more ambiguous than on the SA plate due to its proximity to the edge of the data coverage. To the north of 13°35N, I use the picks of Smith *et al.* (2008; dashed red line in Figure 5.3.2) to annotate the location of anomaly 2 on the AF plate, although our data show no clear anomalies in this area. Several kilometres to the west of here at ~44°50'W is a localised, fairly continuous zone of positive polarity material that could be anomaly 2, although it may be an abandoned spreading centre formed during the Brunhes chron (annotated with 'B?' in Figure 5.3.2).

5.3.1. Spreading rate from anomaly C2n

The rate at which the SA and AF plates are diverging can be calculated by dividing the distance between conjugate anomalies by the time in which the anomalies formed. In the 13°N region, the Brunhes anomaly is highly discontinuous and thus not a good indicator of spreading rate; hence, I use the distance between the position of anomaly 2 on the SA and AF plates (thus giving an average spreading rate over 1.86 Ma; Table 5.3.1). An estimate is made by measuring the maximum (i.e. between the oldest part of each anomaly – 1.95 Ma), minimum (i.e. between the youngest part of each anomaly – 1.77 Ma) and peak-to-peak (i.e. the median point of the anomaly 2 interval – 1.86 Ma) distances where possible.

The average full-spreading rate calculated in this way is 25.5±1.5 km/My (the error is ± one standard deviation of all measurements). The spreading rate considering only the peak-to-peak measurements is 25.7±1.5 km/My (on the basis of Figure 5.2.1, the peak-to-peak measurements should not be affected greatly by the addition of any magnetic annihilator). In contrast, the full-spreading rate between the SA and AF plates calculated from the NUVEL-1a plate model is 25.7±1.0 km/My (DeMets *et al.*, 1990;

with uncertainty estimated from the error ellipse of the poles of rotation); furthermore, Fujiwara *et al.* (2003) calculate the full-spreading rate as 25 km/My in the area around the Fifteen-Twenty FZ. Thus, the anomaly identification in Figure 5.3.2 appears reliable as it gives a good match with the expected spreading rate across the region.

Survey line	Latitude	Distance between conjugate anomaly 2 on SA and AF plates (kilometres)			Spreading rate (km/My)	Confidence
		Min. (1.77 Ma)	Peak-to-peak (1.86 Ma)	Max. (1.95 Ma)		
1	13°16'N	47.6	53.2	-	27.9	2
2	13°19'N	46.0	50.3	55.8	27.2	3
3	13°22'N	40.9	47.6	-	24.4	3
4	13°25'N	40.5	45.9	53.0	25.0	2
5	13°28'N	46.0	50.0	-	26.5	2
6	13°30'N	-	-	-	-	-
7	13°32'N	43.5	48.7	55.4	26.4	3
8	13°35'N	42.0	46.6	50.5	24.8	2
9	13°38'N	43.7	46.4	-	24.8	2
10	13°41'N	-	49.7	-	26.7	1
11	13°44'N	-	47.9	-	25.8	2
12	13°48'N	38.0	44.5	49.6	23.6	2
13	13°51'N	40.1	43.5	-	23.0	1
	Average:	42.8	47.9	52.9	25.5	-
Standard deviation:		-	-	-	1.5	-

Table 5.3.1. Spreading rate calculated from the position of anomaly 2. Confidence levels are: 1) anomaly location is ambiguous on both plates, 2) anomaly location is well-resolved on one plate, and 3) anomaly location is well-resolved on both plates. The average spreading rate is 25.5 km/My for the anomaly locations shown in Figure 5.3.2. See text for discussion.

5.3.2. Spreading rate asymmetry & relationship with OCC formation

Spreading-rate asymmetry, defined as the difference in half-spreading rate divided by the full-spreading rate at a particular latitude, is correlated with OCC formation; this has been inferred from a number of magnetic studies (e.g. Fujiwara *et al.*, 2003; Searle *et al.*, 2003; Okino *et al.*, 2004; Baines *et al.*, 2008). Estimates of this asymmetry range from 30 – 70% averaged over 1 My at the Fifteen-Twenty FZ (Fujiwara *et al.*, 2003), ~70% during the 0.63 My formation of FUJI Dome (Searle *et al.*, 2003), ~70% during the ~1 My formation of a large corrugated surface at the AAD (Okino *et al.*, 2004), and on the

basis of geochemical data, possibly 100% during formation of Atlantis Massif (Grimes *et al.*, 2008). In each of these cases, spreading is observed to be faster across the plate which exhibits OCC formation.

In order to calculate asymmetry from magnetic anomalies, it is first necessary to estimate the position at which anomalies form. As I have shown in previous chapters, in the 13°N region this position is not fixed but appears to wander across the axial valley (e.g. *Section 3.4.1* and *Section 4.3.4*), therefore making it difficult to unambiguously define the location at which anomaly 2 formed. Thus I measure asymmetry relative to the ridge axis defined by four different datasets and consider the implications for each (Figure 5.3.3). The 'neovolcanic ridge axis' is identified from sidescan sonar data as the area of highest backscatter intensity (geological map – Figure 3.2.15a-b); within this zone, hummocky lineaments are picked as the ridge axis (Figure 5.3.3a). The 'bathymetric ridge axis' is defined as the most prominent/largest volcanically constructed ridge within the axial valley (Figure 5.3.3b). The 'magnetic ridge axis' coincides with peaks in magnetisation of the central anomaly within the axial valley (Figure 5.3.3c), and the 'gravitational ridge axis' is picked as the RMBA low that runs N-S through the region (Figure 5.3.3d). The four axes range from ~1 – 10 km apart; they appear to almost coincide at the position of the largest seamount in the region at 44°59'W, 13°40'N (geological map – Figure 3.2.15a). They are distributed across the widest area where the axial valley is also at its widest – within the NTO at 13°38'N. Here, presumably, the wide axial valley allows for melt to wander across-axis more freely, as has been suggested by Macdonald (1977) for the FAMOUS region of the MAR.

Distances were measured from each of these axes to the peak of anomaly 2 on the SA and AF plates and converted to half-spreading rates by dividing by 1.86 Ma (peak-to-peak distances were measured in order to reduce errors associated with the magnetic annihilator; Table 5.3.2). Asymmetries were calculated for each pair of half-spreading rates (i.e. half-rate west and half-rate east relative to each axis, giving four estimates of asymmetry for each survey profile) by dividing the difference between the two half-rates by the full spreading rate and multiplying by 100. Thus, asymmetries of +100% and -100% indicate that the AF and SA plate have accommodated all plate separation during the last 1.86 Ma, respectively. Table 5.3.2 shows the minimum, maximum and average of the four estimates for each survey line.

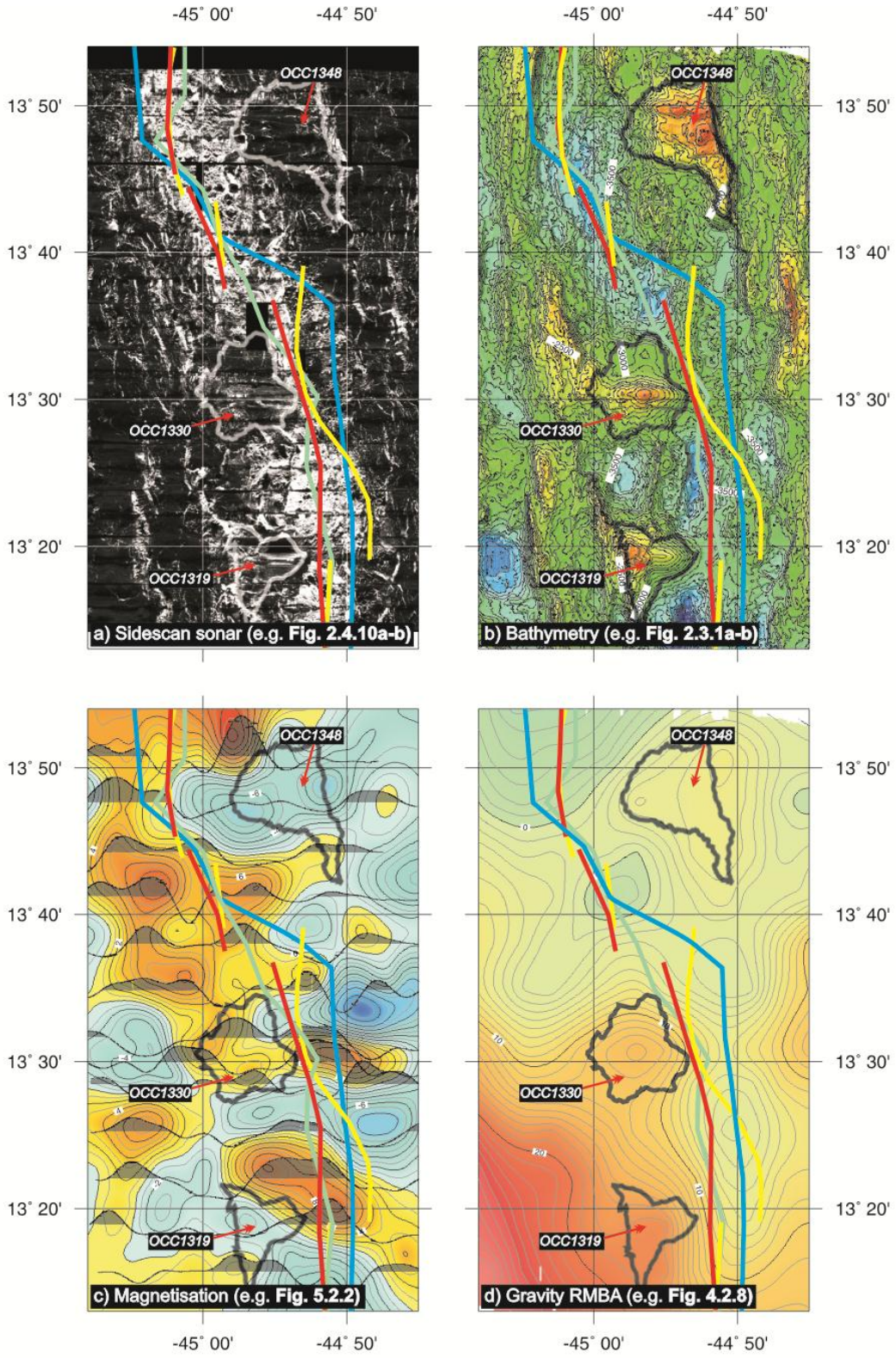


Figure 5.3.3a-d. The MAR axis, as defined by: **a)** sidescan sonar (red), **b)** bathymetry (yellow), **c)** deep-towed magnetic (green) and **d)** gravity data (blue). The various axes do not match as they are averaged over different volumes/thicknesses of material and thus deviations reflect changes in the locus of melt emplacement. See text for discussion.

Survey	Half-rate (west; km/My) from:				Half-rate (east; km/My) from:				% Asymmetry		
line	NVZ	Bath.	Mag.	Grav.	NVZ	Bath.	Mag.	Grav.	Min.	Max.	Ave.
1	14.7	15.1	15.1	16.8	13.9	13.5	13.5	11.8	-3.0	-17.3	-7.9
2	14.5	15.2	15.4	16.8	12.6	11.8	11.7	10.3	-7.0	-24.1	-14.3
3	13.1	16.5	13.1	15.3	12.5	9.1	12.5	10.3	-2.1	-28.6	-13.0
4	12.6	14.8	11.6	14.3	12.1	9.8	13.1	10.4	+5.9	-20.3	-8.1
5	14.0	14.7	14.0	16.2	12.9	12.2	12.9	10.6	-4.0	-20.8	-9.6
6	-	-	-	-	12.2	11.8	11.4	9.5	-	-	-
7	14.1	14.6	11.6	16.8	12.1	14.6	11.6	9.4	0.0	-28.1	-8.9
8	14.3	15.5	13.0	17.9	10.8	9.6	12.0	7.2	-3.9	-42.9	-21.1
9	10.9	16.3	12.5	16.3	14.1	8.6	12.5	8.6	+12.9	-31.0	-12.3
10	12.7	13.4	13.4	13.4	12.3	13.3	13.3	13.3	-0.2	-1.7	-0.6
11	11.4	10.9	12.4	11.9	14.4	14.8	13.4	13.9	+15.2	+4.0	+9.6
12	9.3	9.3	8.4	7.4	14.6	14.6	15.5	16.5	+38.0	+22.2	+28.0
13	9.2	9.2	10.3	7.0	14.2	14.2	13.1	16.3	+39.8	+12.2	+23.7

Table 5.3.2. Spreading rate asymmetry calculated from the position of anomaly 2. Four different ridge axes are used, defined from: sidescan sonar data, bathymetry data, magnetic data and gravity data. Positive asymmetries are faster to the east, and *vice versa*.

In the southern part of the survey area (e.g. survey lines 1 – 7) asymmetry values indicate that the SW-quadrant of the survey area has spread faster, on average, than the SE-quadrant during the last 1.86 Ma (Figure 5.3.4). The average spreading rate asymmetry integrated across lines 1 – 7 is ~-10%. However, the data also show that in some places, if the distance to anomaly 2 is measured relative to the bathymetric ridge axis, this value may be as high as ~-30%. Similarly, measuring relative to the neovolcanic ridge axis and central magnetic anomaly results in very low levels of asymmetry (~-2%, with asymmetry on line 4 measured relative to the magnetic ridge axis showing faster half-spreading rates across the AF plate). North of the NTO (e.g. survey lines 11 – 13), the opposite sense of asymmetry is recorded by anomaly 2 (Figure 5.3.4). Here, the asymmetry is on average ~+20% and thus the AF plate is apparently spreading away from the ridge axis faster than the SA plate. As with survey lines to the south, this value may be as great as ~+40% or as little as ~+4% depending on how the ridge axis is defined. In addition to this, anomaly 2 is poorly recorded north of the NTO, which may contribute to the overall uncertainty. However, from Figure 5.3.1 it appears that this sense of asymmetry (and also the sense of asymmetry south of the NTO) is also recorded by magnetic anomaly 2a, which is generally well resolved and continuous along the length of the 13°N region.

Magnetic data therefore suggest that regular extension on detachment faults in the 13°N accompanies periods of asymmetric spreading. The sense of asymmetry is that plates which contain OCCs and exhibit higher tectonic strains (*Section 3.5.2*) spread faster from the ridge axis than the conjugate plate. This relationship is recorded to the north and south of the NTO in the ridge axis at ~13°38'N, which effectively creates two second-order inside-corner locations and marks a change in the polarity of OCCs. For example, to the south of the NTO increased tectonism and OCC formation is observed on the SA plate, whereas to the north this is observed on the AF plate (OCC distribution – Figure 3.3.1). The precise magnitude of spreading rate asymmetry is unclear as it is not possible to unambiguously identify the location at which conjugate anomalies formed. If anomaly 2 is measured relative to hummocky lineaments within the NVZ (i.e. the point where magnetic anomalies are currently forming) then the asymmetry could be very little or even non-existent in some places (as noted by MacLeod *et al.*, 2009). However, this position is unlikely to be stable for long periods of time and thus the present day NVZ may not be in the same location as it was at 1.86 Ma.

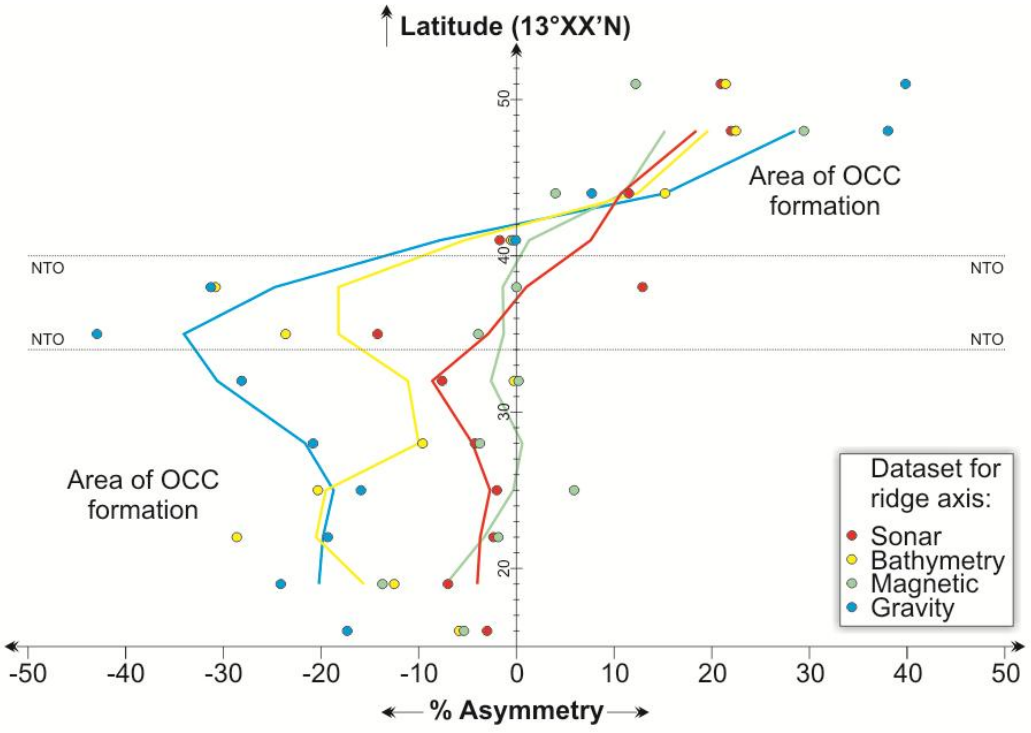


Figure 5.3.4. Spreading rate asymmetry from magnetic anomaly 2 measured for each survey profile. Coloured dots and lines refer to the ridge axis which has been used for each calculation (indicated in the key; see also **Figure 5.3.3a-d**). Lines are 3-point running averages, with positive asymmetries representing faster sprading to the east (i.e. on the African plate). See text for discussion.

Measuring anomaly distances from the low in the RMBA, which most likely represents a more stable ridge position over long periods, suggests that asymmetry may be up to ±40% on each plate. This value is similar to the value of tectonic strain, Tε, measured for the SW- and NE-quadrants of the survey, which were ~30% and ~25%, respectively (*Section 3.5.2*), and is within the 30 – 70% range of spreading rate asymmetries proposed by Fujiwara *et al.* (2003) for 1 My of spreading near the Fifteen-Twenty FZ. It is, however, less than the ~70 – 100% asymmetry estimations made at FUJI Dome (Searle *et al.*, 2003), the AAD (Okino *et al.*, 2004) and Atlantis Massif (Grimes *et al.*, 2008). Thus it appears likely that averaging over 1.86 Ma masks shorter-scale, higher-amplitude variations in asymmetry associated with the formation of a single OCC.

To test this, I use the MATLAB-based program *MODMAG* (Mendel et al., 2005). Magnetic anomaly data (in nanotesla) are modelled at an across-axis resolution of 10 metres by a 500 metre thick magnetic source layer. Figure 5.3.5a shows the predicted anomaly pattern for a full-spreading rate of 26 km/My along survey line 2 (which crosses OCC1319). Asymmetry is -20% (i.e. faster spreading to the west) about the ridge axis as defined by the RMBA low in the gravity data, and is assumed to persist throughout the entire duration of the model. On-axis blocks are modelled with a magnetisation of 5 A/m and off-axis blocks have a magnetisation of 3 A/m. This model adequately matches the off-axis location of anomaly 2 on each plate (note that modelling of the central magnetic anomaly across the ridge axis and OCC1319 is discussed in the next section; at this stage I am only considering the across-track position of anomaly 2). Using the same basic model set-up, an adequate fit to the observed data can also be obtained if asymmetry is assumed to be -75% during the last 0.39 My (Figure 5.3.5b), thus simulating a period of higher-asymmetry during the formation of OCC1319. Note that this period of asymmetry, ~0.40 My, would construct ~10 km of seafloor at a full-spreading rate of 26 km/My, which is approximately the same as the across-axis extent of OCC1319. Thus it is feasible that during this period the OCC acts as the ridge axis (e.g. Figure 3.5.6 and discussed by MacLeod *et al.*, 2009) and forms at the full-spreading rate; the degree of asymmetry would mean that the footwall/hanging-wall boundary would migrate east towards the ridge axis and along-axis projection of the NVZ, which may ultimately cause termination of extension on the detachment fault (Figure 5.3.6, see also *Section 3.5.3*).

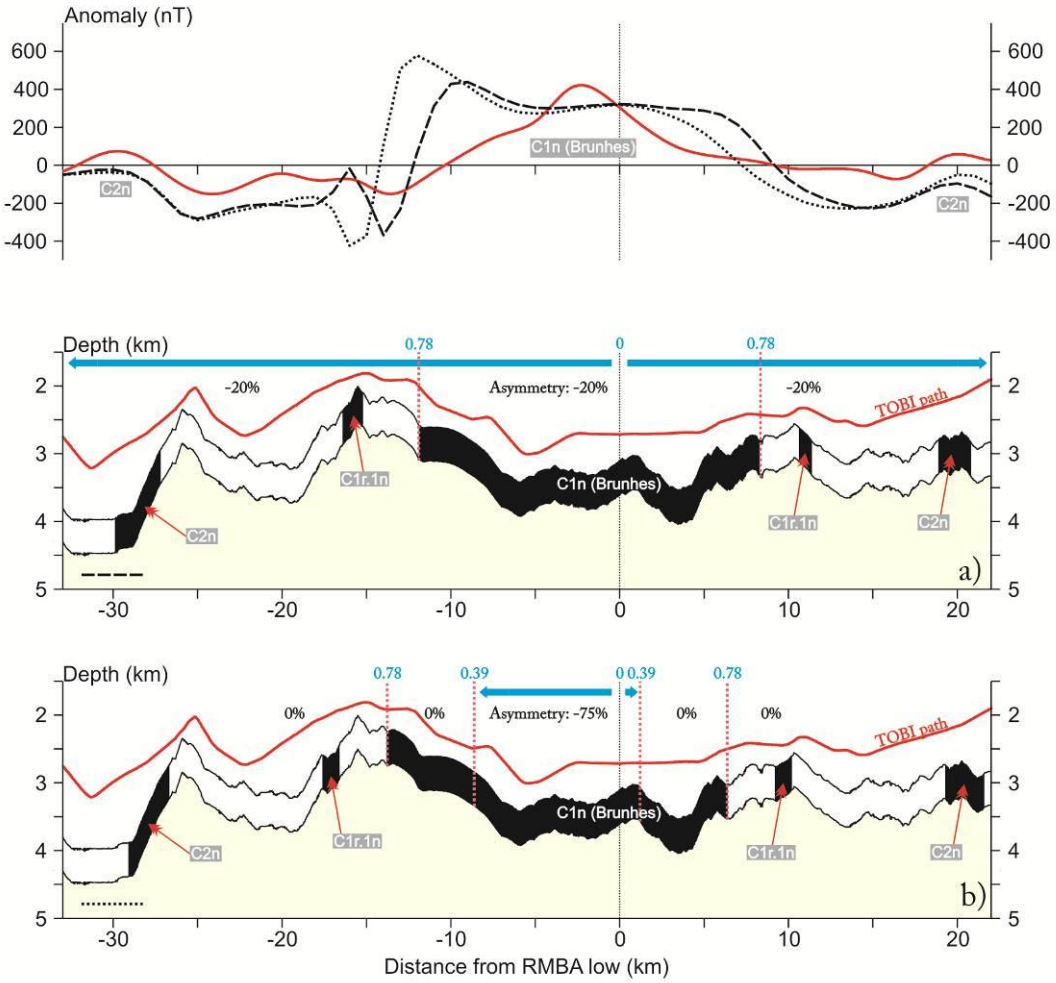


Figure 5.3.5a-b. Spreading rate asymmetry from the position of anomaly 2. Observed anomaly is red line in upper panel and data are from survey line 2. Seafloor ages are annotated in blue, degree of asymmetry annotated in black and period of asymmetry highlighted by blue arrows. **a)** The position of anomaly 2 is modelled by -20% asymmetric spreading for the duration of the model (predicted anomaly is dashed line in upper panel). **b)** Alternatively, a period of -75% asymmetric spreading for the last 0.39 My can match the off-axis positions of anomaly 2 (dotted line in upper panel). Spreading rate is 26 km/My in each case. See text for discussion.

Assuming that OCC1319 has formed in this way, this degree of asymmetry would also suggest that the OCC initiated at approximately the same longitude as the axial-valley wall fault immediately to the north at ~44°54'W, 13°25°N (which is a location where it has been suggested that an OCC may currently be initiating; Smith *et al.*, 2006). In the next section, I examine how magnetic anomalies may be recorded in the footwalls of OCCs and present a spreading reconstruction for the last 0.80 My in the 13°N region.

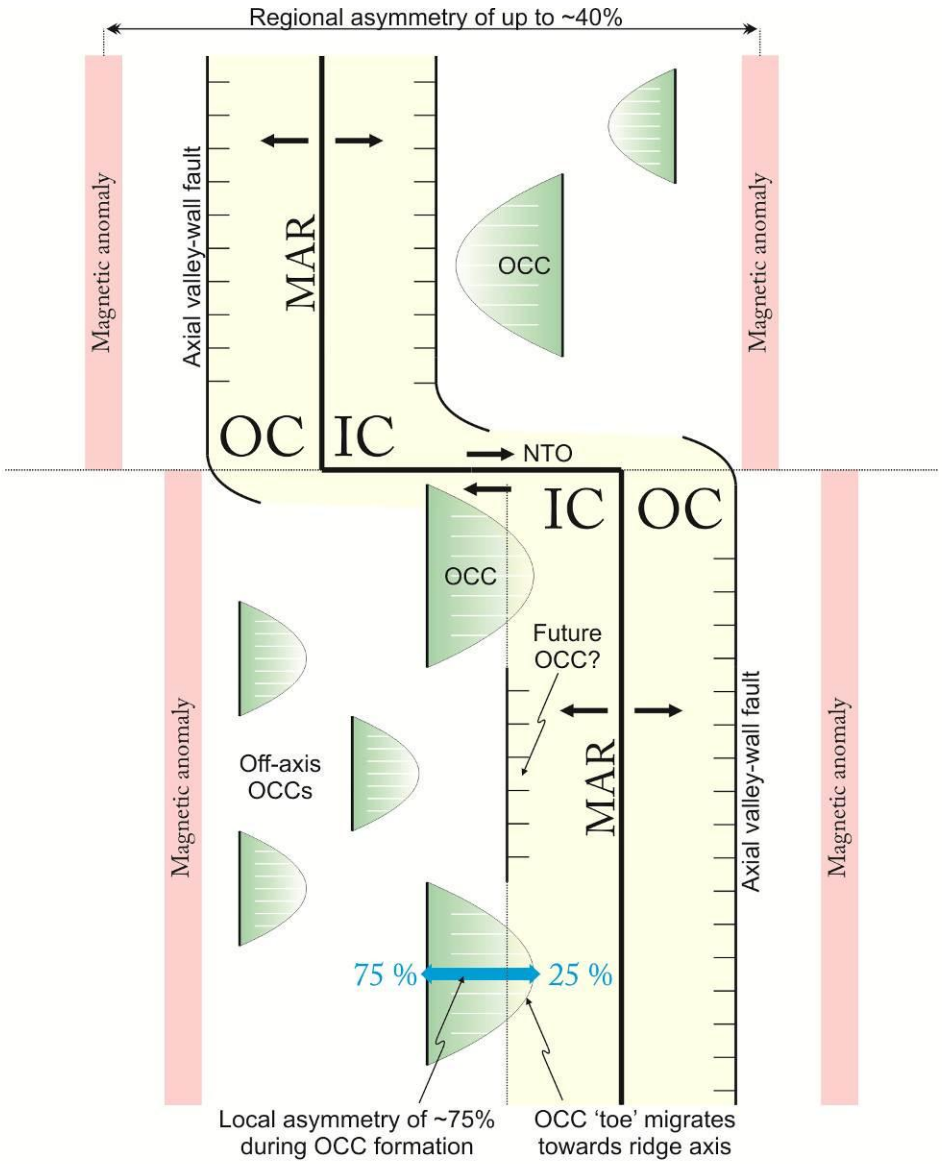


Figure 5.3.6. Schematic interpretation of spreading rate asymmetry across the 13°N region. There are two possible models that fit the data - a constant (regional) asymmetry of ~20-40% or a local asymmetry of ~75% during formation of individual OCCs. Note that in the 13°N region, OCCs are observed within the second-order inside corner ('IC'; conjugate outside corners are marked with 'OC') environment of the ridge NTO. See text for discussion.

5.3.3. Age of formation of near-axis OCCs

Having calculated the regional spreading rate and sense of asymmetry, it is possible to reconstruct the spreading history of the 13°N region. In *Section 3.3.1* I calculated the average duration of 27 OCCs in the area to be 0.44 My. These durations were calculated for a half-spreading rate of 13 km/My so as to be analogous to the durations calculated by Tucholke *et al.* (1998) for some 17 OCCs on the MAR between 21°18'N-31°17'N. In this section, I consider the possibility that OCCs act as the plate separation axis during their life times, thus forming at the full-spreading rate of 25.7 km/My.

OCC1319 is between 8.8 km and 11.1 km wide – the precise distance is uncertain due to the ambiguous position of the OCC's breakaway (*Section 3.3.1.3*). If OCC1319 is forming at half the regional spreading rate of 25.7 km/My (i.e. assuming there is no asymmetry in crustal accretion), the detachment must have been active for 0.68 – 0.86 My. Note, however, that if an OCC forms at only half the spreading rate this implies that other processes must also contribute to plate separation, such as magmatic accretion within the hanging-wall. This is consistent with numerical modelling results (e.g. Buck *et al.*, 2005; Behn & Ito, 2008; Tucholke *et al.*, 2008; Olive *et al.*, 2010), but does not fit the observation that volcanism appears to be absent during part or all of the OCC life cycle in the 13°N region (*Section 3.4.2*). If OCC footwalls capture ascending melt, they may accommodate all of the plate separation. In this scenario, the duration of OCC1319 becomes 0.34 – 0.43 My (see also Table 3.3.1 for the duration of other OCCs in the 13°N region). This estimate is a maximum as introducing any melt into the hanging-wall during OCC formation will accommodate some amount of plate separation. Essentially, increasing M_{HW} (the component of magmatic plate separation in the hanging-wall) consequently increases the duration of each OCC (Figure 5.3.7). The across-axis distances of OCC1330 and OCC1348 are 8.7 – 11.8 km and 8.2 – 11.6 km, and thus formation at the full-spreading rate (i.e. when M_{HW} is zero) gives a duration for these OCCs of 0.34 – 0.46 My and 0.32 – 0.45 My, respectively.

Sidescan sonar data show that OCC1319 and OCC1330 have relatively thin sediment cover, which, combined with their proximity to the ridge axis, suggests that they are presently, or very recently, active. Thus their durations also give an estimate of the time at which they formed. Assuming OCCs form when M_{HW} is zero, OCC1319 and OCC1330 are interpreted to have initiated between 0.34 – 0.43 Ma and 0.34 – 0.46 Ma, respectively.

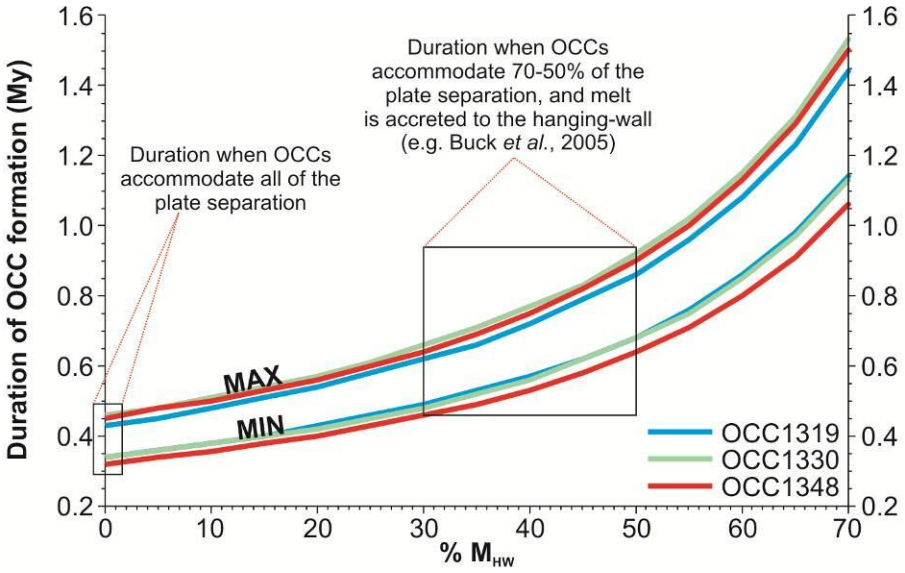


Figure 5.3.7. Duration of near-axis OCCs as a function of magmatic accretion in the hanging-wall. If OCCs form with no melt accreted within the hanging-wall, each OCC accommodates all the plate separation and forms relatively quickly (within ~0.4 My). If melt is accreted to the hanging-wall, OCCs accommodate less of the plate separation and take longer to form (within ~0.8 My for 50% magmatic accretion within the hanging-wall). Minimum and maximum durations for each OCC are the result of ambiguity in across-axis OCC extent. See text for discussion.

OCC1348 is highly sedimented and sub-horizontal and is thus interpreted as inactive. In this case an estimate of the age of formation can be made by making a few assumptions about the spreading history of the OCC. Firstly, it is assumed that the current location of the OCC's breakaway ridge initially formed at the along-axis projection of the present-day axial valley-wall fault (Figure 5.3.8a-b). Secondly, it is assumed that during the active phase of the life cycle of OCC1348, the detachment fault accommodated all of the plate separation – i.e. M_{HW} was zero. The 8.2 – 11.6 km across-axis extent of OCC1348 thus slipped at the full-spreading rate of 25.7 km/My within 0.32 – 0.45 My (Figure 5.3.8c). Finally, it is assumed that after the OCC became terminated the breakaway ridge migrated to its current location by conventional seafloor spreading processes; sidescan sonar data show that magma-rich crustal accretion resumed after termination, and so it is assumed that the breakaway moved east with the AF plate to its current location at the half-spreading rate (Figure 5.3.8d). The ages of initiation and termination of OCC1348, assuming that it acts as the ridge axis during its lifetime and M_{HW} is zero, are therefore 0.82 – 0.89 Ma and 0.37 – 0.57 Ma, respectively. If the OCC had slipped at half the spreading rate when M_{HW} = 50%, then the distance from the axial valley-wall fault to the breakaway indicates that it may have initiated at ~1.04 Ma and terminated at 0.15 – 0.40 Ma.

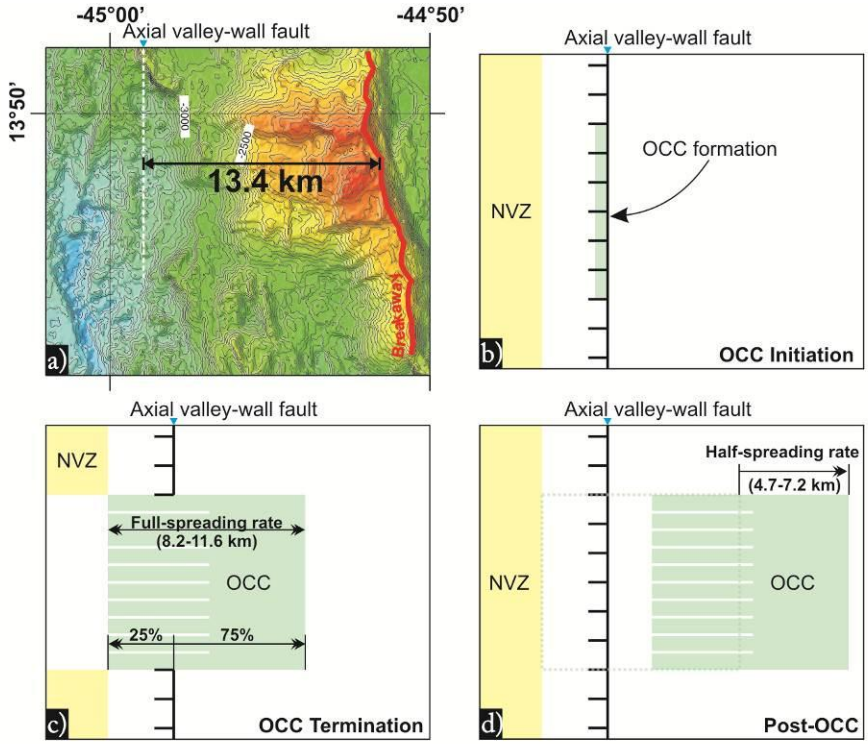


Figure 5.3.8a-d. Calculating the age of formation of OCC1348. **a)** Bathymetry data with 50 metre contours. The breakaway is currently 13.4 km from the along-axis projection of the axial valley-wall fault. **b)** It is assumed that the OCC originally formed about the axial valley-wall fault in the configuration shown. **c)** The OCC accommodates 100% of the plate separation and forms within 0.32 – 0.45 My at the full-spreading rate of 25.7 km/My. At termination, the breakaway is assumed to lie ~6.2 – 8.7 km east of the axial valley-wall fault. **d)** Magmatic accretion resumes and the OCC is rafted off-axis at the half-spreading rate; this must take ~0.37 – 0.57 My to reach its present-day distance of 13.4 km from the axial valley-wall fault. The ages of initiation and termination of OCC1348 are thus 0.82 – 0.89 Ma and 0.37 – 0.57 Ma, respectively. See text for discussion.

Figure 5.3.9 shows the expected spreading history for the last 0.80 Ma in the 13°N region. It is assumed that OCCs slip at the full-spreading rate (i.e. when M_{HW} is zero – note the break in the stippled NVZ when OCCs are active – Figure 5.3.9) and grow about axial-valley wall faults. In this model, OCC1348 begins forming within the northern IC area of the NTO in the ridge axis at 0.80 Ma (Figure 5.3.9a). OCC1348 is active between 0.40 – 0.80 Ma and during this time there is no magmatic accretion or magnetic anomaly formation by conventional processes within the axial valley – this area becomes sedimented and volcanically inactive similar to the present-day axial valley floor adjacent to OCC1319.

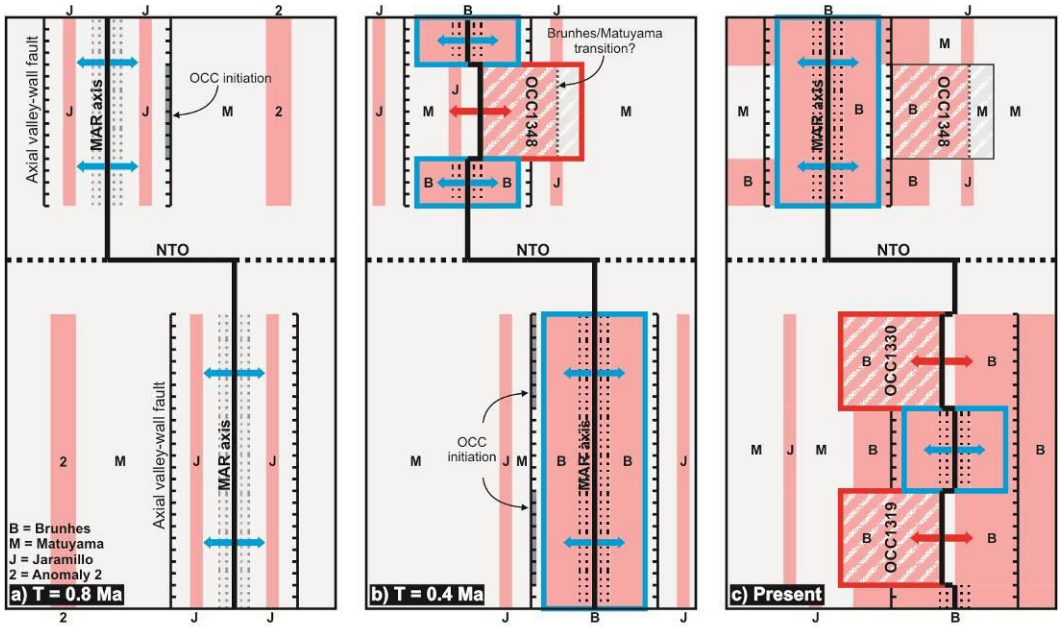


Figure 5.3.9a-c. Spreading history and age of formation of near-axis OCCs in the 13°N region relative to fixed plate boundary. Grey tones represent negatively-magnetised crust, red tones represent material accreted during positively/normal-magnetised magnetic intervals. Diagonally striped effect is detachment surface/OCC, stipled effect is NVZ (these may be grey or red depending on the polarity of the chron within which they formed). Blue arrows represent extension by magmatic accretion, red arrows represent extension by detachment faulting/OCC formation. Blue and red boxes in b) and c) delineate crust formed within last 0.4 My by 100% magmatic and tectonic processes, respectively. **a)** 0.8 Ma: Crustal accretion and magnetic anomaly formation are assumed to occur via conventional processes across the whole region. **b)** 0.4 Ma: OCC1348 forms within the IC north of the NTO between 0.4 – 0.8 Ma. During this time it acts as the spreading axis (note that there is no NVZ adjacent to active OCCs) and may partially record Matuyama and Brunhes events. OCC1319 and OCC1330 begin forming south of the NTO on the SA plate at 0.4 Ma. **c)** Present: OCC1319 and OCC1330 have reached their current extent of ~10 km and have recorded Brunhes-age events. Note that the magmatically constructed portion of the Brunhes (i.e. solid red tones - *not* diagonally striped OCCs) may exhibit significant along-axis variations in width. See text for discussion.

Instead, and if OCCs are able to acquire a magnetisation (either thermo-remanent in intruded gabbro or chemical remanent via serpentinisation of peridotite; e.g. Searle *et al.*, 2003), it may be expected that magnetic anomaly formation is recorded in the footwall of OCC1348. Thus, the oldest, breakaway and upper-massif part of OCC1348 may comprise negatively-magnetised Matuyama-age material, whereas the younger, domal section may comprise positively-magnetised Brunhes-age material. If magmatic accretion within the hanging-wall persisted throughout formation of OCC1348, it may be expected that the OCC began forming earlier to reach its current across-axis width and position, and therefore comprise a greater proportion of Matuyama-age material.

At approximately the same time that OCC1348 was being terminated (0.40 Ma), OCC1319 and OCC1330 began forming within the IC south of the NTO (Figure 5.3.9b). On the basis of backscatter intensity, it seems likely that OCC1330 initiated slightly

earlier than OCC1319, although the magnitude of this difference in the age of OCC initiation is most likely insignificant in terms of the expected magnetic anomaly pattern. These OCCs are thus expected to have formed entirely within the Brunhes chron. It is plausible that the present-day axial valley-floor may contain positively-magnetised, Brunhes-age material that formed by conventional magmatic processes prior to OCC formation between 0.40 – 0.80 Ma (which is discussed in the following section). Figure 5.3.9c shows the expected present day configuration of magnetic anomalies about the ridge axis. However, it should be noted that the existence of numerous off-axis OCCs on the SA plate south of the NTO may significantly modify this anomaly pattern (i.e. the model shown in Figure 5.3.9a-c assumes that crustal accretion and magnetic anomaly formation prior to 0.8 Ma was magma-rich, when in reality OCC formation and widespread detachment faulting is assumed to have been the dominant form of extension and magnetic anomaly formation in this region for perhaps > 4 My).

In the following section, I compare the predicted magnetic anomaly pattern shown in Figure 5.3.9c with the observed magnetisation across near-axis core complexes and intervening regions. Deviations between the predicted and observed pattern are then interpreted and modelled as heterogeneities in melt supply and crustal accretion processes.

5.4. OCC magnetisation & implications for melt emplacement

In the previous section I showed that the central positive anomaly (which reflects material accreted magmatically during the Brunhes chron) is discontinuous and chaotic in nature, and, based on the estimated ages of core complexes, I predicted the magnetic anomaly pattern across near-axis OCC footwalls. It was also shown that the CPA is often considerably narrower than the expected width of the Brunhes (~20 km), and I suggested that OCC formation may be responsible for this apparent Brunhes-age 'deficit'.

There are a hierarchy of factors that control the overall pattern of magnetisation recorded at the ridge axis, the most significant of which is melt supply. For example, rather than forming a continuous Vine-Matthews-Morley magnetic lineation, the CPA appears to form discrete 'highs' of positively magnetised crust that are similar to ridge-centred RMBA lows (which have previously been interpreted as centres of magmatic upwelling; *Section 4.3.4*). These areas most likely reflect discrete accumulations of highly-magnetised, neovolcanic material that have formed in response to further partitioning of the melt supply at shallow depths. In turn, local variations in melt supply are expected to regulate the initiation, formation and termination of OCCs at the ridge axis. Although an OCC formed entirely within the Brunhes chron would be expected to record a positive magnetisation (e.g. through serpentinisation of peridotite), there are several processes that conspire to add further complexity to the pattern of magnetisation. For example, lower crustal material (i.e. sheeted dikes and gabbro) exposed by detachment faults may record very little magnetisation and magnetic minerals may be hydrothermally de-magnetised in the presence of OCCs (as is observed at TAG; Tivey *et al.*, 2003). In addition to this, mass wasting and denudation of the OCC during uplift and flattening of the detachment surface may physically segment the magnetic source layer to the point where it has no resolvable magnetisation. Finally, irregular melt supply and footwall capture of ascending melt, combined with local variations in the extent of serpentinisation beneath OCCs, may also contribute to the 'chaotic' pattern of magnetisation at the ridge axis. In this section I will discuss the magnetic anomaly patterns across near-axis OCCs in terms of these factors and consider the history of melt emplacement in the region.

5.4.1. OCC1319: Magnetisation

OCC1319 is generally associated with low amplitude negatively-magnetised crust, having a minimum value of -3 A/m over the centre of the upper massif (Point 1 - Figure 5.4.1). Across the NE part of the domal section, the OCC has a slightly positive magnetisation of ~3 A/m (Point 2 – Figure 5.4.1), although this is poorly constrained by the data. This area of positive magnetisation gently grades into the local peak in magnetisation associated with robust magmatism and volcanic activity in the hanging-wall to the NE (Point 3 – Figure 5.4.1). Across the SE part of the dome, there is no such positive magnetisation associated with the footwall; thus if the positive to the NE is associated with material forming the OCC then this indicates that the structure of the footwall is magnetically heterogeneous. It is possible that the 3D solution is not a good representation of footwall magnetisation in areas where data coverage is low (i.e. between survey lines), and thus the 2D magnetisation solution along survey line 2 most likely gives the best estimate of footwall composition (which has a weak, positive magnetisation across the youngest part of the OCC dome; upper panel – Figure 5.4.1).

Across-axis, on the younger side of OCC1319, the CPA is well-formed, displaying a peak in magnetisation centred at 44°51’W, 13°19’N (Point 4 – Figure 5.4.1). From the 2D and 3D magnetisation solutions this peak in the CPA is between ~8 – 13 km wide and therefore constitutes around 0.30 – 0.50 My of magmatic accretion during the Brunhes chron at a full-spreading rate of 26 km/My; thus there is a deficit in the width of the Brunhes which has lasted for 0.28 – 0.48 My. This is consistent with sidescan sonar data that show this area of high magnetisation to correlate with low backscatter intensity and therefore thick sediment cover, indicative of a volcanic hiatus that has persisted for a few 100 Ky (*Section 3.4.2*). This gives the impression that magmatism persisted for 0.30 – 0.50 My, forming a peak in the CPA, then ceased for a period of similar length creating the sedimented axial valley-floor observed in this region. This pattern of magnetisation is thus similar to that which has been predicted in *Section 5.3.3* (Figure 5.3.9c).

The deficit in the width of the Brunhes can be accounted for by the formation of OCC1319, which is ~9 – 11 km wide (the precise width is dependent on the location of the breakaway ridge, which cannot be unambiguously identified – *Section 3.3.1.3*). Thus the footwall of OCC1319 formed during the Brunhes chron, yet across its upper massif it displays a weakly-magnetised, negative polarity signature.

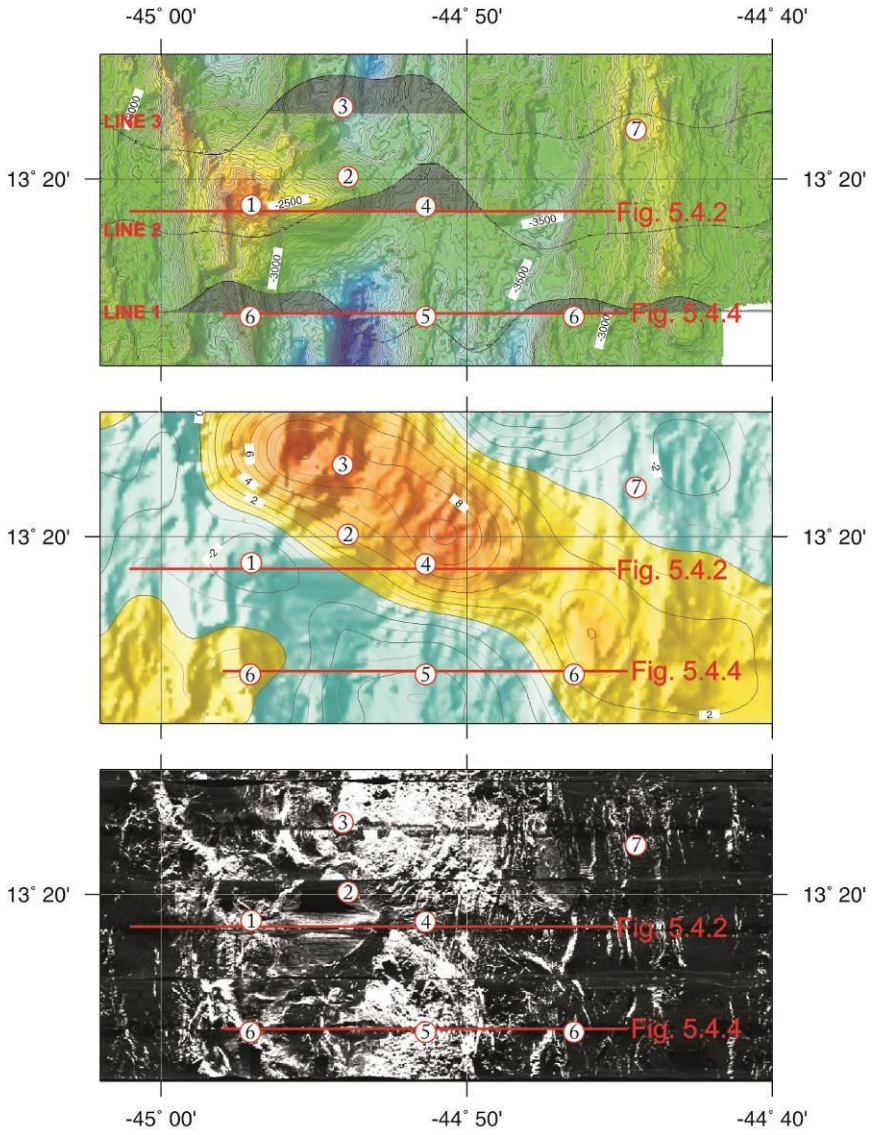


Figure 5.4.1. Magnetisation pattern across OCC1319. Upper panel shows 2D magnetisation solutions for survey lines 1-3 across bathymetry data (with 50 metre contours). Centre panel is 3D magnetisation solution (colour scale as **Figure 5.3.2**). Lower panel is sidescan sonar data, allowing for the position of magnetisation highs and the NVZ to be compared. Red line is position of profile in **Figure 5.4.2** and **Figure 5.4.4**. Numbered points are referred to in the text.

A similar relationship is observed at TAG, where ~0.35 My of extension on a fault that is ~3.9 km across-axis has created a negatively-magnetised trough with amplitude of ~-5 A/m within the Brunhes (Tivey *et al.*, 2003). Tivey *et al.* (2003) suggest that the primary mechanism for forming this low within the Brunhes is exhumation of non-magnetic dikes and gabbro, and that the contribution of hydrothermal alteration and mass-wasting to demagnetisation is likely to be insignificant; i.e. they imply that there is no negative polarity crust exposed by the fault and that the trough within the Brunhes is merely created by an 'overshoot' of the inversion process.

To test possible models for the magnetic structure of the footwall of OCC1319, I forward model a short section of survey line 2 (13°19'N) using *Gravmag* (*Section 4.4.2*). The basic model set-up assumes that magnetic source material is confined to the upper 0.5 km of the crust and has a 10 km wide section of Brunhes-age material across the axial valley (Figure 5.4.2). The peak in magnetic anomaly can be approximately matched by partitioning the Brunhes-age material into a number of smaller blocks, the central-most one of which has relatively high magnetisation (15 A/m) and is bounded by blocks that have a magnetisation of ~6 A/m. Matuyama-age material is assumed to have a magnetisation of -4 A/m, and the block which forms the outer-slope of the OCC's breakaway is rotated counter-clockwise by 45°.

The first model I test assumes that magnetisation across the entire footwall of OCC1319 is zero ('predicted 1' – dotted black line – Figure 5.4.2). This is analogous to the model proposed for TAG by Tivey *et al.* (2003), yet it does not give a particularly good match to the observed data across OCC1319; the zero magnetisation of the footwall causes the predicted anomaly to flatten-out at zero nanotesla so that it is less than the observed anomaly over the younger part of the OCC and greater than the observed anomaly over the older part of the OCC by ~100 – 200 nT. Increasing the magnetisation of the Brunhes-age hanging-wall material that is juxtaposed against the footwall or changing the dip of the detachment surface does not significantly improve the fit between the two datasets. Instead, a better fit to the data is attained when the OCC is partitioned at the upper massif/domal section boundary and the older block is assumed to have a magnetisation of -4 A/m and the younger block is assumed to have a magnetisation of +3 A/m ('predicted 2' – solid black line – Figure 5.4.2). Each of these footwall blocks are rotated by 45° counter-clockwise in the model, simulating exhumation and flattening of the detachment surface. The precise degree of rotation is dependent on the subsurface detachment geometry which in this region is largely unknown, although palaeomagnetic studies from other OCCs suggest that rotation may be within the range 46±6° (Morris *et al.*, 2009) and 50 – 80° (Garces & Gee, 2007; *Section 1.3.3*). Increasing the degree of rotation of footwall material requires that the magnetisation and/or thickness of the blocks must be increased to create a similar amplitude anomaly, and *vice versa*.

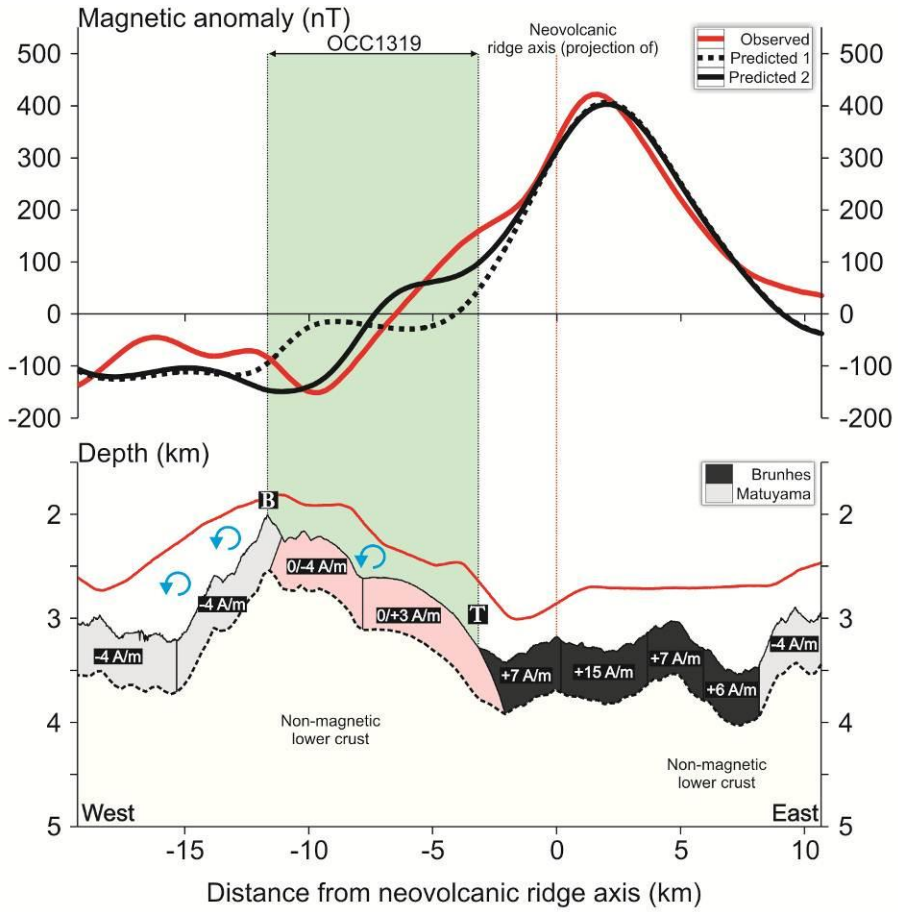


Figure 5.4.2. Forward model of magnetisation distribution across OCC1319 (survey line 2). Upper panel shows observed and predicted magnetic anomalies, lower panel shows magnetisation distribution. In the first model (dotted black line - predicted 1) the footwall of the OCC (pink shading) has no magnetisation. In the second model (solid black line - predicted 2) the upper massif of the OCC has a negative magnetisation (-4 A/m) and the domal section has a positive magnetisation (+3 A/m). The footwall and outer slope of the OCC have been rotated by 45°. Regional position marked in **Figure 5.4.1**. See text for discussion.

Geologically, the positive magnetisation across the domal section of the OCC may represent serpentinised peridotites and captured melt that have acquired a relatively weak magnetisation whilst being unroofed during the Brunhes (3 – 4 A/m is within the range of magnetisations for each of these rock types – Table 1.2.2). The negative magnetisation across the upper massif suggests that it may comprise a significant proportion of Matuyama-age material. This seems unusual as based on the across-axis deficit in the width of Brunhes-age hanging-wall material, it is expected that the OCC formed entirely during the Brunhes chron (e.g. Figure 5.3.9c). However, I note that although the OCC may have formed entirely within the Brunhes chron, it may have physically initiated off-axis within Matuyama-age crust (Figure 5.4.3).

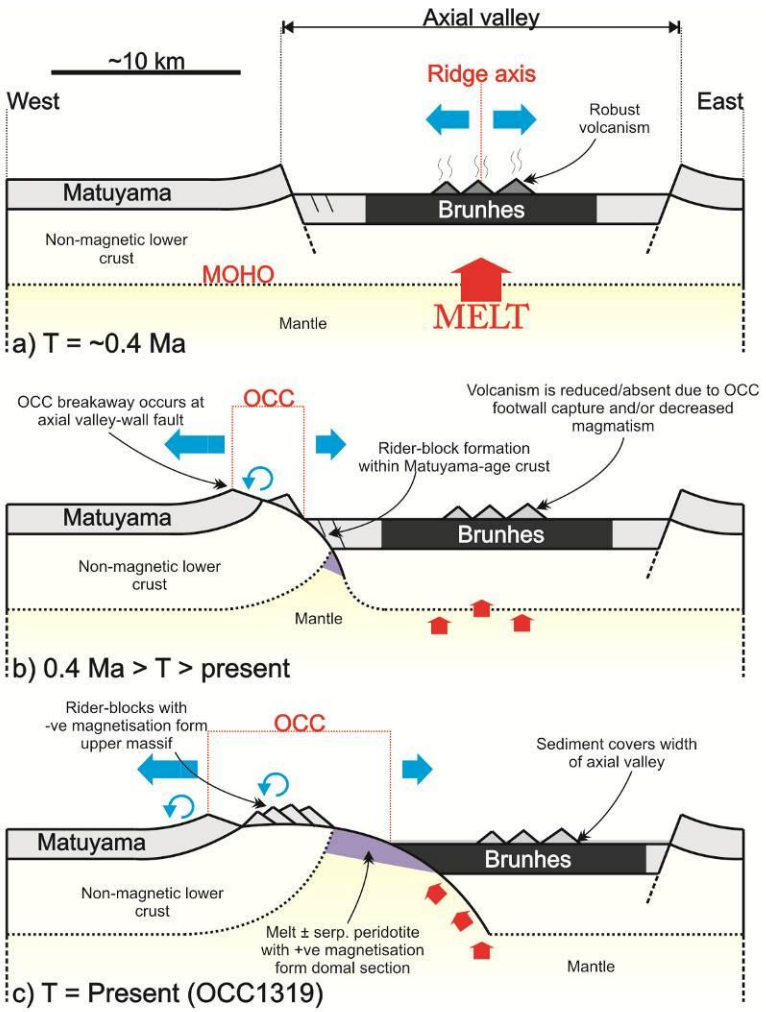


Figure 5.4.3a-c. Interpretation of magnetic structure and spreading history of OCC1319. Blue arrows indicate spreading rates; red arrows indicate melt migration. **a)** ~0.4 Ma: the Brunhes is ~10 km wide and volcanism covers the axial valley. **b)** Melting conditions at the ridge axis instigate OCC formation, the breakaway of which forms at the axial valley-wall fault which lies within negatively magnetised, Matuyama-age crust. **c)** As the footwall/hanging-wall boundary migrates towards the ridge axis, Matuyama-age material is transferred from the hanging-wall to the footwall as rider-blocks. This gives the older (western) part of the OCC a negative magnetisation. Prolonged extension causes the footwall and outer slope of the OCC to rotate and flatten out. Ultimately, a mixture of positively-magnetised serpentinised peridotite and captured melt is unroofed at the younger (eastern) part of the OCC. Sediment builds up across the axial valley during the volcanic hiatus. See text for discussion.

In such a model, the upper massif at depth may be composed primarily of non-magnetic lower-crustal material (as implied for TAG), but during extension on the OCC-forming detachment fault, the footwall may have clipped Matuyama-age rider-blocks off of the hanging-wall. If these rider-blocks sit atop the OCC in the location of the upper massif (as suggested by Smith *et al.*, 2008), this may give the area a negative magnetisation. Alternatively, Matuyama-age lower-crustal material – which has previously been assumed to have no magnetisation – may have a weak negative magnetisation. However,

as we shall see in the following section, based on seafloor morphology OCC1330 does not have any rider-blocks and is associated with an area of zero magnetisation across the upper massif, suggesting that lower-crustal material acquires no magnetisation during OCC formation.

The main limitation with this model is that Matuyama-age rider-blocks cannot account for the negative magnetisation observed within the 3D magnetisation solution across the SE part of the domal section. This area is clearly not part of a rider-block, and it seems unlikely that the basaltic scree sampled from the dome of the OCC has the magnetic homogeneity to contribute significantly to the magnetic field. It is also difficult to envisage any realistic scenario by which material accreted within the footwall during the Brunhes chron may acquire a negative magnetisation; hydrothermal de-magnetisation would have to be highly extensive and localised across only the southern part of the dome, or material would have to undergo > 90° of rotation. Therefore, it seems that the 3D magnetisation solution is not a good indicator of footwall structure in this area due to low data coverage and the influence of negatively-magnetised crust in the hanging-wall to the SE of the OCC (the formation of which I discuss below). It would be ideal to have a series of short magnetic profiles collected at the seabed across the footwall/hanging-wall contact to clarify the exact nature of footwall magnetisation.

South of OCC1319 there is only a minor peak in magnetisation within the axial valley (Point 5 – Figure 5.4.1), with the bulk of the CPA/Brunhes-age material displaced from the ridge axis forming an area of positive magnetisation across the axial valley-wall fault in the east and southern tip of the OCC breakaway ridge in the west (Points 6 – Figure 5.4.1). The area of weakly-magnetised crust within the axial valley corresponds to robust, widespread neovolcanism (sidescan sonar – Figure 5.4.1). Therefore, the NVZ to the south must form only a thin veneer of Brunhes-age volcanism which overlies a much thicker accumulation of negatively-magnetised (Matuyama-age?) material; the amplitude of magnetisation determined by the inversion process is essentially an average over 0.5 km, it does not take into consideration vertical changes in magnetisation. This can be demonstrated by using *Gravmag* to forward model a section of data collected along survey line 1 (Figure 5.4.4, with profile location shown in Figure 5.4.1). In this model I assume that magnetic source material is confined to a continuous 0.5 km thick layer and that Brunhes-age material (< 0.78 Ma) is erupted through and on top of Matuyama-age material (> 0.78 Ma). By assigning Brunhes-age

material a magnetisation of 12 A/m and the underlying Matuyama-age material a magnetisation of -8 A/m, I find that the Brunhes layer must be < 50 metres thick at the ridge axis and across most of the central part of the axial valley floor at this latitude. The Brunhes layer must thicken towards and across the edges of the axial valley (so that it becomes ~200 – 250 metres thick) to match the relatively high amplitude positive anomalies in these regions. If a more realistic magnetisation distribution were used in which the youngest, ridge-centred material had higher magnetisation compared with the older, off-axis material, this would require the thickness of the layer at the ridge axis to be even thinner and thicknesses off-axis to be greater; hence the overall pattern of thickness variations would stay the same.

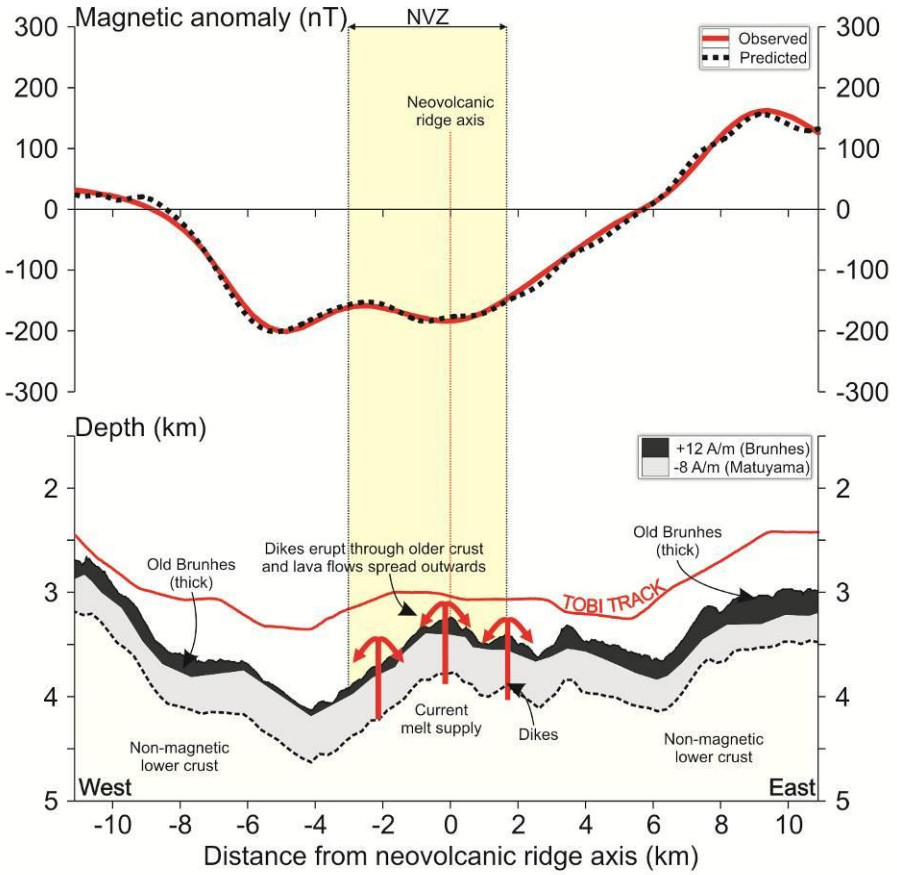


Figure 5.4.4. Forward model of magnetisation distribution within the axial valley beneath survey line 1 (13°16'N). Upper panel shows observed and predicted magnetic anomalies, lower panel shows magnetisation distribution. In this area, the NVZ (yellow vertical bar) is associated with a low magnetic anomaly/magnetisation; this is unusual as it would be expected that young lava flows should be associated with a high magnetic anomaly/magnetisation. This can be accounted for if it is assumed that Brunhes-age material is fed by dikes and forms only a thin veneer above predominantly Matuyama-age material. See text for discussion.

The across-axis magnetic symmetry of survey profile 1 indicates accretion has been more-or-less fixed in the same location; across-axis variations in the thickness of

Brunhes-age material therefore imply that the local melt supply has waxed and waned during the last 0.78 Ma. The depression within the Brunhes anomaly to the south of OCC1319 is ~10 km wide and is therefore of similar width (and thus age) to the OCC. This suggests that although volcanism may have persisted in this area throughout formation of the nearby OCC, it appears to have been at a reduced strength. If OCCs are able to control melt emplacement pathways at depth by footwall capture (as is suggested by the gaps in the NVZ adjacent to OCC1319 and OCC1330 – *Section 3.4.2*), it may be the case that OCC1319 has siphoned some of the rising melt from beneath the axial valley to the south, creating the waning effect observed in the magnetic data at 13°16'N. However, the magnetisation pattern observed to the south of the OCC is not repeated immediately north of the OCC, where high magnetisation and robust neovolcanism (evident from sidescan sonar data) coincide – suggesting that magmatism and magnetic anomaly formation have been relatively robust throughout the formation of OCC1319. It is possible that the slight peak in magnetisation at 44°45'W, 13°22'N is of Brunhes-age (which would give rise to an intra-Brunhes depression along survey line 3 similar to that which is observed along survey line 1), but it is also possible that this peak arises from de-magnetisation of Matuyama-age material across relatively large faults in this region (Point 7 – Figure 5.4.1). If the Brunhes anomaly only forms in one place north of the OCC (i.e. Point 3 – Figure 5.4.1), there must be significant local variations in patterns of upwelling melt at scales < 12 km (i.e. the distance between survey lines 1 and 3). It is also possible that the depression in the Brunhes anomaly south of OCC1319 is not directly related to footwall capture of ascending melt, but relates to a natural periodicity in which melt emplacement goes through robust and weak phases.

5.4.2. OCC1330: Magnetisation

OCC1330 was surveyed by three deep-towed profiles 3 km apart and this added data coverage helps to highlight the complexity of crustal magnetisation across the footwall and adjacent axial valley. For example, the 2D magnetisation solution along survey line 6 indicates that the summit of OCC1330 is associated with weakly-magnetised, negative polarity material (Point 1 – Figure 5.4.5); this area of reduced magnetisation coincides with the across-axis limits of the OCC (although the exact location of the breakaway is ambiguous – *Section 3.3.1.4*). The 3D magnetisation solution, which may be better constrained in the presence of complex topography (and is better constrained by

increased data coverage over OCC1330 compared with OCC1319), shows a similar depression in magnetisation over this area, albeit with an overall positive magnetisation of ~1 – 2 A/m. The northern and southern halves of the OCC appear to be associated with areas of positive magnetisation (in both the 2D and 3D solutions; Points 2 – Figure 5.4.5). If magnetisation is recorded in the footwall by serpentinisation of peridotite and accretion of melt (as may be the case for OCC1319 – *Section 5.4.1*), the discontinuous nature and variations in amplitude of magnetisation across the OCC might reflect localised variations in these processes.

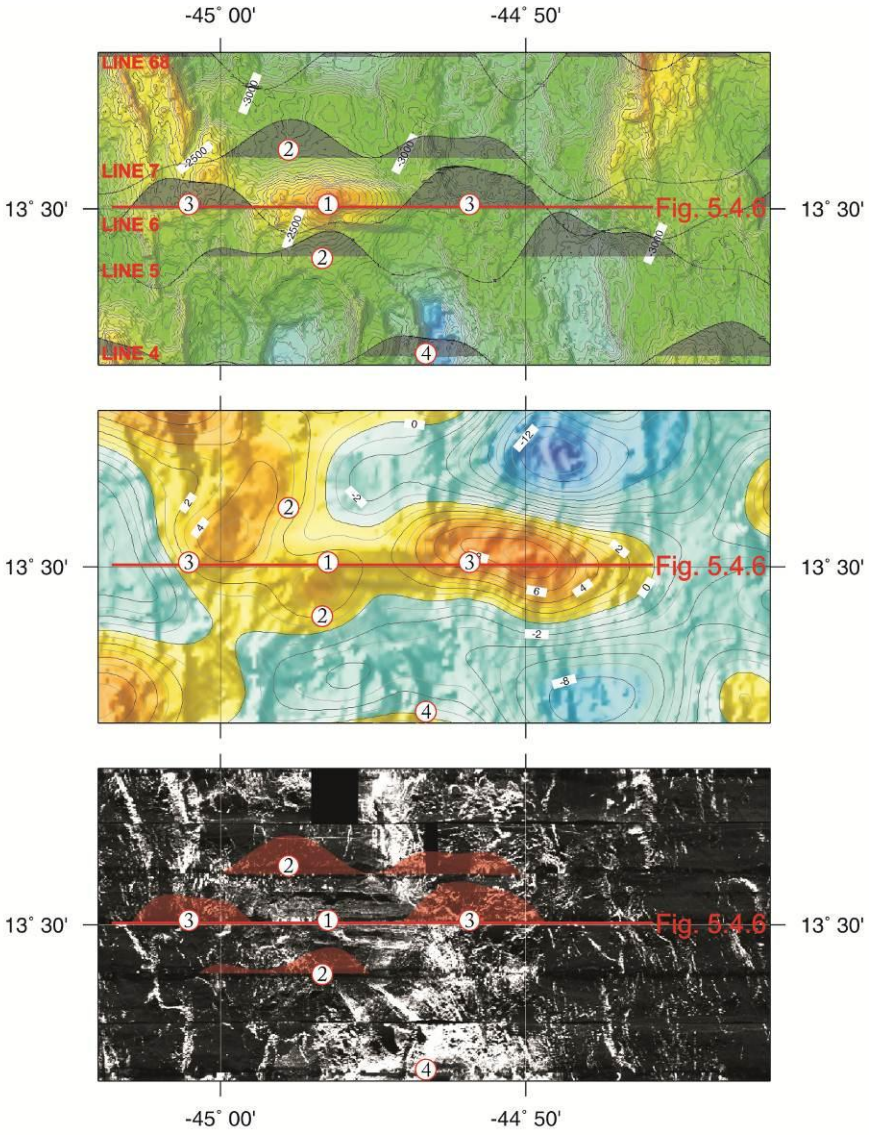


Figure 5.4.5. Magnetisation pattern across OCC1330. Upper panel shows 2D magnetisation solutions for survey lines 4-8 across bathymetry data (with 50 metre contours). Centre panel is 3D magnetisation solution (colour scale as **Figure 5.3.2**). Lower panel is sidescan sonar data, allowing for the position of magnetisation highs and the NVZ to be compared. Red line is position of profile in **Figure 5.4.6.** Numbered points are referred to in the text.

Widespread lithological heterogeneity of OCC footwalls has also been inferred from detailed seabed sampling of Kane Massif (Dick *et al.*, 2008) and seismic imaging of Atlantis Massif (Canales *et al.*, 2008). Canales *et al.* (2008) use seismic data to show that the upper part (depths < 1.5 km) of the 'Central Dome' of Atlantis Massif is underlain by a high velocity body that is ~8 km in diameter and is most likely of gabbroic composition. Furthermore, this gabbroic body does not account for all of the OCC footwall, with relatively low velocity material – interpreted as an area of widespread serpentinisation – forming the 'Southern Ridge' of the core complex. At Kane Massif, lithological variation over similar wavelengths is also predicted to occur (Dick *et al.*, 2008). Thus it seems plausible that the magnetic heterogeneity of the footwall of OCC1330 (and other near-axis OCCs in the 13°N region) may represent significant lithological variations that occur over distances of ~6 km (i.e. the distance between the points numbered '2' in Figure 5.4.5). These lithological variations may take the form of predominantly serpentinite-rich zones and gabbro-rich zones.

The area of reduced magnetisation across the OCC is bounded on its older and younger sides by peaks in positive magnetisation; thus the Brunhes anomaly appears to have been split by formation of the OCC. This can be demonstrated by using *Gravmag* to set up a model in which magnetic source material is confined to a 0.5 km thick layer and positively-magnetised material of Brunhes-age exists across the axial valley and beyond the breakaway of the OCC (Figure 5.4.6). Peaks and troughs away from the OCC can be approximately matched by varying the magnetisation of the source material by 3 to 12 A/m (Brunhes) and -2 to -4 A/m (Matuyama). As has been shown for OCC1319 in the previous section, assuming that the footwall of OCC1330 has zero magnetisation does not give a particularly good match between observed and predicted data, having a mismatch of ~100 – 150 nT across the OCC ('predicted 1' – dotted black line – Figure 5.4.6). If, however, the summit and domal part of the OCC are assigned a magnetisation of 4 A/m and assumed to have undergone 45° of rotation, the overall fit between observed and predicted anomalies is improved dramatically ('predicted 2' – solid black line – Figure 5.4.6). In this second model the oldest part of the OCC has zero magnetisation and the overall misfit is everywhere < 30 nT. It is not necessary to have negative polarity material forming the OCC to give an accurate match to the observed data, as is the case for OCC1319. This is consistent with the fact that the Brunhes anomaly is detected on the older side of the OCC; thus Matuyama-age rider-blocks are unlikely to have ever formed on OCC1330 (in addition to this, the OCC does

not have a distinct topographic upper massif that may be built by rider-blocks, as is observed at OCC1319 – e.g. Figure 5.4.3). As I have suggested in the previous section, positively magnetised material across the younger parts of OCCs most likely represents a combination of serpentinised peridotite and gabbroic material that has been captured by the footwall during the Brunhes; 4 A/m is within the range for each of these rock types (Table 1.2.2). The older part of OCC1330 most likely comprises non-magnetic lower-crustal material exposed at the seafloor.

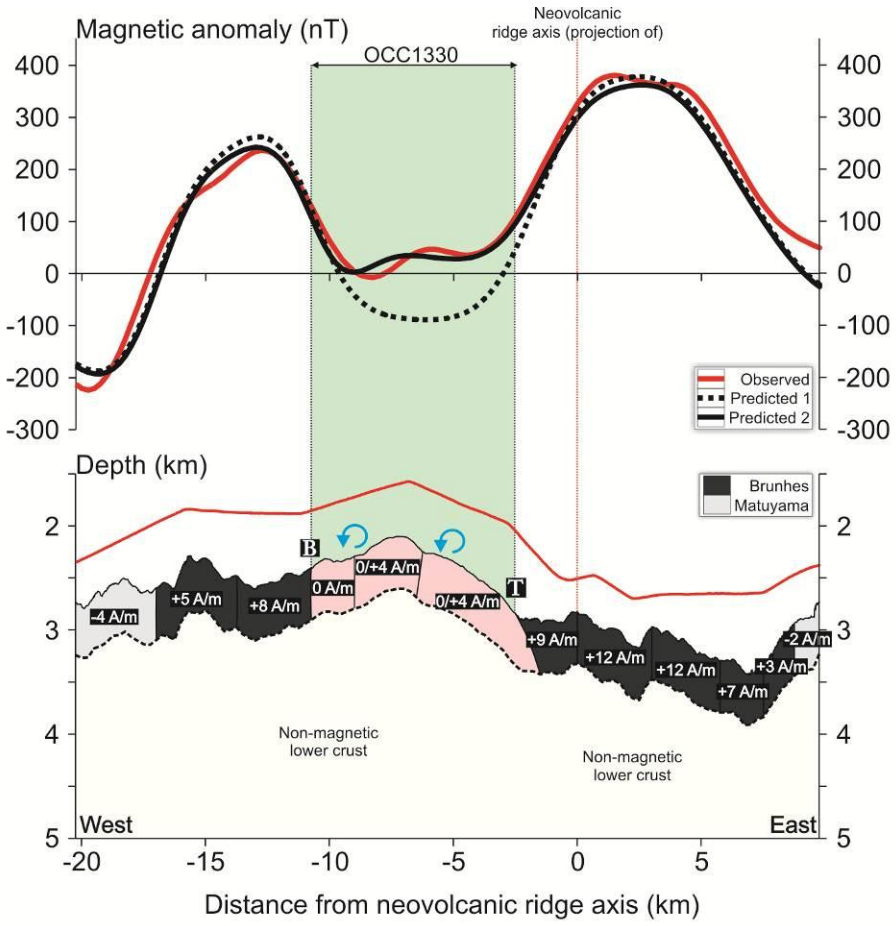


Figure 5.4.6. Forward model of magnetisation distribution across OCC1330 (survey line 6). Upper panel shows observed and predicted magnetic anomalies, lower panel shows magnetisation distribution. In the first model (dotted black line - predicted 1) the footwall of the OCC (pink shading) has no magnetisation. In the second model (solid black line - predicted 2) the oldest part of the OCC still has no magnetisation but the domal section has a positive magnetisation (+4 A/m). The footwall and outer slope of the OCC have been rotated by 45°. Regional position marked in **Figure 5.4.5.** See text for discussion.

The most striking difference between the magnetisation associated with OCC1319 and that associated with OCC1330 is that the latter exhibits crust with positive magnetisation on the older, western side of the OCC. Positive peaks in crustal

magnetisation are symmetrical about OCC1330, having a width of ~7 – 8 km on both the older and younger sides (Point 3 – Figure 5.4.5). This is unusual as, based on backscatter intensity, the footwall of OCC1330 is slightly older than OCC1319 and thus OCC1330 may be expected to have formed within older crust. It appears from the magnetic data, however, that OCC1319 initiated in Matuyama-age crust (and formed rider-blocks) whereas OCC1330 initiated in Brunhes-age crust. This is not predicted by the relatively straight-forward model presented in Figure 5.3.9, but may be accounted for if the across-axis location of material accreted during the Brunhes is highly variable along-axis (which appears to be the case in the 13°N region – *Section 5.3*). For example, in the region between OCC1319 and OCC1330, the bulk of the Brunhes anomaly is displaced from the bathymetric ridge axis and is centred over the western axial valley-wall fault (Point 4 – Figure 5.4.5; see also Point 3 – Figure 5.4.1). This area is volcanically active (as shown by sidescan sonar data), and thus it seems that the Brunhes is actively being constructed close to the axial valley wall-fault – possibly due to footwall capture of ascending melt (e.g. MacLeod *et al.,* 2009; Standish & Sims, 2010) – rather than simply being rafted away from the centre of the axial valley which occurs several kilometres to the east. It is possible that the large bathymetric depression running parallel to this fault has formed in response to downward bending of the hanging-wall. Subsequent compression within the hanging-wall may have resulted in melt preferentially being erupted towards this location. If this normal fault subsequently develops into an OCC-forming detachment fault (as suggested by Smith *et al.,* 2008), the Brunhes would be split in two and the magnetic data would give the impression that the OCC formed about the ridge axis, when in reality if formed about the axial valley-wall. Thus it appears that the early portion of the Brunhes constructed between 0.40 – 0.78 Ma (Figure 5.3.9b) may actually have been centred over the axial valley wall-fault about which OCC1330 formed. This implies that very large normal faults – precursory structures to detachment faults (MacLeod *et al.,* 2009) – may act to focus melt emplacement prior to OCC formation. However, the fact that there is no Brunhes on the older side of the apparently younger OCC1319 suggests that although melt focussing prior to OCC formation is observed in some places, it is not necessarily a requirement.

5.4.3. OCC1348: Magnetisation

OCC1348 is generally associated with negatively-magnetised material (Figure 5.4.7). The 3D inversion solution indicates that the most negative values occur over the breakaway ridge (~-7 A/m; Point 1 – Figure 5.4.7), and that the domal section is slightly less magnetised (~-4 A/m; Point 2 – Figure 5.4.7). The 2D inversion solution along survey line 12 also shows that the younger part of the OCC has a higher magnetisation (~1 A/m) compared with the older part of the OCC (~-8 A/m).

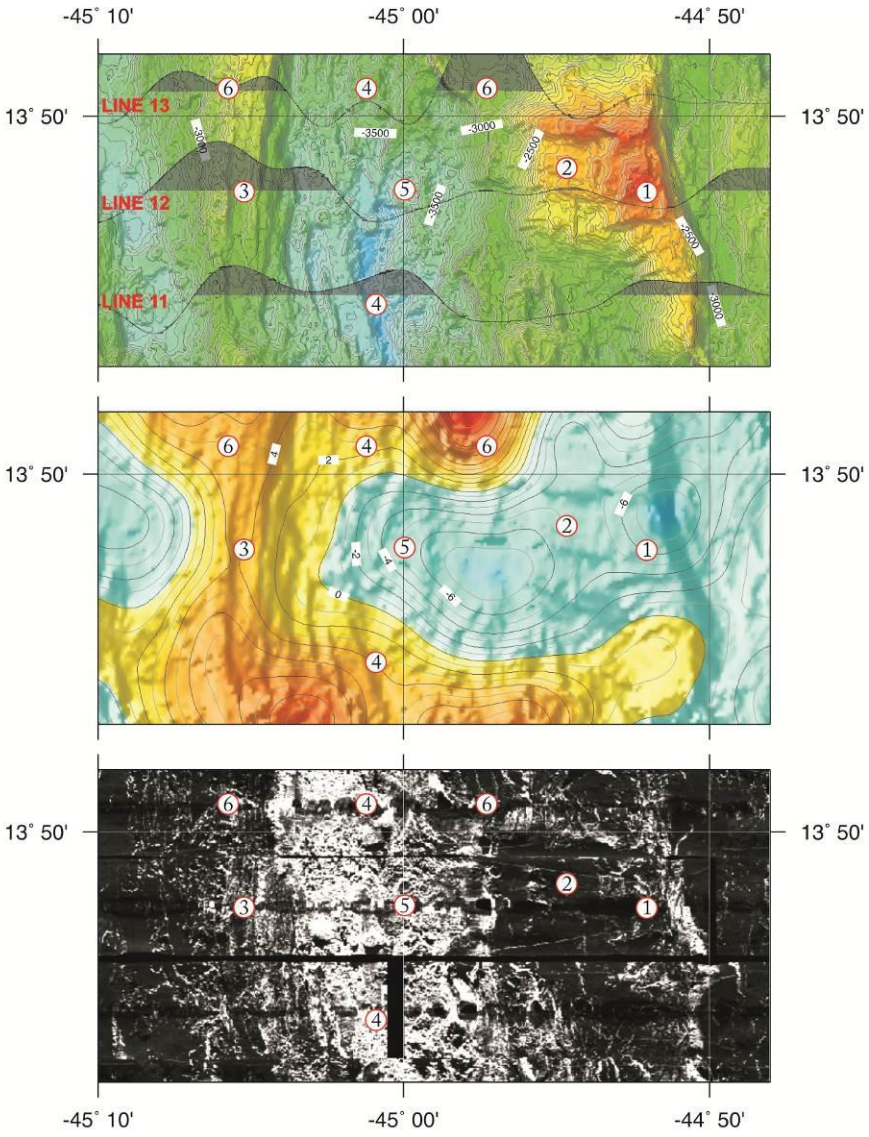


Figure 5.4.7. Magnetisation pattern across OCC1348. Upper panel shows 2D magnetisation solutions for survey lines 11-13 across bathymetry data (with 50 metre contours). Centre panel is 3D magnetisation solution (colour scale as **Figure 5.3.2**). Lower panel is sidescan sonar data, allowing for the position of magnetisation highs and the NVZ to be compared. Numbered points are referred to in the text.

This pattern of magnetisation is consistent with the age of formation for OCC1348 of 0.37 – 0.89 Ma discussed in *Section 5.3.3*; the OCC may have recorded Matuyama and Brunhes events, with the older parts tending to be more negative than the younger parts. In addition to this, the upper massif of OCC1348 is similar in morphology to that observed across OCC1319 and may thus also comprise rider-blocks of Matuyama-age material that contribute to the overall negative magnetisation of this area.

The CPA is narrow at the latitude of OCC1348 (Point 3 – Figure 5.4.7) and wider immediately to the north and south of the OCC (Points 4 – Figure 5.4.7). This is similar to the magnetic anomaly pattern predicted in Figure 5.3.9, and suggests that magmatic accretion was more widespread at locations along-axis from where the OCC formed. Along survey line 13 (northern-most survey line in upper panel of Figure 5.4.7), there is a depression within the CPA that coincides with widespread neovolcanism in the axial valley (45°02'W). This pattern is remarkably similar to that which is observed along survey lines 1 and 5, which are immediately south of OCC1319 and OCC1330, respectively. The width of this depression, ~8 km, implies that magmatism has been relatively weak during the last ~0.32 My, and forms only a thin layer of Brunhes-age material in this area (and also to the south, immediately adjacent to OCC1348, where widespread neovolcanism is associated with low/negatively-magnetised crust; Point 5 – Figure 5.4.7). The pattern of magnetisation within the axial valley north of OCC1348 is unusual as it implies that melt supply is presently weaker than it was during formation of OCC1348. For example, it may be expected that the older parts of the Brunhes anomaly (Points 6 – Figure 5.4.7), which are associated with a high magnetisation and thus presumably robust magmatic accretion, were formed at the same time as OCC1348. However, the most recent part of the Brunhes anomaly, which has been constructed after the OCC has terminated, has a weak magnetisation and thus suggests poorly magmatic crustal accretion. This suggests that the weakly-magmatic processes responsible for initiating OCC formation near the beginning of the Brunhes chron were localised into an area that extended for < 6 km along-axis (i.e. at along-axis distance > 6 km the ridge may potentially be in a different phase of the magmatic/amagmatic cycle).

5.5. Chapter summary

In this chapter I have calculated crustal magnetisation from the magnetic total field anomaly and used this to assess OCC structure and quantify spreading rate asymmetry. In general, magnetic anomalies are highly discontinuous and, in most cases, poorly resolved across the 13°N region. This is consistent with the findings of a number of magnetic studies across magma-poor environments (e.g. Fujiwara *et al.*, 2003; Okino *et al.*, 2004; Smith *et al.*, 2008). Essentially, there is a hierarchy of factors that contribute to the low fidelity with which crustal accretion records magnetic anomalies along this section of the MAR. At the top of the hierarchy, intermittent and irregular melt supply causes anomalies to be 'blotchy' about the ridge axis. This is most clearly evident about the NTO at 13°38'N, where the Brunhes anomaly appears to have accreted in at least two separate locations. Regionally elevated tectonism, which may be controlled by magmatism, further contributes to the degradation of magnetic anomalies. Detachment faults may thin the magnetic source layer so that non-magnetic lower crustal material is exposed at the seafloor. OCC formation may then ultimately expose serpentinised peridotite and gabbro emplaced by ascending melt captured by the footwall at depth. This acquires a magnetisation parallel with the ambient geomagnetic field, but may become rotated with prolonged extension and flattening of the footwall. Focusing of hydrothermal alteration within the footwall of OCCs and mass wasting of magnetic source material may also increase the local complexity of the magnetisation. Despite these factors, I summarise the main findings of this chapter as follows:

Asymmetry in rate of crustal accretion

- There is evidence that plate separation spreading rates have been asymmetric during at least the last 1.86 My. The sense of asymmetry matches the pattern of tectonic strain discussed in *Section 3.5.2*; areas of increased tectonic strain and OCC formation (such as the SW- and NE-quadrants of the survey area) are associated with faster spreading. I note, however, that the precise degree of asymmetry is uncertain due to the temporally unstable position of the ridge axis. For example, if asymmetry is averaged over 1.86 My and calculated from the position of anomaly 2 relative to the low in the RMBA, it may in places be as great as 20 – 40% faster for plates that form OCCs. If asymmetry is calculated relative to the present day NVZ, asymmetry may be negligible (i.e. < 5%).

However, on the basis that the region is characterised by intermittent and weak melt supply, it seems unlikely that the present-day NVZ is a good indicator of the locus of magmatic accretion at ~1.86 Ma.

- If asymmetry is calculated relative to the ridge-centred RMBA low (which may provide the most stable estimate of the locus of melt emplacement over relatively long periods), the regional asymmetry is 20 – 40% averaged over 1.86 My. This could also be explained by shorter-periods of higher-asymmetry (~75 % for 0.40 My) that coincide with the formation of individual OCCs. This latter value is comparable with other studies which indicate that OCC formation occurs during periods in which the rate of plate separation is ~70 – 100% asymmetric (e.g. Fujiwara *et al.*, 2003; Searle *et al.*, 2003; Okino *et al.*, 2004; Baines *et al.*, 2008; Grimes *et al.*, 2008).

Magnetisation of OCCs & footwall structure

- OCC footwalls display highly heterogeneous magnetisation patterns. OCC1330, which was crossed by three closely-spaced magnetic profiles, gives the best indication of the magnetic structure of a near-axis OCC; considerable variations in magnetisation exist over distances of < 6 km. This may occur due to heterogeneity in footwall structure, which may be related to localised variations in the thickness and composition of the magnetic source layer. Compositional variations may reflect areas that formed under melt-rich (i.e. gabbroic) and melt-poor (i.e. serpentinised) conditions, as has been proposed for Kane Massif (Dick *et al.*, 2008) and Atlantis Massif (Canales *et al.*, 2008).

- Forward modelling of magnetic anomalies indicates that the footwalls of OCCs record a magnetisation during their formation. For a 0.5 km thick magnetic source layer, the domal parts of OCCs may have a magnetisation of ~3 – 4 A/m if they are assumed to have undergone 45° of rotation. This value of magnetisation is consistent with serpentinised peridotite and gabbroic material, and the degree of rotation is similar to the palaeomagnetic inclination of footwall material studied at Atlantis Massif (Morris *et al.*, 2009). If footwall material is rotated by a greater amount (e.g. Garces & Gee, 2007), it would need to have a greater magnetisation and/or thickness to maintain the same predicted anomaly. The older part of OCC1330 seemingly has no magnetisation, which may coincide with exhumed non-magnetic lower crust, as is observed at TAG (Tivey *et*

al., 2003). The negative magnetisation observed across the upper massifs of OCC1319 and OCC1348 may be created by crust of Matuyama-age being clipped from the hanging-wall in the form of rider-blocks during the early stages of OCC formation.

Chapter Six

Discussion & Conclusions

6.1. Introduction

This thesis has documented the acquisition, processing and interpretation of geophysical data collected across the MAR between 13 – 14°N during research cruise JC07. One of the key aims of this study has been to further our understanding of the mechanisms that govern oceanic core complex formation and crustal accretion along magma-poor sections of the MOR system. In previous chapters I have made observations and discussed the implications for these issues on the basis of sidescan sonar imagery together with bathymetry data and seafloor sampling results (Chapter Three), shipboard gravity data (Chapter Four) and deep-towed TOBI magnetic data (Chapter Five). It is the purpose of this chapter to combine these observations and give an overview of the volcanic and tectonic controls on OCC formation and, in a wider context, magma-poor crustal accretion along this section of the MAR. Where relevant I have also drawn comparison with other magma-poor sections of the MOR. At the end of this chapter I present a final model for the evolution of oceanic core complexes that accommodates observations made in previous chapters, and give suggestions for future work within the 13°N region and involving core complexes in general.

6.2. Crustal accretion in the 13°N region: Regional observations

6.2.1. Melt supply

Along the MAR there are considerable and well-documented long wavelength, segment-scale heterogeneities in the distribution and style with which melt is emplaced at the ridge axis. In this study I have used a combination of geophysical datasets collected across the 13°N region to assess these processes and to place OCCs in a regional context. This has primarily involved analysis of bathymetry and gravity data,

with variations in melt supply resulting in the formation of distinct morphological provinces (i.e. magma-rich abyssal hill terrain and magma-poor areas of widespread detachment faulting) and variations in RMBA (i.e. ridge-centred lows that reflect centres of robust magmatic upwelling). I have also considered magnetic anomalies and sidescan sonar data in relation to melt supply (which are discussed with respect to the formation of individual OCCs in *Section 6.3*). It is the purpose of this section to discuss and combine these observations into a coherent model for the 13°N region. Firstly, I give a brief summary of previous work that relates to melt supply in this region.

The Fifteen-Twenty and Marathon FZs are first-order ridge discontinuities (D1) that define a first-order ridge segment (S1) of the MAR (herein referred to as the FT-MA segment; Figure 6.2.1). Within this segment melt supply is highly variable at all scales (Collette *et al.*, 1979; Escartin & Cannat, 1999; Fujiwara *et al.*, 2003; Smith *et al.*, 2006; Smith *et al.*, 2008) and there are also a number of second-order, non-transform ridge discontinuities (D2) that define a series of smaller, second-order ridge segments (S2). Seafloor constructed around the first-order segment centre at 14°10'N displays lineated, abyssal-hill morphology; this is bounded to the north and south by irregular terrain containing numerous OCCs. Numerical models of strain rate at the ridge axis have recreated these 'styles' of seafloor by varying the ratio of magmatic to tectonic crustal accretion processes (e.g. Buck *et al.*, 2005; Behn & Ito, 2008; Ito & Behn, 2008; Tucholke *et al.*, 2008; Olive *et al.*, 2010). Lineated terrain, such as that formed about 14°10'N, forms at high degrees of magmatic accretion (where magmatic processes – M_{TOTAL} – accommodate > 95% of plate separation); irregular, OCC-forming terrain occurs at relatively low degrees of magmatic accretion (where M_{TOTAL} = 30 – 50%). This distinct partitioning between zones of predominantly magmatic and predominantly tectonic plate separation is also recorded in seismicity patterns, with sections of the FT-MA segment that display widespread OCC formation and detachment faulting being associated with relatively high amounts of seismic activity compared with the seismically 'quiet' segment centre (Escartin *et al.*, 2003b; Smith *et al.*, 2006). Furthermore, focused magmatism at 14°10'N has been inferred from the recovery of depleted peridotite and enriched basalt samples, which suggest that the ridge axis at 14°10'N is underlain by a zone of metasomatized mantle or a 'hot-spot'-type temperature anomaly in the asthenosphere (Collette *et al.*, 1979; Bonatti *et al.*, 1992; Dosso *et al.*, 1993).

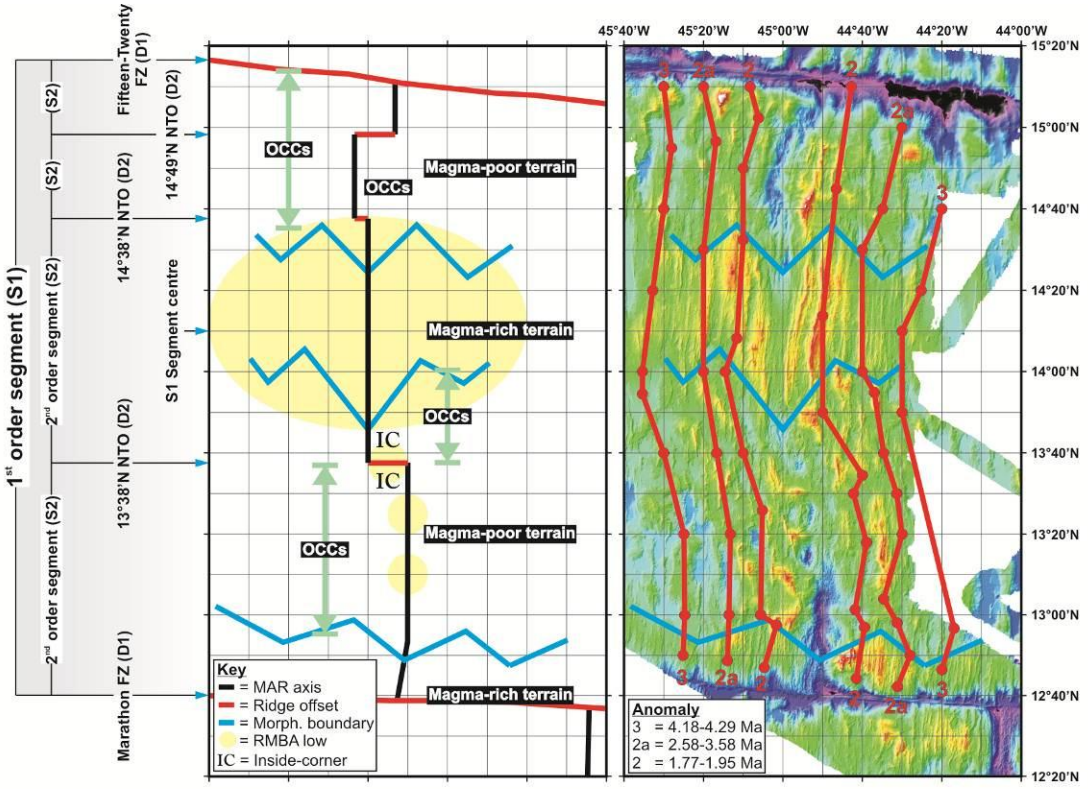


Figure 6.2.1. Simplified ridge geometry between the Fifteen-Twenty and Marathon FZs, showing main morphological and structural elements of the seafloor. The FT-MA segment is a first-order ridge segment (S1), but comprises a number of smaller second-order segments (S2) defined by non-transform offsets. There is also a morphological and structural segmentation of seafloor terrain (blue lines) and various RMBA lows (yellow shades). Right-hand panel shows magnetic anomaly picks of Fujiwara *et al.* (2003) and Smith *et al.* (2008). See text for discussion.

With regard to the contrasting style of seafloor morphology exhibited along the FT-MA segment, Escartin & Cannat (1999) suggest that the long wavelength partitioning of melt supply has led to crust forming the segment centre at 14°10'N becoming compositionally, and thus rheologically, homogeneous with respect to the relatively heterogeneous crust formed at the segment end immediately south of the Fifteen-Twenty FZ[7]. In areas where melt supply is weak and the lithosphere is heterogeneous (e.g. OCC-forming areas) the magmatic crust is thin and peridotite may be more readily serpentinised by exposure to seawater. The abrupt, along-axis transition in faulting style from lineated to irregular terrain may thus be controlled by threshold amounts of serpentinised peridotite within the lithosphere; below this threshold (i.e. when the volume of serpentinised material in the lithosphere is relatively low) the lithosphere is mechanically homogeneous and this promotes the formation of long,

[7] Escartin & Cannat (1999)'s discussion is based on data from around the Fifteen-Twenty FZ, although their reasoning is equally applicable to the transition from magma-rich to magma-poor terrain south of the segment centre at 14°10'N.

narrow faults (i.e. abyssal hill terrain; Escartin & Cannat, 1999). Above this serpentinisation threshold, rheological heterogeneities are sufficiently important and result in irregular stress fields that create irregular fault patterns (i.e. 'chaotic' terrain). The subsequent development of oceanic core complexes is discussed in *Section 6.3*.

Further south, the Marathon FZ is bounded on its northern and southern flanks by abyssal hill topography – an observation first made by Smith *et al.* (2008). This indicates that magmatic conditions are locally enhanced across the Marathon FZ relative to the 13°N region. An OCC has developed at the inside-corner (IC) high at the western end of the Marathon FZ (Smith *et al.*, 2008), and is flanked on its older side by lineated, abyssal hill terrain (formed during magma-rich conditions). This suggests that the 'serpentinisation thresholds' used to explain along-axis changes in fault style by Escartin & Cannat (1999) may also be temporal features that are able to switch on and off with waxing and waning magmatic conditions, giving rise to across-axis variations in seafloor morphology.

On the basis of seafloor morphology, it appears that the magmatic source beneath the segment centre at 14°10'N has persisted for > 4 Ma (*Section 3.3*). During this period, the along-axis length of abyssal hills has increased from ~45 km to ~65 km over the last ~3 My; this may indicate a recent increase in the strength and/or extent of magmatism (Figure 3.3.1 and Figure 6.2.1). In addition to this, I also calculate that the magmatic source has not been fixed in space but appears to have episodically migrated north and south along the ridge axis relative to the SA and AF plates at rates of ~15 – 20 km/My, creating zigzag patterns in off-axis topography (*Section 3.3*). This is not uncommon as migratory melt sources have also been observed along other parts of the MAR (e.g. Tucholke *et al.*, 1997; Briais & Rabinowicz, 2002). Furthermore, I note that the along-axis length of abyssal hills paralleling the ridge axis immediately to the north and south of the Marathon FZ varies with a similar periodicity to those flanking the magmatic segment centre at 14°10'N. For example, the recent (0 – 1.8 Ma) southward propagation of abyssal hills at 14°10'N coincides with southward propagation of abyssal hills to the north of the Marathon FZ. The fact that the two magmatic sources have migrated over the same period suggests that they may be controlled by the same processes at depth within the asthenosphere.

To the south of the lineated terrain formed about 14°10'N, isolated exposures of abyssal hills are observed off-axis within the 13°N region (Figure 3.3.1). This suggests that short-lived periods of relatively robust, focused melting along the ridge axis are not

wholly uncommon in otherwise magma-poor environments (on the basis of gravity data, Cannat *et al.* (2009) come to a similar conclusion for a magma-poor section of the SWIR).

A number of OCCs have formed along the transition between lineated terrain that has formed about the segment centre at 14°10'N and the region of chaotic terrain to the south (i.e. OCC1348, OCC1352, and OCC1356; see Figure 3.3.1). These OCCs appear to 'follow' the magmatic terrain as it has wandered back-and-forth along the ridge axis, suggesting that they may have been regulated by waxing and waning magmatic conditions about the first-order segment centre (i.e. as robust magmatism propagated southwards the locus of OCC initiation also propagated southwards; older OCCs became terminated by locally increasing magmatic conditions). There is also some evidence that within the 13°N region to the south, OCCs have formed along the edge of a discrete area of robust magmatism as it has propagated southwards along the ridge axis (*Section 3.3.1.1*). There are, however, a considerable number of OCCs in the SW-quadrant of the survey area that do not appear to have been directly regulated by the along-axis migration of abyssal-hill terrain. This suggests that OCC formation and termination may be controlled by the distribution of less extensive and temporally short-lived magmatic events at the ridge axis, which are not associated with the formation of distinct magma-rich terrain (which is discussed further in *Section 6.3*).

On the SWIR, Cannat *et al.* (2009) make the observation that the majority of corrugated surfaces have formed along the boundaries of volcanic/magma-rich terrain and avolcanic/'smooth' seafloor; they use this observation to suggest that OCCs form at an intermediate level of melt supply, as has been suggested by numerical modelling (e.g. Buck *et al.*, 2005; Tucholke *et al.*, 2008). However, in the 13°N region I note that there does not appear to be any distinctive regions of smooth seafloor which Cannat *et al.* (2006) propose forms during periods of avolcanism, and thus it is difficult to conclude from their distribution alone that OCCs in the 13°N region form at intermediate levels of magmatism.

The formation of abyssal hill terrain, formed during a relatively magma-rich period, about the Marathon FZ (Smith *et al.*, 2008) is unusual as the juxtaposition of the ridge axis against old, cold lithosphere at large offset fracture zones is expected to impede the delivery of melt to the surface (e.g. Fox & Gallo, 1984). However, although melting is likely to be depressed, I note that abyssal hills in such close proximity to fracture zones are common along much of the MAR, and thus the inferred relative level

of magmatism around the Marathon FZ is not dissimilar from other large ridge offsets. The main implication of this observation is that the 13°N region is bounded to the north and south by magmatic terrain, and thus displays the characteristics of a distinctive 'cold-spot' in ridge morphology. Essentially, the formation of OCCs in this region cannot simply be explained by their proximity to the end of the segment and attributed to the cooling effects associated with the nearby transform fault – as may be proposed for traditional inside-corner highs such as Kane and Atlantis Massif. Furthermore, Escartin & Cannat (1999) have noted that the magma-poor terrain immediately south of the Fifteen-Twenty FZ is anomalously widespread compared with other OCC-forming parts of the MAR, which also implies that transform offsets do not control the along-axis extent over which OCCs may form.

Analysis of globally available bathymetry data using *GeoMapApp* (Ryan *et al.*, 2009) indicates that similar ridge morphology to that flanking the Marathon FZ has formed on the MAR near 04°00'N, where the Strakhov FZ is bounded by abyssal hills and the intra-segment area to the north apparently exhibits chaotic seafloor diagnostic of widespread OCC formation (Figure 6.2.2).

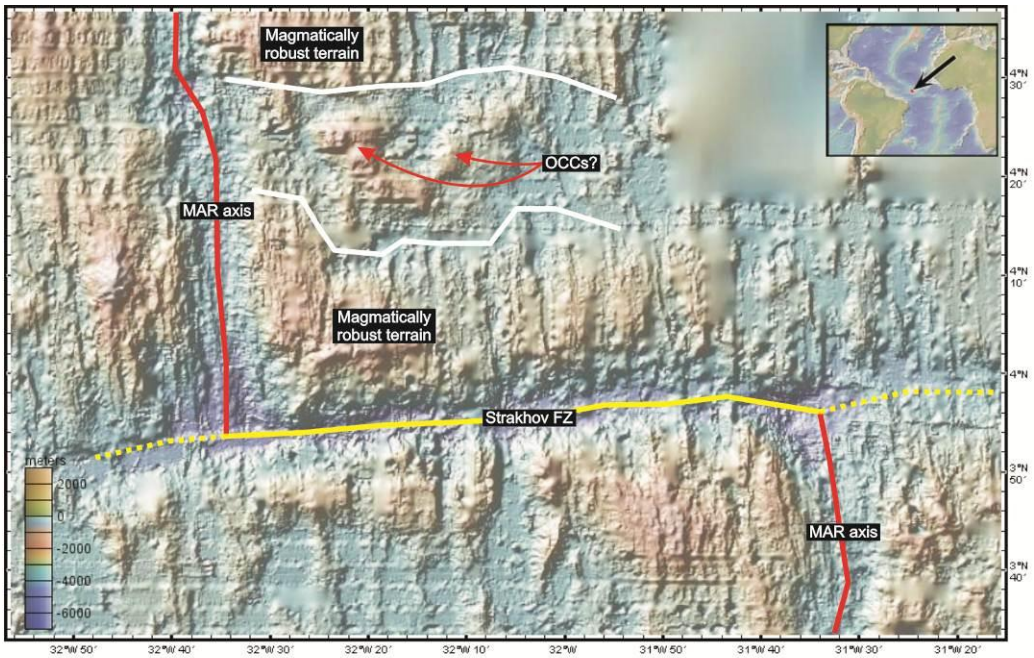


Figure 6.2.2. Interpretation of seafloor morphology near the the Strakhov FZ, which appears to be bounded by abyssal hill terrain and is therefore associated with enhanced magmatism relative to the area of irregular seafloor to the north (04°20'N), which may exhibit OCC formation. Bathymetry data were accessed via *GeoMapApp* (Ryan *et al.*, 2009).

Immediately north of the Marathon FZ, the two most recent maxima in magmatic robustness (i.e. the points at which abyssal hills are longest along-axis) are separated across-axis by ~40 km of seafloor in which abyssal hills gradually become shorter. This suggests that magmatism waxes and wanes from robust-weak-robust over a period of ~3 My (*Section 3.3.1.2*; Figure 6.2.1). Furthermore, south of the fracture zone the minimum in magmatic robustness at ~4 Ma was marked by the formation of a single large OCC (Marathon OCC). These observations are consistent with a model in which crustal accretion at the MAR undergoes a magmatic/amagmatic cycle that occurs over a timescale of ~2 – 4 My (e.g. Tucholke & Lin, 1994; Tucholke *et al.*, 1997; Skolotnev *et al.*, 1999; Fujiwara *et al.*, 2003). In such a model, Tucholke *et al.* (1997) suggest that magmatic accretion is not continuous, but that melt accumulates at the base of the crust during an amagmatic phase, gradually building-up until it episodically breaks through the crust and erupts at the seafloor during a magmatic phase. It is possible that these phases are self-limiting processes. For example, Behn *et al.* (2006) show that during a magmatic phase, an axial valley is formed which subsequently causes compression at the base of the crust and inhibits further melt emplacement at the ridge axis; this compressive force remains until sufficient tectonism (during the amagmatic phase) has taken place. I discuss this idea in the context of OCC formation, and also consider the timescale of the magmatic/amagmatic cycle on the basis of OCC durations, in *Section 6.3.2*.

Long wavelength variations in melt supply to the ridge axis not only influence the regional seafloor morphology, but also greatly affect the long wavelength geophysical signature of the entire segment. For example, elevated RMBA across the 13°N region indicates that magma-poor plate separation processes have been the primary mode of crustal accretion in this region for > 4 My (*Section 4.3*). Assuming standard crustal density contrasts, gravity data collected throughout JC07 indicate that crustal thicknesses, which can be used as a proxy for magmatic robustness, are > 1.5 km thinner in the 13°N region compared with the segment centre. This degree of thinning is comparable to that measured by Fujiwara *et al.* (2003) for terrain bounding the Fifteen-Twenty FZ, and by Okino *et al.* (2004) for an area of OCC formation near the AAD. However, this value is likely to be an underestimate as the precise contribution of low density serpentinised mantle (which, in terms of density, may be indistinguishable from gabbroic material) to the 'crustal' thickness is largely unknown.

In addition to regionally thinned crust, within the JC07 survey area there is an along-axis gradient in RMBA of ~0.25 mGal/km (*Section 4.3.4*). This may be accounted for by a decrease in Moho depth of ~0.75 km from north to south and/or a temperature gradient in the upper mantle associated with the zone of robust magmatism beneath the segment centre. Similar along-axis gradients are often observed in the presence of major ridge hot-spots, such as along the Reykjanes Ridge south of Iceland (e.g. Gardiner, 2003; Peirce *et al.*, 2005). Superimposed on this regional gradient in RMBA are numerous, shorter-wavelength RMBA lows which indicate that beyond the long wavelength segment-scale partitioning of melt supply (i.e. towards the segment centre and Marathon FZ), melt is further partitioned to a number of discrete zones. Forward modelling of gravity anomalies suggest that this partitioning must occur within the brittle lithosphere and most likely does not exist at depths of > 6 km (*Section 4.3.4* – Figure 4.3.8a-b). These areas are associated with robust, surficial volcanism (Figure 4.3.6) but they do not appear to be directly related to off-axis abyssal hill topography in the same way that the robust centres of magmatism to the north and south of the survey area are. This may indicate that these circular, ridge-centred anomalies are temporally short-lived features, which is supported by the fact that they do not appear to form across-axis 'ribbons' of low amplitude RMBA like traditional bull's-eye anomalies (such as that formed across the centre of the FT-MA segment at 14°10'N).

On a smaller-scale, numerous, discrete magnetisation highs exist within the axial valley, suggesting that melt emplacement is partitioned even further at shallower levels (*Section 5.4*). The magnetic anomaly formed during the Brunhes chron is generally quite poorly resolved and negatively magnetised crust is commonly observed within the axial valley. Multiple Brunhes-age events coexisting at the same latitude also suggest that the locus of melt emplacement is able to jump across-axis by several kilometres over a period of ~0.3 – 0.5 My. This short wavelength instability is also recorded in surficial volcanism, with numerous volcanic lineaments of various ages spanning the axial valley (*Section 3.4.1*). In the area between OCC1319 and OCC1330, for example, a large, sedimented volcanic lineament exists ~6 km to the east of several, minor hummocky lineaments which have formed within the NVZ near the western axial valley-wall fault. Intensity of acoustic backscatter suggests that the larger volcanic lineament may have been inactive for ~0.19 – 0.77 My (*Section 3.4.2*). These shorter-scale fluctuations and discontinuities in magmatism occur within the same depth range

and timescale that OCCs are expected to operate, and hence they are discussed in more detail in *Section 6.3*.

In the following section I consider how the magmatic processes discussed in this section relate to asymmetric crustal accretion, and consider the effects this has on crustal structure in the 13°N region. In particular, I discuss the morphological contrast between areas of OCC formation and their conjugate ridge flanks.

6.2.2. OCC distribution & asymmetry

Along the MAR, widespread detachment faulting and OCC formation is commonly observed to be an asymmetric process that may manifest itself in a number of different ways. For example, OCCs may be preferentially formed within the inside-corner, rather than the outside-corner, environments of major ridge offsets (e.g. Cann *et al.*, 1997; Tucholke *et al.*, 1998). There are a few OCCs located on the outside-corners of the eastern and western intersections of the Fifteen-Twenty FZ with the MAR (e.g. Escartin & Cannat, 1999; MacLeod *et al.*, 2002), but Fujiwara *et al.* (2003) suggest these OCCs may have actually formed in an inside-corner environment and subsequently been transferred to the outside-corner by a series of ridge jumps and/or changes in the polarity of relatively small offsets in the ridge axis. Crustal thickness estimates from gravity measurements may also show considerable across-axis asymmetry, with areas of OCC formation being associated with thinner crust and higher density material near the surface relative to conjugate ridge flanks (e.g. Fujiwara *et al.*, 2003; Smith *et al.*, 2008). In addition to this, magnetic anomalies have been used to show that spreading rates may be ~70 – 100% faster on plates that form oceanic core complexes (e.g. Fujiwara *et al.*, 2003; Searle *et al.*, 2003; Okino *et al.*, 2004; Baines *et al.*, 2008), as have zircon crystallisation ages plotted against across-axis distance (e.g. Grimes *et al.*, 2008).

Asymmetric crustal accretion most likely arises as strain is efficiently localised into weak minerals such as serpentine and talc (Escartin *et al.*, 1997b; 2001; Escartin *et al.*, 2008a), which form along the detachment faults of oceanic core complexes and may ultimately lead to runaway slip displacement along one edge of the axial valley (MacLeod *et al.*, 2009). These minerals are abundant across the domal sections of near-axis OCCs sampled in the 13°N region (*Section 3.2.2*) and along other parts of the MOR where asymmetric crustal accretion is widespread (e.g. Bougault *et al.*, 1993; Cann *et*

al., 1997; Cannat *et al.*, 1997; Escartin & Cannat, 1999; Ohara *et al.*, 2001; Tucholke *et al.*, 2001; MacLeod *et al.*, 2002; Reston *et al.*, 2002; Searle *et al.*, 2003).

In the 13°N region there are a large number of OCCs; on the basis of seafloor morphology alone, Smith *et al.* (2008) identify some 44 core complexes between the Marathon and Fifteen-Twenty FZs (OCC distribution: *Section 3.3.1*). Using higher resolution bathymetry data and sidescan sonar imagery collected during JC07, an additional 4 core complexes have been identified on the SA plate within the zone of intense OCC formation first identified by Smith *et al.* (2008) (*Section 3.3.1.1*). The overall distribution of these OCCs is highly asymmetric across-axis, the polarity of which switches across the NTO at 13°38'N. To the south of the NTO, OCCs have preferentially formed on the SA plate, whereas to the north they have formed on the AF plate (Figure 3.3.1). In each case, no OCCs appear to have formed on the conjugate plate; this sense of asymmetry is maintained in crust up to ~4 Ma. Essentially, OCC formation in the 13°N region conforms with the broad observation that OCCs generally form within inside-corner settings (in this case, however, it is the inside-corners of the second-order ridge offset at 13°38'N, rather than a first-order transform offset).

OCC distribution across the 13°N region is therefore unusual as it appears that the relatively minor ridge offset of ~20 km at 13°38'N exerts more widespread influence on the polarity of OCC formation than the Marathon FZ (which offsets the ridge by ~70 km). OCC1259, for example, is located within the widespread zone of OCCs that are forming within the inside-corner of the NTO at 13°38'N, rather than the inside-corner of the much larger and considerably closer Marathon FZ (Figure 3.3.1). This suggests that the formation and distribution of OCCs is not directly controlled by offsets of the ridge axis, but by more fundamental local variations in melt supply and magmatic discontinuities (which in turn may also control the locations of ridge offsets). This is supported by data from the MAR at 22°30'N, where an extremely large (~250 km^2), less well-studied near-axis OCC has seemingly formed in conjunction with only a very small (< 5 km) offset in the ridge axis (Figure 6.2.3; Escartin *et al.*, 2008b).

Asymmetric crustal accretion processes in the 13°N region are also reflected in analyses of sidescan sonar images (*Section 3.5.1*). Sidescan data show that the average tectonic strain since 1.86 Ma has been elevated at $T\varepsilon$ = ~25 – 30% in the SW- and NE-quadrants of the survey area, which are effectively the insider-corners of the NTO at 13°38'N, compared with $T\varepsilon$ = ~10 – 15% at the SE- and NW-quadrants, which may be considered outside-corners of the NTO (Table 6.2.1, with quadrants of the survey area

shown in Figure 3.5.1). In addition to this, the SW-quadrant is associated with elevated RMBA that is indicative of tectonically-thinned crust and the presence of high density material at relatively shallow depths (*Section 4.3.1*).

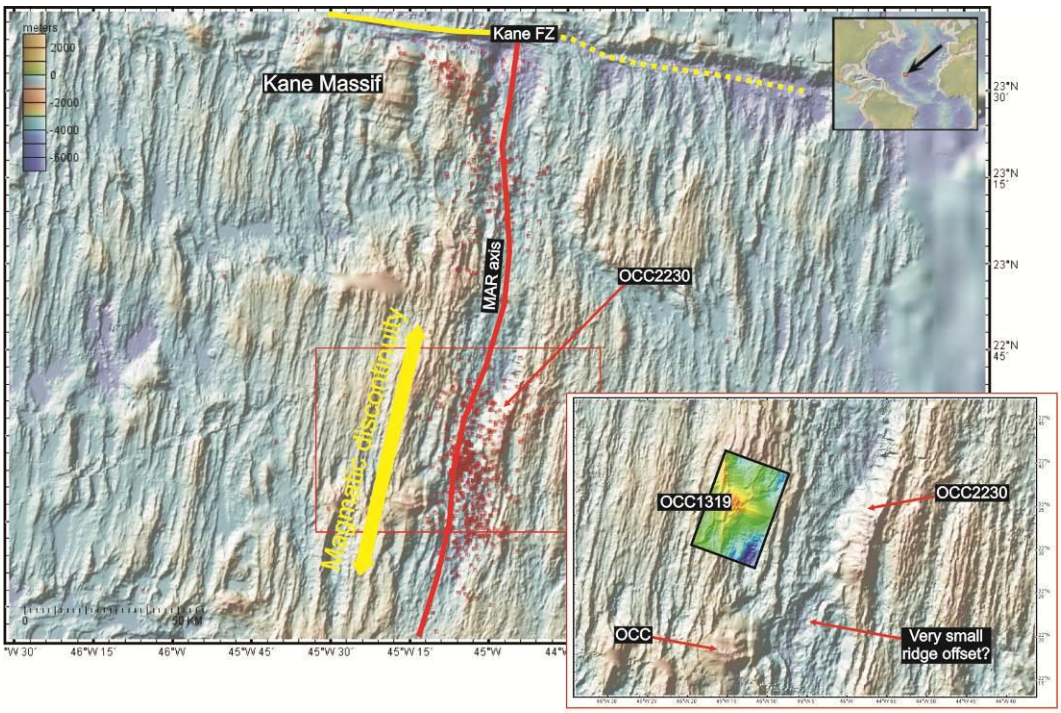


Figure 6.2.3. Seafloor morphology for ~150 km of the MAR south of Kane FZ. There is a very large OCC situated at 22°30'N that is not associated with a clear offset in the ridge axis. The formation of this OCC is associated with elevated seismicity (red dots) suggesting it has been controlled primarily by a significant discontinuity in magmatism. Inset shows detail of OCC with approximate size of OCC1319 for comparison. Bathymetry data were accessed via *GeoMapApp* (Ryan *et al.*, 2009).

Ridge flanks conjugate to zones of intense OCC-related deformation are characterised by numerous, closely spaced, small faults that have an average surface area of ~2 km^2 (Table 6.2.1; *Section 3.5.1*). Gravity data show that non-OCC-forming ridge flanks are associated with crust that is typically ~0.5 – 1.0 km thicker than OCC-forming ridge flanks, which is consistent with a more magmatically robust mode of crustal accretion in these areas (*Section 4.3.2*). However, even within these areas where no OCCs are observed, gravity anomalies still reveal crustal thickness variations of up to ~0.5 km which may indicate significant variations in the relative strength and distribution of melt accreted to the hanging-wall over the last 1.86 My. The relatively long wavelength of these thickness variations compared with the average size of OCCs makes it difficult to correlate specific areas of thin or thick crust in outside-corner settings with individual OCCs or magma-poor events recorded within inside-corners.

	Inside-corners	**Outside-corners**
No. faults	~60	~110
Average fault surface area (km^2)	10.1	2.1
Average OCC surface area (km^2)	97.8	0
Fault density (1 fault per XX km^2)	36.1	15.8
Tectonic strain (%)	25 – 30	10 – 15
Range in crustal thickness (km)	4.8 – 5.9	5.5 – 6.0
Average half-spreading rate (km/My)	15.7	10.0

Table 6.2.1. Summary of inside-/outside-corner asymmetry across the 13°N region. These values are determined based on the quadrants defined in *Section 3.5.1* and shown in Figure 3.5.1 (e.g. 'inside-corner' averages are calculated across SW- and NE-quadrants). Tectonic statistics are inferred from sidescan sonar imagery and crustal thicknesses are inferred from gravity data. Half-spreading rates are calculated from the position of magnetic anomaly 2 relative to the ridge-centred RMBA low (i.e. the 'gravitational ridge axis' defined in *Section 5.3.2*). All values represent averages over 0 – 1.86 Ma.

Magnetic data show that in the 13°N region the rate of plate separation has been asymmetric during the last 1.86 My (*Section 5.3.2*). The sense of asymmetry is that OCC-forming areas appear to have spread faster than conjugate areas of the ridge. The degree of asymmetry is largely dependent on the definition of the ridge axis which is used and is thus uncertain as, for example, the NVZ, bathymetric ridge axis, CAMH and ridge-centred RMBA low are typically distributed across-axis by several kilometres. If asymmetry is measured from the position of anomaly 2 relative to the RMBA low, which – given that gravity data are averaged over a greater volume of crustal material – may be stable for relatively long periods, spreading rate may be as much as 20 – 40% asymmetric across areas which display OCC formation (i.e. the SW- and NE-quadrants of the survey area; *Section 5.3.2*). This gives an average half-spreading rate of ~15.7 km/My for OCC-forming areas compared with ~10.0 km/My for conjugate areas (Table 6.2.1). Alternatively, if half-spreading rates are measured relative to the position of the present day NVZ then this asymmetry becomes very small – perhaps < 5% (i.e. half-spreading rates are ~12.9 km/My). However, it seems likely that the location of the NVZ is relatively unstable and is able to wander across-axis by significant amounts over timescales of ~0.5 My (*Section 3.4.1*), and thus asymmetry measured from the present-day NVZ may be unreliable.

Spreading rate asymmetry measured relative to the 'gravitational' ridge axis (~20 – 40%) is less than estimates of asymmetry made for other OCC-forming parts of the MOR. For example, previous studies have shown that spreading rates may be up to ~70 – 100% asymmetric across oceanic core complexes (e.g. Searle *et al.*, 2003; Okino *et al.*, 2004; Baines *et al.*, 2008; Grimes *et al.*, 2008), with Fujiwara *et al.* (2003) also showing that over the last ~1 My spreading rate asymmetry has been ~30 – 70% in crust bounding the Fifteen-Twenty FZ. However, the value measured across the 13°N region is averaged over the last 1.86 My and may therefore mask shorter-wavelength fluctuations in asymmetry that relate to periods of predominantly tectonic or magmatic extension. For example, at 13°19'N a period of asymmetry lasting 0.4 My with a magnitude of 75% (relating to the formation of OCC1319, i.e. faster spreading on SA plate) can also account for the regional asymmetry of 20% over 1.86 My (*Section 5.3.2*).

In the following section I present a summary and model for the magmatic and tectonic processes that control the regional crustal structure and morphology of the FT-MA segment. Following this, in *Section 6.3* I discuss local observations that relate to the morphology and variability in melt supply in the presence of individual OCCs.

6.2.3. Summary & model of regional crustal structure in the 13°N region

The 13°N region is an intra-segment area of widespread detachment faulting and oceanic core complex formation. The region is characterised by low melt supply and distinct morphological differences compared with the more magmatically robust segment centre to the north and the strip of seafloor formed about the Marathon FZ to the south. Table 6.2.2 gives a summary of the main morphological and geophysical observations made throughout this study that relate to the fundamental differences between magma-rich and magma-poor settings. Observations from other studies have also been incorporated into Table 6.2.2 to allow further comparison between these two styles of seafloor.

In summary: Across the FT-MA segment, melt emplacement at the segment centre (14°10'N) is strong and gives rise to thick crust and closely-spaced, long, linear faults (Figure 6.2.4). Escartin & Cannat (1999) suggest that the homogenous nature of the lithosphere in this region, created by the robust magmatic supply, is responsible for the faulting pattern; in contrast, within the 13°N region – where melt supply is weak and intermittent (*Section 3.4.1* and *Section 4.3.4*) – it may be expected that the lithosphere is

largely heterogeneous at depth, comprising a mixture of gabbro bodies that have crystallised in peridotite host rock (similar to 'plum-pudding' crust – *Section 1.2.4*).

Crustal accretion across the region is a highly asymmetric process, with plates containing OCCs exhibiting higher tectonic strain, thinner crust and faster spreading rates compared with conjugate plates in which strain is partitioned across numerous, closely-spaced small faults (Figure 6.2.4).

	Magma-rich terrain (Terrain 1 in Fig. 6.2.4)	**Magma-poor terrain**	
		Inside-corner (IC; Terrain 2 in Fig. 6.2.4)	**Outside-corner (OC; Terrain 3 in Fig. 6.2.4)**
Geographic location	Usually, although not limited to, segment centre.	Segment end or intra-segment 'cold-spot'.	
Surficial morphology	Long, linear faults that are closely spaced and parallel with ridge axis.	Large OCC-forming detachment faults.	Numerous, relatively small faults that are closely-spaced relative to IC.
Lithospheric rheology (after Escartin & Cannat, 1999)	Homogeneous	Heterogeneous – seawater is accessible to mantle peridotite	
Tectonic strain (Te) inferred from fault exposures	8 – 15% at 29°N (low) (Escartin *et al.*, 1999)	25 – 30% (relatively high)*	10 – 15% (low)*
Inferred component of magmatic extension (M_{TOTAL}) from tectonic strain	85 – 92% at 29°N (high) (Escartin *et al.*, 1999)	70 – 75% (relatively low)*	85 – 90% (high)*
Along- and across-axis magmatic variability	May wander along-axis at rates of ~15 – 20 km/My. Fluctuates in strength over ~3 My timescale.	Zone of melt emplacement is unstable and may jump across-axis by several km over period of ~0.5 My. Along-axis gaps in volcanism may occur adjacent to active OCCs (*Section 6.3*).	
Relative crustal thickness	Thick	Thin	Moderate
OCCs?	N	Y	N
Spreading rate asymmetry?	Not in FT-MA segment (Fujiwara *et al.*, 2003).	Y (faster spreading)	Y (slower spreading)
Magnetic anomaly pattern	Lineated and well-resolved.	Intermittent and difficult to unambiguously identify anomalies.	

Table 6.2.2. Summary of observations regarding morphology, structure and magmatic processes that occur along the FT-MA segment made during this study. Data from outside this study are also included to fill-in the gaps in observations (e.g. at the segment centre). * denotes that value is averaged over 0-1.86 Ma, and thus shorter-wavelength variability may exist (discussed in text).

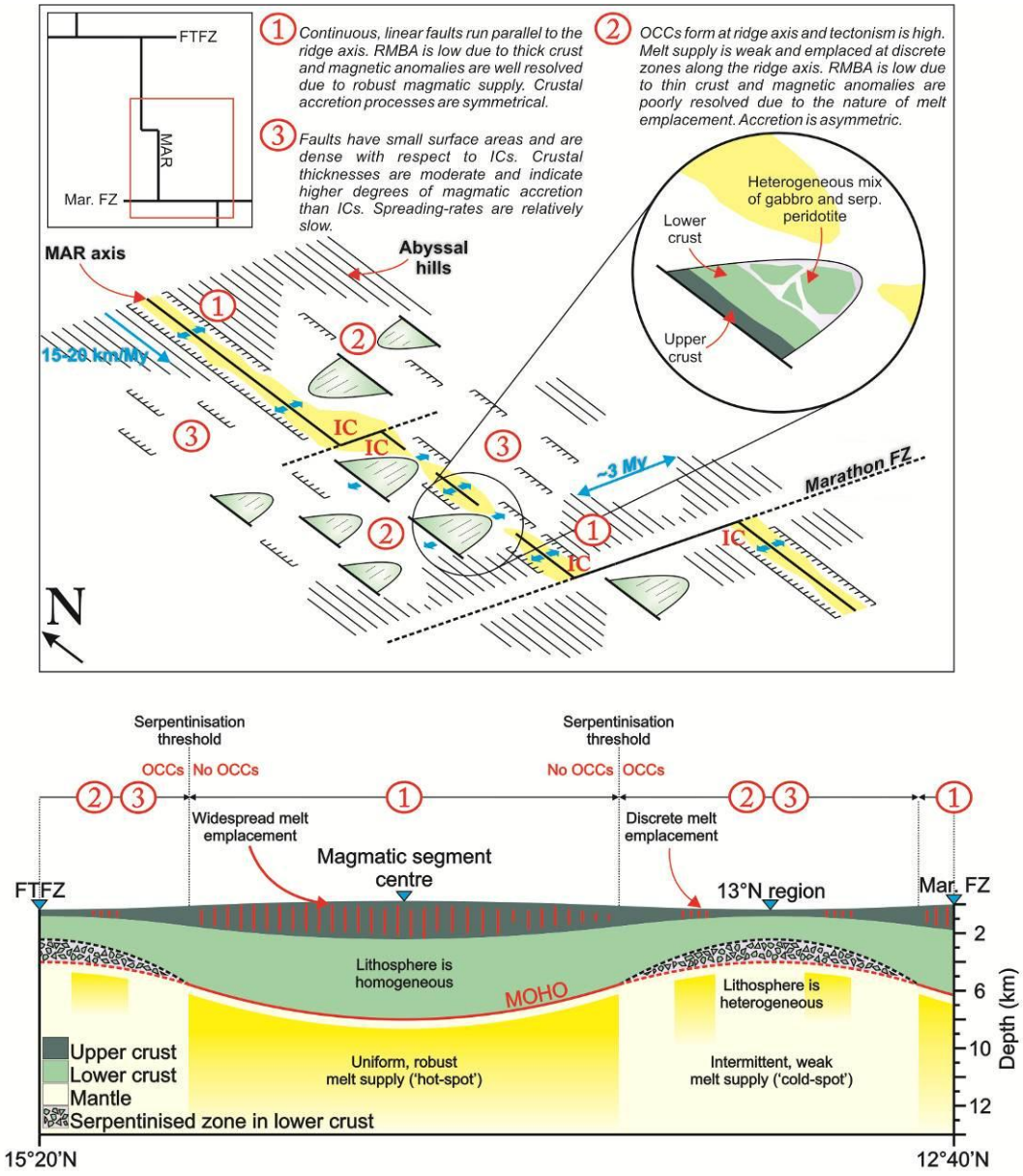


Figure 6.2.4. Regional interpretation of seafloor structure and morphology across 13°N region. Terrains are numbered 1-3 for: 1) Magma-rich terrain, 2) inside-corner magma-poor terrain and 3) outside-corner magma-poor terrain. Lower panel is along-axis cross-section between the Fifteen-Twenty and Marathon FZs. Morphologies are described in detail in the text and also in **Table 6.2.2**.

This asymmetry may develop as seawater percolates along fault planes and reacts with peridotite (which occurs at relatively shallow depths when the magmatic crust is thin) to form serpentinised peridotite and other weak minerals that localise strain on one side of the axial valley and ultimately leads to runaway slip displacement. This may eventually result in the exposure of deep-seated crustal rocks and mantle material, and to the formation of OCCs, which forms the basis of the following section.

6.3. The life cycle of oceanic core complexes

Crustal accretion along the MOR occurs via a combination of tectonic and magmatic processes; far-field tensile stresses are accommodated by tectonic extension along fault surfaces and by periodic emplacement of melt at the ridge axis. In this section, I discuss observations from the 13°N region that relate to the magmato-tectonic ratio of crustal accretion processes and consider its relationship with actively forming OCCs, and also discuss the mechanisms by which OCCs form and how footwall structure and OCC morphology evolve temporally.

6.3.1. The role of melt supply in OCC initiation

In areas where melt supply to the ridge axis is reduced, such as at segment ends or a mantle 'cold-spot' (as appears to be the case in the 13°N region), the magmatic crust is thin and the lithosphere is primarily heterogeneous in nature (Tucholke & Lin, 1994; Escartin & Cannat, 1999). In these areas, the mantle is more readily exposed to seawater, allowing for the formation of serpentinised peridotite and extension along long-lived detachment faults. Thus melt supply and the temporal and geographical locus of OCC formation are intimately linked.

Numerical modelling of strain rate suggests that the regional reduction in magmatic accretion processes must fall within a finite range – a 'Goldilocks' scenario – for OCCs to subsequently form (e.g. Buck *et al.,* 2005). For example, magma-rich/abyssal hill terrain forms when magmatic accretion accommodates ~95% of the regional plate separation (i.e. M_{TOTAL} – the total proportion of magmatic extension – is 95%, with the remaining 5% being accommodated by tectonic processes). Core complexes are expected to form when M_{TOTAL} falls between ~30 – 50%; on the basis of numerical modelling OCCs are not expected to form for values of M_{TOTAL} < 30% (e.g. Buck *et al.*, 2005; Behn & Ito, 2008; Tucholke *et al.*, 2008). In this latter scenario, it is expected that faults remain active for no longer than ~0.2 My and alternately break along either side of the axial valley with irregular positions and dips (Tucholke *et al.*, 2008). Furthermore, Olive *et al.* (2010) show that M_{TOTAL} does not control OCC formation, and that it is M_{HW} (the relative amount of magmatic accretion within the hanging-wall) that must fall between ~30 – 50% to promote extension on a single, long-

lived detachment fault. With this latter model, M_{TOTAL} could effectively take any value between ~30 – 100%, with the excess melt above the ~30 – 50% window being accreted within the footwall of the OCC (M_{FW}) such that $M_{TOTAL} = M_{HW} + M_{FW}$.

An independent estimate of the proportion of plate separation that is accommodated magmatically can be calculated across the 13°N region by assuming that magmatism is the complement of tectonic strain, Tε, which can be quantified by mapping fault surfaces apparent within sidescan sonar imagery (*Section 3.5*). In the SW-quadrant of the survey area Tε is ~25 – 30%; this value is temporally averaged over 0 – 1.86 Ma and along ~40 km of the ridge axis. On the conjugate flank, Tε across the SE-quadrant of the survey area has been ~10 – 15% over the same period. Thus for the entire southern half of the survey area, the average tectonic strain over the last 1.86 My has been ~20% and the inferred magmatic component of crustal accretion, M_{TOTAL}, has been ~80%. A similar estimate of M_{TOTAL} = ~70% can be obtained by measuring the ratio of the crustal thickness at the ridge axis in proximity to actively forming OCCs in the 13°N region to the thickness of crust produced at the magmatically-robust segment centre (*Section 4.3.3*). These values are maxima as intra-crustal deformation and serpentinised mantle material within the crust are not taken into consideration when analysing sidescan sonar and gravity data, respectively.

Estimates of M_{TOTAL} during OCC formation, calculated from fault exposures and crustal thickness estimates, are therefore considerably larger than that which has been predicted by the numerical modelling work of, for example, Buck *et al.* (2005) and Tucholke *et al.* (2008). Tucholke *et al.* (2008) summarise that at such high levels of magmatic accretion (i.e. M_{TOTAL} = ~70 – 80%) faults migrate off-axis and become inactive as their integrated strength increases in older, colder lithosphere, and seafloor terrain should have a morphology akin to that of the magmatically-robust segment centre, rather than displaying widespread OCC formation. It therefore appears that estimates of M_{TOTAL} made during this study of the 13°N region, which have been averaged over a relatively large area, mask significant, higher-amplitude variations in the magmato-tectonic ratio; essentially, the analysis method averages over numerous periods of predominantly tectonic (i.e. OCC-forming) extension and intervening magmatic interludes. This is clearly demonstrated by MacLeod *et al.* (2009) who show that by considering only a single across-axis profile of tectonic heave which crosses OCC1319, rather than an entire quadrant of the survey area, the estimated value of M_{TOTAL} during OCC formation is reduced from ~70 – 80% to ~60%. Thus it may be

expected that if the area over which fault patterns are analysed is constrained yet further, M_{TOTAL} may increase accordingly. As demonstrated in *Section 5.3*, however, magnetic anomalies are inherently poorly-resolved in magma-poor environments and thus it is not possible to unambiguously define more recent anomalies on each flank, particularly relatively short duration anomalies such as the Jaramillo. The process of calculating shorter-period variations in M_{TOTAL} is further complicated by the fact that the precise location and extent of crustal accretion within the hanging-wall during OCC formation (if any) is unknown.

In lieu of more precise tie-points on either side of the ridge axis, the width of the magmatically constructed part of the Brunhes anomaly (central positive anomaly – CPA – *Section 5.3*) can be used to make qualitative estimates of the nature of the magmato-tectonic ratio during OCC formation (*Section 5.4*). For example, adjacent to OCC1319 the CPA has a width of ~10 km, which is approximately the same as the active core complex. Assuming that the CPA is constructed entirely by magmatic processes (i.e. tectonic widening of the anomaly is negligible) this might imply that the ridge is spreading with roughly equal amounts tectonic and magmatic extension (i.e. magmatic accretion within the Brunhes chron widens the CPA whilst tectonic extension forms OCC1319; Scenario 1 – Figure 6.3.1). However, it is equally plausible that the CPA formed entirely prior to OCC1319, and that the OCC formed when the CPA was no longer being widened (Scenario 2 – Figure 6.3.1; this scenario is also represented in Figure 5.3.9a-c). Neither scenario requires any change in M_{TOTAL} during the life cycle of the OCC (note that the OCC lifetime in scenario 2 is only from 0 – 0.4 Ma), but the fundamental difference is that with the latter scenario M_{HW} must become approximately zero as the OCC accommodates all of the plate separation.

Sidescan sonar data strongly indicate that M_{HW} accommodates ~0% of the local plate separation during some stage of the OCC life cycle, as surficial volcanism is presently absent adjacent to OCC1319 and OCC1330 (*Section 3.4*). This is suggestive of a model whereby OCCs are able to accommodate all of the plate separation, such as scenario 2 in Figure 6.3.1. If no variation in M_{TOTAL} were invoked throughout OCC formation, the drop in M_{HW} would also imply that M_{FW} increases and that magmatic accretion within the footwall occurs. This is supported by widespread evidence that the cores of OCC footwalls comprise significant proportions of gabbroic material (e.g. Dick *et al.*, 2000; MacLeod *et al.*, 2002; Reston *et al.*, 2002; Ildefonse *et al.*, 2007). However, it is also possible that there is a natural periodicity in melt supply to the ridge axis (i.e.

the magmatic/amagmatic cycle) that causes M_{TOTAL} to vary over time – this could be the primary factor that controls OCC formation (which is discussed in more detail in the next section).

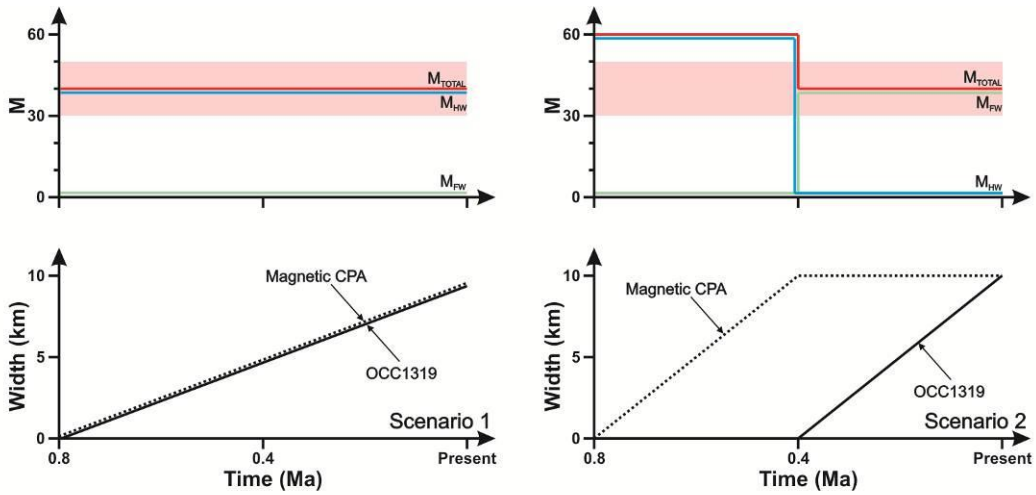


Figure 6.3.1. Two possible scenarios for the history of magmatic accretion during formation of OCC1319. In scenario 1, magmatic accretion in the hanging-wall persists throughout OCC formation and the magnetic CPA and detachment fault grow synchronously between 0.8 – 0 Ma. In scenario 2, the CPA forms between 0.8 – 0.4 Ma, and the OCC forms between 0.4 – 0 Ma. Upper panels show changes in M_{TOTAL}, M_{HW} and M_{FW} during each scenario. Note that in scenario 2 M_{HW} becomes approximately zero during the active part of the OCC life cycle, and melt becomes accreted within the footwall (as shown by the increase in M_{FW}). Components of magmatic accretion (M) after Buck *et al.*, (2005). See text for discussion.

It is important to note that OCC1319 and OCC1330 are, in a regional context, very mature and may be nearing the end of their life cycle, as their across-axis extents are roughly the same as the inactive OCC1348 and they are also considerably larger than other OCCs in the region (OCC durations – Table 3.3.1). Thus the inferred strength of M_{HW} from the present-day melting configuration within the hanging-wall may not be a good indicator of melting conditions throughout the whole OCC life cycle. This is demonstrated by measuring backscatter intensities which show that the volcanic 'hiatus' may be as young as ~0.2 My (*Section 3.4.2*), thus volcanism may have persisted throughout the early stages of OCC formation, and ceased towards the end (i.e. the scenarios in Figure 6.3.1 are end-member models). For example, it may be expected that rather than the component of magmatic plate separation in the hanging-wall instantaneously 'switching-off' as soon as OCC1319 began forming (as in scenario 2), it was more likely a gradual waning, whereby magmatic accretion persisted during the early stages of OCC formation and then became absent more recently. This is supported by evidence for widespread, robust volcanism occurring adjacent to the western axial

valley wall-fault at 13°25'N (geological map – Figure 3.2.15b), which Smith *et al.* (2008) have proposed is a site of OCC inception. Furthermore, the NVZ in this area appears to have been displaced from the centre of the axial valley towards the west, suggesting that the axial valley wall-fault, even before it has developed into a fully-fledged OCC, may exert some influence on melt emplacement pathways beneath the ridge axis. Additional evidence that fault capture plays a significant role in crustal accretion processes occurs on a magma-poor section of the SWIR, where Standish & Sims (2010) show that the youngest, neovolcanic lava flows are located up to ~10 km from the ridge axis and form in close proximity to major fault scarps (although not necessarily OCC-forming detachment faults).

It therefore seems likely that as detachments mature and grow beneath the surface, their potential to capture ascending melt increases such that M_{HW} decreases steadily as M_{FW} increases (MacLeod *et al.*, 2009). The precise rate at which this happens is most likely governed by the width over which ascending melt is distributed across the axial-valley; if melt accretes over a wide area (which on the basis of backscatter intensities and magnetic anomaly patterns appears to be the case in the 13°N region) then M_{FW} may begin to increase and M_{HW} may decrease almost as soon as the OCC begins forming. If magmatic accretion is focused into a narrow zone, then M_{FW} may remain low and increase dramatically as the detachment crosses the vertical projection of the ridge axis at depth. In either case, M_{HW} is expected to decrease as the OCC grows larger, eventually to the point where volcanism is absent in the hanging-wall. At this stage of the OCC life cycle, slip on the OCC's detachment fault may terminate, the processes for which I discuss in the following section.

6.3.2. OCC termination

Numerous studies have shown that beyond the regional low melting conditions in magma-poor environments, OCC formation may actually be regulated by either a locally increasing or decreasing melt supply (e.g. Karson & Winters, 1992; Tucholke *et al.*, 1998; Reston *et al.*, 2002; Buck *et al.*, 2005; Behn & Ito, 2008; Tucholke *et al.*, 2008). Tucholke *et al.* (2008) demonstrate this by showing that relict OCC footwalls may be associated with either an RMBA high or an RMBA low relative to younger, hanging-wall crust, suggesting that this indicates that detachment faulting was abandoned when magmatic conditions locally increased (i.e. M_{TOTAL} or $M_{HW} > 50\%$) or

decreased (i.e. M_{TOTAL} or M_{HW} < 30%). Renewed magmatism is expected to promote the formation of younger faults inboard of the detachment surface within weakened axial valley crust (Tucholke *et al.*, 1998), causing the OCC to become terminated and rafted off-axis by conventional seafloor-spreading processes as extension is preferentially accommodated along younger faults and intrusive dikes.

On the basis of gravity data, Tucholke *et al.* (2008) suggest that amagmatic termination of an OCC at 15°45'N occurred as this OCC is associated with low RMBA relative to crust on its younger, ridge-proximal side which shows elevated RMBA (the relationship between RMBA, crustal thickness and the inferred level of melt supply is discussed in *Section 4.3*). However, on the basis of seafloor sampling results across the same OCC, MacLeod *et al.* (2002) suggest that slip termination was actually associated with synkinematic emplacement of dikes into and across the detachment, which implies enhanced magmatic conditions. This suggests that gravity anomalies may only record prevailing long wavelength variations in magmatism that are not necessarily a good indicator of localised magmatic conditions at the exact moment of OCC termination. For example, Tucholke *et al.* (1998) state that termination may be caused by a relatively minor episode of magmatism within an amagmatic phase of crustal accretion, rather than initiation of a new magmatic phase at the ridge axis. Furthermore, Cannat *et al.* (2006) show that of 39 corrugated surfaces studied on the SWIR, most are associated with locally high RMBA, which suggests that termination by amagmatism, at all scales, is rare.

Contrary to this, on the MAR at 05°00'S, a single, large OCC has been split by a rifting event and forms both an IC-high and conjugate OC-high; crust formed between the two massifs is unusually thin and does not exhibit a well-developed neovolcanic ridge. This suggests that tectonic processes, rather than renewed magmatism, have been the primary control on rifting and OCC termination in this area (Reston *et al.*, 2002).

Direct geological evidence for magmatic termination of slip on detachment surfaces has previously been observed at Kane Massif, which is believed to have formed during a period of amagmatic extension that persisted for about ~0.5 My, before becoming terminated by the emplacement of a neovolcanic ridge (Karson *et al.*, 1987; Karson & Winters, 1992). In addition to this, on the MAR at 26°40'N, basaltic cones have been observed across the detachment surface of Dante's Domes OCC, which are interpreted to have formed as magmatism became enhanced at the end of the OCC's lifetime (Tucholke *et al.*, 2001). Tucholke *et al.* (2001) further suggest that compressive

forces associated with bending of the footwall may facilitate melt migration towards the surface which ultimately cause the formation of a new fault nearer the ridge axis; in this scenario OCC extension and termination may be a self-limiting process, although it is unclear whether this mechanism is secondary compared with broader magmatic/amagmatic cycles.

Using the rationale of Tucholke *et al.* (2008), in the 13°N region I suggest that termination of OCCs has occurred primarily by renewed magmatic conditions at the ridge axis, as each OCC is associated with a peak in RMBA of several mGal compared with younger crust which exhibits relatively low RMBA (*Section 4.3.3*). However, I note that a limitation of Tucholke *et al.* (2008)'s method may occur if magmatic accretion is assumed to persist within the hanging-wall throughout OCC formation (e.g. Buck *et al.*, 2005; Behn & Ito, 2008; Tucholke *et al.*, 2008; Olive *et al.*, 2010). In this scenario, to truly assess the magmatic conditions during OCC formation it would be necessary to analyse the RMBA pattern across the conjugate area of the hanging-wall, not just across the OCC itself. For example, an OCC may be associated with a peak in RMBA relative to younger crust, which implies that it formed during a magma-poor interlude and was terminated by renewed magmatism, but if magmatic accretion persisted within the hanging-wall during OCC formation then for termination to be associated with renewed magmatism there must also be an RMBA high in the hanging-wall conjugate to the OCC.

With this ambiguity in mind, sidescan sonar imagery may provide the best evidence that OCCs in the 13°N region become terminated by renewed magmatic accretion (*Section 3.4.2*). Whereas it appears that surficial volcanism is absent within the hanging-wall towards the end of the active stage of the OCC life cycle, volcanism is widespread and robust within the axial valley adjacent to the older, inactive near-axis OCC1348 (this study; MacLeod *et al.*, 2009). With regard to the precise mechanisms of OCC termination by renewed magmatism, sidescan sonar imagery show that melt-rich NVZs are currently propagating from the north and south towards OCC1319 and OCC1330. This most likely occurs as melt is preferentially channelled towards the stress-free surface at the footwall/hanging-wall boundary of near-axis OCCs (*Section 3.5*). Eventually, these NVZs may merge and significant volumes of melt may be erupted around the 'toe' of each OCC that on-lap onto the respective detachment surfaces. It is possible that this event will provide the necessary heating of axial valley

lithosphere on the ridge-proximal side of each OCC that will promote the formation of younger faults and terminate slip on OCC-forming detachment surfaces.

In addition to the along-axis propagation of NVZs, there are a number of other processes by which OCCs in the region may be terminated. For example, it is expected that a significant volume of melt is captured by OCC footwalls during their lifetime (e.g. Dick *et al.*, 2000; MacLeod *et al.*, 2002; Reston *et al.*, 2002; Ildefonse *et al.*, 2007). This can also be inferred from the gap in the NVZ adjacent to active OCCs and the assumed transition from melt emplacement primarily into the hanging-wall to the footwall as OCCs mature (*Section 3.4.2*). Melt captured by the footwall may episodically break through the detachment and erupt at the seafloor, resulting in dike emplacement through the detachment surface that subsequently leads to OCC termination (MacLeod *et al.*, 2009). As noted previously, rollover and flattening of the detachment surface may cause compressive forces at depth within the OCC's footwall that enhance this process by helping to drive captured melt towards the surface (Tucholke *et al.*, 2001). In addition to this, Cannat *et al.* (2009) suggest that melt accumulation causes the footwall to become uplifted, and that when melt has cooled sufficiently rheological changes occur which increase the rigidity of the footwall and promote the formation of 'termination scarps'. These faults subsequently dissect the footwall and prohibit extension on the master detachment fault. This latter process is demonstrated in the 13°N region, where the oldest of the three near-axis OCCs exhibits the flattest detachment surface and also displays the most cross-cutting faults (*Section 3.3.1.5*). Footwall structure and OCC evolution is discussed in the following section.

From the preceding discussion, it is clear that no overall change in melt supply to the ridge axis (i.e. M_{TOTAL}) is required to cause termination of OCCs; M_{TOTAL} could in theory remain constant throughout the OCC life cycle, but towards the later, mature stage of OCC formation become preferentially accreted within the footwall, rather than the hanging-wall, and cause termination by the processes discussed above. However, significant variations in M_{TOTAL} *are expected* to occur at the ridge axis; this is clearly demonstrated on a regional scale by long wavelength variability in the location and extent of abyssal hill terrain, and more locally by ridge-centred RMBA lows within the 13°N region (summarised in *Section 6.2.1*). Thus it is possible that OCC formation is primarily regulated by relatively long wavelength waxing and waning of M_{TOTAL}, and only secondarily by preferential accretion of melt into the footwall. Detachment faulting may occur within amagmatic periods and become terminated as a new phase of melt

emplacement occurs, with the critical control on OCC formation therefore being the recurrence time of magmatic events at the ridge axis (Tucholke *et al.*, 1998).

The average duration of OCCs across the 13°N region implies that amagmatic cycles persist for ~0.2 – 0.5 My, and therefore it might be expected that one entire magmatic/amagmatic cycle lasts ~0.4 – 1.0 My. This is slightly quicker than the full-cycle predicted on the basis of regional seafloor morphology along the FT-MA segment (~3 My; *Section 3.3*) and by various other studies (2 – 4 My; e.g. Tucholke & Lin, 1994; Tucholke *et al.*, 1997; Skolotnev *et al.*, 1999; Fujiwara *et al.*, 2003). It therefore seems that OCCs may operate in response to shorter-wavelength variations in melt supply that are superimposed on longer-wavelength, regional trends. The fact that the average duration of OCCs in the 13°N region is shorter than that of OCCs in the vicinity of Kane FZ (e.g. Tucholke *et al.*, 1998) thus implies that relatively frequent periods of short-lived magmatism, and subsequently relatively frequent periods of short-lived OCC formation, are the dominant crustal accretion processes in the 13°N region.

It is also possible that the cyclicity predicted to occur in M_{TOTAL} is in fact *controlled* by OCC formation. For example, Behn *et al.* (2006) show that magmatic phases may be a self-limiting process, and that as axial valley topography forms when M_{TOTAL} is high, compressive forces occur beneath the ridge axis at the base of the crust that inhibit further melt emplacement. At this point, it might be expected that an OCC begins to form to compensate for the deficit in magmatic accretion. If the detachment fault of the OCC is able to penetrate into the area where melt is being trapped at the base of the crust, it is possible this may relieve the compressive forces inhibiting melt ascent, instigating a new magmatic phase that subsequently overwhelms the OCC and terminates slip on the detachment surface.

In the following sections I discuss observations regarding the morphology and structure of OCC footwalls on the basis of sidescan sonar data and forward modelling of gravity and magnetic data, and also consider the possibility of linked detachment surfaces. At the end of this section I then present a model for OCC formation and give a summary of my observations regarding melt emplacement and the controls on OCC initiation and termination.

6.3.3. Footwall structure

The footwalls of oceanic core complexes studied in the 13°N region exhibit highly variable morphology and structure. OCC1319 is the youngest (termination/initiation: ~0 – 0.4/0.8 Ma) of the three near-axis OCCs and is characterised by two distinct morphological provinces, comprising: a smoothly domed section on the younger side of the OCC, and a rugged, elevated massif that includes the linear breakaway region on the older side. Bathymetry and sidescan sonar data reveal that the domal section exhibits slickensides that parallel the spreading direction at wavelengths ranging from several hundreds of metres (corrugations) down to only a few tens of metres (striations); the azimuth of these kinematic indicators faithfully record the regional spreading direction (*Section 3.3.1.3*). Serpentinised peridotite is a major constituent of the detachment surface forming the domal section and thus it appears that corrugations may form by continuous casting of relatively ductile footwall material against the underside of the brittle, basaltic hanging-wall (Spencer, 1999). A distinct light scattering sensor (LSS) anomaly was detected in the water column midway across the domal section of OCC1319, which suggests that the serpentine-rich footwall hosts active hydrothermal vents (*Section 3.2.4*; although none were imaged with the deep-towed video, which has a limited field of view). In terms of its location, this vent is similar to a Rainbow-type ultramafic-hosted hydrothermal system (McCaig *et al.*, 2007).

Sparse striations are observed across the elevated, upper massif of OCC1319, where basaltic material and upper crustal rocks were predominantly sampled (*Section 3.3.1.3*). This suggests that the presence of striations does not necessarily indicate the presence of ultramafic lithologies. Rotation of these features by ~10° from the spreading direction and the existence of numerous small faults (apparent within the sidescan sonar imagery) indicate that the upper massif has undergone large amounts of tectonic deformation. The upper massif is also associated with negatively magnetised crust (*Section 5.4.1*). Assuming that the OCC formed entirely during the Brunhes chron, this suggests that the OCC may have initiated off-axis in Matuyama-age crust, and that the upper massif may primarily comprise rider-blocks of negatively-magnetised Matuyama-age material that were clipped-off the hanging-wall during extension on the detachment fault (e.g. Figure 5.4.3a-c).

To the north, OCC1330 has similar dimensions to OCC1319 and is also similarly located in close proximity to the ridge axis. However, based on the more

irregular and sedimented domal section (*Section 3.3.1.4*), it is interpreted as being the slightly older of the two core complexes (termination/initiation: ~0 – 0.4/0.8 Ma). This can also be inferred from the gap in the NVZ adjacent to OCC1330, which is slightly smaller than opposite OCC1319, possibly indicating that OCC1330 is in a later stage of the OCC life cycle (*Section 3.4.2*). Although less extensively sampled, the domal section of OCC1330 has been shown to comprise large amounts of serpentinised peridotite and hydrothermally altered material (*Section 3.2.2*). Deep-towed video footage collected during JC07 confirm the existence of beehive-shaped hydrothermal vents on the detachment surface of OCC1330; hydrothermal fields have previously been inferred from electrical potential anomalies in the water column ('Semyenov sulphide district'; Beltenev *et al.*, 2007; Beltenev *et al.*, 2009).

Morphologically, the most striking difference between OCC1319 and OCC1330 is that the latter does not display a distinctive, elevated upper massif. Instead, the breakaway region and area of seafloor on the older side of the domal section forms a low-lying patch of seafloor that exhibits an irregular, 'mottled' backscatter texture (*Section 3.3.1.4*). This indicates that OCC1330 does not have any rider-blocks, which is also confirmed by a deep-towed magnetic profile across the detachment surface which shows that there is not an area of anomalous positive or negative magnetisation across the older part of the OCC as there is with OCC1319 (*Section 5.4.2*). Instead, forward modelling of magnetic anomalies reveals that the low-lying patch of seafloor has no magnetisation, which is consistent with the presence of non-magnetic sheeted dykes and lower crust (Section 5.4.2; a similar sequence of crustal material has been shown to have no magnetisation across a large fault at TAG – Tivey *et al.*, 2003).

Of the three near-axis OCCs surveyed during JC07, OCC1348 is the oldest and is also the only detachment that is interpreted as being inactive (termination/initiation: ~0.4 – 0.6/0.8 – 0.9 Ma). The domal section is sub-horizontal and is obscured by a thick sediment blanket, and widespread neovolcanism fills the entire width of the adjacent axial valley (*Section 3.3.1.5*). In addition, the detachment surface is cut by numerous faults that are much larger than the few, minor faults that are observed cutting-through the footwall of OCC1330 (there do not appear to be any faults deforming the domal section of OCC1319). These faults have most likely formed in response to a combination of rheological changes within the footwall (e.g. Cannat *et al.*, 2009) and dikes erupting through the detachment surface to the seafloor, each of which may be associated with enhanced magmatism or melt becoming preferentially accreted within

the footwall at the latter stages of the OCC life cycle (as discussed in the previous section). There is not, however, any evidence for surficial volcanism on the detachment surface of the OCC, as may rarely be observed across other inactive detachments on the MAR (e.g. Tucholke *et al.*, 2001).

Gravity data confirm that each of the near-axis OCCs in the 13°N region is associated with an area of relatively low density rock that probably reflects gabbro and/or serpentinised peridotite, within the footwall (*Section 4.4*). Gravity anomalies across OCCs are relatively weak, thus it is not possible to match predicted and observed anomalies with a model that assumes unserpentinised mantle peridotite (ρ = 3300 kg/m^3) outcrops at the seafloor (note that such a model is plausible at FUJI Dome, where RMBA values over the OCC are considerably higher – Searle *et al.*, 2003). Instead, between the assumed outcrop of the Moho and the footwall/hanging-wall boundary, OCCs must comprise rock of significantly lower density – the precise value of which is dependent on the thickness of the low density sequence. For example, within the footwall of OCC1319, the low density zone (LDZ) must have a density of ~2900 kg/m^3 if it is assumed to have a thickness of ~3 – 4 km (*Section 4.4.2.1*); this density is similar to that of gabbroic lower crust or partially serpentinised peridotite (~50% serpentinisation). Most of the peridotite samples taken across the domes of OCCs in this region were serpentinised by > 75% (*Section 3.2.2*), but it is important to remember that, in terms of degree of serpentinisation, rocks dredged from the surface are unlikely to be representative of the whole footwall sequence. Thus 50% serpentinisation is more likely an average value between extremes, with serpentinisation decreasing with depth as it becomes progressively more difficult for seawater to penetrate into the OCC.

The footwalls of OCC1330 and OCC1348 must also be associated with a LDZ in order to match predicted and observed gravity anomalies (*Sections 4.4.2.2-3*). However, the LDZ within these older OCCs must be either ~1 – 2 km thicker, or of lower density (~2750 kg/m^3), relative to the LDZ which is modelled in the footwall of the younger OCC at 13°19'N; this is supported in both 2.5D and 3D models of subsurface OCC density structure. The possible reasons for this are discussed below.

The composition of the LDZ has important implications for the conditions in which OCCs form. If the LDZ comprises entirely serpentinised peridotite, and it was assumed that no melt was accreted to the hanging-wall during at least some part of the OCC life cycle (inferred from the gaps in the NVZ adjacent to active OCCs), this would imply that each OCC formed entirely amagmatically. Conversely, if the LDZ comprised

some degree of gabbroic intrusions, this would imply that magmatism persisted and was accreted within the footwall during OCC formation (e.g. Figure 4.4.5a-b).

At Atlantis Massif, a ~1 km thick low density layer has been attributed to a serpentinisation front in the footwall running sub-parallel with the detachment surface (Nooner *et al.*, 2003). On the basis that recent sampling studies have shown the cores of OCC footwalls to comprise significant volumes of gabbroic material at depths < 1 km (e.g. Dick *et al.*, 2000; MacLeod *et al.*, 2002; Reston *et al.*, 2002; Ildefonse *et al.*, 2007), I suggest that the LDZ beneath near-axis OCCs in the 13°N region is likely to be formed primarily by magmatic accretion but still contain some degree of serpentinised peridotite. The base of the LDZ may represent a serpentinisation front within the footwall – as predicted for Atlantis Massif by Nooner *et al.* (2003) – but the overlap between the density ranges of partially serpentinised peridotite and gabbro does not preclude the possibility that the latter forms a significant part of the footwall of OCCs at shallow depths. Deeper, detailed sampling studies and seismic data acquisition would be necessary to fully quantify the subsurface nature of OCC footwalls in this region.

Magnetic heterogeneity of OCCs supports the idea that the LDZ comprises a mixture of gabbroic intrusions and serpentinised peridotite (*Section 5.4*). For example, if the domal sections of OCCs are assumed to be built entirely by a single lithology (i.e. serpentinised peridotite), it seems unlikely that the degree of serpentinisation and/or depth to a serpentinisation front would vary to such an extent that major along- and across-OCC discontinuities in magnetisation form. It seems more reasonable that significant lithological variations, whereby the domal sections of OCCs comprise a mixture of partially serpentinised peridotite and gabbroic intrusions, as has been observed at Kane Massif (Dick *et al.*, 2008) and Atlantis Massif (Canales *et al.*, 2008), plays a major role in shaping the magnetisation patterns across OCC footwalls.

There appears to be a first-order relationship between LDZ extent and OCC age, with the older of the two near-axis OCCs (OCC1330 and OCC1348) seemingly being associated with thicker and/or lower density material than OCC1319 (*Section 4.4*). There are a number of reasons as to why this may be the case. Firstly, it may be expected that the degree and extent of serpentinisation increases with age, and thus older OCCs may be underlain by a greater extent of low density, serpentinised mantle. Serpentinisation may also become accelerated towards the end of the OCC life cycle as the terminated detachment fault becomes dissected by cross-cutting faults (as appears to have occurred across OCC1348 – *Section 3.3.1.5*). The across-axis thickness variations

in the LDZ within the footwall of OCC1348 may therefore reflect the fact that the eastern part of the dome, being older, has undergone more pervasive serpentinisation than the western part. Secondly, if magmatism persists throughout OCC formation, older OCCs may have undergone a longer period of melt capture and magmatic accretion within the footwall, thus explaining why they exhibit a greater ratio of low density material relative to high density unserpentinised mantle compared with the youngest OCC in the region. Across-axis variations in the thickness of the LDZ may therefore reflect localised variations in magmatic intensity. Thickening of the LDZ towards the footwall/hanging-wall boundary of OCC1348 may have occurred as the detachment fault progressively crossed the axial valley at depth, dramatically increasing melt input into the footwall immediately prior to OCC termination (as discussed in *Section 6.3.2*).

In the following section I discuss the possibility of along- and across-axis linked detachment surfaces. I then present a summary of the local melting conditions and mechanisms that necessitate OCC formation and also regulate OCC termination, and also present a model for footwall structure at different stages of the OCC life cycle.

6.3.4. Linked detachment surfaces

It has been proposed that apparently isolated oceanic core complexes in the 13°N region may be linked beneath the seafloor by a single, master detachment surface (e.g. Smith *et al.*, 2008; Schouten *et al.*, 2010). Whilst this provides an elegant model for crustal accretion in magma-poor environments, as yet there is very little data to test such a model. The data collected during JC07 show little evidence in favour of this process occurring in the 13°N region (although it should be noted that the geophysical data collected were not specifically designed to test this hypothesis). Ambiguity primarily arises due to the similarities in the density range over which serpentinised peridotite and gabbro can exist. Thus the composition of intervening areas of seafloor between OCCs cannot be distinguished from either large tracts of ‘normal’ gabbroic seafloor (i.e. magmatic crustal accretion) or a mixture of serpentinised peridotite and gabbroic melt captured by the footwall of a single, large detachment fault (i.e. magma-poor plate separation and linked-OCC formation; *Section 4.4.2.4*).

Seismic imaging or an along- and across-axis transect of deep boreholes could potentially resolve this ambiguity. In lieu of this data, it is possible to make qualitative

comparisons between the 13°N region and other magma-poor environments along the MOR to determine if widespread detachment faulting and linked OCC formation is a plausible mechanism for crustal accretion in this area. For example, it has been proposed that OCC1319 and OCC1330 may be two parts of the same detachment surface (e.g. Smith *et al.*, 2008). In this model the area of seafloor between the two comprises rider-blocks that sit atop a topographic corrugation of much longer-wavelength and amplitude than corrugations on the exposed part of each detachment surface (Figure 6.3.2). If these detachment faults were linked beneath the surface, however, this would imply that formation of this single, large detachment surface marks a considerably different mode of crustal accretion to other detachment faults that are continuous along-axis over similar distances; Dante's Domes OCC on the MAR at 26°40'N, for example, is continuous along-axis for ~25 – 40 km and exhibits a predominantly flat topography – there is no evidence for very large topographic corrugations (Figure 6.3.2; Tucholke *et al.*, 1998; Tucholke *et al.*, 2001).

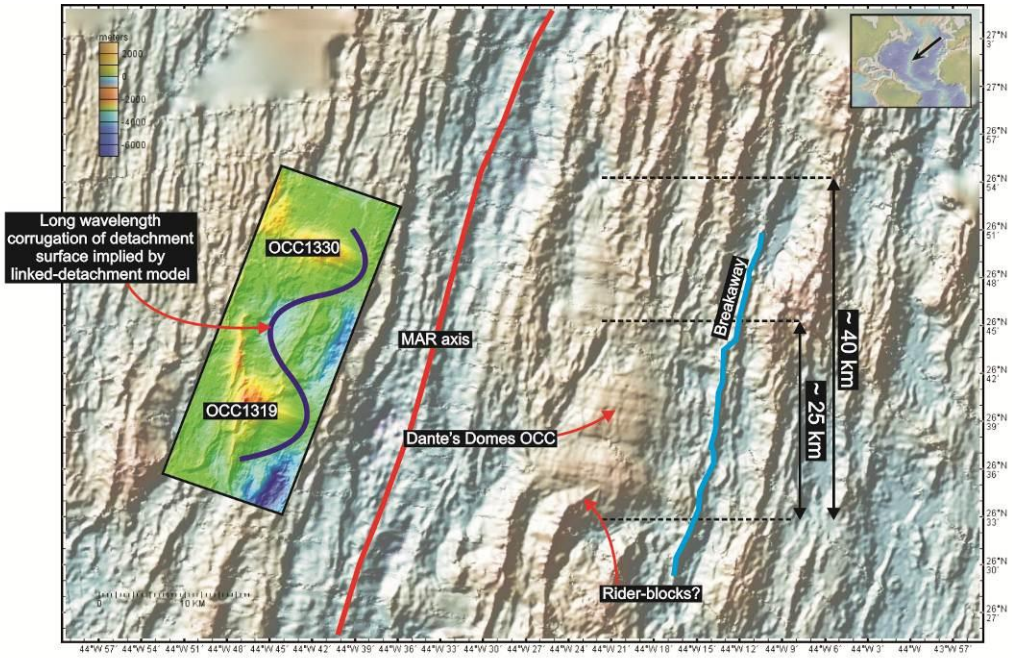


Figure 6.3.2. Seafloor morphology in the vicinity of a large detachment surface on the MAR at 22°40'N (~70 km north of TAG). The corrugated detachment surface extends for between ~25-40 km along-axis and does not exhibit very-long wavelength topographic corrugations implied by a linked detachment model in the 13°N region (the relative size and spacing of OCC1319 and OCC1330 are superimposed on the conjugate, western flank). Breakaway location of Dante's Domes after Tucholke *et al.*, 1998. Bathymetry data were accessed via *GeoMapApp* (Ryan *et al.*, 2009).

Thus a model in which OCCs in the 13°N region are linked beneath the surface by a single, master detachment surface cannot be unequivocally proven or disproven using data collected throughout JC07. However, comparison with a single, large detachment fault at 26°40'N on the MAR suggests that the surficial morphology of OCC1319 and OCC1330 (and the intervening area of seafloor) is greatly different from this area, and therefore continuous crustal accretion by detachment faults that extend for > 10 km along-axis seems unlikely in the 13°N region. Instead, within the 13°N region I envisage that magmatism is weak and discontinuous, yet significant volumes of melt are still emplaced regularly enough at the ridge axis to punctuate detachment faults and limit the along- and across-axis dimensions of core complexes (a model for which is presented in the following section).

6.3.5. Summary & model for OCC formation

Oceanic core complexes form when magmatic accretion at the ridge axis is diminished; on the basis of faults exposed within sidescan sonar imagery and crustal thickness estimates, M_{TOTAL} must be ~70 – 80% for this to take place. This is an average value along ~40 km of the ridge axis and over 1.86 My. It may therefore be expected that shorter-wavelength, higher-amplitude variations in M_{TOTAL} take place.

The large axial valley-wall fault on the western side of the ridge axis at 13°25'N is associated with a peak in magnetisation and widespread neovolcanism, and therefore appears to be the present-day locus of magmatic accretion (Figure 6.3.3a). MacLeod *et al.* (2009) show that the dip of this fault is no different from the initial dip of OCC-forming detachment faults, thus it may be expected that this axial valley-wall fault may eventually develop into an OCC (which has also been proposed by Smith *et al.*, 2008). Neovolcanism in close proximity to this fault thus supports a model whereby OCCs initiate under magmatic conditions (i.e. M_{TOTAL} = 30 – 50%; e.g. Buck *et al.*, 2005; Behn & Ito, 2008; Tucholke *et al.*, 2008; Olive *et al.*, 2010). This is also supported by the fact that back-tilted, hummocky seafloor is often observed on the outer slopes of OCC breakaway ridges (e.g. MacLeod *et al.*, 2009). In addition to this, the NVZ at 13°35'N is offset towards the western axial valley-wall fault, which suggests that the fault may be able to influence melt emplacement pathways at depth within the crust.

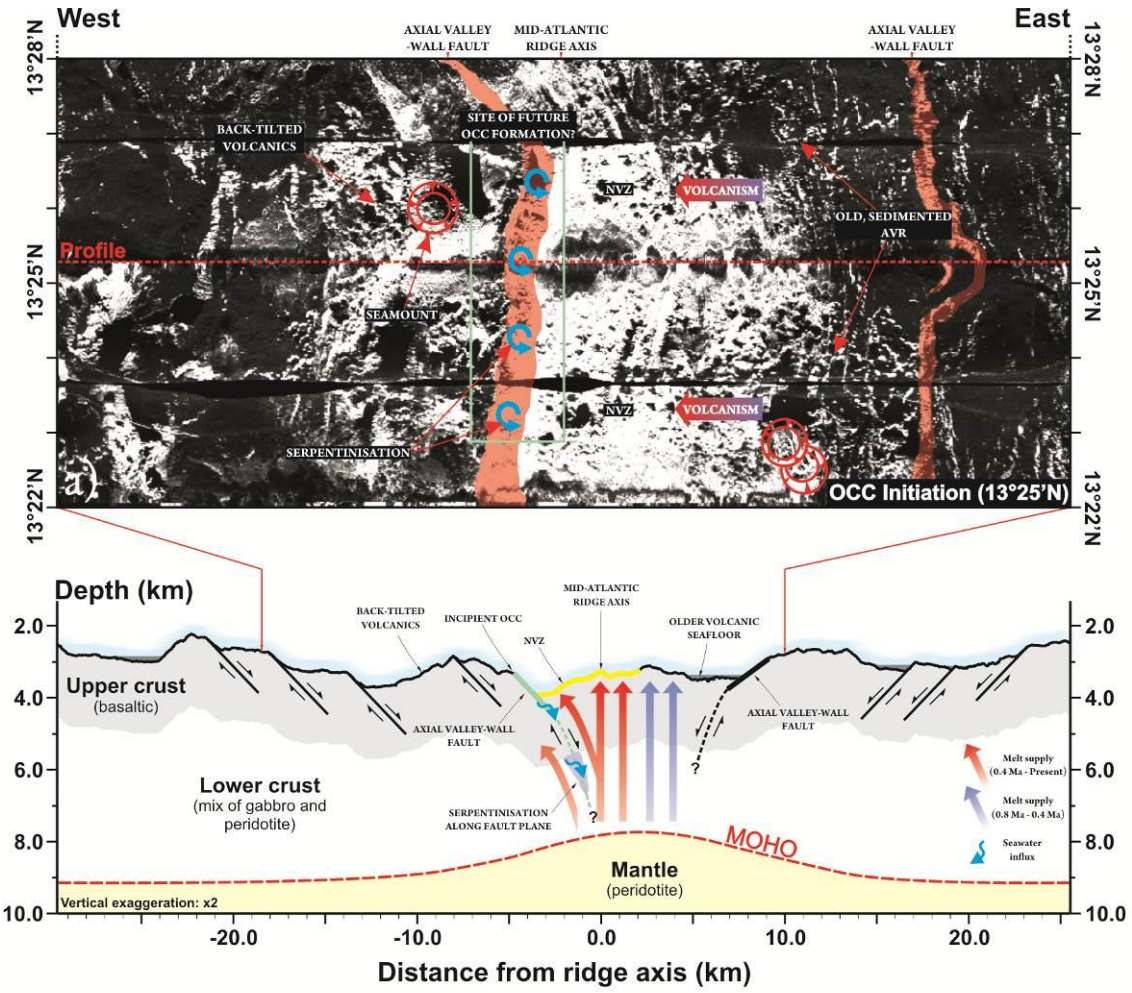


Figure 6.3.3a. OCC formation and structure: OCC initiation. Sidescan sonar (upper panel) and bathymetry data (cross-section; lower panel) are across axial valley at 13°25'N. Note that the cross-section extends beyond the limits of the sonar data. In this region, the magmatic crust is thin and the lithosphere is heterogeneous. Seawater reacts with peridotite (which may be present in the lower crust) and localises strain on a single fault (green line in cross-section). Widespread neovolcanism occurs in close proximity to this fault at the surface, due to melt becoming captured at depth. Magnetisation profiles confirm this, with the central positive anomaly occurring across the western half of the axial valley (e.g. **Line 4 - Figure 5.2.1[2]**). See text for discussion.

The mechanisms by which this may occur are not well understood, but this also appears to be the case along a section of the SWIR (Standish & Sims, 2010). Thus footwall capture of ascending melt appears to occur during crustal accretion by magma-poor processes, yet it is not clear if this is a fundamental process that leads to OCC formation. Furthermore, the breakaway region of OCC1319 is not associated with a peak in magnetisation indicative of robust magmatism prior to OCC formation (*Section 5.4.1*). Instead, low magnetisation in this area suggests that the OCC initiated within older seafloor, where volcanism may have been sparse. Thus it is likely that additional factors other than footwall capture of ascending melt are able to control OCC formation, which are discussed below.

In environments where the magmatic crust is thin and heterogeneous, and where faults are able to grow large due to the deficit in magmatic accretion, peridotite is more readily accessible to seawater which infiltrates the crust along fault planes (Figure 6.3.3a). Seawater reacts with high-temperature mantle material to form serpentinised peridotite and other weak minerals (such as talc) which efficiently localise strain onto the incipient detachment fault (Escartin *et al.*, 1997b; 2001; Escartin *et al.*, 2008a); these lithologies are ubiquitously sampled from OCC-forming detachment faults in the 13°N region (*Section 3.2.2*). Thus footwall capture of ascending melt and focusing of volcanism around the incipient OCC may be a secondary process, which is elevated if serpentinisation has taken place and strain has localised onto a single, large fault at the ridge axis.

The across-axis extent of OCCs in the region suggests that serpentinisation causes strain to occur preferentially along a single fault for ~0.2 – 0.5 My (*Section 3.3.1*). During this time, OCCs gradually roll over and flatten, exhuming lower crustal and mantle rocks (e.g. OCC1319; Figure 6.3.3b). Surficially, basalts and dolerites are exposed on the older parts of OCCs (i.e. the upper massif) whereas the younger part of each OCC (i.e. the domal section) comprises predominantly serpentinised peridotite (*Section 3.2.2*). Gabbro outcrops are sparse although it is expected that this lithology makes up a significant volume of OCC footwalls at depths greater than those sampled during JC07 (e.g. Dick *et al.*, 2000; MacLeod *et al.*, 2002; Reston *et al.*, 2002; Ildefonse *et al.*, 2007). Rider-blocks may be clipped from the hanging-wall onto the footwall so that they lie unconformably on detachment surfaces (although this does not appear to be the case for *all* near-axis OCCs in the 13°N region – e.g. OCC1330; Figure 6.3.3c). Mature core complexes exhibit corrugations and striations that have wavelengths of several hundreds of metres and a few tens of metres, respectively (*Section 3.3.1.3-5*). These features parallel the spreading direction and may form by continuous-casting of the footwall against the underside of the hanging-wall (Spencer, 1999).

During the active phase of the OCC life cycle there is a dramatic change in the style with which melt is emplaced at the ridge axis; melt no longer becomes accreted to the hanging-wall (*Section 3.4.2*). Sidescan sonar data clearly show that there is a gap in neovolcanism adjacent to the mature, active OCCs at 13°19'N and 13°30'N (sidescan sonar – Figure 6.3.3a-b). Smith *et al.* (2008) also show that this is the case for the near-axis OCC at 13°06'N. The seafloor in these areas is highly sedimented and has lacked volcanism for ~0.2 – 0.7 My.

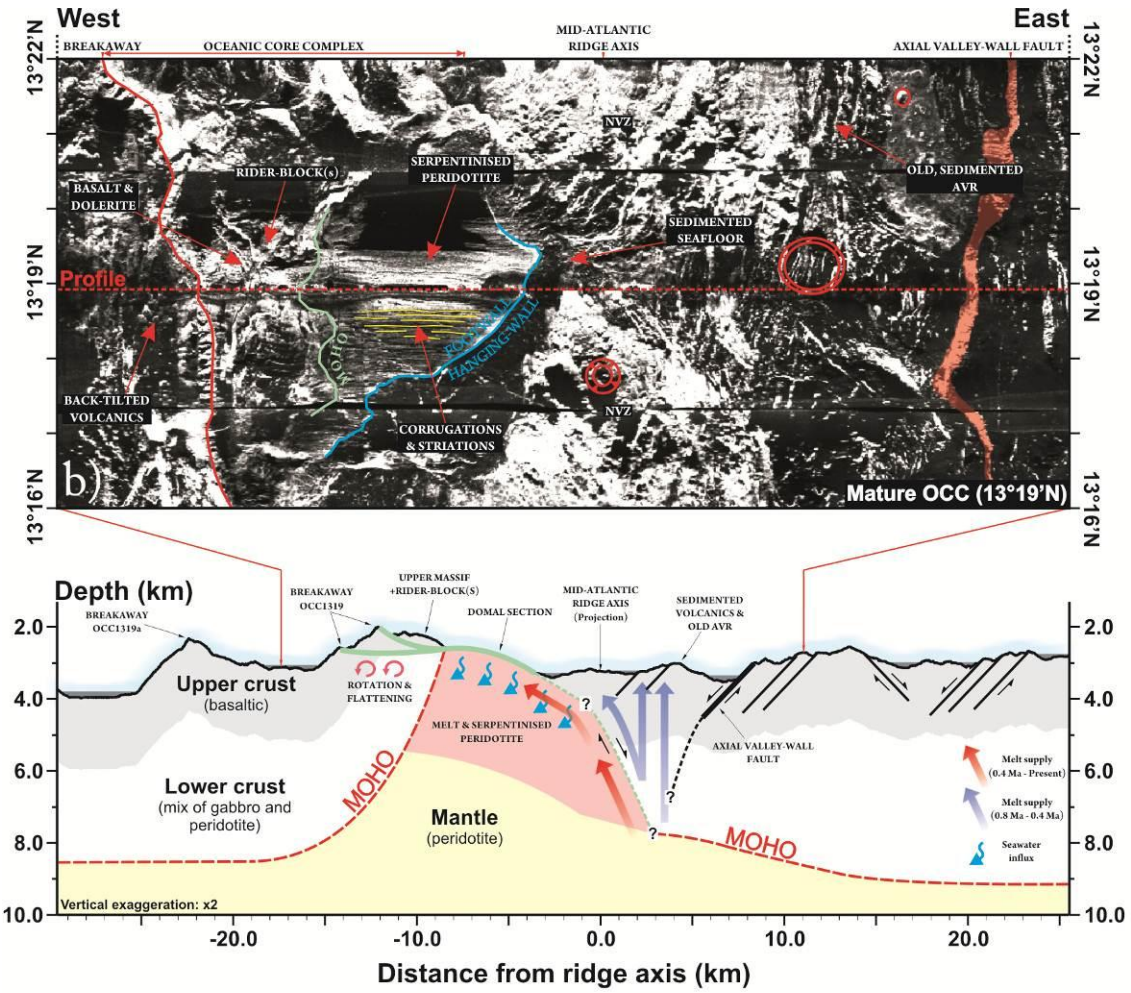


Figure 6.3.3b. OCC formation and structure: Mature OCC [version 1]. Sidescan sonar (upper panel) and bathymetry data (cross-section; lower panel) are across OCC1319. Low density zone is red shaded area in OCC footwall. The mature phase of the OCC life cycle is characterised by absent volcanism across the axial valley, which is predicted to occur as increasing amounts of ascending melt become captured by the detachment fault (green line in cross-section) at depth and accreted within the footwall of the OCC. Rider-blocks have formed on the summit of OCC1319 and represent material clipped-off the hanging-wall in the early stages of OCC formation. Subsurface structure of OCC1319a is not sketched, but can be seen in **Figure 4.4.8a-d**. See text for discussion.

This may arise due to a natural cyclicity in melt supply to the ridge axis (i.e. M_{TOTAL} varies in time), with OCCs forming during amagmatic phases of crustal accretion (e.g. Tucholke *et al.*, 1998). Alternatively, total melt input (M_{TOTAL}) may remain unchanged, but as the OCC grows beneath the surface and across the axial valley melt may become captured by the footwall so that it no longer erupts at the seafloor.

A zone of relatively low density material forms within mantle rock exposed within the footwalls of active OCCs (*Section 4.4*). If OCC formation occurs entirely amagmatically, this LDZ may comprise serpentinised peridotite. Alternatively, if magmatic accretion within the footwall persists throughout OCC formation (which, on

the basis of sampling results from OCCs outside the 13°N region, is more likely; e.g. Dick *et al.*, 2000; MacLeod *et al.*, 2002; Reston *et al.*, 2002; Ildefonse *et al.*, 2007) then the LDZ may comprise gabbroic material. In reality, a combination of magmatic accretion and serpentinisation most likely occurs as this is the only model that can potentially explain sampling results and gravity anomalies across OCCs in the region.

The overlap in the density range for gabbro and peridotite that has been ~50% serpentinised makes it difficult to accurately define the extent and composition of the LDZ using gravity modelling techniques. However, for an assumed density of 2900 kg/m^3 the LDZ must be ~3 – 4 km thick beneath OCC1319 (Section 4.4.2.1) and ~4 – 5 km thick beneath OCC1330 and OCC1348 (Section 4.4.2.2-3). The apparently more extensive (or lower density) LDZ beneath older OCCs may reflect more extensive serpentinisation of peridotite or a greater volume of material accreted magmatically within older footwalls; i.e. the low density zone may grow with time.

The subsequent termination of a mature OCC is most likely associated with renewed magmatic accretion at the ridge axis (Figure 6.3.3d); sidescan sonar data show that widespread neovolcanism covers the width of the axial valley adjacent to the inactive OCC at 13°48'N (*Section 3.4.2*). There are a number of factors that may contribute to this process: renewed magmatism may occur naturally as magma supply temporarily increases during the magmatic phase of the magmatic/amagmatic cycle (i.e. M_{TOTAL} increases), volcanism may propagate from adjacent melt-rich NVZs towards the stress-free footwall/hanging-wall boundary of the OCC (*Section 3.5.3*), and melt capture by the footwall may episodically break through the detachment surface resulting in cross-cutting diking (e.g. MacLeod *et al.*, 2002; MacLeod *et al.*, 2009). This latter process may be enhanced by compressive forces generated within the OCC by flexure of the footwall, which drive melt towards the surface (Tucholke *et al.*, 2001). In each case, renewed magmatism is expected to warm and weaken the axial lithosphere on the younger side of the OCC, thus making it easier to break a new fault in this area rather than maintain slip on the low-angle detachment fault.

It is also possible that OCC formation is a self-limiting process. For example, Behn *et al.* (2006) show that at high melt supplies (i.e. M_{TOTAL} = ~100%) an axial valley forms that generates compressive forces at the base of the crust. This compressive force may potentially inhibit melt emplacement at the ridge axis and remain until sufficient far-field extension has taken place (Behn *et al.*, 2006).

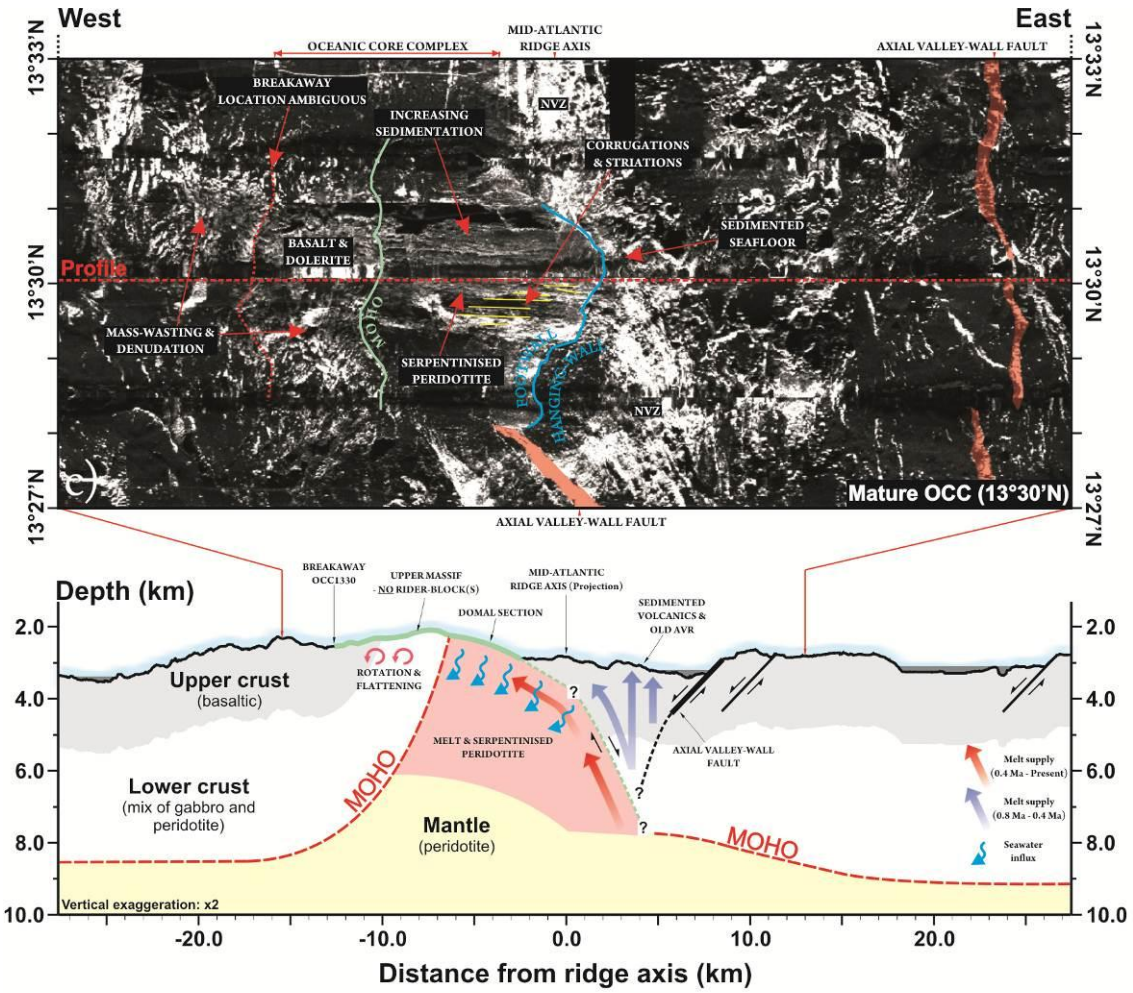


Figure 6.3.3c. OCC formation and structure: Mature OCC [version 2]. Sidescan sonar (upper panel) and bathymetry data (cross-section; lower panel) are across OCC1330. Low density zone is red shaded area in OCC footwall. OCC1330 is slightly older than OCC1319, and thus the detachment surface is more heavily sedimented and has a slightly more irregular domal structure. Neovolcanism is absent adjacent to the OCC at 13°30.5'N, although volcanism occurs in close proximity to the northern and southern halves of the OCC. This implies that a new phase of magmatic accretion is beginning at the ridge axis, and that the OCC is in the process of becoming terminated. Unlike OCC1319, there do not appear to be any rider-blocks on the summit of OCC1330. See text for discussion.

During this amagmatic period an OCC may begin to accommodate plate separation, and if the detachment surface exists for long enough and roots near the base of the lithosphere it may eventually relieve the compressive forces that inhibit melt emplacement, thus triggering a new magmatic phase and terminating the OCC. The average duration of OCCs in the 13°N region suggests that this magmatic/amagmatic cycle may occur over a period of ~0.4 – 1.0 My.

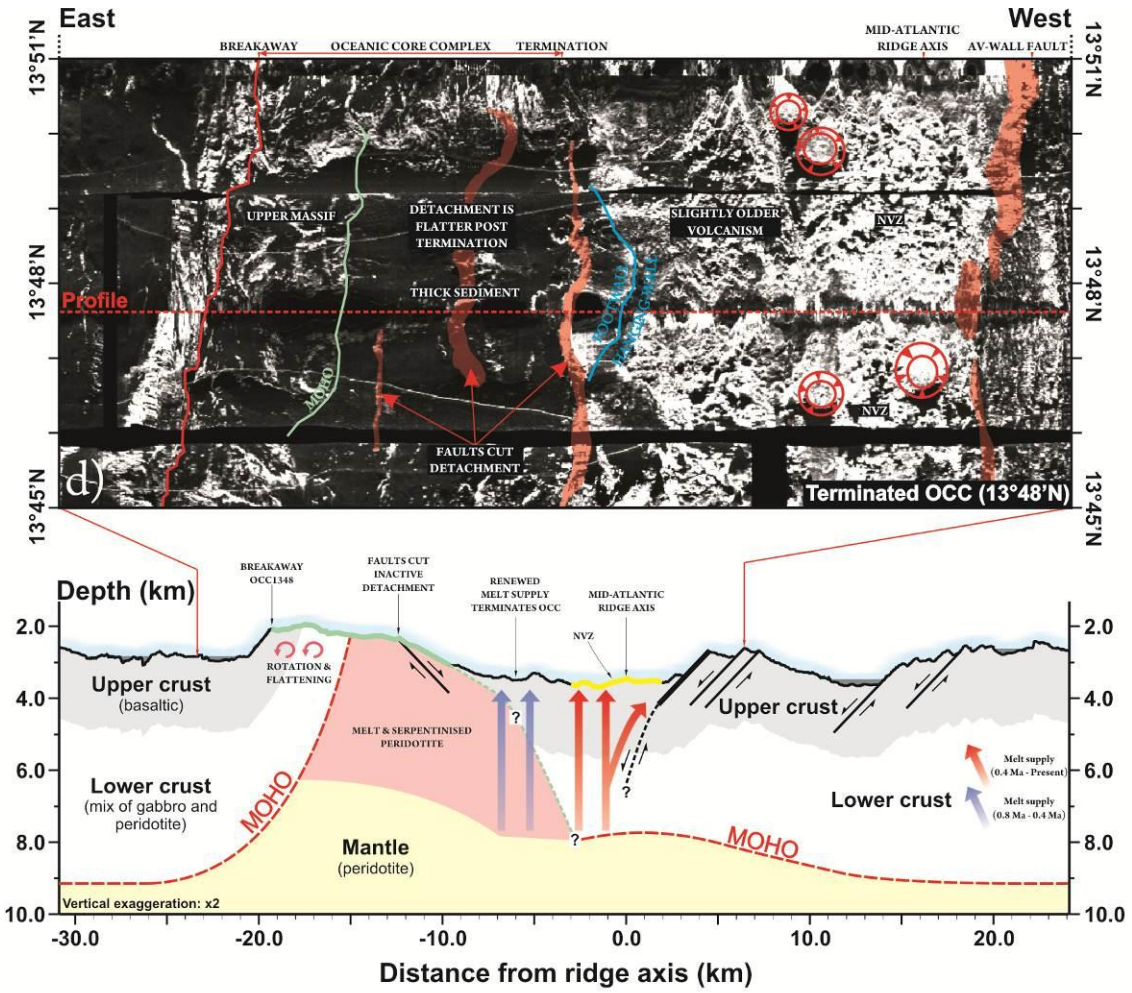


Figure 6.3.3d. OCC formation and structure: Terminated OCC. Sidescan sonar (upper panel) and bathymetry data (cross-section; lower panel) are across OCC1348. Note that this diagram has been mirrored E-W so that it is comparable with **Figure 6.3.3a-c**. Low density zone is red shaded area in OCC footwall. Extension on the OCC's detachment fault has become terminated by renewed magmatic accretion at the ridge axis which has created widespread volcanism across the axial valley. The relict OCC has become heavily sedimented and flattened-out considerably as it becomes cut by a number of ridge-parallel faults. See text for discussion.

After termination, OCCs flatten out and become less domed as flexural forces in the footwall are relieved by cross-cutting faults (*Section 3.3.1.5*). Renewed and relatively robust magmatic accretion occurs at the ridge axis, which causes the sedimented and inactive OCC to become rafted off-axis by conventional seafloor spreading process.

6.4. Conclusions

This thesis has documented the acquisition, processing and analysis of geophysical data collected across a section of the slow-spreading Mid-Atlantic Ridge between 13 – 14°N. In this area crustal accretion involves regular nucleation and extension along OCC-forming detachment faults. The primary aim of this study has been to assess the relationship between magmatic and tectonic processes in such an environment, and also to use geophysical techniques to model and assess local variations in OCC structure and regional crustal architecture (thesis aims are outlined in detail in *Section 1.4*). The main conclusions of this study are as follows:

(1) The 13°N region is an intra-segment area of widespread detachment faulting and oceanic core complex formation (*Section 3.3*). The terrain in this region is distinct from linear, abyssal hill (magma-rich) terrain which flanks the ridge axis near the centre of the FT-MA segment to the north. Magmatic terrain has also formed around the Marathon FZ to the south. Therefore, formation of the 13°N region cannot simply be attributed to the cooling effects associated with the large-offset Marathon FZ, and may thus be the result of a relatively long wavelength mantle 'cold-spot'.

(2) Long wavelength melt supply to the MAR segment bounded by the Fifteen Twenty and Marathon FZs wanders along axis at rates of ~15 – 20 km/My (*Section 3.3*). At this scale, the intensity of magmatism waxes and wanes over a period of ~3 My. In some places, waning magmatism is observed to result in OCC formation (such as the newly identified Marathon OCC – *Section 3.3.1.2*), and waxing magmatism appears to terminate OCCs. However, long wavelength variations in melt supply, inferred from the location of abyssal hill terrain, cannot account for initiation and termination of all of the OCCs in the 13°N region, and thus OCC formation may be regulated by a shorter cycle in magmatism.

(3) Circular RMBA lows show that melt is delivered to discrete points along the ridge axis in the 13°N region; the wavelengths of these anomalies suggest that this zone of anomalous material is confined to the crust and does not exist at depths > ~6 km (*Section 4.3.4*). Bathymetry and sidescan sonar imagery also show that the locus of melt

emplacement at the ridge axis is highly unstable and is able to wander across axis by several km within ~0.5 My (*Section 3.4.1*).

(4) Widespread OCC formation occurs when magmatic processes accommodate ~70 – 80% of the total plate separation over ~1.86 My; this estimate is determined from tectonic strain over the four quadrants of the survey area, and is thus spatially (along-axis) averaged over 40 km (*Section 3.5.2*). Higher-amplitude, shorter-wavelength fluctuations in the relative contribution of magmatic accretion to plate separation are expected to occur during the life cycle of individual OCCs (so that during OCC formation magmatic accretion approaches the theoretical value of M_{TOTAL} = 30 – 50%). Magnetic data lack the resolution to identify younger tie-points that can constrain this.

(5) Although OCCs may initiate at intermediate levels of magmatism, surficial volcanism is absent at the ridge axis during the latter part of the OCC life cycle (*Section 3.4.2*). This marks a dramatic change in the style of crustal accretion at the ridge axis, whereby ascending melt is preferentially emplaced within the footwall of the detachment fault, rather than the hanging-wall, as OCCs mature.

(6) During the active phase of the OCC life cycle, melt captured by the detachment fault forms a low density zone within the footwall of the OCC (*Section 4.4*). Forward modelling of gravity anomalies show that for a density of 2900 kg/m^3, this zone must be ~3 – 4 km thick beneath OCC1319 and ~4 – 5 km thick beneath OCC1330 and OCC1348. The LDZ may thus comprise a heterogeneous mix of partially serpentinised peridotite and gabbroic material. Thicker successions of material beneath older OCCs may reflect a greater accumulation of melt, or more pervasive serpentinisation by seawater infiltration as OCCs gradually become weathered and dissected by faults.

(7) Magnetisation patterns across OCC footwalls are highly disorganised and discontinuous (*Section 5.4*). Assuming the lower crust acquires relatively little magnetisation, the negatively magnetised crust across the upper massif of OCC1319 may thus represent rider-blocks of older (Matuyama-age) basaltic material that have been clipped from the hanging-wall during OCC extension (*Section 5.4.1*). This is supported by the fact that to the north, OCC1330 does not display any morphological evidence for rider-block formation and also only exhibits an area of zero magnetisation

across the upper massif (*Section 5.4.2*). OCC1330 does, however, display considerable along-axis variations in magnetisation over distances of ~3 km, which may be associated with local variations in the composition of the footwall (i.e. melt-rich and melt-poor areas). The wavelength of this intra-footwall compositional heterogeneity is similar to that which has been observed at Atlantis Massif (Canales *et al.*, 2008).

(8) Slip termination on OCC-forming detachment faults is associated with renewed magmatism at the ridge axis (*Section 3.5.3*). This may occur due to a natural periodicity in the strength of magmatism, by melt captured within the footwall occasionally breaking through the detachment fault and erupting at the seafloor, by laterally propagating NVZs from adjacent melt-rich zones, or a combination of these processes. It is also plausible that detachment faults are able to relieve compressive forces at the base of the crust which inhibit melt emplacement at the ridge axis (e.g. Behn *et al.*, 2006). In this latter scenario, OCC formation would be a self-limiting process that occurs over a timescale of ~0.2 – 0.5 My (i.e. the average duration of OCCs in the region; *Section 3.3.1*). The entire magmatic/amagmatic cycle may thus last for ~0.4 – 1.0 My.

(9) Crustal accretion by OCC formation is highly asymmetric compared with magmatically-robust forms of plate separation (such as at segment centres). In the 13°N region, across- and along-axis asymmetry is present in nearly all datasets collected during JC07. For example, bathymetry data and sidescan sonar imagery show that OCC formation is focused within the inside-corners of the NTO at 13°38'N. These areas are associated with elevated tectonic strain ($T\varepsilon$ = ~25 – 30%) compared with conjugate outside-corners ($T\varepsilon$ = ~10 – 15%), which are characterised by numerous, low-heave faults (*Section 3.5.1-2*). Gravity data indicate that in the 13°N region crustal thicknesses are > 1.5 km thinner than the magmatically-robust segment centre (*Section 4.3.2*); the thinnest crust is observed across an area of intense OCC formation in the SW of the survey area. Across-axis asymmetry in crustal thicknesses result in areas of OCC formation being up to ~0.5 – 1.0 km thinner than conjugate ridge flanks, although this may be an underestimate as the precise contribution of low density serpentinised mantle peridotite to the 'crustal' thickness in areas of OCC formation is uncertain. Finally, magnetic anomalies reveal that spreading rates may be up to ~75% asymmetric as tectonic strain and plate separation is preferentially accommodated along long-lived, OCC-forming detachment faults (*Section 5.3.2*).

(**10**) OCCs display striations and corrugations that precisely follow the predicted relative plate motion and reflect a change from NA-AF to SA-AF across the survey area. This suggests that the 13°N region is very close to the NA-SA-AF triple junction.

6.5. Suggestions for further work

6.5.1. Existing data

Palaeomagnetic studies have shown that the footwalls of OCCs may initiate at high angles and become rotated and flattened by flexure and isostatic uplift (Garces & Gee, 2007; Morris *et al.*, 2009). Garcés & Gee (2007) suggest that footwall rotations of 50 – 80° are common along both sides of the ridge axis in the Fifteen-Twenty FZ region, and Morris *et al.* (2009) show that the footwall of Atlantis Massif has rotated by 46±6° away from the ridge axis. These estimates are consistent with seismic imaging and seismicity studies, which have been used to show that at TAG, a large offset fault dips by ~20° towards the ridge axis and steepens to an angle of ~70° at a depth of ~3 km (deMartin *et al.*, 2007).

The outward rotation and flattening of core complexes in the 13°N region should be recorded by the existing three-component magnetometer data collected using TOBI during JC07 (shown in Figure 2.6.14) by magnetic minerals that form along the plane of the detachment fault (e.g. serpentinite). These minerals are initially magnetised parallel with the ambient geomagnetic field, and during formation of the OCC, unroofing and rollover of the footwall causes them to become rotated. The components of the magnetic field in the plane of the spreading direction (in the case of the 13°N region, this would be the eastward and downward components) should record the magnitude of this rotation. For example, if it was assumed that the ambient geomagnetic field was near vertical throughout formation of the OCC, then in theory the vertical/downward component of the magnetic field should decrease across the footwall of OCCs (Figure 6.5.1). In contrast, the horizontal/eastward component should show an increase in magnetic field strength. The ratio of vertical to horizontal magnetic field strength is therefore related to the degree of rotation experienced by magnetic minerals.

The heterogeneous nature of OCC footwalls and the poor along-track continuity of magnetic anomalies, combined with the fact that the magnetic inclination is low in the 13°N region, require that careful 3D forward modelling of the three components of the magnetic field are used to constrain footwall rotations accurately. It should be possible, however, to measure the rollover of detachment faults to see if there is any variability between core complexes in the 13°N region, and also to see how this region compares with OCCs studied elsewhere along the MAR.

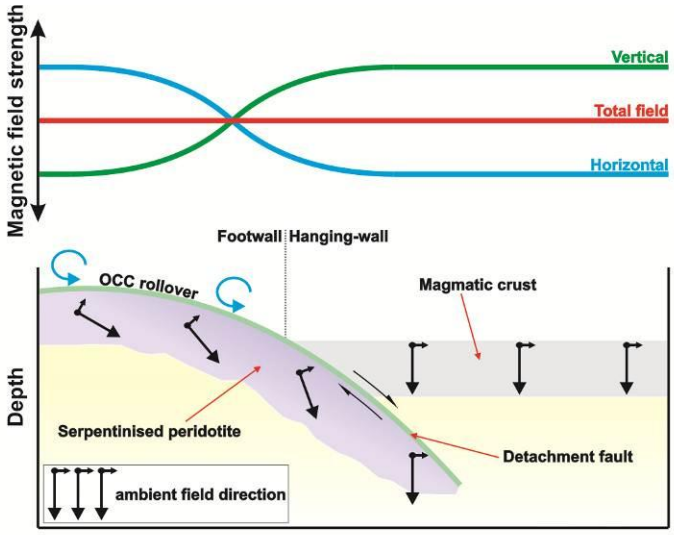


Figure 6.5.1. Theoretical variation in intensity of magnetic field strength across rotated magnetic minerals in OCC footwall. Assuming the ambient geomagnetic field is strong in the vertical direction and weak in the horizontal direction, as the detachment fault rolls over and flattens the observed horizontal magnetic field strength should increase and the vertical field strength should decrease. See text for discussion.

Furthermore, it should also be possible to use the existing TOBI sidescan sonar mosaic to better constrain the magmato-tectonic ratio within which OCCs are expected to form. For example, in *Section 3.5.2* fault surface areas were used to measure tectonic strain across the region and from this M_{TOTAL} during OCC formation was inferred. However, it was noted that as diffuse intra-crustal deformation was not taken into consideration, that the resultant value for M_{TOTAL} was an upper bound. In theory, it should be possible to use the existing fault map (Figure 3.2.15a-b) to estimate fractal fault populations. This would give a better estimate of tectonic strain by taking into consideration intra-crustal deformation that is not apparent on the sidescan sonar mosaic, thus providing a more accurate inferred component of magmatic accretion (M_{TOTAL}) during OCC formation and magma-poor crustal accretion.

6.5.2. Further data acquisition

One of the key findings of this study is that surficial volcanism is absent adjacent to the mature, near-axis OCCs at 13°19’N and 13°30’N, and renewed adjacent to the inactive/terminated near-axis OCC at 13°48’N. This suggests that magmatic accretion in the hanging-wall does not contribute to plate separation during part of the OCC life

cycle, and that melt is able to accrete within the footwalls of active OCCs. Although magmatic accretion within OCC footwalls has been inferred from a number of previous studies (i.e. studies which have sampled gabbro from the OCC 'core'), there has been very little evidence until now that surficial volcanism is absent during the active part of the OCC life cycle and renewed after OCC termination.

Contrary to these findings, numerical modelling results suggest that OCCs should not form at such low levels of magmatic accretion within the hanging-wall (e.g. Olive *et al.*, 2010). In order to validate the observation that volcanism is absent during part of the OCC life cycle (this study; MacLeod *et al.*, 2009), it would thus be useful to acquire more data across the hanging-walls of actively forming OCCs on the MOR. This would help to establish if 'avolcanism' is a fundamental process during OCC formation, or if this observation is unique to the 13°N region. In a broader context, this would help constrain our understanding of the range of magmato-tectonic conditions within which OCCs are expected to form.

As has been shown in this study, sidescan sonar data provide a rapid means for assessing the volcanic conditions in the hanging-wall during OCC formation. The preliminary results of a recent TOBI sidescan sonar survey conducted across the Cayman Trough also suggest that OCC formation is associated with avolcanic crustal accretion (R. Searle; cruise JC44, *personal comm.*). In the future, I suggest that the MAR in the vicinity of TAG would be an ideal location to conduct further TOBI surveys designed to assess the relationship between OCC formation and volcanism as, on the basis of seismicity and seafloor morphology, there appears to be ~5 active, near-axis OCCs currently forming along this section of the MAR (Figure 6.5.2). Reanalysis of existing sidescan sonar data collected along the ridge axis from 26°20'N to 27°00'N and from 24°50'N to 25°50'N (Smith *et al.*, 1995) may also provide further constraints on volcanic conditions during OCC formation.

It should be noted, however, that seafloor dating using sidescan sonar backscatter intensity is associated with large errors, which primarily arise due to the ambiguity regarding sedimentation rates and the depth of sonar penetration into the seabed (e.g. *Section 3.4.2*). Thus to determine the exact relationship between OCC formation and volcanism, it would be necessary to accurately date samples collected across the axial valley (i.e. to measure the age of the volcanic hiatus) and the breakaway and termination areas of detachment surfaces (i.e. to measure the age of the OCC). Drill and dredge samples collected during JC07 between 13° – 14°N on the MAR lack the

necessary resolution to test this model, but it is possible that such a sampling survey could be conducted in the future in the 13°N region.

Finally, seismic data acquisition across the 13°N region would provide valuable constraints on the gravity and magnetic modelling results presented as part of this study. Seismic data could potentially determine the thickness of footwall LDZs (thus allowing gravity models to be inverted to determine footwall density), confirm the existence (or absence) of rider-blocks on the summit of OCC1319 (as predicted by magnetic modelling) and also test the hypothesis of across-axis linked OCCs. Combined with microseismicity data, seismic imaging could also be used to determine subsurface detachment geometry, in order to assess whether the dip of mature detachment faults in the 13°N region differs from that which has been proposed at TAG (e.g. deMartin *et al.*, 2007). In addition to across-axis profiles, along-axis profiles might be used to determine the true nature of the ridge-centred RMBA lows present in the gravity field, and to address the possibility of along-axis linking of detachment faults. This would help to further our understanding of the structural and magmatic conditions within which core complexes are expected to form.

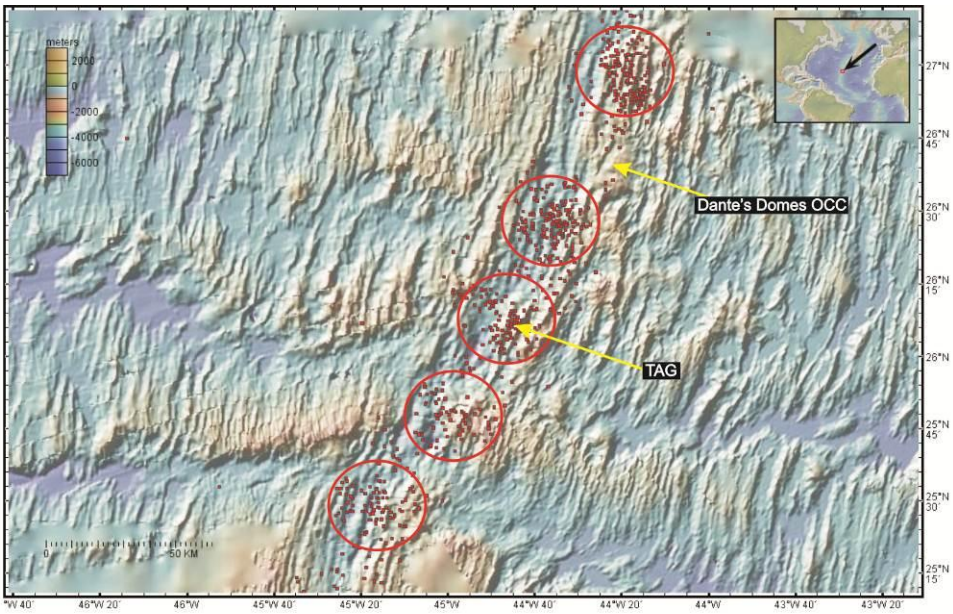


Figure 6.5.2. The MAR in the vicinity of TAG and Dante's Domes OCC (labelled) is an ideal area to assess the volcanic conditions during OCC formation. Red circles highlight areas of high seismicity that may delineate near-axis OCCs (red dots are individual seismic events). Bathymetry and seismicity data were accessed via *GeoMapApp* (Ryan *et al.*, 2009).

References

Ade-Hall, J., F. Aumento, P. J. C. Ryall & R. E. Gerstein, 1973. Mid-Atlantic Ridge near 45°N: 21 Magnetic results from basalt drill cores from the median-valley, *Canadian Journal of Earth Sciences,* **10,** 679-696

Allerton, S., J. Escartin & R. C. Searle, 2000. Extremely asymmetric magmatic accretion of oceanic crust at the ends of slow-spreading ridge segments, *Geology,* **28,** 179-182

Allerton, S., B. J. Murton, R. C. Searle & M. Jones, 1995. Extensional faulting and segmentation of the Mid-Atlantic Ridge north of the Kane Fracture-Zone (24°00'N to 24°40'N), *Marine Geophysical Researches,* **17,** 37-61

Amante, C. & B. W. Eakins, 2009. ETOPO1 1 arc-minute global relief model: Procedures, data sources and analysis, *NOAA Technical Memorandum NESDIS NGDC-24***,** 19pp

Atwater, T. & J. D. Mudie, 1973. Detailed near-bottom geophysical study of Gorda Rise, *Journal of Geophysical Research,* **78,** 8665-8686

Baines, A. G., M. J. Cheadle, H. J. B. Dick, A. H. Scheirer, B. E. John, N. J. Kusznir & T. Matsumoto, 2003. Mechanism for generating the anomalous uplift of oceanic core complexes: Atlantis Bank, southwest Indian Ridge, *Geology,* **31,** 1105-1108

Baines, A. G., M. J. Cheadle, B. E. John & J. J. Schwartz, 2008. The rate of oceanic detachment faulting at Atlantis Bank, SW Indian Ridge, *Earth and Planetary Science Letters,* **273,** 105-114

Ballard, R. D. & T. H. Van Andel, 1977. Morphology and tectonics of inner rift valley at lat. 36°50'N on Mid-Atlantic Ridge, *Geological Society of America Bulletin,* **88,** 507-530

Barclay, A. H., D. R. Toomey & S. C. Solomon, 1998. Seismic structure and crustal magmatism at the Mid-Atlantic Ridge, 35°N, *Journal of Geophysical Research,* **103,** 17827-17844

Beard, J. S., B. R. Frost, P. Fryer, A. McCaig, R. Searle, B. Ildefonse, P. Zinin & S. K. Sharma, 2009. Onset and progression of serpentinization and magnetite formation in olivine-rich troctolite from IODP Hole U1309D, *Journal of Petrology,* **50,** 387-403, doi: 10.1093/petrology/egp004

Behn, M. D., W. R. Buck & I. S. Sacks, 2006. Topographic controls on dike injection in volcanic rift zones, *Earth and Planetary Science Letters,* **246,** 188-196

Behn, M. D. & G. Ito, 2008. Magmatic and tectonic extension at mid-ocean ridges: 1. Controls on fault characteristics, *Geochemistry Geophysics Geosystems,* **9**, doi: 10.1029/2008GC001965

Beltenev, V., A. Ivanov, I. Rozhdestvenskaya, G. Cherkashov, T. Stepanova, V. Shilov, A. Pertsev, M. Davydov, I. Egorov, I. Melekestseva, E. Narkevsky & V. Ignatov, 2007. A new hydrothermal field at 13°30'N on the Mid-Atlantic Ridge, *InterRidge News,* **16,** 9-10

Beltenev, V., V. Ivanov, I. Rozhdestvenskaya, G. Cherkashov, T. V. Stepanova, V. V. Shilov, M. Davydov, A. Laiba, V. Kaylio, E. Narkevsky, A. Pertsev, I. Dobretsova, A. Gustaytis, Y. Popova, Y. Amplieva, C. Evrard, L. Moskalev & A. Gebruk, 2009. New data about hydrothermal fields on the Mid-Atlantic Ridge between 11°-14°N: 32nd Cruise of R/V Professor Logatchev, *InterRidge News,* **18,** 13-17

Bina, M. M. & B. Henry, 1990. Magnetic properties, opaque mineralogy and magnetic anisotropies of serpentinized peridotites from ODP Hole 670a near the Mid-Atlantic Ridge, *Physics of the Earth and Planetary Interiors,* **65,** 88-103

Blackman, D. K., J. R. Cann, B. Janssen & D. K. Smith, 1998. Origin of extensional core complexes: Evidence from the Mid-Atlantic Ridge at Atlantis Fracture Zone, *Journal of Geophysical Research,* **103,** 21315-21333

Blackman, D. K. & D. W. Forsyth, 1991. Isostatic compensation of tectonic features of the Mid-Atlantic Ridge - 25-27°30'S, *Journal of Geophysical Research,* **96,** 11741-11758

Blackman, D. K., B. Ildefonse, B. E. John, Y. Ohara, C. J. MacLeod & the Expedition 304/305 scientists, 2006. Oceanic core complex formation, Atlantis Massif. *In Proceedings of the Integrated Ocean Drilling Program.* Integrated Ocean Drill. Program Manage. Int., Inc., College Station, Tex.

Blackman, D. K., G. D. Karner & R. C. Searle, 2008. Three-dimensional structure of oceanic core complexes: Effects on gravity signature and ridge flank morphology, Mid-Atlantic Ridge, 30°N, *Geochemistry Geophysics Geosystems,* **9**, doi: 10.1029/2008GC001951

Blondel, P. & B. J. Murton, 1997. *Handbook of seafloor sonar imagery,* First edn., Wiley and Sons, Chichester, UK.

Bonatti, E., A. Peyve, P. Kepezhinskas, N. Kurentsova, M. Seyler, S. Skolotnev & G. Udintsev, 1992. Upper mantle heterogeneity below the Mid-Atlantic Ridge, 0°-15°N, *Journal of Geophysical Research*, **97,** 4461-4476

Bougault, H., J. L. Charlou, Y. Fouquet, H. D. Needham, N. Vaslet, P. Appriou, P. J. Baptiste, P. A. Rona, L. Dmitriev & S. Silantiev, 1993. Fast and slow-spreading ridges - structure and hydrothermal activity, ultramafic topographic highs and CH4 output, *Journal of Geophysical Research*, **98,** 9643-9651

Bougault, H., L. Dmitriev, J. G. Schilling, A. Sobolev, J. L. Joron & H. D. Needham, 1988. Mantle heterogeneity from trace-elements - MAR Triple Junction near 14°N, *Earth and Planetary Science Letters*, **88,** 27-36

Briais, A. & M. Rabinowicz, 2002. Temporal variations of the segmentation of slow to intermediate spreading mid-ocean ridges - 1. Synoptic observations based on satellite altimetry data, *Journal of Geophysical Research*, **107**, doi: 10.1029/2001jb000533

Briais, A., H. Sloan, L. M. Parson & B. J. Murton, 2000. Accretionary processes in the axial valley of the Mid-Atlantic Ridge 27°N-30°N from TOBI side-scan sonar images, *Marine Geophysical Researches*, **21,** 87-119

Buck, W. R., L. L. Lavier & A. N. B. Poliakov, 2005. Modes of faulting at mid-ocean ridges, *Nature*, **434,** 719-723, doi: 10.1038/Nature03358

Bullard, E. C. & R. G. Mason, 1961. The magnetic field astern of a ship, *Deep-Sea Research*, **8,** 20-27

Canales, J. P., R. A. Sohn & B. J. Demartin, 2007. Crustal structure of the Trans-Atlantic Geotraverse (TAG) segment (Mid-Atlantic Ridge, 26°10'N): Implications for the nature of hydrothermal circulation and detachment faulting at slow spreading ridges, *Geochemistry Geophysics Geosystems*, **8**, doi: 10.1029/2007GC00162

Canales, J. P., B. E. Tucholke & J. A. Collins, 2004. Seismic reflection imaging of an oceanic detachment fault: Atlantis megamullion (Mid-Atlantic Ridge, 30°10N), *Earth and Planetary Science Letters*, **222,** 543-560

Canales, J. P., B. E. Tucholke, M. Xu, J. A. Collins & D. L. DuBois, 2008. Seismic evidence for large-scale compositional heterogeneity of oceanic core complexes, *Geochemistry Geophysics Geosystems*, **9**, doi: 10.1029/2008GC002009

Cande, S. C. & D. V. Kent, 1992. Ultrahigh resolution marine magnetic anomaly profiles - a record of continuous paleointensity variations, *Journal of Geophysical Research,* **97,** 15075-15083

Cande, S. C. & D. V. Kent, 1995. Revised calibration of the geomagnetic polarity timescale for the Late Cretaceous and Cenozoic, *Journal of Geophysical Research,* **100,** 6093-6095

Cann, J. R., D. K. Blackman, D. K. Smith, E. McAllister, B. Janssen, S. Mello, E. Avgerinos, A. R. Pascoe & J. Escartin, 1997. Corrugated slip surfaces formed at ridge-transform intersections on the Mid-Atlantic Ridge, *Nature,* **385,** 329-332

Cann, J. R. & D. K. Smith, 2005. Evolution of volcanism and faulting in a segment of the Mid-Atlantic Ridge at 25°N, *Geochemistry Geophysics Geosystems,* **6**, doi: 10.1029/2005GC000954

Cann, J. R., D. K. Smith, J. Escartin & H. Schouten, 2008. Bathymetric Signatures of Oceanic Detachment Faulting and Potential Ultramafic Lithologies at Outcrop or in the Shallow Subseafloor, *Eos Trans. AGU,* Fall Meet. Suppl., Abstract T43C-2039

Cannat, M., 1996. How thick is the magmatic crust at slow spreading oceanic ridges?, *Journal of Geophysical Research,* **101,** 2847-2857

Cannat, M., Y. Lagabrielle, H. Bougault, J. Casey, N. deCoutures, L. Dmitriev & Y. Fouquet, 1997. Ultramafic and gabbroic exposures at the Mid-Atlantic Ridge: Geological mapping in the 15°N region, *Tectonophysics*, **279,** 193-213

Cannat, M., C. Mevel, M. Maia, C. Deplus, C. Durand, P. Gente, P. Agrinier, A. Belarouchi, G. Dubuisson, E. Humler & J. Reynolds, 1995. Thin crust, ultramafic exposures, and rugged faulting patterns at Mid-Atlantic Ridge (22°-24°N), *Geology*, **23,** 49-52

Cannat, M., C. Rommevaux-Jestin & H. Fujimoto, 2003. Melt supply variations to a magma-poor ultra-slow spreading ridge (Southwest Indian Ridge 61° to 69°E), *Geochemistry Geophysics Geosystems,* **4**, doi: 10.1029/2002GC000480

Cannat, M., D. Sauter, J. Escartin, L. Lavier & S. Picazo, 2009. Oceanic corrugated surfaces and the strength of the axial lithosphere at slow spreading ridges, *Earth and Planetary Science Letters,* **288,** 174-183, doi:10.1016/j.epsl.2009.09.020

Cannat, M., D. Sauter, V. Mendel, E. Ruellan, K. Okino, J. Escartin, V. Combier & M. Baala, 2006. Modes of seafloor generation at a melt-poor ultraslow-spreading ridge, *Geology,* **34,** 605-608

Carbotte, S. M. & K. C. Macdonald, 1990. Causes of variation in fault-facing direction on the ocean-floor, *Geology,* **18,** 749-752

Carbotte, S. M. & K. C. Macdonald, 1994. Comparison of seafloor tectonic fabric at intermediate, fast, and super fast spreading ridges - influence of spreading rate, plate motions, and ridge segmentation on fault patterns, *Journal of Geophysical Research,* **99,** 13609-13631

Carlut, J. & D. V. Kent, 2002. Grain-size-dependent paleointensity results from very recent mid-oceanic ridge basalts, *Journal of Geophysical Research,* **107**, doi: 10.1029/2001jb000439

Cheadle, M. & C. Grimes, 2010. Structural geology: To fault or not to fault, *Nature Geoscience,* **3,** 454-456

Chen, Y. S. & W. J. Morgan, 1990. A non-linear rheology model for mid-ocean ridge axis topography, *Journal of Geophysical Research,* **95,** 17583-17604

Christenson, N. I., 1972. Abundance of serpentinites in oceanic crust, *Journal of Geology,* **80,** 709-719

Christeson, G. L., K. D. McIntosh & J. A. Karson, 2007. Inconsistent correlation of seismic layer 2a and lava layer thickness in oceanic crust, *Nature,* **445,** 418-421

Christie, D. M., B. P. West, D. G. Pyle & B. B. Hanan, 1998. Chaotic topography, mantle flow and mantle migration in the Australian-Antarctic discordance, *Nature,* **394,** 637-644

Collette, B. J., A. P. Slootweg & W. Twigt, 1979. Mid-Atlantic Ridge crest topography between 12°N and 15°N, *Earth and Planetary Science Letters,* **42,** 103-108

Cormier, M. H., R. S. Detrick & G. M. Purdy, 1984. Anomalously thin crust in oceanic fracture zones - new seismic constraints from the Kane Fracture Zone, *Journal of Geophysical Research,* **89,** 249-266

Cowie, P., 1998. Normal fault growth in three-dimensions in continental and oceanic crust. *In Faulting and Magmatism at Mid-Ocean Ridges,* Volume 106, pp 325-348, eds. Buck, W. R., P. T. Delaney, J. A. Karson & Y. Lagabrielle. American Geophysical Union, Washington, D. C.

Crane, K. & R. D. Ballard, 1981. Volcanics and structure of the Famous Narrowgate Rift - evidence for cyclic evolution - AMAR-1, *Journal of Geophysical Research,* **86,** 5112-5124

CYAMEX, 1981. First manned submersible dives on the East Pacific Rise at 21°N (project RITA): General results *Marine Geophysical Researches,* **4,** 345-379

Davies, R. J., C. J. MacLeod, R. Morgan & S. E. Briggs, 2005. Termination of a fossil continent-ocean fracture zone imaged with three-dimensional seismic data: The Chain Fracture Zone, eastern equatorial Atlantic, *Geology,* **33,** 641-644

Davis, K. S., N. C. Slowey, I. H. Stender, H. Fiedler, W. R. Bryant & G. Fechner, 1996. Acoustic backscatter and sediment textural properties of inner shelf sands, northeastern Gulf of Mexico, *Geo-Marine Letters,* **16,** 273-278

Dehlinger, P., 1978. *Marine gravity,* First edn., Elsevier Scientific Pub. Co., Amsterdam; New York.

deMartin, B. J., R. A. R. Canales, J. P. Canales & S. E. Humphris, 2007. Kinematics and geometry of active detachment faulting beneath the Trans-Atlantic Geotraverse (TAG) hydrothermal field on the Mid-Atlantic Ridge, *Geology,* **35,** 711-714

DeMets, C., R. G. Gordon, D. F. Argus & S. Stein, 1990. Current plate motions, *Geophysical Journal International,* **101,** 425-478

DeMets, C., R. G. Gordon, D. F. Argus & S. Stein, 1994. Effect of recent revisions to the geomagnetic reversal time-scale on estimates of current plate motions, *Geophysical Research Letters,* **21,** 2191-2194

Detrick, R. S., H. D. Needham & V. Renard, 1995. Gravity anomalies and crustal thickness variations along the Mid-Atlantic Ridge between 33°N and 40°N, *Journal of Geophysical Research,* **100,** 3767-3787

Dick, H. J. B., J. Lin & H. Schouten, 2003. An ultraslow-spreading class of ocean ridge, *Nature,* **426,** 405-412

Dick, H. J. B., J. H. Natland, J. C. Alt, W. Bach, D. Bideau, J. S. Gee, S. Haggas, J. G. H. Hertogen, G. Hirth, P. M. Holm, B. Ildefonse, G. J. Iturrino, B. E. John, D. S. Kelley, E. Kikawa, A. Kingdon, P. J. LeRoux, J. Maeda, P. S. Meyer, D. J. Miller, H. R. Naslund, Y. L. Niu, P. T. Robinson, J. Snow, R. A. Stephen, P. W. Trimby, H. U. Worm & A. Yoshinobu, 2000. A long in-situ section of the lower ocean crust: Results of ODP Leg 176 drilling at the Southwest Indian Ridge, *Earth and Planetary Science Letters,* **179,** 31-51

Dick, H. J. B., G. Thompson & W. B. Bryan, 1981. Low angle faulting and steady-state emplacement of plutonic rocks at ridge-transform intersections, *Eos Trans. AGU,* **62,** 406

Dick, H. J. B., M. A. Tivey & B. E. Tucholke, 2008. Plutonic foundation of a slow-spreading ridge segment: Oceanic core complex at Kane Megamullion, 23°30'N,

45°20'W, *Geochemistry Geophysics Geosystems*, **9**, doi: 10.1029/2007GC001645

Dosso, L., H. Bougault & J. L. Joron, 1993. Geochemical morphology of the north Mid-Atlantic Ridge, 10°-24°N - trace element-isotope complementarity, *Earth and Planetary Science Letters*, **120,** 443-462

Dosso, L., B. B. Hanan, H. Bougault, J. G. Schilling & J. L. Joron, 1991. Sr-Nd-Pb Geochemical morphology between 10°N and 17°N on the Mid-Atlantic Ridge - a new MORB isotope signature, *Earth and Planetary Science Letters*, **106,** 29-43

Drolia, R. K. & C. DeMets, 2005. Deformation in the diffuse India-Capricorn-Somalia triple junction from a multibeam and magnetic survey of the northern Central Indian ridge, 3°S-10°S, *Geochemistry Geophysics Geosystems*, **6**, doi: 10.1029/2005gc000950

Dusunur, D., J. Escartin, V. Combier, T. Seher, W. Crawford, M. Cannat, S. C. Singh, L. M. Matias & J. M. Miranda, 2009. Seismological constraints on the thermal structure along the Lucky Strike segment (Mid-Atlantic Ridge) and interaction of tectonic and magmatic processes around the magma chamber, *Marine Geophysical Researches*, **30,** 105-120, doi: 10.1007/s11001-009-9071-3

Escartin, J., M. Andreani, G. Hirth & B. Evans, 2008a. Relationships between the microstructural evolution and the rheology of talc at elevated pressures and temperatures, *Earth and Planetary Science Letters*, **268,** 463-475, doi: 10.1016/j.epsl.2008.02.004

Escartin, J. & M. Cannat, 1999. Ultramafic exposures and the gravity signature of the lithosphere near the Fifteen-Twenty Fracture Zone (Mid-Atlantic Ridge, 14°-16.5°N), *Earth and Planetary Science Letters*, **171,** 411-424

Escartin, J., P. A. Cowie, R. C. Searle, S. Allerton, N. C. Mitchell, C. J. MacLeod & A. P. Slootweg, 1999. Quantifying tectonic strain and magmatic accretion at a slow spreading ridge segment, Mid-Atlantic Ridge, 29°N, *Journal of Geophysical Research*, **104,** 10421-10437

Escartin, J., G. Hirth & B. Evans, 1997a. Effects of serpentinization on the lithospheric strength and the style of normal faulting at slow-spreading ridges, *Earth and Planetary Science Letters*, **151,** 181-189

Escartin, J., G. Hirth & B. Evans, 1997b. Nondilatant brittle deformation of serpentinites: Implications for Mohr-Coulomb theory and the strength of faults, *Journal of Geophysical Research,* **102,** 2897-2913

Escartin, J., G. Hirth & B. Evans, 2001. Strength of slightly serpentinized peridotites: Implications for the tectonics of oceanic lithosphere, *Geology,* **29,** 1023-1026

Escartin, J., C. Mevel, C. J. MacLeod & A. M. McCaig, 2003a. Constraints on deformation conditions and the origin of oceanic detachments: The Mid-Atlantic Ridge core complex at 15°45'N, *Geochemistry Geophysics Geosystems,* **4**, doi: 10.1029/2002GC000472

Escartin, J., D. K. Smith, J. Cann, H. Schouten, C. H. Langmuir & S. Escrig, 2008b. Central role of detachment faults in accretion of slow-spreading oceanic lithosphere, *Nature,* **455,** 790-795

Escartin, J., D. K. Smith & M. Cannat, 2003b. Parallel bands of seismicity at the Mid-Atlantic Ridge, 12-14°N, *Geophysical Research Letters,* **30**, doi: 10.1029/2003GL01722

Flewellen, C., N. Millard & I. Rouse, 1993. TOBI, a vehicle for deep ocean survey, *Electronics & Communication Engineering Journal,* **5,** 85-93

Forsyth, D. W. & B. Wilson, 1984. 3-Dimensional Temperature Structure of a Ridge-Transform Ridge System, *Earth and Planetary Science Letters,* **70,** 355-362

Fouquet, Y., G. Cherkashov, J. L. Charlou & H. Ondreas, 2008. Serpentine cruise - ultramafic hosted hydrothermal deposits on the Mid-Atlantic Ridge: First submersible studies on Ashadze 1 and 2, Logatchev 2 and Krasnov vent fields, *InterRidge News,* **17,** 15-19

Fowler, C. M. R., 1976. Crustal structure of Mid-Atlantic Ridge crest at 37°N, *Geophysical Journal of the Royal Astronomical Society,* **47,** 459-491

Fowler, C. M. R., 1978. Mid-Atlantic Ridge - structure at 45°N, *Geophysical Journal of the Royal Astronomical Society,* **54,** 167-183

Fox, P. J. & D. G. Gallo, 1984. A model for ridge-transform-ridge plate boundaries: implications for the structure of oceanic lithosphere, *Tectonophysics,* **104,** 205-242

Francis, T. J. G., 1981. Serpentinization faults and their role in the tectonics of slow-spreading ridges, *Journal of Geophysical Research,* **86,** 1616-1622

Fujiwara, T., J. Lin, T. Matsumoto, P. B. Kelemen, B. E. Tucholke & J. F. Casey, 2003. Crustal evolution of the Mid-Atlantic Ridge near the Fifteen-Twenty Fracture

Zone in the last 5 Ma, *Geochemistry Geophysics Geosystems*, **4**, doi: 10.1029/2002GC000364

Garces, M. & J. S. Gee, 2007. Paleomagnetic evidence of large footwall rotations associated with low-angle faults at the Mid-Atlantic Ridge, *Geology*, **35,** 279-282

Gardiner, A., 2003. Segmentation and cycle of crustal accretion at mid-ocean ridges: A study of the Reykjanes Ridge, Ph.D. Thesis, Durham University, Durham, U.K.

Gee, J., D. A. Schneider & D. V. Kent, 1996. Marine magnetic anomalies as recorders of geomagnetic intensity variations, *Earth and Planetary Science Letters,* **144,** 327-335

Gente, P., R. A. Pockalny, C. Durand, C. Deplus, M. Maia, G. Ceuleneer, C. Mevel, M. Cannat & C. Laverne, 1995. Characteristics and evolution of the segmentation of the Mid-Atlantic Ridge between 20°N and 24°N during the last 10 million years, *Earth and Planetary Science Letters,* **129,** 55-71

German, C. R., A. Bowen, M. L. Coleman, D. L. Honig, J. A. Huber, M. V. Jakuba, J. C. Kinsey, M. D. Kurz, S. Leroy, J. M. McDermott, B. M. de Lepinay, K. Nakamura, J. S. Seewald, J. L. Smith, S. P. Sylva, C. L. Van Dover, L. L. Whitcomb & D. R. Yoerger, 2010. Diverse styles of submarine venting on the ultraslow spreading Mid-Cayman Rise, *Proceedings of the National Academy of Sciences of the United States of America,* **107,** 14020-14025, doi: 10.1073/pnas.1009205107

German, C. R., G. P. Klinkhammer & M. D. Rudnicki, 1996. The Rainbow hydrothermal plume, 36°15'N, MAR, *Geophysical Research Letters,* **23,** 2979-2982

Gracia, E., D. Bideau, R. Hekinian & Y. Lagabrielle, 1999. Detailed geological mapping of two contrasting second-order segments of the Mid-Atlantic Ridge between Oceanographer and Hayes fracture zones (33°30'N-35°N), *Journal of Geophysical Research,* **104,** 22903-22921

Grimes, C. B., B. E. John, M. J. Cheadle & J. L. Wooden, 2008. Protracted construction of gabbroic crust at a slow spreading ridge: Constraints from Pb-206/U-238 zircon ages from Atlantis Massif and IODP Hole U1309D (30°N, MAR), *Geochemistry Geophysics Geosystems,* **9**, doi: 10.1029/2008gc002063

Grindlay, N. R. & P. J. Fox, 1993. Lithospheric stresses associated with non-transform offsets of the Mid-Atlantic Ridge - Implications from a finite-element analysis, *Tectonics,* **12,** 982-1003

Grindlay, N. R., P. J. Fox & K. C. Macdonald, 1991. 2nd-Order ridge axis discontinuities in the South Atlantic - morphology, structure, and evolution, *Marine Geophysical Researches,* **13,** 21-49

Guspi, F., 1987. Frequency-domain reduction of potential-field measurements to a horizontal plane, *Geoexploration,* **24,** 87-98

Hall, J. M., 1976. Major problems regarding magnetization of oceanic crustal layer 2, *Journal of Geophysical Research,* **81,** 4223-4230

Head, J. W., L. Wilson & D. K. Smith, 1996. Mid-ocean ridge eruptive vent morphology and substructure: Evidence for dike widths, eruption rates, and evolution of eruptions and axial volcanic ridges, *Journal of Geophysical Research,* **101,** 28265-28280

Honsho, C., J. Dyment, K. Tamaki, M. Ravilly, H. Horen & P. Gente, 2009. Magnetic structure of a slow spreading ridge segment: Insights from near-bottom magnetic measurements on board a submersible, *Journal of Geophysical Research,* **114**, doi: 10.1029/2008JB005915

Hussenoeder, S. A., M. A. Tivey, H. Schouten & R. C. Searle, 1996. Near-bottom magnetic survey of the Mid-Atlantic Ridge axis, 24°-24°40'N: Implications for crustal accretion at slow spreading ridges, *Journal of Geophysical Research,* **101,** 22051-22069

Ildefonse, B., D. K. Blackman, B. E. John, Y. Ohara, D. J. Miller, C. J. MacLeod & I. O. D. Program, 2007. Oceanic core complexes and crustal accretion at slow-spreading ridges, *Geology,* **35,** 623-626

Isezaki, N., 1986. A new shipboard 3-component magnetometer, *Geophysics,* **51,** 1992-1998

Ito, G. & M. D. Behn, 2008. Magmatic and tectonic extension at mid-ocean ridges: 2. Origin of axial morphology, *Geochemistry Geophysics Geosystems,* **9**, doi: 10.1029/2008gc001970

Jackson, D. R., A. M. Baird, J. J. Crisp & P. A. G. Thomson, 1986. High-frequency bottom backscatter measurements in shallow water, *Journal of the Acoustical Society of America,* **80,** 1188-1199

Johnson, H. P. & M. Helferty, 1990. The geological interpretation of side-scan sonar, *Reviews of Geophysics,* **28,** 357-380

Johnson, H. P. & M. A. Tivey, 1995. Magnetic-properties of zero-age oceanic crust - a new submarine lava flow on the Juan-De-Fuca ridge, *Geophysical Research Letters,* **22,** 175-178

Juarez, M. T. & L. Tauxe, 2000. The intensity of the time-averaged geomagnetic field: the last 5 Myr, *Earth and Planetary Science Letters,* **175,** 169-180

Juarez, M. T., L. Tauxe, J. S. Gee & T. Pick, 1998. The intensity of the Earth's magnetic field over the past 160 million years, *Nature,* **394,** 878-881

Karson, J. A., 1990. Seafloor spreading on the Mid-Atlantic Ridge: Implications for the structure of ophiolites and oceanic lithosphere produced in slow-spreading environments. *In Proceedings of the Symposium "TROODOS 1987"*, eds. Malpas, J., E. M. Moores, A. Panayiotou & C. Xenophontos. Geological Survey Dept., Nicosia.

Karson, J. A., 1998. Internal structure of oceanic lithosphere: A perspective from tectonic windows. *In Faulting and Magmatism at Mid-Ocean Ridges,* Volume 106, pp. 177-218, eds. Buck, W. R., P. T. Delaney, J. A. Karson & Y. Lagabrielle. American Geophysical Union, Washington, D. C.

Karson, J. A., 1999. Geological investigation of a lineated massif at the Kane Transform Fault: implications for oceanic core complexes, *Philosophical Transactions of the Royal Society of London Series A: Mathematical Physical and Engineering Sciences,* **357,** 713-736

Karson, J. A. & H. J. B. Dick, 1983. Tectonics of ridge-transform intersections at the Kane Fracture Zone, *Marine Geophysical Researches,* **6,** 51-98

Karson, J. A., G. Thompson, S. E. Humphris, J. M. Edmond, W. B. Bryan, J. R. Brown, A. T. Winters, R. A. Pockalny, J. F. Casey, A. C. Campbell, G. Klinkhammer, M. R. Palmer, R. J. Kinzler & M. M. Sulanowska, 1987. Along-axis variations in seafloor spreading in the MARK area, *Nature,* **328,** 681-685

Karson, J. A. & A. T. Winters, 1992. Along-axis variations in tectonic extension and accommodation zones in the MARK area, Mid-Atlantic Ridge 23°N latitude. *In Ophiolites and their Modern Oceanic Analogues,* 107-116, eds. Parson, L. M., B. J. Murton & P. Browning. Geological Society Special Publication, London, UK.

Kelemen, P. B., E. Kikawa, D. J. Miller & the Shipboard Scientific Party, 2004. Drilling mantle peridotite along the Mid-Atlantic Ridge from 14°-16°N: Sites 1268-1275.

In Proceedings of the Ocean Drilling Program, Initial reports, 209, College Station, Texas.

Kennett, B. L. N., 1977. Towards a more detailed seismic picture of oceanic crust, *Geophysical Journal of the Royal Astronomical Society,* **49,** 285-285

Kennett, B. L. N. & J. A. Orcutt, 1976. Comparison of travel time inversions for marine refraction profiles, *Journal of Geophysical Research,* **81,** 4061-4070

Kong, L. S. L., R. S. Detrick, P. J. Fox, L. A. Mayer & W. B. F. Ryan, 1989. The morphology and tectonics of the MARK area from Sea Beam and Sea Marc-I observations (Mid-Atlantic Ridge 23°N), *Marine Geophysical Researches,* **10,** 59-90

Kong, L. S. L., S. C. Solomon & G. M. Purdy, 1992. Microearthquake characteristics of a mid-ocean ridge along-axis high, *Journal of Geophysical Research,* **97,** 1659-1685

Korenaga, J., 1995. Comprehensive analysis of marine magnetic vector anomalies, *Journal of Geophysical Research,* **100,** 365-378

Kuo, B. Y. & D. W. Forsyth, 1989. Gravity anomalies of the ridge-transform system in the South Atlantic between 31°S and 34.5°S - upwelling centers and variations in crustal thickness, *Marine Geophysical Researches,* **10,** 205-232

Lacoste, L., 1973. Cross-correlation method for evaluating and correcting shipboard gravity data, *Geophysics*, **38,** 701-709

Laughton, A. S., R. C. Searle & D. G. Roberts, 1979. Reykjanes Ridge crest and the transition between its rifted and non-rifted regions, *Tectonophysics,* **55,** 173-177

Lawson, K., R. C. Searle, J. A. Pearce & P. Kempton, 1996. Detailed volcanic geology of the MARNOK area, Mid-Atlantic Ridge north of Kane transform. *In Tectonic, Magmatic, Hydrothermal and Biological Segmentation of Mid-Ocean Ridges*, 61-102, eds. Macleod, C., P. Tyler & C. L. Walker. Geological Society Publishing House, London, UK.

Lawson, N. K., 1996. Crustal accretion near ridge-transform intersection: Kane Fracture Zone, Mid-Atlantic Ridge, Doctor of Philosophy, Durham University, Durham, U.K.

Le Bas, T. P., 2005. PRISM processing of remotely-sensed imagery for seafloor mapping - Version 4.0, pp. 192, Unpublished manuscript, National Oceanography Centre, Southampton, UK.

Le Bas, T. P., D. C. Mason & N. C. Millard, 1995. TOBI image processing - the state-of-the-art, *Ieee Journal of Oceanic Engineering,* **20,** 85-93

Lin, J. & E. M. Parmentier, 1990. A finite-amplitude necking model of rifting in brittle lithosphere, *Journal of Geophysical Research,* **95,** 4909-4923

Lin, J., G. M. Purdy, H. Schouten, J. C. Sempere & C. Zervas, 1990. Evidence from gravity data for focused magmatic accretion along the Mid-Atlantic Ridge, *Nature,* **344,** 627-632

Luis, J. F., 2007. Mirone: A multi-purpose tool for exploring grid data, *Computers & Geosciences,* **33,** 31-41

Luyendyk, B. P. & K. C. Macdonald, 1976. Spreading center terms and concepts, *Geology,* **4,** 369-370

Luyendyk, B. P. & K. C. Macdonald, 1977. Physiography and structure of inner floor of Famous Rift Valley - observations with a deep-towed instrument package, *Geological Society of America Bulletin,* **88,** 648-663

Macdonald, K., B. P. Luyendyk, J. D. Mudie & F. N. Spiess, 1975. Near-bottom geophysical study of Mid-Atlantic Ridge median valley near 37°N - preliminary observations, *Geology,* **3,** 211-215

Macdonald, K. C., 1977. Near-bottom magnetic anomalies, asymmetric spreading, oblique spreading, and tectonics of Mid-Atlantic Ridge near 37°N, *Geological Society of America Bulletin,* **88,** 541-555

Macdonald, K. C., 1982. Mid-ocean ridges - fine scale tectonic, volcanic and hydrothermal processes within the plate boundary zone, *Annual Review of Earth and Planetary Sciences,* **10,** 155-190

Macdonald, K. C., 1986. The crest of the Mid-Atlantic Ridge: Models for crustal generation processes and tectonics. *In The Geology of North America: the Western North Atlantic Region*, 51-68, eds. Vogt, P. R. & B. E. Tucholke. Geological Society of America, Boulder.

Macdonald, K. C., 2001. Mid-ocean ridge tectonics, volcanism and geomorphology. *In Encyclopedia of Ocean Sciences,* 1798-1813, eds. Steele, J., S. Thorpe & K. Turekian. Academic Press.

Macdonald, K. C. & T. M. Atwater, 1978. Evolution of rifted ocean ridges, *Earth and Planetary Science Letters,* **39,** 319-327

Macdonald, K. C., P. J. Fox, L. J. Perram, M. F. Eisen, R. M. Haymon, S. P. Miller, S. M. Carbotte, M. H. Cormier & A. N. Shor, 1988. A new view of the mid-ocean ridge from the behavior of ridge-axis discontinuities, *Nature,* **335,** 217-225

Macdonald, K. C., D. S. Scheirer & S. M. Carbotte, 1991. Mid-ocean ridges - discontinuities, segments and giant cracks, *Science,* **253,** 986-994

MacLeod, C. J., J. Escartin & D. Banerji, 2001. RRS James Clark Ross Cruise JR63 Report: Recife, Brazil - Ponta Delgada, Azores, 14th April - 23rd May 2001: The Mid-Atlantic Ridge, 15°45'N, Cardiff University, Cardiff, UK.

MacLeod, C. J., J. Escartin, D. Banerji, G. J. Banks, M. Gleeson, D. H. B. Irving, R. M. Lilly, A. M. McCaig, Y. L. Niu, S. Allerton & D. K. Smith, 2002. Direct geological evidence for oceanic detachment faulting: The Mid-Atlantic Ridge, 15°45'N, *Geology,* **30,** 879-882

MacLeod, C. J., R. C. Searle, B. J. Murton, J. F. Casey, C. Mallows, S. C. Unsworth, K. L. Achenbach & M. Harris, 2009. Life cycle of oceanic core complexes, *Earth and Planetary Science Letters,* **287,** 333-344

Macmillan, S. & S. Maus, 2005. International geomagnetic reference field - the tenth generation, *Earth Planets and Space,* **57,** 1135-1140

Magde, L. S. & D. W. Sparks, 1997. Three-dimensional mantle upwelling, melt generation, and melt migration beneath segment slow spreading ridges, *Journal of Geophysical Research,* **102,** 20571-20583

Martinez, F., J. Karsten & E. M. Klein, 1998. Recent kinematics and tetonics of the Chile Ridge, *Eos Trans. AGU,* **79,** F836

Masson, D. G. & J. V. Gardner, 1991. MV Farnella Cruise 6/90 Report: 19th June - 13th July, 1990: TOBI surveys of Monterey Fan, Institute of Oceanographic Sciences, Wormley, UK.

McCaig, A. M., R. A. Cliff, J. Escartin, A. E. Fallick & C. J. MacLeod, 2007. Oceanic detachment faults focus very large volumes of black smoker fluids, *Geology,* **35,** 935-938, doi: 10.1130/G23657a.1

Mello, S. L. M., J. R. Cann & C. M. R. Fowler, 1999. Anomalous mantle at 45°N Mid-Atlantic Ridge?, *Journal of Geophysical Research,* **104,** 29335-29349

Mendel, V., M. Munschy & D. Sauter, 2005. MODMAG, a MATLAB program to model marine magnetic anomalies, *Computers & Geosciences,* **31,** 589-597, doi: 10.1016/j.cageo.2004.11.007

Mienert, J. & P. Weaver, 2002. *European margin sediment dynamics: side-scan sonar and seismic images,* First edn., Springer, New York.

Mitchell, N. C., 1993. A model for attenuation of backscatter due to sediment accumulations and its application to determine sediment thicknesses with GLORIA sidescan sonar, *Journal of Geophysical Research,* **98,** 22477-22493

Mitchell, N. C., S. Allerton & J. Escartin, 1998a. Sedimentation on young ocean floor at the Mid-Atlantic Ridge, 29 degrees N, *Marine Geology,* **148,** 1-8

Mitchell, N. C., J. Escartin & S. Allerton, 1998b. Detachment faults at Mid-Ocean Ridges garner interest, *Eos Trans. AGU,* **79,** 127

Morley, L. W. & A. Larochelle, 1964. Palaeomagnetism as a means of dating geological events. *In Geochronology in Canada*, Spec. Publ., 8, pp. 39-51, ed. Osborne, F. F. Roy. Soc. Canada, Ottawa, Ont.

Morris, A., J. S. Gee, N. Pressling, B. E. John, C. J. MacLeod, C. B. Grimes & R. C. Searle, 2009. Footwall rotation in an oceanic core complex quantified using reoriented Integrated Ocean Drilling Program core samples, *Earth and Planetary Science Letters,* **287,** 217-228

Mutter, J. C. & J. A. Karson, 1992. Structural processes at slow-spreading ridges, *Science,* **257,** 627-634

Nazarova, K. A., 1994. Serpentinized peridotites as a possible source for oceanic magnetic anomalies, *Marine Geophysical Researches,* **16,** 455-462

Needham, H. D. & J. Francheteau, 1974. Some characteristics of rift valley in Atlantic Ocean near 36°48'N, *Earth and Planetary Science Letters,* **22,** 29-43

Niu, Y. L., D. Bideau, R. Hekinian & R. Batiza, 2001. Mantle compositional control on the extent of mantle melting, crust production, gravity anomaly, ridge morphology, and ridge segmentation: a case study at the Mid-Atlantic Ridge 33-35°N, *Earth and Planetary Science Letters,* **186,** 383-399

Nooner, S. L., G. S. Sasagawa, D. K. Blackman & M. A. Zumberge, 2003. Structure of oceanic core complexes: Constraints from seafloor gravity measurements made at the Atlantis Massif, *Geophysical Research Letters,* **30**, doi: 10.1029/2003gl017126

Ohara, Y., T. Yoshida, Y. Kato & S. Kasuga, 2001. Giant megamullion in the Parece Vela Backarc Basin, *Marine Geophysical Researches,* **22,** 47-61

Okino, K., K. Matsuda, D. M. Christie, Y. Nogi & K. Koizumi, 2004. Development of oceanic detachment and asymmetric spreading at the Australian-Antarctic

Discordance, *Geochemistry Geophysics Geosystems*, **5**, doi: 10.1029/2004GC000793

Olive, J.-A., M. D. Behn & B. E. Tucholke, 2010. The structure of oceanic core complexes controlled by the depth distribution of magma emplacement, *Nature Geoscience,* **3,** 491-495

Oufi, O., M. Cannat & H. Horen, 2002. Magnetic properties of variably serpentinized abyssal peridotites, *Journal of Geophysical Research,* **107**, doi: 10.1029/2001JB000549

Pariso, J. E., J. C. Sempere & C. Rommevaux, 1995. Temporal and spatial variations in crustal accretion along the Mid-Atlantic Ridge (29°-31°30'N) over the last 10 My - implications from a 3-dimensional gravity study, *Journal of Geophysical Research,* **100,** 17781-17794

Parker, R. L., 1972. Rapid calculation of potential anomalies, *Geophysical Journal of the Royal Astronomical Society,* **31,** 447-455

Parker, R. L. & S. P. Huestis, 1974. Inversion of magnetic anomalies in presence of topography, *Journal of Geophysical Research,* **79,** 1587-1593

Parson, L. M., B. J. Murton, R. C. Searle, D. Booth, J. Evans, P. Field, J. Keeton, A. Laughton, E. Mcallister, N. Millard, L. Redbourne, I. Rouse, A. Shor, D. Smith, S. Spencer, C. Summerhayes & C. Walker, 1993. En-echelon axial volcanic ridges at the Reykjanes Ridge - a life cycle of volcanism and tectonics, *Earth and Planetary Science Letters,* **117,** 73-87

Pedley, R. C., 1991. *GRAVMAG - Interactive 2.5D Gravity and Magnetic Modelling Program,* First edn., British Geological Survey, Keyworth, Nottingham, U.K.

Peirce, C., A. Gardiner & M. Sinha, 2005. Temporal and spatial cyclicity of accretion at slow-spreading ridges - evidence from the Reykjanes Ridge, *Geophysical Journal International,* **163,** 56-U31

Planert, L., E. R. Flueh & T. J. Reston, 2009. Along- and across-axis variations in crustal thickness and structure at the Mid-Atlantic Ridge at 5°S obtained from wide-angle seismic tomography: Implications for ridge segmentation, *Journal of Geophysical Research,* **114**, doi: 10.1029/2008jb006103

Prince, R. A. & D. W. Forsyth, 1988. Horizontal extent of anomalously thin crust near the Vema Fracture Zone from the 3-dimensional analysis of gravity anomalies, *Journal of Geophysical Research,* **93,** 8051-8097

Purdy, G. M., 1987. New observations of the shallow seismic structure of young oceanic crust, *Journal of Geophysical Research,* **92,** 9351-9362

Purdy, G. M. & R. S. Detrick, 1986. Crustal structure of the Mid-Atlantic Ridge at 23°N from seismic refraction studies, *Journal of Geophysical Research,* **91,** 3739-3762

Purdy, G. M., L. S. L. Kong, G. L. Christeson & S. C. Solomon, 1992. Relationship between spreading rate and the seismic structure of mid-ocean ridges, *Nature,* **355,** 815-817

Rabain, A., M. Cannat, J. Escartin, G. Pouliquen, C. Deplus & C. Rommevaux-Jestin, 2001. Focused volcanism and growth of a slow spreading segment (Mid-Atlantic Ridge, 35°N), *Earth and Planetary Science Letters,* **185,** 211-224

Raitt, R. W., 1956. Seismic refraction studies of the Pacific Ocean basin .1. Crustal thickness of the central equatorial Pacific, *Geological Society of America Bulletin,* **67,** 1623-1639

Raitt, R. W., 1963. The crustal rocks. *In The Sea*, 85-102, ed. Hill, M. N. Wiley-Interscience, London, U. K.

Ranero, C. R. & T. J. Reston, 1999. Detachment faulting at ocean core complexes, *Geology,* **27,** 983-986

Rao, D. G. & K. S. Krishna, 2002. Magnetic rock properties of the gabbros from the ODP Drill Hole 1105 A of the Atlantis Bank, Southwest Indian Ridge, *Proceedings of the Indian Academy of Sciences-Earth and Planetary Sciences,* **111,** 467-481

Reston, T. J., W. Weinrebe, I. Grevemeyer, E. R. Flueh, N. C. Mitchell, L. Kirstein, C. Kopp, H. Kopp & Meteor 47-2 Scientific Party, 2002. A rifted inside corner massif on the Mid-Atlantic Ridge at 5°S, *Earth and Planetary Science Letters,* **200,** 255-269

Roest, W. R. & B. J. Collette, 1986. The 15°20'N Fracture Zone and the North American South American plate boundary, *Journal of the Geological Society,* **143,** 833-843

Ryan, W. B. F., S. M. Carbotte, J. O. Coplan, S. O'Hara, A. Melkonian, R. Arko, R. A. Weissel, V. Ferrini, A. Goodwillie, F. Nitsche, J. Bonczkowski & R. Zemsky, 2009. Global multi-resolution topography synthesis, *Geochemistry Geophysics Geosystems,* **10**, doi: 10.1029/2008gc002332

Schouten, H., D. K. Smith, J. R. Cann & J. Escartin, 2010. Tectonic versus magmatic extension in the presence of core complexes at slow-spreading ridges from a visualization of faulted seafloor topography, *Geology,* **38,** 615-618, doi: 10.1130/G30803.1

Searle, R. C., 1984. Gloria survey of the East Pacific Rise near 3.5°S - tectonic and volcanic characteristics of a fast-spreading mid-ocean rise, *Tectonophysics,* **101,** 319-344

Searle, R. C., 1992. The volcano-tectonic setting of oceanic lithosphere generation. *In Ophiolites and their Modern Oceanic Analogues*, 65-79, eds. Parson, L. M., B. J. Murton & P. Browning. Geological Society Special Publication, London, UK.

Searle, R. C., M. Cannat, K. Fujioka, C. Mevel, H. Fujimoto, A. Bralee & L. Parson, 2003. FUJI Dome: A large detachment fault near 64°E on the very slow-spreading southwest Indian Ridge, *Geochemistry Geophysics Geosystems,* **4**, doi: 10.1029/2003GC000519

Searle, R. C., P. A. Cowie, N. C. Mitchell, S. Allerton, C. J. MacLeod, J. Escartin, S. M. Russell, P. A. Slootweg & T. Tanaka, 1998. Fault structure and detailed evolution of a slow spreading ridge segment: the Mid-Atlantic Ridge at 29°N, *Earth and Planetary Science Letters,* **154,** 167-183

Searle, R. C. & A. S. Laughton, 1977. Sonar studies of Mid-Atlantic Ridge and Kurchatov Fracture Zone, *Journal of Geophysical Research,* **82,** 5313-5328

Searle, R. C., C. J. MacLeod, B. J. Murton, J. Casey, C. Mallows, S. C. Unsworth, K. Achenbach & M. Harris, 2007. RRS James Cook Cruise JC07 Report: Geological and geophysical studies of the Mid-Atlantic Ridge: 12°30'N to 14°30'N, pp. 75, Unpublished manuscript, Durham University, UK.

Searle, R. C., N. C. Mitchell, A. P. Slootweg, S. Russell, P. Cowie, S. Allerton, C. J. MacLeod & T. Tanaka, 1996. RRS Charles Darwin Cruise CD99 Report: Near-bottom geophysical studies of the Broken Spur spreading segment, Mid-Atlantic Ridge 29°N, pp. 61, Unpublished manuscript, Durham University, UK.

Searle, R. C., B. J. Murton, K. Achenbach, T. P. Le Bas, M. Tivey, I. Yeo, M. H. Cormier, J. Carlut, P. Ferreira, C. Mallows, K. Morris, N. Shroth, P. van Calsteren & C. Waters, 2010. Structure and development of an Axial Volcanic Ridge: Mid-Atlantic Ridge, 45°N, *Earth and Planetary Science Letters (submitted),*

Searle, R. C., B. J. Murton, C. Mallows, I. Yeo & K. L. Achenbach, 2008. RRS James Cook Cruise JC24 Report: 45°N, Durham University, UK.

Sempere, J. C., P. Blondel, A. Briais, T. Fujiwara, L. Geli, N. Isezaki, J. E. Pariso, L. Parson, P. Patriat & C. Rommevaux, 1995. The Mid-Atlantic Ridge between 29°N and 31°30'N in the last 10 Ma, *Earth and Planetary Science Letters,* **130,** 45-55

Sempere, J. C., J. Lin, H. S. Brown, H. Schouten & G. M. Purdy, 1993. Segmentation and morphotectonic variations along a slow-spreading center - the Mid-Atlantic Ridge (24°00'N-30°40'N), *Marine Geophysical Researches,* **15,** 153-200

Sempere, J. C. & K. C. Macdonald, 1987. Marine tectonics - processes at mid-ocean ridges, *Reviews of Geophysics,* **25,** 1313-1347

Shaw, P. R., 1992. Ridge segmentation, faulting and crustal thickness in the Atlantic Ocean, *Nature,* **358,** 490-493

Shih, J. S. F., T. Atwater & M. Mcnutt, 1978. Near-bottom geophysical traverse of Reykjanes Ridge, *Earth and Planetary Science Letters,* **39,** 75-83

Singh, S. C., W. C. Crawford, H. Carton, T. Seher, V. Combier, M. Cannat, J. P. Canales, D. Dusunur, J. Escartin & J. M. Miranda, 2006. Discovery of a magma chamber and faults beneath a Mid-Atlantic Ridge hydrothermal field, *Nature,* **442,** 1029-1032

Skolotnev, S. G., A. A. Peyve & S. M. Lyapunov, 1999. Tectono-volcanic activity at the axial zone of the Mid-Atlantic Ridge between the Fifteen Twenty and Mercurius fracture zones, central Atlantic, *Petrology,* **7,** 556-573

Sleep, N. H., 1969. Sensitivity of heat flow and gravity to mechanism of seafloor spreading, *Journal of Geophysical Research,* **74,** 542-549

Sleep, N. H. & B. R. Rosendahl, 1979. Topography and tectonics of mid-oceanic ridge axes, *Journal of Geophysical Research,* **84,** 6831-6839

Smith, D. K. & J. R. Cann, 1990. Hundreds of small volcanos on the median valley floor of the Mid-Atlantic Ridge at 24-30°N, *Nature,* **348,** 152-155

Smith, D. K. & J. R. Cann, 1992. The role of seamount volcanism in crustal construction at the Mid-Atlantic Ridge (24°-30°N), *Journal of Geophysical Research,* **97,** 1645-1658

Smith, D. K. & J. R. Cann, 1993. Building the crust at the Mid-Atlantic Ridge, *Nature,* **365,** 707-715

Smith, D. K., J. R. Cann, M. E. Dougherty, J. Lin, S. Spencer, C. J. MacLeod, J. Keeton, E. Mcallister, B. Brooks, R. Pascoe & W. Robertson, 1995. Mid-Atlantic Ridge volcanism from deep-towed sidescan sonar images, 25°-29°N, *Journal of Volcanology and Geothermal Research,* **67,** 233-262

Smith, D. K., J. R. Cann & J. Escartin, 2006. Widespread active detachment faulting and core complex formation near 13°N on the Mid-Atlantic Ridge, *Nature,* **442,** 440-443, doi: 10.1038/Nature04950

Smith, D. K., J. Escartin, M. Cannat, M. Tolstoy, C. G. Fox, D. R. Bohnenstiehl & S. Bazin, 2003. Spatial and temporal distribution of seismicity along the northern Mid-Atlantic Ridge (15°-35°N), *Journal of Geophysical Research,* **108**, doi: 10.1029/2002jb001964

Smith, D. K., J. Escartin, H. Schouten & J. R. Cann, 2008. Fault rotation and core complex formation: Significant processes in seafloor formation at slow-spreading mid-ocean ridges (Mid-Atlantic Ridge, 13°-15°N), *Geochemistry Geophysics Geosystems,* **9**, doi: 10.1029/2007GC001699

Smith, D. K., M. A. Tivey, H. Schouten & J. R. Cann, 1999. Locating the spreading axis along 80 km of the Mid-Atlantic Ridge south of the Atlantis Transform, *Journal of Geophysical Research,* **104,** 7599-7612

Smith, W. H. F. & D. T. Sandwell, 1994. Bathymetric prediction from dense satellite altimetry and sparse shipboard bathymetry, *Journal of Geophysical Research,* **99,** 21803-21824

Sparks, D. W., E. M. Parmentier & J. P. Morgan, 1993. 3-Dimensional mantle convection beneath a segmented spreading center - implications for along-axis variations in crustal thickness and gravity, *Journal of Geophysical Research,* **98,** 21977-21995

Spencer, J. E., 1999. Geologic continuous casting below continental and deep-sea detachment faults and at the striated extrusion of Sacsayhuaman, Peru, *Geology,* **27,** 327-330

Spudich, P. & J. Orcutt, 1980. A new look at the seismic velocity structure of the oceanic crust, *Reviews of Geophysics,* **18,** 627-645

Standish, J. J. & K. W. W. Sims, 2010. Young off-axis volcanism along the ultraslow-spreading Southwest Indian Ridge, *Nature Geoscience,* **3,** 286-292, Doi 10.1038/Ngeo824

Talwani, M. & M. Ewing, 1960. Rapid computation of gravitational attraction of three-dimensional bodies of arbitrary shape, *Geophysics,* **25,** 203-225

Talwani, M., X. Le Pichon & M. Ewing, 1965. Crustal structure of the mid-ocean ridges 2. Computed model from gravity and seismic refraction data, *Journal of Geophysical Research,* **70,** 341-352

Tapponnier, P. & J. Francheteau, 1978. Necking of lithosphere and mechanics of slowly accreting plate boundaries, *Journal of Geophysical Research,* **83,** 3955-3970

Telford, W. M., L. P. Geldart & R. E. Sheriff, 1990. *Applied Geophysics,* Second edn., pp. 770, Cambridge University Press, Cambridge, UK.

Tilmann, F., E. Flueh, L. Planert, T. Reston & W. Weinrebe, 2004. Microearthquake seismicity of the Mid-Atlantic Ridge at 5°S: A view of tectonic extension, *Journal of Geophysical Research,* **109**, doi: 10.1029/2003jb002827

Tivey, M. A., H. Schouten & M. C. Kleinrock, 2003. A near-bottom magnetic survey of the Mid-Atlantic Ridge axis at 26°N: Implications for the tectonic evolution of the TAG segment, *Journal of Geophysical Research,* **108**, doi: 10.1029/2002JB001967

Toft, P. B., J. Arkanihamed & S. E. Haggerty, 1990. The effects of serpentinization on density and magnetic susceptibility - a petrophysical model, *Physics of the Earth and Planetary Interiors,* **65,** 137-157

Tolstoy, I., 1987. *Ocean acoustics: theory and experiment in underwater sound,* New edn., American Institute of Physics, New York.

Tolstoy, M., A. J. Harding & J. A. Orcutt, 1993. Crustal thickness on the Mid-Atlantic Ridge - bull's-eye gravity anomalies and focused accretion, *Science,* **262,** 726-729

Toomey, D. R., S. C. Solomon & G. M. Purdy, 1988. Microearthquakes beneath median valley of Mid-Atlantic Ridge near 23°N - tomography and tectonics, *Journal of Geophysical Research,* **93,** 9093-9112

Toomey, D. R., S. C. Solomon, G. M. Purdy & M. H. Murray, 1985. Microearthquakes beneath the median valley of the Mid-Atlantic Ridge near 23°N - hypocenters and focal mechanisms, *Journal of Geophysical Research,* **90,** 5443-5458

Tucholke, B. E., M. D. Behn, W. R. Buck & J. Lin, 2008. Role of melt supply in oceanic detachment faulting and formation of megamullions, *Geology,* **36,** 455-458, doi: 10.1130/G24639a.1

Tucholke, B. E., K. Fujioka, T. Ishihara, G. Hirth & M. Kinoshita, 2001. Submersible study of an oceanic megamullion in the central North Atlantic, *Journal of Geophysical Research,* **106,** 16145-16161

Tucholke, B. E. & J. Lin, 1994. A geological model for the structure of ridge segments in slow-spreading ocean crust, *Journal of Geophysical Research,* **99,** 11937-11958

Tucholke, B. E., J. Lin & M. C. Kleinrock, 1998. Megamullions and mullion structure defining oceanic metamorphic core complexes on the Mid-Atlantic Ridge, *Journal of Geophysical Research,* **103,** 9857-9866

Tucholke, B. E., J. Lin, M. C. Kleinrock, M. A. Tivey, T. B. Reed, J. Goff & G. E. Jaroslow, 1997. Segmentation and crustal structure of the western Mid-Atlantic Ridge flank, 25°25'-27°10'N and 0-29 My, *Journal of Geophysical Research,* **102,** 10203-10223

Urick, R. J., 1983. *Principles of underwater sound,* 3rd edn., McGraw-Hill, New York.

Vine, F. J. & D. H. Matthews, 1963. Magnetic anomalies over oceanic ridges, *Nature,* **199,** 947-949

Wessel, P., 1989. XOVER - a crossover error detector for track data, *Computers & Geosciences,* **15,** 333-346

Wessel, P. & W. H. F. Smith, 1998. New, improved version of the Generic Mapping Tools, *Eos Trans. AGU,* **79,** 579

White, R. S., R. S. Detrick, J. C. Mutter, P. Buhl, T. A. Minshull & E. Morris, 1990. New seismic images of oceanic crustal structure, *Geology,* **18,** 462-465

White, R. S., D. Mckenzie & R. K. Onions, 1992. Oceanic crustal thickness from seismic measurements and rare-Earth element inversions, *Journal of Geophysical Research,* **97,** 19683-19715

Whitehead, J. A., H. J. B. Dick & H. Schouten, 1984. A mechanism for magmatic accretion under spreading centers, *Nature,* **312,** 146-148

Williams, C. M., M. A. Tivey & M. D. Behn, 2006. The magnetic structure of Kane megamullion: Results from marine magnetic anomalies, palaeomagnetic data and thermal modeling, *Eos Trans. AGU,* **87,** Fall meeting suppl. T42A-03

Wolfe, C. J., G. M. Purdy, D. R. Toomey & S. C. Solomon, 1995. Microearthquake characteristics and crustal velocity structure at 29°N on the Mid-Atlantic Ridge: The architecture of a slow spreading segment, *Journal of Geophysical Research,* **100,** 24449-24472

Woollard, G. P., 1979. New gravity system - changes in international gravity base values and anomaly values, *Geophysics,* **44,** 1352-1366